

**STUDIES OF
PHYSICOCHEMICAL PROCESSES IN ATMOSPHERIC PARTICLES
AND ACID DEPOSITION**

Thesis by
Spyros N. Pandis

In Partial Fulfillment of the Requirements
for the Degree of
Doctor of Philosophy

California Institute of Technology
Pasadena, California

1991

(Submitted July 2, 1990)

Πολυνοίην ού πολυμαθίην άσκέειν χρή.

Δημόκριτος

One should avoid memorizing and try understanding.

Demokritos

Στούς γονείς μου Νίκο και Ελένη

Dedicated to my parents Nikos and Helen

ACKNOWLEDGEMENTS

I feel obliged at this point to thank several persons that contributed directly or indirectly to the completion of this work and made it possible for me not only to survive during these four years of graduate studies but to be happy doing it.

First, I want to thank my adviser John Seinfeld for giving me the opportunity to work in an exciting field, for trusting me enough to let me choose my own way through the labyrinth of problems, for never pressing me to do something against my will and supporting me even when I wanted to try my luck as an experimentalist. If I had to go through graduate studies all over again I would choose him once more as my adviser. Rick Flagan had always several solutions to my experimental problems and taught me what aerosol experimentation is all about. The comments and advice of Glen Cass about my work is greatly appreciated.

During these four years, I have been fortunate to have two wonderful officemates and friends. Christodoulos Pilinis made my studies much easier, passing to me his experience about mathematical modeling, and he also has been a great friend for all these years. I owe him a lot. Tony Wexler has been a valuable source of inspiration and help, not only with his computing expertize, but also with the never ending discussions and arguments about every scientific subject that came along. The thought that these two guys would be in the office made the every day experience of leaving my bed and coming to work much easier for me.

My luck did not abandon me during my roof days, when Suzanne Paulson was a great company and help. With her, waking up at 5 a.m. every other day, praying for the disappearance of clouds, crawling under the smog chamber on hands and knees, skipping lunch, etc., was not half as bad as it sounds.

The help and camaraderie of the air pollution group has been one of the many good points of my graduate studies. Special thanks to Brian Wong, Shih-Chen Wang, Steve Rogak, Barbara Wyslouzil, Hung Nguyen, Fangdong Yin and Xiaoming Li who helped each with his own way to the completion of my experiments. The comments and friendship of Ken Wolfenbarger, Rob Harley, Chak Chan, Yong Kim and David Huang are greatly appreciated.

Several persons contributed with their company and friendship to my well being away from the office and the lab. Tasso Kaper has been a great friend and a perfect roommate. I hope that moving to another continent will not be a strong enough reason for me to lose his friendship. Moving across an ocean and two continents did not prevent Panos Pantzikas from following me and offering his friendship. I do thank him for that. I also want to thank Natassa Kotronarou, Panos Georgopoulos and Ivan Claeys for having been such special friends and Alex Seressiotis, Garrett Biehle, David Loren, Sarah Galt, Panos Papanikolaou, Phoebos Rosakis and Jay Lee for their help and encouragement during some rough times.

From several thousand kilometers away my parents and my sister Rubini have provided me with constant love and support. I finally get the chance to thank them for everything that they have done for me.

Most importantly, I want to thank my wife Angeliki for being there for me when I needed her love, friendship and support and for restraining herself when I had to work long hours, when I could not get my mind off my work or when I came back from a soccer match with a broken ankle or an injured knee. Thanks, Angeliki.

ABSTRACT

Atmospheric particles, or particulate matter, can be solid or liquid with diameters varying from around $0.002 \mu\text{m}$ to roughly $100 \mu\text{m}$. Atmospheric aerosol sources can be classified as primary or secondary, with the primary aerosol being directly emitted from the corresponding sources and the secondary particles being formed in the atmosphere, for example, from gas-phase chemical reactions that produce condensable vapors. At the same time aerosol particles are ultimately connected with the formation of water droplets and equivalently with the formation of clouds and fogs in the atmosphere.

The first part of this thesis concerns the mathematical modeling of wet and dry acid deposition and of the relevant physicochemical processes. Acid deposition consists of the delivery of acidic substances, principally sulfuric and nitric acid, from the atmosphere to the earth's surface. Upon emission to the atmosphere, SO_2 and NO_x are photochemically oxidized, yielding sulfuric and nitric acid vapors. Sulfuric acid is rapidly incorporated into aerosol particles, while nitric acid may be scavenged by particles or droplets or remain in the gas phase. Even in the absence of an aqueous phase (no clouds or fog), the acidic gases and dry particles can be transported to and deposited at ground level; this process is called dry deposition. When an aqueous phase is present (inside a cloud or a fog), gas-phase species like SO_2 , HNO_3 , NH_3 and aerosol particles are scavenged by water droplets resulting in a solution that can be significantly acidic. Additional cloudwater or fogwater acidity beyond that attained purely from scavenging of gases and particles results from aqueous-phase chemistry, most notably oxidation of dissolved SO_2 to sulfuric acid. These acidic droplets can reach the earth's surface either as precipitation or as impacted cloud and fogwater, in the processes termed wet deposition. If they are not rained or deposited out the aqueous droplets can evaporate leaving as residue

new aerosol particles that may themselves undergo dry deposition to the earth's surface. The effects of acid deposition include soil and lake acidification, forest decline and deterioration of cultural monuments.

Mathematical models are a major tool in our effort to understand and ultimately control acid deposition. The development of such a mathematical model represents a major challenge as it requires the ability to describe the entire range of atmospheric physicochemical phenomena.

As a first step in the modeling, a comprehensive chemical mechanism for aqueous-phase atmospheric chemistry was developed and its detailed sensitivity analysis was performed. The main aqueous-phase reaction pathways for the system are the oxidation of S(IV) to S(VI) by H_2O_2 , OH, O_2 (catalysed by Fe^{3+} and Mn^{2+}), O_3 and HSO_5^- . The dominant pathway for $\text{HNO}_3(\text{aq})$ acidity is scavenging of nitric acid from the gas phase. HCOOH is produced because of the reaction of $\text{HCHO}(\text{aq})$ with $\text{OH}(\text{aq})$. The gas-phase concentrations of SO_2 , H_2O_2 , HO_2 , OH, O_3 , HCHO , NH_3 , HNO_3 and HCl are of primary importance. Increase of the liquid water content of the cloud results in a decrease of the sulfate concentration, but an increase of the total sulfate amount in the aqueous-phase. On the basis of the sensitivity analysis, a condensed mechanism was derived.

The next step was the development of a model that actually predicts the amount of liquid water in the atmosphere solving the energy balance. This Lagrangian model combines for the first time a detailed description of gas and aqueous-phase atmospheric chemistry with a treatment of the dynamics of radiation fog, that is the fog that is created due to the radiative cooling of the earth's surface to the space during the night. The model was evaluated against a well documented radiation fog episode in Bakersfield in the San Joaquin Valley of California over the period January 4-5, 1985. This application showed that the model predictions for

temperature profile, fog development, liquid water content, gas-phase concentrations of SO_2 , HNO_3 , and NH_3 , pH, aqueous-phase concentrations of SO_4^{2-} , NH_4^+ and NO_3^- , and finally deposition rates of the above ions match well the observed values. The fog was found to lead to a drastic increase of deposition rates over those in its absence for the major ionic species, with most notable being the increase of sulfate deposition. Several important differences were found to exist between the characteristics of a radiation fog and a representative cloud environment. Radiation fogs typically develop under stable conditions (very low wind speed) resulting in weak mixing and significant vertical gaseous species concentration gradients. Because of the proximity of the fog to ground-level sources of pollutants like SO_2 and NO_x , the corresponding gas-phase concentrations can reach much higher levels than in a cloud. In such a case, pathways for aqueous-phase sulfate production that are of secondary importance in a cloud environment may become significant in a fog.

The next level of treatment beyond assuming that all the water droplets have the size and chemical composition is to explicitly model the size-composition distribution of droplets as a result of nucleation on aerosol particles. A third model was developed to study the distribution of acidity and solute concentration among the various droplet sizes in a fog or a cloud. The major finding of this study was that significant solute concentration differences can occur in aqueous droplets inside a fog or a cloud. For the fog simulated, during the period of dense fog, the solute concentration in droplets larger than $10 \mu\text{m}$ diameter increased with size, in such a way that droplets of diameter $20 \mu\text{m}$ attain a solute concentration that is a factor of 3.6 larger than that in the $10 \mu\text{m}$ droplets. Chemical processes tend to decrease the total solute mass concentration differences among the various droplet sizes. Low cooling rates of the system also tend to decrease these concentration differences while high cooling rates have exactly the opposite effect. The mass/size distribu-

tion of the condensation nuclei influences quantitatively, but not qualitatively, the above concentration differences.

The effects of equilibration processes on wet and dry deposition were then investigated and furthermore the accuracy of the currently used modelling approaches of these phenomena was examined. Atmospheric equilibration processes between two phases with different deposition velocities have the potential to affect significantly the amount of total material deposited on the ground. The magnitude of the effects of the equilibration processes depends primarily on the ratio of the deposition velocities of the two phases, on the production/emission rate of the gas-phase species, and on the initial distribution of species between the two phases.

At this point all the tools were available for the detailed investigation of the cyclical relationship between the aerosol and aqueous droplets; a polluted atmosphere with high aerosol concentration assists the formation of the aqueous phase which itself appears to enhance smog production, visibility reduction and aerosol sulfate levels after its dissipation. A model including descriptions of aerosol and droplet microphysics, gas and aqueous-phase chemistry and deposition was used to study the transformation of aerosol to fog droplets and back to aerosol in an urban environment. Fogs in polluted environments have the potential to increase aerosol sulfate concentrations, but at the same time to cause reductions in the aerosol concentration of nitrate, chloride, ammonium and sodium as well as in the total aerosol mass concentration. The sulfate produced during fog episodes favors the aerosol particles that have access to most of the fog liquid water which are usually the large particles. Aerosol scavenging efficiencies of around 80% were calculated for urban fogs. Sampling and subsequent mixing of fog droplets of different sizes may result in measured concentrations that are not fully representative of the fog-water chemical composition and can introduce errors in the reported values of the

ionic species deposition velocities. Differences in the major ionic species deposition velocities can be explained by their distribution over the aerosol size spectrum and can be correlated with the species average diameter.

The second part of this work was focused on the experimental study of the mechanisms of formation of secondary aerosol particles due to the atmospheric photooxidation of hydrocarbons. In this smog chamber the aerosol forming potential of natural hydrocarbons was investigated. Natural hydrocarbons like the monoterpenes $C_{10}H_{16}$ and isoprene C_5H_8 are emitted by various trees and plants in significant quantities. Isoprene and β -pinene, at concentration levels ranging from a few ppb to a few ppm were reacted photochemically with NO_x in the Caltech outdoor smog chamber facility. Aerosol formation from the isoprene photooxidation was found to be negligible even under extreme ambient conditions due to the relatively high vapor pressure of its condensable products. Aerosol carbon yield from the β -pinene photooxidation is as high as 8% and depends strongly on the initial HC/ NO_x ratio. The average vapor pressure of the β -pinene aerosol is estimated to be 37 ± 24 ppt at $31^\circ C$. Monoterpene photooxidation can be a significant source of secondary aerosol in rural environments and in urban areas with extended natural vegetation.

TABLE OF CONTENTS

ACKNOWLEDGEMENTS	iii
ABSTRACT	v
TABLE OF CONTENTS	x
LIST OF TABLES	xvii
LIST OF FIGURES	xix

CHAPTER 1

INTRODUCTION	1
An Overview	2
Research Objectives and Thesis Outline	10
References	16

CHAPTER 2

SENSITIVITY ANALYSIS OF A CHEMICAL MECHANISM FOR AQUEOUS-PHASE ATMOSPHERIC CHEMISTRY		18
Abstract		19
Introduction		19
Aqueous-Phase Chemical Mechanism Formulation		21
Aqueous-Phase Chemistry		21
Mathematical Description		34
Sensitivity Analysis Method		36
S(IV) to S(VI) Transformation and Sulfur Chemistry		40
SO_5^- , SO_4^{2-} , and HSO_5^- Chemistry		47
$\text{HOCH}_2\text{SO}_3^-$ Chemistry		52

Nitrite and Nitrate Chemistry	52
Formaldehyde and Formic Acid Chemistry	56
Other Organic Species	60
Oxygen and Hydrogen Chemistry	61
Chlorine Chemistry	63
Importance of Initial Gas and Aqueous-Phase Concentrations	65
Effects on the S(IV) to S(VI) Conversion	65
Nitrogen Chemistry	67
Formic Acid and Formaldehyde Chemistry	67
HSO ₃ ⁻	69
Liquid Water Content w_L	69
Accommodation Coefficient and Droplet Radius	71
Temperature Effects	73
Condensed Mechanism	75
Comparison of the DDM with the Indirect Method	76
Conclusions	78
Acknowledgment	79
References	79

CHAPTER 3

MATHEMATICAL MODELING OF ACID DEPOSITION DUE TO RADIATION FOG	89
Abstract	90
Introduction	91
Radiation Fog and Acid Deposition	93
Model Description	96

1. Gas-phase Model	98
2. Radiation Fog Model	98
Boundary Conditions	102
3. Aqueous-Phase Model	103
Full Model Description	103
Application of the Model to the San Joaquin Valley of California on 4-5 January 1985	106
Input Data for the Model	107
Fog Development	112
Species Concentrations in the Aqueous and Gas Phase	116
Effect of the Fog Development on the Aerosol Mass	119
Wet Deposition Rates	121
Sulfate Production	127
Sensitivity to Deposition	129
Conclusions	131
Acknowledgments	132
References	133

CHAPTER 4

ON THE RELATION BETWEEN THE SIZE AND COMPOSITION OF FOG AND CLOUD DROPLETS AND THE SIZE AND COMPOSITION OF ATMOSPHERIC AEROSOL	138
Chemical Composition Differences in Fog and Cloud Droplets of Different Sizes	139
Abstract	139
Introduction	140

Model Description	142
1. Conditioning Period	143
Gas-Phase Chemistry Operator	144
Aerosol Operators	145
2. Rapid Growth Period	146
Aqueous-Phase Chemistry and Droplet Microphysics Operator	147
3. Dissipation Period	148
Representative Cases for Evaluation	148
Case 1 (base case)	151
Case 2	151
Case 3	153
Case 4	153
Results and Discussion	153
Size/Composition Distribution of Fog and Cloud Droplets (Base Case)	153
Influence of Gas- and Aqueous-Phase Chemistry	163
Influence of Cooling Rate	164
Influence of Initial Aerosol Distribution	169
Conclusions	169
Acknowledgments	173
References	174

CHAPTER 5

ON THE INTERACTION BETWEEN EQUILIBRATION PROCESSES AND WET OR DRY DEPOSITION	177
Abstract	178

Introduction	179
Problem Description and Numerical Model Formulation	181
Case 1: $A(g) \rightleftharpoons B(s)$	182
Case 2: $A(g) \rightleftharpoons B(aq)$	184
Case 3: $A(g) + B(g) \rightleftharpoons AB(s)$	186
Solution of the Model Equations	188
Case 1	188
Case 2	189
Case 3	190
The Deposition Ratio	190
Effects of Equilibration Processes on Dry and Wet Deposition	191
Case 1	191
Case 2	198
Case 3	203
Effects of the Relative Deposition Velocities of the Gas Species	206
Effects of the Relative Deposition Velocities of the Gas and Aerosol Phases	206
Effects of the Emission/Production Rates of the Gas-Phase Species	208
Monodisperse vs Polydisperse Condensed Phase	217
Implications for Mathematical Modeling	218
Conclusions	221
Acknowledgement	222
References	222

CHAPTER 6

THE SMOG-FOG-SMOG CYCLE AND ACID DEPOSITION	225
Abstract	226
Introduction	227
Aerosol or Droplet?	229
Model Description	230
Representative Fog Episode for Evaluation	233
Effects of Fogs on Aerosol Concentration	235
Effects of Fogs on Aerosol Size/Composition Distribution	240
Aerosol Scavenging Efficiency	241
Sampling a Polydisperse Fog Droplet Population	246
Fogs and Deposition	253
Calculation of Liquid Water Deposition in Fog Models	254
Deposition Velocity of Major Ionic Species	258
Conclusions	260
Acknowledgements	263
References	263

CHAPTER 7

AEROSOL FORMATION IN THE PHOTOOXIDATION OF

ISOPRENE AND β -PINENE	267
Abstract	268
Introduction	269
Experimental Description	271
Aerosol Yields	277
Isoprene	280

β -pinene	284
Saturation Vapor Pressure Estimation	288
Isoprene as an Aerosol Precursor	291
β -pinene as an Aerosol Precursor	294
Pathways for Production of Condensable Species	294
Contribution of β -pinene and Other Monoterpenes to Atmospheric Aerosol Levels	296
Conclusions	299
Acknowledgement	301
References	301

CHAPTER 8

CONCLUSIONS	305
-----------------------	-----

APPENDIX A

BRIEF DOCUMENTATION OF ACID DEPOSITION

MODULES 1-3	308
Module 1	310
Module 2	312
Module 3	315

APPENDIX B

SMOG CHAMBER AEROSOL DATA	321
-------------------------------------	-----

LIST OF TABLES

Chapter 2

1.	Chemical species, initial conditions and model parameters	22
2.	Equilibrium reactions	24
3a.	Oxygen-hydrogen chemistry	26
3b.	Carbonate chemistry	27
3c.	Chlorine chemistry	28
3d.	Nitrite and nitrate chemistry	29
3e.	CH ₄ oxidation chain	30
3f.	Sulfur chemistry	31
4.	Dimensionless sensitivity coefficients for S(IV)(aq)	42
5.	Dimensionless sensitivity coefficients for H ₂ O ₂ (aq)	44
6.	Dimensionless sensitivity coefficients for S(VI)(aq)	48
7.	Dimensionless sensitivity coefficients for HSO ₅ ⁻	49
8.	Dimensionless sensitivity coefficients for some nitrogen compounds at t=1800 s	54
9.	Dimensionless sensitivity coefficients for HCHO(aq)	57
10.	Dimensionless sensitivity coefficients for HCOOH(aq)	59
11.	Dimensionless sensitivity coefficients for O ₃ (aq)	62
12.	Dimensionless sensitivity coefficients for S(IV)(aq), N(V)(aq), and HSO ₅ ⁻ to initial conditions	66
13.	Sensitivity coefficients for HCHO(aq) and HCOOH(aq) to initial con- ditions	68
14.	Dimensionless sensitivity coefficients to the cloud or fog water liquid content w_L	70
15.	Dimensionless sensitivity coefficients to the sticking coefficient a_w and the radius α	72
16.	Concentration of various species after 1 hr for different cloud or fog temperatures	74

17. Comparison of sensitivity analysis methods 77

Chapter 4

1. Base case parameters and initial conditions 149

Chapter 6

1. Base case parameters and initial conditions 234

Chapter 7

1. Initial conditions and results of the smog chamber experiments . . . 278

LIST OF FIGURES

Chapter 1

1. Idealized schematic of the composition of atmospheric aerosols. The principal sources and particle formation mechanisms are indicated (Pili- nis and Seinfeld, 1988) 4
2. Schematic of the mechanisms for the formation of aqueous-phase droplets in the atmosphere 5
3. Schematic of the main physicochemical processes associated with cloud or fog droplets 7
4. Summary of atmospheric processes leading to acid deposition 9
5. Elements of a mathematical model for relating pollutant emissions to ambient air quality and acid deposition 11
6. Schematic of the mechanism of formation of radiation fog 13

Chapter 2

1. Calculated aqueous-phase concentrations in (mol / l water) for the base scenario 37
2. Calculated aqueous-phase concentrations in (mol / l water) and gas- phase concentrations in (mol / l air) for the base scenario 38
3. Main pathways for the sulfur reaction system and the oxidation of S(IV) to S(VI) 53

Chapter 3

1. Atmospheric processes leading to acid deposition and the interactions among the gas, aqueous and aerosol phases 97

2.	Schematic representation of the vertically resolved Lagrangian trajectory model for radiation fog	104
3.	Predicted top of the fog layer	109
4.	Comparison of the predicted vertical temperature profiles with the observations of Waldman (1986)	110
5.	Comparison of the predicted hourly averaged liquid water content for the ground-level grid cell with the observations of Waldman (1986). The uncertainty in the measurements as reported by Waldman is indicated by the data ranges	111
6.	Predicted hourly averaged water deposition rates	113
7.	Predicted vertical liquid water concentration profiles for 2100, 0030, and 0530 PST.	114
8.	Comparison of the predicted hourly averaged (a) pH values, (b) NH_4^+ , (c) S(VI), (d) NO_3^+ concentration for the ground-level grid cell with the observations of Waldman (1986)	115
9.	Comparison of the predicted hourly averaged $\text{SO}_2(\text{g})$ concentration for the ground-level grid cell with the observations of Waldman (1986)	117
10.	Predicted HNO_3 , H_2O_2 and NH_3 vertical gas-phase concentration profiles for 2300 PST.	118
11.	Concentrations of the main ionic species in the aerosol phase (a) vertically averaged concentration before the fog formation (observed values used as initial conditions), (b) predicted vertically averaged concentration after fog dissipation, (c) predicted concentration for the ground level grid cell after fog dissipation	120
12.	Comparison of the predicted average wet deposition rates over three time periods with the observations of Waldman (1986) for (a) S(VI), (b) NH_4^+ , (c) NO_3^-	122
13.	Comparison of the predicted average deposition rates for the same 16 hour period in (a) presence of radiation fog, (b) absence of radiation fog	124
14.	Predicted total sulfur mass balance for the lower 250 m of the atmosphere.	125

15.	Contributions of the main pathways for the production of sulfate during the simulated radiation fog episode	126
-----	---	-----

Chapter 4

1.	Temperature variation profiles used in the various simulations. The profile used in Case 4 is the same as in Case 1	150
2a.	Calculated aerosol size/composition distribution at the beginning of the Case 1 simulation assuming thermodynamic equilibrium for the sulfate, nitrate, sodium, ammonium and water system	152
2b.	Calculated aerosol size/composition distribution at the beginning of the Case 4 simulation assuming thermodynamic equilibrium for the sulfate, nitrate, sodium, ammonium and water system	152
3.	Calculated variation of the mass mean diameter of the seven sections, the system's supersaturation, the liquid water content and the temperature with time. $t=0$ corresponds to 7:20	154
4.	Calculated time evolution of the droplet mass distribution as a function of the droplet diameter	156
5a.	Calculated total (volatile and nonvolatile) solute concentration as a function of droplet diameter for five different times during the growth period	157
5b.	Calculated total (volatile and nonvolatile) solute concentration as a function of droplet diameter for five different times during the fog dissipation	157
6.	Calculated time evolution of the sulfate mass distribution as a function of the droplet diameter. The shaded area corresponds to the sulfate that initially exists in the aerosol particles and the rest is the sulfate produced during the fog evolution	160
7.	Calculated time evolution of the nitrate mass distribution as a function of the droplet diameter	161
8.	Calculated time evolution of the ammonium mass distribution as a function of the droplet diameter	162

9.	The ratio of the total solute concentration at $t=30$ calculated by considering gas and aqueous-phase chemistry over that calculated neglecting chemical processes versus droplet diameter	165
10.	Comparison of the calculated liquid water mass distributions as a function of the droplet diameter for Case 1 (base case, $t=20$ min), Case 2 (small cooling rate, $t=40$ min) and Case 3 (large cooling rate, $t=10$ min)	166
11.	Comparison of the calculated total (volatile and nonvolatile) solute concentration as a function of droplet diameter for Case 1 (base case, $t=20$ min), Case 2 (small cooling rate, $t=40$ min) and Case 3 (large cooling rate, $t=10$ min)	167
12.	Comparison of the calculated total (volatile and nonvolatile) solute mass distribution as a function of droplet diameter for Case 1 (base case, $t=20$ min), Case 2 (small cooling rate, $t=40$ min) and Case 3 (large cooling rate, $t=10$ min)	170
13.	Comparison of the calculated total (volatile and nonvolatile) solute concentration as a function of droplet diameter for Case 1 ($t=20$ min) and Case 4 ($t=20$ min)	171

Chapter 5

1.	Schematic representation of the multiphase systems studied. (a) Case 1 : $A(g) \rightleftharpoons B(s)$ (b) Case 2 : $A(g) \rightleftharpoons B(aq)$ (c) Case 3 : $A(g) + B(g) \rightleftharpoons AB(s)$	180
2.	Deposition ratio $DR_1(t^*)$ (total deposition with equilibration processes over deposition without) as a function of the initial species distribution β and the ratio of the deposition velocities γ for rapid mass transfer ($\alpha=1000$) and two production/emission rates of $A(g)$ δ . (a) $\delta = 0$ No emission. (b) $\delta = 10$ Strong emission source.	194

3.	Deposition ratio $DR_1(t^*)$ (total deposition with equilibration processes over deposition without) as a function of the initial species distribution β and the ratio of the deposition velocities γ for slow mass transfer ($\alpha=10$) and strong emission source of A(g) ($\delta=10$).	197
4.	Deposition ratio $DR_2(t^*)$ (total deposition with equilibration processes over deposition without) as a function of the initial species distribution β and the ratio of the deposition velocities γ for typical mass transfer ($\alpha=1500$) and (a) $\delta = 0$ Zero A(g) emission/production rate. (b) $\delta = 100$ Very high A(g) emission/production rate.	200
5.	Deposition ratio $DR_3(t^*)$ for the base case.	204
6.	Effect of the ratio of the aerosol and gas phase deposition velocities on the deposition ratio $DR_3(t^*)$. (a) $\sigma_4=0.5$ (b) $\sigma_4=10$	207
7.	Effect of the ratio of the gas phase source rates to the gas phase deposition rate on the deposition ratio $DR_3(t^*)$. (a) $\sigma_5 = 0$ (b) $\sigma_5 = 0.3$ (c) $\sigma_5 = 15$	210
8.	Effect of the ratio of the nitric acid production rate on the deposition ratio $DR_3(t^*)$. (a) $\sigma_6 = 0$ (b) $\sigma_6 = 1.5$ (c) $\sigma_6 = 150$	214
9.	Ratio of the total deposited mass as calculated by the operator splitting scheme over the full solution as a function of the operator time step.	220

Chapter 6

1.	Mass balances for the main ionic species for a simulated radiation fog episode. (a) Sulfate, (b) Ammonium (the gaseous ammonia is not included), (c) Nitrate	237
2.	Evolution of the smoothed aqueous droplet mass distribution during the fog episode.	242
3.	Comparison of the smoothed aerosol size/composition distributions before and after the fog episode. (a) At 50% relative humidity before the fog episode. (b) At 50% relative humidity after the fog episode	243
4.	Total solute concentration for particles of different sizes. (a) During the fog growth period. (b) During the fog dissipation period	247

5.	Concentration ratios (concentration measured by the sampler over the concentration of the larger droplet section) for three idealized fog samplers for (a) Sulfate. (b) Ammonium.	250
6.	Calculated values of the sulfate deposition velocity for alternative definitions. Deposition velocity of the condensed phase $v_{d,cond}$. Deposition velocity of the aqueous-phase v_{aq} sampling cutoff $5 \mu\text{m}$. Deposition velocity of the aqueous-phase v_{aq} sampling cutoff $15 \mu\text{m}$	255
7.	Water deposition rates versus fog liquid water content.	257
8.	Condensed phase deposition velocities for the major species in fogwater. (Deposition Velocity)=(Deposition Flux) / [(aerosol concentration) + (droplet concentration)].	259
9.	Calculated deposition velocity of selected species in fog as a function of their average diameter.	261

Chapter 7

1.	Schematic of the Caltech outdoor smog chamber facility.	272
2.	Tandem Differential Mobility Analyzer (TDMA).	276
3.	Number and volume concentrations of aerosol during experiment 13.	279
4.	Aerosol volume yield as a function of time and isoprene reacted for experiment 13.	281
5.	Measured maximum aerosol yields during the isoprene photooxidation versus the isoprene reacted. Also shown the predicted yields from the proposed model.	282
6.	Measured maximum aerosol yields for the β -pinene photooxidation versus the β -pinene reacted.	285
7.	Measured maximum aerosol yields for the β -pinene photooxidation versus r , the ratio of the initial hydrocarbon to the initial NO_x concentration.	287

8.	Measured maximum aerosol yields for the β -pinene photooxidation as a function of p_1 , the fraction of β -pinene that reacted with O_3 . The solid line is the best linear fit.	289
9.	Steady state predicted diurnal variation of the concentrations of isoprene and one of its condensable products ($COND_1$) in a rural environment with atmospheric stagnation.	293
10.	Nuclcation of particles during experiment 5. Also shown are the amounts of β -pinene that have reacted with O_3 and OH	295
11.	Number concentration of particles smaller than $0.21 \mu m$ (DMA range) during experiment 16. Also shown are the amounts of β -pinene that have reacted with O_3 and OH	297

CHAPTER 1

INTRODUCTION

Introduction

An Overview

Atmospheric particles, or particulate matter, can be solid or liquid with diameter varying from around $0.002 \mu\text{m}$ to roughly $100 \mu\text{m}$. It is difficult to define the smallest particle size because there is no accepted criterion when a cluster of molecules becomes a particle. The largest particles are cloud or fog droplets or even very fine sand. There are of course even larger particles in the atmosphere, like raindrops (around 1 mm) and hail (around 10 mm), but these particles are rapidly removed from the atmosphere and are not going to be examined in the present work.

Atmospheric particles can be categorized as either aerosol or droplets but there have been several conflicting attempts in separating the two groups of particles. In principle the distinction between aerosol and droplets appears unnecessary because the same physicochemical processes, mass transfer, chemical reactions, etc., take place in both aerosol and droplets. However, to avoid confusion an exact definition of aerosol and droplets will be presented later. As a rough rule, if the relative humidity of the environment remains under 95%, all the ambient particles are aerosol, while for higher relative humidities some of the particles may be droplets and the rest are described as interstitial aerosol in a cloud or fog.

Atmospheric aerosol sources can be classified as primary or secondary. Primary aerosols are directly emitted from the corresponding sources such as dust due to the wind, or ash due to wood burning. Secondary aerosols are produced in the atmosphere, for example, from gas phase chemical reactions that produce condensable vapors. Sources of primary aerosols produce particles of all sizes but most secondary aerosols are of submicron size.

Most atmospheric aerosols are multicomponent mixtures containing inorganic and organic material (Figure 1). Major inorganic constituents are usually sulfate, nitrate, ammonium, chloride, sodium and water with elements like Si, Ca, Pb, Fe, Al, K, Mn, Mg, etc., completing the inorganic aerosol composition. The organic part of the aerosol consists of elemental carbon and primary organic carbon emitted by combustion sources and secondary organic material formed by the photooxidation of organic compounds in the atmosphere.

The most poorly understood pathway for the production of atmospheric aerosol material is the formation of secondary organic aerosol from the photooxidation of organic compounds. The understanding of this pathway is critical because secondary organic aerosols accumulate in the submicrometer range and therefore may be responsible for adverse health effects and contribute significantly to visibility degradation. This understanding requires identification of the specific hydrocarbon precursors, knowledge of the gas-phase chemical pathways that lead to the formation of condensable species and finally knowledge of the physical properties of these species.

Aerosol particles are also ultimately connected with the formation of droplets and equivalently with the formation of clouds and fogs in the atmosphere. Assume that the temperature of an air parcel containing water vapor, aerosol and pollution gases like SO_2 , NO_x , O_3 , etc., decreases (Figure 2). This temperature change can be the result of mechanical lifting of the air mass over a mountain slope, dynamical lifting due to pressure difference, radiative cooling or advective cooling. The temperature drop results to a relative humidity increase and at a specific relative humidity, which for most soluble components in the atmosphere is well below 100%, aerosol particles that are not already liquid deliquesce into aqueous solution drops. As the relative humidity keeps increasing, water vapor condenses on the aerosol

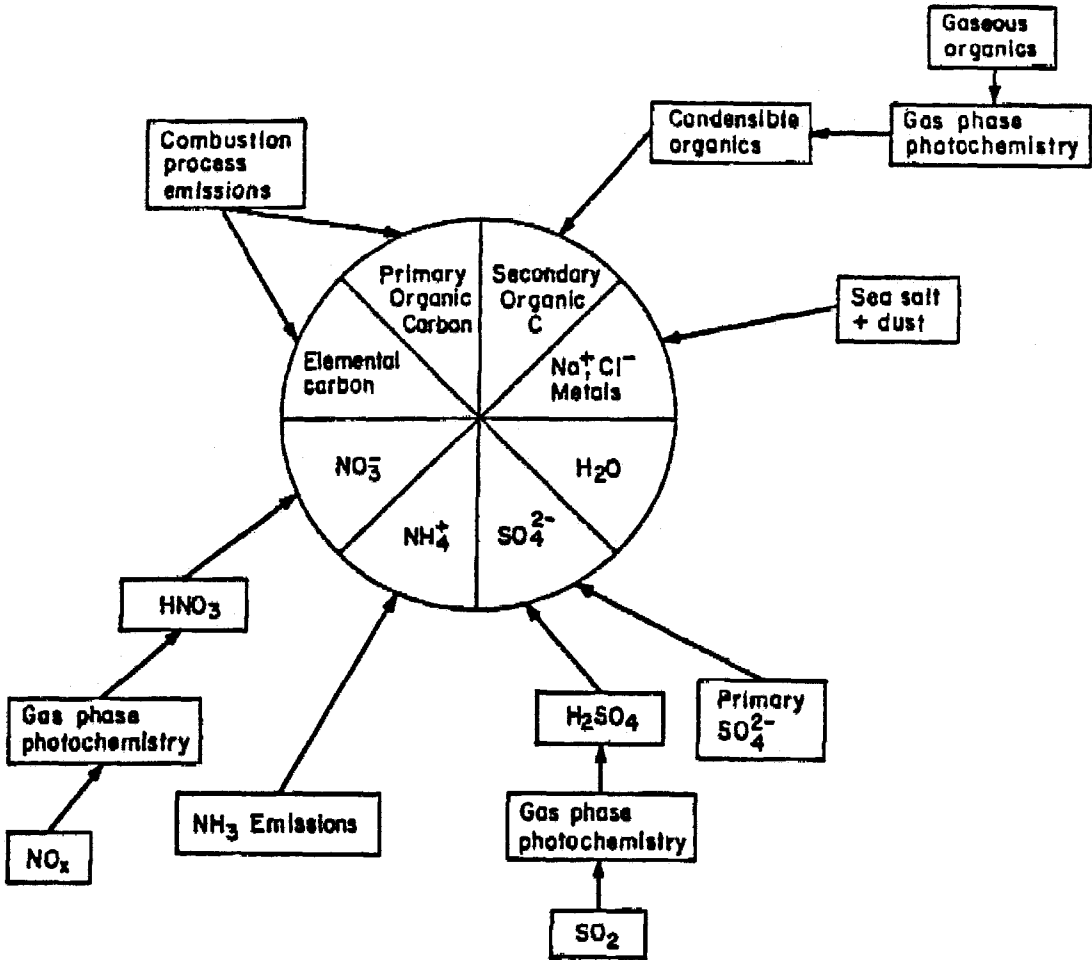


Figure 1. Idealized schematic of the composition of atmospheric aerosols.

The principal sources and particle formation mechanisms are indicated (Pilinis and Seinfeld, 1988).

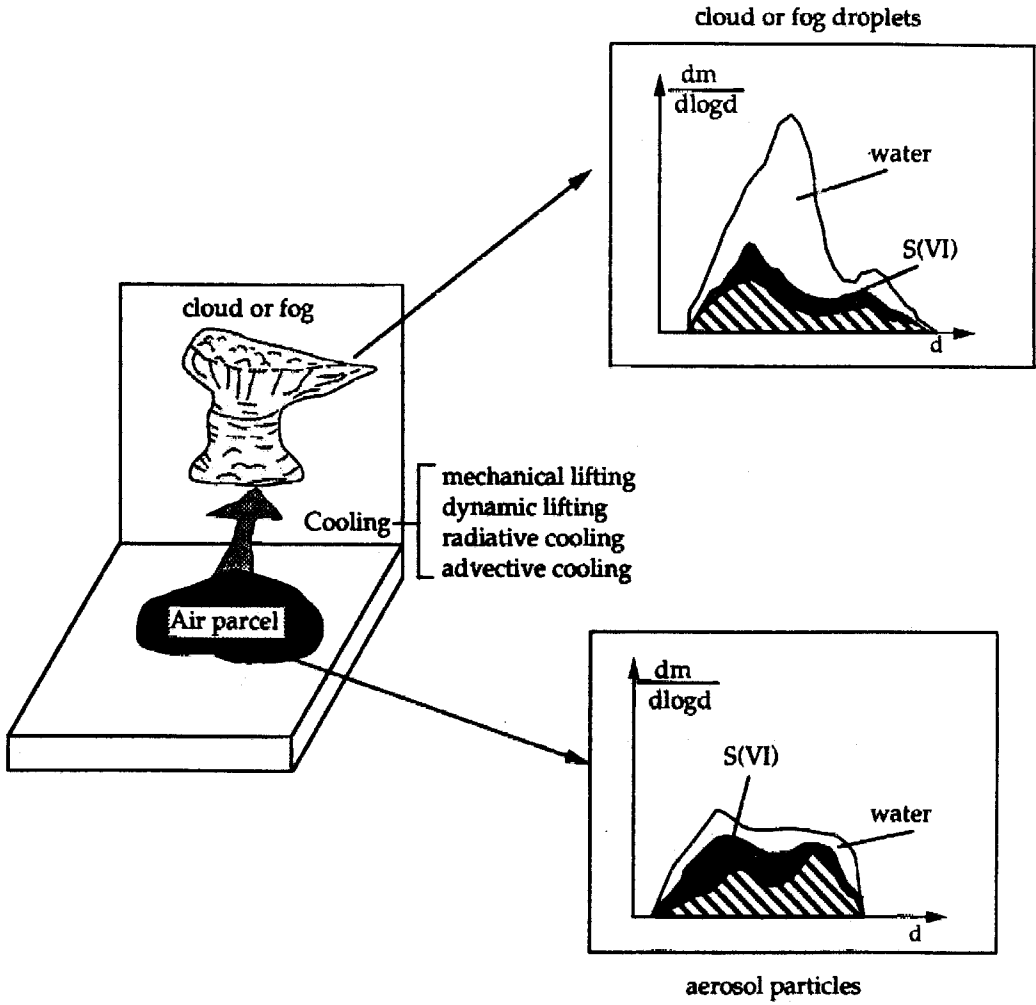


Figure 2. Schematic of the mechanisms for the formation of aqueous-phase droplets in the atmosphere.

particles in accordance with water vapor equilibrium. If the relative humidity of the air parcel reaches a critical supersaturation, the value of which depends on the size and chemical composition of the aerosol present, the particles become activated, grow unstably by water vapor diffusion, and a cloud or fog forms. Soluble gaseous species such as nitric acid, sulfur dioxide and ammonia are transferred to the aqueous phase. At the same time the cloud or fog formation provides the reacting medium, the liquid water, for aqueous-phase reactions (Figure 3). Several species dissolve in the aqueous phase and react giving acidic products, for example the dissolution of SO_2 , its ionization and its subsequent oxidation to sulfate.

Acid deposition consists of delivery of acidic aerosol or droplets or even acid vapors like HNO_3 from the atmosphere to the earth's surface. Upon emission to the atmosphere SO_2 and NO_x are photochemically oxidized, yielding sulfuric and nitric acid vapors. Sulfuric acid is rapidly incorporated into aerosol particles, while nitric acid may be scavenged by particles or droplets or remain in the gas phase. Even in the absence of an aqueous phase (no clouds or fog), the acidic gases and dry particles can be transported to and deposited at ground level; this process is called dry deposition. When an aqueous phase is present (inside a cloud or a fog), gas phase species like SO_2 , HNO_3 , HCl , NH_3 and aerosol particles are scavenged by water droplets resulting in a solution that can be significantly acidic. Additional cloudwater or fogwater acidity beyond the attained purely from scavenging of gases and particles results from aqueous-phase chemistry, most notably oxidation of dissolved SO_2 to sulfuric acid. These acidic water droplets can reach the earth's surface either as precipitation or as impacted cloud and fog drops, in a process termed wet deposition. If they are not rained or deposited out, the aqueous droplets can evaporate leaving as residue fresh acidic aerosol particles that may themselves undergo dry deposition to the earth's surface. The atmospheric paths leading to wet and

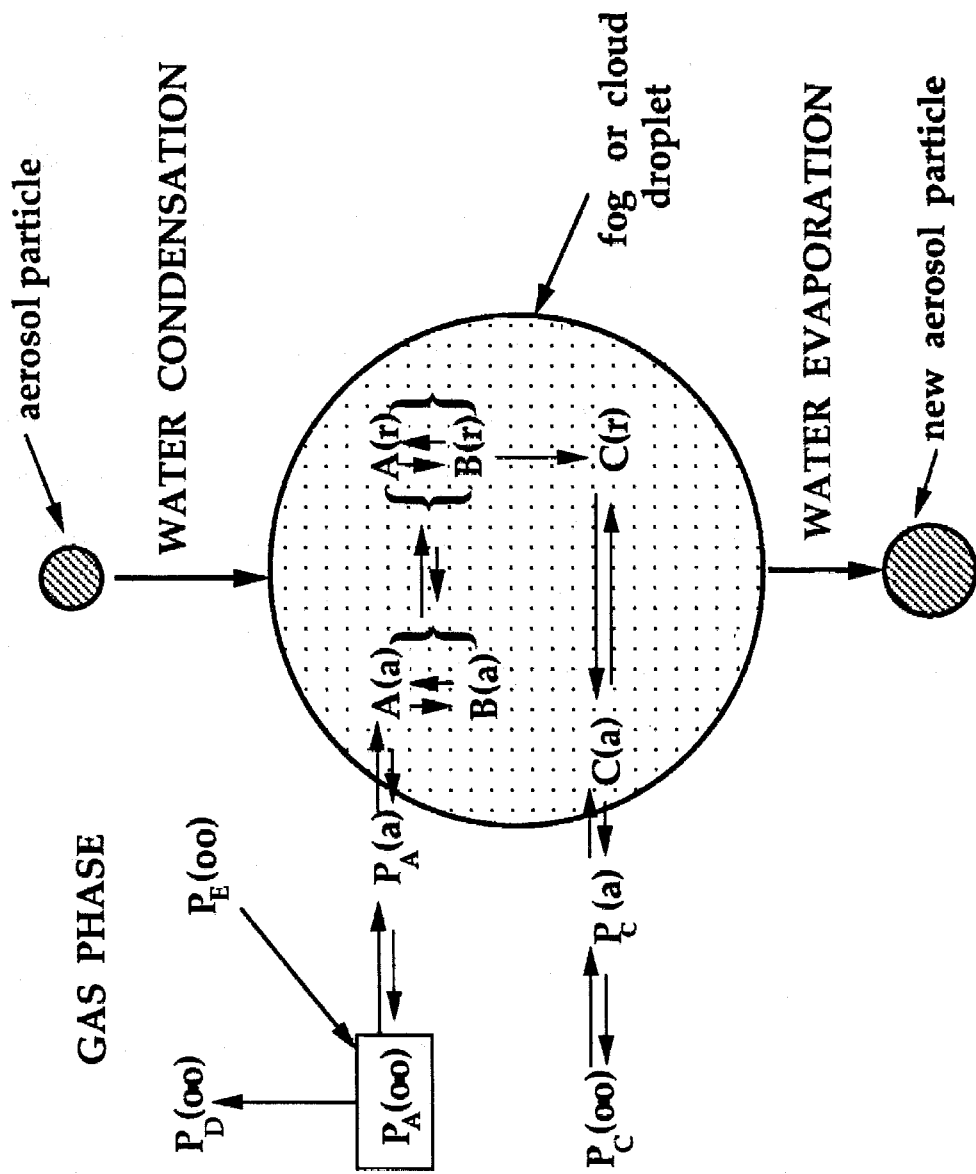


Figure 3. Schematic of the main physicochemical processes associated with cloud or fog droplets.

dry acidic deposition are depicted in Figure 4.

The effects of acid deposition or what is commonly identified as acid rain, including soil and lake acidification, forest decline, and deterioration of cultural monuments, have attracted lately the increasing attention of scientists and the public. Significant progress has been achieved the last few years but several questions still remain partially or completely unanswered. They mainly concern the relative importance of the various pathways contributing to acid deposition as well as the interactions among the various phases present in the atmosphere.

Mathematical models will eventually be a major tool in our effort to understand and ultimately to control acid deposition. The development of such a mathematical model represents a major challenge as it requires the ability to describe the entire range of atmospheric physicochemical phenomena depicted in Figure 4. A complete acid deposition model should include descriptions of:

- emissions of pollutants like NO_x , SO_2 , organics, and primary aerosol particles,
- gas-phase chemistry to produce an array of species including nitric and sulfuric acid vapors,
- aerosol formation,
- formation of cloud or fog droplets by condensation of water vapor on the aerosol particles that serve as condensation nuclei, and evaporation of droplets to leave an aerosol residue,
- scavenging of gaseous species by the water droplets, followed by ionization,
- aqueous-phase reactions and,
- dry and wet deposition mechanisms as the ultimate modes of delivery of acidity to the earth's surface.

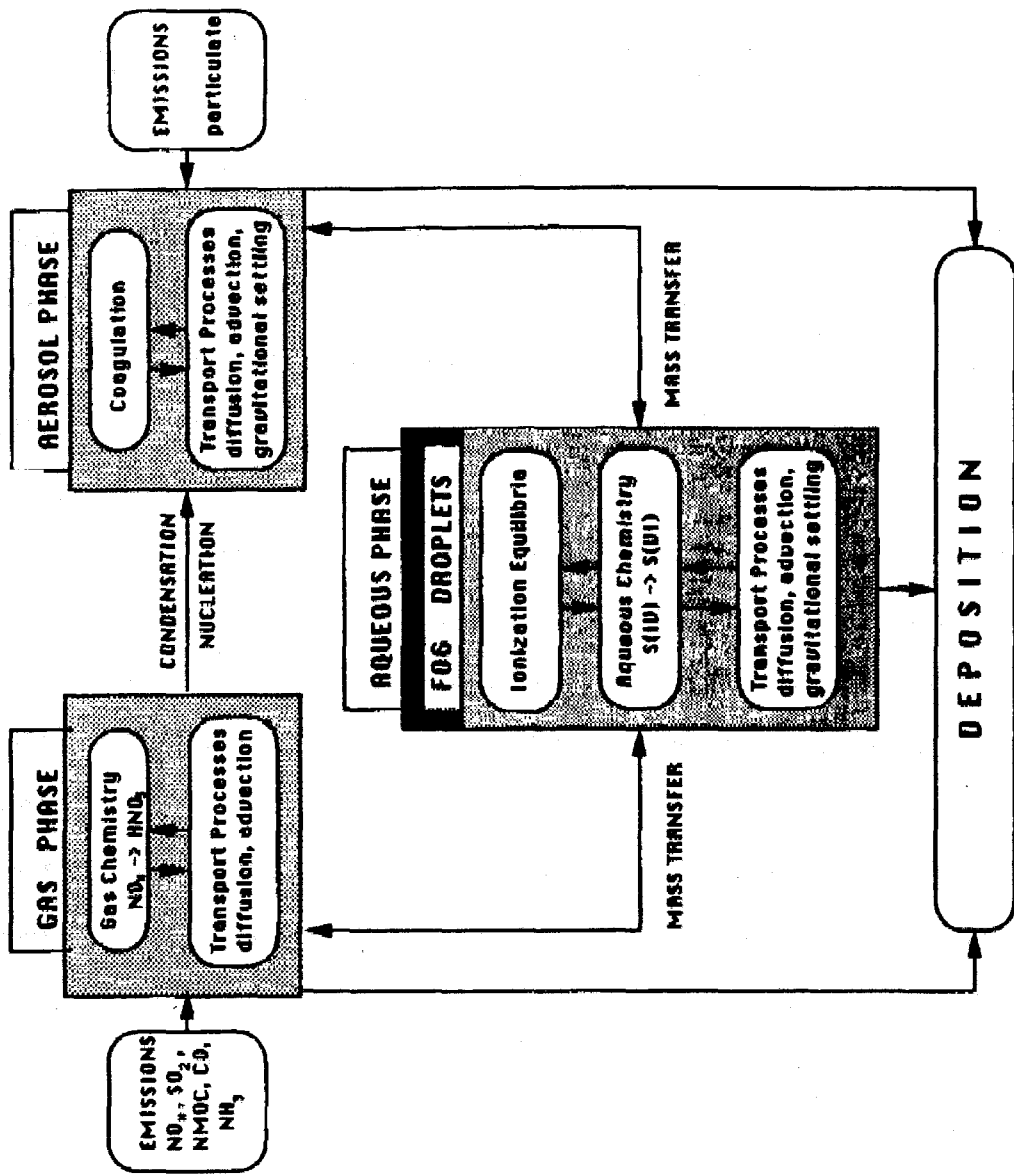


Figure 4. Summary of atmospheric processes leading to acid deposition.

Research objectives and thesis outline

The first part of this thesis concerns the mathematical modeling of wet and dry acid deposition and of the relevant physicochemical process. The main emphasis of this project has been the development of a state-of-the-art acid deposition model and at the same time the improvement of our understanding of the corresponding phenomena. A detailed description of all the physicochemical processes shown in Figure 4 would produce a complicated model whose main elements are depicted in Figure 5.

First a comprehensive atmospheric aqueous-phase chemistry model for cloud and fog water chemistry is developed and a detailed sensitive analysis is performed (Chapter 2). This model treats both the aqueous-phase chemical reactions and the dynamic exchange of species between the gas and aqueous phases in a homogeneous parcel of air inside a cloud or a fog. The sensitivity analysis results lead to a ranking of the most important reaction pathways for the various species. Additionally, the influence of the initial gas-phase concentrations and of parameters such as the liquid water content, the sticking coefficient, the droplet radius, the temperature, etc., is investigated. Based on these results a condensed mechanism is proposed and tested. Also, a brief comparison of some sensitivity analysis methods is presented.

In the course of this work it became apparent that the amount of liquid water present in the atmosphere is a parameter of major importance for acidic deposition and that a state-of-the-art aqueous-phase chemistry module should predict the liquid water content of a fog or cloud. Fogs are much better testing grounds for our understanding of the chemical processes compared to clouds, because their proximity to the ground makes field measurements much easier. At the same time, acid deposition due to acidic fogs is of primary importance for several areas, for example, California (Air Resources Board, 1988). Additionally, the human health danger as-

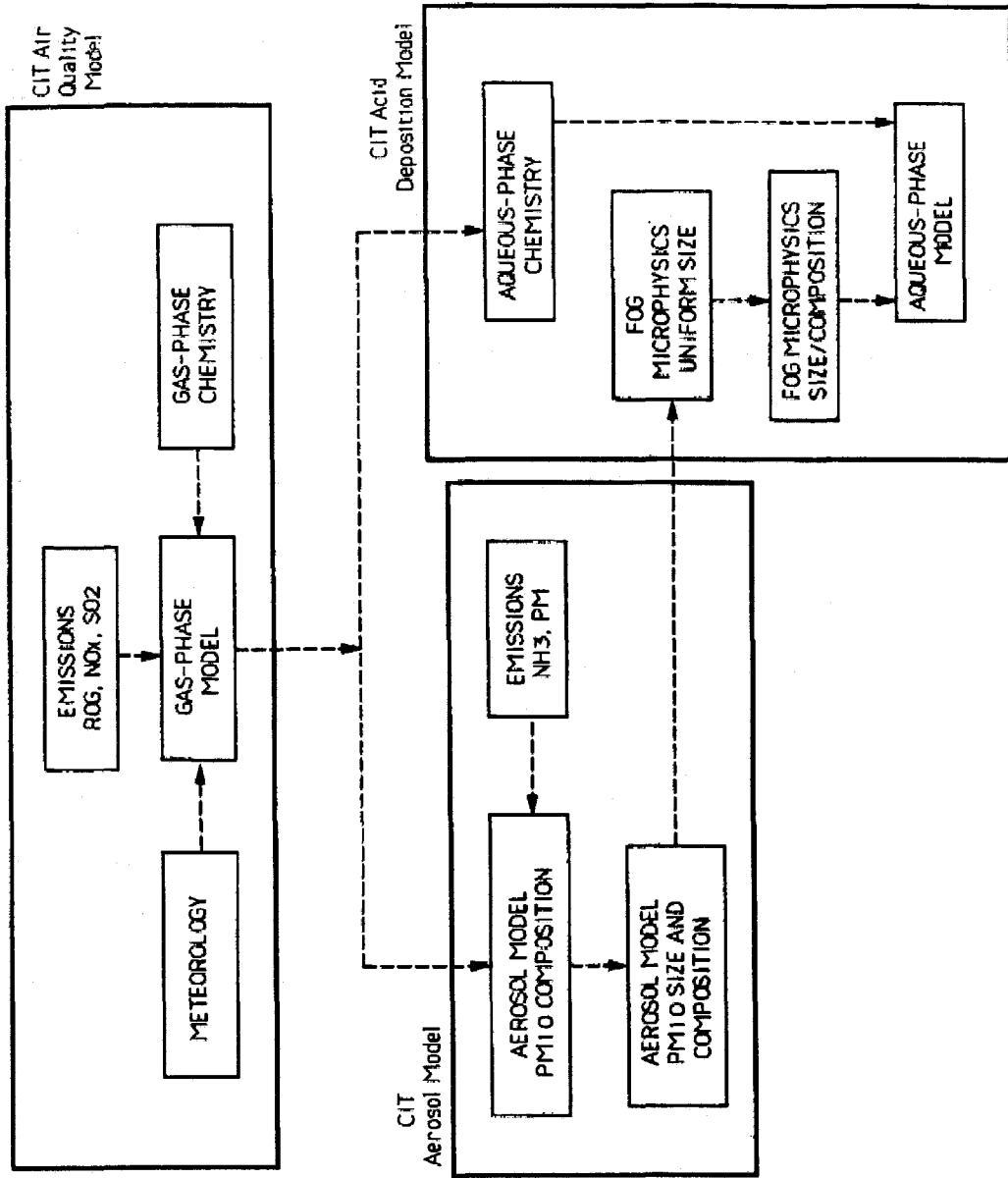


Figure 5. Elements of a mathematical model for relating pollutant emissions to ambient air quality and acid deposition.

sociated with acidic fogs is much greater than for clouds because human beings are obliged to live, work, exercise, etc., inside the fogs. Hoffmann and co-workers have reported highly acidic fogs in California, with pH values as low as 1.69 (Waldman et al., 1982). In these fogs concentrations of anions and cations such as SO_4^{2-} , NO_3^- , and NH_4^+ were higher by one to two orders of magnitude than in precipitation in the same areas. Field measurements have provided valuable information concerning the chemical composition of acid fogs, but the physicochemical processes leading to this composition have yet to be elucidated.

In this work we combined for the first time a detailed description of gas and aqueous-phase atmospheric chemistry with a description of radiation fog dynamics. The inclusion of the fog dynamics enables us to study the wet deposition of pollutants during fog episodes, the vertical variability of acidity and pollutants in a fog, and the changes of concentration of aqueous and gaseous species during the various stages of fog development. In Chapter 3 we begin with a physical description of the system of interest, with emphasis on the physics of radiation fog (Figure 6). Next we present separately the gas-phase chemistry, aqueous-phase chemistry and radiation fog dynamics submodels and then the complete model. The full model is then evaluated against data obtained during a well documented radiation fog episode in the San Joaquin Valley. Sensitivity studies address the effects of fog formation on the deposition rates and on the aerosol mass and the chemical pathways that contribute to sulfate formation.

Despite the suggestion of cloud microphysics, all the theoretical studies and the field measurements have assumed that all the droplets inside a cloud or a fog have the same chemical composition. In Chapter 4 this assumption is investigated by combining for the first time a detailed description of the gas and aqueous-phase chemistry occurring inside a cloud or a fog with the microphysics of the condensa-

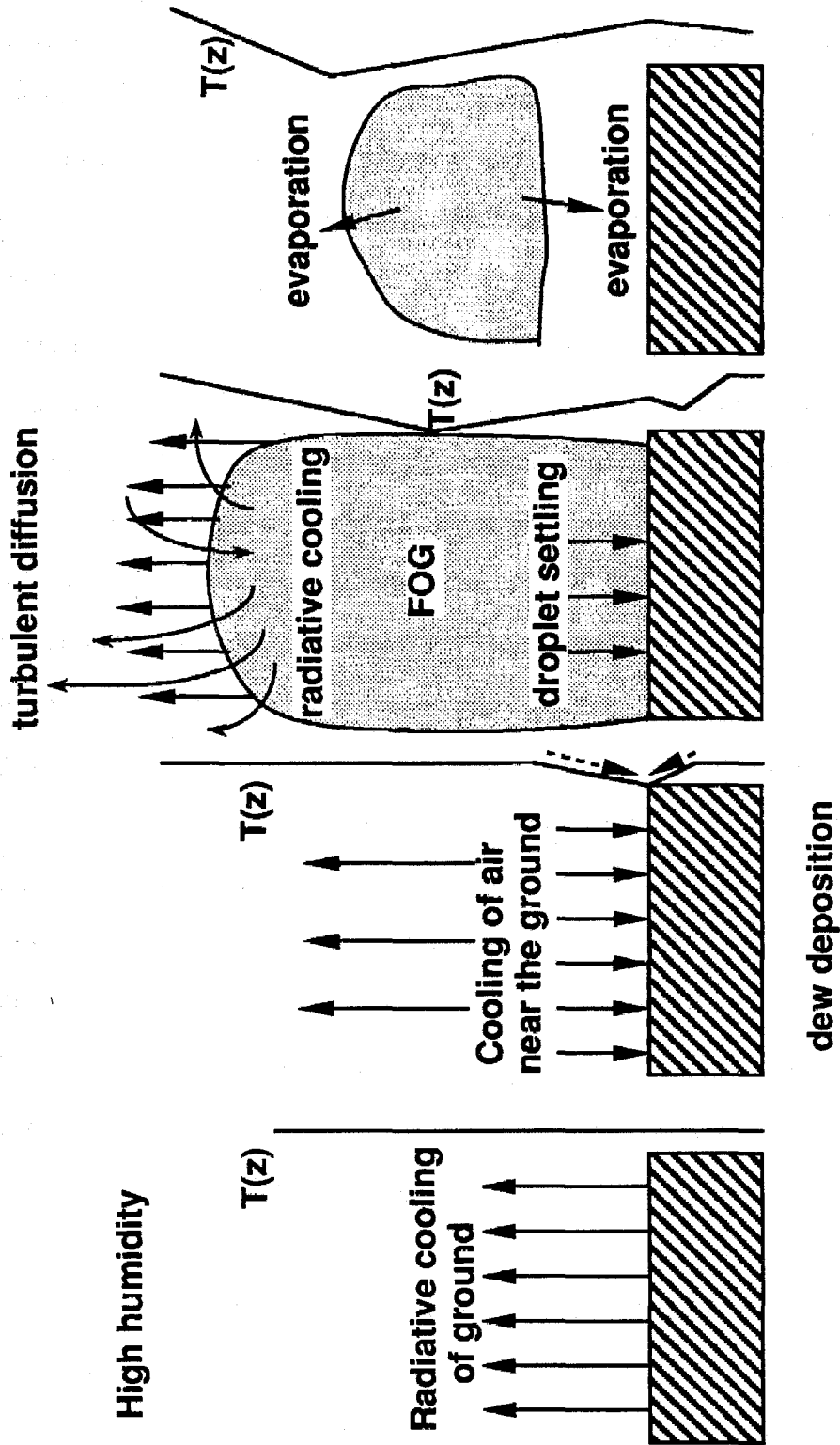


Figure 6. Schematic of the mechanism of formation of radiation fog.

tional growth of an aqueous droplet distribution. The thermodynamics and dynamics of multicomponent aerosols are described explicitly for the period before the fog (or cloud) formation and that after the aqueous phase dissipation. The coupling of the descriptions of all the above physical and chemical processes enables us to simulate the concentration/size dependence of cloud and fog droplets under a variety of conditions.

Processes such as condensation of vapor on aerosol particles, dissolution of material in aqueous droplets, and evaporation of species from aerosol particles or droplets move in the direction of establishing and maintaining thermodynamic equilibrium between the gas and aerosol or gas and aqueous phases in the atmosphere. These equilibration processes change the species' distribution among the various phases present and transfer material between phases that often have very different deposition characteristics. It is reasonable to expect therefore that the equilibration processes may affect significantly the amounts of material deposited on the ground, either enhancing or suppressing the removal processes over those from gas-phase processes alone. In Chapter 5 we investigate the effects of the equilibration processes on wet and dry deposition and furthermore examine the accuracy of the currently used modelling approaches of these phenomena.

Historically, urban fogs have frequently been interconnected with severe pollution episodes. A cyclical relationship between the occurrence of smog and fog in the Los Angeles basin has been proposed by Munger et al. (1983) and was termed the smog-fog-smog cycle. A polluted atmosphere with high aerosol concentration assists the formation of late night and early morning fogs which appear to enhance smog production, visibility reduction, and aerosol sulfate levels during the following day. In Chapter 6 a rigorous theoretical investigation of the smog-fog-smog cycle is performed using the modeling tools that have been developed in this work. Sev-

eral questions are addressed including the aerosol scavenging efficiencies of urban fogs, the uncertainties introduced by measuring in bulk a polydisperse fog droplet distribution, the difference in deposition velocities of different ionic species during fog episodes, and expression of the liquid water flux as a function of the liquid water content for fog models that do not include explicit treatment of droplet microphysics.

In Chapter 7 we focus our attention on the formation and growth of aerosol particles due to the atmospheric photooxidation of hydrocarbons. In this smog chamber study the aerosol forming potential of natural hydrocarbons is investigated. Natural hydrocarbons like the monoterpenes $C_{10}H_{16}$ and isoprene C_5H_8 are emitted by various types of trees and plants. In the United States the biogenic hydrocarbon sources are estimated to produce 30 to 60 Mt of carbon per year (isoprene and monoterpenes) whereas anthropogenic hydrocarbon sources have been estimated to account for 27 Mt of carbon per year (Lamb et al., 1987; Zimmerman, 1979; Altshuller, 1983). Despite the magnitude of the estimated amounts of biogenic hydrocarbons emitted and their considerable reactivity, our understanding of their role in atmospheric chemistry remains incomplete. The formation of aerosol from the oxidation of the biogenic hydrocarbons is one of the poorer understood phenomena.

This study was undertaken to investigate the significance of biogenic hydrocarbons as aerosol precursors in both rural and urban environments. The present study is focused on two representative natural hydrocarbons, namely isoprene and β -pinene. Isoprene is one of the major non-terpenoid compounds emitted by vegetation (Lamb et al., 1987) and is very efficient at forming O_3 when photooxidized in the presence of NO_x (Arnts and Gay, 1979). β -pinene is a representative monoterpene accounting for a major portion of the total terpene emissions (Zimmerman,

1979), and, together with α -pinene, is the most abundant monoterpene (Altshuller, 1983; Roberts et al., 1983, 1985). Chapter 7 starts with a description of our experimental facility. Next we present our results concerning the aerosol yields during the isoprene and β -pinene photooxidation together with our measurements of the average vapor pressures of the corresponding condensable products. Finally, the implications of our findings for the aerosol production from biogenic hydrocarbons in urban and rural areas are discussed.

The conclusions drawn in this study are summarized in Chapter 8.

References

- Air Resources Board, The Fifth Annual Report to the Governor and the Legislature on the Air Resources Board's Acid Deposition Research and Monitoring Program, California Air Resources Board, Sacramento, CA, 1988.
- Altshuller A. P., Review: Natural volatile organic substances and their effect on air quality in the United States, *Atmos. Environ.*, 17, 2131-2165, 1983.
- Arnts R. R. and B. G. Gay, Photochemistry of some naturally emitted hydrocarbons, Rep. EPA-600/3-79-081, 1979.
- Lamb B., A. Guenther, D. Gay and H. Westberg, A national inventory of biogenic hydrocarbon emissions, *Atmos. Environ.*, 21, 1695-1705, 1987.
- Munger J. W., D. J. Jacob, J. M. Waldman and M. R. Hoffmann, Fogwater chemistry in an urban atmosphere, *J. Geophys. Res.* 88, 5109-5121, 1983.
- Pilinis C. and J. H. Seinfeld, Development and evaluation of a eulerian photochemical gas-aerosol model, *Atmos. Environ.*, 22, 1985-2001, 1988.
- Roberts J. M., F. C. Fehsenfeld, D. L. Albitton, and R. E. Sievers, Measurement of monoterpene hydrocarbons at Niwot Ridge, CO, *J. Geophys. Res.*, 88, 10,667-10,678, 1983.

- Roberts J. M., C. J. Hahn, F. C. Fehsenfeld, J. M. Warnock, D. L. Albritton, and R. E. Sievers, Monoterpene hydrocarbons in the nighttime troposphere, *Environ. Sci. Technol.*, 19, 364-369, 1985.
- Waldman J. M., J. W. Munger, D. J. Jacob, R. C. Flagan, J.J. Morgan, and M. R. Hoffmann, Chemical composition of acid fog, *Science*, 218, 677-680, 1982.
- Zimmerman P. R., Testing for hydrocarbon emissions from vegetation leaf litter and aquatic surfaces, and development of a methodology for compiling biogenic emission inventories, Rep. EPA 450/4-4-79-004, 1979.

CHAPTER 2

SENSITIVITY ANALYSIS OF A CHEMICAL MECHANISM FOR AQUEOUS-PHASE ATMOSPHERIC CHEMISTRY

(Published in *Journal of Geophysical Research*, **94**, 1105-1126, 1989)

Sensitivity Analysis of a Chemical Mechanism for Aqueous-Phase Atmospheric Chemistry

Spyros N. Pandis and John H. Seinfeld

*Department of Chemical Engineering, California Institute of Technology,
Pasadena, CA 91125, U.S.A.*

Abstract

The sensitivity analysis of a comprehensive chemical mechanism for aqueous-phase atmospheric chemistry is performed. The main aqueous-phase reaction pathways for the system are the oxidation of S(IV) by H_2O_2 , OH, O_2 (catalysed by Fe^{3+} and Mn^{2+}), O_3 and HSO_5^- . The $\text{HO}_2(\text{aq})$ and $\text{OH}(\text{aq})$ radicals contribute indirectly to this process by producing and consuming $\text{H}_2\text{O}_2(\text{aq})$ respectively. The dominant pathway for $\text{HNO}_3(\text{aq})$ acidity is scavenging of nitric acid from the gas phase. HCOOH is produced because of the reaction of $\text{HCHO}(\text{aq})$ with $\text{OH}(\text{aq})$. The gas phase concentrations of SO_2 , H_2O_2 , HO_2 , OH, O_3 , HCHO, NH_3 , HNO_3 and HCl are of primary importance. Increase of the liquid water content of the cloud results to a decrease of the sulfate concentration but increase of the total sulfate amount in the aqueous-phase. A condensed mechanism is derived from the analysis.

Introduction

Acid precipitation may be causing significant damage to various ecosystems, for example acidification of lakes, tree damage, etc., [Havas et al., 1984 ; Schofield, 1982]. To identify and describe the physicochemical pathways leading to acid deposition, several models have been developed describing the gas- and aqueous- phase chemistry as well as the mass transport processes coupling the two phases [Graedel

et al. 1981, 1983; Chameides et al. 1982, 1984; Jacob and Hoffmann, 1983; Seigneur and Saxena, 1984; Young and Lurmann, 1984; Hoffmann and Jacob, 1984; Jacob, 1986]. In these models the treatment of the aqueous-phase chemistry has been continuously evolving as more and more experimental kinetic information becomes available. Some of the recent improvements have been the recognition of the potential importance of the metal (Fe^{3+} and Mn^{2+}) catalysed oxidation of SO_2 by O_2 [Hoffmann and Jacob, 1984], the aqueous-phase free radical chemistry [Chameides and Davis, 1982; Schwartz, 1984] and the chemistry of formic acid and formaldehyde [Chameides, 1984; Jacob 1986].

As atmospheric aqueous-phase reaction mechanisms increase in size and complexity, identification of the important and unimportant kinetic pathways has become an increasingly difficult task. Although the qualitative features of the aqueous-phase reaction system appear to be reasonably well understood, there are questions that still remain partially or completely unanswered. They concern the relative importance of the pathways included in the latest mechanisms, the role of every species in the entire reaction system and the influence of the mechanism's parameters such as the liquid water content, the sticking coefficient, the droplet radius, the temperature, etc., on the behavior of the reaction system.

Our goal in this paper is to address quantitatively the above questions through a sensitivity analysis. To accomplish this goal we have developed an aqueous-phase mechanism that represents the current understanding of the physicochemical processes taking place in cloudwater.

This work begins with a presentation of the aqueous-phase chemical mechanism. Next a brief description of the sensitivity analysis method [Decoupled Direct Method (DDM)] employed here is given; details are available in the cited references. The sensitivity analysis results are then presented and discussed, leading to a rank-

ing of the most important reaction pathways for the various species. Additionally, the influence of the gas-phase concentrations and the mechanism's parameters on the aqueous-phase species concentrations is addressed. Based on these results a condensed mechanism can be proposed and tested for the base scenario. Finally, we briefly summarize the sensitivity methods available and actually compare the DDM with the indirect or brute force method.

Aqueous-Phase Chemical Mechanism Formulation

The aqueous-phase model treats the chemistry of the aqueous-phase (no gas-phase reactions are included), and the dynamic exchange of species between the two phases, in a homogeneous parcel of air in a cloud. At $t = 0$ an air parcel containing an initial gas mixture with high water vapor concentration and aerosol particles consisting of SO_4^{2-} , NO_3^- , Cl^- , NH_4^+ , Na^+ , Fe^{3+} and Mn^{2+} is assumed to be suddenly cooled by an isobaric process. The cloud droplets that are formed then are assumed to be chemically homogeneous and to attain instantaneously the same radius α that remains constant. Transport processes such as entrainment and mixing of outside air into the cloud are neglected as are the effects of temporal variations in temperature and liquid water content.

Aqueous-Phase Chemistry

The chemical mechanism that we have developed is based on the work of Graedel et al. [1981,1983], Chameides [1982,1984], Schwartz [1984], Seigneur and Saxena [1984], Hoffman and Calvert [1985], Jacob [1986], and Systems Applications, Inc. [1987]. The mechanism includes 49 individual aqueous-phase species and 20 gas-phase species (Table 1), 17 aqueous-phase ionic equilibria (Table 2), 20 gas-phase aqueous-phase reversible reactions (Table 2) and 109 aqueous-phase

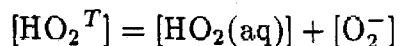
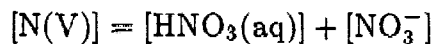
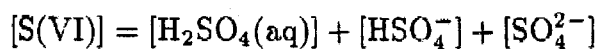
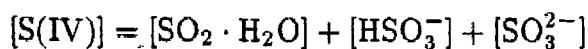
TABLE 1
Chemical Species, Initial Concentrations and Model Parameters

Aqueous - Phase Species	Concentration (μM)	Gas - Phase Species	Concentration (ppb)
$\text{SO}_2 \cdot \text{H}_2\text{O}, \text{HSO}_3^-, \text{SO}_3^{2-}$	0	SO_2	0.98
$\text{H}_2\text{SO}_4, \text{HSO}_4^-, \text{SO}_4^{2-}$	8.0		
$\text{HNO}_2, \text{NO}_2^-$	0	$\text{HNO}_2(\text{g})$	4×10^{-4}
$\text{HNO}_3, \text{NO}_3^-$	2.0	HNO_3	0.55
$\text{CO}_2 \cdot \text{H}_2\text{O}, \text{HCO}_3^-, \text{CO}_3^{2-}$	11.9	CO_2	340×10^3
$\text{H}_2\text{O}_2, \text{HO}_2^-$	0	H_2O_2	0.95
$\text{HCHO}, \text{H}_2\text{C}(\text{OH})_2$	0	HCHO	0.29
$\text{HCOOH}, \text{HCOO}^-$	0	HCOOH	0.007
NO	0	NO	0.016
NO_2	0	NO_2	0.039
O_3	0	O_3	53.2
$\text{CH}_3\text{C}(\text{O})\text{O}_2\text{NO}_2$	0	$\text{CH}_3\text{C}(\text{O})\text{O}_2\text{NO}_2$	0.6
$\text{CH}_3\text{C}(\text{O})\text{OOH}$	0	$\text{CH}_3\text{C}(\text{O})\text{OOH}$	1×10^{-4}
CH_3OOH	0	CH_3OOH	1.0
HCl, Cl^-	8.0	HCl	0.5
OH	0	OH	3×10^{-4}
$\text{HO}_2, \text{O}_2^-$	0	HO_2	0.04
NO_3	0	NO_3	4×10^{-6}
$\text{NH}_4\text{OH}, \text{NH}_4^+$	2.0	NH_3	0.6
CH_3O_2	0	CH_3O_2	0.02
CH_3OH	0	CH_3OH	0.8
H^+	14.74		
OH^-	6.78×10^{-4}		
Fe^{3+}	0.4		
Mn^{2+}	0.2		
Na^+	0.8		
<i>Aqueous Phase Only Species</i>			
<i>With Zero Initial Concentrations</i>			
$\text{Cl}_2^-, \text{Cl}, \text{ClOH}^-$			
$\text{SO}_4^-, \text{SO}_5^-, \text{HSO}_5^-$			
$\text{HOCH}_2\text{SO}_3^-, ^-\text{OCH}_2\text{SO}_3^-$			
CO_3^-			
<i>Fixed Model Parameters</i>		<i>Value</i>	
Temperature, T		298K	
Liquid Water Content, w_L		4×10^{-7} (l water/l air)	
Droplet Radius, α		10 μm	
Zenith Angle, θ		30°	
Cloud Transmissivity		0.5	

reactions (Table 3). The proposed mechanism combines most of the aqueous-phase reactions that have been used in previous studies. It includes detailed aqueous-phase free radical chemistry, chlorine chemistry, chemistry of formaldehyde and formic acid as well as a complete description of sulfur chemistry. The reactions of the mechanism have been divided into the following six groups:

- (a) Oxygen-Hydrogen Chemistry
- (b) Carbonate Chemistry
- (c) Chlorine Chemistry
- (d) Nitrite and Nitrate Chemistry
- (e) Methane oxidation Chemistry
- (f) Sulfur Chemistry

It is convenient to consider the sum of each reactant species in a particular class that is in rapid equilibrium, because of dissociation or hydration, as a single entity [Schwartz, 1984]. Therefore the 49 aqueous-phase species can actually be represented by 29 different groups, like:



where [I] denotes the concentration of aqueous-phase species I in mol/l of water.

Some of the products of reactions 51, 53, 62, 86, 99, 100 and 105 are not included in the chemical mechanism because they have no known significant reactions and would only increase the size of our species matrix.

TABLE 2
Equilibrium Reactions

<i>Equilibrium Reaction</i>	K_{298} (<i>M</i> or <i>M/atm</i>) ^a	$-\frac{\Delta H}{R}$ (K)	<i>Reference</i>
$\text{SO}_2(\text{g}) \rightleftharpoons \text{SO}_2 \cdot \text{H}_2\text{O}$	1.23	3120	Smith and Martell (1976)
$\text{SO}_2 \cdot \text{H}_2\text{O} \rightleftharpoons \text{HSO}_3^- + \text{H}^+$	1.23×10^{-2}	1960	Smith and Martell (1976)
$\text{HSO}_3^- \rightleftharpoons \text{SO}_3^{2-} + \text{H}^+$	6.61×10^{-8}	1500	Smith and Martell (1976)
$\text{H}_2\text{SO}_4(\text{aq}) \rightleftharpoons \text{HSO}_4^- + \text{H}^+$	1000		Perrin(1982)
$\text{HSO}_4^- \rightleftharpoons \text{SO}_4^{2-} + \text{H}^+$	1.02×10^{-2}	2720	Smith and Martell (1976)
$\text{H}_2\text{O}_2(\text{g}) \rightleftharpoons \text{H}_2\text{O}_2(\text{aq})$	7.45×10^4	6620	Lind and Kok (1986)
$\text{H}_2\text{O}_2(\text{aq}) \rightleftharpoons \text{HO}_2^- + \text{H}^+$	2.2×10^{-12}	-3730	Smith and Martell (1976)
$\text{HNO}_3(\text{g}) \rightleftharpoons \text{HNO}_3(\text{aq})$	2.1×10^5		Schwartz (1984)
$\text{HNO}_3(\text{aq}) \rightleftharpoons \text{NO}_3^- + \text{H}^+$	15.4	8700 ^b	Schwartz (1984)
$\text{HNO}_2(\text{g}) \rightleftharpoons \text{HNO}_2(\text{aq})$	49.	4780	Schwartz and White (1981)
$\text{HNO}_2(\text{aq}) \rightleftharpoons \text{NO}_2^- + \text{H}^+$	5.1×10^{-4}	-1260	Schwartz and White (1981)
$\text{O}_3(\text{g}) \rightleftharpoons \text{O}_3(\text{aq})$	1.13×10^{-2}	2300	Kozac and Heltz (1983)
$\text{NO}_2(\text{g}) \rightleftharpoons \text{NO}_2(\text{aq})$	1.00×10^{-2}	2500	Schwartz (1984)
$\text{NO}(\text{g}) \rightleftharpoons \text{NO}(\text{aq})$	1.9×10^{-3}	1480	Schwartz and White (1981)
$\text{CH}_3\text{O}_2(\text{g}) \rightleftharpoons \text{CH}_3\text{O}_2(\text{aq})$	6.0	5600	Jacob (1986)
$\text{CH}_3\text{OH}(\text{g}) \rightleftharpoons \text{CH}_3\text{OH}(\text{aq})$	2.2×10^2	4900	Snider and Dawson (1985)
$\text{CO}_2(\text{g}) \rightleftharpoons \text{CO}_2 \cdot \text{H}_2\text{O}$	3.40×10^{-2}	2420	Smith and Martell (1976)
$\text{CO}_2 \cdot \text{H}_2\text{O} \rightleftharpoons \text{HCO}_3^- + \text{H}^+$	4.46×10^{-7}	-1000	Smith and Martell (1976)
$\text{HCO}_3^- \rightleftharpoons \text{CO}_3^{2-} + \text{H}^+$	4.68×10^{-11}	-1760	Smith and Martell (1976)
$\text{NH}_3(\text{g}) \rightleftharpoons \text{NH}_4\text{OH}$	75	3400	Hales and Drewes (1979)
$\text{NH}_4\text{OH} \rightleftharpoons \text{NH}_4^+ + \text{OH}^-$	1.75×10^{-5}	-450	Smith and Martell (1976)
$\text{H}_2\text{O} \rightleftharpoons \text{H}^+ + \text{OH}^-$	1.0×10^{-14}	-6710	Smith and Martell (1976)

TABLE 2 - continuation
Equilibrium Reactions

<i>Equilibrium Reaction</i>	K_{298} (<i>M</i> or <i>M/atm</i>)	$\frac{-\Delta H}{R}$ (K)	<i>Reference</i>
$\text{CH}_3\text{C}(\text{O})\text{O}_2\text{NO}_2(\text{g}) \rightleftharpoons$			
$\text{CH}_3\text{C}(\text{O})\text{O}_2\text{NO}_2(\text{aq})$	2.9	5910	Lee (1984b)
$\text{HCHO}(\text{g}) \rightleftharpoons \text{HCHO}(\text{aq})$	6.30×10^3	6460	Ledbury and Blair (1925)
$\text{HCHO}(\text{aq}) \xrightleftharpoons{\text{H}_2\text{O}} \text{H}_2\text{C}(\text{OH})_2(\text{aq})$	1.82×10^3	4020	Le Hanaf (1968)
$\text{HCOOH}(\text{g}) \rightleftharpoons \text{HCOOH}(\text{aq})$	3.5×10^3	5740	Latimer (1953)
$\text{HCOOH}(\text{aq}) \rightleftharpoons \text{HCOO}^- + \text{H}^+$	1.78×10^{-4}	-20	Martell and Smith (1977)
$\text{HCl}(\text{g}) \rightleftharpoons \text{HCl}(\text{aq})$	7.27×10^2	2020	Marsh and McElroy (1985)
$\text{HCl}(\text{aq}) \rightleftharpoons \text{H}^+ + \text{Cl}^-$	1.74×10^6	6900	Marsh and McElroy (1985)
$\text{Cl}_2^- \rightleftharpoons \text{Cl} + \text{Cl}^-$	5.26×10^{-6}		Jayson et al. (1973)
$\text{CH}_3\text{OOH}(\text{g}) \rightleftharpoons \text{CH}_3\text{OOH}(\text{aq})$	2.27×10^2	5610	Lind and Kok (1986)
$\text{CH}_3\text{C}(\text{O})\text{OOH}(\text{g}) \rightleftharpoons$			
$\text{CH}_3\text{C}(\text{O})\text{OOH}(\text{aq})$	4.73×10^2	6170	Lind and Kok (1986)
$\text{NO}_3(\text{g}) \rightleftharpoons \text{NO}_3(\text{aq})$	2.1×10^5	8700	Jacob (1986)
$\text{OH}(\text{g}) \rightleftharpoons \text{OH}(\text{aq})$	25	5280	Jacob (1986)
$\text{HO}_2(\text{g}) \rightleftharpoons \text{HO}_2(\text{aq})$	2.0×10^3	6640	Jacob (1986)
$\text{HO}_2(\text{aq}) \rightleftharpoons \text{H}^+ + \text{O}_2^-$	3.50×10^{-5}		Perrin (1982)
$\text{HOCH}_2\text{SO}_3^- \rightleftharpoons$			
$^- \text{OCH}_2\text{SO}_3^- + \text{H}^+$	2.00×10^{-12}		Sorensen et al. (1970)

^a The temperature dependence is represented by:

$$K = K_{298} \exp \left[\frac{-\Delta H}{R} \left(\frac{1}{T} - \frac{1}{298} \right) \right]$$

where K is the equilibrium constant at temperature T (in K).

^b Value for equilibrium:

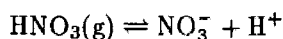


TABLE 3(a)
Oxygen-Hydrogen Chemistry

	Reaction	Rate Expression		Reference
		$M^n \text{ (sec)}^{-1}$	$-E/R$	
1.	$\text{H}_2\text{O}_2 \xrightarrow{h\nu} 2\text{OH}$			Graedel and Weschler (1981)
2.	$\text{O}_3 \xrightarrow{h\nu, \text{H}_2\text{O}} \text{H}_2\text{O}_2 + \text{O}_2$			Graedel and Weschler (1981)
3.	$\text{OH} + \text{HO}_2 \longrightarrow \text{H}_2\text{O} + \text{O}_2$	7.0×10^9	-1500	Sehested et al. (1968)
4.	$\text{OH} + \text{O}_2^- \longrightarrow \text{OH}^- + \text{O}_2$	1.0×10^{10}	-1500	Sehested et al. (1968)
5.	$\text{OH} + \text{H}_2\text{O}_2 \longrightarrow \text{H}_2\text{O} + \text{HO}_2$	2.7×10^7	-1700	Christensen et al. (1982)
6.	$\text{HO}_2 + \text{HO}_2 \longrightarrow \text{H}_2\text{O}_2 + \text{O}_2$	8.6×10^5	-2365	Bielski (1978)
7.	$\text{HO}_2 + \text{O}_2^- \xrightarrow{\text{H}_2\text{O}} \text{H}_2\text{O}_2 + \text{O}_2 + \text{OH}^-$	1.0×10^8	-1500	Bielski (1978)
8.	$\text{O}_2^- + \text{O}_2^- \xrightarrow{2\text{H}_2\text{O}} \text{H}_2\text{O}_2 + \text{O}_2 + 2\text{OH}^-$	< 0.3	0	Bielski (1978)
9.	$\text{HO}_2 + \text{H}_2\text{O}_2 \longrightarrow \text{OH} + \text{O}_2 + \text{H}_2\text{O}$	0.5	0	Weinstein and Bielski (1979)
10.	$\text{O}_2^- + \text{H}_2\text{O}_2 \longrightarrow \text{OH} + \text{O}_2 + \text{OH}^-$	0.13	0	Weinstein and Bielski (1979)
11.	$\text{OH} + \text{O}_3 \longrightarrow \text{HO}_2 + \text{O}_2$	2×10^9	0	Staehelin et al. (1984)
12.	$\text{HO}_2 + \text{O}_3 \longrightarrow \text{OH} + 2\text{O}_2$	$< 1 \times 10^4$	0	Sehested et al. (1984)
13.	$\text{O}_2^- + \text{O}_3 \xrightarrow{\text{H}_2\text{O}} \text{OH} + 2\text{O}_2 + \text{OH}^-$	1.5×10^9	-1500	Sehested et al. (1983)
14.	$\text{OH}^- + \text{O}_3 \xrightarrow{\text{H}_2\text{O}} \text{O}_2^- + \text{HO}_2$	70	0	Staehelin and Hoigne (1982)
15.	$\text{HO}_2^- + \text{O}_3 \longrightarrow \text{OH} + \text{O}_2^- + \text{O}_2$	2.8×10^6	0	Staehelin and Hoigne (1982)
16.	$\text{H}_2\text{O}_2 + \text{O}_3 \longrightarrow \text{H}_2\text{O} + 2\text{O}_2$	$7.8 \times 10^{-3}[\text{O}_3]^{-0.5}$	0	Martin et al. (1983)

TABLE 3(b)
Carbonate Chemistry

	Reaction	Rate Expression		Reference
		$M^n \text{ (sec)}^{-1}$	$-E/R$	
17.	$\text{HCO}_3^- + \text{OH}^- \longrightarrow \text{H}_2\text{O} + \text{CO}_3^{2-}$	1.5×10^7	-1910	Weeks and Rabani (1966)
18.	$\text{HCO}_3^- + \text{O}_2^- \longrightarrow \text{HO}_2^- + \text{CO}_3^{2-}$	1.5×10^6	0	Schmidt (1972)
19.	$\text{CO}_3^{2-} + \text{O}_2^- \xrightarrow{\text{H}_2\text{O}} \text{HCO}_3^- + \text{O}_2 + \text{OH}^-$	4.0×10^8	-1500	Behar (1970)
20.	$\text{CO}_3^{2-} + \text{H}_2\text{O}_2 \longrightarrow \text{HO}_2 + \text{HCO}_3^-$	8.0×10^5	-2820	Behar (1970)

TABLE 3(c)
Chlorine Chemistry

	<i>Reaction</i>	<i>Rate Expression</i>		<i>Reference</i>
		$M^n \text{ (sec)}^{-1}$	$-E/R$	
21.	$\text{Cl}^- + \text{OH} \longrightarrow \text{ClOH}^-$	4.3×10^9	-1500	Jayson et al. (1973)
22.	$\text{ClOH}^- \longrightarrow \text{Cl}^- + \text{OH}$	6.1×10^9	0	Jayson et al. (1973)
23.	$\text{ClOH}^- \xrightarrow{\text{H}^+} \text{Cl} + \text{H}_2\text{O}$	$2.1 \times 10^{10} [\text{H}^+]$	0	Jayson et al. (1973)
24.	$\text{Cl} \xrightarrow{\text{H}_2\text{O}} \text{ClOH}^- + \text{H}^+$	1.3×10^3	0	Jayson et al. (1973)
25.	$\text{HO}_2 + \text{Cl}_2^- \longrightarrow 2\text{Cl}^- + \text{O}_2 + \text{H}^+$	4.5×10^9	-1500	Ross and Neta (1979)
26.	$\text{O}_2^- + \text{Cl}_2^- \longrightarrow 2\text{Cl}^- + \text{O}_2$	1.0×10^9	-1500	Ross and Neta (1979)
27.	$\text{HO}_2 + \text{Cl} \longrightarrow \text{Cl}^- + \text{O}_2 + \text{H}^+$	3.1×10^9	-1500	Graedel and Goldberg (1983)
28.	$\text{H}_2\text{O}_2 + \text{Cl}_2^- \longrightarrow 2\text{Cl}^- + \text{HO}_2 + \text{H}^+$	1.4×10^5	-3370	Hagesawa and Neta (1978)
29.	$\text{H}_2\text{O}_2 + \text{Cl} \longrightarrow \text{Cl}^- + \text{HO}_2 + \text{H}^+$	4.5×10^7	0	Graedel and Goldberg (1983)
30.	$\text{OH}^- + \text{Cl}_2^- \longrightarrow 2\text{Cl}^- + \text{OH}$	7.3×10^6	-2160	Hagesawa and Neta (1978)

TABLE 3(d)
Nitrite and Nitrate Chemistry

	Reaction	Rate Expression		Reference
		$M^n \text{ (sec)}^{-1}$	$-E/R$	
31.	$\text{NO} + \text{NO}_2 \xrightarrow{\text{H}_2\text{O}} 2\text{NO}_2^- + 2\text{H}^+$	2.0×10^8	-1500	Lee (1984a)
32.	$\text{NO}_2 + \text{NO}_2 \xrightarrow{\text{H}_2\text{O}}$ $\text{NO}_2^- + \text{NO}_3^- + 2\text{H}^+$	1.0×10^8	-1500	Lee (1984a)
33.	$\text{NO} + \text{OH} \longrightarrow \text{NO}_2^- + \text{H}^+$	2.0×10^{10}	-1500	Strehlow and Wagner (1982)
34.	$\text{NO}_2 + \text{OH} \longrightarrow \text{NO}_3^- + \text{H}^+$	1.3×10^9	-1500	Gratzel et al. (1970)
35.	$\text{HNO}_2 \xrightarrow{h\nu} \text{NO} + \text{OH}$			Rettich (1970)
36.	$\text{NO}_2^- \xrightarrow{h\nu, \text{H}_2\text{O}} \text{NO} + \text{OH} + \text{OH}^-$			Graedel and Weschler (1981)
37.	$\text{HNO}_2 + \text{OH} \longrightarrow \text{NO}_2 + \text{H}_2\text{O}$	1.0×10^9	-1500	Rettich (1978)
38.	$\text{NO}_2^- + \text{OH} \longrightarrow \text{NO}_2 + \text{OH}^-$	1.0×10^{10}	-1500	Treinin and Hayon (1978)
39.	$\text{HNO}_2 + \text{H}_2\text{O}_2 \xrightarrow{\text{H}^+}$ $\xrightarrow{\text{H}^+} \text{NO}_3^- + 2\text{H}^+ + \text{H}_2\text{O}$	$6.3 \times 10^3 [\text{H}^+]$	-6693	Lee and Lind (1986)
40.	$\text{NO}_2^- + \text{O}_3 \longrightarrow \text{NO}_3^- + \text{O}_2$	5.0×10^5	-6950	Damschen and Martin (1983)
41.	$\text{NO}_2^- + \text{CO}_3^- \longrightarrow \text{NO}_2 + \text{CO}_3^{2-}$	4.0×10^5	0	Lilie et al. (1978)
42.	$\text{NO}_2^- + \text{Cl}_2^- \longrightarrow \text{NO}_2 + 2\text{Cl}^-$	2.5×10^8	-1500	Hagesawa and Neta (1978)
43.	$\text{NO}_2^- + \text{NO}_3 \longrightarrow \text{NO}_2 + \text{NO}_3^-$	1.2×10^9	-1500	Ross and Neta (1979)
44.	$\text{NO}_3^- \xrightarrow{h\nu, \text{H}_2\text{O}} \text{NO}_2 + \text{OH} + \text{OH}^-$			Graedel and Weschler (1981)
45.	$\text{NO}_3 \xrightarrow{h\nu} \text{NO} + \text{O}_2$			Graedel and Weschler (1981)
46.	$\text{NO}_3 + \text{HO}_2 \longrightarrow$ $\text{NO}_3^- + \text{H}^+ + \text{O}_2$	4.5×10^9	-1500	Jacob (1986)
47.	$\text{NO}_3 + \text{O}_2^- \longrightarrow \text{NO}_3^- + \text{O}_2$	1.0×10^9	-1500	Jacob (1986)
48.	$\text{NO}_3 + \text{H}_2\text{O}_2 \longrightarrow$ $\text{NO}_3^- + \text{H}^+ + \text{HO}_2$	1.0×10^6	-2800	Chameides (1984)
49.	$\text{NO}_3 + \text{Cl}^- \longrightarrow \text{NO}_3^- + \text{Cl}$	1.0×10^8	-1500	Ross and Neta (1979)

TABLE 3(e)
CH₄ Oxidation Chain

	Reaction	Rate Expression		Reference
		M^n (sec) ⁻¹	$-E/R$	
50.	$H_2C(OH)_2 + OH \xrightarrow{O_2}$ $HCOOH + HO_2 + H_2O$	2.0×10^9	-1500	Bothe et al. (1980)
51.	$H_2C(OH)_2 + O_3 \rightarrow$ products	0.1	0	Hoigne and Bader (1983a)
52.	$HCOOH + OH \xrightarrow{O_2} CO_2 + HO_2 + H_2O$	1.6×10^8	-1500	Scoles and Willson (1967)
53.	$HCOOH + H_2O_2 \rightarrow$ product + H_2O	4.6×10^{-6}	-5180	Shapilov et al. (1974)
54.	$HCOOH + NO_3 \xrightarrow{O_2}$ $NO_3^- + H^+ + CO_2 + HO_2$	2.1×10^5	-3200	Dogliotti and Hayon (1967)
55.	$HCOOH + O_3 \rightarrow CO_2 + HO_2 + OH$	5.0	0	Hoigne and Bader (1983b)
56.	$HCOOH + Cl_2^- \xrightarrow{O_2}$ $CO_2 + HO_2 + 2Cl^- + H^+$	6.7×10^3	-4300	Hagesawa and Neta (1978)
57.	$HCOO^- + OH \xrightarrow{O_2} CO_2 + HO_2 + OH^-$	2.5×10^9	-1500	Anbar and Neta (1967)
58.	$HCOO^- + O_3 \rightarrow CO_2 + OH + O_2^-$	100.0	0	Hoigne and Bader (1983b)
59.	$HCOO^- + NO_3 \xrightarrow{O_2} NO_3^- + CO_2 + HO_2$	6.0×10^7	-1500	Jacob (1986)
60.	$HCOO^- + CO_3^- \xrightarrow{O_2, H_2O} CO_2 + HCO_3^- +$ $+HO_2 + OH^-$	1.1×10^5	-3400	Chen et al. (1973)
61.	$HCOO^- + Cl_2^- \xrightarrow{O_2} CO_2 + HO_2 + 2Cl^-$	1.9×10^6	-2600	Hagasawa and Neta (1978)
62.	$CH_3C(O)O_2NO_2 \rightarrow NO_3^- +$ products	4.0×10^{-4}	0	Lee (1984b)
63.	$CH_3O_2 + HO_2 \rightarrow CH_3OOH + O_2$	4.3×10^5	-3000	Jacob (1986)
64.	$CH_3O_2 + O_2^- \xrightarrow{H_2O} CH_3OOH + O_2 + OH^-$	5.0×10^7	-1600	Jacob (1986)
65.	$CH_3OOH + h\nu \xrightarrow{O_2} HCHO + OH + HO_2$			Graedel and Wechsler (1981)
66.	$CH_3OOH + OH \rightarrow CH_3O_2 + H_2O$	2.7×10^7	-1700	Jacob (1986)
67.	$CH_3OH + OH \rightarrow HCHO + HO_2 + H_2O$	4.5×10^8	-1500	Anbar and Neta (1967)
68.	$CH_3OH + CO_3^- \xrightarrow{O_2}$ $HCHO + HO_2 + HCO_3^-$	2.6×10^3	-4500	Chen et al. (1973)
69.	$CH_3OH + Cl_2^- \xrightarrow{O_2}$ $HCHO + HO_2 + H^+ + 2Cl^-$	3.5×10^3	-4400	Hagesawa and Neta (1978)
70.	$CH_3OOH + OH \rightarrow HCHO + OH + H_2O$	1.9×10^7	-1800	Jacob (1986)
71.	$CH_3OH + NO_3 \xrightarrow{O_2}$ $NO_3^- + H^+ + HCHO + HO_2$	1.0×10^5	-2800	Dogliotti and Hayon (1967)

TABLE 3(f)
Sulfur Chemistry

	Reaction	Rate Expression		Reference
		$M^n \text{ (sec)}^{-1}$	$-E/R$	
72. ^a	$\text{S(IV)} + \text{O}_3 \longrightarrow \text{S(VI)} + \text{O}_2$	2.4×10^4		
		3.7×10^5	-5530	Hoffmann and
		1.5×10^9	-5280	Calvert (1985)
73. ^a	$\text{S(IV)} + \text{H}_2\text{O}_2 \longrightarrow \text{S(VI)} + \text{H}_2\text{O}$	1.3×10^6	-4430	McArdle (1983)
74. ^a	$\text{S(IV)} + \frac{1}{2}\text{O}_2 \xrightarrow{\text{Mn}^{2+}, \text{Fe}^{3+}} \text{S(VI)}$	4.7	-13,700	
		0.82	-11,000	
		5.0×10^3	-13,700	
		1.0×10^7	-11,000	Martin (1984)
75.	$\text{SO}_3^{2-} + \text{OH}^- \xrightarrow{\text{O}_2} \text{SO}_5^- + \text{OH}^-$	4.6×10^9	-1500	Huie and Neta (1987)
76.	$\text{HSO}_3^- + \text{OH}^- \xrightarrow{\text{O}_2} \text{SO}_5^- + \text{H}_2\text{O}$	4.2×10^9	-1500	Huie and Neta (1987)
77.	$\text{SO}_5^- + \text{HSO}_3^- \xrightarrow{\text{O}_2} \text{HSO}_5^- + \text{SO}_5^-$	3.0×10^5	-3100	Huie and Neta (1987)
	$\text{SO}_5^- + \text{SO}_3^{2-} \xrightarrow{\text{O}_2} \text{HSO}_5^- + \text{SO}_5^-$	1.3×10^7	-2000	Huie and Neta (1987)
78.	$\text{SO}_5^- + \text{O}_2 \xrightarrow{\text{H}_2\text{O}} \text{HSO}_5^- + \text{OH}^- + \text{O}_2$	1.0×10^8	-1500	Jacob (1986)
79.	$\text{SO}_5^- + \text{HCOOH} \xrightarrow{\text{O}_2}$ $\text{HSO}_5^- + \text{CO}_2 + \text{HO}_2$	200	-5300	Jacob (1986)
80.	$\text{SO}_5^- + \text{HCOO}^- \xrightarrow{\text{O}_2}$ $\text{HSO}_5^- + \text{CO}_2 + \text{O}_2^-$	1.4×10^4	-4000	Jacob (1986)
81.	$\text{SO}_5^- + \text{SO}_5^- \longrightarrow 2\text{SO}_4^- + \text{O}_2$	2.0×10^8	-1500	Jacob (1986)
82.	$\text{HSO}_5^- + \text{HSO}_3^- \xrightarrow{\text{H}^+} 2\text{SO}_4^{2-} + 3\text{H}^+$	7.5×10^7	-4755	Jacob (1986)
83.	$\text{HSO}_5^- + \text{OH}^- \longrightarrow \text{SO}_5^- + \text{H}_2\text{O}$	1.7×10^7	-1900	Jacob (1986)
84.	$\text{HSO}_5^- + \text{SO}_4^- \longrightarrow$ $\text{SO}_5^- + \text{SO}_4^{2-} + \text{H}^+$	$< 1.0 \times 10^5$	0	Jacob (1986)
85.	$\text{HSO}_5^- + \text{NO}_2^- \longrightarrow \text{HSO}_4^- + \text{NO}_3^-$	0.31	-6650	Jacob (1986)
86.	$\text{HSO}_5^- + \text{Cl}^- \longrightarrow \text{SO}_4^{2-} + \text{product}$	1.8×10^{-3}	-7050	Jacob (1986)

TABLE 3(f) - continuation

Sulfur Chemistry

	Reaction	Rate Expression		Reference
		$M^n \text{ (sec)}^{-1}$	$-E/R$	
87.	$\text{SO}_4^- + \text{HSO}_3^- \xrightarrow{\text{O}_2} \text{SO}_4^{2-} + \text{H}^+ + \text{SO}_5^-$	1.3×10^9	-1500	Jacob (1986)
88.	$\text{SO}_4^- + \text{SO}_3^{2-} \xrightarrow{\text{O}_2} \text{SO}_4^{2-} + \text{SO}_5^-$	5.3×10^8	-1500	Jacob (1986)
89.	$\text{SO}_4^- + \text{HO}_2 \longrightarrow \text{SO}_4^{2-} + \text{H}^+ + \text{O}_2$	5.0×10^9	-1500	Jacob (1986)
90.	$\text{SO}_4^- + \text{O}_2^- \longrightarrow \text{SO}_4^{2-} + \text{O}_2$	5.0×10^9	-1500	Jacob (1986)
91.	$\text{SO}_4^- + \text{OH}^- \longrightarrow \text{SO}_4^{2-} + \text{OH}$	8.0×10^7	-1500	Jacob (1986)
92.	$\text{SO}_4^- + \text{H}_2\text{O}_2 \longrightarrow \text{SO}_4^{2-} + \text{H}^+ + \text{HO}_2$	1.2×10^7	-2000	Ross and Neta (1979)
93.	$\text{SO}_4^- + \text{NO}_2^- \longrightarrow \text{SO}_4^{2-} + \text{NO}_2$	8.8×10^8	-1500	Jacob (1986)
94.	$\text{SO}_4^- + \text{HCO}_3^- \longrightarrow \text{SO}_4^{2-} + \text{H}^+ + \text{CO}_3^-$	9.1×10^6	-2100	Ross and Neta (1979)
95.	$\text{SO}_4^- + \text{HCOO}^- \xrightarrow{\text{O}_2} \text{SO}_4^{2-} + \text{CO}_2 + \text{HO}_2$	1.7×10^8	-1500	Jacob (1986)
96.	$\text{SO}_4^- + \text{Cl}^- \longrightarrow \text{SO}_4^{2-} + \text{Cl}$	2.0×10^8	-1500	Ross and Neta (1979)
97.	$\text{SO}_4^- + \text{HCOOH} \xrightarrow{\text{O}_2} \text{SO}_4^{2-} + \text{H}^+ + \text{CO}_2 + \text{HO}_2$	1.4×10^6	-2700	Jacob (1986)
98. ^a	$\text{S(IV)} + \text{CH}_3\text{C(O)O}_2\text{NO}_2 \longrightarrow \text{S(VI)}$	6.7×10^{-3}	0	Lee (1984)
99.	$\text{HSO}_3^- + \text{CH}_3\text{OOH} \xrightarrow{\text{H}^+} \text{SO}_4^{2-} + 2\text{H}^+ + \text{prd}$	1.9×10^7	-3800	Hoffmann (1985)
100. ^a	$\text{HSO}_3^- + \text{CH}_3\text{C(O)OOH} \longrightarrow \text{SO}_4^{2-} + \text{H}^+ + \text{prd}$	5.0×10^7	-4000	
		6.0×10^2		Hoffmann (1985)
101.	$\text{S(IV)} + \text{HO}_2 \longrightarrow \text{S(VI)} + \text{OH}$	1.0×10^6	0	Hoffmann (1985)
	$\text{S(IV)} + \text{O}_2^- \xrightarrow{\text{H}_2\text{O}} \text{S(VI)} + \text{OH} + \text{OH}^-$	1.0×10^5	0	Hoffmann (1985)
102.	$\text{SO}_4^- + \text{CH}_3\text{OH} \xrightarrow{\text{O}_2} \text{SO}_4^{2-} + \text{HCHO}$			
	$\quad\quad\quad + \text{H}^+ + \text{HO}_2$	2.5×10^7	-1800	Dogliotti (1967)

TABLE 3(f) - continuation

Sulfur Chemistry

	Reaction	Rate Expression		Reference
		M^n (sec) ⁻¹	-E/R	
103.	$2\text{HSO}_3^- + \text{NO}_3 \xrightarrow{\text{O}_2}$ $\text{NO}_3^- + 2\text{H}^+ + \text{SO}_4^{2-} + \text{SO}_4^-$	1.0×10^8	0	Chameides (1984)
104.	$2\text{NO}_2 + \text{HSO}_3^- \xrightarrow{\text{H}_2\text{O}} \text{SO}_4^{2-} + 3\text{H}^+ + 2\text{NO}_2^-$	2.0×10^6	0	Lee and Schwartz (1983)
105a. ^b	$\text{S(IV)} + \text{N(III)} \longrightarrow \text{S(VI)} + \text{product}$	1.4×10^2	0	Martin (1984)
105b. ^c	$2\text{HSO}_3^- + \text{NO}_2^- \longrightarrow \text{OH}^- + \text{product}$	4.8×10^3	-6100	Oblath et al. (1981)
106.	$\text{HCHO} + \text{HSO}_3^- \longrightarrow \text{HOCH}_2\text{SO}_3^-$	2.9×10^2	-4900	Boyce and Hoffmann (1984)
	$\text{HCHO} + \text{SO}_3^{2-} \xrightarrow{\text{H}_2\text{O}} \text{HOCH}_2\text{SO}_3^- + \text{OH}^-$	2.5×10^7	-1800	Boyce and Hoffmann (1984)
107.	$\text{HOCH}_2\text{SO}_3^- + \text{OH}^- \longrightarrow$ $\text{SO}_3^{2-} + \text{HCHO} + \text{H}_2\text{O}$	3.6×10^3	-4500	Munger et al. (1986)
108.	$\text{HOCH}_2\text{SO}_3^- + \text{OH}^- \xrightarrow{\text{O}_2}$ $\text{SO}_5^- + \text{HCHO} + \text{H}_2\text{O}$	1.4×10^9	-1500	Jacob (1986)
109.	$\text{HSO}_3^- + \text{Cl}_2 \xrightarrow{\text{O}_2} \text{SO}_5^- + 2\text{Cl}^- + \text{H}^+$	3.4×10^8	-1500	Huie and Neta (1987)
	$\text{SO}_3^{2-} + \text{Cl}_2 \xrightarrow{\text{O}_2} \text{SO}_5^- + 2\text{Cl}^-$	1.6×10^8	-1500	Huie and Neta (1987)

^a Reaction with "non-elementary" rate expression.

^b For pH ≤ 3.

^c For pH > 3.

Mathematical Description

The dynamics of the aqueous-phase and gas-phase species are described by a set of mass balance differential equations, the general form of which, for an aqueous-phase species with concentration $c_i(aq)$ (moles/l of water), is given by

$$\frac{dc_i(aq)}{dt} = k_{mt}c_i(g) - k_{mt}\frac{1}{K_{Hi}RT}c_i(aq) + R_i \quad (1.1)$$

where k_{mt} is a combined rate coefficient for gas-phase plus interfacial mass transport,

$$k_{mt} = \frac{3\eta D_{g,i}}{\alpha^2} \quad (1.2)$$

and where $c_i(g)$ (moles/l of gas) is the concentration of species i in the gas phase, K_{Hi} is the effective Henry's law constant of species i , R is the ideal gas constant (0.082058 l atm/ mole K), T is the temperature (K), R_i (moles/ l of water s) is the reaction rate of i in the aqueous-phase, $D_{g,i}$ is the diffusivity of species i in air, α is the cloud droplet radius and finally η is a coefficient correcting for free molecular effects. This coefficient can be approximated by [Fuchs and Sutugin, 1971]:

$$\eta = \left\{ 1 + \left[\frac{1.33 + 0.71Kn^{-1}}{1 + Kn^{-1}} + \frac{4(1 - a_w)}{3a_w} \right] Kn \right\}^{-1} \quad (1.3)$$

Here Kn is the Knudsen number, that is the ratio of the mean free path of air to the droplet radius and a_w is the sticking coefficient. The sticking coefficient represents the probability that a gas molecule reaching the droplet surface will adhere to it. For cloud droplets Kn is much smaller than unity so as a_w approaches unity, η approaches 1. As a_w decreases approaching zero, η also decreases. For example, for a cloud droplet of radius 10 μm and a species with $a_w = 10^{-4}$, $\eta = 0.01$.

The sticking coefficient a_w for gaseous species on small droplets has been an elusive quantity. In recent measurements of the sticking coefficients of SO_2 [Gardner

et al.,1987] and HO₂ [Mozurkewich et al.,1987] onto aqueous solutions it has been found that the corresponding values of a_w are slightly larger than 0.01. Such values of a_w would imply that interfacial mass-transport does not substantially inhibit the rate of aqueous-phase reactions of these species under representative conditions [Schwartz, 1986]. In the absence of other data a value of $a_w = 0.01$ has been used in our base case simulation for all species.

The effective (or modified) Henry's law coefficient K_{Hi} for a species i that undergoes ionic dissociation differs from the Henry's law coefficient H_i as it contains all the ionic forms of the dissolved gas. For example,

$$K_{H,S(IV)} = H_{S(IV)} \left[1 + \frac{K_1}{[H^+]} + \frac{K_1 K_2}{[H^+]^2} \right] \quad (1.4)$$

where K_1 and K_2 are the first and the second ionic dissociation constants for SO₂·H₂O (Table 2).

Finally the temporal variations in the concentrations of the gas-phase species $c_i(g)$ (Table 1) are given by equations of the general form :

$$\frac{dc_i(g)}{dt} = -k_{mt}w_L c_i(g) + k_{mt}w_L \frac{1}{K_{Hi}RT} c_i(aq) \quad (1.5)$$

where w_L is the water liquid content (1 water/1 air) of the cloud.

In our description of the process we assume that aqueous equilibrium and electroneutrality are continuously maintained [Seinfeld, 1986], so that the electroneutrality equation can be expressed in the form:

$$f\left([H^+]; [S(IV)], [S(VI)], [N(III)], \dots, [CO_3^-], [Fe^{3+}], [Mg^{2+}], [Na^+]\right) = 0 \quad (1.6)$$

and as all the lumped concentrations (S(IV), S(VI), etc.,) are known at any time equation (1.6) reduces to one nonlinear equation with one unknown, [H⁺].

The initial conditions for the base case (Table 1) have been chosen to be representative of a day-time cloud environment in the northeastern United States region

[Systems Applications Inc., 1987; Jacob, 1986; Chameides, 1982]. Some of the results of the base case simulation are shown in figures 1 and 2. The pH changes from an initial value of 4.9 to 3.6 after two hours. Both $\text{SO}_2(\text{g})$ and $\text{H}_2\text{O}_2(\text{g})$ concentrations decrease significantly as both species are transported to the aqueous-phase where they react rapidly to produce $\text{S}(\text{VI})$. The scavenging of $\text{HNO}_3(\text{g})$ appears to be the only source of nitrate acidity in the cloud. The presence of the cloud results in a net production of formic acid and a small decrease in the amount of formaldehyde. Peroxymonosulfate concentration reaches a maximum and then decreases.

Sensitivity Analysis Method

The sensitivity analysis can provide a direct means for determining the important reactions in a chemical mechanism, the effects of uncertainties in the input parameters on the mechanism's predictions and generally provide considerable insight into the entire system. Sensitivity analysis has been used for the identification of the most important reactions, initial and boundary conditions in atmospheric and combustion mechanisms [Falls et al. 1979; Dickinson and Gelinas, 1976; Dougherty et al. 1979, 1980; Dunker 1980,1984].

Two classes of methods have been used for sensitivity analysis. The local or deterministic methods produce information on how the uncertainty to one parameter, for example, k_i , affects one of the dependent variables, for example, y_j [Oran and Boris, 1987]. The global or stochastic methods consider the effects of simultaneously varying parameters over a range of values [Cukier et al.,1978; Koda et al. 1979; Stolarski et al.,1978].

Since our main goal is the determination of the relative importance of the 109 reactions in the mechanism local sensitivity analysis methods are sufficient. There are four main candidates :

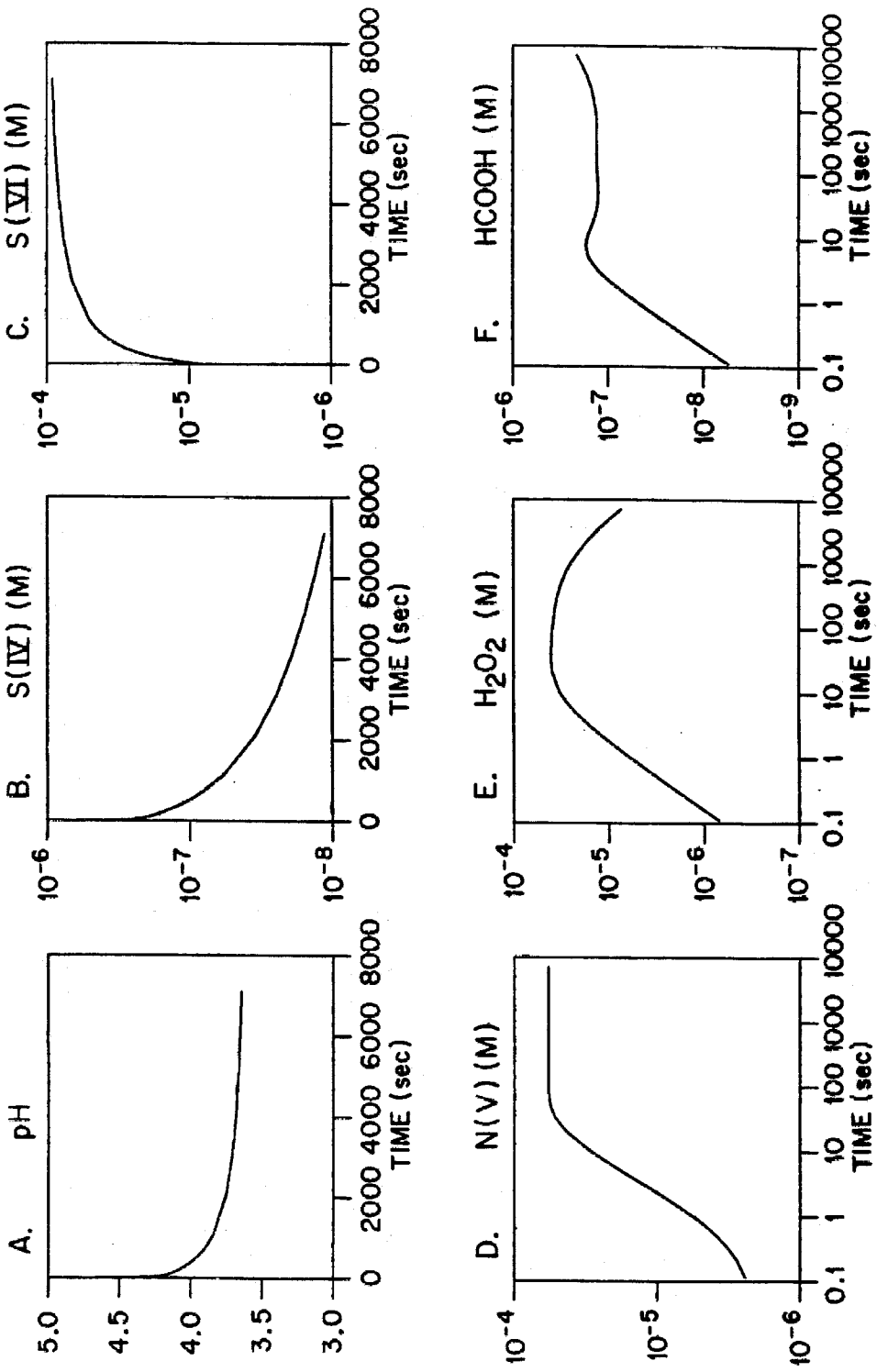


Figure 1. Calculated aqueous-phase concentrations in (mol / l of water) for the base scenario.

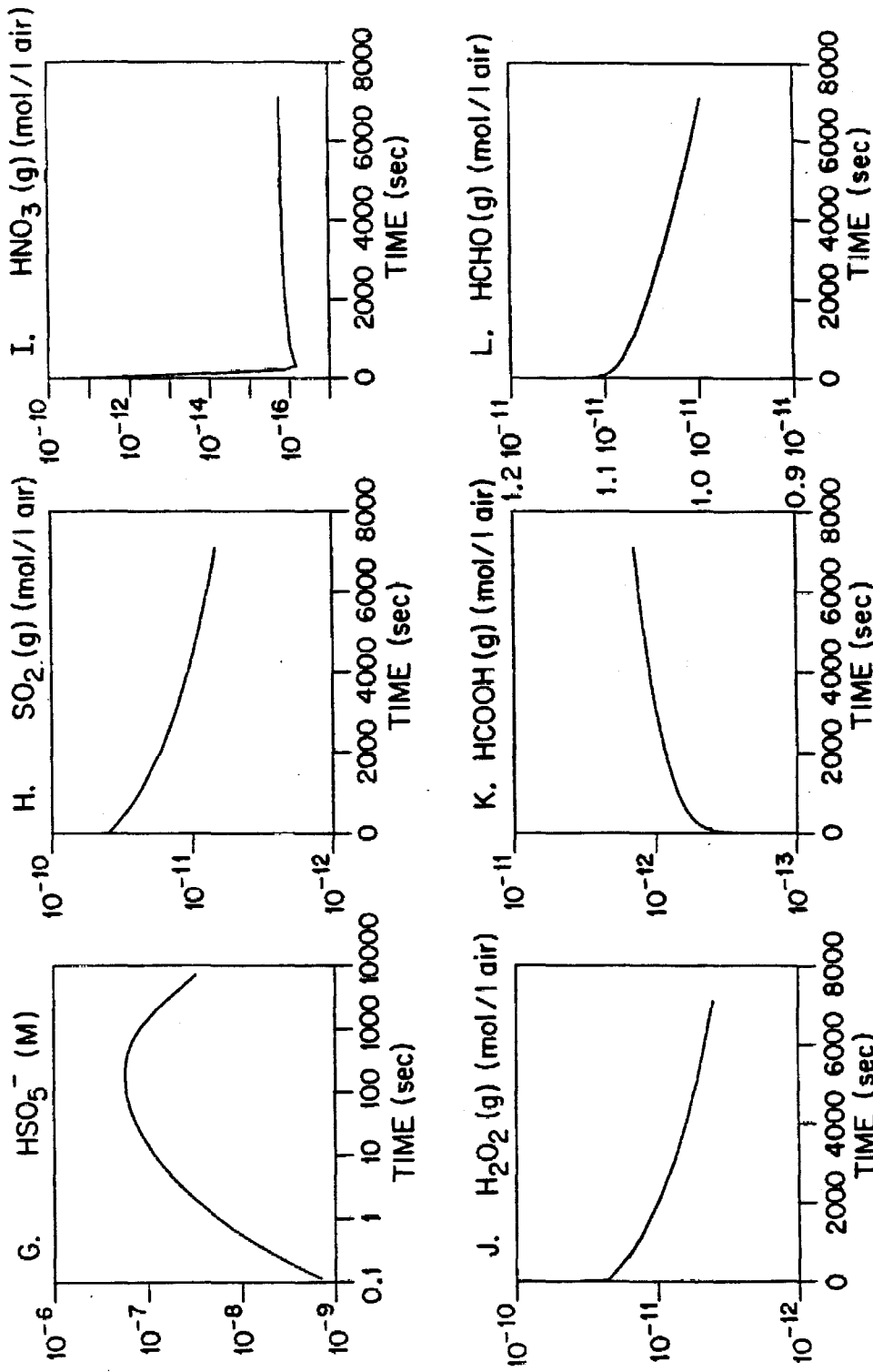


Figure 2. Calculated aqueous-phase concentrations in (mol / l of water) and gas-phase concentrations in (mol / l of air) for the base scenario.

- (a) The indirect or brute force method [Dunker, 1980]
- (b) The coupled direct method [Dickinson et al., 1976; Frank, 1978]
- (c) The Green's function method [Dougherty et al., 1979]
- (d) The decoupled direct method [Dunker, 1984]

Most appropriate for the current problem is the decoupled direct method (DDM) because of its efficiency in the calculation of large numbers of sensitivity coefficients, its simplicity, accuracy and stability.

The system of ordinary differential equations for the aqueous and gas-phase concentrations can be written in the form :

$$\frac{dy}{dt} = \mathbf{f}(y, t; \lambda), \quad \mathbf{y}(t_0) = \mathbf{y}_0 \quad (2.1)$$

where \mathbf{y} is the N-dimensional vector of concentrations, λ is the M-dimensional time-independent vector of input parameters, and \mathbf{y}_0 is the initial condition on \mathbf{y} . The first-order sensitivity coefficients are defined as

$$s_{ki} = \frac{\partial y_k}{\partial \lambda_i}. \quad (2.2)$$

The N-dimensional vector \mathbf{s}_i , consisting of the sensitivity coefficients s_{ji} of the N species concentrations to the parameter λ_i , satisfies the differential equation:

$$\frac{d\mathbf{s}_i}{dt} = \mathbf{J}(y, t; \lambda) \mathbf{s}_i + \mathbf{f}_i(y, t; \lambda), \quad \mathbf{s}_i(t_0) = \frac{\partial \mathbf{y}_0}{\partial \lambda_i} \quad (2.3)$$

where the elements of \mathbf{J} , the Jacobian matrix, and the vector \mathbf{f}_i are

$$J_{mn} = \frac{\partial f_m}{\partial y_n} \quad \mathbf{f}_i = \frac{\partial \mathbf{f}}{\partial \lambda_i}. \quad (2.4)$$

The basic idea behind the DDM is that systems (2.1) and (2.3) are decoupled but solved simultaneously, alternating the solution of (2.1) with the solution of (2.3) [Dunker, 1984].

We have calculated the sensitivity coefficients of the mechanism in Table 3 with respect to the reaction constants that appear in it. Results will be presented in terms of the dimensionless sensitivity coefficients \bar{s}_{ij} defined as

$$\bar{s}_{ij} = \frac{\lambda_j}{y_i} \frac{\partial y_i}{\partial \lambda_j} = \frac{\partial \ln y_i}{\partial \ln \lambda_j} \quad (2.5)$$

in order to make comparison between them easier [Dougherty and Rabitz, 1980]. The use of dimensional sensitivity coefficients can result in difficulty in assessing the sensitivity to the nonzero initial concentrations [Cho et al., 1986]. However, the dimensionless sensitivity coefficient will always be zero for a zero initial concentration because the nonzero $\partial y_i / \partial \lambda_j$ is multiplied by $\lambda_j = 0$. In this case dimensional sensitivity coefficients should be calculated.

One way of interpreting the dimensionless sensitivity coefficients is the use of a Taylor series expansion of formula (2.5). Then

$$y_i(t, \lambda_j + \Delta \lambda_j) - y_i(t, \lambda_j) = \bar{s}_{ij} y_i(t, \lambda_j) \frac{\Delta \lambda_j}{\lambda_j}. \quad (2.6)$$

Note that the net effect of parameter λ_j on y_i at time t depends not only on $\bar{s}_{ij}(t)$ but on $y_i(t)$ too.

We have calculated the sensitivity of the concentrations of our species to 150 parameters of the mechanism (reaction constants, initial conditions, liquid water content, etc.). This required the solution of almost 7500 stiff ODE's and consumed 19 hours of CPU time on a microvax II.

S(IV) to S(VI) Transformation and Sulfur Chemistry.

The conversion of S(IV) to S(VI) is a dominant chemical process in cloudwater. Absorption of $\text{SO}_2(\text{g})$ in cloudwater results in the ionic dissociation of $\text{SO}_2 \cdot \text{H}_2\text{O}$ to HSO_3^- and SO_3^{2-} . Because of this dissociation the solubility of $\text{SO}_2(\text{g})$ in water is

enhanced and the total amount of dissolved sulfur always exceeds that predicted by Henry's law for SO₂ alone. The total amount of dissolved S(IV) is therefore quite pH-dependent. The Henry's law coefficient for SO₂ alone, H_{SO₂}, is 1.23 M/atm at 298 K, while for the same temperature the effective Henry's law coefficient for S(IV), K_{H,S(IV)} (equation 1.4), is 1524 M/atm for pH=5, 152 M/atm for pH=4 and 16.4 M/atm for pH=3. Furthermore, at the pH range of interest (pH 2-8) virtually all of the S(IV) is in the form of HSO₃⁻, whereas at low pH (pH<2) all of the S(IV) occurs as SO₂·H₂O.

The pathways for S(IV) transformation that have been included in the present mechanism involve reactions of S(IV) with O₃, H₂O₂, O₂ (catalysed by Mn²⁺ and Fe³⁺), OH, SO₅⁻, HSO₅⁻, SO₄⁻, PAN, CH₃OOH, CH₃C(O)OOH, HO₂, NO₃, NO₂, N(III), HCHO and Cl₂⁻. For the oxidation of S(IV) by OH we have adopted here the mechanism proposed by Jacob [1986]. The products of the above S(IV) reactions include S(VI), SO₄⁻, SO₅⁻, HSO₅⁻ and HOCH₂SO₃⁻. The dimensionless sensitivity coefficients for S(IV) to the various chemical reaction constants appear in Table 4.

The dominant reaction throughout the simulation is the oxidation of S(IV) by H₂O₂(aq),



Hydrogen peroxide is clearly the most effective oxidant of S(IV) for the pH range of our simulation as for pH>2 the rate of this reaction is pH independent [Martin and Damschen, 1981; McArdle and Hoffmann, 1983]. Under the conditions of the present simulation the rate of the reaction at $t = 30$ s was 2.57 ppb SO₂/hr or equivalently 253% SO₂/hr.

The other reactions that influence [S(IV)(aq)] can be divided into two categories:

a) Reactions that influence S(IV) indirectly by producing or consuming H₂O₂ and

TABLE 4. Dimensionless Sensitivity Coefficients for S(IV)(aq)^a

Time	100 sec	400 sec	800 sec	1800 sec
	React. Sens.Coef.	React. Sens.Coef.	React. Sens.Coef.	React. Sens.Coef.
	73 -0.198	73 -0.519	73 -0.662	73 -0.799
	78 -0.323(-2) ^b	7 -0.939(-2)	74 -0.142(-1)	74 -0.262(-1)
	7 -0.298(-2)	78 -0.531(-2)	7 -0.138(-1)	7 -0.216(-1)
	76 -0.263(-2)	74 -0.363(-2)	78 -0.507(-2)	78 -0.628(-2)
	81 -0.228(-2)	76 -0.258(-2)	82 -0.320(-2)	5 0.447(-2)
	72 -0.138(-2)	82 -0.228(-2)	76 -0.280(-2)	82 -0.394(-2)
	74 -0.930(-3)	72 -0.221(-2)	72 -0.249(-2)	76 -0.387(-2)
	82 -0.855(-3)	81 -0.191(-2)	5 0.239(-2)	72 -0.311(-2)
	50 -0.506(-3)	5 0.139(-2)	18 -0.171(-2)	18 -0.281(-2)
	77 -0.372(-3)	18 -0.112(-2)	81 -0.157(-2)	20 0.215(-2)
	87 -0.365(-3)	20 0.804(-3)	20 0.127(-2)	99 -0.186(-2)
	5 0.341(-3)	13 0.701(-3)	13 0.110(-2)	13 0.159(-2)
	18 -0.332(-3)	77 -0.685(-3)	99 -0.103(-2)	81 -0.126(-2)
	96 -0.258(-3)	99 -0.662(-3)	77 -0.736(-3)	77 -0.104(-2)
	99 -0.223(-3)	50 -0.603(-3)	1 0.325(-3)	1 0.998(-3)
	109 -0.223(-3)	87 -0.377(-3)	109 -0.323(-3)	29 0.596(-3)
	20 0.217(-3)	109 -0.280(-3)	87 -0.312(-3)	109 -0.452(-3)
	13 0.184(-3)	96 -0.272(-3)	29 0.287(-3)	6 -0.271(-3)
	101 -0.134(-3)	29 0.136(-3)	96 -0.215(-3)	87 -0.268(-3)
	92 -0.118(-3)	1 0.112(-3)	6 -0.166(-3)	96 -0.149(-3)

^a Dimensionless sensitivity coefficient for reaction *i* with reaction constant K_i :

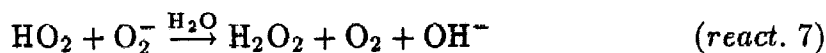
$$\frac{\partial \ln[S(IV)(aq)]}{\partial \ln K_i}$$

^b Read -0.323(-2) as -0.323×10^{-2} .

therefore by changing the rate of reaction 73.

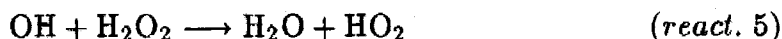
b) Reactions that consume S(IV), influencing S(IV) directly.

We shall start by examining the indirect influences. The sensitivity coefficients for H_2O_2 are shown in Table 5. The main aqueous-phase source of H_2O_2 is



and therefore it accelerates the oxidation of S(IV) to S(VI). Reaction 7 is in fact more influential to S(IV) oxidation, in the case considered here, than most of the other direct oxidation reactions for the conversion of S(IV) to S(VI). The rate of this reaction is initially 100% H_2O_2 /hr and, as HO_2 is depleted, it slows down.

The second most important sink of H_2O_2 , after the oxidation of S(IV), is its reaction with OH to produce HO_2 :



This reaction results in a slowing of the conversion of S(IV) by H_2O_2 and after 30 minutes of simulation it is found to be relatively significant for S(IV). The importance of this reaction is less than what its rate suggests because its product, HO_2 , leads to H_2O_2 by reaction 7.

Of next importance for the $[\text{H}_2\text{O}_2(\text{aq})]$ is the reaction of the superoxide ion, O_2^- , with bicarbonate ion to form HO_2^- and carbonate radical ion:



Reaction 18 was initially reported by Schmidt [1972], although subsequently Schwartz [1984] concluded that there is insufficient evidence for its occurrence in cloudwater. Assuming that the rate constant given in Table 3 is correct, the sensitivity analysis shows that this reaction represents a relatively important aqueous-phase source of H_2O_2 . Hence, some additional studies are necessary to confirm or exclude the occurrence of this reaction.

TABLE 5. Dimensionless Sensitivity Coefficients for H₂O₂(aq)^a

Time	100 sec	400 sec	800 sec	1800 sec
	React. Sens. Coef.	React. Sens. Coef.	React. Sens. Coef.	React. Sens. Coef.
	73 -0.606(-1) ^b	73 -0.203	73 -0.336	73 -0.531
	7 0.156(-1)	7 0.175(-1)	7 0.189(-1)	7 0.235(-1)
	5 -0.200(-2)	5 -0.319(-2)	5 -0.406(-2)	5 -0.604(-2)
	18 0.176(-2)	18 0.219(-2)	18 0.249(-2)	74 0.526(-2)
	20 -0.124(-2)	20 -0.165(-2)	20 -0.192(-2)	18 0.327(-2)
	13 -0.117(-2)	13 -0.141(-2)	13 -0.190(-2)	13 -0.324(-2)
	29 -0.246(-3)	76 0.757(-3)	76 0.151(-2)	76 0.324(-2)
	6 0.179(-3)	1 -0.422(-3)	74 0.973(-3)	20 -0.258(-2)
	76 0.172(-3)	29 -0.411(-3)	1 -0.859(-3)	1 -0.204(-2)
	1 -0.105(-3)	6 0.214(-3)	29 -0.538(-3)	78 0.111(-2)
		72 0.125(-3)	78 0.328(-3)	72 0.901(-3)
		74 0.114(-3)	72 0.320(-3)	29 -0.824(-3)
			82 0.241(-3)	82 0.660(-3)

^a Dimensionless sensitivity coefficient for reaction *i* with reaction constant *K_i*:

$$\frac{\partial \ln[\text{H}_2\text{O}_2(\text{aq})]}{\partial \ln K_i}$$

^b Read -0.606(-1) as -0.606×10^{-1} .

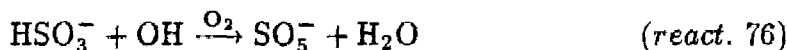
Another significant sink of H_2O_2 is found to be its reaction with the carbonate radical ion:



This reaction is the inverse of reaction 18.

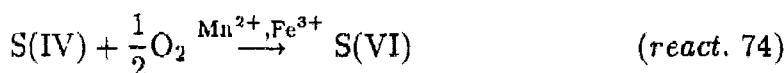
Finally, other sinks or sources of H_2O_2 are reactions 1, 29 and 6. The influence of these reactions on H_2O_2 explains their appearance among the sensitive reactions for S(IV) and S(VI).

For the first five minutes of simulation the second most important direct pathway for S(IV) conversion is its oxidation by OH to produce SO_5^- :



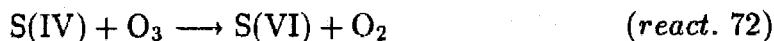
After this initial time period, the rate of reaction 76 decreases because of the pH decrease and the depletion of OH. We should note that the various gas-phase sources and sinks of OH, which have not been included here, would have as a net result a slower OH depletion. Hence, as OH(g) concentration can be higher than the value calculated by our model, the above reaction can be even more influential than shown here. Reaction 76 takes place in two steps; first oxidation of HSO_3^- and SO_3^{2-} by OH(aq) produces the SO_3^- radical and then SO_3^- reacts very rapidly with O_2 to produce SO_5^- [Huie and Neta, 1984]. The fate of SO_5^- is reaction via various pathways to produce HSO_6^- , SO_4^- and S(VI) creating a relatively complicated reaction system that we shall examine later.

After the first 10 minutes (Table 4) of the simulation, the second most important pathway for conversion of S(IV) to S(VI) is oxidation by O_2 catalysed by Fe^{3+} and Mn^{2+} :



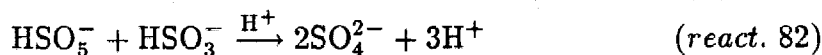
This reaction has been the subject of considerable interest [Hoffmann and Boyce, 1983; Martin, 1984; Hoffmann and Jacob, 1984; Hoffmann and Calvert, 1985; Clarke and Radojevic, 1986] and important differences in the measured reaction rates, rate laws and pH dependencies have been found [Hoffmann and Jacob, 1984]. Recently Martin [1987] has proposed that the reaction is inhibited by ionic strength, sulfate ion and is self-inhibited, and furthermore, that most of the literature discrepancies may be explained by differences in the above factors. Our sensitivity study in which the previous expressions proposed by Martin [1984] have been used shows that the metal (Fe^{3+} and Mn^{2+}) catalysed oxidation of S(IV) is of major importance for the aqueous-phase sulfate production. Due to the uncertainties existing in the transition metal chemistry and the wide variations of the concentrations of dissolved transition metal ions [Graedel et al., 1986], our analysis of the role of the transition metals is limited only to reaction 74.

The oxidation of S(IV) by O_3 :



decreases rapidly as the pH decreases [Hoffmann et al., 1985], and so for the pH range of our simulation, its final contribution to the S(IV) oxidation is far less significant than oxidation of S(IV) by H_2O_2 , OH and O_2 (Table 4).

A pathway that becomes progressively important is the oxidation of S(IV) by HSO_5^- to produce sulfate :



For the first 15 minutes of simulation the HSO_5^- concentration and the contribution of this pathway to the S(IV) oxidation increase. Later as the pH continues to decrease, HSO_5^- is converted to sulfate and therefore reaction 82 starts slowing down.

There are some reactions that under the conditions used in this study are found moderately significant. They include the oxidation of S(IV) by SO_5^- (reaction 77), oxidation by $\text{CH}_3\text{OOH}(\text{aq})$ (reaction 99), oxidation by SO_4^- (reaction 87) and oxidation by HO_2 (reaction 101).

The remainder of the reaction pathways for S(IV) included in the present mechanism are found to be insignificant. The oxidation by PAN is very slow for pH less than 5.5. The oxidation of S(IV) by formaldehyde is found to be unimportant, as the corresponding reaction rate decreases dramatically with decreasing pH and will be quite small unless the pH exceeds 5.5. Finally, oxidation by nitrogen compounds, NO_3 , NO_2 and N(III), is found to be a negligible sink of S(IV) and is not expected to play a role under ordinary conditions.

SO_5^- , SO_4^- and HSO_5^- chemistry

Among the reactions that play an important role in the oxidation of S(IV) (Table 4) appears a group, such as reactions 78 and 81, that do not involve S(IV) directly. These reactions represent intermediate steps in the conversion of S(IV) to S(VI) and involve species like SO_5^- , SO_4^- and HSO_5^- .

The SO_5^- , SO_4^- , HSO_5^- reaction subsystem appears to be rather complicated; therefore, we shall try first to identify the important sinks and sources for each of the above species and then we shall examine the influences exerted by these reactions on S(IV) and S(VI). We attempt to gain some insight by looking at the corresponding sensitivity coefficients from three different points of view:

- (1) the sensitivity coefficients for S(IV) (Table 4)
- (2) the sensitivity coefficients for S(VI) (Table 6) and
- (3) the sensitivity coefficients for HSO_5^- (Table 7).

Using the above information we arrive at the following conclusions.

TABLE 6. Dimensionless Sensitivity Coefficients for S(VI)(aq)^a

Time	100 sec		400 sec		800 sec		1800 sec	
	React.	Sens.Coef.	React.	Sens.Coef.	React.	Sens.Coef.	React.	Sens.Coef.
	73	0.361	73	0.558	73	0.508	73	0.377
	7	0.524(-2) ^b	7	0.101(-1)	74	0.108(-1)	74	0.123(-1)
	72	0.257(-2)	78	0.516(-2)	7	0.106(-1)	7	0.108(-1)
	81	0.241(-2)	82	0.386(-2)	78	0.511(-2)	78	0.474(-2)
	82	0.229(-2)	74	0.363(-2)	82	0.358(-2)	82	0.248(-2)
	78	0.218(-2)	72	0.238(-2)	76	0.241(-2)	76	0.247(-2)
	74	0.171(-2)	76	0.218(-2)	72	0.192(-2)	5	-0.210(-2)
	76	0.112(-2)	81	0.171(-2)	5	-0.182(-2)	72	0.147(-2)
	96	0.918(-3)	5	-0.148(-2)	18	0.131(-2)	18	0.132(-2)
	87	0.891(-3)	18	0.120(-2)	81	0.130(-2)	20	-0.101(-2)
	5	-0.603(-3)	20	-0.861(-3)	20	-0.968(-3)	99	0.871(-3)
	18	0.537(-3)	99	0.710(-3)	99	0.784(-3)	13	-0.813(-3)
	99	0.407(-3)	13	-0.521(-3)	13	-0.705(-3)	1	-0.466(-3)
	20	-0.392(-3)	96	0.497(-3)	77	0.359(-3)	77	0.370(-3)
	13	-0.364(-3)	87	0.414(-3)	96	0.351(-3)	81	0.328(-3)
	92	0.325(-3)	77	0.336(-3)	1	-0.247(-3)	96	0.246(-3)
	101	0.225(-3)	92	0.199(-3)	87	0.243(-3)	29	-0.186(-3)
	90	0.165(-3)	29	-0.134(-3)	29	-0.158(-3)	87	0.137(-3)
	89	0.123(-3)	1	-0.129(-3)	92	0.128(-3)	6	0.127(-3)
			101	0.125(-3)	6	0.127(-3)	109	-0.101(-3)

^a Dimensionless sensitivity coefficient for reaction *i* with reaction constant K_i :

$$\frac{\partial \ln[S(VI)(aq)]}{\partial \ln K_i}$$

^b Read 0.542(-2) as 0.542×10^{-2} .

TABLE 7. Dimensionless Sensitivity Coefficients for $\text{HSO}_5^- (\text{aq})^a$

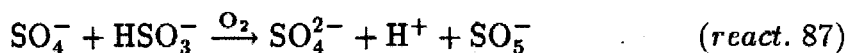
Time	100 sec		400 sec		800 sec		1800 sec	
	React.	Sens.Coef.	React.	Sens.Coef.	React.	Sens.Coef.	React.	Sens.Coef.
	78	0.924	78	0.896	78	0.879	82	-1.122
	81	-0.141	82	-0.335	82	-0.618	78	0.859
	82	-0.823(-1) ^b	81	-0.158	81	-0.167	73	0.252
	77	0.687(-1)	77	0.966(-1)	77	0.113	81	-0.183
	73	-0.188(-1)	73	-0.120(-1)	73	0.484(-1)	77	0.133
	83	-0.226(-2)	83	-0.356(-2)	83	-0.436(-2)	74	0.669(-2)
	80	0.112(-2)	80	0.215(-2)	80	0.305(-2)	7	-0.600(-2)
	72	-0.359(-3)	76	0.991(-3)	76	0.215(-2)	83	-0.576(-2)
	87	-0.264(-3)	50	0.544(-3)	50	0.110(-2)	80	0.481(-2)
	7	-0.243(-3)	72	-0.297(-3)	7	0.106(-2)	76	0.475(-2)
	74	-0.163(-3)	87	-0.225(-3)	74	0.908(-3)	5	-0.115(-2)
	76	0.113(-3)	74	-0.124(-3)	5	-0.193(-3)	18	0.759(-3)
			7	-0.119(-3)	87	-0.178(-3)	72	0.744(-3)

^a Dimensionless sensitivity coefficient for reaction i with reaction constant K_i :

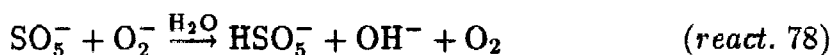
$$\frac{\partial \ln[\text{HSO}_5^- (\text{aq})]}{\partial \ln K_i}$$

^b Read -0.823(-1) as -0.823×10^{-1} .

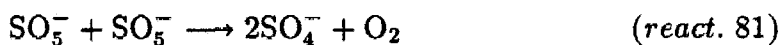
The main source of SO_5^- is under the present conditions the oxidation of HSO_3^- by OH (reaction 76). A additional source is the oxidation of S(IV) by SO_4^- :



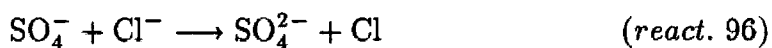
There are two competing reactions consuming SO_5^- . The first one is its reaction with O_2^- to produce SO_5^- :



and the second is its autoconversion to SO_4^- :

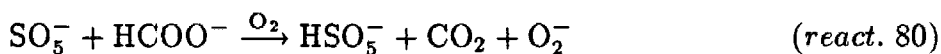


There is only one significant source of SO_4^- , the autoconversion of SO_5^- by reaction 81. The fate of SO_4^- is mainly conversion to S(VI). There are two main pathways for this conversion, its reaction with Cl^- :



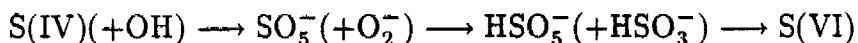
and its reaction with HSO_3^- (reaction 87). Additional pathways for the above conversion, like the reaction of SO_4^- with H_2O_2 (reaction 92), its reaction with HO_2 and O_2^- (reactions 89 and 90) and finally its reaction with HCOO^- (reaction 95), are of minor importance.

The main sources of HSO_5^- (Table 7) appear to be the fast reaction of SO_5^- with O_2^- (reaction 78) and the oxidation of HSO_3^- by SO_5^- (reaction 77). There is one more minor source, the reaction of SO_5^- with HCOO^- :



The main sink is by far its reaction with HSO_3^- to produce sulfate (reaction 82). A secondary sink is its reaction with OH (reaction 83).

The main reactions that produce and consume SO_4^- , HSO_5^- and SO_3^- are found to be influential on both the S(IV) and S(VI) concentrations. Under the conditions used in this study there are two main pathways involving the above species and resulting in the conversion of S(IV) to S(VI). The first is:



and the second :

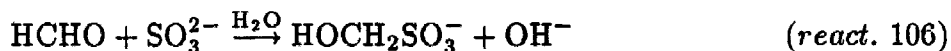


The first of these two pathways appears to be faster than the second under the present conditions (Tables 4, 6 and 7) after at least the first few minutes.

An interesting feature of the reaction system is the production and consumption of HSO_5^- . For the first five minutes of our simulation the concentration of HSO_5^- keeps increasing; it then reaches a maximum value and starts decreasing (figure 2). Reaction 78, which is mainly responsible for HSO_5^- production, slows down at this time and reaction 82 becomes dominant (Table 7). Notable is the influence of reaction 73 on the HSO_5^- concentration. Initially one finds that this reaction indirectly negatively influences the HSO_5^- concentration because it consumes S(IV) and therefore inhibits the HSO_5^- production which is at this time the dominant process for HSO_5^- . Subsequently as the consumption of HSO_5^- by HSO_3^- becomes the dominant process, reaction 73 starts enhancing the HSO_5^- concentration as it consumes HSO_3^- . The same change of sign at 300 s is noted for the sensitivity coefficients for reactions 72, 7 and 74 for exactly the same reasons.

HOCH₂SO₃⁻ chemistry

Under the pH conditions studied here hydroxymethanesulfonate ion (HMSA) is produced by the reaction of SO₃²⁻ with formaldehyde:



HMSA concentration attains a maximum value and then is converted to SO₅⁻ because of the OH(aq) attack:



The dissociation of HOCH₂SO₃⁻ by nucleophilic displacement of HSO₃⁻ by OH⁻ [Munger et al., 1986] :



is slow under the current conditions and is not expected to be influential under ordinary cloud conditions (non-alkaline conditions).

The main features of the sulfur chemistry are summarized in figure 3.

Nitrite and Nitrate Chemistry

From Table 8 we note there is no significant reaction producing HNO₃ in the aqueous phase. The main reaction concerning N(V) is, under the present conditions, the photolysis of NO₃⁻:



which consumes nitric acid at the negligible rate of 0.03%/hr. Hence the rates of all the nitric acid aqueous-phase reactions are too small to influence the HNO₃(aq)

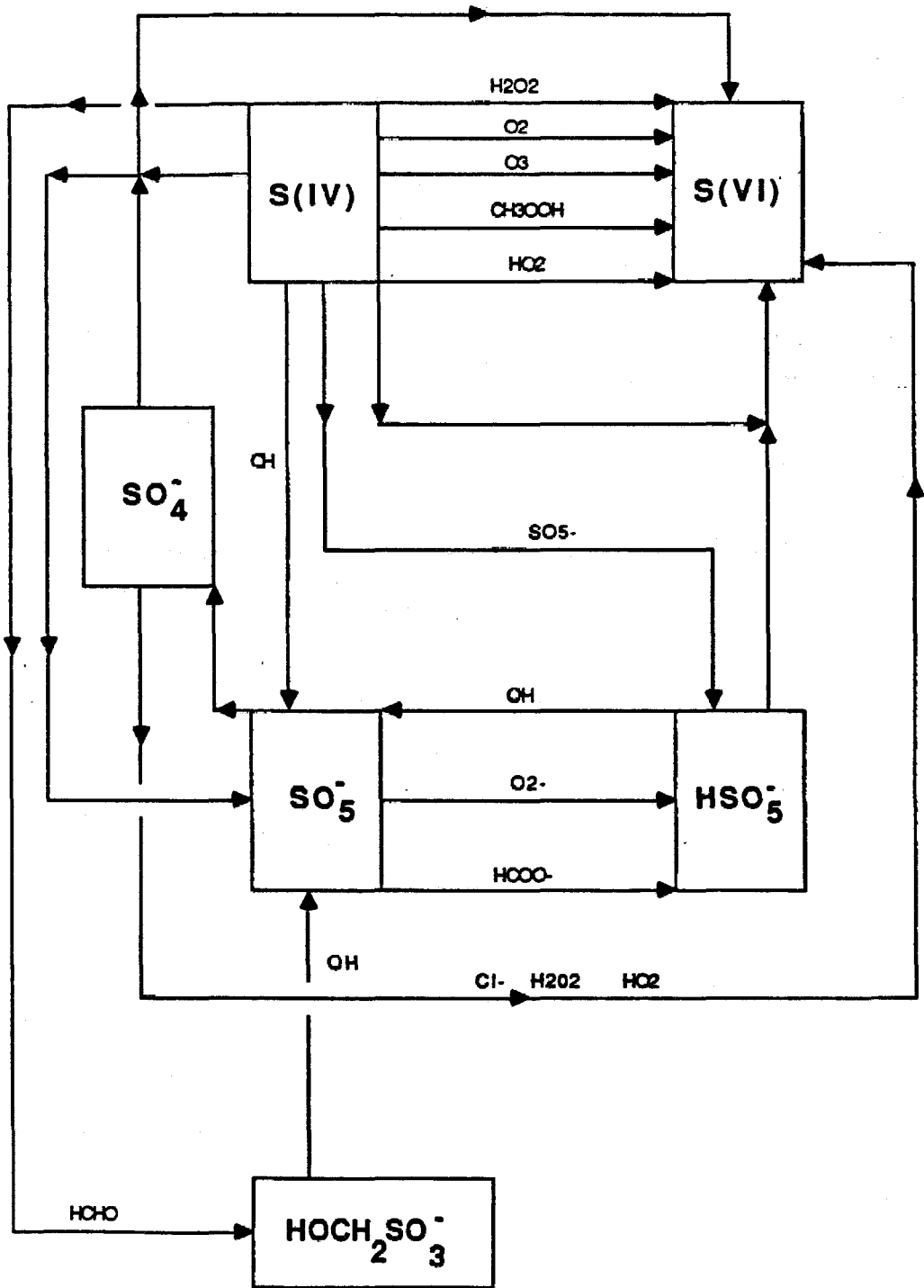


Figure 3. Main pathways for the sulfur reaction system.

TABLE 8. Dimensionless Sensitivity Coefficients for Nitrogen compounds at t=1800 s

Species	HNO ₃ (aq) ^a		PAN(aq) ^b		NO(aq) ^c		NO ₂ (aq) ^d	
	React.	Sens.Coeff.	React.	Sens.Coeff.	React.	Sens.Coeff.	React.	Sens.Coeff.
	44	-0.178(-3) ^e	62	-0.204(-4)	35	0.785(-6)	44	0.260(-2)
	62	0.215(-4)	98	-0.324(-6)	36	0.576(-6)	38	0.178(-3)
	73	-0.168(-5)	73	0.191(-6)	33	-0.183(-6)	104	-0.618(-4)
	40	0.772(-6)			73	-0.152(-6)	73	-0.517(-4)
	46	0.218(-6)			38	-0.209(-7)	42	0.482(-5)
	103	0.128(-6)					37	0.234(-5)

^a Dimensionless sensitivity coefficient for reaction *i* with reaction constant K_i :

$$\frac{\partial \ln[\text{HNO}_3(\text{aq})]}{\partial \ln K_i}$$

^b Dimensionless sensitivity coefficient for reaction *i* with reaction constant K_i :

$$\frac{\partial \ln[\text{PAN}(\text{aq})]}{\partial \ln K_i}$$

^c Dimensionless sensitivity coefficient for reaction *i* with reaction constant K_i :

$$\frac{\partial \ln[\text{NO}(\text{aq})]}{\partial \ln K_i}$$

^d Dimensionless sensitivity coefficient for reaction *i* with reaction constant K_i :

$$\frac{\partial \ln[\text{NO}_2(\text{aq})]}{\partial \ln K_i}$$

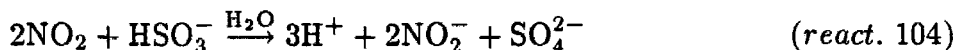
^e Read -0.178(-3) as -0.178×10^{-3} .

concentration under any circumstances. The dominant pathway for determining the aqueous-phase HNO_3 concentration is scavenging of nitric acid from the gas phase.

In the present mechanism (Table 3) there are two aqueous-phase reactions of PAN, its decomposition to NO_3^- (reaction 62) and the oxidation of S(IV) by PAN (reaction 98). Both reactions are found to be very slow and therefore do not influence the PAN(aq) concentration (Table 8). The rate of consumption of PAN by these reactions is about 0.004%/hr.

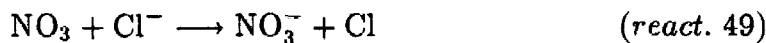
The results in Table 8 show that there is no reaction influencing NO(aq), which is just in Henry's law equilibrium with NO(g).

NO_2 also does not play an important role in the aqueous-phase chemistry (Table 8). The production of NO_2 by NO_3^- photolysis (reaction 44) occurs at about 0.5% NO_2 /hr. Reactions that consume NO_2 are also slow because of the low NO_2 solubility in the aqueous phase. The main one is the reaction with S(IV):



which consumes NO_2 at an average rate of 0.02%/hr.

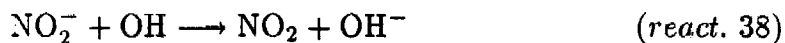
NO_3 is the only highly reactive nitrogen containing species in the aqueous phase. It is consumed rapidly by its reaction with Cl^- :



Additional reactions that consume NO_3 are those with HO_2 (reactions 46 and 47), with H_2O_2 (reaction 48) and with HSO_3^- (reaction 103). The lifetime (time for 99.9 % depletion) of NO_3 in our simulation was in the order of a few minutes.

NO_3 aqueous-phase chemistry may become much more important during the night and under the appropriate conditions NO_3 can constitute a relatively significant aqueous-phase source of NO_3^- [Chameides, 1986].

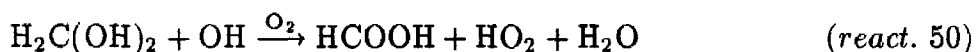
An important feature of HNO_2 is that as the cloudwater pH decreases, its solubility also decreases and it is transferred from the aqueous to the gas phase. Thus, the reactions that influence the $\text{HNO}_2(\text{aq})$ concentration are both those that involve HNO_2 and those that influence the cloudwater pH, such as reactions 73, 78 and 7. The main reaction involving HNO_2 is, under the present conditions, its attack by OH:



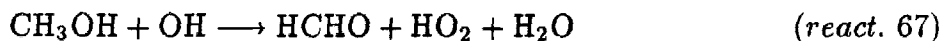
which consumes HNO_2 at an average rate of 0.9%/hr. Hence, the resulting change of $[\text{HNO}_2(\text{aq})]$ is small (the corresponding sensitivity coefficient is -0.02). Other slightly important reactions for HNO_2 include reaction 104, which is the main aqueous-phase source of HNO_2 , and reaction 40.

Formaldehyde and Formic Acid Chemistry

The main aqueous-phase reaction involving organic species is the attack of OH on the diol:



This reaction consumes 12% HCHO /hr and therefore we expect a small decrease in the concentration of $\text{HCHO}(\text{g})$ because of the presence of the cloud. The main aqueous-phase source of formaldehyde is the attack of OH on CH_3OH :



but this source is more than an order of magnitude less important for HCHO than reaction 50 (Table 9). An additional small sink for HCHO is reaction 106, while some sources of HCHO that under different conditions may play a small role are the reaction of CH_3OOH with OH (reaction 70), the photolysis of CH_3OOH (reaction 65), and the reaction of CH_3OH with SO_4^- (reaction 102).

TABLE 9. Dimensionless Sensitivity Coefficients for HCHO(aq)^a

Time	100 sec		400 sec		800 sec		1800 sec	
	React.	Sens.Coef.	React.	Sens.Coef.	React.	Sens.Coef.	React.	Sens.Coef.
	50	-0.243(-1) ^b	50	-0.357(-1)	50	-0.429(-1)	50	-0.559(-1)
	13	-0.417(-2)	13	-0.531(-2)	13	-0.628(-2)	13	-0.684(-2)
	67	0.558(-3)	67	0.857(-3)	67	0.103(-2)	67	0.134(-2)
	106	-0.381(-4)	106	-0.541(-4)	106	-0.627(-4)	106	-0.761(-4)
	70	0.321(-4)	70	0.467(-4)	70	0.561(-4)	70	0.732(-4)
	102	0.297(-5)	102	0.351(-5)	102	0.375(-5)	65	0.779(-5)

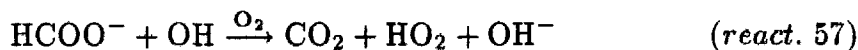
^a Dimensionless sensitivity coefficient for reaction *i* with reaction constant K_i :

$$\frac{\partial \ln[\text{HCHO(aq)}]}{\partial \ln K_i}$$

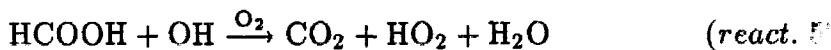
^b Read -0.243(-1) as -0.243×10^{-1} .

Reaction 50 is primarily responsible for the production of formic acid in the aqueous-phase. The average rate of this reaction for the present pH range is 250% HCOOH/hr and therefore the presence of the cloud enhances the HCOOH(g) concentration. Reaction 73 causes a decrease of the pH and therefore results in a decrease of [HCOOH(aq)] (Table 10). In our case the effects of reaction 50 are stronger but the sensitivity coefficient of reaction 73 is of the same order of magnitude as that of reaction 50. Hence, in other cases (high SO₂(g) concentration) the effects of reaction 73 may dominate. As in the previous cases the [HCOOH(aq)] is influenced by the pH determining reactions such as 74, 7, 78, 72, etc.

The main aqueous-phase sink of HCOOH is its reaction with OH(aq):



and



Under the conditions considered here these reactions are two orders of magnitude less significant than reaction 50. The above two reactions can be considered as competitive with reaction 50 as they both consume OH. The ratio of the rate of reaction 50 (R50) over the sum of the rates of reactions 52 and 57 (R52+R57) can be expressed as a function of the pH and the ratio of the gas-phase pressures ($p_{\text{HCHO}}/p_{\text{HCOOH}}$) for a constant temperature. The ratio of the gas-phase pressures is under ordinary conditions (before cloud formation) higher than 10 and for all the pH of interest we expect a net production of formic acid.

Some additional sinks of formic acid include its reactions with SO₅⁻ (reaction 80) and SO₄⁻ (reaction 95). The remainder of the aqueous-phase sinks of HCOOH appear to be negligible.

Table 10. Dimensionless Sensitivity Coefficients for HCOOH(aq)^a

Time	100 sec		400 sec		800 sec		1800 sec	
	React.	Sens.Coef.	React.	Sens.Coef.	React.	Sens.Coef.	React.	Sens.Coef.
	50	0.495	50	0.589	50	0.629	50	0.682
	73	-0.829(-1) ^b	73	-0.174	73	-0.170	73	-0.123
	57	-0.425(-1)	57	-0.484(-1)	13	0.637(-1)	13	0.914(-1)
	13	0.361(-1)	13	0.425(-1)	57	-0.502(-1)	57	-0.515(-1)
	78	-0.194(-2)	7	-0.316(-2)	74	-0.367(-2)	74	-0.417(-2)
	7	-0.120(-2)	78	-0.245(-2)	7	-0.355(-2)	7	-0.339(-2)
	52	-0.795(-3)	74	-0.119(-2)	78	-0.210(-2)	78	-0.167(-2)
	72	-0.572(-3)	52	-0.109(-2)	52	-0.126(-2)	52	-0.158(-2)
	81	-0.411(-3)	82	-0.873(-3)	82	-0.872(-3)	76	-0.827(-3)
	82	-0.393(-3)	72	-0.723(-3)	76	-0.811(-3)	5	0.707(-3)
	74	-0.391(-3)	76	-0.683(-3)	5	0.616(-3)	82	-0.596(-3)
	76	-0.260(-3)	5	0.467(-3)	72	-0.613(-3)	67	0.519(-3)
	95	-0.221(-3)	18	-0.376(-3)	18	-0.439(-3)	72	-0.466(-3)
	67	0.212(-3)	67	0.315(-3)	67	0.385(-3)	18	-0.442(-3)
	87	-0.196(-3)	80	-0.298(-3)	80	-0.354(-3)	80	-0.404(-3)
	80	-0.185(-3)	81	-0.284(-3)	20	0.326(-3)	20	0.338(-3)
	96	-0.148(-3)	20	0.270(-3)	99	-0.263(-3)	99	-0.291(-3)
	18	-0.138(-3)	95	-0.214(-3)	95	-0.202(-3)	95	-0.178(-3)

^a Dimensionless sensitivity coefficient for reaction *i* with reaction constant *K_i*:

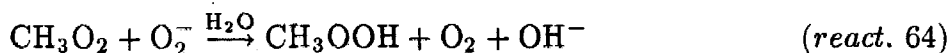
$$\frac{\partial \ln[\text{HCOOH(aq)}]}{\partial \ln K_i}$$

^b Read -0.829(-1) as -0.829×10^{-1} .

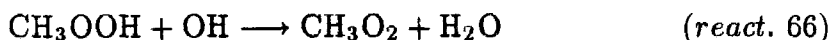
Other Organic Species

The main sink for methanol, CH_3OH , is its transformation to formaldehyde by OH (reaction 67), which occurs at a rate of 0.09% $\text{CH}_3\text{OH}/\text{hr}$. Since methanol is not produced in the aqueous-phase, one expects a very small decrease in the $\text{CH}_3\text{OH}(\text{g})$ because of the cloud's presence.

A moderate sink for CH_3OOH is the oxidation of $\text{S}(\text{IV})$ via reaction 99. The average rate of this reaction is 0.2% $\text{CH}_3\text{OOH}/\text{hr}$, a rate that is not particularly important for CH_3OOH under the present circumstances but may be influential in case of larger $\text{S}(\text{IV})$ concentrations. The main source for CH_3OOH is the reaction of CH_3O_2 with O_2^- :

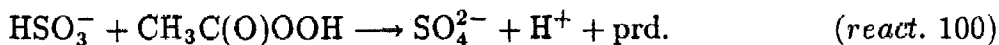


The main sink of CH_3O_2 is reaction 64, with an average rate of 0.5% $\text{CH}_3\text{O}_2/\text{hr}$. Its main aqueous phase source is its production by the attack of OH on CH_3OOH :



As both these reactions are of minor importance, (sensitivity coefficients less than 0.006) we do not expect a substantial change in $\text{CH}_3\text{O}_2(\text{g})$ concentration because of the aqueous-phase CH_3O_2 sinks.

The only reaction of $\text{CH}_3\text{C}(\text{O})\text{OOH}$ included in the mechanism is the oxidation of HSO_3^- :



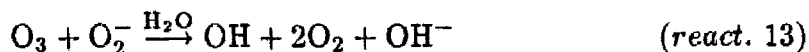
This reaction occurs with a rate of 0.7% $\text{CH}_3\text{C}(\text{O})\text{OOH}/\text{hr}$ and does not play a major role in the reaction system.

The carbonate radical ion is a highly reactive species. It is produced by the rapid reaction of HCO_3^- with O_2^- (reaction 18), the occurrence of which, as we noted,

is still a subject of discussion. The main sinks are first the reaction of CO_3^- with hydrogen peroxide (reaction 20) and second its reaction with O_2^- (reaction 19).

Oxygen and Hydrogen Chemistry

Ozone is not produced at all in the aqueous-phase but is consumed via 12 different reactions. Because of the small solubility of ozone, most of these reactions are too slow to influence $[\text{O}_3(\text{aq})]$ (Table 11). Its main aqueous-phase sink is its reaction with O_2^- :



Although the rate of this reaction is just 0.03 % O_3/hr , because of the small ozone solubility this rate results in a lifetime of $\text{O}_3(\text{aq})$ of the order of 1 s. The oxidation of S(IV) via reaction 72 decreases as pH decreases and therefore is an order of magnitude less important for ozone than reaction 13.

There are 16 reactions producing the hydroxyl radical, OH, and 19 consuming it. Its main sink is the reaction with the diol $\text{H}_2\text{C}(\text{OH})_2$ (reaction 50). Other sinks are the reactions with hydrogen peroxide (reaction 5), with HCOO^- (reaction 57) and with HSO_3^- (reaction 76). Moderate sinks are the reactions of OH with methanol (reaction 67) and HO_2 (reactions 3 and 4). The main aqueous-phase sources of OH are the reaction of O_2^- with ozone (reaction 13) and the photolysis of hydrogen peroxide (reaction 1). Secondary sources are the photolysis of NO_3^- (reaction 44) and the oxidation of S(IV) by HO_2 (reaction 101).

HO_2 is another highly reactive radical produced by 29 reactions and consumed by 22 reactions. The main aqueous-phase sources of HO_2 include reactions 50, 5, 20, 57, 67 and 29. Main sinks are reactions 13, 7, 18 and 78. Secondary sinks are reactions 3, 4 and 6.

TABLE 11. Dimensionless Sensitivity Coefficients for O₃(aq)^a

Time	100 sec		400 sec		800 sec		1800 sec	
	React.	Sens.Coef.	React.	Sens.Coef.	React.	Sens.Coef.	React.	Sens.Coef.
	13	-0.153(-3) ^b	13	-0.218(-3)	13	-0.251(-3)	13	-0.307(-3)
	72	-0.697(-5)	72	-0.140(-4)	72	-0.189(-4)	72	-0.245(-4)
	73	0.525(-6)	73	0.192(-5)	73	0.316(-5)	7	-0.216(-4)
	16	-0.130(-6)	16	-0.507(-6)	16	-0.930(-6)	16	-0.173(-5)
							11	-0.109(-6)

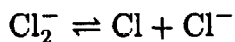
^a Dimensionless sensitivity coefficient for reaction *i* with reaction constant *K_i*:

$$\frac{\partial \ln[\text{O}_3(\text{aq})]}{\partial \ln K_i}$$

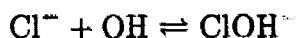
^b Read -0.153(-3) as -0.153×10^{-3} .

Chlorine Chemistry

Chlorine chemistry is characterised by various equilibria. First an equilibrium exists between two forms of radical chlorine [Jayson et al., 1973]:

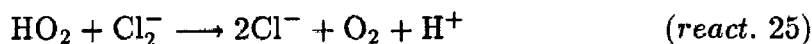


Reactions 21 and 22 result in an equilibrium between Cl^- and ClOH^- :



Because both reactions are quite fast, the equilibrium is established in our simulation in about 1s. Reactions 23 and 24 are relatively fast also and reach equilibrium after the first two minutes of simulation.

Using the above aqueous-phase equilibria, the reactions between Cl_2^- and HO_2 and O_2^- :



can be combined, the intermediate chlorine compounds can be eliminated and the net result is that reactions 25 and 26 constitute an alternate pathway for the reactions of HO_2 and O_2^- with OH^- :



Comparison of the rates of the above reactions at 298 K results in the following:

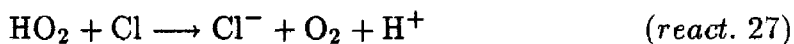
$$r_{25} = 5.3 \cdot 10^{13} [\text{Cl}^-]^2 [\text{H}^+] r_3 \quad \text{M/s}$$

and

$$r_{26} = 8.3 \cdot 10^{12} [\text{Cl}^-]^2 [\text{H}^+] r_4 \quad \text{M/s}$$

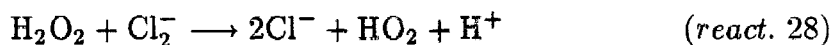
Thus the relative importance of these pairs of pathways depends on the pH and the concentration of Cl^- . For our simulation the maximum value of $[\text{H}^+]$ is $200 \mu\text{M}$ and that of $[\text{Cl}^-]$ $60 \mu\text{M}$. For these values the pathway starting with reaction 25 can be one order of magnitude faster than reaction 3, and the pathway starting with reaction 26 one-half an order of magnitude faster than reaction 4. Reactions 3 and 4 are moderate sinks of HO_2 and so reactions 25 and 26, even if sometimes faster, are still of minor importance. The sensitivity coefficient of H_2O_2 to the reaction 25 after 1800 s is just -0.3×10^{-3} .

Using the same procedure as above, the reaction of Cl with HO_2 :



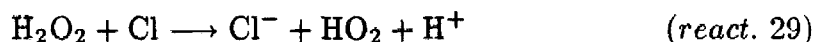
can be viewed as one more alternate pathway for reaction 3. The rate of reaction 27 in our case can be the most comparable to reaction 3 and therefore it is unimportant for HO_2 .

The reaction between H_2O_2 and Cl_2^- :



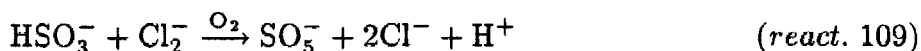
is an alternate pathway for the reaction of H_2O_2 and OH (reaction 5). The maximum rate of this pathway in our case is one order of magnitude less than the rate of the direct reaction 5 and therefore it is of minor importance for H_2O_2 . The sensitivity coefficient of H_2O_2 to this reaction after 1800 s is -0.4×10^{-3} .

Another alternate pathway for reaction 5 is the reaction of H_2O_2 with Cl :



Kinetic calculations show that the rate of this pathway can be at most 8 times faster than the direct pathway 5 and therefore reaction 29 is a relatively important sink of hydrogen peroxide even if it is less influential than reaction 5 (Table 5).

The oxidation reaction of S(IV) by Cl_2^- :



constitutes an additional pathway for the oxidation of S(IV) by OH (reactions 75 and 76). The kinetic calculations show that the rate of this reaction can be at most comparable to the rate of reaction 76 and therefore reaction 109 is only slightly important for S(IV).

The reactions of Cl^- with NO_3 (reaction 49) and SO_4^- (reaction 96) have already been discussed. Other reactions of chlorine species like reactions 30, 42 and 61 are quite slow.

Importance of Initial Gas and Aqueous-Phase Concentrations

The sensitivity coefficients for all the species with respect to all the initial gas phase concentrations as well as the initial aqueous-phase concentrations of S(VI), N(V), HCl and NH_3 have been calculated. This calculation serves a dual purpose. First it demonstrates quantitatively the dependence of the whole reaction process on the initial conditions used in this study and it provides further insight to the interaction between the two phases.

Effects on the S(IV) to S(VI) conversion

The major variables among the initial conditions influencing the sulfate concentration are the gas-phase concentrations of $\text{SO}_2(\text{g})$ and $\text{H}_2\text{O}_2(\text{g})$ (Table 12). The calculated dimensionless sensitivity coefficients are about 0.6. This result has an important consequence on the control of cloud acidity. Based on the calculated sensitivity coefficient if ambient levels of $\text{SO}_2(\text{g})$ are decreased by 10%, the sulfate concentration in cloudwater will approximately decrease by 6%. This important

TABLE 12

Dimensionless Sensitivity Coefficients for S(VI)(aq), N(V)(aq) and HSO₅⁻ to initial conditions

Time	100 sec		400 sec		800 sec		1200 sec	
	Species	Sens.Coef.	Species	Sens.Coef.	Species	Sens.Coef.	Species	Sens.Coef.
<i>S(VI)(aq)</i> ^a								
	[S(VI)] _o ^b	0.579	(SO ₂) _o ^c	0.664	(SO ₂) _o	0.681	(SO ₂) _o	0.672
	(SO ₂) _o	0.405	(H ₂ O ₂) _o	0.632	(H ₂ O ₂) _o	0.638	(H ₂ O ₂) _o	0.626
	(H ₂ O ₂) _o	0.381	[S(VI)] _o	0.287	[S(VI)] _o	0.189	[S(VI)] _o	0.159
	(HO ₂) _o	0.027	(NH ₃) _o	0.029	(HO ₂) _o	0.014	(HO ₂) _o	0.013
	(O ₃) _o	0.010	(HNO ₃) _o	-0.020	(OH) _o	0.010	(OH) _o	0.009
	(NH ₃) _o	0.007	(HCl) _o	-0.019	(NH ₃) _o	0.006	(O ₃) _o	0.002
	(HNO ₃) _o	-0.007	(HCO ₂) _o	0.018	(HNO ₃) _o	-0.003	(NH ₃) _o	0.002
	(HCl) _o	-0.006	(OH) _o	0.010	(O ₃) _o	0.003	(HNO ₃) _o	-0.001
	(OH) _o	0.005	(O ₃) _o	0.006	(HCl) _o	-0.002	(HCl) _o	-0.001
	(HCHO) _o	-0.004	(HCHO) _o	-0.002	(HCHO) _o	-0.001		
	[HCl] _o	-0.002	[HCl] _o	-0.001				
<i>N(V)(aq)</i> ^a								
	(HNO ₃) _o	0.966	(HNO ₃) _o	0.965	(HNO ₃) _o	0.965	(HNO ₃) _o	0.905
	[N(V)] _o	0.034	[N(V)] _o	0.034	[N(V)] _o	0.034	[N(V)] _o	0.034
							(PAN) _o	0.131(-4)
<i>HSO₅⁻(aq)</i> ^a								
	(NH ₃) _o	1.050	(HO ₂) _o	1.490	(HO ₂) _o	1.378	(HO ₂) _o	1.322
	(HNO ₃) _o	-0.970	(NH ₃) _o	1.066	(NH ₃) _o	1.067	(NH ₃) _o	1.061
	(HCl) _o	-0.898	(HNO ₃) _o	-0.984	(HNO ₃) _o	-0.986	(HNO ₃) _o	-0.980
	[S(VI)] _o	-0.652	(HCl) _o	-0.920	(HCl) _o	-0.922	(HCl) _o	-0.916
	(SO ₂) _o	0.464	[S(VI)] _o	-0.588	(OH) _o	0.674	(OH) _o	0.697
	[HCl] _o	-0.341	(HCHO) _o	-0.323	[S(VI)] _o	-0.565	[S(VI)] _o	-0.552
	(HCHO) _o	-0.331	[HCl] _o	-0.308	(HCHO) _o	-0.327	(SO ₂) _o	-0.356
	(HO ₂) _o	0.182	(OH) _o	0.301	[HCl] _o	-0.296	(HCHO) _o	-0.330
	(O ₃) _o	0.153	(O ₃) _o	0.186	(O ₃) _o	0.200	[HCl] _o	-0.289
	(H ₂ O ₂) _o	-0.129	(SO ₂) _o	0.177	(SO ₂) _o	-0.146	(O ₃) _o	0.207
	[N(V)] _o	-0.082	(H ₂ O ₂) _o	-0.149	(H ₂ O ₂) _o	-0.131	(H ₂ O ₂) _o	-0.090
	[NH ₃] _o	0.082	[N(V)] _o	-0.074	[N(V)] _o	-0.071	[N(V)] _o	-0.069
	(OH) _o	0.041	[NH ₃] _o	0.074	[NH ₃] _o	0.071	[NH ₃] _o	0.069

^a Dimensionless sensitivity coefficient of species I (concentration c_i) to the initial concentration of species J, c_{j0} :

$$\frac{\partial \ln c_i}{\partial \ln c_{j0}}$$

^b [I]_o is the initial aqueous-phase concentration of species I

^c (I)_o is the initial gas-phase concentration of species I.

feature of the reaction system can be explained considering the complicated interaction among the S(IV), S(VI) concentrations and the cloudwater pH [Chameides, 1982].

Species that directly affect the cloudwater pH determine to a large extent the [S(IV)(aq)] and therefore influence the sulfate formation. They include gases like $\text{NH}_3(\text{g})$, HNO_3 , HCl , and species that initially exist in cloudwater like SO_4^{2-} , Cl^- , NO_3^- and NH_4^+ (Table 14).

Additional species whose initial concentrations influence the sulfate formation include those that oxidize S(IV), like OH and O_3 , and species that produce $\text{H}_2\text{O}_2(\text{aq})$, like HO_2 . Formaldehyde is of some influence also as its reaction in the aqueous-phase with OH constitutes a major sink of $\text{OH}(\text{aq})$ and at the same time a major source of $\text{HO}_2(\text{aq})$.

Nitrogen Chemistry

The negligibly small sensitivity coefficients for all other species for nitrate (Table 12) show that the only pathway for nitric acid cloud acidity is the scavenging of the gaseous and aerosol phase nitric acid.

Formic acid and Formaldehyde chemistry

The conversion of formaldehyde to formic acid is relatively sensitive to the $\text{OH}(\text{g})$ concentration, to species that affect the $\text{OH}(\text{aq})$ concentration like ozone (because of reaction 13), and finally to species that influence the cloudwater pH (Table 13).

The concentration of formic acid in the aqueous-phase is much more sensitive to the various gas-phase concentrations than $[\text{HCHO}(\text{aq})]$ is. The hydroxyl radical concentration is once more of primary importance here with a sensitivity coefficient of about 0.6. As the aqueous-phase solubility of HCOOH is a strong function of pH,

TABLE 13
Sensitivity Coefficients for HCHO(aq) and HCOOH(aq) to initial conditions

Time	100 sec	400 sec	800 sec	1200 sec
	Species Sens.Coeff.	Species Sens.Coeff.	Species Sens.Coeff.	Species Sens.Coeff.
HCHO(aq) ^a				
	(HCHO) _o ^b 0.998	(HCHO) _o 0.996	(HCHO) _o 0.993	(HCHO) _o 0.990
	(O ₃) _o -0.016	(OH) _o -0.022	(OH) _o -0.040	(OH) _o -0.045
	(OH) _o -0.011	(O ₃) _o -0.016	(O ₃) _o -0.022	(O ₃) _o -0.024
	(HNO ₃) _o 0.005	(NH ₃) _o -0.009	(NH ₃) _o -0.011	(NH ₃) _o -0.012
	(HCl) _o 0.005	(HNO ₃) _o 0.008	(HNO ₃) _o 0.010	(HNO ₃) _o 0.011
	(NH ₃) _o -0.005	(HCl) _o 0.008	(HCl) _o 0.010	(HCl) _o 0.011
	(SO ₂) _o 0.004	(SO ₂) _o 0.006	(SO ₂) _o 0.008	(SO ₂) _o 0.009
	(H ₂ O ₂) _o 0.002	(H ₂ O ₂) _o 0.004	(H ₂ O ₂) _o 0.005	(H ₂ O ₂) _o 0.005
	[S(VI)] _o ^c 0.002	[S(VI)] _o 0.003	[S(VI)] _o 0.003	[S(VI)] _o 0.003
			(CH ₃ OH) _o 0.001	(CH ₃ OH) _o 0.001
HCOOH(aq) ^a				
	(NH ₃) _o 0.623	(NH ₃) _o 0.501	(OH) _o 0.601	(OH) _o 0.627
	(HNO ₃) _o -0.578	(HCOOH) _o 0.466	(HCOOH) _o 0.414	(HCOOH) _o 0.388
	(HCOOH) _o 0.569	(HNO ₃) _o -0.461	(NH ₃) _o 0.412	(O ₃) _o 0.385
	(HCl) _o -0.530	(HCl) _o -0.427	(HNO ₃) _o -0.377	(NH ₃) _o 0.379
	(O ₃) _o 0.248	(OH) _o 0.376	(O ₃) _o 0.369	(SO ₂) _o -0.377
	(HCHO) _o 0.211	(O ₃) _o 0.335	(SO ₂) _o -0.364	(HNO ₃) _o -0.346
	(SO ₂) _o -0.180	(SO ₂) _o -0.322	(HCl) _o -0.353	(HCl) _o -0.326
	[S(VI)] _o -0.168	(H ₂ O ₂) _o -0.274	(H ₂ O ₂) _o -0.295	(H ₂ O ₂) _o -0.293
	(H ₂ O ₂) _o -0.143	(HCHO) _o 0.247	(HCHO) _o 0.259	(HCHO) _o 0.263
	(OH) _o -0.095	[S(VI)] _o -0.134	[S(VI)] _o -0.110	[S(VI)] _o -0.101
	[HCl] _o -0.085	[HCl] _o -0.068	[HCl] _o -0.057	[HCl] _o -0.052
	[NH ₃] _o 0.021	[NH ₃] _o 0.017	[NH ₃] _o 0.014	[NH ₃] _o 0.014
	[N(V)] _o -0.021	[N(V)] _o -0.017	[N(V)] _o -0.014	[N(V)] _o -0.014
	(CH ₃ OH) _o -0.005	(CH ₃ OH) _o -0.006	(CH ₃ OH) _o -0.007	(CH ₃ OH) _o -0.008
	(HO ₂) _o -0.003	(HO ₂) _o -0.004	(HO ₂) _o -0.004	(HO ₂) _o -0.004

^a Dimensionless sensitivity coefficient of species I (concentration c_i) to the initial concentration of species J, c_{j0} :

$$\frac{\partial \ln c_i}{\partial \ln c_{j0}}$$

^b (I)_o is the initial gas-phase concentration of species I.

^c [I]_o is the initial aqueous-phase concentration of species I.

the influence of species like ammonia and nitric acid is important to $[\text{HCOOH}(\text{aq})]$. The sensitivity of the $\text{HCOOH}(\text{aq})$ concentration to the $\text{HCOOH}(\text{g})$ concentration decreases rapidly so that one expects that after sufficient time the aqueous-phase concentration will be almost independent of the initial gas-phase concentration of HCOOH (Table 13).

HSO_5^- Since the fate of HSO_5^- is a strong function of pH, the $\text{HSO}_5^-(\text{aq})$ concentration is found to depend on the concentrations of ammonia, nitric acid, etc. Decrease of the pH, or increase of $\text{HNO}_3(\text{g})$ and $\text{HCl}(\text{g})$ results in a dramatic drop of the HSO_5^- aqueous-phase concentration (Table 12).

Liquid Water Content w_L

The liquid water content is one of the important input parameters of a cloud-chemistry model [Chameides, 1982]. Typical values of w_L are $10^{-7} - 10^{-6}$ (1 water/ 1 air) for clouds and $5 \times 10^{-8} - 5 \times 10^{-7}$ (1 water/ 1 air) for fogs [Pruppacher, 1980]. In our simulation a value of 4×10^{-7} (1 water/ 1 air) has been used.

In order to investigate the importance of w_L on the whole system, we have calculated the sensitivity coefficients of all species in both phases with respect to w_L . We shall restrict ourselves here to the importance of w_L on the sulfate and formic acid formation.

Since a change of w_L represents a change of the amount of the aqueous-phase, it is crucial to calculate not only the sensitivity of the $\text{S}(\text{IV})(\text{aq})$ and $\text{S}(\text{VI})(\text{aq})$ concentrations to w_L but also to examine how the total sulfate, $\text{S}(\text{VI})_{\text{tot}}$ and the total $\text{S}(\text{IV})_{\text{tot}}$ in the system vary with w_L (Table 14).

Increase of the cloud liquid water content has as its main effect the dissolution of larger quantities of $\text{SO}_2(\text{g})$ in the aqueous-phase and therefore increase of the $\text{S}(\text{IV})$ amount available to be oxidized. Thus the total sulfate increases with increasing

Table 14.

Dimensionless Sensitivity Coefficients to the Water Liquid Content w_L ^a

Species	400 sec	800 sec	1200 sec	3600 sec
S(IV)(aq)	0.707	0.607	0.544	0.435
S(VI)(aq)	-0.698	-0.748	-0.764	-0.874
S(IV) _{tot}	-0.126	-0.187	-0.232	-0.361
S(VI) _{tot}	0.302	0.252	0.236	0.126
HCOOH(g)	0.052	0.101	0.127	0.231
HSO ₅ ⁻ (aq)	0.994	0.896	0.861	0.841

^a Dimensionless sensitivity coefficient for species I with concentration c_i :

$$\frac{\partial \ln c_i}{\partial \ln w_l}$$

w_L and the total S(IV) actually decreases. But as increased w_L results in higher dilution, the concentration of S(VI) is found to decrease, even if the global amount of sulfate increases. This higher dilution results in a pH increase and increase of the S(IV)(aq) concentration. Summarizing, an increase of w_L results in an increase of the S(IV)(aq) concentration but decrease of the total amount of S(IV), decrease of the sulfate concentration but increase of the total sulfate amount and finally to a pH increase (sensitivity coefficient for the H^+ concentration is -0.7).

The above results demonstrate the importance of the liquid water content. Using the above sensitivity coefficients as an approximation, we can extrapolate and predict that for an increase of w_L from 4×10^{-7} to 1.3×10^{-6} (1 water/ 1 air), a change that is possible inside the same cloud [Pruppacher, 1980], the sulfate produced after one hour will increase by 30%.

Since the increase of the liquid water content results in an important pH increase, it influences all the pH-sensitive species. For example, $[HSO_5^-]$ will increase rapidly (Table 14) with increasing w_L .

The production of formic acid is enhanced by the increase of the liquid water content (Table 14) as the sensitivity coefficient of $HCOOH(g)$ to w_L is 0.23 after the first hour. This increase can be explained by the pH increase and the subsequent increase of the aqueous-phase OH production rate.

Accommodation Coefficient and Droplet Radius

The sensitivity coefficients of some key species with respect to the accommodation coefficient a_w and the droplet radius α are shown in Table 15. The same accommodation coefficient for all the species has been used in the above calculation.

Our results are consistent with the predictions of Jacob [1986], Schwartz [1984] and Chameides [1984]. When a_w is in the order of 0.01, as in our case, the interfacial

TABLE 15. Dimensionless Sensitivity Coefficients to a_w and the Radius α

Species	100 sec	400 sec	1200 sec	3600 sec
<i>Accommodation coefficient a_w ^a</i>				
S(VI)(aq)	0.007	0.005	0.003	0.002
H ₂ O ₂ (aq)	0.003	0.004	0.006	0.008
OH(aq)	0.063	0.081	0.101	0.187
HO ₂ (aq)	0.022	0.014	0.010	0.014
HCOOH(g)	0.005	0.013	0.014	0.018
<i>Droplet radius α ^b</i>				
S(VI)(aq)	-0.010	-0.008	-0.005	-0.003
H ₂ O ₂ (aq)	-0.004	-0.006	-0.010	-0.012
OH(aq)	-0.095	-0.122	-0.154	-0.281
HO ₂ (aq)	-0.033	-0.021	-0.015	-0.020
HCOOH(g)	-0.008	-0.021	-0.022	-0.028

^a Dimensionless sensitivity coefficient of species I with concentration c_i :

$$\frac{\partial \ln c_i}{\partial \ln a_w}$$

^b Dimensionless sensitivity coefficient of species I with concentration c_i :

$$\frac{\partial \ln c_i}{\partial \ln \alpha}$$

mass transport does not substantially influence the concentrations of most species in our reaction system. The increase of a_w has as its main effect the acceleration of the transfer of the OH and HO₂ radicals from the gas to the aqueous-phase. Therefore, the production of HCOOH and H₂O₂ increases in the aqueous phase. The positive contribution of this increase to the conversion of S(IV) to S(VI) appears to be very small for this range of a_w . Species like HCHO(aq), HNO₃(aq), NH₃(aq), that for the present a_w reach Henry's law equilibria in a few minutes [Jacob, 1985], are not influenced at all by a_w , at least after this equilibration period.

Increase of cloud droplet radius has exactly the same effects as decrease of the accommodation coefficient, that is decrease of the mass-transfer rate between the gas and the aqueous-phase. The corresponding sensitivity coefficients, calculated for the present case, are larger than the coefficients for a_w and exactly the opposite phenomena are observed.

Temperature Effects

The temperature influences the reaction system in various ways. A change of temperature results in changes in the cloud water liquid content w_L , in the rate of the gas-phase reactions, in the rate of mass transport between the two phases, in the solubilities of the species in the aqueous-phase, in the rate of the reactions in the aqueous-phase, etc. Our study of the temperature effects will be necessarily preliminary not only because of the restrictions of our model (w_L independent of temperature, no gas-phase reactions), but additionally because of the uncertainties on the temperature dependence of the various reaction, Henry's law, equilibria, etc., constants.

We have studied four cases for different temperatures and the results after one hour of simulation are presented in Table 16. A temperature decrease mainly results

TABLE 16. Concentrations of Various Species After 1 hr for Different Temperatures

Species	298°K	283°K	273°K	263°K
pH	3.71	3.69	3.69	3.69
S(IV)(aq) (μM)	0.025	0.050	0.090	0.191
S(VI)(aq) (μM)	75.1	75.7	80.2	80.3
H ₂ O ₂ (aq) (μM)	13.5	15.6	25.1	30.7
HCOOH(aq) (μM)	0.161	0.423	0.708	1.71
SO ₂ (g) (mol/l)	1.31(-10) ^a	1.29(-10)	1.10(-10)	1.10(-10)
H ₂ O ₂ (g) (mol/l)	7.51(-12)	2.72(-12)	1.96(-12)	1.00(-12)
HCOOH(g) (mol/l)	1.00(-13)	1.01(-13)	1.03(-13)	1.05(-13)
(HCOOH) _{tot} (mol/l)	1.64(-13)	2.70(-13)	3.86(-13)	7.89(-13)

^a Read 1.31(-10) as 1.31×10^{-10} .

in the increase of the solubility of the gas-phase species in the aqueous-phase and at the same time in the decrease of the rates of the aqueous-phase reactions. As it can be seen in Table 16 these effects almost cancel each other resulting in the same pH, sulfate concentration and HCOOH(g) concentrations. Additionally, the S(IV)(aq), H₂O₂(aq), HCOOH(aq) concentrations increase substantially if temperature decreases.

Condensed Mechanism

The sensitivity analysis has shown that 48 reactions in the mechanism are completely unimportant under the initial conditions studied. The corresponding dimensionless sensitivity coefficients are less than 10⁻⁵. Therefore, it is possible to propose a condensed mechanism consisting of the following reactions:

Oxygen-Hydrogen Chemistry: 1, 3, 4, 5, 6, 7, 13, 16.

Carbonate Chemistry: 17, 18 (if the reaction rate in Table 3 is correct), 19, 20.

Chlorine Chemistry: 21, 22, 23, 24, 25, 26, 28, 29.

Nitrogen Chemistry: 38, 40, 44, 47, 49.

CH₄ Oxidation Chemistry: 50, 52, 57, 60, 61, 62, 63, 64, 66, 67, 70.

Sulfur Chemistry: 72, 73, 74, 75, 76, 77, 78, 80, 81, 82, 83, 87, 89, 90, 92, 93, 95, 96, 99, 100, 101, 104, 106, 108, 109.

The results of a simulation, for the initial conditions of Table 1, using the above simplified reaction mechanism, differ by only the numerical error from the results of the full mechanism of Table 3. Because the above mechanism has been derived by local sensitivity analysis, its validity cannot be guaranteed very far from the conditions used in this study. Even if the condensed mechanism has been tested for several additional sets of conditions (with pH < 6) and the results were again within numerical error from the results of the full mechanism, caution should be employed

before its use for conditions very different than ours.

Comparison of the DDM with the Indirect Method

In order to check the accuracy of the results obtained using the Direct Decoupled Method, we have calculated several sensitivity coefficients using the Indirect Method. For the latter we have employed the simple one sided difference formula:

$$s_{ij} = \frac{\partial y_i}{\partial \lambda_j} \Big|_{\lambda_k} \approx \frac{y_i(\lambda_j + \Delta\lambda_j; \lambda_k \ j \neq k) - y_i(\lambda_j; \lambda_k \ j \neq k)}{\Delta\lambda_j} \quad (5.1)$$

and in nondimensionalized form:

$$\bar{s}_{ij} = \frac{\lambda_j}{y_i} \frac{\partial y_i}{\partial \lambda_j} \Big|_{\lambda_k} \approx \frac{1}{\delta} \frac{y_i(\lambda_j + \Delta\lambda_j; \lambda_k \ j \neq k) - y_i(\lambda_j; \lambda_k \ j \neq k)}{y_i(\lambda_j; \lambda_k \ j \neq k)} \quad (5.2)$$

where $\delta = \Delta\lambda_j/\lambda_j$.

Another alternative is the use of a centered difference formula instead of formula (5.2).

$$\bar{s}_{ij} = \frac{\lambda_j}{y_i} \frac{\partial y_i}{\partial \lambda_j} \Big|_{\lambda_k} \approx \frac{1}{2\delta} \frac{y_i(\lambda_j + \Delta\lambda_j; \lambda_k \ j \neq k) - y_i(\lambda_j - \Delta\lambda_j; \lambda_k \ j \neq k)}{y_i(\lambda_j; \lambda_k \ j \neq k)} \quad (5.3)$$

One of the main disadvantages of the indirect method is that cancellation can occur in the numerator of formula (5.2). In our calculation only the first three or four digits appear free of round-off error. Hence for small δ 's some of the sensitivity coefficients calculated with the indirect method are inaccurate because of the round-off error in the y_i 's. If we attempt to use a larger δ , the finite difference approximation becomes progressively inaccurate. We have found that in this case the indirect method gives usually unreliable results if $\bar{s}_{ij} \leq 0.001$. As some of the sensitivity coefficients are large and some small, it is impossible to compute all of them accurately with one choice of δ [Dunker, 1980]. In our calculations we have used $\delta = 0.05$ and for some small sensitivity coefficients (≤ 0.005) $\delta = 0.5$.

TABLE 17. Comparison of Sensitivity Analysis Methods

Time	100 sec		400 sec		1100 sec	
	DDM	Indirect	DDM	Indirect	DDM	Indirect
<i>Reaction 73^a</i>						
S(IV) (aq)	-0.211	-0.210	-0.518	-0.517	-0.723	-0.693
S(VI) (aq)	0.361	0.353	0.522	0.543	0.463	0.446
N(III) (aq)	-0.125	-0.127	-0.258	-0.245	-0.247	-0.238
H ₂ O ₂ (aq)	-0.060	-0.058	-0.203	-0.201	0.410	-0.405
HCOOH (aq)	-0.088	-0.102	-0.174	-0.116	-0.155	-0.175
NH ₃ (aq)	0.001	0.001	0.002	0.003	0.002	0.003
HSO ₅ ⁻ (aq)	-0.020	-0.078	-0.012	-0.069	0.107	0.043
HOCH ₂ SO ₃ ⁻ (aq)	-0.095	-0.087	-0.291	-0.340	-0.456	-0.440
SO ₂ (g)	-0.053	-0.051	-0.203	-0.204	-0.406	-0.393
HNO ₃ (g)	≤ 0.001		0.304	0.306	0.318	0.319
H ₂ O ₂ (g)	-0.051	-0.049	-0.197	-0.198	-0.406	-0.389
NH ₃ (g)	-0.104	-0.130	-0.302	-0.302	-0.316	-0.310
<i>Reaction 50^b</i>						
HCHO (aq)	-0.024	-0.025	-0.036	-0.041	-0.047	-0.057
HCOOH (aq)	0.495	0.512	0.588	0.612	0.649	0.697
HCHO (g)	-0.023	-0.023	-0.035	-0.040	-0.047	-0.057
HCOOH (g)	0.480	0.498	0.586	0.629	0.648	0.698
<i>Reaction 74^c</i>						
S(IV) (aq)	-0.0009	-0.0008	-0.0036	-0.0034	-0.018	-0.019
S(VI) (aq)	.0017	.0016	.0036	.0032	0.012	0.012
N(III) (aq)	-0.0005	-0.0005	-0.0017	-0.0015	-0.0063	-0.0061
SO ₂ (g)	-0.0023	-0.0021	-0.0017	-0.0012	-0.0101	-0.0106
HNO ₃ (g)	≤ 0.0001		.0017	.0016	0.0081	.0077

^a Dimensionless sensitivity coefficient of species *i* with concentration *c_i* to reaction 73:

$$\frac{\partial \ln c_i}{\partial \ln K_{73}}$$

^b Dimensionless sensitivity coefficient of species *i* with concentration *c_i* to reaction 50:

$$\frac{\partial \ln c_i}{\partial \ln K_{50}}$$

^c Dimensionless sensitivity coefficient of species *i* with concentration *c_i* to reaction 74:

$$\frac{\partial \ln c_i}{\partial \ln K_{74}}$$

Results obtained by both methods are shown in Table 17. The results appear to be in very good agreement. One main advantage of the DDM is that the sensitivity coefficients are calculated exactly. If T is the time required for the execution of one simulation, the calculation of our 150 sensitivity coefficients costs $151 T$ using the Indirect Method with one sided differences and $300 T$ using the numerically better centered differences. Use of the DDM requires $11 T$ for four sensitivity coefficients and $39 T$ for the calculation of the whole set of 150. The DDM is expected to perform even better for smaller Jacobians [Dunker, 1980].

Conclusions

A sensitivity analysis of a comprehensive chemical mechanism for aqueous-phase atmospheric chemistry has been performed, using the Direct Decoupled Method (DDM). The dominant reaction throughout the simulation is the oxidation of S(IV) by H_2O_2 . Other important oxidation pathways for S(IV) include reactions with O_2 (catalysed by Fe^{3+} and Mn^{2+}), with OH to produce SO_5^- , with ozone, and with HSO_5^- . Reactions that produce or consume H_2O_2 influence the conversion of S(IV) to S(VI) directly and to a large extent. Such reactions are the production of H_2O_2 in the aqueous-phase by HO_2 , the reaction of H_2O_2 with OH, and the reaction of the superoxide ion with bicarbonate ion. The concentration of peroxymonosulfate is found to be a strong function of pH.

The rate of all the aqueous-phase reactions for nitric acid, NO and NO_2 are too small to influence their aqueous-phase concentrations. Therefore, the dominant pathway for the HNO_3 acidity is scavenging of nitric acid from the gas phase.

The presence of a cloud enhances the production of formic acid. Formaldehyde reacts with OH to produce HCOOH which (at least for pH less than 5) is transferred to the gas-phase. This reaction is more important for $\text{HCOOH}(\text{g})$ than for

HCHO(g). The main aqueous-phase sink for HCOOH is its reaction with OH.

The initial gas-phase concentrations of SO₂, H₂O₂, HO₂, OH, O₃, HCHO, NH₃, HNO₃, HCl and the initial aqueous-phase concentrations of S(VI), N(V), NH₃ and HCl are the initial conditions of primary importance for the reaction system.

The liquid water content is one of the most important parameters of the mechanism. Increase of w_L results in an increase of the S(IV)(aq) concentration but decrease of the total amount of S(IV), decrease of the sulfate concentration but increase of the total sulfate amount.

For the value of the accommodation coefficient used in this study ($a_w=0.01$), the rates of the aqueous-phase reactions are not substantially limited by interfacial or gas-phase mass-transport. Therefore, the importance of the accommodation coefficient and the average droplet radius is small. The temperature has opposite effects on the solubility of the various species and on the reaction constants. The net result is a small temperature influence.

Acknowledgement

This work was supported by State of California Air Resources Board Agreement A732-043.

References

- Anbar, M., and P. Neta, A compilation of specific bimolecular rate constants for the reactions of hydrated electrons, hydrogen atoms and hydroxyl radicals with inorganic and organic compounds in aqueous solution, *Int. J. Appl. Radiat. Isot.*, 18, 493-523, 1967.
- Behar, D., G. Czapski, and I. Duchovny, Carbonate radical in flash photolysis and pulse radiolysis of aqueous carbonate solutions, *J. Phys. Chem.*, 74, 2206-2210, 1970.

- Bielski, B. H. J., Reevaluation of the spectral and kinetic properties of HO₂ and O₂⁻ free radicals, *Photochem. Photobiol.*, 28, 645-649, 1978.
- Bothe, E., and D. Schulte-Frohlinde, Reaction of dihydroxymethyl radical with molecular oxygen in aqueous solution, *Z. Naturforsch. B, Anorg. Chem. Org. Chem.*, 35, 1035-1039, 1980.
- Boyce, S. D., and M. R. Hoffmann, Kinetics and mechanism of the formation of hydroxymethanesulfonic acid at low pH, *J. Phys. Chem.*, 88, 4740-4746, 1984.
- Chameides, W. L., and D. D. Davis, The free-radical chemistry of cloud droplets and its impact upon the composition of rain, *J. Geophys. Res.*, 87:4863-4877, 1982.
- Chameides, W. L., The photochemistry of a marine stratiform cloud, *J. Geophys. Res.*, 89:4739-4755, 1984.
- Chameides, W. L., Possible role of NO₃ in the nighttime chemistry of a cloud, *J. Geophys. Res.*, 91:5331-5337, 1986.
- Chen, S., V. W. Cope, and M. Z. Hoffman, Behavior of CO₃⁻ radicals generated in the flash photolysis of carbonatoamines complexes of cobalt(III) in aqueous solution, *J. Phys. Chem.*, 77, 1111-1116, 1973.
- Cho, S., and G. R. Carmichael, Sensitivity analysis of the role of free radical, organic and transition metal reactions in sulfate production in clouds, *Atmos. Environ.*, 20, 10, 1959-1968, 1986.
- Christensen, H., K. Sehested, and H. Corfitzen, Reactions of hydroxyl radicals with hydrogen peroxide at ambient and elevated temperatures, *J. Phys. Chem.*, 86, 1588-1590, 1982.
- Clarke, A. G., and M. Radojevic, Oxidation of SO₂ in rainwater and its role in acid rain chemistry, *Atmos. Environ.*, 21, 1115-1123, 1987.
- Cukier R. I., H. B. Levine and K. E. Shuler, Nonlinear Sensitivity analysis of Multi-

Parameter Model Systems, *J. Comp. Phys.*, 26, 1-42, 1978.

Damschen, D. E., and L. R. Martin, Aqueous aerosol oxidation of nitrous acid by O_2 , O_3 , and H_2O_2 , *Atmos. Environ.*, 17, 2005-2011, 1983.

Dickinson, R. P., and Gelinas R. J., Sensitivity analysis of ordinary differential equation systems—a direct method *J. Comp. Phys.*, 21,123-143, 1976.

Dogliotti, L., and E. Hayon, Flash photolysis of persulfate ions in aqueous solutions. Study of the sulfate and ozonide radical ions, *J. Phys. Chem.*, 71, 2511-2516, 1967.

Dougherty, E. P., Hwang J. T., and Rabitz H., Further developments and applications of the Green's function method of sensitivity analysis in chemical kinetics, *J. Chem. Phys.*, 71, 1794-1808, 1979.

Dougherty, E. P., and Rabitz H., Computational kinetics and sensitivity analysis of hydrogen-oxygen combustion, *J. Chem. Phys.*, 72, 6571-6586, 1980.

Dunker, A. M., The response of an atmospheric reaction-transport model to changes in input functions, *Atmos. Environ.*, 14, 671-678, 1980.

Dunker, A. M., The decoupled direct method for calculating sensitivity coefficients in chemical kinetics. *J. Chem. Phys.*, 81, 2385-2393, 1984.

Falls, A. H., G. J. McRae , and J. H. Seinfeld, Sensitivity and uncertainty of reaction mechanisms for photochemical air pollution, *Int. J. Chem. Kinet.*, 11, 1137-1162, 1979.

Frank, P. M., Introduction to system Sensitivity Theory, Academic, New York, 1978.

Fuchs, N. A., and A. G. Sutugin, High-dispersed aerosols, in International Reviews of aerosol Physics and Chemistry, vol. 2, edited by G. M. Hidy and J. R. Brock, pp. 1-60, Pergamon, New York, 1971.

Gardner J. A., Watson L. R., Adewuyi Y. G., Davidovits P., Zahniser M. S.,

- Worsnop D. R., and C. E. Kolb, Measurement of the mass accommodation coefficient of $\text{SO}_2(\text{g})$ on water droplets. *J. Geophys. Res.*, 92, 10887-10895, 1987.
- Graedel, T. E., and C. J. Weschler, Chemistry within aqueous atmospheric aerosols and raindrops. *Rev. Geophys. Space Phys.*, 19:505-539, 1981.
- Graedel, T. E., and K. I. Goldberg, Kinetic studies of raindrop chemistry, 1. Inorganic and organic processes. *J. Geophys Res.*, 88C:10, 865-10, 882, 1983.
- Graedel, T. E., M. L. Mandich and C. J. Weschler, Kinetic model studies of atmospheric droplet chemistry 2. Homogeneous transition metal chemistry in raindrops, *J. Geophys Res.*, 91: 5205-5221, 1986.
- Gratzel, M., A. Henglein, and S. Taniguchi, Pulsradiolytische Beobachtungen über die Reduktion des NO_3^- -Ions und über Bildung und Zerfall der persalpetrigen Säure in wässriger Lösung, *Ber. Bundessenges. Phys. Chem.*, 74, 292-298, 1970.
- Hagesawa, K., and P. Neta, Rate constants and mechanisms of reaction for Cl_2^- radicals, *J. Phys. Chem.*, 82, 854-857, 1978.
- Hales, J. M., and D. R. Drewes, Solubility of ammonia in water at low concentrations, *Atmos. Environ.*, 13, 1133-1147, 1979.
- Havas, M., Hutchinson, T.C., and Likens, G.E., Red herrings in acid rain research, *Environ. Sci. Technol.*, 18, 176A-186A, 1984.
- Hoffmann, M. R., and S.D. Boyce, Catalytic Autoxidation of Aqueous Sulfur Dioxide in Relationship to Atmospheric Systems, *Adv. Environ. Sci. Tech.*, 12, 148-189, Wiley-Interscience, New York, 1983.
- Hoffmann, M. R., and J. G. Calvert, Chemical Transformation Modules for Eulerian Acid Deposition Models. Vol. 2 - The Aqueous-phase chemistry, U.S. Environmental Protection Agency, Research Triangle Park, North Carolina (EPA/600/3-85/017), 1985.

- Hoffmann, M. R., and D. J. Jacob, Kinetics and Mechanisms of the catalytic oxidation of dissolved sulfur dioxide in aqueous solution: an application to nighttime fog water chemistry, SO₂, NO and NO₂ Oxidation Mechanisms, edited by Calvert J. G., pp. 101-172, Butterworth, Boston, Mass., 1984.
- Hoigne, J., and H. Bader, Rate constants of reactions of ozone with organic and inorganic compounds in water, 1, Non-dissociating organic compounds, *Water Res.*, 17, 173-183, 1983a.
- Hoigne, J., and H. Bader, Rate constants of reactions of ozone with organic and inorganic compounds in water, 2, Dissociating organic compounds, *Water Res.*, 17, 185-194, 1983b.
- Huie, R. E., and P. Neta, Chemical behavior of SO₃⁻ and SO₅⁻ radicals in aqueous solutions, *J. Phys. Chem.*, 88, 5665-5669, 1984.
- Huie, R. E., and P. Neta, Rate constants for some oxidations of S(IV) by radicals in aqueous solutions, *Atmos. Environ.*, 21, 8, 1743-1747, 1987.
- Jacob, D. J., and M. R. Hoffmann, A dynamic model for the production of H⁺, NO₃⁻, and SO₄²⁻, in urban fog, *J. Geophys. Res.*, 88, 6611-6621, 1983.
- Jacob, D. J., Comment on "The photochemistry of a remote marine stratiform cloud" by William L. Chameides, *J. Geophys. Res.*, 90, 5864, 1985.
- Jacob, D. J., Chemistry of OH in remote clouds and its role in the production of formic acid and peroxymonosulfate, *J. Geophys. Res.*, 91 (D9), 9807-9826, 1986.
- Jayson, G. G., B. J. Parsons, and A. J. Swallow, Some simple, highly reactive, inorganic chlorine derivatives in aqueous-solution, *Trans. Farad. Soc.*, 69, 1597-1607, 1973.
- Koda M., Dogru A. H., and J. H. Seinfeld, Sensitivity analysis of partial differential equations with application to reaction and diffusion processes, *J. Comp. Phys.*,

30, 259-282, 1979.

Kozac-Channing, L. F., and G. R. Heltz, Solubility of ozone in aqueous solutions of 0-0.6 M ionic strength at 5-30°C, *Environ. Sci. Technol.*, 17(3), 145-149, 1983.

Latimer, W. M., *The Oxidation States of the Elements and Their Potentials in Aqueous Solutions*, Prentice-Hall, New York, pp. 70-89, 1952.

Ledbury, W., and E. W. Blair, The partial formaldehyde vapour pressure of aqueous solutions of formaldehyde, Part II, *J. Chem. Soc.*, 127, 2832-2839, 1925.

Lee, Y-N, Kinetics of oxidation of aqueous sulfur(IV) by nitrogen dioxide, in *Precipitation Scavenging, Dry Deposition, and Resuspension, Volume I*, H. R. Pruppacher, R. G. Semonin, and W. G. N. Slinn, eds., Elsevier, New York, 1983.

Lee, Y-N, Kinetics of some aqueous-phase reactions of peroxyacetyl Nitrate, in *Gas-Liquid Chemistry of Natural Waters, Vol. 1*, 21/1-21/7, Brookhaven National Laboratory (BNL 51757), 1984a.

Lee, Y-N, Atmospheric aqueous-phase reactions of nitrogen species, in *Gas-Liquid Chemistry of Natural Waters*, Brookhaven National Laboratory, 1984b.

Lee, Y-N, and J. A. Lind, Kinetics of aqueous-phase oxidation of nitrogen(III) by hydrogen peroxide, *J. Geophys. Res.*, 91(D2), 2793-2800, 1986.

Le Henaf, P., Methodes d'etude et proprietes des hydrates, hemiacetals et hemiacetals derives des aldehydes et des cetonas, *Bull. Soc. Chim. France*, 4687-4700, 1968.

Lilie, J., A. Henglein, and R. J. Haurahan, Reactions of the carbonate radical anion with organic and inorganic solutes in aqueous solution, presented at the 176th meeting of the American Chemical Society, Miami Beach, Florida, 1978.

Lind, J. A., and G. L. Kok, Henry's law determinations for aqueous solutions of

- hydrogen peroxide, methylhydroperoxide, and peroxyacetic acid, *J. Geophys. Res.*, 91(D7), 7889-7895, 1986.
- Marsh A. R. W., and W. J. McElroy, The dissociation constant and Henry's law constant of HCl in aqueous solution, *Atmos. Environ.*, 19, 1075-1080, 1985.
- Martin, L. R., and Damschen, D. E., Aqueous Oxidation of Sulfur Dioxide by Hydrogen Peroxide at low pH, *Atmos. Environ.*, 15, 1615-1622, 1981.
- Martin, L. R., Kinetic Studies of Sulfite Oxidation in Aqueous Solution, in SO₂, NO, and NO₂ Oxidation Mechanisms: Atmospheric Considerations, edited by Calvert J. G., pp. 63-100, Butterworth, Boston, Mass., 1984.
- Martin, L. R., and M. W. Hill, The iron catalysed oxidation of sulfur: recociliation of the literature rates, (preliminary communication), *Atmos. Environ.*, 6, 1487-1490, 1987.
- McArdle, J. V., and Hoffmann, M. R., Kinetics and Mechanism of the Oxidation of Aqueated Sulfur Dioxide by Hydrogen Peroxide at Low pH, *J. Phys. Chem.*, 87, 5425-5429, 1983.
- Mozurkewich, M., P. H. McMurry, A. Gupta, and J. G. Calvert, Mass accomodation coefficient for HO₂ radicals on aqueous particles, *J. Geophys. Res.*, 92, 4163-4170, 1987.
- Munger, J. W., C. Tiller, and M. R. Hoffmann, Identification of hydroxymethanesulfonate in fog water, *Science*, 231, 247-249, 1986.
- Oblath, S. B., S. S. Markowitz, T. Novakov, and S. G. Chang, Kinetics of the formation of hydroxylamine disulfonate by reaction of nitrite with sulfites, *J. Phys. Chem.*, 85, 1017-1021, 1981.
- Oran, E. S., and J.P. Boris, Numerical Simulation of reactive flow, Elsevier Science Publishing Co., Inc., New York, 1987.
- Perrin, D. D., Ionization Constants of Inorganic Acids and Bases in Aqueous Solu-

- tion, 2nd edition, Pergamon Press, New York, 1982.
- Pruppacher, H. R., and J. D. Klett, *Microphysics of Cloud and Precipitation*, D. Reidel, Dordrecht, The Netherlands, 1980.
- Rettich, T. R., Some photochemical reactions of aqueous nitric acid, *Diss. Abstr. Int. B.*, 38, 5968, 1978.
- Ross, A. B., and P. Neta, Rate constants for reactions of inorganic radicals in aqueous solution, U.S. Department of Commerce, Washington, D. C., (NSRDS-NBS 65), 1979.
- Schmidt, K. H., Electrical conductivity techniques for studying the kinetics of radiation-induced chemical reactions in aqueous solutions, *Int. J. Radiat. Phys. Chem.*, 4, 439-468, 1972.
- Schofield, C.L., Acid rain/fisheries, Proceedings International Symposium on Acidic Precipitation and Fishery impacts in Northeast North America, R.E. Johnson (Ed.), Ithaca, NY, 57-67, 1982.
- Scholes, G., and R. L. Willson, γ -radiolysis of aqueous thymine solutions. Determination of relative reaction rates of OH radicals, *Trans. Faraday Soc.*, 63, 2982-2993, 1967.
- Schwartz, S. E., Mass-transport considerations pertinent to aqueous-phase reactions of gases in liquid-water clouds, in *Chemistry of Multiphase Atmospheric Systems* (W. Jaeschke, ed.), Heidelberg: Springer, 415-471, 1986.
- Schwartz, S. E., Gas- and aqueous-phase chemistry of HO_2 in liquid water clouds. *J. Geophys. Res.*, 89, 11,589-11,598, 1984.
- Schwartz, S. E., and W. H. White, Solubility equilibrium of the nitrogen oxides and oxyacids in dilute aqueous solution, *Adv. Environ. Sci. Eng.*, 4, 1-45, 1981.
- Sehested, K., O. L. Rasmussen, and H. Fricke, Rate constants of OH with HO_2 , O_2^- , and H_2O_2^+ from hydrogen peroxide formation in pulse-irradiated oxygenated

- water, *J. Phys. Chem.*, 72, 626-631, 1968.
- Sehestad, K., J. Holcman, and E. J. Hart, Rate constants and products of the reactions of e_{aq}^- , O_2^- , and H with ozone in aqueous solutions, *J. Phys. Chem.*, 87, 1951-1954, 1983.
- Sehestad, K., J. Holcman, E. Bjergbakke, and E. J. Hart, A pulse radiolytic study of the reaction $OH + O_3$ in aqueous medium, *J. Phys. Chem.*, 88, 4144-4147, 1984.
- Seigneur, C., and P. Saxena, A study of atmospheric acid formation in different environments, *Atmos. Environ.*, 18:2109-2124, 1984.
- Seinfeld, J. H., *Atmospheric Chemistry and Physics of Air Pollution*, John Wiley, New York, 1986.
- Shapilov, O. D., and Y. L. Kostyukovskii, Reaction kinetics of hydrogen peroxide with formic acid in aqueous solutions, *Kinet. Katal.*, 15, 1065-1067, 1974.
- Smith, R. M., and A. E. Martell, *Critical Stability Constants*, Vol. 4: Inorganic Complexes, Plenum Press, New York, 1976.
- Snider, J. R., and G. A. Dawson, Tropospheric light alcohols, carbonyls, and acetonitrile: Concentrations in the southwestern United States and Henry's law data, *J. Geophys. Res.*, 90, 3797-3805, 1985.
- Sorensen, P. E., and V. S. Andersen, The formaldehyde-hydrogen sulphite system in alkaline aqueous solution: kinetics, mechanism, and equilibria, *Acta Chem. Scand.*, 24, 1301-1306, 1970.
- Staehelin, J., R. E. Buhler, and J. Hoigne, Ozone decomposition in water studied by pulse radiolysis, 2, OH, and HO_4 as chain intermediates, *J. Phys. Chem.*, 88, 5999-6004, 1984.
- Staehelin, J., and J. Hoigne, Decomposition of ozone in water: rate of initiation by hydroxide ions and hydrogen peroxide, *Environ. Sci. Technol.*, 16, 676-681,

1982.

Stolarski, R. S., Butler D. M., and R. D. Rundel, Uncertainty propagation in a stratospheric model, II. Monte Carlo analysis of Imprecision due to reaction rates, *J. Geophys. Res.*, 83(C6), 3074-3078, 1978.

Strehlow, H., and I. Wagner, Flash photolysis in aqueous nitrite solutions, *Z. Phys. Chem. Wiesbaden*, 132, 151-160, 1982.

Systems Applications, Inc., Development of a Comprehensive Chemistry Acid Deposition Model (CCADM) Volume I: Technical Document, SYSAPP-87/002, 1987.

Treinin, A., and E. Hayon, Absorption spectra and reaction kinetics of NO_2 , N_2O_3 , and N_2O_4 in aqueous solutions, *J. Am. Chem. Soc.*, 92, 5821-5828, 1970.

Weeks, J. L., and J. Rabani, The pulse radiolysis of deaerated aqueous carbonate solutions, I, Transient optical spectrum and mechanism; II, pK for OH radicals, *J. Phys. Chem.*, 70, 2100-2106, 1966.

Weinstein, J., and B. H. J. Bielski, Kinetics of the interaction of HO_2 and O_2^- radicals with hydrogen peroxide; the Haber-Weiss reaction, *J. Am. Chem. Soc.*, 101, 58-62, 1979.

Young, J.R., and F.W. Lurmann, ADOM/TADAP Model Development Program: Volume 7 - Aqueous Phase Chemistry. ERT Doc. No. P-B980-535, Environmental Research and Technology, Inc., Newbury Park, CA, 1984.

CHAPTER 3

**MATHEMATICAL MODELLING OF ACID DEPOSITION DUE TO
RADIATION FOG**

(Published in *Journal of Geophysical Research*, **94**, 12,911-12,923, 1989)

Mathematical Modeling of Acid Deposition Due to Radiation Fog

Spyros N. Pandis and John H. Seinfeld

*Department of Chemical Engineering and Environmental Quality Laboratory,
California Institute of Technology, Pasadena, CA 91125, USA*

Abstract

A Lagrangian model has been developed to study acidic deposition due to radiation fog. The model couples submodels describing the development and dissipation of radiation fog, the gas-phase chemistry and transfer and the aqueous-phase chemistry. The model is applied to a radiation fog episode in Bakersfield in the San Joaquin Valley of California over the period January 4-5, 1985. Model predictions for temperature profile, fog development, liquid water content, gas-phase concentrations of SO_2 , HNO_3 and NH_3 , pH, aqueous-phase concentrations of SO_4^{2-} , NH_4^+ and NO_3^- , and finally deposition rates of the above ions are compared with the observed values. The deposition rates of the major ions are predicted to increase significantly during the fog episode with the most notable being the increase of sulfate deposition. Pathways for sulfate production that are of secondary importance in a cloud environment may become significant in a fog. Expressing the mean droplet settling velocity as a function of the liquid water content is found to be quite influential in the model's predictions.

Introduction

The importance of acid fog as a component of the general acidic deposition phenomenon has recently been recognized. For example, Hoffmann and co-workers [Waldman et al., 1982; Munger et al., 1983; Jacob et al., 1985] have reported pH values of fogs in Southern California as low as 1.69. These fogs were much more acidic, and concentrations of anions and cations such as SO_4^{2-} , NO_3^- and NH_4^+ were higher by one to two orders of magnitude than in precipitation in the same areas. Field measurements have provided valuable information concerning the chemical composition of acid fog, but the physicochemical processes leading to this composition have yet to be elucidated.

Mathematical models describing atmospheric processes are a major tool in our effort first to understand and then to control acidic deposition. The first step in acidic deposition processes is the emission to the atmosphere of SO_2 and NO_x . SO_2 and NO_x can be oxidized in the atmosphere, yielding sulfuric and nitric acid vapors. Due to its very low vapor pressure, sulfuric acid is rapidly incorporated into aerosol particles, while nitric acid may be scavenged by particles or droplets or remain in the gas-phase. Inside a cloud or a fog, gas-phase species like SO_2 , HNO_3 , NH_3 , H_2O_2 , and aerosol particles are scavenged by water droplets resulting in a solution that can be significantly acidic. It was initially believed that the scavenging of these acids by cloud, fog and rain droplets was the major source of sulfuric and nitric acid observed in precipitation. It is now recognized that cloudwater and fogwater acidity may result not only from incorporation of strong acids present in clear air but also from aqueous-phase oxidation reactions, most notably oxidation of S(IV) to S(VI). Several analyses of aqueous-phase atmospheric chemistry have been performed using mechanisms of varying complexity [Graedel and Goldberg, 1983; Jacob and Hoffmann, 1983; Chameides, 1984; Seigneur and Saxena, 1984;

Schwartz, 1984; Jacob, 1986; Pandis and Seinfeld, 1989]. These studies are based on reaction mechanisms of the aqueous-phase chemistry in clouds or fog with or without gas-phase reactions, but with no treatment of cloud or fog dynamics. The importance of parameters such as amount of liquid water, the droplet lifetime, and the amount of polluted air mixed in the cloud system to the chemical composition of the aqueous-phase has been stressed in these studies.

Tremblay and Leighton [1984, 1986] developed a model of cloud dynamics with a simple treatment of cloud chemistry. Their initial one-dimensional model [1984] was later extended to a three-dimensional model [1986]. Walcek and Taylor [1986] used a one-dimensional steady-state cumulus cloud model with detailed aqueous but no gas-phase chemistry to study vertical distribution of acidity and sulfate production. Seigneur and Saxena [1988] presented a model with a simple treatment of cloud physics (updraft and precipitation) and detailed cloud chemistry and investigated sulfate formation in stratus and cumulus clouds. Several attempts have been made to model the life-cycle of radiation fog with no treatment of atmospheric chemistry [Fisher and Caplan, 1963; Zdunkowski and Nielsen, 1969; Lala et al., 1975; Brown and Roach, 1976; Brown, 1980; Forkel et al., 1983; Turton and Brown, 1987; Forkel et al., 1987].

Each of all the above studies has focused either on the chemical processes associated with the gas and aqueous-phase or the physics of clouds and fog. This study combines for the first time a detailed description of gas and aqueous-phase atmospheric chemistry with a basic treatment of radiation fog dynamics. The inclusion of the fog dynamics enables us to study the wet deposition of pollutants during fog episodes, the vertical variability of acidity and pollutant concentrations in a fog, and the changes of concentration of aqueous and gaseous species during the various stages of fog development.

A Lagrangian trajectory model has been used in this study for the description of the radiation fog development and gas and aqueous-phase chemistry. A trajectory model that follows a parcel of air as it traverses the airshed has been found to be a valuable tool for the simulation of the chemical and physical processes occurring in a particular location. Even if such a model is not ideally suited for the prediction of concentration changes over extended spatial and temporal scales where an Eulerian description is preferable, the small computing cost of a trajectory model compared to an Eulerian grid model makes it ideal for the testing of chemical reaction mechanisms and model assumptions and for studying the sensitivity of the model to various inputs and parameters. Furthermore, the relatively low computing cost allows the use of higher vertical resolution than in a three-dimensional model and thus affords the opportunity to explore phenomena sensitive to height above the ground.

In this paper, we begin with a physical description of the system of interest, with emphasis on the physics of radiation fog. Next we present separately the gas-phase chemistry, aqueous-phase chemistry and radiation fog dynamics submodels and then describe the complete model. The full model is then evaluated against data obtained during a well-documented radiation fog episode in the San Joaquin Valley of California [Waldman, 1986; Jacob et al., 1987]. Sensitivity studies address the effects of fog formation on the deposition rates and on the aerosol mass and the chemical pathways that contribute to sulfate formation.

Radiation fog and acid deposition

By definition, a fog is a cloud of liquid water droplets near the earth's surface that reduces visibility to less than 1 km [Eagleman, 1985]. If humid air near the ground is cooled sufficiently, it becomes saturated and a fog develops. Typical

fogs are classified according to the process that causes the cooling of the air. The types identified are upslope, advection, frontal and radiation fogs [Eagleman, 1985]. Upslope fog is generated by the cooling of the air as it is forced to rise over hills and mountains. Advection fog is created through contact cooling of warm air with a cold surface or through advection of cold air over warm water. Frontal fog can be created as weather, especially warm fronts, passes through an area. Finally, radiation fog (or ground fog) is generated as the earth's surface cools by loss of radiation to space at night.

This study focuses on the development of radiation fog because it is one of the most frequently encountered fog forms in heavily polluted areas [Munger et al., 1989]. It is important to note, however, that the main ideas concerning the modelling of radiation fog can be extended and applied to other fog categories and especially to advection and upslope fog.

The various stages in the development of a typical radiation fog can be visualized by following the movement of an air parcel during a 24 hour period. During the daytime the air parcel collects water vapor and aerosol particles (sea salt, dust, primary and secondary particles of anthropogenic origin). The air temperature is high and the relative humidity is low. In the late afternoon the heat loss of the ground due to radiation to space exceeds the heating rate due to solar radiation and the ground's temperature starts decreasing. After sunset, as the cooling of the ground continues, the air within the lowest few meters also cools, due to heat transfer to the cooler ground. The radiational heat loss of the surface is partially balanced by heat conducted upwards to the ground surface because of the temperature gradient created in the first few centimeters in the soil. At a specific relative humidity, which for most soluble components in the atmosphere is well below 100%, aerosol particles that are not already liquid deliquesce into aqueous solution drops. As the ambient

relative humidity keeps increasing, the droplets undergo a slow equilibrium growth by water vapor diffusion [Pruppacher and Klett, 1980]. The air near the ground approaches saturation. At this stage dew deposition occurs.

Whether fog forms at this point depends on several factors such as cloud cover (clouds reduce radiative cooling), wind speed (turbulent diffusion tends to dry and may warm the air), and water vapor concentration. If there are no clouds and the wind speed is very low and the water vapor concentration is high enough, then fog starts forming in the lowest few meters. When the relative humidity reaches a critical supersaturation, depending on the size and chemical composition of the aerosol present, the droplets become activated and grow freely by water vapor diffusion.

The air near the top of the fog is cooling rapidly due to radiation of the fog droplets to space and consequently the fog propagates upward. At the same time as the fog's thickness increases, the radiative losses of the ground decrease due to the liquid water shield over it, and the ground temperature starts increasing from heat conduction upward through the soil. The air near the ground thus warms and the fog near the ground thins out.

When the sun comes out, fog dissipation is accelerated and liquid water evaporates rapidly at both the top and bottom of the fog. As the relative humidity decreases, the water evaporates from the fog droplets leaving aerosol particles. The fog life-cycle affects the aerosol concentration and composition in various ways. The aerosol particles grow because of water vapor diffusion and their gravitational settling and subsequent deposition are accelerated. At the same time, fog droplets scavenge soluble gases like nitric acid and ammonia and act as the medium for various aqueous-phase reactions, including the oxidation of absorbed SO_2 to sulfate.

Model Description

A complete model for acidic deposition due to fog should include descriptions of several physicochemical processes for all three phases existing in the atmosphere, namely the gaseous, the aqueous and the aerosol phase (Figure 1). Important processes that should be modelled are the emission of gas-phase species (SO_2 , NH_3 , NO_x , hydrocarbons) and particles, the reactions of species in the gas-phase, the nucleation and condensation of gaseous species to aerosol particles, and the mass transfer (diffusion and advection) and dry deposition of gases and aerosol. Additionally, a description of the physical process that causes the cooling of the moist air (radiative cooling for radiation fog) is necessary. The condensation of water vapor on the aerosol particles that serve as condensation nuclei and the subsequent growth of the water droplets is the next step. After the appearance of the aqueous-phase, one should account for the scavenging of gaseous species by the water droplets, their ionization and aqueous-phase reactions. The gravitational settling of droplets and their deposition on the ground must also be described. The last step of the phenomenon is the evaporation of the aqueous-phase leaving an aerosol residue.

A full description of all the above processes requires a model capable of predicting the changes of the aerosol and water droplet size-chemical composition spectrum. The present study focuses on the chemical changes in both the gas and aqueous-phases and an explicit treatment of the aerosol microphysics has not been included. Size-dependent processes of interest such as the aerosol particle scavenging by fogwater, gravitational settling, and radiative cooling of fog droplets have been parameterized. The model is capable of predicting the liquid water profile, and the gas and aqueous-phase concentration profiles for all species but does not account for the size or composition spectrum of aerosol particles or fog droplets.

The mathematical model employed in this study consists of three interacting submodels simulating gas-phase chemistry, fog development and aqueous-phase

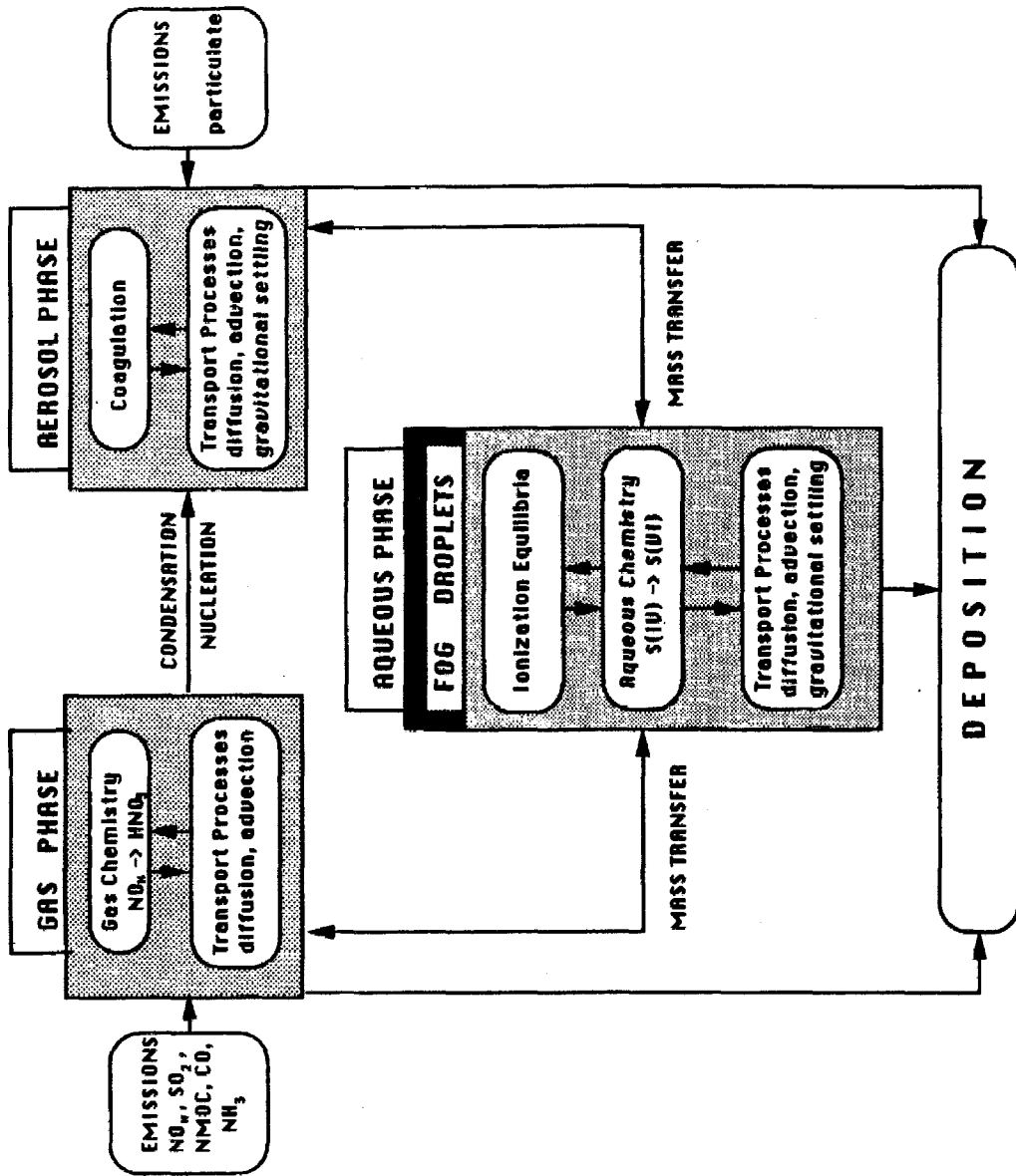


Figure 1 Atmospheric processes leading to acid deposition.

chemistry. These three models will initially be described independently.

1. Gas-phase model

The gas-phase model describes atmospheric chemical reactions, turbulent vertical diffusion, horizontal advective transport, and ground level pollutant deposition. It is based on the numerical solution of the Lagrangian trajectory form of the atmospheric diffusion equation presented in McRae et al. [1982]. Except for the changes mentioned below, the methods employed here are as described by McRae et al. [1982].

The detailed SAPRC/ERT gas-phase chemical reaction mechanism (Carter et al., 1986) with the modifications and extensions of Carter and Atkinson [1988] has replaced the previously used mechanism. It contains 154 reactions and 62 species (39 active, 7 accumulating and 16 steady state species). The photochemical mechanism preparation and emissions processing software of Carter and Atkinson [1988] has been used to prepare the gas-phase mechanism dependent part of the code.

2. Radiation fog model

The governing equations of the radiation model are the one-dimensional continuity equations for heat (for air and soil), water vapor and liquid water:

$$\frac{\partial T}{\partial t} = -\frac{1}{\rho c_p} \frac{\partial F_N}{\partial z} + \frac{\partial}{\partial z} \left[K_h \left(\frac{\partial T}{\partial z} + \Gamma \right) \right] + \frac{L}{\rho c_p} C \quad (1)$$

$$\frac{\partial T_s}{\partial t} = K_s \frac{\partial^2 T_s}{\partial z^2} \quad (2)$$

$$\frac{\partial q}{\partial t} = \frac{\partial}{\partial z} \left(K_q \frac{\partial q}{\partial z} \right) - C \quad (3)$$

$$\frac{\partial w}{\partial t} = \frac{\partial}{\partial z} \left(K_w \frac{\partial w}{\partial z} \right) + \frac{\partial G}{\partial z} + C \quad (4)$$

where T is the air temperature (in K), ρ the air density (in g m^{-3}), c_p the specific heat of air (in $\text{J K}^{-1} \text{g}^{-1}$), F_N the net radiative flux (in W m^{-2}), K_h, K_q, K_w the exchange coefficients for heat, water vapor and liquid water respectively (in $\text{m}^2 \text{s}^{-1}$), Γ is the adiabatic lapse rate ($\Gamma = 0.0098 \text{ K m}^{-1}$), L the latent heat of vaporization (in J / g water), C the condensation rate (in $\text{g water m}^{-3} \text{s}^{-1}$), T_s the temperature in the soil (in K), K_s the soil thermal conductivity (in $\text{m}^2 \text{s}^{-1}$), q is the water vapor concentration (in g water m^{-3}), w is the liquid water concentration (in g water m^{-3}) and G is the gravitational flux of liquid water (in $\text{g water m}^{-2} \text{s}^{-1}$).

The radiation flux F_N is calculated using the radiation scheme of Zdunkowski et al. [1982] for the solar and infrared emission spectrum. This scheme incorporates the effects of atmospheric water vapor, carbon dioxide, ozone, nitrogen dioxide, aerosol particles and multiple layers of clouds or fog. A total of 74 grid points extending from the ground surface to a height of 50 km have been found to provide sufficient accuracy for the solution of the equations for the radiative fluxes in the study.

The exchange coefficients for heat, water vapor and liquid water are assumed equal in this model [Brown and Roach, 1975]. They are given by the [Shir, 1973] :

$$K_{h,q,w} = \frac{K^n}{\phi_{h,q,w}(z/L)} \quad (5)$$

where K^n refers to neutral conditions and is given by :

$$K^n = \frac{1}{2} k u_* z \left[\exp\left(\frac{-4z}{H}\right) + \frac{1}{1 + 16(z/H)^{1.6}} \right] \quad (6)$$

In the above formulas $H = 0.455u_*/f$ scales the boundary layer height [Shir, 1973], u_* is the friction velocity, f the Coriolis parameter, L is the Monin-Obukhov length, and $\phi_{h,q,w}$ is the appropriate Monin-Obukhov profile function. The simplifying assumption is made that $\phi_h = \phi_q = \phi_w$. The Monin-Obukhov profile functions used in this study are [Zdunkowski et al., 1976] :

1) Unstable Regime

$$\phi_h\left(\frac{z}{L}\right) = 0.76\left(1 - 16\frac{z}{L}\right)^{-\frac{1}{2}} \quad \text{for } \frac{z}{L} > -10. \quad (7)$$

The functions are evaluated at $z/L = -10$ if $z/L < -10$.

2.) Stable Regime

$$\phi_h\left(\frac{z}{L}\right) = 0.74 + 9.62\frac{z}{L} + 29.6\left(\frac{z}{L}\right)^2, \quad \frac{z}{L} < 0.08 \quad (8a)$$

$$\phi_h\left(\frac{z}{L}\right) = 1.2 + 6.1\frac{z}{L}, \quad \frac{z}{L} > 0.08 \quad (8b)$$

The thermal conductivity of the soil, K_s , is assumed to remain constant for all depths during the simulation.

The gravitational flux of liquid water G is defined in terms of a mean settling velocity u_{av} by

$$G = w u_{av}. \quad (9)$$

If the droplet size distribution, $n(r, z)$, and the settling velocity of droplets as a function of size, $u(r)$, are known, the mean settling velocity, u_{av} , can be obtained from

$$u_{av} = \frac{\int_0^\infty n(r, z)u(r)r^3 dr}{\int_0^\infty n(r, z)r^3 dr}. \quad (10)$$

Because the fog droplet distribution at height z is not calculated by this model we have parametrized the mean settling velocity u_{av} following Brown and Roach [1976] and Forkel et al. [1983, 1987] as :

$$u_{av} = a_g w \quad (11)$$

Various measured fog droplet spectra [Waldman, 1986] have been used to calculate an average a_g value of $0.120 \text{ m}^4 \text{ g}^{-1} \text{ s}^{-1}$. The terminal velocity of droplets in Equation (10) has been calculated using Stokes law.

To avoid an explicit treatment of the fog microphysics we assume that inside the fog the water vapor pressure always attains its saturation value [Brown and Roach, 1976]. Various field measurements suggest that fogs generally have low supersaturations, with largest values during the initial stage of fog development. Therefore, our assumption leads to a small loss of accuracy in the calculated liquid water values but at the same time reduces drastically the computing time requirements as we do not have to solve the droplet growth equation [Brown, 1980]. The integration of Equations (1), (3) and (4) is performed in two steps. In the first, the equations are integrated for one timestep neglecting the condensation/evaporation term ($C = 0$). This integration results in values of the air temperature, water vapor and liquid water concentrations, T_o, q_o, w_o , respectively. In general, the water vapor concentration will be different from the saturation concentration, q_{so} , at temperature T_o . If the air is supersaturated, some water vapor has to be condensed. If it is subsaturated, some of the existing liquid water is evaporated. Therefore, the three variables are adjusted to T', q', w' , where q' is the saturation concentration corresponding to T' . The new values are calculated by solving the water mass balance, the energy balance and the Clausius-Clapeyron equations simultaneously [McDonald, 1963].

Boundary conditions

Equations (1), (3) and (4) are solved in the region extending from the ground surface to a height of 300 m. This region has been chosen large enough to include the fog top in most radiation fog episodes. Equation (2) is solved from a depth of 1 m below the surface to the ground surface. The grid used is unequally spaced with

52 points above ground level for the solution of Equations (1), (3), and (4), and 13 points inside the soil for the solution of Equation (2). The grid is much denser near the ground surface. This grid selection was proven to provide both accuracy and speed for subsequent calculations.

The boundary conditions applied to the top ($z = 300$ m) of the model region are:

$$T = \text{constant} = T_{\text{top}}$$

$$q = \text{constant} = q_{\text{top}}$$

$$w = 0$$

for the bottom level:

$$T_s = \text{constant} = T_{\text{bot}} \text{ at } z = -1 \text{ m}$$

Finally for the ground surface the liquid water concentration is assumed to be zero, $w = 0$, and the air and soil temperature are considered to be the same, $T = T_s$. From the continuity of heat fluxes at the air-soil interface [Turton and Brown, 1987],

$$-F_N + F_H + F_L - F_S = 0 \text{ at } z = 0$$

where F_N is the net radiative flux (long-wave and short-wave) incident at the surface, F_H and F_S are the sensible heat fluxes reaching the interface through the air and the soil and F_L is the latent heat flux. The surface water vapor concentration q_1 is calculated by [Turton and Brown, 1987] :

$$q_1 = f_p q_{\text{sat}}(T_1) + (1 - f_p) q_2 \quad (12)$$

where $q_{\text{sat}}(T_1)$ is the saturation water vapor concentration of the ground surface which has temperature T_1 , q_2 is the water vapor concentration for the first grid

point above ground level and f_p is given by [Turton and Brown, 1987] :

$$f_p = (z_2/K_{h1})/(z_2/K_{h1} + r_s) \quad (13)$$

where r_s is the surface resistance. A value of 60 s m^{-1} is used in this study following Turton et al. [1987]. For dew deposition that is $q_{\text{sat}}(T_1) < q_2$, f_p is set equal to unity.

The system of the four partial differential equations is solved using the Crank-Nicolson method with a timestep of 1 s. No stability difficulties were encountered for this timestep.

3) Aqueous-phase model

The aqueous-phase chemical reaction mechanism used in this study is described by Pandis and Seinfeld [1989]. The mechanism includes the dynamic exchange of species between the gaseous and aqueous phases in a homogeneous parcel of air containing liquid water droplets. The chemical mechanism includes 49 individual aqueous-phase species, 17 aqueous-phase ionic equilibria, 20 gas-phase aqueous-phase reversible reactions and 109 aqueous-phase reactions.

Full Model Description

The full Lagrangian model describes the physicochemical processes occurring in a vertical column containing a prescribed number of computational grid cells (12, in the present computation). The region where the fog is expected to grow (the first 300 meters above the ground) is divided into 9 cells, while the remaining three cells cover the height from 300 to 1000 m. The size of each vertical cell remains constant during the simulation (Figure 2).

Each simulation is divided in three stages. In the first, the stage before fog development, the model operates like an ordinary air quality trajectory model with

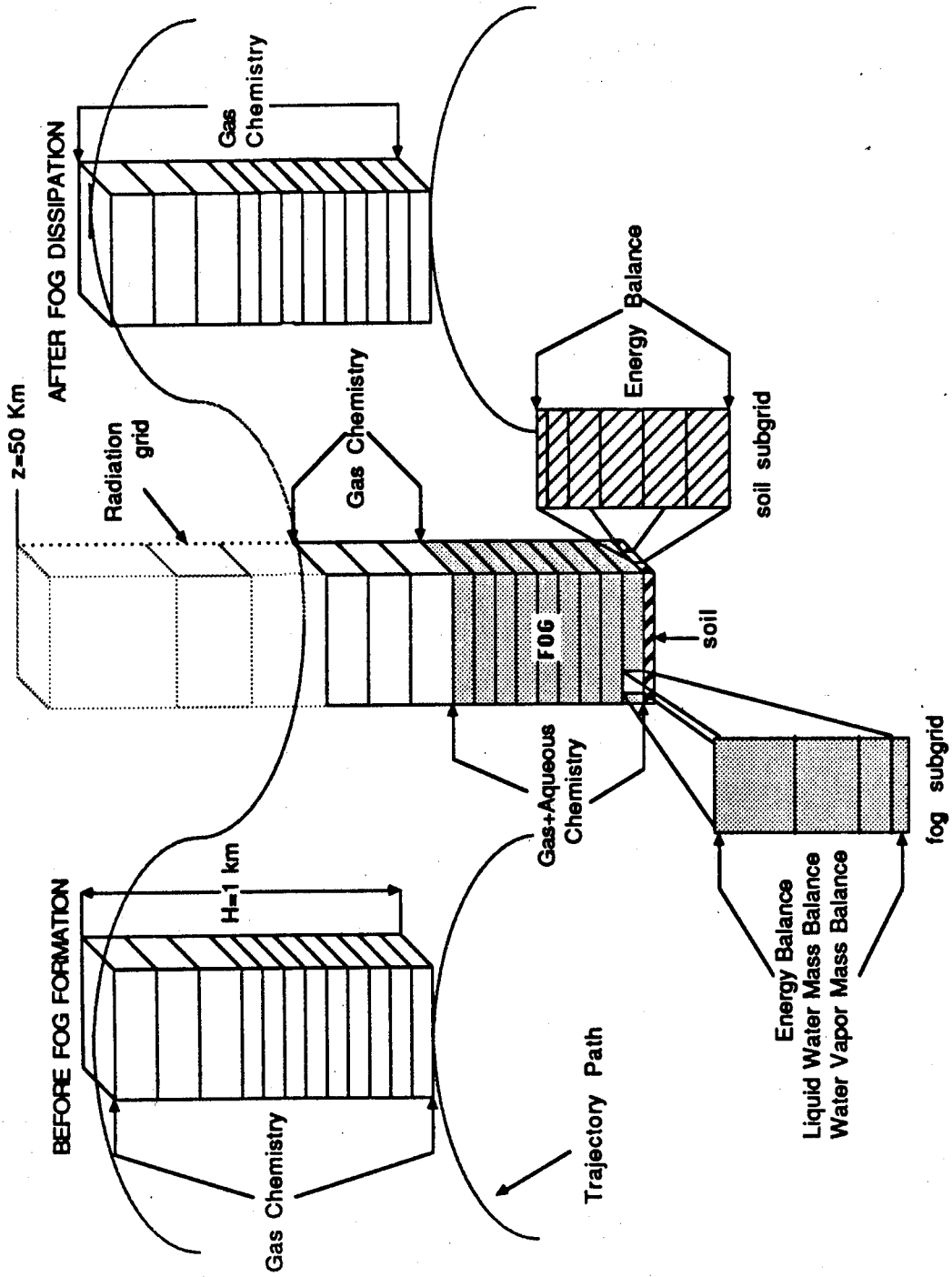


Figure 2 Schematic representation of the vertically resolved Lagrangian trajectory model for radiation fog.

only the gas-phase submodel active [McRae, 1982]. The variables calculated by the model in this stage are the gas-phase concentrations c_{gi} . Their change is calculated by

$$c_g^{(t+\Delta t)} = A_{gas}(\Delta t)c_g^{(t)} \quad (14)$$

where A_{gas} is the gas-phase operator described for the gas phase submodel.

At this stage the temperature and relative humidity constitute an input to the model. When the relative humidity exceeds 90%, the first stage is considered over, and we enter the fog development stage. Initial temperature and relative humidity profiles are provided as an input and the fog submodel becomes active. The first 9 of the 12 major cells of the gas submodel are divided into smaller cells for the solution of the fog model equations (1), (3) and (4). When liquid water is created in a cell, the aqueous-phase chemistry submodel is also used. The existing aerosol particles are assumed to be completely scavenged by fog droplets upon the formation of a liquid water phase [Ten Brink et al., 1987]. In this way the aerosol mass provides the initial concentrations of sulfate, nitrate and ammonia in fogwater.

The aqueous-phase chemistry calculation is performed within the fog region of the main grid. The liquid water content for each of these cells is an average over the liquid water profile provided by the fog submodel.

During radiation fog, wind speeds remain generally under 2 m s^{-1} [Forkel et al., 1987; Waldman, 1986] therefore, during the life cycle of the radiation fog one can assume that the Lagrangian cell is stationary. Under this assumption, the energy balance is valid because the cell remains more or less over the same piece of land throughout the simulation.

The full set of partial differential equations for the fog, gaseous and aqueous phases is solved using an operator splitting technique, in order to decouple the fog growth, the gas-phase chemistry and vertical transport, and the aqueous-phase

chemistry. If F_i is the variable vector containing the gas and aqueous phase concentrations and fog variables, its value at time $t + \Delta t$ is obtained from that at time t by:

$$F_i^{(t+\Delta t)} = A_{gas}(\Delta t)A_{fog}(\Delta t)A_{aq}(2\Delta t)A_{fog}(\Delta t)A_{gas}(\Delta t)F_i^{(t)} \quad (15)$$

where A_{gas} , A_{aq} and A_{fog} are the gaseous-chemistry, aqueous-chemistry and fog operators described above.

The second stage of simulation ends when the fog dissipates. At this point, when all the liquid water has been evaporated the fog and aqueous chemistry operators become inactive, and the model becomes once more an ordinary gas-phase only model.

Application of the Model to the San Joaquin Valley of California on 4-5 January 1985

The Lagrangian radiation fog model has been applied to simulate atmospheric conditions in the San Joaquin Valley of California (Bakersfield's Meadows Field Airport) from 1700 PST on 4 January to 1000 PST on 5 January 1985. The main goals of this simulation are to evaluate the model's performance against a well documented episode and to improve our understanding of the interaction of the various physical and chemical processes taking place during a radiation fog. About 10 CPU hours on a micro-Vax III were required for the simulation.

During the 4th and 5th of January 1985 an extensive sampling network was operated in the San Joaquin Valley of California as a part of a two month study [Waldman, 1986; Jacob et al., 1987]. The gas-phase concentrations of SO_2 , HNO_3 , and NH_3 were monitored. Aerosol samples were collected on open-faced Teflon filters, and fogwater samples were collected with a rotating arm collector. The fog liquid water content was determined from the collection rate of the rotating arm

collector assuming a collection efficiency of 60%. The fogwater pH and the aqueous-phase concentrations of S(IV), HCHO, NH_4^+ , SO_4^{2-} , NO_3^- , Cl^- and trace metals (Fe, Mn, Na, K, Ca, Mg, Pb, and Cu) were measured. The aerosol concentrations of NH_4^+ , NO_3^- , SO_4^{2-} , Cl^- and several trace metals were determined. Additionally, the fog deposition rates for the major ions were monitored using polystyrene petri dishes and polyethylene buckets. Surface winds in the valley were determined at several sites and vertical profiles of temperature, relative humidity, wind speed and wind direction were recorded every 4-8 h using a tether sonde. An inert tracer was continuously released for 23 hours between 1800 PST on 4 January and 1700 PST on 5 January 1985 to monitor the fate of sulfur dioxide in the valley. The complete data sets have been reported by Waldman [1986] along with detailed descriptions of the sampling techniques used.

Input Data for the model

All the field data used are from the work of Waldman [1986] and Jacob et al. [1987] for the Bakersfield site unless another source is mentioned. Measured vertical profiles for temperature are presented in Figure 4. The profiles for 1700 PST have been used as initial conditions for the fog model. The profiles predicted by the fog model are also presented in the same figure. Due to lack of any other information the initial soil temperature has been chosen to vary according to $T_s = 278.25 - 12.25z$ for $-0.4\text{m} < z \leq 0$ and ($T_s = 283.15\text{ K}$) for $-1\text{ m} < z \leq -0.4\text{ m}$ in agreement with Forkel et al. [1984]. Representative soil properties assumed here are, $K_s = 3.210^{-7}\text{ m}^2\text{ s}^{-1}$, $c_s = 1255\text{ J kg}^{-1}\text{ K}^{-1}$ and $\rho_s = 1600\text{ kg m}^{-3}$ [Zdunkowski and Nielsen, 1969]. The wind speeds at the 2.85 m level during this night were lower than 2 m s^{-1} . A constant value of 1.5 m s^{-1} has been assumed for the simulation.

The emissions are taken from the NAPAP 5.2 1980 emissions inventory [U.S.

Environmental Protection Agency, 1986] for a winter weekday, with the exception of SO₂ and NH₃ emissions. The SO₂ emission rate is assumed constant at 7.1×10^{-10} kg m⁻² s⁻¹, obtained from a 1984 SO₂ inventory for the San Joaquin Valley [Aerovironment, Inc., 1984]. An NH₃ emission rate of 3.4×10^{-11} kg m⁻² s⁻¹ has been used for the San Joaquin Valley based on the estimation of Jacob [1985].

Initial gas-phase concentrations for SO₂, NH₃, HNO₃, and aerosol particle mass concentrations for SO₄²⁻, NO₃⁻, and NH₄⁺ are based on the corresponding ground-level measurements. The remainder of the gas-phase concentrations are computed by an extra simulation using the gas-phase submodel from 0000 to 1700 PST on January 4. Due to lack of other information, an initial H₂O₂ vapor concentration of 2 ppb has been assumed based on the measurements of Heikes et al. [1987]. The aqueous phase concentrations of Fe³⁺ and Mn²⁺ are assumed to be 225 and 33 μg / liter water according to the observations of Waldman [1986] for the fog episode.

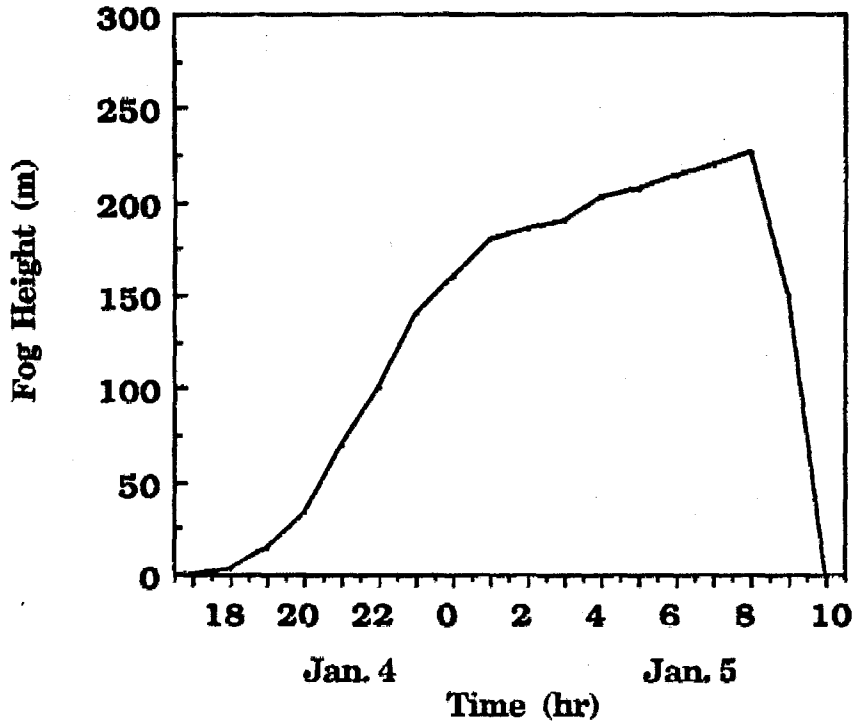


Figure 3 Predicted top of the fog layer.

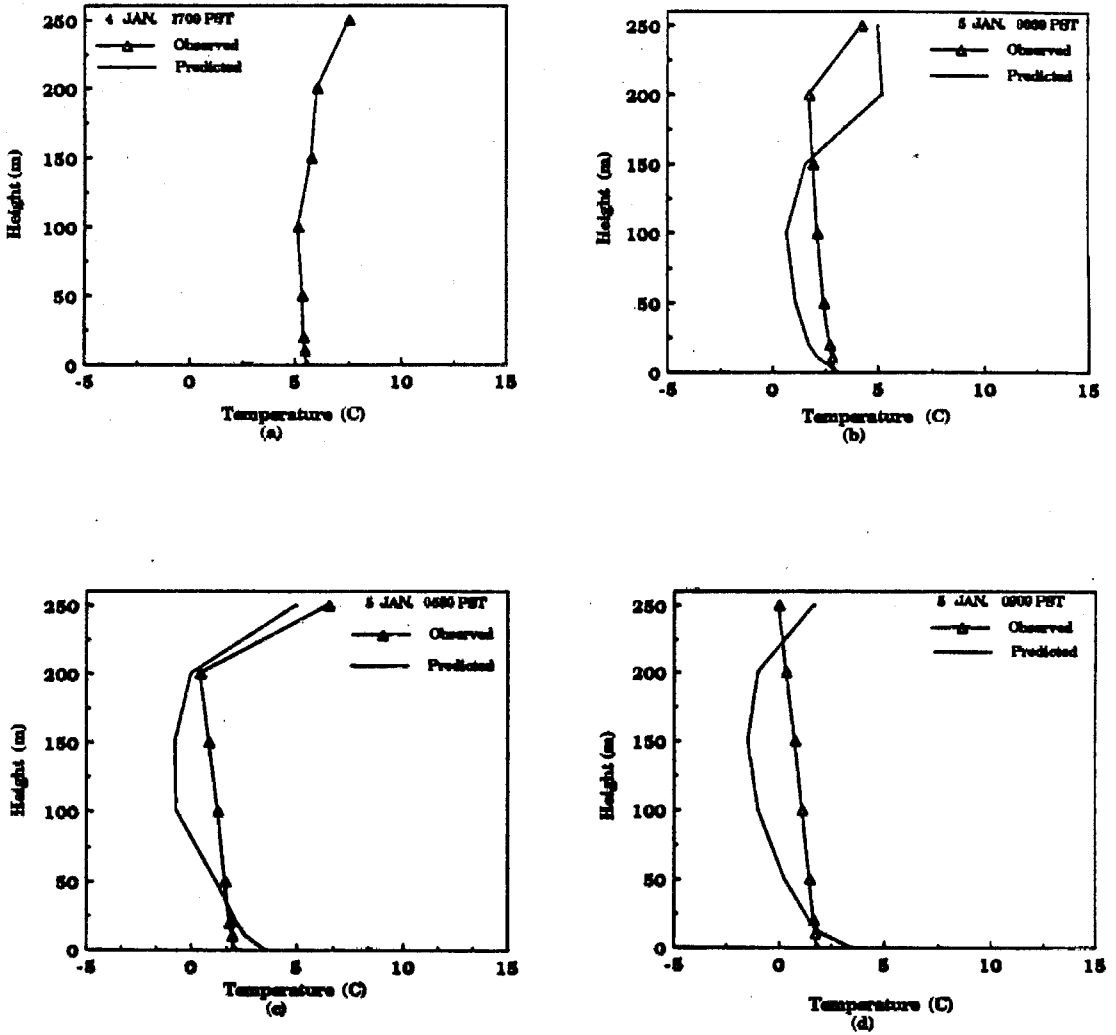


Figure 4 Comparison of the vertical temperature profiles predicted by the model with the observations of Waldman (1986).

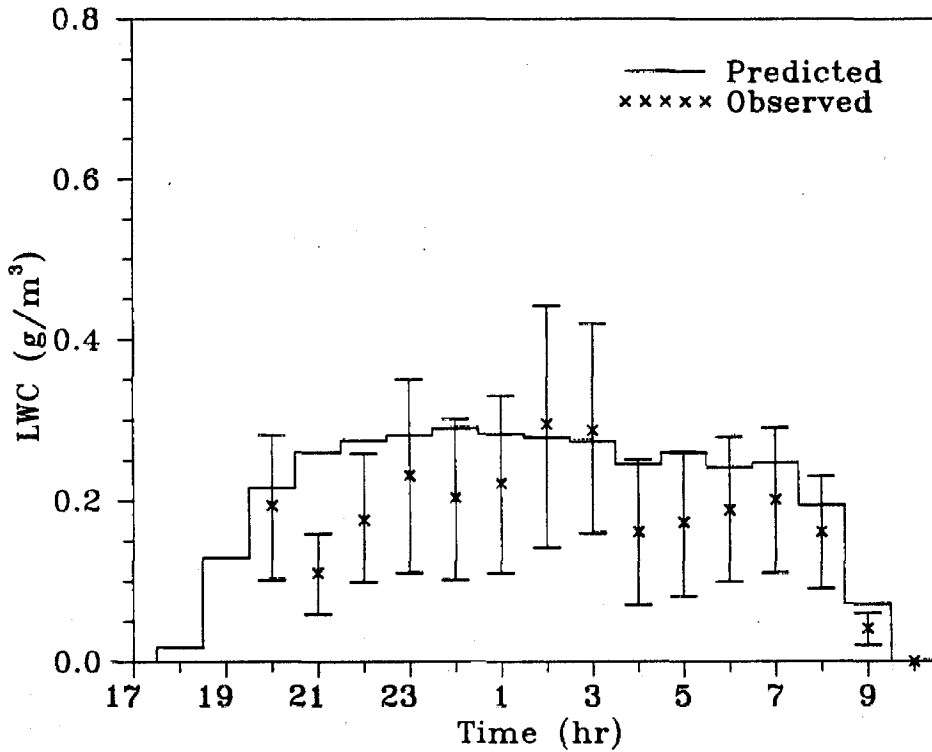


Figure 5 Comparison of the predicted hourly averaged liquid water content for the ground-level grid cell with the observations of Waldman (1986). The uncertainty in the measurements as reported by Waldman (1986) is indicated by the data ranges.

Fog Development

The radiation model predicts that radiation fog starts developing just after sunset (1700 PST), reaches a maximum height of about 230 m, and dissipates by 1000 PST, the morning of the next day. The predicted fog evolution is shown in Figure 3. The predicted start and end of the radiation fog agrees exactly with the observations of Waldman [1986]. The predicted fog height agrees with the relative humidity profiles measured by tethersonde. These profiles suggest that the first 210 m, 240 m and 270 m of the atmosphere were saturated at 0030, 0530 and 0900 PST, respectively. The predicted and observed temperature profiles (Figure 4) are in close agreement.

The hourly averaged liquid water content predicted at ground level is compared to the measured values in Figure 5. The maximum liquid water attained in the fog is predicted to be 0.28 g m^{-3} matching very closely the 0.29 g m^{-3} reported. The model appears to have a tendency of slightly overpredicting the liquid water content of the fog.

The predicted hourly averaged liquid water deposition rates are presented in Figure 6. A maximum of $24.6 \text{ g m}^{-2} \text{ hr}^{-1}$ is attained around midnight. These liquid water rates are closely consistent with the deposition velocities of 1 to 3 cm s^{-1} reported by Waldman [1986].

The results indicate that the radiation fog submodel is very successful in describing the observed fog development and in predicting variables of interest like the liquid water content, the liquid water deposition rates and the fog height.

Three representative calculated liquid water profiles are shown in Figure 7. An interesting feature is that after the initial fog development stage, after midnight in this simulation, the liquid water profile starting at a few meters high and ending near the fog top remains relatively flat.

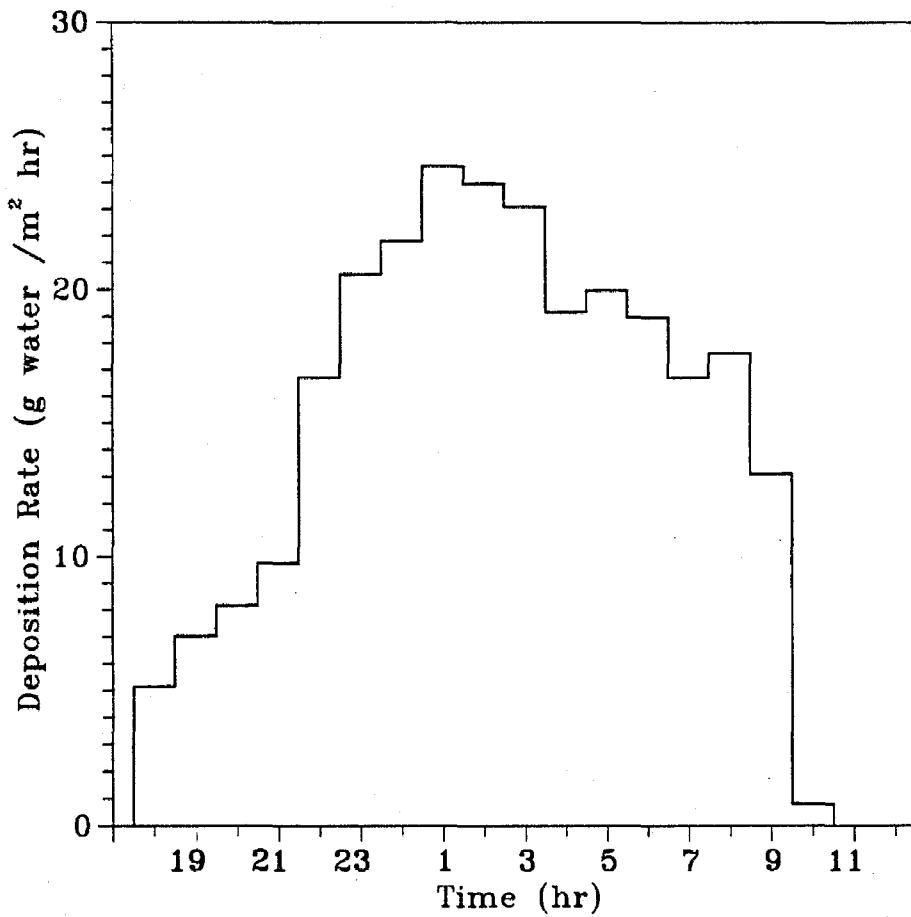


Figure 6 Predicted hourly averaged liquid water deposition rates.

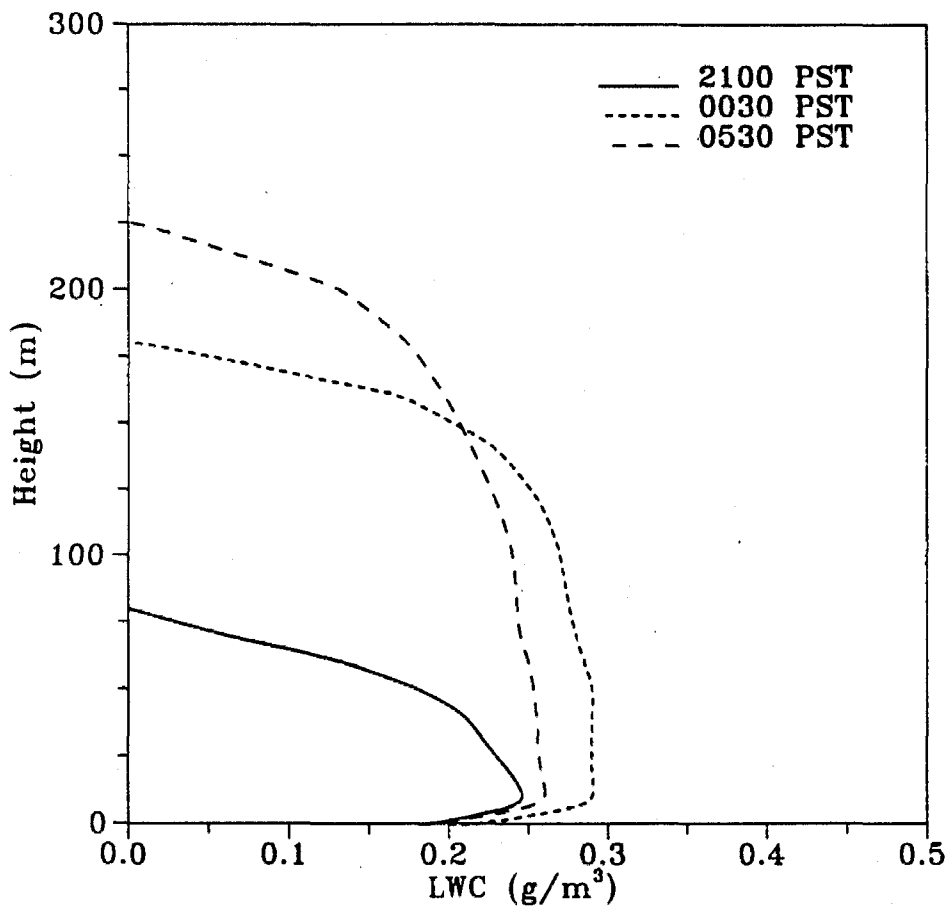


Figure 7 Predicted vertical liquid water concentration profiles for 2100, 0030, and 0530 PST.

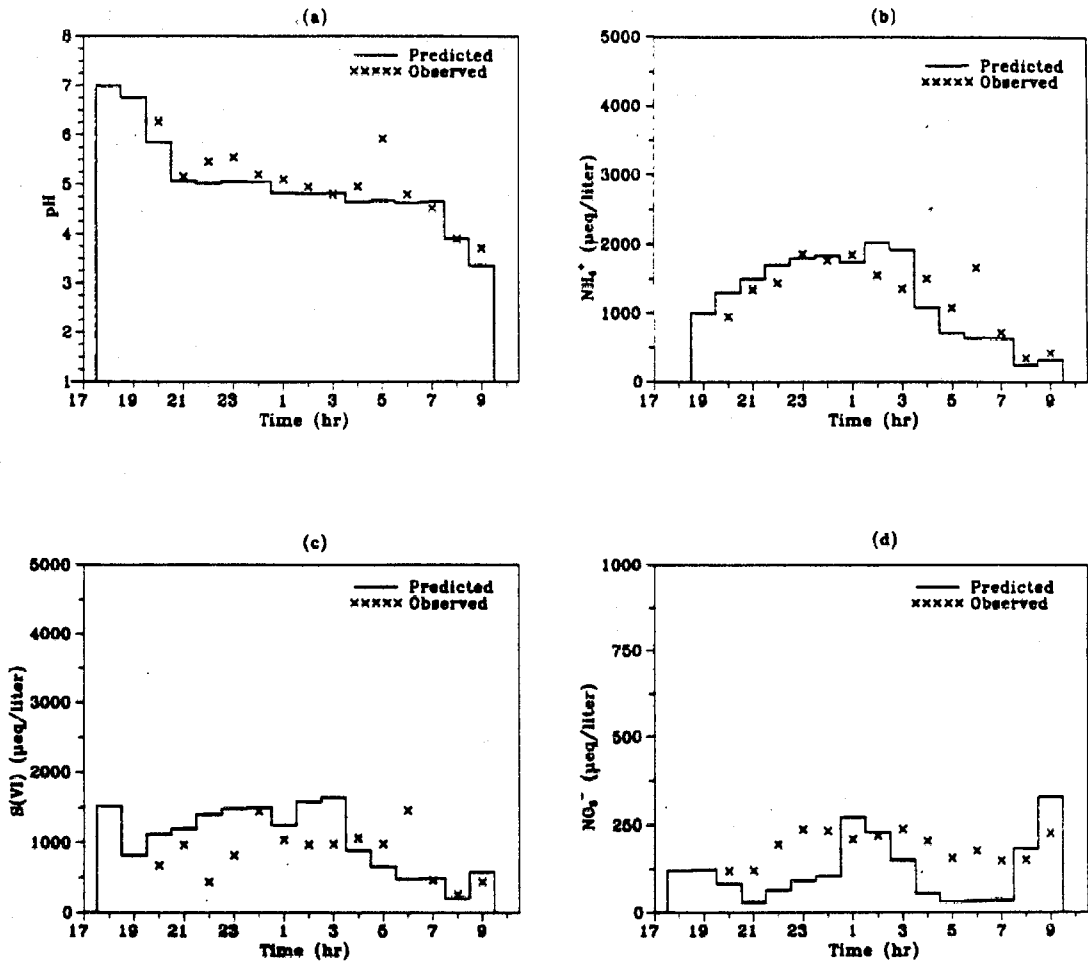


Figure 8 Comparison of the predicted hourly averaged (a) pH values, (b) NH_4^+ , (c) S(VI), (d) NO_3^- concentration for the ground-level grid cell with the observations of Waldman (1986).

Species concentrations in the aqueous and gas-phase

Predicted and observed hourly averaged values for the pH and the aqueous-phase concentrations of NH_4^+ , SO_4^{2-} and NO_3^- are presented in Figure 8.

The pH of the fog at ground level is initially around 7.0, gradually drops to 4.5 at 0700 PST as the fog is developing and in the dissipation stage of the fog it drops further reaching a value of 3.3 at 0900 PST. The pH prediction of the model is very good with a small tendency to underestimate.

The major ionic species in fogwater are in this case NH_4^+ , SO_4^{2-} and NO_3^- . The high pH during most of the fog is a result of the ammonia emissions in the area due to widespread agricultural and livestock activities. The maximum predicted concentration of NH_3 , 2000 μeq /liter, as well as the rest of the predicted values, are in close agreement with the reported values.

The SO_4^{2-} is the anion that closely balances NH_4^+ . The hourly averaged sulfate concentrations do match closely the observed concentrations with a tendency of the model to overpredict the sulfate concentrations. The reasons for this overprediction will be examined later. A result of this sulfate overprediction is the pH underprediction observed above.

The aqueous-phase concentration of nitric acid remains much smaller than the ammonia and sulfate concentrations throughout the simulation until the fog dissipation stage. The maximum predicted concentration (excluding the fog dissipation) of nitric acid is 270 μeq / liter versus the maximum observed value 240 μeq / liter. The model results indicate a larger variation in the nitrate concentrations than observed and generally the observed values are somewhat higher than predicted. Possible explanations include the use of an incorrect initial gas and nitrate aerosol concentration profile, or an underprediction of the gas-phase nitric acid production rate.

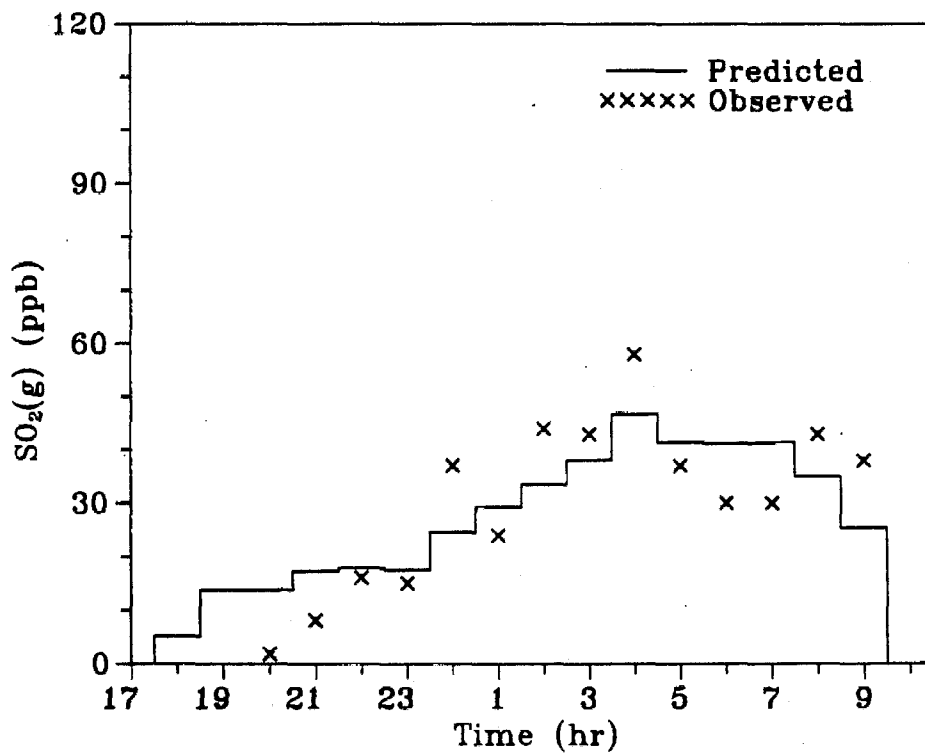


Figure 9 Comparison of the predicted hourly averaged SO₂(g) concentration for the ground-level grid cell with the observations of Waldman (1986).

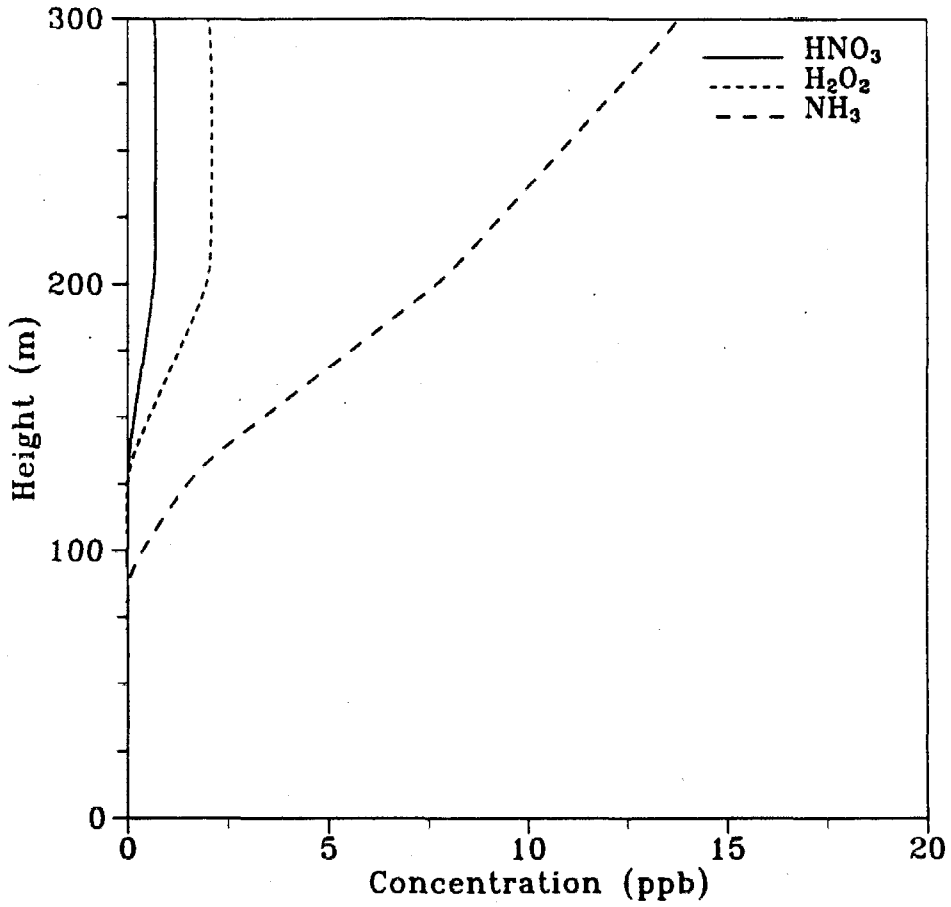


Figure 10 Predicted HNO₃, H₂O₂, and NH₃ vertical gas-phase concentration profiles for 2300 PST.

The predicted and observed gas-phase concentrations of SO_2 at ground level are shown in Figure 9. The model predictions once more match adequately the observed values. An average concentration of 40 ppb is maintained during the night.

The behavior of the gas-phase concentrations of HNO_3 , NH_3 and H_2O_2 is quite interesting (Figure 10). At 2300 the fog has reached a height of 140 meters. When the aqueous phase is not present in a cell these three species exist in the gas-phase. When the fog enters a cell, these species rapidly disappear either because of their high solubility in the aqueous phase (NH_3 and HNO_3) or because of fast reactions in the aqueous-phase (H_2O_2). In this respect the gravitational settling of the fog results in a 'cleaning' of the lower atmosphere of these three species. The above model predictions agree with the reported gas phase concentrations of HNO_3 and NH_3 [Waldman, 1986] and the mutual exclusivity of SO_2 and H_2O_2 in clouds reported by Kelly et al. [1985].

Effect of the fog development on the aerosol mass

The influence of the fog development on the dry aerosol mass concentration in the modelling region can be examined (Figure 11). The concentrations of sulfate, nitrate and ammonium before the fog development are the observed values that have already been used as initial conditions. To estimate the corresponding concentrations after the fog dissipation, we use the concentrations of these species at 0845. The average concentrations refer to the entire modelling region (1000 m). A large part of this region has not been influenced substantially by the fog that occupied the lower 250 m only.

The predicted aqueous-phase concentrations for sulfate and ammonium suggest that for the case studied here, the corresponding aerosol concentrations will be reduced, especially near the ground. The nitrate concentration remains practically

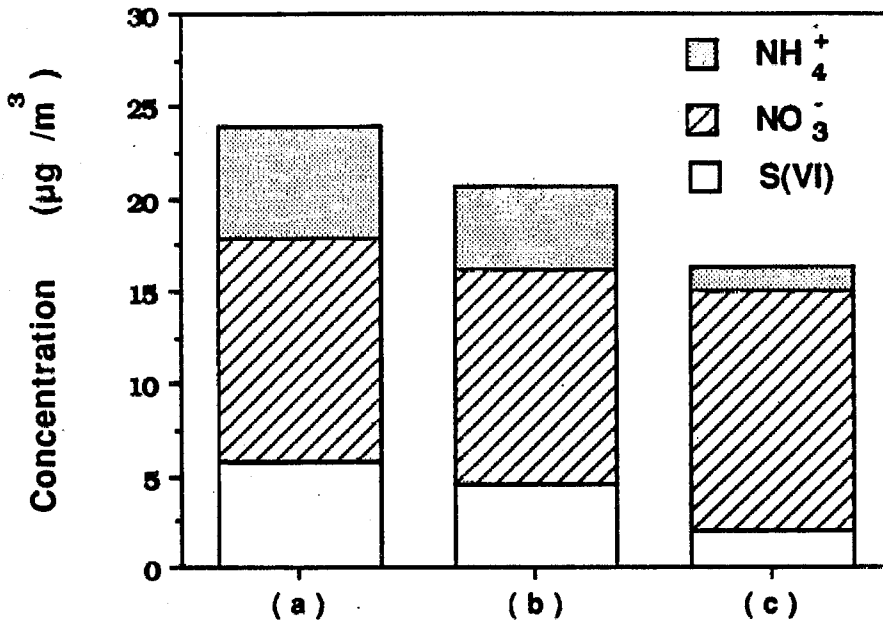


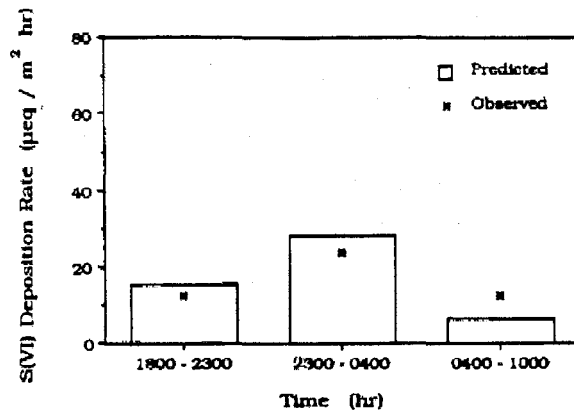
Figure 11 Concentrations of the principal ionic species in the aerosol phase (a) vertically averaged concentration before fog formation (observed values used as initial conditions in the simulation), (b) predicted vertically averaged concentration after fog dissipation, (c) predicted concentration for the ground-level grid cell after fog dissipation.

unchanged. The reasons for this behavior lie in the sinks and sources of these species under foggy conditions. The only source of ammonia is the ground-level emissions. The fog accelerates significantly the deposition of ammonia resulting in a significant decrease of the ammonium concentration in the aerosol phase. The decrease of the sulfate concentration is found to be less than that of ammonium due to the production of sulfate in the aqueous phase. The relatively small change in the nitrate concentrations is due to the production of nitric acid in the gas phase during the last hour of the fog life. This production is much faster near the ground where the NO_2 concentrations are higher in the early morning. This $\text{HNO}_3(\text{g})$ is dissolved rapidly in the still existing aqueous-phase resulting in a higher nitrate concentration.

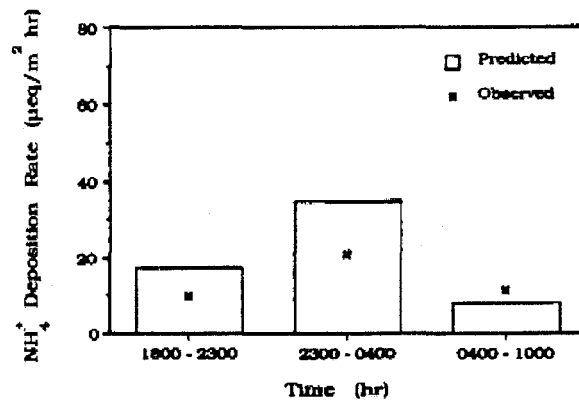
An additional important question that should be addressed in the future concerns the effects of the fog formation on the number concentration of aerosol particles as well as their size distribution. The present model can only predict aerosol mass, and a rigorous description of the aerosol particle microphysics must be added to address the above question.

Wet deposition rates

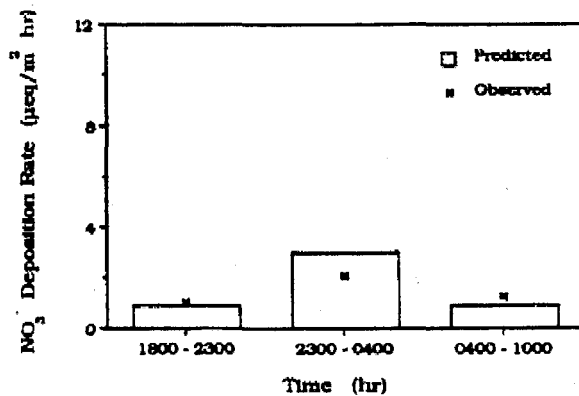
The average predicted and observed wet deposition rates for the major ionic species are presented in Figure 12. The observed values are measured at the ground level. The model tends to overpredict the deposition of all three species. The main reason for this is probably our assumption that the fog deposition velocity depends linearly on the liquid water content. Waldman [1986] reports that during this episode the liquid water variations appeared to be principally a function of droplet number concentration and the mass median diameters remained in a relative narrow range. Therefore we have probably overpredicted the fog deposition velocity,



(a)



(b)



(c)

Figure 12 Comparison of the predicted average wet deposition rates over three time periods with the observations of Waldman (1986) for (a) S(VI), (b) NH₄⁺, (c) NO₃⁻.

especially for the high liquid water values.

During the fog dissipation stage (0400 to 1000), the deposition rates are under-predicted because of the underprediction at this time of the corresponding aqueous-phase concentrations (Figures 8b, 8c and 8d). The observed values of ammonia deposition rates are, according to Waldman, a lower bound due to ammonia losses so disparity between the model and the actual values is less than appears in Figure 12b.

An interesting question that can be addressed is the effect of the fog formation on the total deposition rates. We have performed an additional simulation for the imaginary scenario that no fog was formed during the night of 4 to 5 of January. During this scenario the only mechanism for deposition is the dry deposition of gases and aerosol. The calculation was performed according to the model described by McRae et al. [1982]. Due to the various simplifications used, the dry deposition rates are only reasonable estimates.

The results of this simulation are presented as the average deposition rates for the 16 hour period from 1800 January 4 to 1000 January 5 (Figure 13). These calculations suggest that because of the fog formation, the total average deposition rate increased almost three times. The deposition of S(IV) is found to increase only 25% because the gas-phase concentration decreases during the fog period. The most interesting change is the deposition of sulfate that increases about 30 times because of the sulfate production in fogwater. Ammonia and nitric acid gas phase concentrations are very low inside the fog so the corresponding dry deposition rates are very small and the net increase is only twofold.

Sulfate Production

The main chemical change taking place in fogwater is the oxidation of S(IV) to

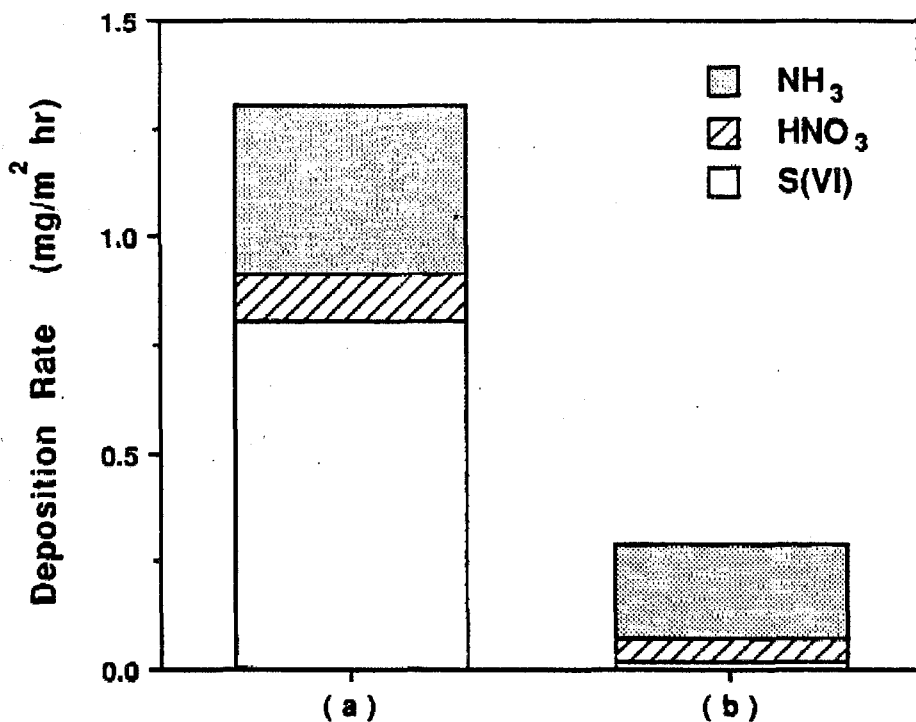


Figure 13 Comparison of the predicted average deposition rates for the same 16 hour period in (a) presence of radiation fog, (b) absence of radiation fog.

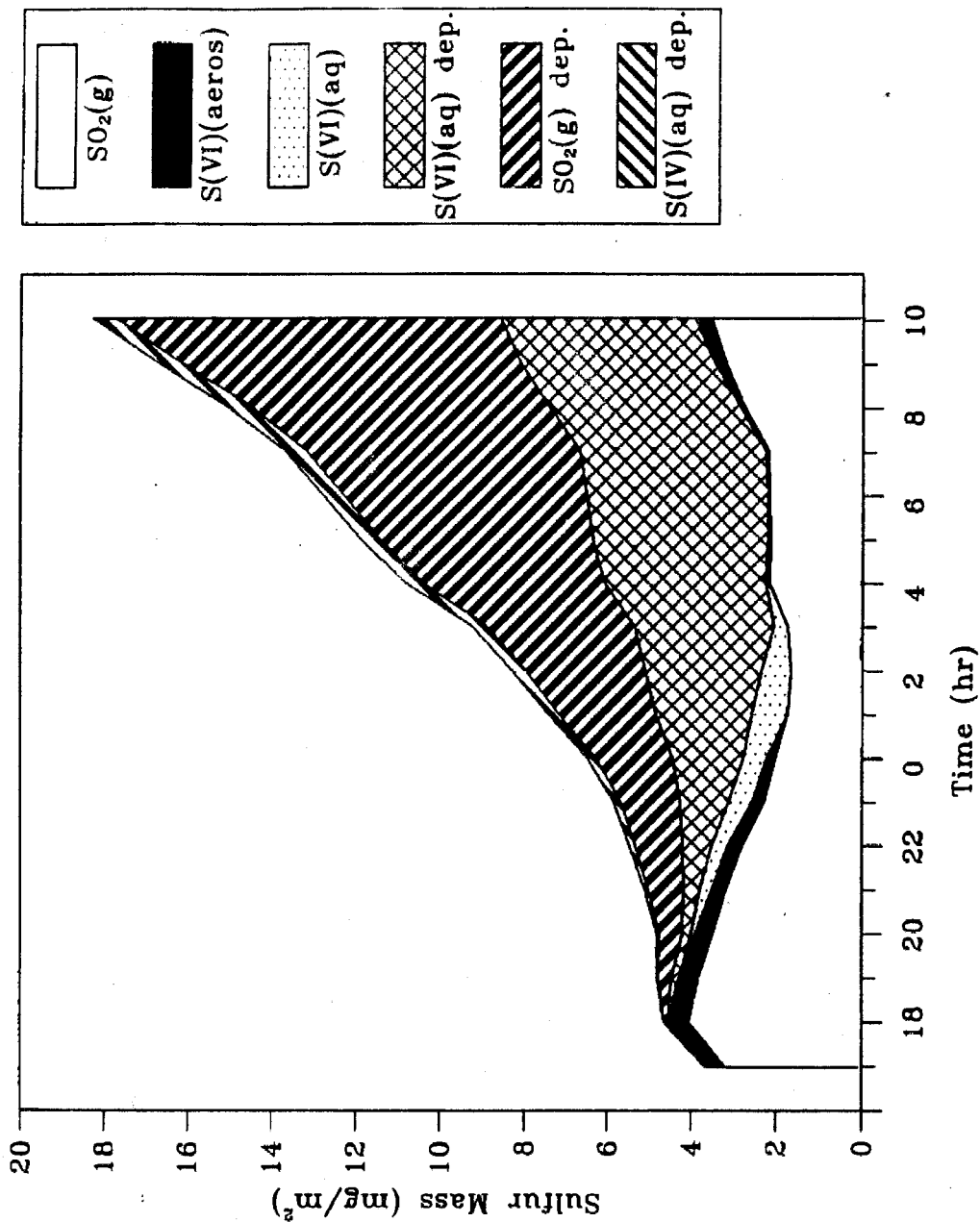


Figure 14 Predicted sulfur mass balance for the lower 250 m of the atmosphere.

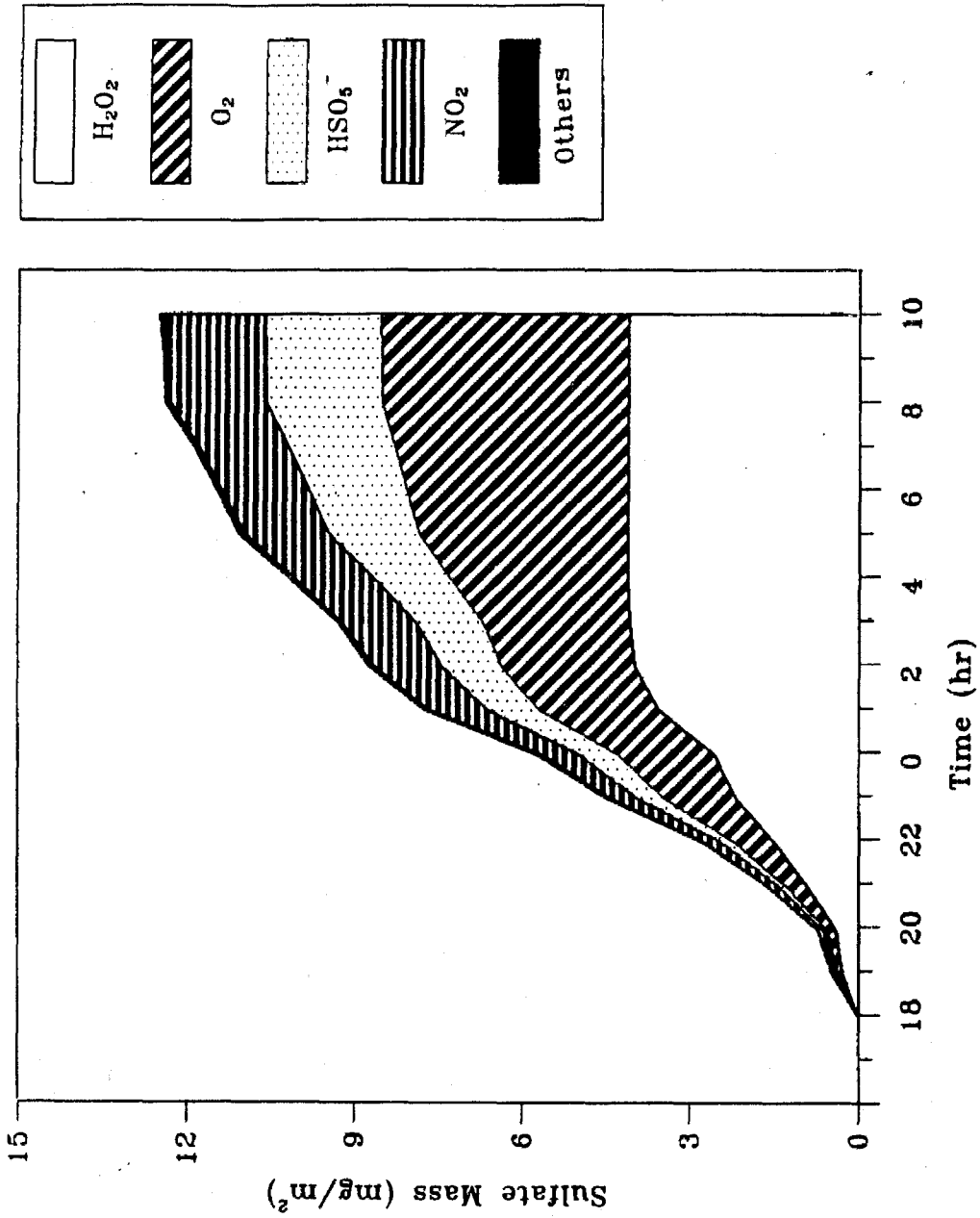


Figure 15 Pathways for the production of sulfate during the radiation fog episode.

S(VI) [Pandis and Seinfeld, 1989]. A mass-balance for sulfur is presented in Figure 14 including the deposited masses of S(IV)(aq), SO₂(g) and S(VI). The mass of sulfur existing as S(IV)(aq) has not been included in the figure because it is much smaller than the rest of the entries.

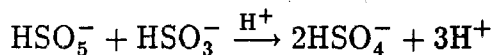
During this fog episode the main pathways for the production of sulfate are the oxidation of S(IV) by H₂O₂, O₂ (catalysed by Fe³⁺ and Mn²⁺), HSO₅⁻ and NO₂ (Figure 15). Hydrogen peroxide oxidizes S(IV) rapidly but is also depleted rapidly because of the excess of SO₂(g) in cases like the present one. One would expect that under these conditions the contribution of hydrogen peroxide to the SO₂ oxidation would be negligible shortly after the fog develops. This is, however, not the case. Due to the very stable conditions during the radiation fog life, hydrogen peroxide continues to exist in significant concentrations above the fog (Figure 10). As the fog continues to grow, new hydrogen peroxide is entrained into the fog and is available to oxidize S(IV). This process continues for almost 8 hours after the beginning of fog development, until 0200. After this time the contribution of hydrogen peroxide to S(IV) oxidation is indeed zero.

Due to the ammonia that gets continuously dissolved in the aqueous-phase, the pH of the fog is always greater than 4 except during the last two hours of fog life. Under these conditions the Fe³⁺ and Mn²⁺-catalysed oxidation of S(IV) is predicted to be a major contributor to sulfate formation. After hydrogen peroxide is depleted from the fog region, this reaction becomes the major pathway for the S(IV) to S(VI) transformation.

The gas phase concentration of ozone during the night remains close to zero, and therefore the oxidation of S(IV) by ozone in the aqueous-phase is negligible. When ozone concentrations start to increase (around 0800), the fog has already begun to dissipate and the fog pH is lower than 4 resulting again in negligible S(IV)

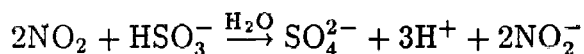
oxidation by ozone.

An important pathway for sulfate production during this fog episode is the oxidation of S(IV) by HSO_5^- :



HSO_5^- is one of the products appearing in the oxidation chain initiated by the attack of $\text{OH}(\text{aq})$ to S(IV) and propagated by further reactions of the radicals SO_4^- , SO_5^- and HSO_5^- [Jacob, 1986; Pandis and Seinfeld, 1989].

A reaction that under the present conditions is found to contribute considerably to the sulfate production is that of S(IV) with NO_2 :



This reaction has been studied by Lee and Schwartz [1983] at pH 6.4, 5.8 and 5.0 and was described as a reaction that is first order in NO_2 and first order in S(IV), with a pH dependent rate constant. The evaluation of this rate expression was considered tentative by Lee and Schwartz in view of evidence for the formation of a long-lived intermediate species. The apparent rate constant was found to increase with increasing pH. This reaction was considered of secondary importance at the concentrations and pH values representative of clouds. Under the conditions of the radiation fog in the San Joaquin Valley, the importance of this reaction increases considerably over that in clouds. The major reason is that the emitted NH_3 is scavenged by the fog droplets maintaining a low fogwater acidity. Therefore, this reaction is not self limiting in fog to the extent that it is in clouds. Other reasons for the significance of this reaction for this case are the relatively high gas phase concentrations of SO_2 and NO_2 . Radiation fogs develop under stable meteorological conditions, and in polluted environments they occur at the same altitude as the

sources of SO_2 and NO_x . Consequently the gas phase concentrations of SO_2 and NO_2 can be much higher in a fog than inside a cloud and the aqueous-phase reaction of S(IV) with NO_2 can be much faster.

Due to the remaining questions concerning the kinetics of this reaction, our results should be considered tentative. The fact that the model overpredicts the sulfate concentrations could be the result of a high initial H_2O_2 concentration, an overprediction of the oxidation of S(IV) by NO_2 , or an overprediction of the S(IV) oxidation rate by O_2 (catalysed by Fe^{3+} and Mn^{2+}).

Sensitivity to deposition

The sensitivity of the model to the expression of the mean settling velocity, u_{av} , as a function of the liquid water content has been investigated by performing an additional simulation using the value $a_g = 0.06$ (case II) instead of $a_g = 0.12$ used for the base case (case I). Therefore, for the same liquid water content, the settling velocity in case II is half the settling velocity of case I. This reduction in settling velocity accelerates the fog growth by 10-20 m, and increases the liquid water content of the fog by almost 30%. The mature fog in case II has a liquid water content of $0.38 \text{ g water m}^{-3}$. The rate of liquid water mass deposited to the ground in case II is only around 10% less than that in case I. This is due to the fact that the decrease of the water deposition rate because of the smaller value of the parameter a_g is partially balanced by the increase of the liquid water content.

The aqueous-phase concentrations of the main ionic species, S(VI), NH_4^+ and NO_3^- in case II, are initially (at 2000 PST) around 25% lower than the corresponding concentrations in case I because the increase of the liquid water causes a higher dilution. Therefore, case I is characterized initially by higher ionic concentrations and higher water deposition rates than case II, or equivalently by higher initial

ionic deposition rates. This difference in the deposition rates of the major ions causes a convergence of the calculated ionic concentrations and after 0400 PST the calculated concentration difference is less than 5%. At the same time the total mass of the ionic species dissolved in the aqueous-phase is for case II as much as 30% larger compared to case I due to the higher liquid water content..

Summarizing, a 50% decrease in the parameter a_g causes an average increase of the fog liquid water content by 30%, an average decrease of the liquid water deposition rate by 10%, an initial decrease of 25% in the aqueous-phase concentrations of the major ions that finally reduces to less than 5% and an increase of the total mass of the major ions in the aqueous-phase by as much as 30%. These results indicate that a good estimate of a_g is required by the model and furthermore that the gravitational settling of fog droplets affects considerably the chemical composition of fogwater.

An additional test has been performed to study the importance of the deposition process in acidic deposition. In an imaginary scenario the water droplet settling has been neglected and the liquid water content has been assigned a constant value of 0.3 g m^{-3} , conditions that can be generally applied to a cloud simulation (case III). Only one computational cell has been used for this simulation and the rest of the conditions (initial gas and aerosol concentrations, emissions, etc.) are the same as in the base case (case I). The fact that all the liquid water remains in the modelling region results in much higher concentrations of the major ionic species. The average S(VI) , NH_4^+ , and NO_3^- are 2.5, 3 and 2.7 times larger in case III than in the base case. The pH in case III remains higher than in the base case until the fog dissipation stage when the pH is practically the same for both case. The higher pH in case III can be explained by the fact that the neutralizing agent, ammonia, is not depleted from the system, keeping the pH at higher values. The gradual increase in

the sulfate and nitrate concentrations finally compensates for this higher ammonia concentration and the pH difference for the two cases becomes essentially zero after 0600 PST.

Conclusions

The physical and chemical processes leading to acidic deposition during a radiation fog episode have been studied using a one-dimensional mathematical model. The model used in this study combines a detailed description of gaseous and aqueous-chemistry with a dynamic model describing radiation fog development. Variables predicted by the model include the vertical profiles of temperature, relative humidity and liquid water content, the vertical concentration profiles of species in the gaseous and aqueous-phase and the wet deposition rates for all species.

Application of the model to a radiation fog episode in Bakersfield in the San Joaquin Valley of California over the period January 4-5, 1985, shows that the model predictions for temperature profile, fog development, liquid water content, gas-phase concentrations of SO_2 , HNO_3 and NH_3 , pH, aqueous-phase concentrations of SO_4^{2-} , NH_4^+ and NO_3^- , and finally deposition rates of the above ions match well the observed values.

The formation of the specific radiation fog causes reduction of the aerosol NH_4^+ and SO_4^{2-} content. The NO_3^- content remains practically the same as that predicted in the absence of a fog due to production of nitric acid in the gas-phase during the last three hours of the fog life and subsequent dissolution of the HNO_3 in the existing aqueous-phase. The deposition rates of the major ions are found to increase drastically during the fog episode with most notable the increase of sulfate deposition.

Several differences exist between a radiation fog and a representative cloud

environment. Radiation fog develops typically under stable conditions resulting in weak mixing and significant gradients in the vertical profiles of species like hydrogen peroxide, ammonia and nitric acid. The deposition process during a dense radiation fog leads to rapid removal from the atmosphere of the major ionic species and tends to keep their corresponding fogwater concentrations to lower values. Because of the proximity of the fog to ground-level sources of pollutants like SO_2 and NO_x , the corresponding gas-phase concentrations can reach much higher levels than in a cloud. In such a case, pathways for the sulfate production that are of secondary importance in a cloud environment may become significant in a fog.

Expressing the mean droplet settling velocity as a function of the liquid water content is found to be very influential in the prediction of the fog liquid water content, the total masses of the major ionic species in the aqueous-phase and the concentrations of these species in the first half of the fog life.

In the present model aerosol or fog droplet size-dependent processes such as aerosol nucleation, condensation and coagulation, droplet growth, evaporation and settling have either been described in terms of overall properties of the fog or have been omitted. The next level of detail in the modelling of acid deposition due to fog episodes requires the coupling of this model with one describing aerosol and fog-droplet microphysics.

Acknowledgements

We would like to thank Prof. W. G. Zdunkowski and Dr. A. Bott, Institut für Meteorologie, Johannes Gutenberg Universität, Mainz, for providing us with the code for the radiation scheme and for their helpful comments. We would also like to thank Dr. W. P. L. Carter, University of California, Riverside, for providing us with his software for the gas-phase mechanism preparation and emissions processing.

This work was supported by the State of California Air Resources Board under Agreement A732-043.

References

- Aerovironment Inc., AVKERN Application Report AV-FR-83/501R2, Pasadena, CA, 1984.
- Brown, R., A numerical study of radiation fog with an explicit formulation of the microphysics, *Quart. J. Roy. Met. Soc.*, 106, 781-802, 1980.
- Brown, R. and Roach W. T., The physics of radiation fog: II - a numerical study, *Quart. J. Roy. Met. Soc.*, 102, 335-354, 1976.
- Carter, W. P. L., Lurmann F. W., Atkinson R. and Lloyd A. C, Development and testing of a surrogate species chemical reaction mechanism, EPA-600/3-86-031, 1986.
- Carter, W. P. L. and Atkinson R., Development and implementation of an up-to-date photochemical mechanism for use in airshed modeling, Summary final report to California Air Resources Board, 1988.
- Chameides, W. L., The photochemistry of a marine stratiform cloud, *J. Geophys. Res.*, 89, 4739-4755, 1984.
- Eagleman, J. R., *Meteorology. The atmosphere in action*, Wadsworth Publishing Company, Belmont, CA, 1985.
- Environmental Protection Agency, Development of the 1980 NAPAP emissions inventory, report EPA/600/7-86/057a, 1986.
- Fisher, E. L. and Caplan, P., An experiment in the numerical prediction of fog and stratus, *J. Atmos. Sci.*, 20, 425-537, 1963.
- Forkel, R., Sievers, U. and Zdunkowski, W., Fog modelling with a new treatment of the chemical equilibrium condition, *Beitr. Phys. Atmosph.*, 60, 340-360,

1987.

- Forkel, R., Panhans, W.-G., Welch, R. and Zdunkowski, W., A one-dimensional numerical study to simulate the influence of soil moisture, pollution and vertical exchange on the evolution of radiation fog, *Beitr. Phys. Atmosph.*, 57, 72-91, 1983.
- Graedel, T. E. and Goldberg K. I., Kinetic studies of raindrop chemistry, 1. Inorganic and organic processes, *J. Geophys. Res.*, 88, 10865-10882, 1983.
- Heikes, B. G., Kok G. L., Walega J. G. and Lazrus A. L., H₂O₂, O₃, and SO₂ measurements in the lower troposphere over the eastern United States during the fall, *J. Geophys. Res.*, 92, 915-931, 1987.
- Jacob, D. J., Chemistry of OH in remote clouds and its role in the production of formic acid and peroxymonosulfonate, *J. Geophys. Res.*, 91, 9807-9826, 1986.
- Jacob, D. J., The origins of inorganic acidity in fogs, Ph.D. Thesis, California Institute of Technology, Pasadena, CA, 1985.
- Jacob, D. J., Waldman J. M., Munger J. W. and Hoffmann M. R., Chemical composition of fogwater collected along the California Coast, *Environ. Sci. Technol.*, 19, 730-736, 1985.
- Jacob, D. J. and Hoffmann M. R., A dynamic model for the production of H⁺, NO₃ and SO₄²⁻ in urban fog, *J. Geophys. Res.*, 88, 6611-6621, 1983.
- Jacob, D. J., Shair F. H., Waldman J. M., Munger J. W. and Hoffmann M. R., Transport and oxidation of SO₂ in a stagnant foggy valey, *Atmos. Environ.*, 21, 1305-1314, 1987.
- Kelly, T. G., Daum, P. H. and Schwartz, S. E., Measurements of peroxides in cloud-water and rain, *J. Geophys. Res.*, 90, 7861-7871, 1985.
- Lala, G. G., Mandel, E. and Jiusto, J. E., A numerical evaluation of radiation fog variables, *J. Atmos. Sci.*, 32, 720-728, 1975.

- Lee, Y-N and Schwartz, S. E., Kinetics of oxidation of aqueous sulfur(IV) by nitrogen dioxide in Precipitation Scavenging, Dry Deposition, and Resuspension, Volume I, H. R. Pruppacher, R. G. Semonin, and W. G. N. Slinn, eds., Elsevier, NY, 1983.
- McDonald, J. E., The saturation adjustment in numerical modelling of fog, *J. Atmos. Sci.*, 20, 476-478, 1963.
- McRae, G. J., Goodin W. R. and Seinfeld J. H., Development of a second generation mathematical model for urban air pollution, I. Model formulation. *Atmospheric Environment*, 16, 679-696, 1982.
- Munger, J. W., Jacob D. J., Waldman J. M., Hoffmann M. R., Fogwater chemistry in an urban atmosphere, *J. Geophys. Res.*, 88, 5109-5121, 1983.
- Munger, J. W., Collett J., Daube B., Hoffmann M. R., Fogwater chemistry at Riverside California, *Atmos. Environ.*, (submitted), 1989.
- Pruppacher, H. R. and Klett J. D., Microphysics of Clouds and Precipitation, Reidel Pub. Comp., 1980.
- Pandis, S. N. and Seinfeld J. H., Sensitivity analysis of a chemical mechanism for aqueous-phase atmospheric chemistry, *J. Geophys. Res.*, 94, 1105-1126, 1989.
- Schwartz, S. E., Gas- and aqueous-phase chemistry of HO₂ in liquid water clouds, *J. Geophys. Res.*, 89, 11589-11598, 1984.
- Seigneur, C. and Saxena P., A theoretical investigation of sulfate formation in clouds, *Atmos. Environ.*, 22, 101-115, 1988.
- Seigneur, C. and Saxena P., A study of atmospheric acid formation in different environments, *Atmos. Environ.*, 18, 2109-2124, 1984.
- Shir, C. C., A preliminary numerical study of atmospheric turbulent flows in the idealized planetary boundary layer, *J. Atmos. Sci.*, 30, 1327-1339, 1973.
- Ten Brink, H. M., Schwartz, S. E. and Daum, P. H., Efficient scavenging of aerosol

- sulfate by liquid water clouds, *Atmos. Environ.*, 21, 9, 2035-2052, 1987.
- Tremblay, A. and Leighton H., The influence of cloud dynamics upon the redistribution and transformation of atmospheric SO₂ - a numerical simulation, *Atmos. Environ.*, 18, 1885-1894, 1984.
- Tremblay, A. and Leighton H., A three-dimensional cloud chemistry model, *J. Climate appl. Met.*, 25, 652-671, 1986.
- Turton, J. D. and Brown R., A comparison of a numerical method of radiation fog with detailed observations, *Quart. J. Roy. Meteor. Soc.*, 113, 37-54, 1987.
- Waldman, J. M., Depositional aspects of pollutant behavior in fog, Ph.D. thesis, California Institute of Technology, 1986.
- Walcek, C. J. and Taylor G. R., A theoretical method for computing vertical distributions of acidity and sulfate production within cumulus clouds, *J. Atmos. Sci.*, 43, 339-355, 1986.
- Waldman, J. M., Munger J. W., Jacob D. J., Flagan R. C., Morgan J. J. and Hoffmann M. R., Chemical composition of acid fog, *Science*, 218, 677-680, 1982.
- Zdunkowski, W. G. and Nielsen, B. C., A preliminary prediction analysis of radiation fog, *Pure and Appl. Geophys.*, 75, 278-299, 1969.
- Zdunkowski, W. G., Welch, R. M. and Paegle, J., One-dimensional numerical simulation of the effects of air pollution on the planetary boundary layer, *J. Atmos. Sci.*, 33, 2399-2414, 1976.
- Zdunkowski, W. G., Panhans W-G., Welch R. M. and Korb G. J., A radiation scheme for circulation and climate models, *Beitr. Phys. Atmosph.*, 55, 215-238, 1982.

CHAPTER 4

**CHEMICAL COMPOSITION DIFFERENCES
IN FOG AND CLOUD DROPLETS OF DIFFERENT SIZES**

(Accepted for publication in *Atmospheric Environment*, June 1989)

Chemical Composition Differences in Fog and Cloud Droplets of Different Sizes

Spyros N. Pandis, John H. Seinfeld

*Department of Chemical Engineering and Environmental Quality Laboratory,
California Institute of Technology, Pasadena, CA 91125, USA*

and

Christodoulos Pilinis

Aero Vironment Inc., 825 Myrtle Ave., Monrovia, CA 91016, USA

Abstract

The distribution of acidity and solute concentration among the various droplet sizes in a fog or cloud and the effect of the evaporation-condensation cycle on the composition and size distribution of atmospheric aerosol is studied. Significant total solute concentration differences can occur in aqueous droplets inside a fog or cloud. For the fog simulated here, during the period of dense fog, the solute concentration in droplets larger than 10 μm diameter increased with size, in such a way that droplets of diameter 20 μm attain a solute concentration that is a factor of 3.6 larger than that in the 10 μm droplets. Droplets on which most of the liquid water condenses have access to most of the reacting medium for in situ S(IV) oxidation and are therefore preferentially enriched in sulfate. The gas and aqueous-phase chemical processes result in an increase of the total solute mass concentration nonuniform over the droplet spectrum for a mature fog. These chemical processes tend to decrease the total solute mass concentration differences among the various droplet sizes. Low cooling rates of the system also tend to decrease these concentration differences while high cooling rates have exactly the opposite effect. The mass/size distribution of the condensation nuclei influences quantitatively, but not qualitatively, the above concentration differences.

Introduction

Atmospheric aerosols are multicomponent particles with sizes ranging roughly from 0.01 to 10 μm in diameter. It is well known now that the chemical composition of these aerosol particles varies significantly with size. At a specific relative humidity, which for most soluble components in the atmosphere is well below 100%, aerosol particles that are not already liquid deliquesce into aqueous solution drops. As the relative humidity keeps increasing, the droplets increase their size in accordance with water vapor equilibrium. If the relative humidity of the air parcel reaches a critical humidity, the value of which depends on the size and chemical composition of the aerosol present, the droplets become activated, grow freely by water vapor diffusion, and a cloud or fog forms. In addition to having solute concentration differences that arise from differences in the composition of the condensation nuclei, fog and cloud droplets scavenge soluble gases like nitric acid and ammonia and act as a medium for various aqueous-phase reactions, including the oxidation of absorbed SO_2 to sulfate.

Despite the fact that cloud microphysics suggests that diffusional growth of aqueous droplets could result in size dependent concentration and composition, the concentration/size distribution of cloud or fog droplets has not been quantitatively modeled. The main available experimental information on chemical composition differences in cloud droplets was reported by Noone et al. (1988) who sampled droplets from a marine stratus cloud and calculated that the volumetric mean solute concentration of the 9- to 18- μm droplets was a factor of 2.7 smaller than that in the 18- to 23- μm droplets. The concentration/size dependence of cloud or fog droplets has been addressed as a secondary problem in a few theoretical studies with inconclusive results. A study of Flossmann et al. (1985), using an entraining air parcel cloud model, suggested that the mass mixing ratio of the aerosol that served

as condensation nuclei or was scavenged by the aqueous droplets is larger inside smaller drops than inside larger drops when condensation and collision-coalescence are the dominant processes. Other theoretical studies (Hegg and Hobbs, 1979; Jensen and Charlson, 1984) have implied that the opposite is true, namely that the total solute mass concentration is smaller inside the smaller drops when nucleation scavenging is the controlling process.

The investigation of the possible chemical heterogeneities among fog or cloud droplets is of primary importance for both the modeling of acid deposition processes and the design of cloud or fog sampling. Measured droplet spectra in clouds and fogs of various types are usually far from monodisperse (Pruppacher and Klett, 1980). A major assumption common to virtually all atmospheric aqueous-phase chemistry models developed to this point, however, (Graedel and Goldberg, 1983; Chameides, 1984; Schwartz, 1984; Jacob, 1986; Seigneur and Saxena, 1988; Pandis and Seinfeld, 1989) is that the cloudwater or fogwater consists of a monodisperse, chemically homogeneous distribution of droplets.

Each of the theoretical studies attempting to address the concentration/size dependence of fog or cloud droplets has focused on cloud microphysics, neglecting chemical processes associated with the gas and aqueous phases. This study combines for the first time a detailed description of the gas and aqueous-phase atmospheric chemistry occurring in a cloud or fog with the microphysics of the condensational growth of an aqueous droplet distribution. The thermodynamics and dynamics of multicomponent aerosols are described explicitly for the period before the fog (or cloud) formation and that after the aqueous phase dissipates. The coupling of the descriptions of all the above physical and chemical processes enables us to simulate the concentration/size dependence of fog and cloud droplets under a variety of conditions and during the various stages of fog (or cloud) development.

We begin with separate descriptions of the gas-phase chemistry, aerosol dynamics and thermodynamics, aqueous-phase chemistry, and droplet microphysics and then describe the complete model used in this study. Model predictions are then presented together with an analysis of the importance of the gas- and aqueous-phase chemical processes. The sensitivity of the results to the initial aerosol size/composition distribution and to the temperature change are also addressed.

Model Description

The mathematical model employed in this study describes the physicochemical processes of gas-phase chemistry, aerosol dynamics and thermodynamics, aqueous-phase chemistry and droplet microphysics, in a closed volume of air in which a fog or a cloud is formed and dissipated. The primary input to the model is the temperature of the system.

The life cycle of a fog or a cloud can be divided into three periods, namely the conditioning period (relative humidity, RH, rises from the initial value to saturation), the rapid growth period (RH exceeds 100%), and the dissipation period (RH drops under 100%). In the first and the last periods the aqueous droplets can exist in equilibrium with the surrounding air and the amount of the aqueous-phase (liquid water content) is small, while in the rapid growth period droplets grow unstably resulting in the creation of a fog or cloud with considerable liquid water content. Therefore, the physics of the problem suggest strongly that the numerical simulation itself should be divided into three stages corresponding to the three different periods of the fog or cloud life cycle. These three stages can be defined by choosing an appropriate relative humidity threshold value, RH_c , so that the first stage lasts until the system's relative humidity reaches RH_c , the rapid growth period is defined by $RH \geq RH_c$, and the dissipation period starts when the relative humidity drops

again under RH_c .

Several factors should be considered in selecting RH_c . The value of RH_c should be low enough so that the available amount of liquid water remains small during the first and third simulation stage, and aqueous-phase reactions can be neglected during these periods. Additionally, the higher the RH_c value, the larger the size of the water drops at this relative humidity, the larger their corresponding relaxation time to equilibrium, and thus the larger the errors introduced by the water equilibrium assumption. At the same time, the lower the RH_c value, the longer the rapid growth period lasts, the longer the complete system of differential equations has to be solved, resulting in excessive computing requirements and numerical problems associated with the inherent stiffness of the differential equations. Several numerical tests showed that the choice of $RH_c = 99\%$ represents a reasonable compromise, preserving the accuracy of the computation while minimizing the computing time requirements.

1. Conditioning period

During this stage as the RH is increasing but still is below RH_c , the model simulates the gas-phase chemistry and the aerosol behavior. Aqueous-phase chemical reactions are neglected because of the relatively small amount of liquid water present, and the water is assumed to be in equilibrium between the gas and aerosol phase. For computational purposes the continuous aerosol size distribution is discretized into n uniform sections (Warren and Seinfeld, 1985). The dependent variable vector $F^{(t)}$, whose evolution in time is calculated by the model during this period, contains the gas-phase concentrations of 62 species arising from the gas-phase chemical mechanism used and the concentrations of 18 particulate-phase species in each of the aerosol sections. The numerical solution of the evolution of

the aerosol size spectrum and gas-phase concentrations is accomplished by using an operator splitting technique, in which one divides the full problem into various subproblems that are solved sequentially. The scheme used to calculate the value of the variable vector F at time $t + h$ is in operator notation:

$$F^{(t+h)} = A_{int}(h)A_{th}(h)A_d(h)A_{gch}(h)F^{(t)} \quad (1)$$

where $A_{gch}(h)$ indicates advancing the gas-phase chemistry over a time step of length h , and A_{int} , A_{th} , A_d indicate similar advancements for the intersectional movement of aerosol particles, the aerosol thermodynamics and aerosol dynamics, respectively (Pilinis and Seinfeld, 1988). These operators will now be explained.

Gas-phase chemistry operator

The gas-phase chemistry operator describes the gas-phase atmospheric chemical reactions occurring inside a homogeneous air parcel. The evolution of the concentration of the i^{th} gaseous species, C_i , is governed by the spatially homogeneous chemical reaction rate equations,

$$\frac{dC_i}{dt} = R_i^g(C_1, C_2, \dots, C_n) \quad (2)$$

where R_i^g is the rate of change of species i via gas-phase chemical reactions. To calculate R_i^g the detailed SAPRC/ERT gas-phase chemical reaction mechanism (Carter et al., 1986) with the modifications and extensions of Carter and Atkinson (1988) is used. This gas-phase chemical mechanism is a state-of-the-art description the complex chemical reactions of hydrocarbon/ NO_x / SO_2 mixtures in a polluted atmosphere, using 154 reactions and 62 species (39 active, 7 accumulating and 16 steady state species). The photochemical mechanism preparation and emissions processing software of Carter and Atkinson (1988) has been used to prepare the gas-phase

mechanism dependent portion of the code.

Aerosol operators

The size and composition of aerosol particles undergoing nucleation, condensation, and coagulation are described by the aerosol general dynamic equation (Seinfeld, 1986). Using the sectional approximation, in which the continuous size distribution is approximated by a series of step functions (Warren and Seinfeld, 1985; Pilinis et al., 1987), the evolution of the mass concentration of species i in the l^{th} size section, Q_{il} , is described by:

$$\frac{dQ_{il}}{dt} = \left[\frac{\partial Q_{il}}{\partial t} \right]_{cond./evap.} + \left[\frac{\partial Q_{il}}{\partial t} \right]_{coag.} + \left[\frac{\partial Q_{il}}{\partial t} \right]_{sources/sinks} \quad (3)$$

where $\left[\frac{\partial Q_{il}}{\partial t} \right]_{cond./evap.}$ and $\left[\frac{\partial Q_{il}}{\partial t} \right]_{coag.}$ are the rates of change of species i in the l^{th} section due to condensation or evaporation and coagulation, respectively, (Gelbard and Seinfeld, 1980; Gelbard et al., 1980; Warren and Seinfeld, 1985; Pilinis et al., 1987) and $\left[\frac{\partial Q_{il}}{\partial t} \right]_{source/sinks}$ is the rate of change due to nucleation, primary aerosol injection and removal. The three aerosol operators, A_{int} , A_{th} , and A_d , applied successively to the variable vector F represent a method for the solution of equation (3).

Typical components in the aqueous aerosol phase are H_2O , NH_4^+ , SO_4^{2-} , NO_3^- , H^+ , Na^+ , Cl^- , HSO_4^- and H_2SO_4 and possible components in the solid phase are Na_2SO_4 , $NaHSO_4$, $NaCl$, $NaNO_3$, NH_4Cl , NH_4NO_3 , $(NH_4)_2SO_4$, NH_4HSO_4 and $(NH_4)_3H(SO_4)_2$ (Pilinis and Seinfeld, 1987). The aerosol thermodynamics operator computes the chemical equilibrium of volatile species such as H_2O , NH_3 , HCl , and HNO_3 between the gas and aerosol phases while the aerosol dynamics operator describes explicitly the diffusion controlled gas-to-particle conversion of non-volatile species such as sulfuric acid (Pilinis and Seinfeld, 1987). During aerosol evaporation

or condensation the operator for the intersectional movement, A_{int} , describes the movement of the aerosol particles from each constant size section to its neighboring sections (Warren and Seinfeld, 1985; Pilinis et al., 1987).

2. Rapid Growth Period

When the relative humidity of the system reaches the threshold value RH_c , major changes take place. The aqueous droplets approach the region of unstable growth and their liquid water content increases considerably. Important processes during this period include gas-phase chemistry, aqueous-phase chemistry, and microphysics of aqueous droplets. The droplet size distribution is discretized as before into n individual size sections, but because of the magnitude of the size changes occurring, each droplet size section is now allowed to move in the time-diameter space increasing its diameter when water condensation is taking place and decreasing its size in case of evaporation.

Let d_l and d_{l+1} denote the boundaries of each fixed size section during the conditioning period. We represent the droplets in each section during the rapid growth period by the mass mean diameter of that section, D_l . In other words, we replace the N_l particles of total mass M_l evenly distributed between diameters from d_l to d_{l+1} from the conditioning period with N_l particles of the same total mass M_l , but with the single diameter D_l , where D_l is calculated by:

$$D_l = \left[\frac{2d_l^2 d_{l+1}^2}{d_l + d_{l+1}} \right]^{1/3} \quad (4)$$

A new dependent variable vector Y is defined that contains the concentrations of all 62 gas-phase species, the concentrations of 49 aqueous-phase species in each of the n sections and the n diameters D_l (one for each section). The gas-phase chemistry is decoupled from the aqueous-phase chemistry and droplet microphysics

by using the following operator splitting scheme:

$$Y^{(t+h)} = A_{ach}(h)A_{gch}(h)Y^{(t)} \quad (5)$$

with A_{ach} being the aqueous-phase chemistry and droplet microphysics operator.

Aqueous-phase chemistry and droplet microphysics operator .

In previous cloud or fog modelling studies, droplets have been defined as aerosol particles that have been activated, with the non-activated particles considered as the interstitial aerosol (Flossman et al., 1985). Here, in the aqueous-phase chemistry and droplet microphysics operator, there need be no explicit difference in the treatment of the interstitial aerosol particles and the aqueous droplets and, for reasons of simplicity, both will be referred to as droplets from now on. The change of the mass concentration of species i in moving section l , q_{il} , is calculated by:

$$\frac{dq_{il}}{dt} = \left[\frac{\partial q_{il}}{\partial t} \right]_{cond./evap.} + R_i^a(q_{1l}, q_{2l}, \dots, q_{nl}) \quad (6)$$

where $\left[\frac{\partial q_{il}}{\partial t} \right]_{cond./evap.}$ is the mass transfer rate of species i from the gas phase to the aqueous droplets in moving section l . For water the detailed growth equation derived by Pruppacher and Klett (1980) is used and for the remainder of the volatile species the expression used by Pandis and Seinfeld (1989) is applied. The reaction rates R_i^a are derived from the aqueous-phase chemical mechanism presented by Pandis and Seinfeld (1989), which includes 49 individual aqueous-phase species, 17 aqueous-phase ionic equilibria and 109 aqueous-phase reactions.

The change in section diameter is calculated by:

$$\frac{dD_l}{dt} = \frac{2}{N_l \rho_l \pi D_l^2} \sum_{i=1}^{N_v} \left[\frac{\partial q_{il}}{\partial t} \right]_{cond./evap.} \quad (7)$$

where N_l is the number, and ρ_l the density of droplets in section l , respectively, and N_v is the number of volatile species. The number of droplets, N_l , is assumed

constant with time since droplet coagulation is neglected and since the section moves in such a way that particles do not grow out of a section.

3. Dissipation period

When the relative humidity becomes less than the critical relative humidity (RH_c), the system passes to the third stage, where the aerosol operators are reactivated and all the calculations are performed exactly as in the conditioning period.

Representative Cases for Evaluation

There has been conflicting opinions in the literature concerning the nature of the solute concentration/size dependence of cloud or fog droplets. At the same time there is no available information concerning the possible differences in chemical composition of the various droplet sizes, e.g., differences in sulfate concentration, etc. To investigate these phenomena, the model described above has been applied under representative conditions to elucidate differences in chemical composition of droplets of different sizes inside a fog or a cloud. Unfortunately, a data set including the size/composition distribution of atmospheric aerosol and aqueous-phase droplets before, during, and after fog or cloud development is not available for the model's evaluation. Therefore, a representative set of initial conditions together with a temporal temperature variation have been chosen. We will henceforth refer to this as Case 1, the parameters of which are given in Table I. The sensitivity of the results to the temperature variation profile used has been studied by performing two additional simulations (Cases 2 and 3). Finally, the effects of the aerosol size distribution before the fog development on the concentration differences in fog and cloud droplets of different sizes have been investigated in the simulation for Case 4.

Case 1 (base case).

Table I. Base case parameters and initial conditions.

<i>Model Parameter</i>	<i>Value</i>
Latitude	34.5
Solar declination	0°
Time at start	7 : 00 PST
Relative humidity at start	95%

<i>Gas – phase species</i>	<i>Initial concentration (ppb)</i>
SO ₂	20.0
NH ₃	3.17
HNO ₃	2.21
HCl	0.55
O ₃	20.0
NO	35.0
NO ₂	70.0
H ₂ O ₂	2.0
HCHO	20.0
PAN	1.0
ETHE	85.0
Parafins	700.0
Olefins	45.0
Aromatics	150.0

<i>Aerosol species</i>	<i>Initial concentration (µg/m³)</i>
Sulfate	3.72
Sodium	1.8

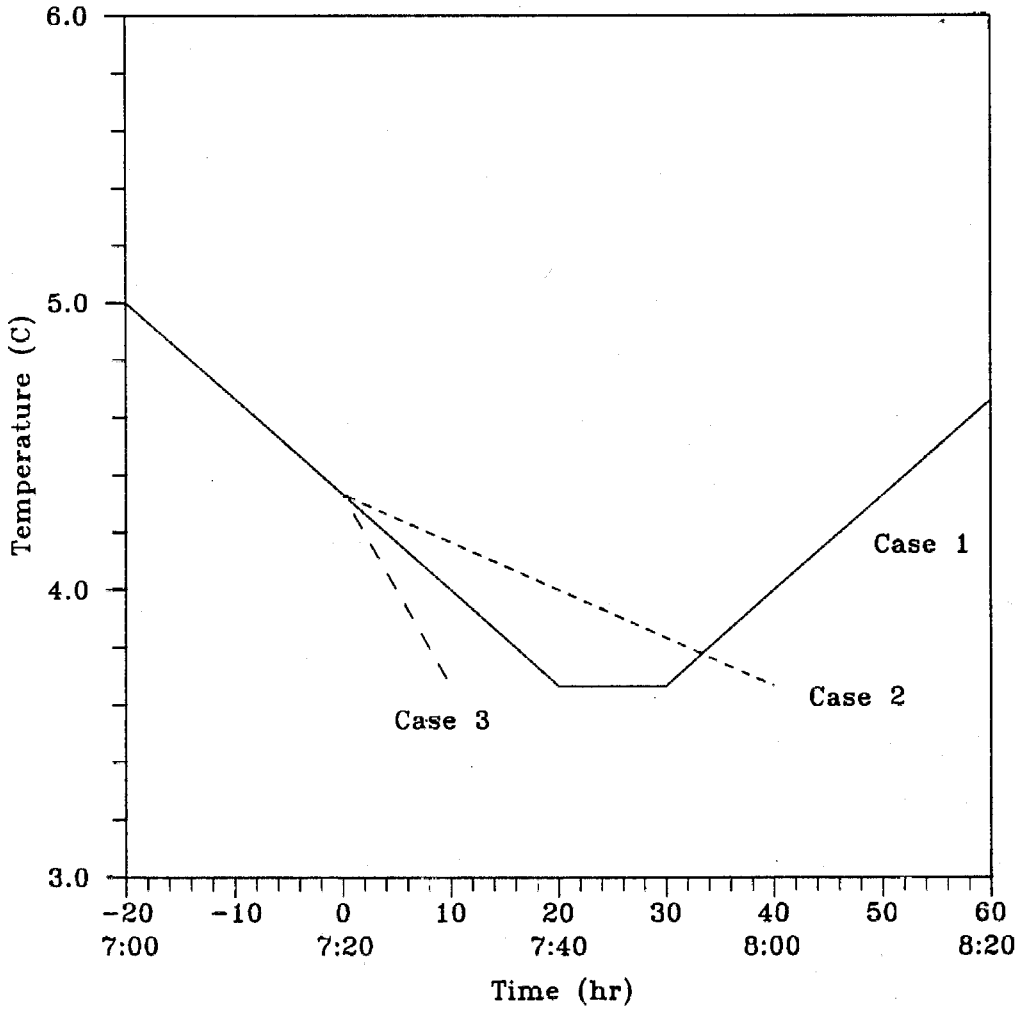


Figure 1 Temperature variation profiles used in the various simulations. The profile used in Case 4 is the same as in Case 1.

In this case a winter maritime urban fog is simulated. The concentrations of ammonia, nitric acid, hydrochloric acid, sulfate and sodium are based on the measurements of Russell and Cass (1984) for Long Beach, California. Due to lack of specific data, an initial hydrogen peroxide concentration of 2 ppb is assumed after Heikes et al. (1987). The remainder of the gas-phase concentrations are derived from Seigneur and Saxena (1984) characteristic of an urban fog in the Los Angeles area.

The system temperature is assumed to vary with time as shown in Figure 1. This temperature variation corresponds to that reported for an early morning winter fog development episode (Roach et al., 1976).

The model has been applied with 7 logarithmically spaced sections covering initially the diameter range from 0.2-8 μm . The size (diameter) sections used are (1) 0.2-0.34 μm , (2) 0.34-0.57 μm , (3) 0.57-0.97 μm , (4) 0.97-1.65 μm , (5) 1.65-2.79 μm , (6) 2.79-4.72 μm , (7) 4.72-8.0 μm . The initial sulfate and sodium have been distributed over these sections based on the measurements of Wall et al. (Wall et al., 1988) for wet maritime air. The initial aerosol mass concentration distribution calculated assuming thermodynamic equilibrium between the gas and aerosol phases for the sulfate, nitrate, chloride, sodium, ammonium, water system (Pilinis and Seinfeld, 1987), is shown in Figure 2a.

Case 2

The conditions used were the same as in Case 1, except for the assumed temperature profile (Figure 1). A cooling rate of 1 $^{\circ}\text{C hr}^{-1}$ was assumed during the growth period compared to the 2 $^{\circ}\text{C hr}^{-1}$ used in Case 1.

Case 3

All the conditions were the same as in the two previous cases but a cooling rate

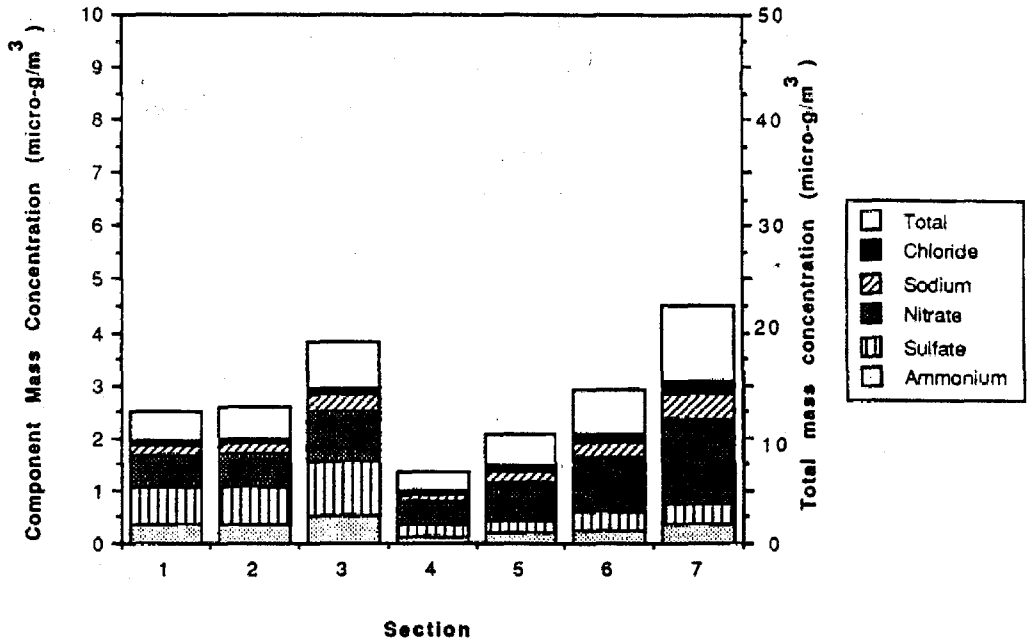


Figure 2a. Calculated aerosol size/composition distribution at the beginning of the Case 1 simulation, 7:00 ($t = -20$ min), assuming thermodynamic equilibrium for the sulfate, nitrate, sodium, ammonium, and water system.

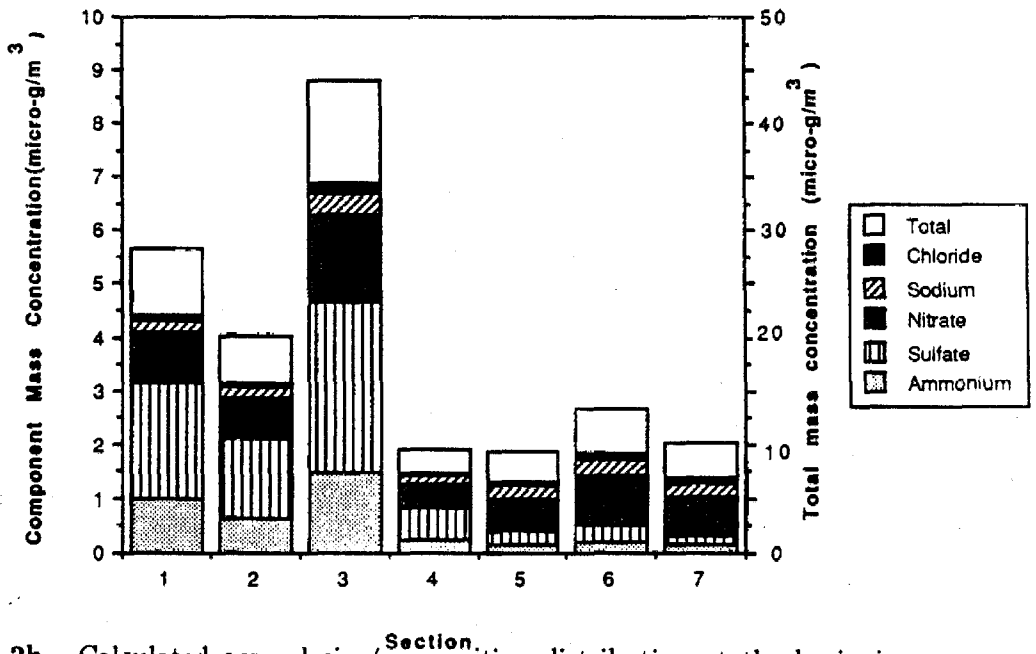


Figure 2b. Calculated aerosol size/composition distribution at the beginning of the Case 4 simulation, 7:00 ($t = -20$ min), assuming thermodynamic equilibrium for the sulfate, nitrate, sodium, ammonium, and water system.

of $4\text{ }^{\circ}\text{C hr}^{-1}$ was assumed during the growth period (Figure 1) resulting in a much faster development of the aqueous phase. This cooling rate corresponds to a vertical velocity of the air parcel around 10 cm s^{-1} , and this simulation is applicable to the initial stages of formation of a stratus cloud (Hänel, 1987).

Case 4

The temperature of the system varied as in Case 1. The aerosol size/composition distribution in the beginning of the simulation was changed by increasing the amount of sulfate from $3.72\text{ }\mu\text{g m}^{-3}$ (Case 1) to $8\text{ }\mu\text{g m}^{-3}$ and the available NH_3 to 6 ppb. The initial aerosol distribution calculated assuming thermodynamic equilibrium for the system at 95% relative humidity is shown in Figure 2b. The main feature of this aerosol distribution compared to that used in Case 1 is the enrichment in solute mass of the three smallest sections covering the range from 0.2 to $1\text{ }\mu\text{m}$ in diameter.

Results and Discussion

Size/Composition Distribution of Fog and Cloud Droplets (Base Case)

In all cases, after 20 minutes the relative humidity of the system reaches 99% (RH_c) and the rapid growth period begins (see Figure 1). We define this time as $t = 0$, at which all the seven size sections are growing. In the base case, by $t = 6$ min, the smallest droplet section reaches a maximum diameter of $0.52\text{ }\mu\text{m}$ and starts evaporating slowly, following the decreasing relative humidity, with the second smallest section soon following. These two smallest sections represent the interstitial aerosol particles. At $t = 6$ min the system supersaturation has reached its maximum value of 0.11% (Figure 3). This maximum is a result of two competing processes, the tendency of the supersaturation to increase due to the system's cooling and the

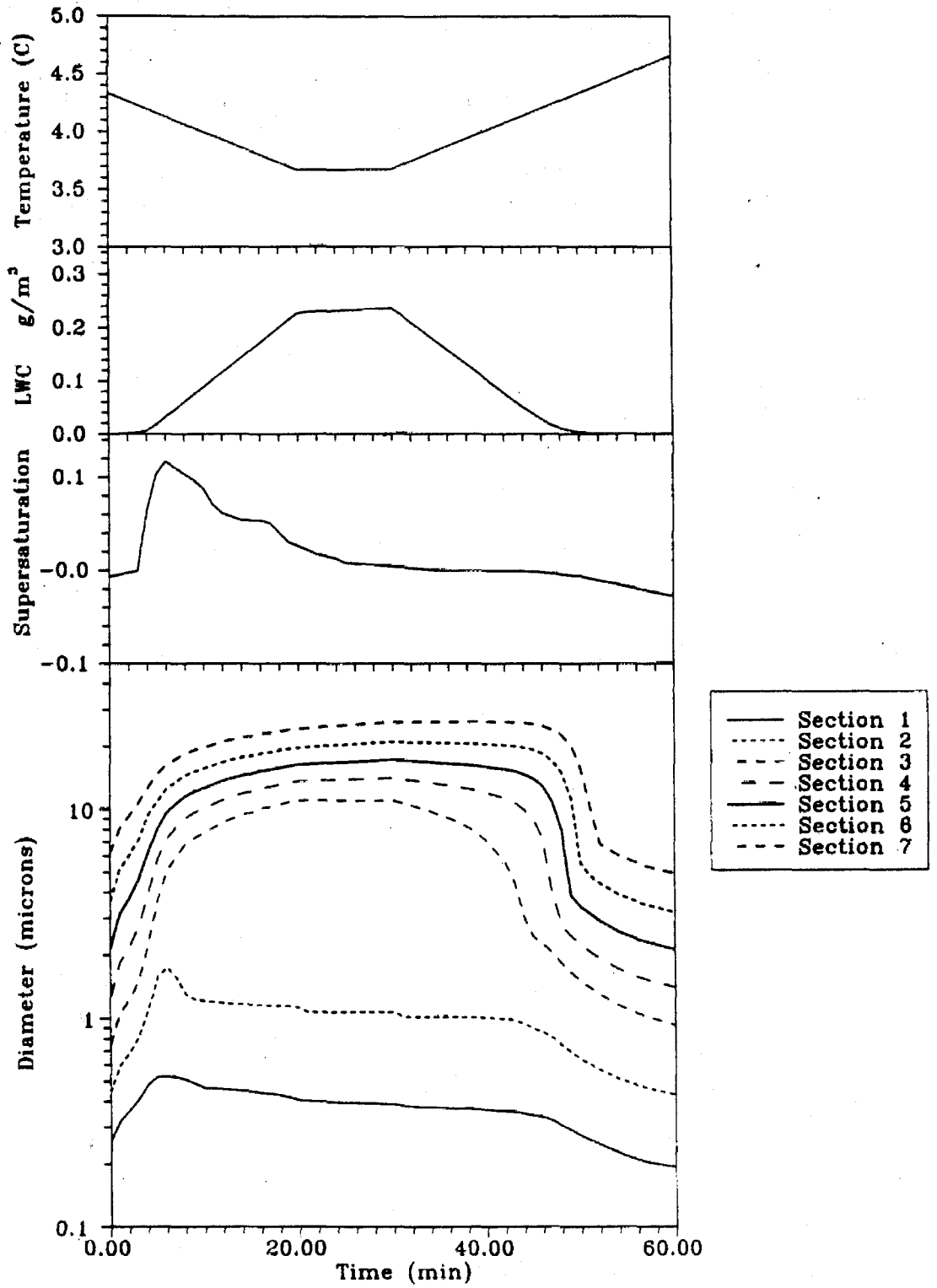


Figure 3. Calculated variation of the mass mean diameter of the 7 sections, the system's supersaturation, the liquid water content and the temperature with time. $t = 0$ corresponds to 7:20.

tendency of the supersaturation to decrease due to the transfer of water vapor to the aqueous-phase. The fog has fully developed at $t = 20$ min reaching a liquid water content of 0.23 g m^{-3} (Figure 3). At this time the two smallest non-activated droplet sections are evaporating because the system's relative humidity remains below their corresponding equilibrium vapor pressures, while the remainder of the size sections are growing. This observation is in agreement with that of Hänel (1987) that after the supersaturation in a cloud has reached its maximum, there are three types of droplets, small non-activated particles shrinking slowly, activated droplets growing unstably, and large droplets growing slowly. The third droplet section starts evaporating slowly at $t = 21$ min and the fog starts dissipating at $t = 31$ min due to the temperature increase. Noticeably, the droplets in the largest section, characterized by a large relaxation time (defined as the time required for the adaptation of the droplets to the changing conditions of their environment), continue to grow slowly for 8 more minutes before commencing to evaporate (Figure 3).

A significant portion of the fogwater is concentrated over a relatively short range of droplet diameters, with a peak at $14 \mu\text{m}$ at the time of maximum liquid water content (Figure 4). This mass distribution is in qualitative agreement with the measurements of Waldman (1986). The distribution of the dissolved compounds over this water droplet spectrum exhibits very interesting behavior. Initially ($t = 0$) all droplets are quite concentrated with solute concentrations of the order of 2×10^4 mg/liter water with the larger droplets being more dilute than the smaller ones. For example, the droplets in section 3 ($D_3(0) = 0.8 \mu\text{m}$) are 15% more concentrated than the droplets of section 4 ($D_4(0) = 1.2 \mu\text{m}$). This monotonic concentration variation changes drastically during the droplet growth period (Figure 5a). The droplets in the 3rd section, that are the smallest activated droplets, are able to

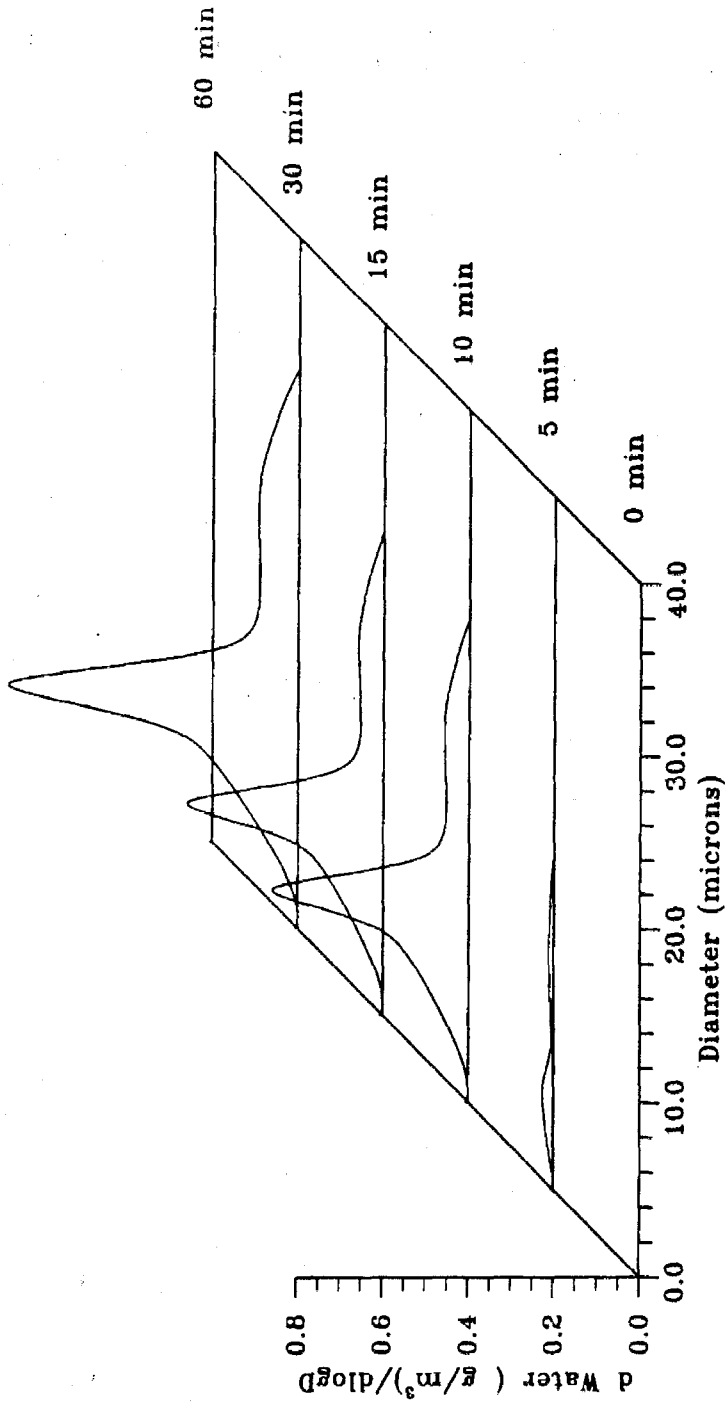


Figure 4 Calculated time evolution of the droplet mass distribution as a function of the droplet diameter.

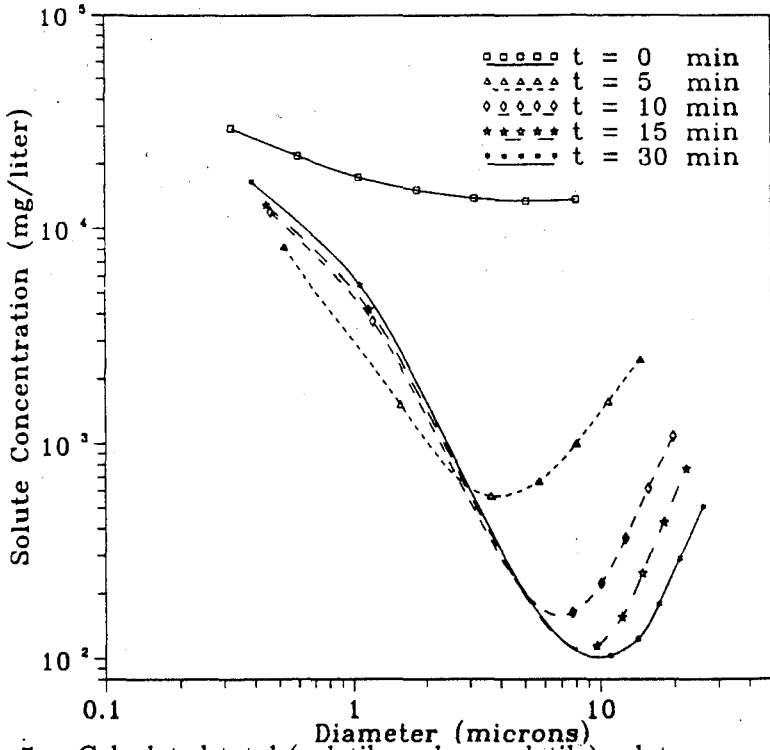


Figure 5a. Calculated total (volatile and nonvolatile) solute concentration as a function of droplet diameter for five different times during the growth period

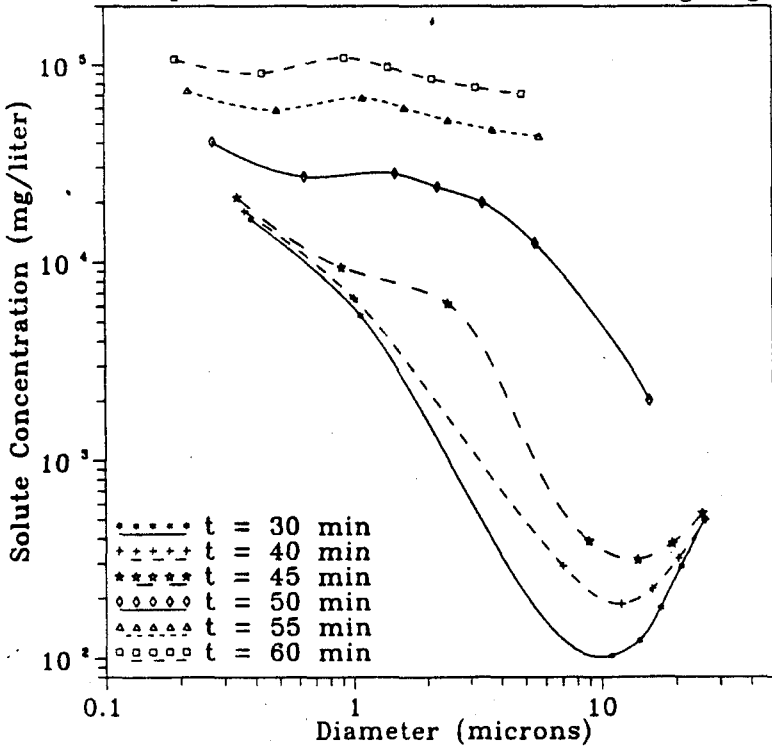


Figure 5b. Calculated total (volatile and nonvolatile) solute concentration as a function of droplet diameter for five different times during the fog dissipation.

grow much faster than the larger droplets. Therefore the resulting dilution rate for the droplets in the 3rd section is much higher than for those in the 4th etc., and these droplets become more dilute than the larger ones. For example, at $t = 20$ the droplets in section 3 ($D_3 = 11\mu\text{m}$) have a total solute concentration (volatile and non-volatile) of $93\ \mu\text{g/liter}$ water while droplets in section 4 ($D_4 = 13.6\mu\text{m}$) have a concentration of $125\ \mu\text{g/liter}$, in 5 ($D_5 = 16.3\mu\text{m}$) $197\ \mu\text{g/liter}$, in 6 ($D_6 = 19.7\mu\text{m}$) $340\ \mu\text{g/liter}$ and finally in 7 ($D_7 = 24.3\mu\text{m}$) $610\ \mu\text{g/liter}$. During the fog evaporation stage, the concentration variation over the droplet distribution returns again to the initial monotonic shape (Figure 5b). The reason for this behavior is that the smaller droplets evaporate faster than the larger ones. The above results are in essential agreement with the measurements of Noone et al. (1988).

These observations of the solute concentration size distribution are a direct result of the fact that droplets of different sizes grow and consequently dilute at different rates, that is smaller droplets grow faster and therefore dilute faster than the larger ones. This can be shown quantitatively using the following simple argument (a similar argument was presented also by Noone et al. (1988)). Assume that the dry aerosol particle size distribution is divided into discrete intervals i with diameters D_s^i . Let the dry particles of diameter D_s^i grow and become aqueous droplets of diameter D_d^i . Assuming for simplicity that the density of the dry particles is $1\ \text{g/cm}^3$, the mass mixing ratio of droplets in section i is $W_i = (D_s^i/D_d^i)^3$. Defining the dilution rate of section i as $DR_i = -(1/W_i)(dW_i/dt)$ and assuming that the mass of scavenged aerosol in droplets in section i remains constant with time (that is neglecting processes like scavenging of gas-species, coagulation, etc.) one gets for sections 1 and 2 with $D_d^1 > D_d^2$ that $(DR_1/DR_2) = (D_d^2/D_d^1)[(dD_d^1/dt)/(dD_d^2/dt)]$. Assuming that the droplets are sufficiently large that $(dD_d^i/dt) = K/D_d^i$ where K is a constant depending on the system's conditions and not on D_d^i (of course K defined by the

growth equation is a weak function of D_d^i , then $(DR_1/DR_2) = (D_d^2/D_d^1)^2 > 1$ and the smaller droplets are diluted at a faster rate than the larger ones if growth by water diffusion is the only process occurring.

Interesting changes in the size/composition spectrum of the droplets take place because of the simultaneous fogwater chemistry and the transfer of species between the gas and the aqueous phases. The amount of sulfate in the aqueous phase increases considerably from $4.0 \mu\text{g m}^{-3}$ at $t = 0$ min to $12.6 \mu\text{g m}^{-3}$ at $t = 30$ min and $12.8 \mu\text{g m}^{-3}$ an hour later. The main pathway for this sulfate production is the aqueous-phase oxidation of S(IV) by hydrogen peroxide. The other chemical pathways for sulfate formation do not contribute significantly because the pH of the aqueous phase remains under 4 at which and these reactions are very slow. Therefore, after the hydrogen peroxide depletion at $t = 20$, the sulfate production is slowed down considerably. The distribution of the produced sulfate is nonuniform over the size spectrum (Figure 6). The peak that is developed can be explained by the fact that most of the liquid water during the fog is in this droplet size regime, that is the 3rd section. These droplets have access to most of the reacting medium for S(IV) oxidation and therefore are preferentially enriched in sulfate. Despite this enrichment the condensational growth effects dominate in this case and these droplets are the most dilute. After the fog dissipation the produced sulfate remains in the aerosol phase resulting in a peak around $1 \mu\text{m}$ at $t = 60$ min.

The same enrichment as in the case of sulfate is observed with nitrate (Figure 7). Nitric acid produced in the gas phase is most efficiently scavenged by the droplets that carry most of the fog liquid water content. During the droplet evaporation stage some of the nitrate returns back to the gas phase as nitric acid. Ammonia is assumed to exist in limited quantities in this base case. During the initial period (before $t = 0$), where thermodynamic equilibrium is assumed, most of the ammonia

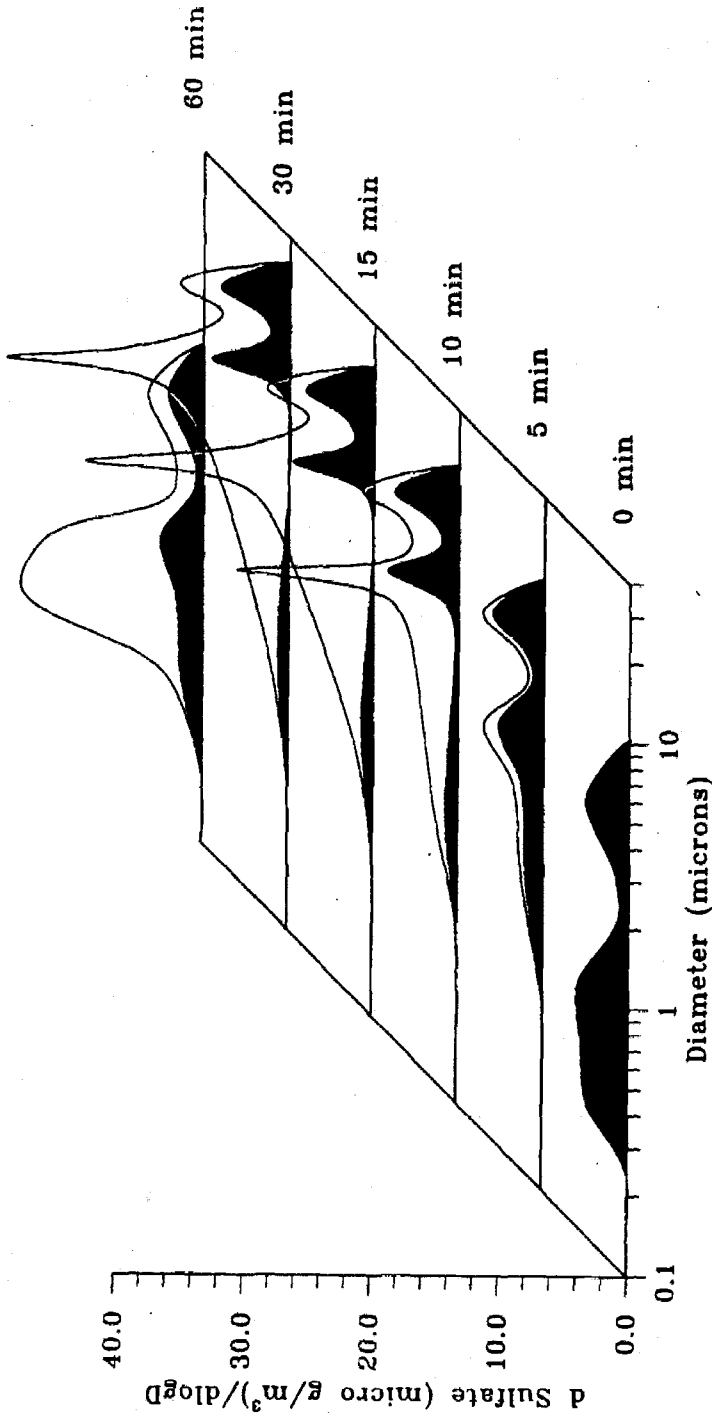


Figure 6 Calculated time evolution of the sulfate mass distribution as a function of the droplet diameter. The shaded area corresponds to the sulfate that initially exists in the aerosol particles and the rest is the sulfate produced during the fog evolution.

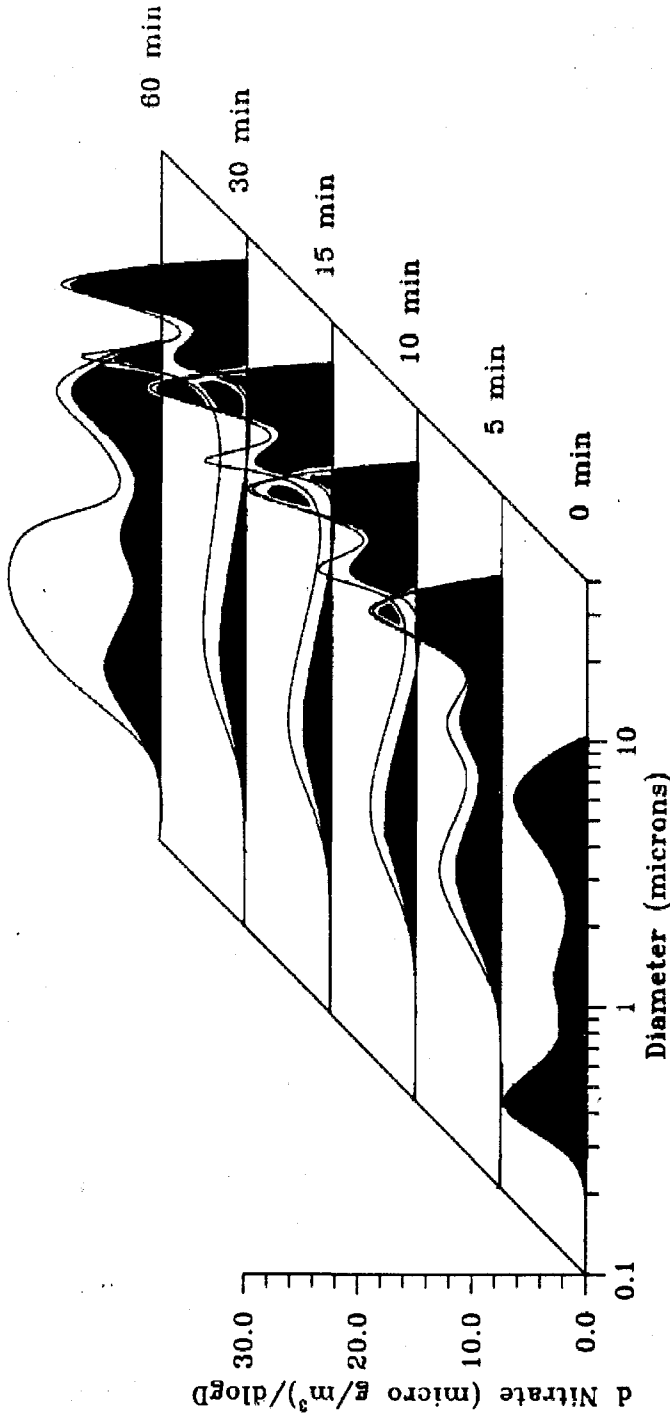


Figure 7 Calculated time evolution of the nitrate mass distribution as a function of the droplet diameter.

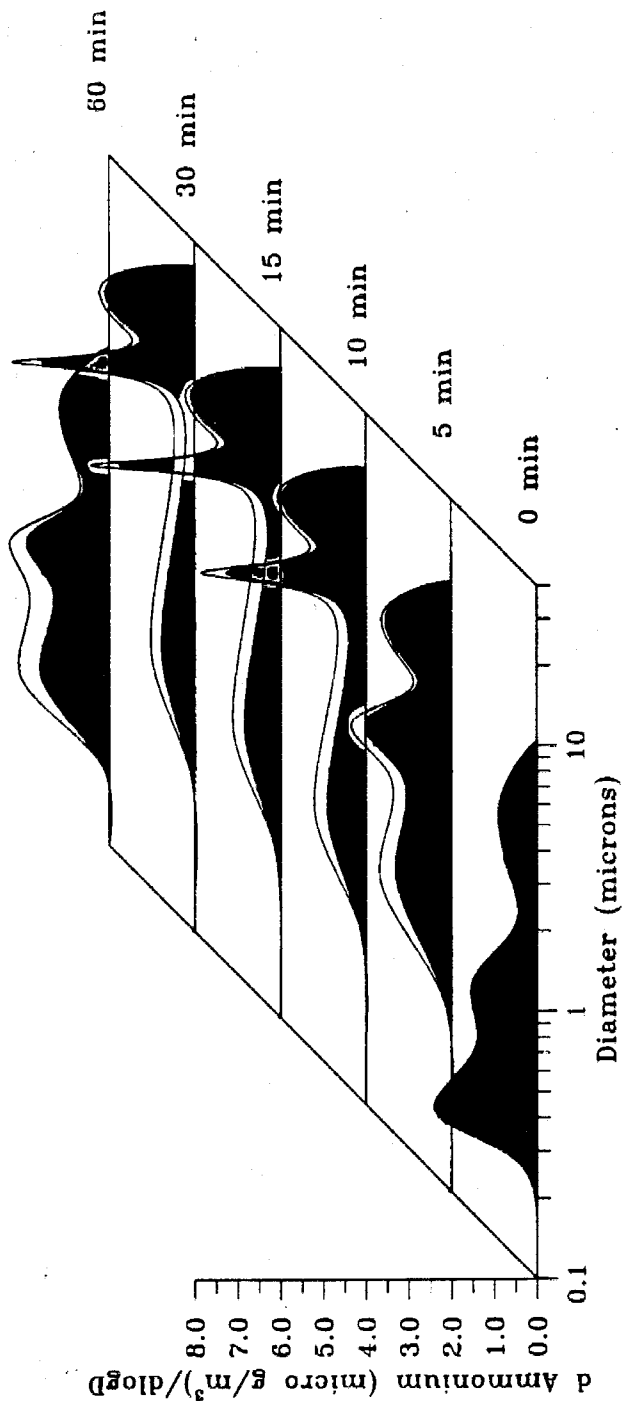


Figure 8 Calculated time evolution of the NH_4^+ mass distribution as a function of the droplet diameter.

resides in the aerosol phase. The small quantities of ammonia that are left in the gas-phase are again preferentially scavenged by the droplets that carry most of the water causing a relatively small change of the distribution. During the latter stages of fog development, no dramatic changes in the ammonium distribution over the droplet size spectrum occur because the available ammonia remains in the acidic aerosol phase and no emissions have been included in this simulation. The small change in the ammonium distribution can be seen by comparing the distributions at $t = 0$ and $t = 60$ min.

Influence of gas- and aqueous-phase chemistry

The importance of the chemical processes in both the gas and aqueous phases for the phenomena described above has been investigated by performing an additional simulation. The base case scenario has been reexamined but with no gas or aqueous-phase chemistry and without scavenging of species from the gas phase from $t = 0$ to $t = 60$ min. Hence, the liquid water is simply allowed to condense on the pre-existing multicomponent aerosol particles as they become activated to form cloud droplets.

The maximum liquid water content attained was again 0.23 g/m^3 and the drop size distribution did not change significantly from the base case suggesting that the liquid water formed is not influenced by the chemical reactions as long as no new condensation nuclei are formed. On the contrary, the solute concentration inside the droplets changes dramatically with the aqueous solutions being much more dilute than the corresponding droplets in the base case. The solute concentration inside the droplets of diameter $11 \mu\text{m}$ is, at $t = 30$ min, 24 mg/liter compared to 103 mg/liter when the gas and aqueous-phase chemical processes are included. The ratios of the total solute mass concentrations of the two cases are shown in Figure

9 for $t = 30$, the point when the liquid water content attains its maximum value. The effect of the gas and aqueous-phase chemical reactions is therefore to enrich droplets of diameters 10 to 15 μm with dissolved species. Bearing in mind that these droplets are more dilute than the others, one concludes that the chemical processes tend to smooth out the minimum solute concentration in the size/concentration distribution (Figure 5) and therefore tend to decrease the concentration differences between the various droplet sizes.

Influence of Cooling Rate

The temperature change is the direct or indirect driving force of the whole series of processes described above. Therefore it is reasonable to expect that in the dynamic framework of the current model, changes are going to occur based on the cooling rate of the system and the ability of the droplets or particles to follow these changes. To investigate these possible changes, two additional simulations have been performed, referred above as Cases 2 and 3.

In Case 2 a cooling rate slower than that used in the base case has been used. The relatively slow rate of change enables the larger droplets to follow more closely the ambient relative humidity. The maximum amount of liquid water that is formed ($t = 40$) is 0.24 g m^{-3} , that is just 5% higher than the liquid water for the base case at $t = 20$ min. The change in the liquid water size distribution is more profound. The distribution is shifted towards the larger droplet sizes proving that the slow cooling rate enables the larger droplets to attract larger quantities of water from the competing small droplets (Figure 10). The attraction of more water to the larger droplets results in the further dilution of these droplets and therefore decreases the solute concentration differences between small and large droplets (Figure 11). For example, the solute concentration of the 10 μm droplets is almost 50% larger

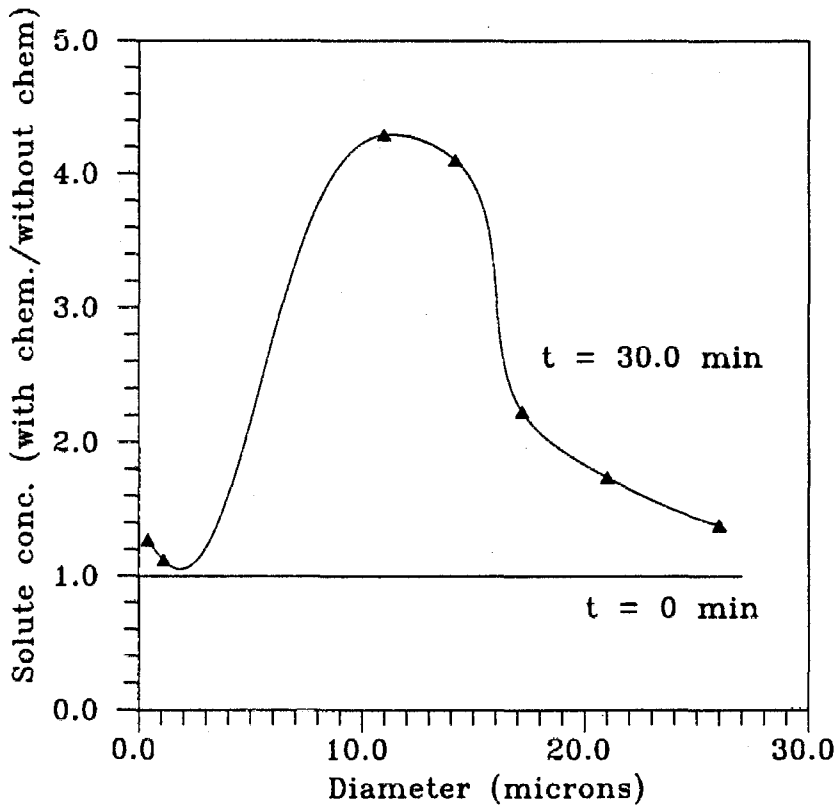


Figure 9. The ratio of the total solute concentration calculated by considering gas and aqueous phase chemistry over the total solute concentration calculated by neglecting chemical processes versus droplet diameter at $t = 30$.

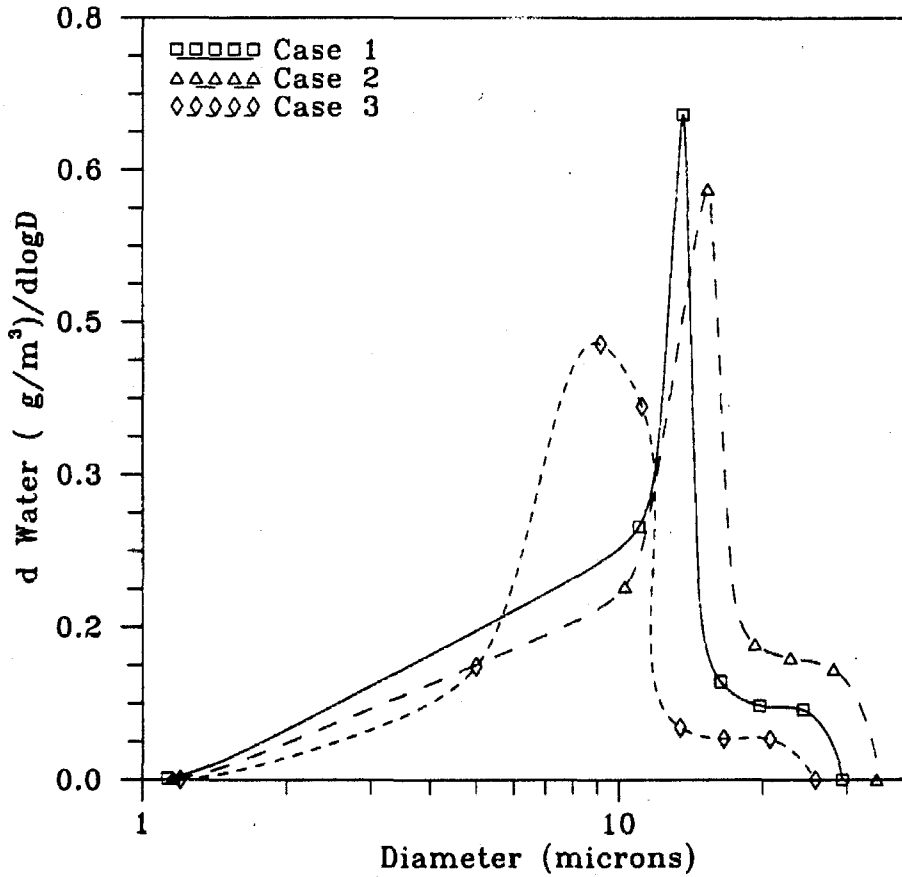


Figure 10 Comparison of the calculated liquid water mass distributions as a function of droplet diameter for Case 1 (base case, $t = 20$ min), Case 2 (small cooling rate, $t = 40$ min) and Case 3 (large cooling rate, $t = 10$ min).

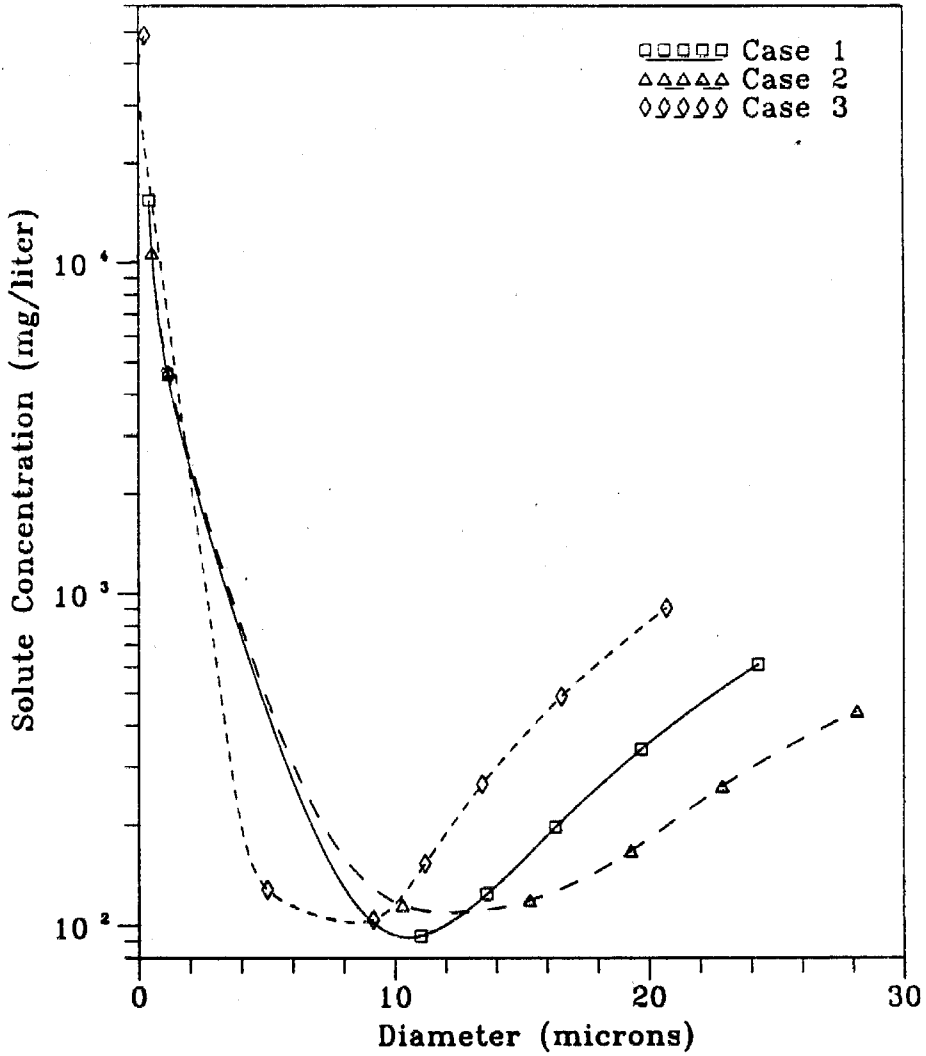


Figure 11 Comparison of the calculated total (volatile and nonvolatile) solute concentration as a function of droplet diameter for Case 1 (base case, $t = 20$ min), Case 2 (small cooling rate, $t = 40$ min) and Case 3 (large cooling rate, $t = 10$ min).

than the concentration of the 20 μm droplets, while in the base case it was 250%. Interesting changes are also observed in the distribution of the total solute mass over the droplet size spectrum (Figure 12). The total solute mass increases from 34.5 $\mu\text{g m}^{-3}$ (base case, $t = 20$ min) to 38.6 $\mu\text{g m}^{-3}$ ($t = 40$ min), an increase that is attributable mainly to the time difference and the subsequent production of more nitrate in the gas phase and secondarily to the increase of the fog liquid water content. Most of this additional solute mass is found in the droplets of diameter larger than 20 μm ($t = 40$).

In Case 3 a relatively rapid cooling of the system has been assumed. In contrast with Case 2 the larger droplets are not able to compete successfully with the smaller ones for the available liquid water. The maximum supersaturation increases to about 0.13% resulting in the activation of the particles in Section 2, leaving only the particles in Section 1 as the interstitial aerosol. The activation of these extra particles has interesting consequences because the number of growing droplets in the system increases significantly. The maximum liquid water ($t = 10$ min) decreases slightly compared to the previous cases to 0.22 g m^{-3} , evidence of the difficulty of the droplets to follow the rapid change of the ambient relative humidity. The liquid water distribution is shifted towards the smaller droplet diameters and at the same time the peak of the distribution is smaller and less sharp due to the fact that more droplets in a wider range are activated (Figure 10). The large droplets attract only small quantities of the condensing water and their solute concentration increases considerably, resulting in an increase of the solute concentration differences among the different droplet sizes (Figure 11). The total solute concentration of the 20 μm droplets is in this case almost 7.5 times larger than the corresponding concentration of the 10 μm droplets at $t = 10$ min. For the same reasons as in Case 2 (small time period) the total solute mass decreases to 32.7 $\mu\text{g m}^{-3}$ and is shifted towards the

smaller droplet diameters (Figure 12).

Influence of Initial Aerosol Distribution (Case 4)

The aerosol distribution before the fog development is a major factor in all the above processes, not only because it usually represents a large percentage of the solute mass (more than 30% in Case 1 at $t = 30$ min), but because it also affects the water distribution. The solute concentration distribution, for the aerosol shown in Figure 4 (at 95% relative humidity), is depicted in Figure 13. The two distributions generally exhibit the same behavior with a minimum around $10 \mu\text{m}$ even if most of the droplets in Case 1 are more dilute. The concentration differences are smaller, with the $20 \mu\text{m}$ droplets 2.4 times more concentrated than the $10 \mu\text{m}$ ones.

The above findings suggest that the quantitative results depend on the aerosol mass/size distribution that serve as condensation nuclei. This dependence is not strong enough, under most conditions, to change qualitatively the conclusions reached above.

Conclusions

A model has been developed to study the interactions between the chemical processes in the gas and aqueous phases and the growth of aerosol particles to fog or cloud droplets. The model assumes thermodynamic equilibrium for volatile components such as NH_3 , HCl , HNO_3 and water between gas and aerosol phases, and diffusion controlled gas-to-particle conversion of H_2SO_4 when the system's relative humidity is less than a critical value (e.g., 99%). When the relative humidity exceeds this critical value, the growth equation for water is solved for the entire particle spectrum, and the mass transfer of all species between gas and aqueous-phases and the aqueous-phase chemical reactions are described in detail.

We have investigated possible differences in chemical composition of droplets of

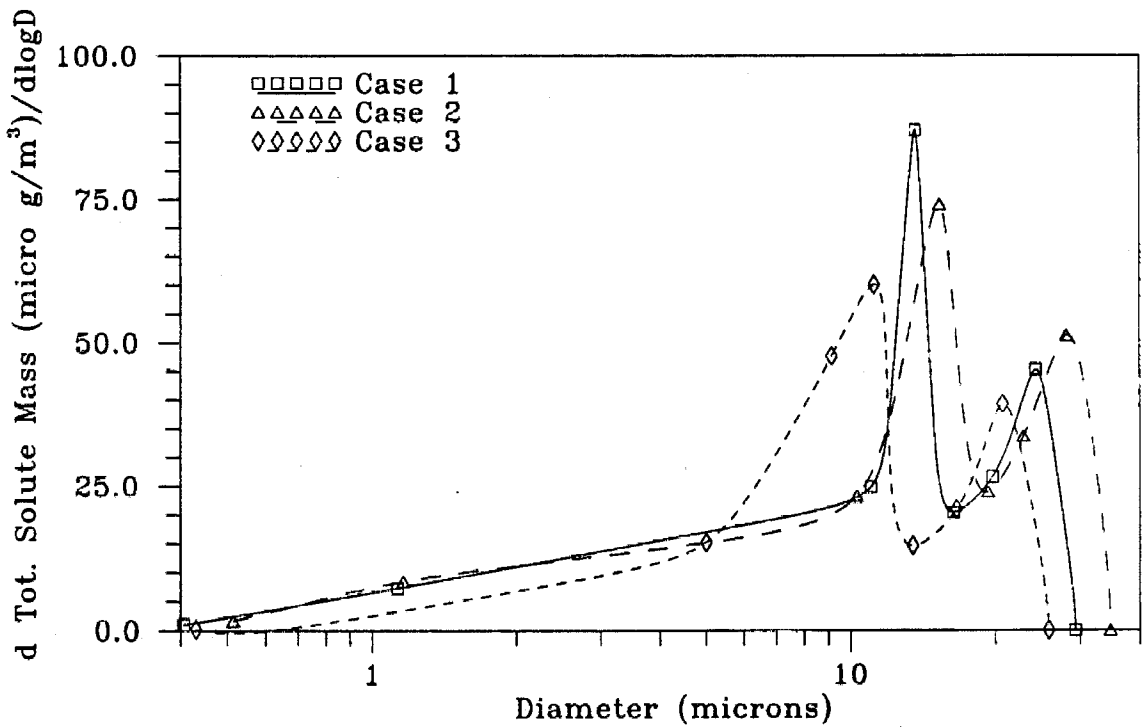


Figure 12. Comparison of the calculated total (volatile and nonvolatile) solute mass distribution as a function of droplet diameter for Case 1 (base case, $t = 20$ min), Case 2 (small cooling rate, $t = 40$ min) and Case 3 (large cooling rate, $t = 10$ min).

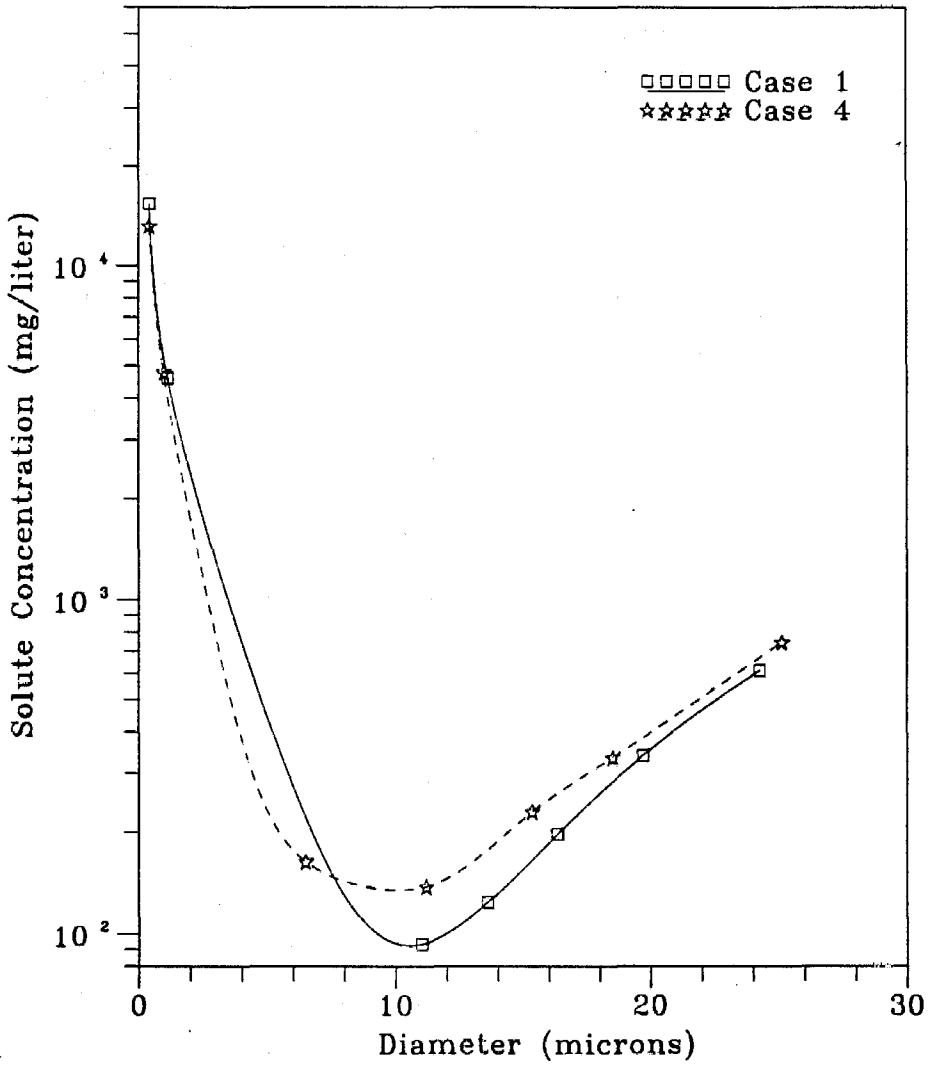


Figure 13. Comparison of the calculated total (volatile and nonvolatile) solute concentration as a function of droplet diameter for Case 1 ($t = 20$ min) and Case 4 ($t = 20$ min).

different sizes in a fog or cloud. The results suggest that significant total solute mass concentration differences can occur in such aqueous droplets. For the fog studied as a base case, during its full development stage, the mass solute concentration in droplets larger than 10 μm diameter increased with size in agreement with the findings of Noone et al. (1988), such that droplets of diameter 20 μm are found to have a solute concentration that is a factor of 3.6 larger than that in the 10 μm droplets. These total mass concentration differences reach a maximum during the fog liquid water peak and decrease during the fog development and dissipation stages.

Significant differences are suggested for the chemical composition of droplets of various sizes. Droplets on which most of the fog liquid water condenses are found to be enriched disproportionately in sulfate, and a peak in the sulfate mass is developed coincident with the peak of the liquid water distribution. This peak continues to exist after the fog dissipates and is due to the aqueous-phase conversion of S(IV) to S(VI). A similar behavior is exhibited by nitrate with the difference that nitric acid is produced in the gas-phase and scavenged by the droplets that have most of the liquid water.

The gas- and aqueous-phase chemical processes result in an increase of the solute total mass concentration for a mature fog over that if only aerosol scavenging is accounted for. This enrichment of fogwater due to gas- and aqueous-phase chemistry is nonuniform over the droplet spectrum, reaching a maximum value of around 4 for the droplets with most of the liquid water. Thus gas- and aqueous-phase chemical processes tend to decrease the total solute mass concentration differences between the various droplet sizes.

The cooling rate of the system is found to have a major impact on the process as it affects directly the distribution of the available water over the droplet size

spectrum. High cooling rates favor the smaller droplets that have small relaxation times as far as liquid condensation is concerned, while low cooling rates favor the larger slowly relaxing droplets. The higher the cooling rates the larger the solute concentration differences between the droplets of different sizes.

The mass/size distribution of the aerosol particles that serve as condensation nuclei affects in a quantitative, but not a qualitative way the concentration differences among droplets of different sizes.

Physical processes like droplet deposition and coagulation have not been included in the present model. A further step is the addition of descriptions of droplet coagulation and gravitational settling and the determination of their effects on the concentration differences between droplets of different sizes.

Acknowledgements

We would like to thank Dr. W. P. L. Carter, University of California, Riverside, for providing us with software for the gas-phase mechanism preparation and emissions processing. This work was supported by State of California Air Resources Board Agreement A732-043.

References

- Carter W. P. L., Lurmann F. W., Atkinson R. and Lloyd A. C. (1986) Development and testing of a surrogate species chemical reaction mechanism. EPA-600/3-86-031.
- Carter W. P. L. and Atkinson R. (1988) Development and implementation of an up-to-date photochemical mechanism for use in airshed modeling. Summary final report to California Air Resources Board.
- Chameides W. L. (1984) The photochemistry of a marine stratiform cloud. *J. Geophys. Res.* **89**, 4739-4755.
- Flossinan A. I., Hall W. D. and Pruppacher H. R. (1985) A theoretical study of the wet removal of atmospheric pollutants, I, The redistribution of aerosol particles captured through nucleation and impaction scavenging by growing cloud drops. *J. Atmos. Sci.* **42**, 583-606.
- Gelbard F. and Seinfeld J. H. (1980) Simulation of multicomponent aerosol dynamics. *J. Colloid Interface Sci.* **78**, 485-501.
- Gelbard F., Tambour Y. and Seinfeld J. H. (1980) Sectional representation for simulating aerosol dynamics *J. Colloid Interface Sci.* **76**, 541-556.
- Graedel T. E. and Goldberg K. I. (1983) Kinetic studies of raindrop chemistry, 1. Inorganic and organic processes *J. Geophys. Res.* **88**, 10865-10882.
- Hänel G. (1987) The role of aerosol properties during the condensational stage of cloud; a reinvestigation of numerics and microphysics *Beitr. Phys. Atmos.* **60**, 321-339.
- Hegg D. A. and Hobbs P. V. (1979) The homogeneous oxidation of sulfur dioxide in cloud droplets. *Atmos. Environ.* **13**, 981-987.
- Heikes B. G., Kok L. G., Walega J. G. and Lazrus A. L. (1987) H₂O₂, O₃ and SO₂ measurements in the lower troposphere over the eastern United States during

- the fall. *J. Geophys. Res.* **92**, 915-931.
- Jacob D. J. (1986) Chemistry of OH in remote clouds and its role in the production of formic acid and peroxymonosulfate *J. Geophys. Res.* **91**, 9807-9826.
- Jensen J. B. and Charlson R. J. (1984) On the efficiency of nucleation scavenging. *Tellus* **36B**, 367-375.
- Noone K. J., Charlson R. J., Covert D. S., Ogren J. A. and Heintzenberg J. (1988) Cloud droplets: solute concentration is size dependent. *J. Geophys. Res.* **93**, 9477-9482.
- Pandis S. N. and Seinfeld J. H. (1989a) Sensitivity analysis of a chemical mechanism for aqueous-phase atmospheric chemistry. *J. Geophys. Res.* **94**, 1105-1126.
- Pandis S. N. and Seinfeld J. H. (1989b) Mathematical modelling of acid deposition due to radiation fog- evaluation of a Lagrangian model. *J. Geophys. Res.*, **94**, 12,911-12,923.
- Pilinis C. and Seinfeld J. H. (1987) Continued development of a general equilibrium model for inorganic multicomponent atmospheric aerosols. *Atmos. Environ.* **21**, 2453-2466.
- Pilinis C., Seinfeld J. H. and Seigneur C. (1987) Mathematical modeling of the dynamics of multicomponent atmospheric aerosols. *Atmos. Environ.* **21**, 943-955.
- Pilinis C. and Seinfeld J. H. (1988) Development and evaluation of an Eulerian photochemical gas-aerosol model. *Atmos. Environ.* **22**, 1985-2001.
- Pruppacher H. R. and Klett J. D. (1980), *Microphysics of Clouds and Precipitation*, Reidel Pub. Co., The Netherlands.
- Roach W. T., Brown R., Caughey S. J., Garland J. A. and Readings C. J. (1976) The physics of radiation fog: I - A field study *Quart. J. R. Met. Soc.* **102**, 313-333.

- Russel A. G. and Cass G. R. (1984) Aquisition of regional air quality model validation data for nitrate, sulfate, ammonium ion and their precursors. *Atmos. Environ.* **18**, 1815-1827.
- Schwartz S. E. (1984) Gas- and aqueous-phase chemistry of HO₂ in liquid water clouds. *J. Geophys. Res.* **89**, 11589-11598.
- Seigneur C. and Saxena P. (1984) A study of atmospheric acid formation in different enviroments. *Atmos. Environ.* **18** 2109-2124.
- Seigneur C. and Saxena P. (1988) A theoretical investigation of sulfate formation in clouds. *Atmos. Environ.* **22** 101-115.
- Seinfeld J. H. (1986) *Atmospheric Chemistry and Physics of Air Pollution*, John Wiley, New York.
- Waldman J. M. (1986) Depositional aspects of pollutant behavior in fog. *Ph.D. thesis* California Institute of Technology.
- Wall S. M., John W. and Ondo J. L. (1988) Measurement of aerosol size distributions for nitrate and major ionic species. *Atmos. Environ.* **22**, 1649-1656.
- Warren D. R. and Seinfeld J. H. (1985) Simulation of aerosol size-distribution evolution in systems with simultaneous nucleation, condensation and coagulation. *Aerosol Sci. Technol.*, **4**, 31-43.

CHAPTER 5

**ON THE INTERACTION BETWEEN
EQUILIBRATION PROCESSES AND WET OR DRY DEPOSITION**

(Accepted for publication in *Atmospheric Environment*, March 1990)

On the Interaction between Equilibration Processes and Wet or Dry Deposition

Spyros N. Pandis and John H. Seinfeld

Department of Chemical Engineering and Environmental Quality Laboratory

California Institute of Technology, Pasadena, CA 91125, USA

Abstract

Atmospheric equilibration processes between two phases with different deposition velocities have the potential to affect significantly the amount of total material deposited on the ground. The magnitude of the effects of the equilibration processes depends primarily on the ratio of the deposition velocities of the two phases, on the production/emission rate of the gas-phase species, and on the initial distribution of species between the two phases. The deposition of a condensible species equilibrating between gas and aerosol phases can increase by as much as 20 times over that when equilibration processes are not present under appropriate conditions (very large aerosol particles, most of the material initially in the gas phase and high gas-phase production rate) or to decrease by as much as 15 times (very small aerosol particles, most of the material initially in the gas phase and high gas-phase production rate). In fog episodes, the deposition of a gaseous species with a Henry's law constant between 10^3 and 10^6 M atm⁻¹ (e.g., SO₂ for pH between 4.5 and 7, H₂O₂, HCHO, etc.) can be enhanced by as much as a factor of 3 because of its transfer to the aqueous phase. For the NH₃ - HNO₃ - NH₄NO₃ system the total deposition can be reduced by as much as a factor of 3 for typical conditions in a polluted atmosphere and small initial concentration of aerosol NH₄NO₃ with NH₃ initially dominating HNO₃ in the gas phase. If an operator splitting scheme is used in a mathematical model, both equilibration and removal processes should

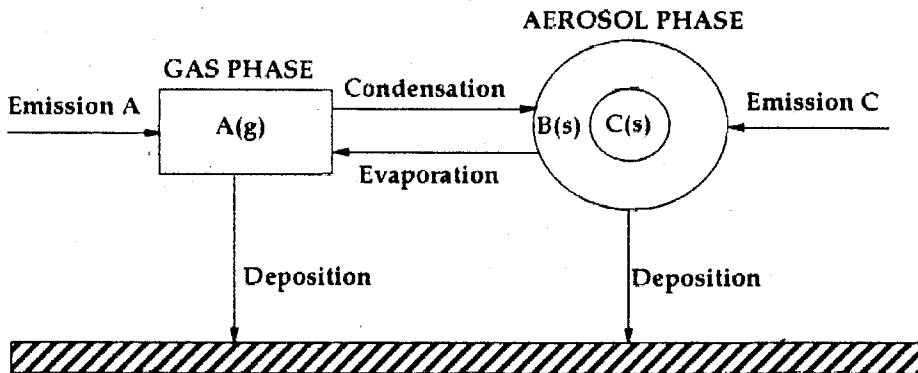
be included in the same operator or very small operator time steps (typically less than one minute) will be necessary.

Introduction

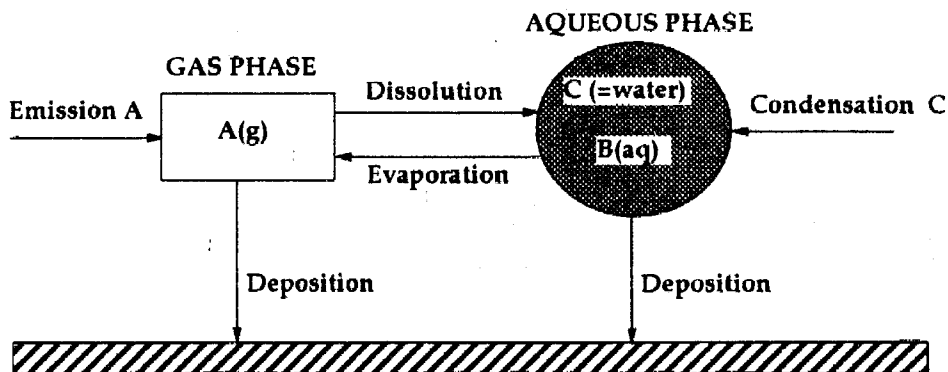
Processes such as condensation of vapor on aerosol particles, dissolution of material in aqueous droplets, and evaporation of species from aerosol particles or droplets move in the direction of establishing and maintaining thermodynamic equilibrium between the gas and aerosol or gas and aqueous phases in the atmosphere. These equilibration processes change the species' distribution among the various phases present and transfer material between phases that often have very different deposition characteristics. It is reasonable to expect therefore that the equilibration processes may affect significantly the amounts of material deposited on the ground, either enhancing or suppressing the removal processes over those from gas-phase processes alone. The goal of this study is to investigate the effects of the equilibration processes on wet and dry deposition and furthermore to examine the accuracy of the currently used modelling approaches of these phenomena.

The importance of equilibration processes in interpreting vertical concentration profiles and turbulent fluxes of HNO_3 , NH_3 and NH_4NO_3 near the surface of the Earth has been discussed by Brust et al. (1988). Bidleman (1988) suggested that the wet and dry deposition of organic compounds are controlled by their vapor-particle partitioning but his analysis was limited by experimental uncertainties and the lack of data concerning semivolatile organic compounds. Stafford [1988] has recently criticized the independent modeling of gas and aerosol deposition, neglecting gas-aerosol transfer. He suggested that coupled, reversible reactions are the more realistic representation of deposition.

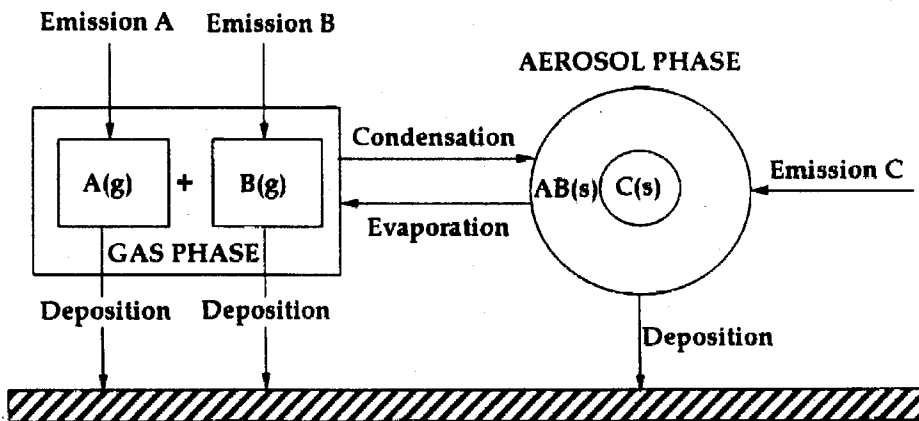
In the present work, three cases will be examined to obtain useful insight



(a)



(b)



(c)

Figure 1 Schematic representation of the multiphase systems studied.

(a) Case 1 : $A(g) \rightleftharpoons B(s)$

(b) Case 2 : $A(g) \rightleftharpoons B(aq)$

(c) Case 3 : $A(g) + B(g) \rightleftharpoons AB(s)$

into the relationship between equilibration processes and deposition. The first case concerns a gas phase species $A(g)$ that can be reversibly transferred to the aerosol phase as $B(s)$ (Figure 1a). In the second case the gas-phase species (e.g., $HCHO$, H_2O_2 , O_3) in the presence of droplets of liquid water content C is transferred reversibly to the aqueous-phase as $B(aq)$ (Figure 1b). Finally, in the third case two gases $A(g)$ and $B(g)$ react to give a volatile aerosol $AB(s)$, and in general all three species have different deposition velocities. This case is typified by the system of $NH_3(g)$, $HNO_3(g)$, and $NH_4NO_3(s)$.

We begin with the formulation of the governing differential equations that will be used to describe the system dynamics for the three representative cases. To reduce the large number of parameters involved in these equations and obtain valuable physical insight, the solutions of the systems of dimensionless differential equations will be presented in dimensionless form. Next, the effects of the equilibration processes on dry or wet deposition will be studied for various typical mass transfer rates, vapor, aqueous, and aerosol deposition velocities, emission and production rates, and initial gas and aerosol phase concentrations. Finally the accuracy of the currently employed modeling approaches will be discussed and suggestions for improvement will be presented.

Problem description and numerical model formulation

We will consider interphase mass transfer processes taking place inside a homogeneous air parcel, the height of which coincides with the mixing height of the atmosphere and is assumed to remain constant. The vapor phase is assumed to be initially in thermodynamic equilibrium with the aerosol or aqueous phase and at $t = 0$ the ground surface is added and the deposition starts. Due to the different rates of removal of the present phases and the emission or production of the vapor

species the system deviates from thermodynamic equilibrium and mass is transferred from the one phase to the other in an attempt to reestablish equilibrium. This transfer of material from a slowly depositing phase to a rapidly depositing one or vice versa can enhance or suppress the removal processes under favorable conditions. Processes described in the models include the reversible mass transfer between the phases present, the emission or production of the gas-phase species and the deposition of all species.

Case 1 : $A(g) \rightleftharpoons B(s)$

In Case 1 a condensible vapor species $A(g)$ is reversibly transferred (condensation/evaporation) to the aerosol phase as $B(s)$. We assume that the aerosol phase also contains non-volatile species $C(s)$. The vapor species and the aerosol particles are deposited on the ground with different deposition velocities (Figure 1a).

Let M_A , M_B , M_C be the mass concentrations of species A in the gas phase and of species $B(s)$ and $C(s)$ in the aerosol phase, respectively. Let $S_A(t)$ and $S_B(t)$ be the amounts of $A(g)$ and $B(s)$ that have been deposited on the ground up to the time t . For simplicity it is assumed that the aerosol particles are monodisperse (diameter d_p), $M_C \gg M_B$ at all times and that there is a source of $C(s)$ particles balancing their deposition so that M_C and the number of particles can be considered constant with time. As a result of these assumptions the particle diameter is not influenced by the condensation/evaporation of $A(g)$ and is assumed to be constant with time.

Within the air parcel M_A , M_B , S_A and S_B are governed by the following four ordinary differential equations (the aerosol mass concentration remains constant at M_C^0):

$$\frac{dM_A}{dt} = -k_m M_C^0 (M_A - M_{eq}) - k_{da} M_A + E_A \quad (1)$$

$$\frac{dM_B}{dt} = k_m M_C^o (M_A - M_{eq}) - k_{dc} M_B \quad (2)$$

$$\frac{dS_A}{dt} = k_{da} M_A \quad (3)$$

$$\frac{dS_B}{dt} = k_{dc} M_B \quad (4)$$

where $k_m = 12D_A/(\rho_p d_p^2)$ is the constant for the mass transfer of 'A' between the gas and aerosol phases for the continuum regime (the particle diameter is assumed to be large compared to the mean free path of the diffusing molecules), assuming unity accommodation coefficient [Seinfeld, 1986] and where D_A is the diffusion coefficient of A in the gas phase, ρ_p is the density of the aerosol particles, M_{eq} is the mass concentration of A(g) at equilibrium, k_{da} , k_{dc} are the deposition rate constants for A(g) and the aerosol particles defined as the ratio of their deposition velocities to the mixing height H , and E_A is the emission or gas-phase production rate of the gas species A.

The following initial conditions are used:

$$M_A(0) = M_{eq} = M_A^o, \quad M_B(0) = M_B^o, \quad S_A(0) = 0, \quad S_B(0) = 0 \quad (5)$$

Non-dimensionalising the above differential equations one gets

$$\frac{dm_A}{d\tau} = -\alpha(m_A - 1) - m_A + \delta \quad (6)$$

$$\frac{dm_B}{d\tau} = \alpha \beta(m_A - 1) - \gamma m_B \quad (7)$$

$$\frac{ds_A}{d\tau} = m_A \quad (8)$$

$$\frac{ds_B}{d\tau} = \gamma m_B \quad (9)$$

with initial conditions, $m_A(0) = 1$, $m_B(0) = 1$, $s_A(0) = 0$, and $s_B(0) = 0$ where the dimensionless dependent variables are defined as

$$m_A = \frac{M_A}{M_A^o}, \quad m_B = \frac{M_B}{M_B^o}, \quad s_A = \frac{S_A}{M_A^o}, \quad s_B = \frac{S_B}{M_B^o} \quad (10)$$

and the dimensionless parameters are

$$\tau = tk_{da}, \quad \alpha = \frac{k_m M_C^o}{k_{da}}, \quad \beta = \frac{M_A^o}{M_B^o}, \quad \gamma = \frac{k_{dc}}{k_{da}}, \quad \delta = \frac{E_A}{k_{da} M_A^o}. \quad (11)$$

The dimensionless time has been defined relative to the characteristic time for vapor deposition, α is the ratio of the evaporation rate to the vapor deposition rate, β is the ratio of the initial gas-phase concentration of A(g) to the corresponding concentration of B(s), γ is the ratio of the aerosol deposition velocity to the vapor deposition velocity, and δ is the ratio of the emission rate of A to the initial vapor deposition rate.

Case 2 : A(g) \rightleftharpoons B(aq)

In Case 2 a vapor species A(g) is reversibly transferred to the aqueous phase consisting of droplets of liquid water C. The liquid water of the fog, M_C (1 water/ 1 air), is assumed to remain constant with time, applicable during the rapid growth period of the fog (Pandis and Seinfeld, 1989b). The fog is assumed to consist of monodisperse droplets of constant diameter d_p and to be spatially homogeneous. Let H be the constant height of the fog. The vapor species and the aqueous droplets are both deposited with different deposition velocities (Figure 1b).

The main difference between Cases 1 and 2 is that in Case 2 the flux of A from the aqueous to the gas phase depends on its aqueous phase concentration, whereas in Case 1 the flux of A from the dry aerosol phase to the gas phase is independent of the quantity of A that exists in the aerosol particles as B(s). Let M_A now be the mass concentration of species A in the gas phase, and M_B its mass concentration in the aqueous phase. The equations that describe the evolution of the mass concentrations of A and B are (Pandis and Seinfeld, 1989a):

$$\frac{dM_A}{dt} = -k_m (M_C^o M_A - K_H M_B) - k_{da} M_A + E_A \quad (12)$$

$$\frac{dM_B}{dt} = k_m (M_C^0 M_A - K_H M_B) - k_{dc} M_B \quad (13)$$

where k_m is the combined rate coefficient for gas-phase plus interfacial mass transport, K_H , a numerical constant (no units) defined by $K_H = 1/K_{Ha} RT$ with K_{Ha} the effective Henry's law constant of species A, R , the ideal gas constant, and T , the temperature (Pandis and Seinfeld, 1989a). The remainder of the symbols are the same as in Case 1. The deposited amounts S_A and S_B are described once more by equations (3) and (4). Initially, as in Case 1, equilibrium is assumed between the two phases and from Henry's law, $M_A^0 = K_H M_B^0 / M_C^0$.

To simplify the present problem, we assume that the effective Henry's law constant of the species remains constant with time. This is exactly true for species that do not dissociate upon dissolution (e.g., O_3 , NO_2 , $HCHO$) and a very good assumption for species that weakly dissociate for the pH range of interest (1-8) like H_2O_2 . To use the above assumption for species like SO_2 with a strongly pH dependent solubility, we have to assume that the pH of the aqueous droplets remains constant. Non-dimensionalising equations (12) and (13), one obtains together with the equations (8) and (9) that describe the dimensionless deposited amounts:

$$\frac{dm_A}{d\tau} = -\alpha(m_A - m_B) - m_A + \delta \quad (14)$$

$$\frac{dm_B}{d\tau} = \alpha \beta(m_A - m_B) - \gamma m_B \quad (15)$$

with the same initial conditions as in Case 1 and dimensionless dependent variables defined by equation (10). The dimensionless parameters are the same as in Case 1 (equation 11) except β that is defined as $\beta = M_A^0 / M_B^0 = K_H / M_C^0$. The parameter β physically represents the distribution ratio of A between the gas and aqueous phases at equilibrium.

Case 3 : $A(g) + B(g) \rightleftharpoons AB(s)$

In Case 3 two gas-phase species react to produce volatile aerosol AB(s) and all three species are deposited on the ground. The aerosol particles are assumed to consist of AB(s) with mass concentration M_{AB} and nonvolatile material that is not influenced by the above equilibration process and has mass concentration M_{nv} . Hence, the total aerosol concentration is $M_{AB} + M_{nv}$ (Figure 1c). Assuming that the reaction of A and B takes place on the surface of the aerosol particles and is mass transfer limited, the differential equations of the model are

$$\frac{dM_A}{dt} = -k_m(M_{AB} + M_{nv})(M_A - M_{A_s}) - k_{da}M_A + E_A \quad (16)$$

$$\frac{dM_B}{dt} = -k_m(M_{AB} + M_{nv})(M_B - M_{B_s}) - k_{db}M_B + E_B \quad (17)$$

$$\frac{dM_{AB}}{dt} = k_m(M_{AB} + M_{nv})(M_A + M_B - M_{A_s} - M_{B_s}) - k_{ds}M_{AB} \quad (18)$$

$$\frac{dS_A}{dt} = k_{da}M_A \quad (19)$$

$$\frac{dS_B}{dt} = k_{db}M_B \quad (20)$$

$$\frac{dS_{AB}}{dt} = k_{ds}M_{AB}. \quad (21)$$

Once more equilibrium is assumed initially between the gas species A and B and AB in the aerosol phase. At $t = 0$ the surface is introduced,

$$M_A(0) = M_A^o, \quad M_B(0) = M_B^o = M_{eq}/M_A^o, \quad M_{AB}(0) = M_{AB}^o \quad (22)$$

$$S_A(0) = S_B(0) = S_{AB}(0) = 0. \quad (23)$$

The mass concentrations of A(g) and B(g) on the aerosol surface are calculated using the equality of the molar fluxes of A and B to the aerosol surface and the equilibrium condition $M_{A_s}M_{B_s} = M_{eq}$. Their values are

$$M_{A_s} = \frac{M_{eq}}{M_{B_s}} \quad M_{B_s} = 0.5 \left[M_B - \mu M_A + ((M_B - \mu M_A)^2 + 4\mu M_{eq})^{0.5} \right] \quad (24)$$

with $\mu = \mu_B/\mu_A$ the ratio of the molecular weights of the two gases.

Non-dimensionalising equations (16) to (21) one gets

$$\frac{dm_A}{d\tau} = -\sigma_1(m_A - m_{As})(1 + \sigma_2 m_{AB}) - m_A + \sigma_5 \quad (25)$$

$$\frac{dm_B}{d\tau} = -\sigma_1\left(m_B - \frac{m_{Bs}}{\sigma_7}\right)(1 + \sigma_2 m_{AB}) - \sigma_3 m_B + \frac{\sigma_5 \sigma_6}{\sigma_7} \quad (26)$$

$$\frac{dm_{AB}}{d\tau} = \sigma_1 \sigma_8 (1 + \sigma_2 m_{AB})(m_A + \sigma_7 m_B - m_{As} - m_{Bs}) - \sigma_4 m_{AB} \quad (27)$$

$$\frac{ds_A}{d\tau} = m_A \quad (28)$$

$$\frac{ds_B}{d\tau} = \sigma_3 m_B \quad (29)$$

$$\frac{ds_{AB}}{d\tau} = \sigma_4 m_{AB} \quad (30)$$

with initial conditions

$$m_A(0) = 1, \quad m_B(0) = 1, \quad m_{AB}(0) = 1, \quad s_A(0) = 0, \quad s_B(0) = 0, \quad s_{AB}(0) = 0 \quad (31)$$

where the dimensionless dependent variables are defined as

$$m_A = \frac{M_A}{M_A^o}, \quad m_B = \frac{M_B}{M_B^o}, \quad m_{AB} = \frac{M_{AB}}{M_{AB}^o}, \quad s_A = \frac{S_A}{M_A^o}, \quad s_B = \frac{S_B}{M_B^o}, \quad s_{AB} = \frac{S_{AB}}{M_{AB}^o} \quad (32)$$

and the dimensionless parameters are

$$\tau = tk_{da}, \quad \sigma_1 = \frac{k_m M_{nv}}{k_{da}}, \quad \sigma_2 = \frac{M_{AB}^o}{M_{nv}}, \quad \sigma_3 = \frac{k_{db}}{k_{da}}, \quad \sigma_4 = \frac{k_{ds}}{k_{da}}$$

$$\sigma_5 = \frac{E_A}{k_{da} M_A^o}, \quad \sigma_6 = \frac{E_B}{E_A}, \quad \sigma_7 = \frac{M_{eq}}{M_A^{o2}} = \frac{M_B^o}{M_A^o}, \quad \sigma_8 = \frac{M_A^o}{M_{AB}^o}. \quad (33)$$

The dimensionless time has been once more defined relative to the characteristic time for vapor deposition, σ_1 is the ratio of the mass transfer rate to the gas-phase deposition rate, σ_2 is the ratio of the initial aerosol concentration of AB to the

corresponding concentration of the rest of the aerosol species, σ_3 is the ratio of the deposition velocities of the two gas-phase species, σ_4 is the ratio of the aerosol deposition velocity to the deposition velocity of A(g), σ_5 is the ratio of the emission (or gas-phase chemical reactions) of A to its initial deposition rate, σ_6 is the ratio of the emission rates of A and B, σ_7 is the ratio of the initial gas phase concentrations of A and B, and finally σ_8 is the ratio of the initial concentrations of gas species A and aerosol AB.

Solution of the model equations

Case 1

The solutions of equations (6) to (9) with the corresponding initial conditions are

$$m_A = m_A^s + (1 - m_A^s) e^{-(1+\alpha)\tau} \quad (34)$$

$$m_B = m_B^s + \frac{\alpha\beta(1-\delta)}{(1+\alpha)(\gamma-1-\alpha)} e^{-(1+\alpha)\tau} + P e^{-\gamma\tau} \quad (35)$$

$$s_A = m_A^s \tau + \frac{1-\delta}{(1+\alpha)^2} (1 - e^{-(1+\alpha)\tau}) \quad (36)$$

$$s_B = \gamma m_B^s \tau + \frac{\alpha\beta\gamma(1-\delta)}{(\gamma-1-\alpha)(1+\alpha)^2} (1 - e^{-(1+\alpha)\tau}) + P(1 - e^{-\gamma\tau}) \quad (37)$$

where

$$P = 1 + \frac{\alpha\beta(\delta-1)}{1+\alpha} \left[\frac{1}{\gamma-1-\alpha} - \frac{1}{\gamma} \right] \quad (38)$$

and

$$m_A^s = \frac{\alpha + \delta}{1 + \alpha}, \quad m_B^s = \frac{\alpha\beta(\delta-1)}{\gamma(1+\alpha)}. \quad (39)$$

In the above formulas m_A^s and m_B^s are the steady-state values of m_A and m_B in equations (6) and (7). These steady-states are nonnegative and therefore physically significant only if $\delta \geq 1$. Note that for $\alpha = 0$, the above equations give

us the solution of the deposition problem if one neglects the equilibration processes between the two phases. Such quantities are noted using a (*) :

$$m_A^* = \delta + (1 - \delta)e^{-\tau} \quad m_B^* = e^{-\gamma \tau}$$

$$s_A^* = \delta \tau + (1 - \delta)(1 - e^{-\tau}) \quad s_B^* = 1 - e^{-\gamma \tau} \quad (40)$$

Case 2

The solutions of equations (14), (15), (8), and (9) with the corresponding initial conditions are

$$m_A = Qe^{\lambda_1 \tau} + We^{\lambda_2 \tau} + m_A^s \quad (41)$$

$$m_B = Q \frac{1 + \alpha + \lambda_1}{\alpha} e^{\lambda_1 \tau} + W \frac{1 + \alpha + \lambda_2}{\alpha} e^{\lambda_2 \tau} + m_B^s \quad (42)$$

$$s_A = m_A^s \tau - \frac{Q}{\lambda_1} (1 - e^{\lambda_1 \tau}) - \frac{W}{\lambda_2} (1 - e^{\lambda_2 \tau}) \quad (43)$$

$$s_B = \gamma m_B^s \tau - \frac{\gamma Q (1 + \alpha + \lambda_1)}{\alpha \lambda_1} (1 - e^{\lambda_1 \tau}) - \frac{\gamma W (1 + \alpha + \lambda_2)}{\alpha \lambda_2} (1 - e^{\lambda_2 \tau}) \quad (44)$$

with λ_1 and λ_2 the eigenvalues of the system given by

$$\lambda_{1,2} = -\frac{1}{2} \left[(1 + \alpha + \alpha\beta + \gamma) \pm \left((1 + \alpha - \alpha\beta - \gamma)^2 + 4\alpha^2\beta \right)^{\frac{1}{2}} \right] \quad (45)$$

and with m_A^s and m_B^s the steady-state values of m_A and m_B ,

$$m_A^s = \frac{\delta(\alpha\beta + \gamma)}{\alpha\beta + \alpha\gamma + \gamma}, \quad m_B^s = \frac{\delta\alpha\beta}{\alpha\beta + \alpha\gamma + \gamma} \quad (46)$$

and

$$Q = \frac{1 + \lambda_2 - m_A^s (1 + \alpha + \lambda_2) + \alpha m_B^s}{\lambda_2 - \lambda_1} \quad (47)$$

$$W = -\frac{1 + \lambda_1 - m_A^s (1 + \alpha + \lambda_1) + \alpha m_B^s}{\lambda_2 - \lambda_1} \quad (48)$$

If one neglects the equilibration processes between the two phases, the corresponding variables are given by equations (40).

Case 3

The system of ordinary equations (25) to (30) with initial conditions given by equation (31) is solved numerically using a standard Gear routine.

Neglecting the gas-aerosol phase equilibration processes is equivalent to setting $\sigma_1 = 0$ in equations (25) to (30). The corresponding solutions of this simplified system are denoted by using a (*) and are

$$\begin{aligned}
 m_A^* &= \sigma_5 + (1 - \sigma_5)e^{-\tau} & m_B^* &= \frac{\sigma_5\sigma_6}{\sigma_3\sigma_7} + \left(1 - \frac{\sigma_5\sigma_6}{\sigma_3\sigma_7}\right)e^{-\sigma_3\tau} \\
 m_{AB}^* &= e^{-\sigma_4\tau} & s_A^* &= \sigma_5\tau + (1 - \sigma_5)(1 - e^{-\tau}) \\
 s_B^* &= \frac{\sigma_5\sigma_6}{\sigma_3\sigma_7}\tau + \left(1 - \frac{\sigma_5\sigma_6}{\sigma_3\sigma_7}\right)(1 - e^{-\sigma_3\tau}) & s_{AB}^* &= 1 - e^{-\sigma_4\tau}.
 \end{aligned} \tag{49}$$

The Deposition Ratio

A simple way of assessing the effects of the equilibration processes on wet or dry deposition is to compare the predictions of the full models described above with those of the corresponding models where the equilibration processes are neglected. To facilitate this comparison we define the deposition ratio at the time t , $DR(t)$, as the ratio of the total species mass that has been deposited since $t = 0$ in gas, aerosol and aqueous solution forms, when the equilibration processes are taken into account, to the same quantity when the equilibration processes have been neglected. Values of the deposition ratio close to unity mean that the equilibration processes do not affect significantly the deposition of species. Values of the deposition ratio larger than one correspond to deposition enhancement by the equilibration processes while values smaller than one represent deposition suppression.

Using the above definition for the deposition ratio, one obtains for the three cases presented above:

$$DR_1(t) = DR_2(t) = \frac{\beta s_A + s_B}{\beta s_A^* + s_B^*} \quad DR_3(t) = \frac{\sigma_8 s_A + \sigma_7 \sigma_8 s_B + s_{AB}}{\sigma_8 s_A^* + \sigma_7 \sigma_8 s_B^* + s_{AB}^*} \quad (50)$$

The deposition ratio is a function of time and due to the initial assumed equilibrium state in all the above three cases, $DR(0) = 1$. This can be easily shown because the mass transfer terms in all the differential equations vanish at $t = 0$ and the equations for both approaches to the deposition problem are the same. The behavior of DR as $t \rightarrow \infty$ depends on whether emissions of material are occurring. If no emissions of material enter the system it is clear that for both approaches all the initially present material will eventually be deposited on the ground and therefore $DR(\infty) = 1$. The cases with vapor emissions present will be examined independently below.

In order to facilitate comparisons, it is useful to define a specific time t^* at which all the comparisons will be made. In direct analogy to the half life of a species, we define, for Cases 1 and 2, t^* as the time at which the total deposited mass of A (in both gas and aerosol or gas and aqueous forms) equals half the initially present mass of A. Therefore, when there are no emissions of A, t^* equals the half life of A. For Case 3 at time t^* , the total deposited mass of A, B and AB equals half their initially present mass. Henceforth, all the results will refer to the time t^* unless specifically stated.

Effects of equilibration processes on dry and wet deposition

Case 1

The model developed for Case 1 is applicable, for example, to secondary organic condensible species. Possible examples include nitro-cresol from the gas-phase photooxidation of toluene, glutaric and adipic acid from the photooxidation of cy-

clopente and cyclohexene. Species C then corresponds to the remainder of the material found in the aerosol phase.

Relatively little is known about the vapor pressures of organic species that are found in secondary organic aerosols. For the purposes of this study the range of 5×10^{-6} to 5×10^{-5} Pa (Stern et al., 1987; Tao and McMurry, 1989) will be investigated. This range corresponds to values of M_{eq} between 0.3 and $3 \mu\text{g m}^{-3}$. The mass of condensible organics has been predicted to vary roughly from zero to $10 \mu\text{g m}^{-3}$ (Pilinis and Seinfeld, 1988). Average particle mass concentrations range from $20 \mu\text{g m}^{-3}$ in clean air to values up to $200 \mu\text{g m}^{-3}$. A value of $80 \mu\text{g m}^{-3}$ representative of a polluted urban atmosphere will be used for our calculations. The deposition velocity of aerosol particles depends on particle diameter, wind speed, atmospheric stability, and surface characteristics. It varies roughly from 0.003 cm s^{-1} for particles of $0.5 \mu\text{m}$ diameter to 10 cm s^{-1} for the $10 \mu\text{m}$ particles (McMahon and Denison, 1979; National Center for Atmospheric Research, 1982; Wesely and Shannon, 1984) and for a mixing height varying between 100 and 2000 m the aerosol deposition constant k_{dc} is in the range between 10^{-8} to 10^{-3} s^{-1} . There is little information available on the dry deposition velocities of condensible organic vapors, so based on reported values for species like PAN (McRae and Russel, 1984), we assume a range of 0.1 to 0.5 cm s^{-1} , corresponding to a vapor deposition rate constant k_{da} between 5×10^{-7} and $5 \times 10^{-5} \text{ s}^{-1}$. The mass transfer constant k_m varies from $10^{-6} \text{ m}^3 \text{ s}^{-1} \mu\text{g}^{-1}$ for $10 \mu\text{m}$ diameter particles to $10^{-2} \text{ m}^3 \text{ s}^{-1} \mu\text{g}^{-1}$ for $0.1 \mu\text{m}$ particles. The source of these condensible organics in the atmosphere is the gas-phase photooxidation of their parent hydrocarbons. The source rate E_A can be estimated from the average concentrations of the primary organic precursors and the corresponding rate constants to be between $\leq 0.001 \mu\text{g m}^{-3} \text{ s}^{-1}$.

Using the above information one can derive the range of the dimensionless variables of our model applicable to condensible organics. They are approximately:

$$2 \leq \alpha \leq 2 \times 10^6, \quad 0.01 \leq \beta, \quad 10^{-3} \leq \gamma \leq 10^3, \quad 0 \leq \delta \leq 3 \times 10^3$$

The first case discussed is for rapid mass transfer between the gas and aerosol phases, $\alpha = 1000$. The deposition ratios are presented in Figure 2 as a function of β and γ . When no source of the organic species A is present ($\delta = 0$), and because the system starts from equilibrium, the gas-phase concentration of A cannot exceed its saturation value. Therefore in this case A does not condense at any time to the aerosol phase and the particles evaporate in an attempt to maintain equilibrium. This non-symmetry in the system is depicted in Figure 2a and for $\gamma \geq 1$ (deposition velocity of the particles exceeds the deposition velocity of the vapor) the equilibration process does not significantly affect the deposition. The material in the aerosol phase is preferentially deposited on the ground and only small quantities are transferred to the gas phase. On the contrary, when $\gamma < 1$ (deposition velocity of particles is less than that of the vapor) the equilibration processes can become very important depending on the relative quantities of the initial concentrations. As the gas-phase material is rapidly deposited, the material in the slowly deposited aerosol phase evaporates in an effort to maintain equilibrium. This transfer of material from the slowly depositing phase to the rapidly depositing phase enhances significantly the total deposition, and the larger the difference in the deposition velocities of the two phases, the larger the enhancement. Additionally, the significant enhancement is observed only when the initial concentration of the organic in the aerosol phase exceeds its initial gas-phase concentration ($\beta < 1$). If the initial mass of A exceeds significantly the aerosol mass ($\beta \gg 1$), the transfer of relatively small quantities of A from the aerosol to the gas phase and their subsequent rapid deposition does

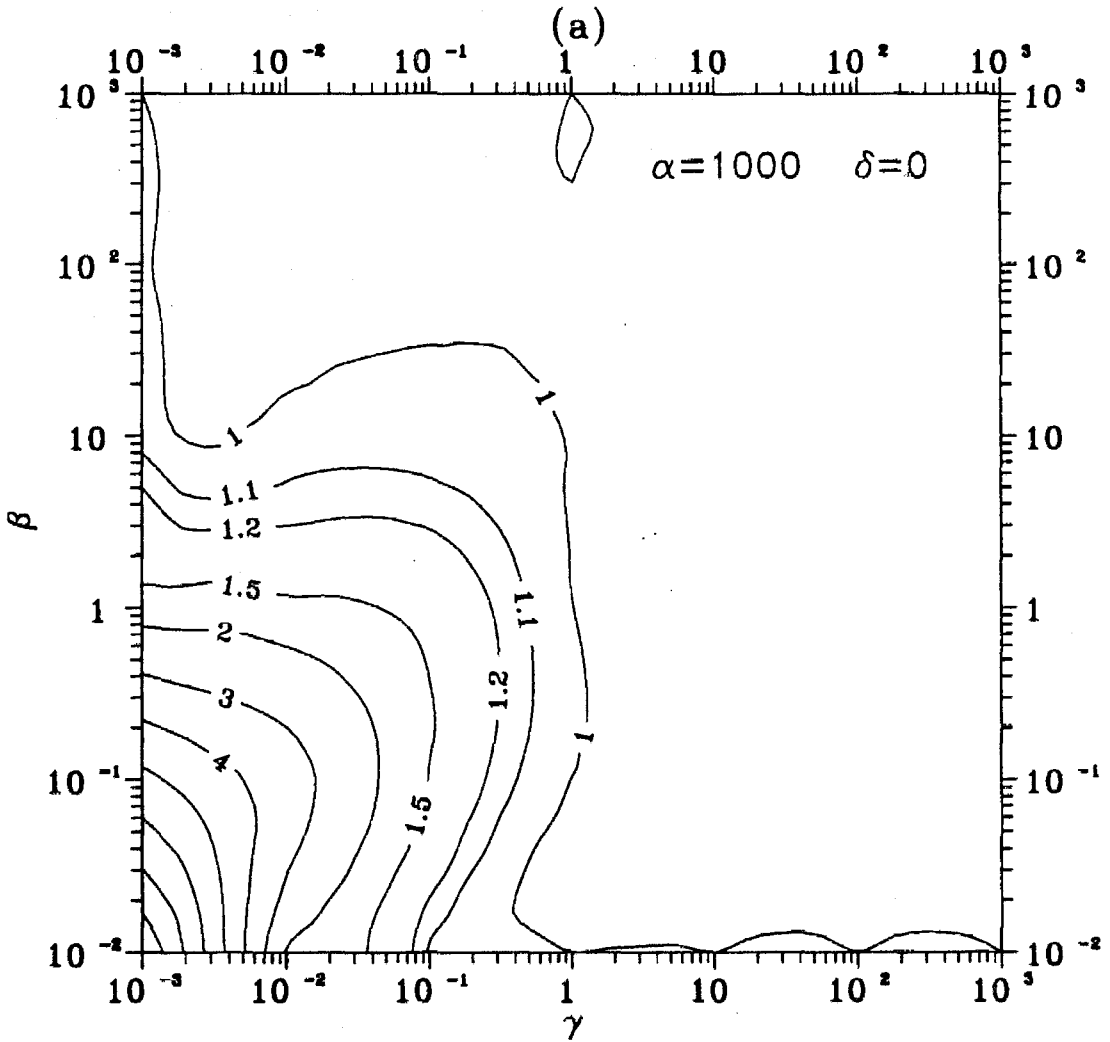


Figure 2a Deposition ratio $DR_1(t^*)$ (total deposition with equilibration processes over deposition without) as a function of the initial species distribution β and the ratio of the deposition velocities γ for rapid mass transfer ($\alpha=1000$) and two production/emission rates of $A(g)$ δ .

(a) $\delta = 0$ No emission.

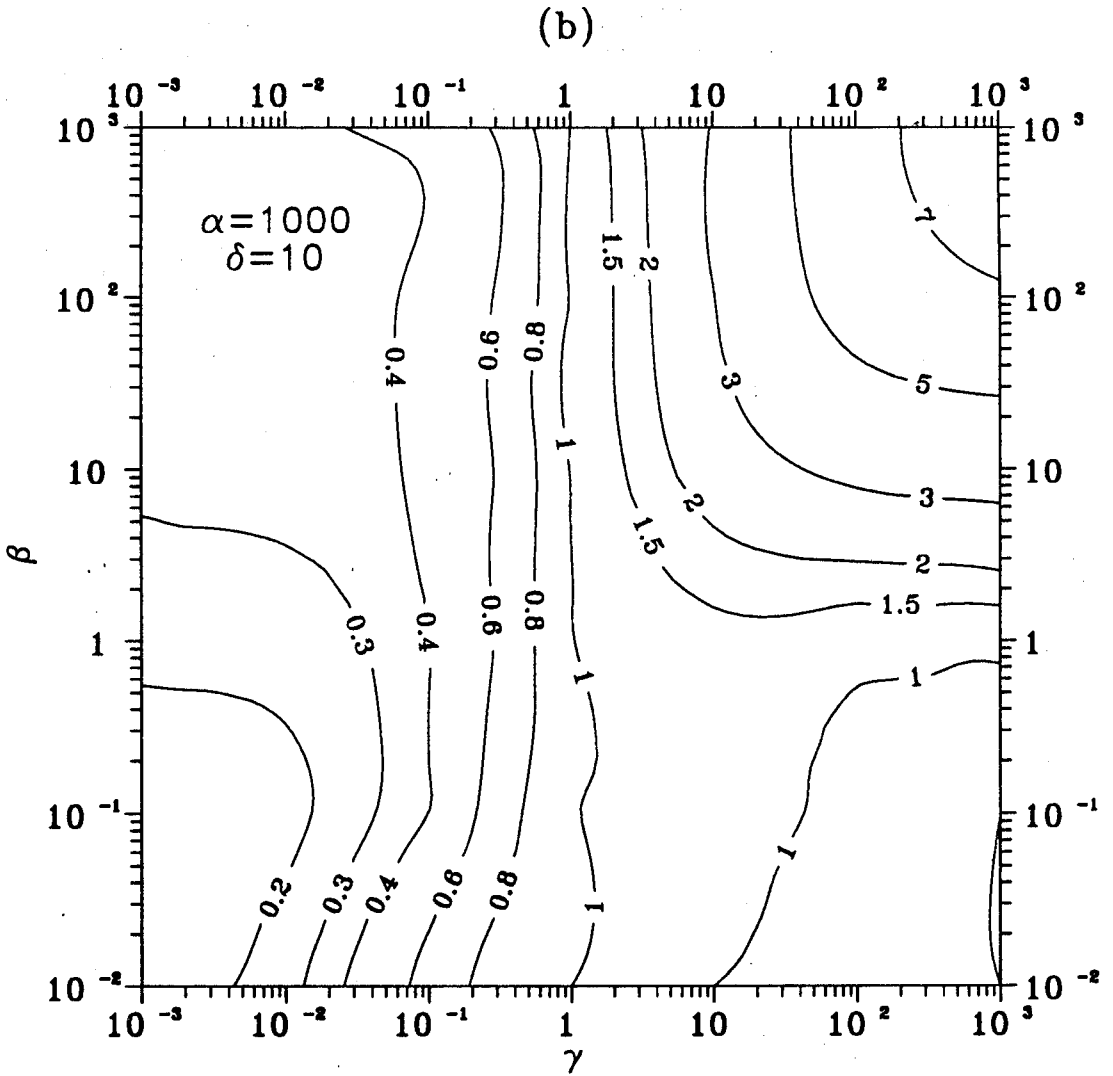


Figure 2b Deposition ratio $DR_1(t^*)$ (total deposition with equilibration processes over deposition without) as a function of the initial species distribution β and the ratio of the deposition velocities γ for rapid mass transfer ($\alpha=1000$) and two production/emission rates of $A(g)$ δ .
(b) $\delta = 10$ Strong emission source.

not affect the total amount of A deposited. When $\beta = 0.01$ and $\gamma = 0.001$ the equilibration processes result in a ninefold increase of the total deposition.

If the organic condensible species A is produced in the gas phase much slower than it is deposited ($\delta = 0.1$), the behavior of the system is qualitatively the same as in the case of $\delta = 0$. The main effect of this small source of A is the reduction of the deposition enhancement observed for $\gamma < 1$ and $\beta < 1$ because of the increase of the mass of A in the gas-phase. Under optimum conditions ($\beta = 0.01, \gamma = 0.001$) the enhancement of deposition is fivefold.

When the gas-phase production rate of A equals its deposition rate ($\delta = 1$), the gas-phase concentration of A remains constant and equal to its equilibrium value. Hence, no transfer of mass takes place between the two phases and the equilibration processes do not play any role. In this case, $DR_1(t) = 1$, for all t .

If the gas phase production rate exceeds the deposition rate ($\delta = 10$), the gas phase becomes supersaturated in A and condensation of A to the aerosol phase takes place. If the vapor deposits faster than the aerosol phase ($\gamma < 0.1$), this transfer of A causes significant reduction of the total deposition (Figure 1b). This reduction is more pronounced for organics with low vapor pressures or high initial aerosol concentration of the organic and it can be as much as eightfold. On the contrary, if the aerosol particles deposit faster than the vapor itself, the condensation of vapor results in a significant enhancement of total deposition if the mass of A in the gas phase exceeds the corresponding mass in the aerosol phase ($\beta > 1$).

A further increase of the production rate of A compared to its vapor deposition rate ($\delta = 100$) results in the same qualitative features as the case with $\delta = 10$. Quantitatively this increased production rate enhances the significance of the equilibration processes. Under the appropriate conditions the total deposition rate decreases 50 times ($\beta = 0.1, \gamma = 0.001$) or increases 48 times ($\beta = 1000, \gamma = 1000$).

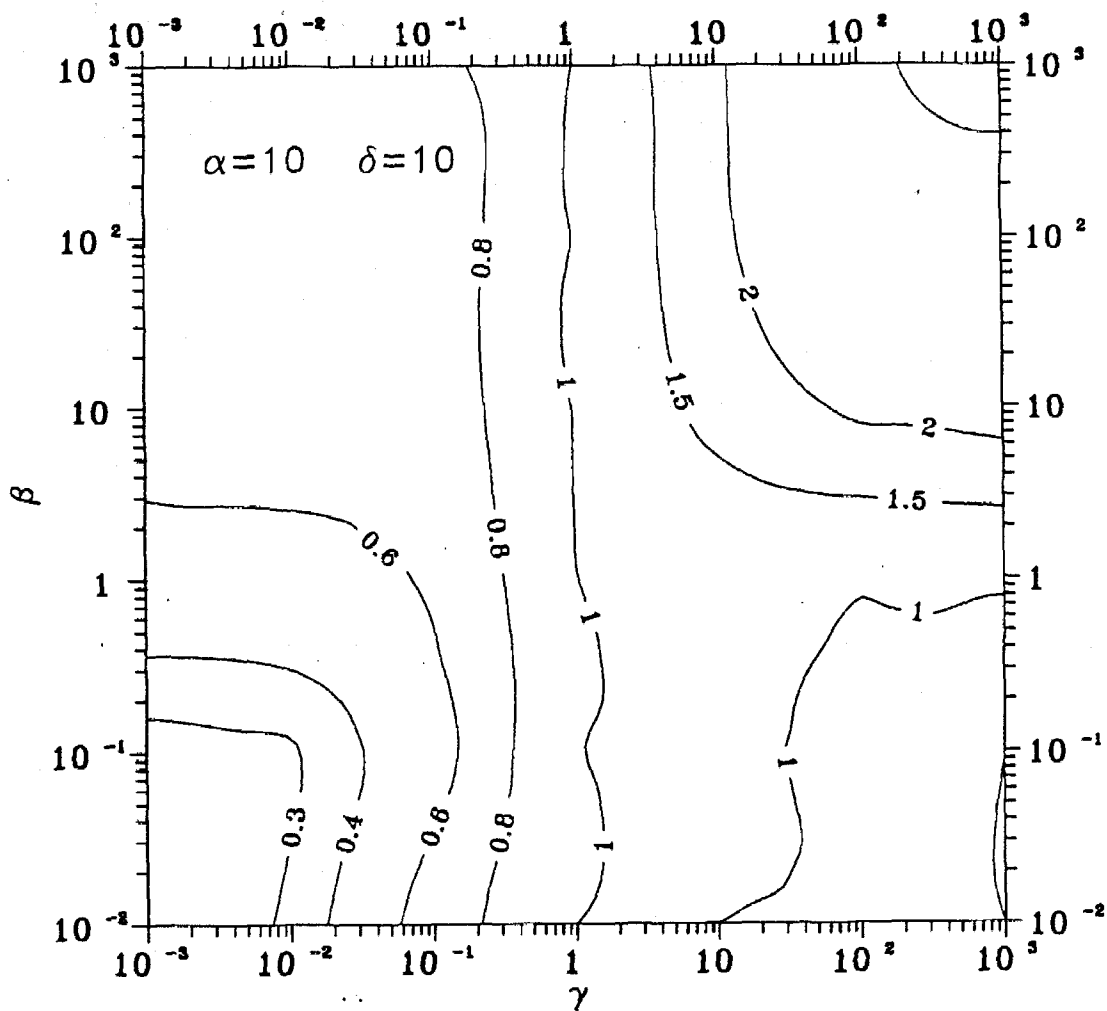


Figure 3 Deposition ratio $DR_1(t^*)$ (total deposition with equilibration processes over deposition without) as a function of the initial species distribution β and the ratio of the deposition velocities γ for slow mass transfer ($\alpha=10$) and strong emission source of A(g) ($\delta=10$).

The effects of the rate constant of mass transfer can be studied by comparing Figure 2b with Figure 3. A decrease of the parameter α (due to low total aerosol loading or larger average particle diameter, etc.) by two orders of magnitude does not change the qualitative behavior of the system but decreases the importance of the equilibration processes. For example, for $\delta = 0$ the maximum deposition enhancement is reduced from 9 ($\alpha = 1000$) to 8.4, for $\delta = 10$ from 7.7 to 3.2 (Figure 3) and for $\delta = 100$ from 48 to 6.

Case 2

The model developed for Case 2 can be applied to species that do not dissociate upon dissolution in water like O_3 , NO_2 , NO , $HCHO$ and PAN or dissociate weakly in the pH range of interest (from 1 to 8) like H_2O_2 . Several important pollutants like SO_2 , HNO_3 , etc., dissociate upon dissolution and therefore their solubility depends on the droplets' pH. To apply the same model to these species, one must assume that the pH is not affected by the dissolution of species A and neglect aqueous phase reactions.

The liquid water content of a fog has been found to vary between 0.05 to 0.5 $g\ m^{-3}$ that corresponds to values of M_C^0 between 5×10^{-8} and 5×10^{-7} (1 water/1 air) (Seinfeld, 1986). The effective Henry's law constant K_H ranges from 2×10^{-3} $M\ atm^{-1}$ for species like NO (Schwartz and White, 1981) to 10^{16} $M\ atm^{-1}$ for HCl for $pH=7$. Because of the assumptions outlined above, the range of pH around 7 where strong acids like HNO_3 and HCl have such a large solubility that they cause a dramatic pH decrease will be omitted from this discussion. Therefore, this study concentrates on a range of K_H from 5×10^{-8} to 5 and to a corresponding range of β from 0.1 to 10^8 .

The typical diameter of a fog droplet varies between 10 and 40 μm correspond-

ing to mass transfer constants k_m between 10^6 s^{-1} and 7×10^4 . The gas-phase deposition velocity is between 0.1 and 1 cm s^{-1} and, assuming a fog height of 100 m , the gas phase deposition rate constant k_{da} is between 10^{-5} and 10^{-4} s^{-1} and the dimensionless variable α is $30 \leq \alpha \leq 5 \times 10^4$.

Experimental data provided by Dollard and Unsworth (1983) suggest that during fog episodes the turbulent droplet flux to a grass surface is 1.8 ± 0.9 times the droplet sedimentation rate for wind speeds $3\text{-}4 \text{ m s}^{-1}$. At wind speeds less than 2 m s^{-1} , typical of radiation fog episodes, their measurements showed that the total droplet deposition rate was almost equal to the droplet sedimentation rate. Based on the above data, the droplet deposition velocity varies roughly between 0.3 and 3 cm s^{-1} resulting in k_{db} values between 3×10^{-5} and 5×10^{-4} and γ values in the range $0.3 \leq \gamma \leq 50$.

The case examined here is for a typical mass transfer rate ($d_p = 20 \mu\text{m}$), $\alpha = 1500$, with gas-phase sources of A ranging from nonexistent ($\delta=0$) to strong ($\delta=100$). The calculated values of the deposition ratio DR_2 for t^* are shown in Figure 4. If there are no sources of A in the gas phase ($\delta = 0$) then the equilibration processes affect significantly (more than 20%) the total deposition of A over a relatively small range of the dimensionless parameters β and γ , namely when $\gamma > 7$ and $1 < \beta < 100$. Therefore, the fog droplets should deposit seven times faster than the vapor species before a maximum 20% increase in total deposition occurs. When the deposition velocity of the aqueous phase becomes 50 times larger than the corresponding vapor deposition velocity, the deposition is enhanced 2.5 times by the equilibration processes. If the deposition velocities of the two phases are sufficiently different, the solubility of A in the aqueous phase determines the importance of the equilibration processes. The maximum influence is observed for values of β around 10 that correspond to effective Henry's constants from around $8 \times 10^3 \text{ M atm}^{-1}$ for

(a)

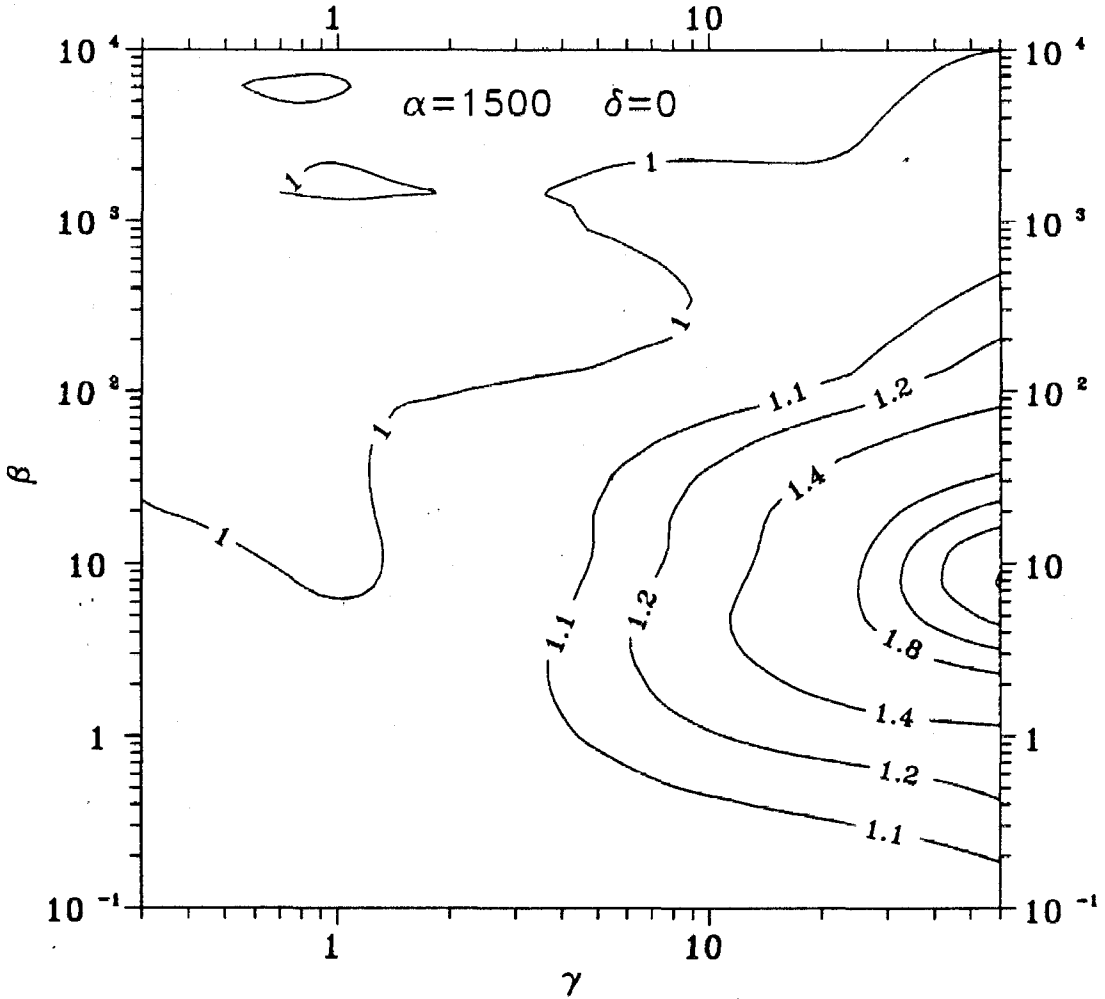


Figure 4a Deposition ratio $DR_2(t^*)$ (total deposition with equilibration processes over deposition without) as a function of the initial species distribution β and the ratio of the deposition velocities γ for typical mass transfer ($\alpha=1500$) and

(a) $\delta = 0$ Zero A(g) emission/production rate.

dense fogs (liquid water content 0.5 g m^{-3}) to $8 \times 10^4 \text{ M atm}^{-1}$ for light fogs (liquid water content 0.05 g m^{-3}).

In Case 2 the emission/production rate of A influences the deposition ratio considerably less than in Case 1. This is mainly due to the fact that the aqueous phase has a limited A dissolution capacity, while unlimited amounts of A can condense on the dry aerosol phase. The extent of these effects can be realized by comparing Figures 4a and 4b. For a strong source of A in the gas phase ($\delta=100$) the maximum deposition enhancement is threefold. An extra interesting region appears when the deposition velocity of the droplets is less than half of the vapor deposition velocity. Then for very soluble species (Henry's law constant 10^6 to 10^7 M atm^{-1}), the equilibration processes cause a reduction of the total deposition by as much as a factor of 2.

In conclusion, the deposition of species with very low solubilities like O_3 , NO_2 , NO and PAN for which $\beta > 10^4$ is generally not affected by their transfer to the aqueous phase. The deposition of highly soluble species like HNO_3 and HCl for which $\beta < 0.1$ will be affected only if their gas-phase deposition velocity exceeds the fog droplet deposition velocity. In that case the total deposition will decrease significantly in the presence of the fog. The deposition of species with small solubilities like CH_3OH ($K_{Hi} = 220 \text{ M atm}^{-1}$) will be enhanced slightly (around 15 to 20%) under optimum conditions. Finally, the deposition of species that have solubilities in the optimum range, (10^3 to 10^6 M atm^{-1}) like SO_2 (for $4.5 \leq \text{pH} \leq 7$), H_2O_2 (pH independent), HNO_2 ($4.8 \leq \text{pH} \leq 7$), HCHO (pH independent), and HCOOH ($2 \leq \text{pH} \leq 6.5$) can be enhanced by as much as 3 times by equilibration processes.

Case 3

(b)

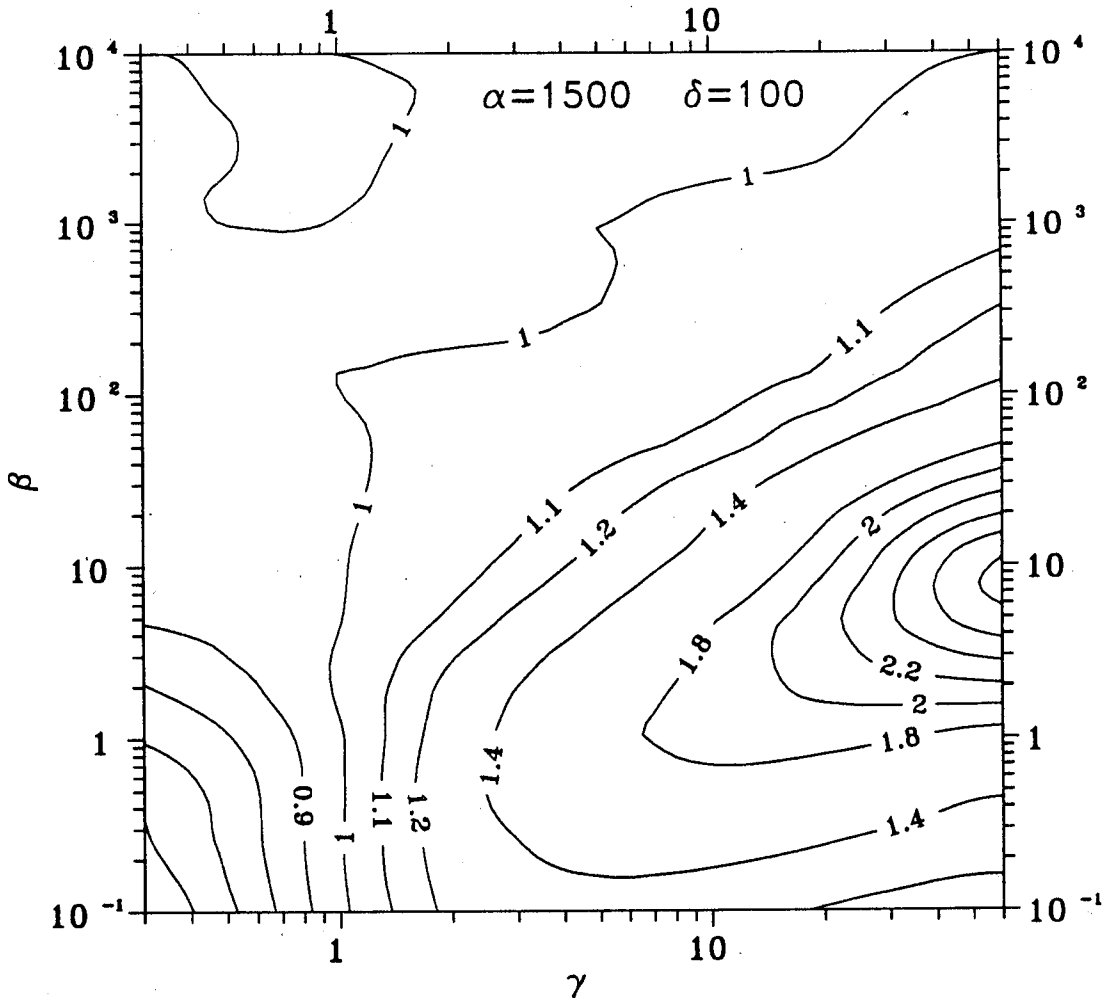


Figure 4b Deposition ratio $DR_2(t^*)$ (total deposition with equilibration processes over deposition without) as a function of the initial species distribution β and the ratio of the deposition velocities γ for typical mass transfer ($\alpha=1500$) and
(b) $\delta = 100$ Very high $A(g)$ emission/production rate.

The most important example of a system corresponding to Case 3 is that of NH_3 , HNO_3 and NH_4NO_3 particles, and therefore the dimensionless parameters σ_1 to σ_8 will be chosen to correspond to the conditions encountered relevant to that system under polluted urban conditions. Let A denote NH_3 and B the HNO_3 vapor. Gas-phase concentrations of NH_3 vary from $0.5\text{-}20 \mu\text{g m}^{-3}$ (Seinfeld, 1986), the equilibrium constant of ammonium nitrate at 298 K is $49.8 \mu\text{g}^2 \text{m}^{-6}$ (Stelson and Seinfeld, 1982) and measurements of Russel and Cass (1984) indicate concentrations of NH_4NO_3 in the Los Angeles basin from 5 to $50 \mu\text{g m}^{-3}$. An average mixing height of 600 m is assumed. For this mixing height ammonia emissions calculations of Russel and Cass (1986) for the LA basin and of Jacob (1985) for San Joaquin Valley, California, suggest an average value of $5 \times 10^{-5} \mu\text{g m}^{-3} \text{s}^{-1}$. A nitric acid vapor production rate of $8 \times 10^{-4} \mu\text{g m}^{-3} \text{s}^{-1}$ is assumed corresponding to an NO_2 concentration of 100 ppb and an OH concentration of 10^{-5} ppb. The deposition velocities of NH_3 and HNO_3 are assumed equal to 1 cm s^{-1} and the aerosol particle deposition velocities vary between 0.005 cm s^{-1} and 5 cm s^{-1} .

In the base case the averages of the above ranges of parameters are used, and assuming a particle diameter of $1 \mu\text{m}$, the following values of the dimensionless parameters are obtained:

$$\sigma_1 = 250, \quad \sigma_2 = 0.2, \quad \sigma_3 = 1, \quad \sigma_4 = 0.01, \quad \sigma_5 = 1.5, \quad \sigma_6 = 15$$

σ_7 is allowed to vary between 0.1 and 1000 while σ_8 varies between 0.01 and 100. The sensitivity of the results to the above chosen values of σ_1 to σ_6 will also be examined.

The calculated values of the deposition ratio for $t = t^*$ are presented in Figure 5 as a function of σ_7 and σ_8 for the base case. The results indicate that there

Base Case

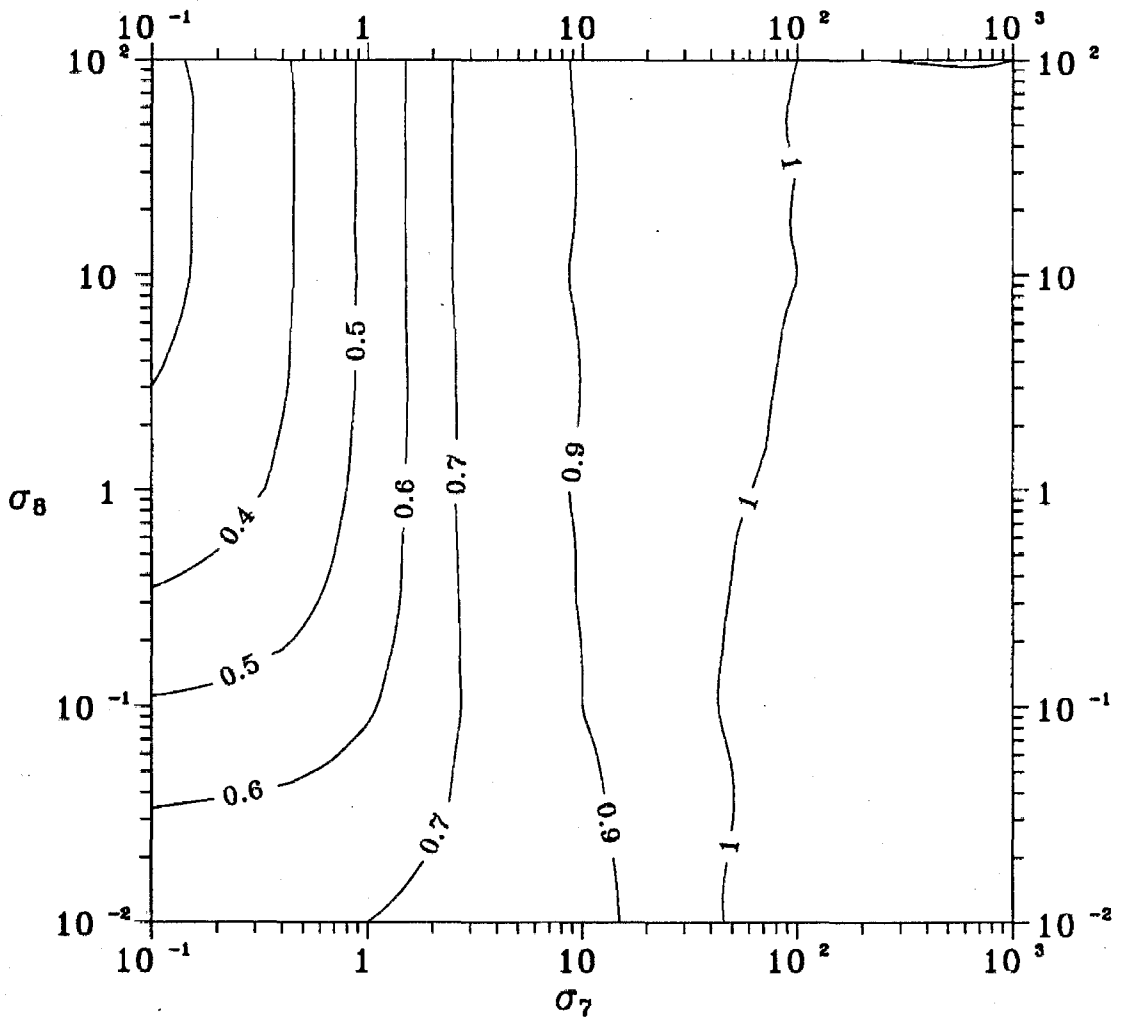


Figure 5 Deposition ratio $DR_3(t^*)$ for the base case.

are three regions of behavior. The first region is for $\sigma_7 > 20$ where for all values of σ_8 of interest the equilibration processes do not affect significantly the total deposition. In this region the initial concentration of nitric acid exceeds the initial concentration of ammonia, and nitric acid is deposited faster than it is produced. At the same time the ammonia emission rate exceeds its deposition rate. Therefore the ammonia concentration increases and the equilibrium is maintained without significant evaporation of the aerosol ammonium nitrate. Most of the material deposited for this region is nitric acid vapor. The second region extends roughly between $\sigma_7 = 20$ and $\sigma_7 = 2$. The deposition ratio drops from 0.95 to 0.75 and does not depend on the initial ammonium nitrate concentration. In this region the emission rates for both ammonia and nitric acid exceed their corresponding initial deposition rates and therefore they are both transferred to the aerosol phase and ammonium nitrate is formed. This transfer of material from a rapidly depositing phase to a slowly depositing one causes a decrease of the total deposition. In this second region the nitric acid deposition also dominates and therefore changes in the initial ammonium nitrate concentration affect the amount of aerosol deposition but have minimal effects on the nitric acid-dominated total deposition. Finally, in the third region for $\sigma_7 < 2$, the deposition ratio varies between 0.75 and 0.3 and the initial ammonium nitrate concentration is important. The smaller the initial ammonium nitrate concentration, the more the entire process changes by the transfer of material from the gas phase to the aerosol phase and the smaller the deposition ratio.

In conclusion, in the base case, the equilibration processes are found to affect the deposition the most when both ammonia and nitric acid production rates exceed their initial deposition rates and most of the material exists initially in the gas-phase primarily as ammonia.

Effect of the relative deposition velocities of the gas species

In the base case discussed the two gas-phase species were assumed to have the same deposition velocity ($\sigma_3 = 1$). The sensitivity of the model results to this value has been determined by examining the cases of $\sigma_3 = 0.5$ and $\sigma_3 = 2$. In both cases this variation of the relative deposition velocity of the gas species caused only small changes in the values of the deposition ratio in Figure 5. Namely, if the deposition velocity of HNO_3 is half the deposition velocity of NH_3 ($\sigma_3 = 0.5$), then the minimum value of the deposition ratio in Figure 5 (for $\sigma_7 = 0.1, \sigma_8 = 1000$) increases from 0.28 to 0.31. If the deposition velocity of HNO_3 is twice the deposition velocity of NH_3 ($\sigma_3 = 2$), the same minimum value decreases from 0.28 to 0.24. Thus, long as the deposition velocities of the two gases do not differ significantly, the exact value of the parameter σ_3 does not affect the deposition ratio by more than 15%. In the discussion that follows, we will assume that both gas-phase species have the same deposition velocity and we will refer to that value as the 'gas phase deposition velocity.'

Effect of the relative deposition velocities of the gas and aerosol phases

The effects of the aerosol deposition velocity on the deposition ratio can be studied by varying the parameter σ_4 (Figure 6). A tenfold increase of the aerosol deposition velocity compared to its base value (σ_4 increases from 0.01 to 0.1) has only minor effects on the deposition ratio. The base case deposition ratio surface moves slightly upwards. For example, its minimum value increases from 0.28 to 0.33 while its value for $\sigma_7 = 0.1$ and $\sigma_8 = 0.01$ increases from 0.68 to 0.81. If the aerosol deposition velocity increases further approaching the velocity of the gas phase ($\sigma_4=0.5$), the effects of the equilibration processes on the total deposition decrease, and the deposition ratio surface approaches the plane $DR_3 = 1$ (Figure

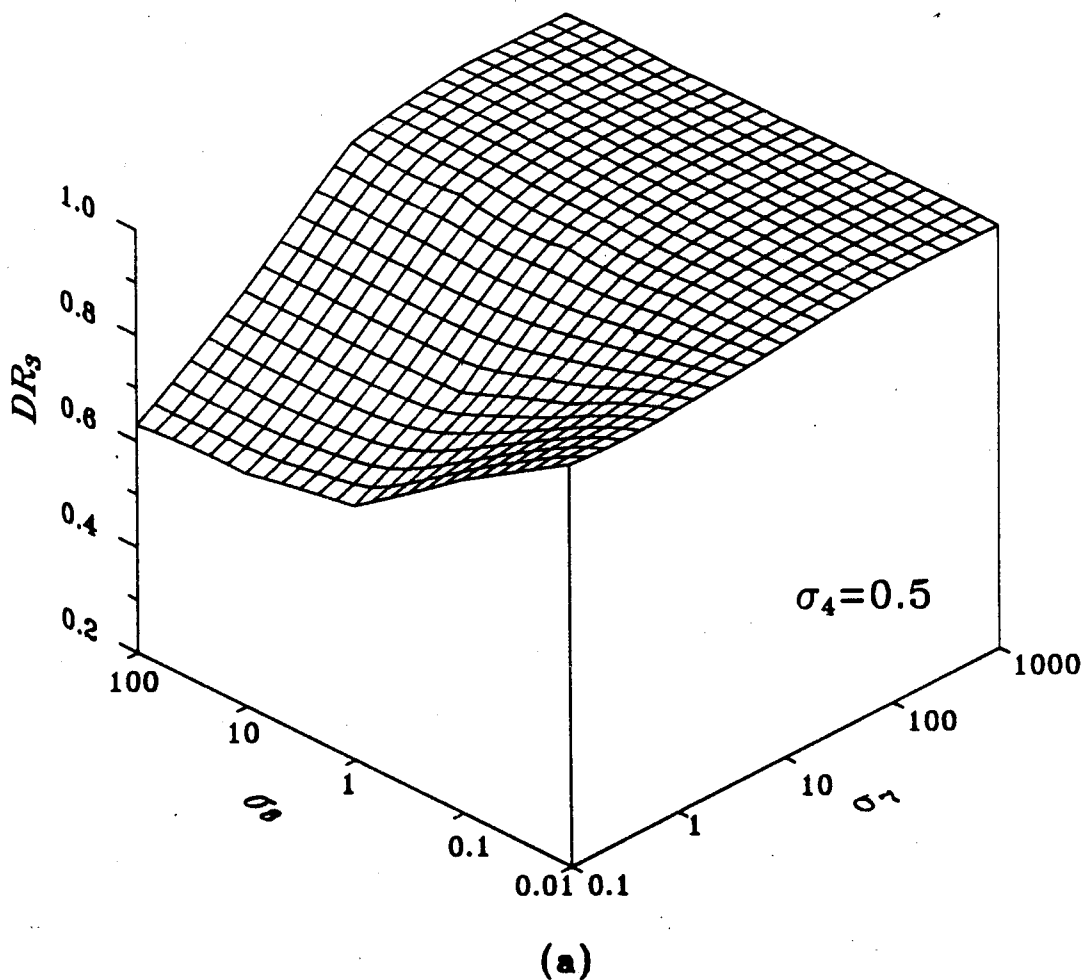


Figure 6a Effect of the ratio of the aerosol and gas phase deposition velocities on the deposition ratio $DR_3(t^*)$.

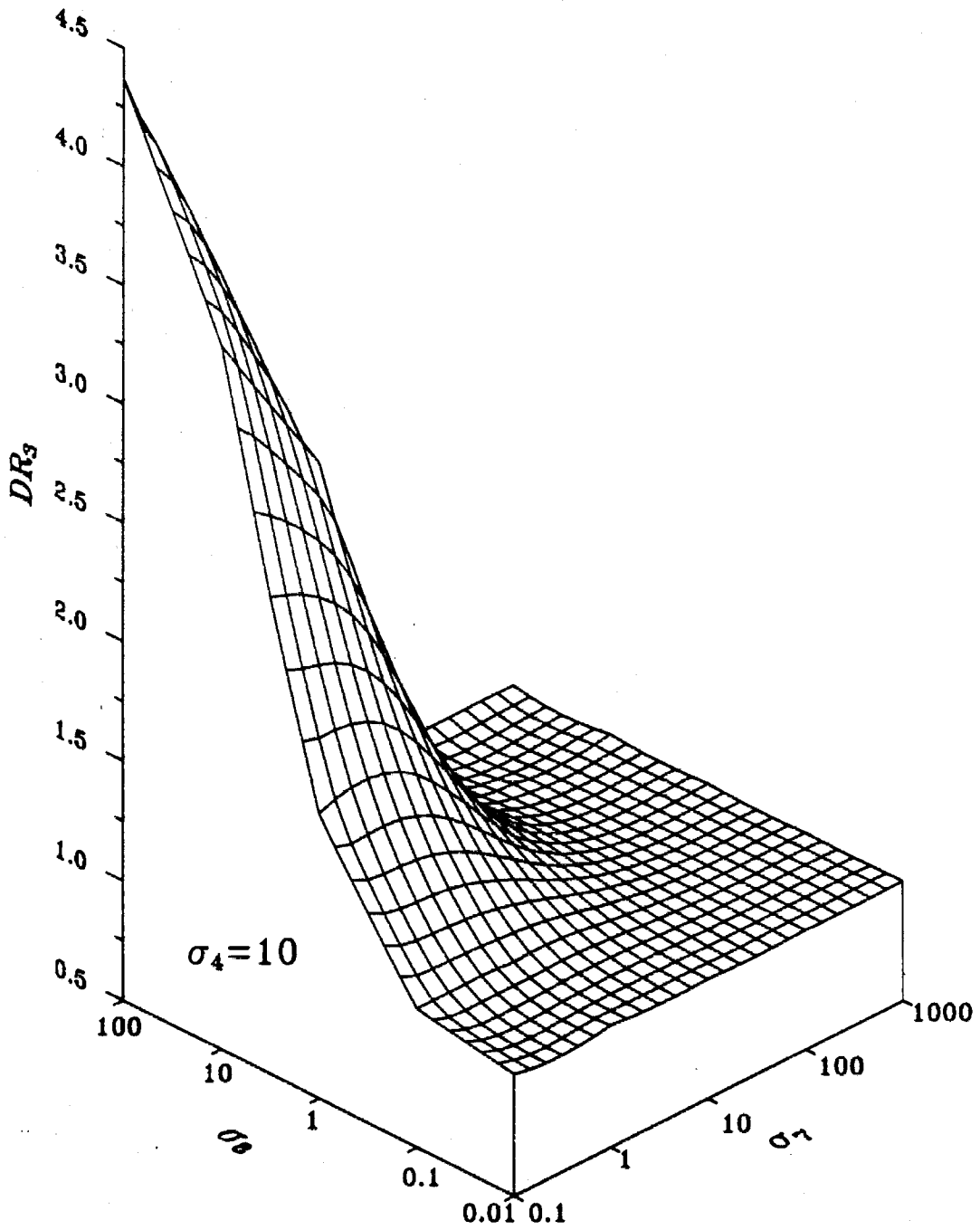
(a) $\sigma_4 = 0.5$

6a). If the deposition velocities of the two phases are the same, the transfer of mass between the two phases has no effect on the total mass deposited and the deposition ratio is one everywhere.

The behavior of the system changes drastically when the parameter σ_4 exceeds unity. Ammonia and nitric acid are still produced faster than they deposit, so they are transferred to the aerosol phase enhancing in this way the total deposition. This enhancement is maximized once more for high ammonia concentrations and small initial concentrations of ammonium nitrate and for $\sigma_4 = 2$ it can be as much 60%. These effects are magnified when the aerosol deposition velocity increases further and for $\sigma_4 = 10$ the total deposition increases by as much as 4.5 times (Figure 6b).

Effects of the emission/production rates of the gas-phase species

The effects of the gas-phase sources of ammonia and nitric acid have been investigated by varying the parameters σ_5 and σ_6 . A change in σ_5 can be viewed as change of both emission/production rates E_A and E_B by equal percentages, keeping all the deposition rates constant. For no gas-phase sources ($\sigma_5 = 0$) the deposition ratio exhibits a maximum value of 4.2 (Figure 7a). This maximum value is observed for roughly equal initial mass concentrations of ammonia and nitric acid and an initial ammonium nitrate concentration almost three times smaller. This peak is due to the fact that both $DR_3(t^*, \sigma_7)$ for a constant σ_8 and $DR_3(t^*, \sigma_8)$ for a constant σ_7 have maxima. If initially one of the two gases is in much higher concentration than the other, for example $M_{HNO_3}^0 \gg M_{NH_3}^0$, then the deviations from equilibrium created by the depositional losses can be suppressed by the evaporation of only small quantities of ammonium nitrate. On the contrary, as the two initial concentrations approach each other, a small depositional loss causes a larger ammonium nitrate evaporation, and more material is transferred from the aerosol to the gas phase



(b)

Figure 6b Effect of the ratio of the aerosol and gas phase deposition velocities on the deposition ratio $DR_3(t^*)$.

(b) $\sigma_4 = 10$

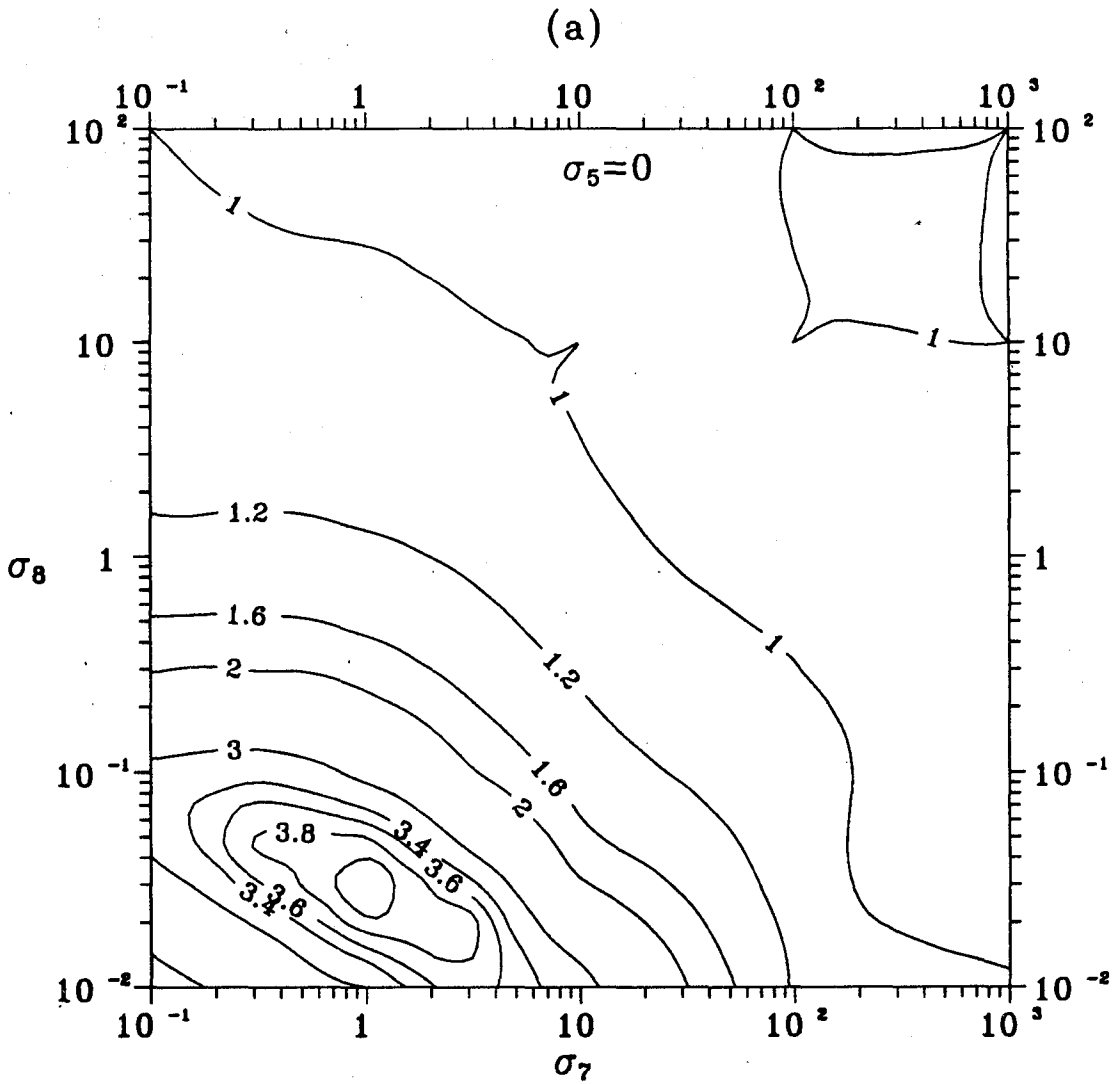


Figure 7a Effect of the ratio of the gas phase source rates to the gas phase deposition rate on the deposition ratio $DR_3(t^*)$.

(a) $\sigma_5 = 0$

enhancing the total deposition.

For an emission rate of NH_3 that is initially slower than its deposition ($\sigma_5 = 0.3$) there are two interesting regions (Figure 7b). If $\sigma_7 < 1$, then nitric acid is produced fast enough so that its concentration increase compensates for the ammonia concentration decline and material condenses to the aerosol phase, slowing down the total deposition rate by as much as a factor of 3. In the second region where $2 < \sigma_7 < 100, \sigma_8 < 0.2$, the gas-phase production is not able to compensate for the depositional losses and ammonium nitrate evaporates trying to maintain equilibrium, enhancing total deposition by as much as 50% .

An increase of σ_5 to 1.5 corresponds to the base case discussed previously. A further increase to $\sigma_5 = 15$ (Figure 7c) causes additional reduction of the total deposition as the strong sources of ammonia and nitric acid cause high supersaturations and rapid condensation to the slow depositing aerosol phase. For almost all conditions of interest, total deposition is slowed down by as much as 2.3 times.

The effect of the variation of the nitric acid production rate keeping all other variables constant has been examined by varying the parameter σ_6 . For no sources of nitric acid, $\sigma_6 = 0$, the increase of the ammonia concentration compensates for the decrease of nitric acid concentration unless $0.5 < \sigma_7 < 50, \sigma_8 < 0.1$ (Figure 8a). In this region ammonia emissions are not sufficient for the equilibrium maintenance and evaporation of the ammonium nitrate is necessary. The total deposition is enhanced by as much as 2 times. An increase of the nitric acid production (Figure 8b) causes the appearance of the two familiar regions with maximum enhancement 45% and maximum reduction 2.7 times. As σ_6 increases to 15, the enhancement region disappears (see base case). For very high nitric acid production rates, the total deposition decreases by as much as 35% (Figure 8c).

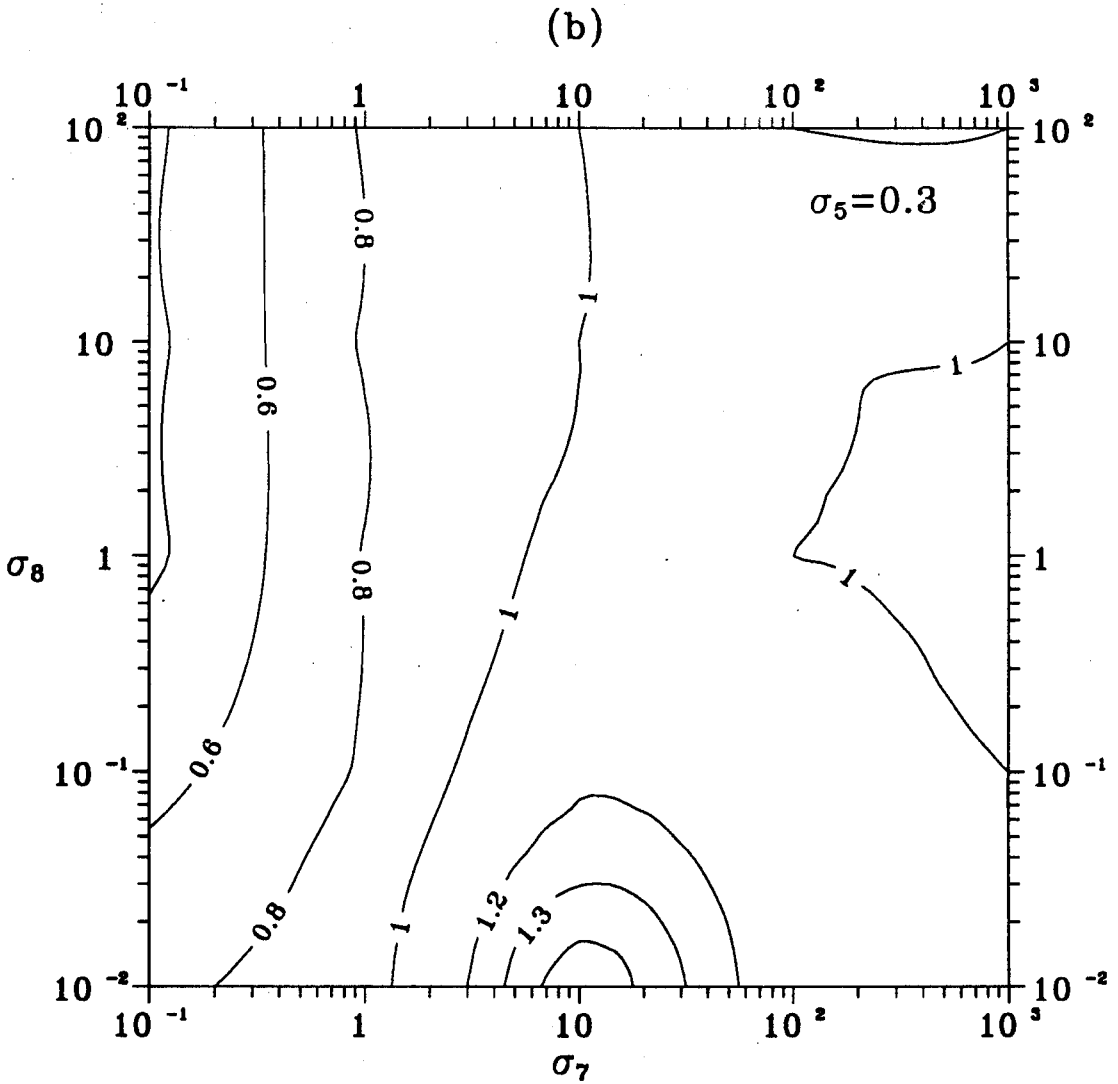


Figure 7b Effect of the ratio of the gas phase source rates to the gas phase deposition rate on the deposition ratio $DR_3(t^*)$.

(b) $\sigma_5 = 0.3$

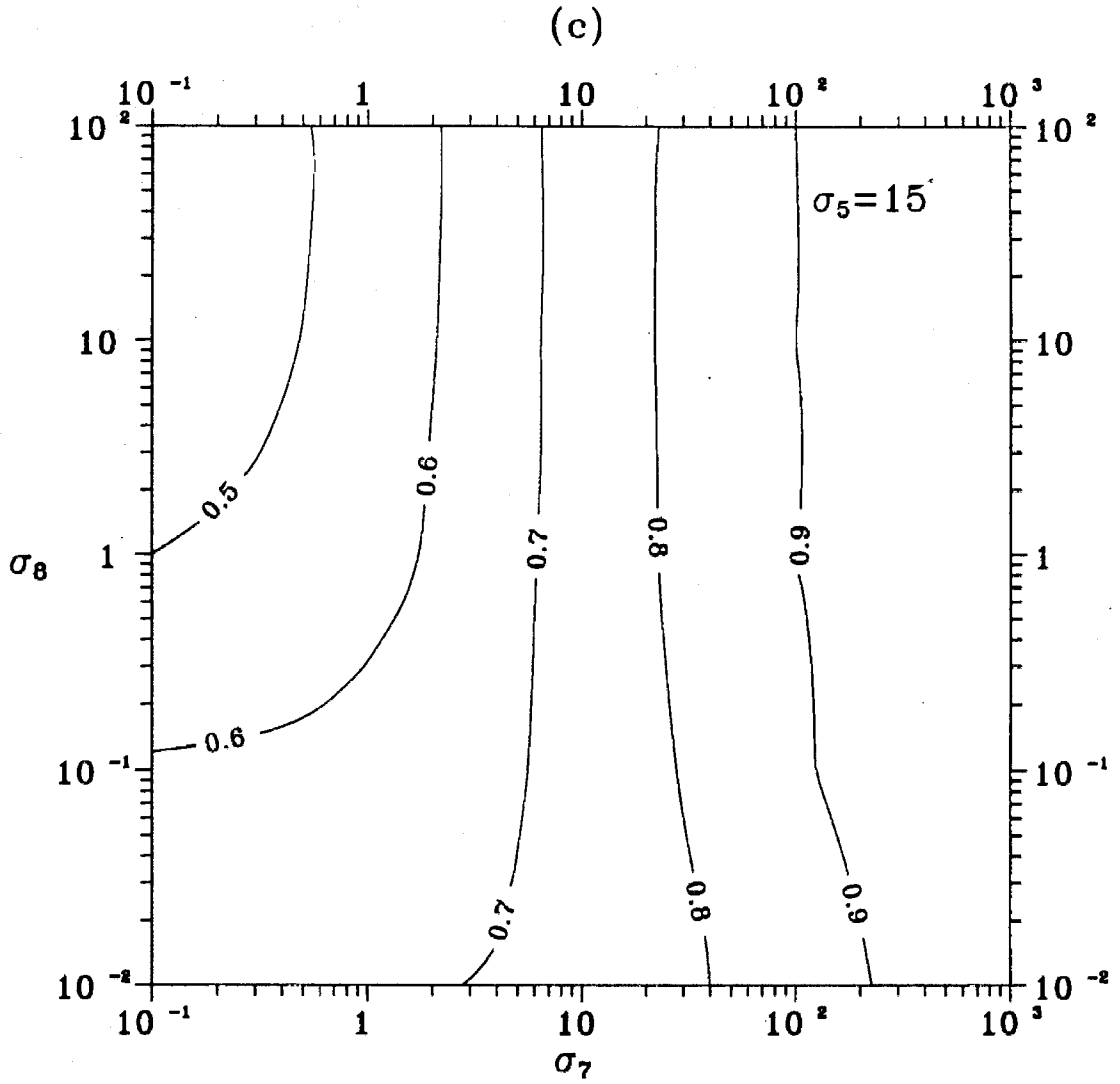


Figure 7c Effect of the ratio of the gas phase source rates to the gas phase deposition rate on the deposition ratio $DR_3(t^*)$.

(c) $\sigma_5 = 15$

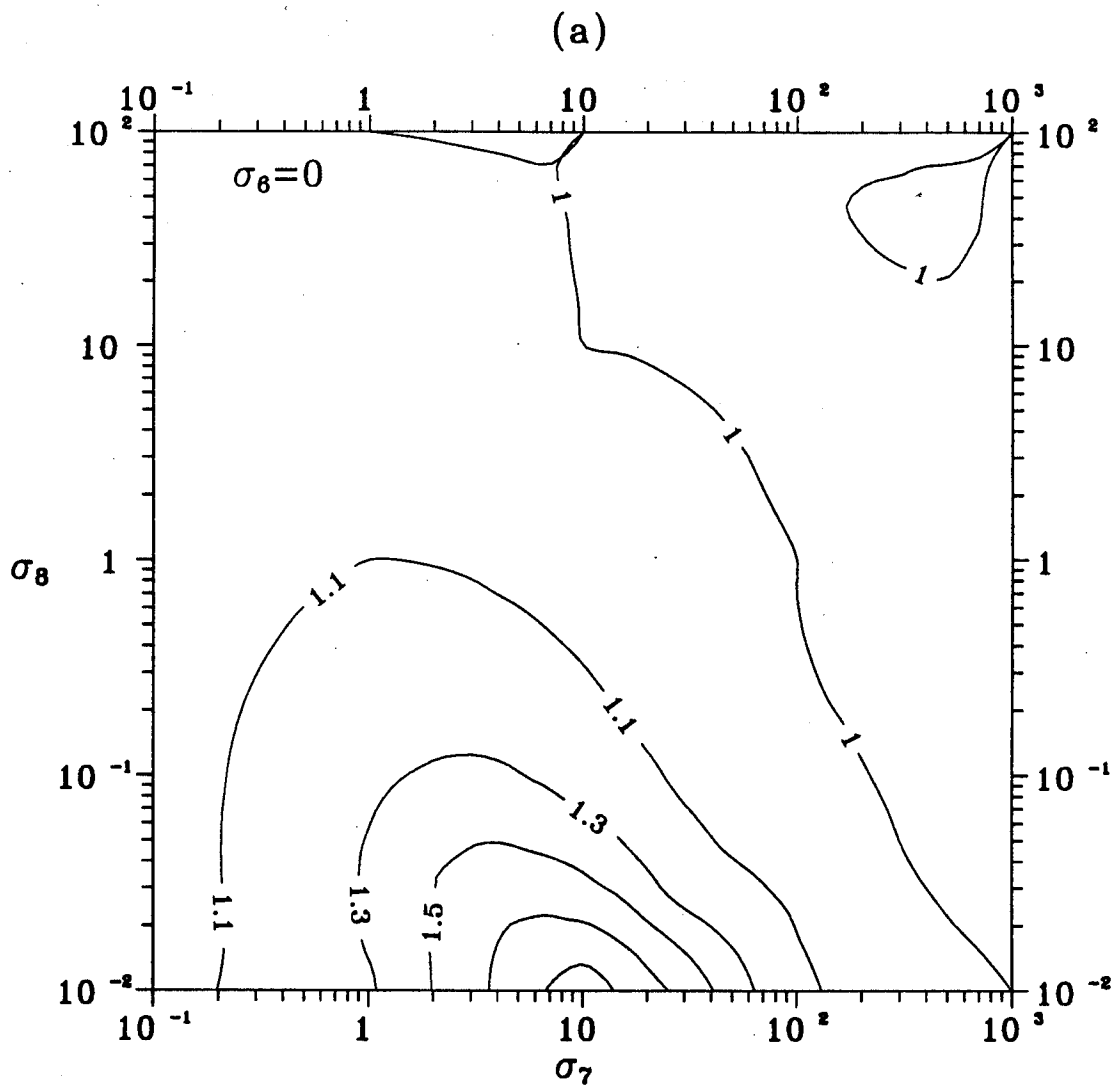


Figure 8a Effect of the ratio of the nitric acid production rate on the deposition ratio $DR_3(t^*)$.

(a) $\sigma_6 = 0$

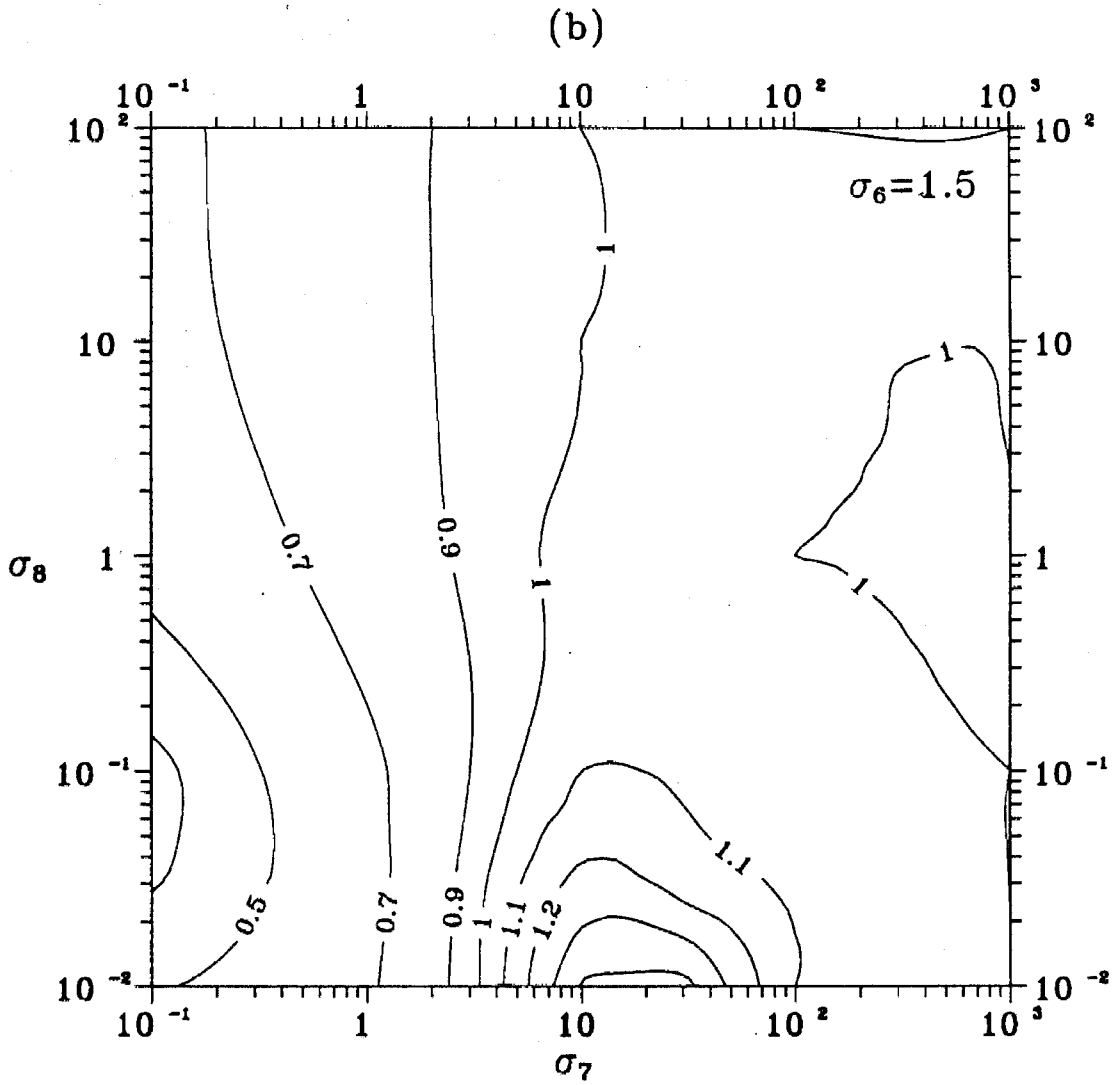


Figure 8b Effect of the ratio of the nitric acid production rate on the deposition ratio $DR_3(t^*)$.

(b) $\sigma_6 = 1.5$

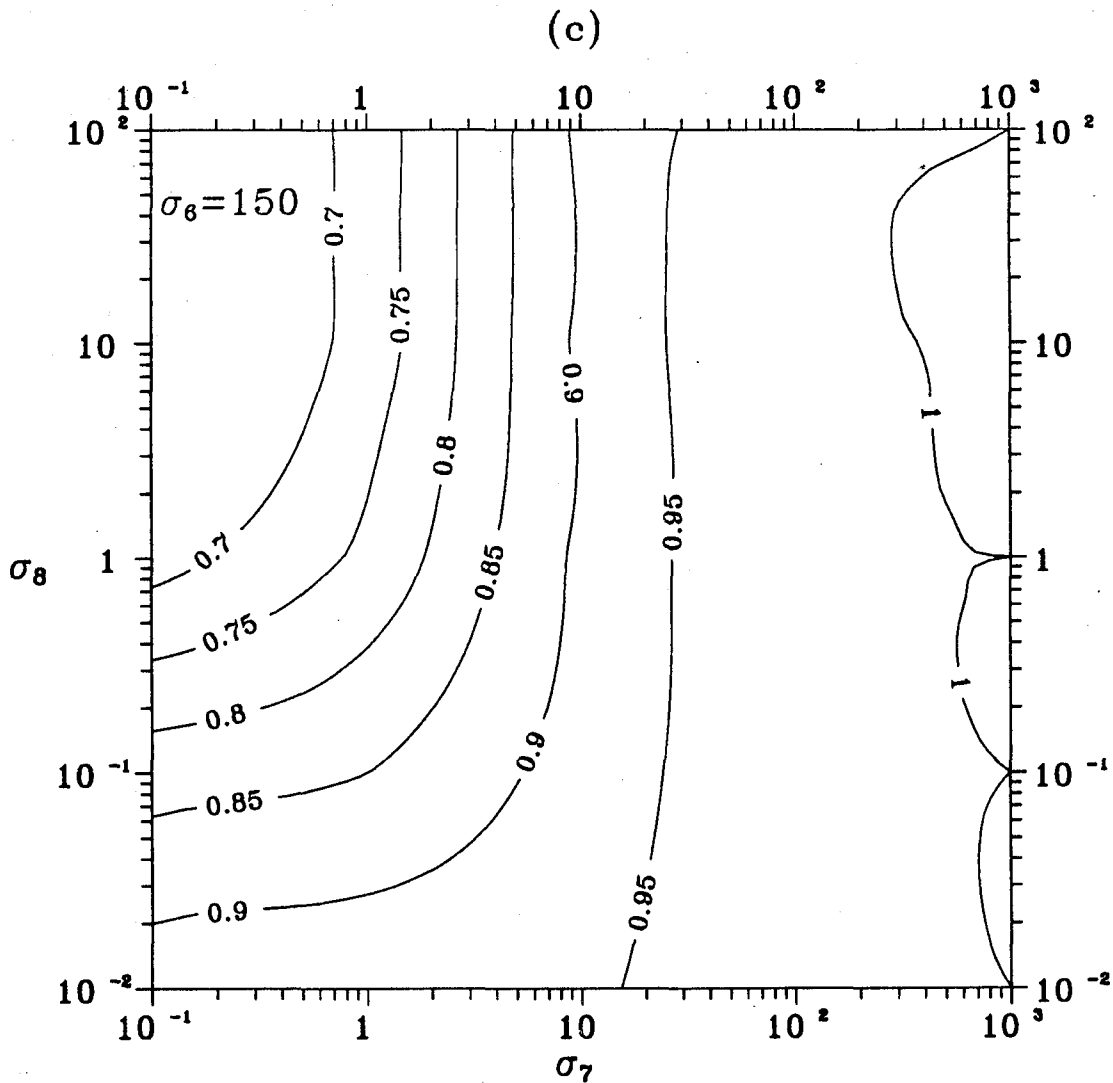


Figure 8c Effect of the ratio of the nitric acid production rate on the deposition ratio $DR_3(t^*)$.

(c) $\sigma_6 = 150$

Monodisperse vs Polydisperse Condensed Phase

A major assumption in the three models presented is the monodispersity of the aerosol or aqueous phase. Atmospheric aerosols sizes range roughly from 0.01 μm to 10 μm , and fog or cloud droplets range from a few μm to a few hundred μm and their distributions are usually far from monodisperse. All the above models can easily be extended to account for polydispersity of the condensed phases by discretizing the continuous aerosol or droplet distribution into n size sections.

Nondimensionalization of the resulting system of $n + 3$ equations suggests that the solutions depend on $3n + 1$ dimensionless parameters, the initial mass fraction of species B in section i , $x_i = M_{B_o}^i / \sum_i M_{B_o}^i$, the initial partitioning of the species between gas and aerosol phases, $\beta = M_A^o / \sum_i M_{B_o}^i$, the ratios of deposition constants of sections i to the gas phase deposition constant, $\gamma_i = k_{dc}^i / k_{da}$, the ratio δ of the emission rate of A to the initial vapor deposition rate, and the ratios of the mass transfer rates of section i to the vapor deposition rate, $\alpha_i = k_m^i M_C^i / k_{da}$.

Because of the large number of parameters involved in the model a thorough investigation of the importance of the equilibration processes on the $(3n + 1)$ dimensional parameter space is beyond the scope of the present work. In the case of a polydisperse aerosol one can obtain a rough estimate of the importance of the equilibration processes on deposition by treating the aerosol as monodisperse and using for Case 1

$$M_B = \sum_{i=1}^n M_B^i, \quad M_C^o = \sum_{i=1}^n M_C^i, \quad k_m = \frac{\sum_{i=1}^n k_m^i M_C^i}{M_C^o}, \quad k_{dc} = \sum_{i=1}^n x_i k_{dc}^i.$$

The inaccuracy of the above treatment arises in calculating an average aerosol deposition velocity using as weighting factors the initial fractions x_i . The distribution of B over the aerosol size spectrum usually changes with time due to mass transfer and deposition and the average deposition velocity follows this change. An accurate

solution can only be obtained by actually solving the system of differential equations and comparing with the solution if one neglects equilibration processes.

The models for Cases 2 and 3 can be similarly extended to describe a poly-disperse aerosol or droplet phase. A treatment of Case 2 with a full fog droplet spectrum has been presented by Pandis et al. (1990).

Implications for Mathematical Modeling

The values of the deposition ratio presented up to this point can be interpreted as the errors introduced in deposition calculations by completely neglecting equilibration processes. The first point suggested by this work is that the equilibration processes between different phases should be included in all mathematical models attempting to predict deposition. The problem that should be addressed next is how should these processes be modelled.

The common practice in gas-aerosol or gas-aqueous phase models has been the splitting of the whole problem into subproblems that are solved sequentially. In this method, called operator splitting, there is usually one operator describing the processes in each phase. For example in an Eulerian photochemical gas-aerosol model, Pilinis and Seinfeld (1988) used the following operator scheme to calculate the variable vector F_i at time $t + 2h$:

$$F_i^{(t+2h)} = A_i(2h)A_{th}(2h)A_d(2h)A_x(h)A_y(h)A_{zc}(2h)A_y(h)A_x(h)F_i^{(t)}$$

where A_x , A_y , A_{zc} are the x -transport, y -transport, z -transport and gas-phase chemistry operators, respectively, while A_i , A_{th} , A_d are the operators for the inter-sectional movement of the aerosol particles, the aerosol thermodynamics, respectively. In this model the gas and aerosol deposition have been included in the z -transport and gas-phase chemistry operator while the equilibration processes have

been included in the thermodynamics operator. The operator step $2h$ used was 10 minutes.

The separation of the equilibration processes and the deposition into different operators is expected to introduce errors in the calculations when the operator time step used is not sufficiently small. To investigate the magnitude of these errors we have compared the models developed in this study with the corresponding operator splitting schemes.

For Case 1 we have chosen the point $\alpha = 1000, \beta = 1, \gamma = 0.01, \delta = 100$ for which neglect of the equilibration processes would cause an overprediction of total deposition by 16 times (Figure 2d). Selecting $M_{eq} = 1 \mu\text{g m}^{-3}$ and gas deposition velocity 0.5 cm s^{-1} we find that the smallest time scale in the problem is the emission time scale equal to 17 minutes. The errors introduced by the operator splitting scheme are shown in Figure 9. For a time step of 10 minutes, the error is almost a 100% deposition overprediction. Timesteps less than 2 minutes should be used to avoid errors more than 10%.

For Case 3 the Base Case with $\sigma_7 = 0.1, \sigma_8 = 100$ has been examined. Complete omission of the equilibration processes results in an overprediction of the total deposition by a factor of 3.6 (Figure 5). The results of the corresponding operator splitting scheme are depicted in Figure 9 for $k_{da} = 10^{-4} \text{ s}^{-1}$. The smallest time scale of the problem is the production of HNO_3 at 1 minute. The performance of the operator splitting scheme is better, but it still overpredicts total deposition by 40% for a time step of 10 minutes.

In conclusion, when equilibration processes significantly affect deposition one should try to include both processes in the same numerical operator. If this is not possible, then one should be prepared to use very small time steps in the operator splitting scheme to avoid the above described errors.

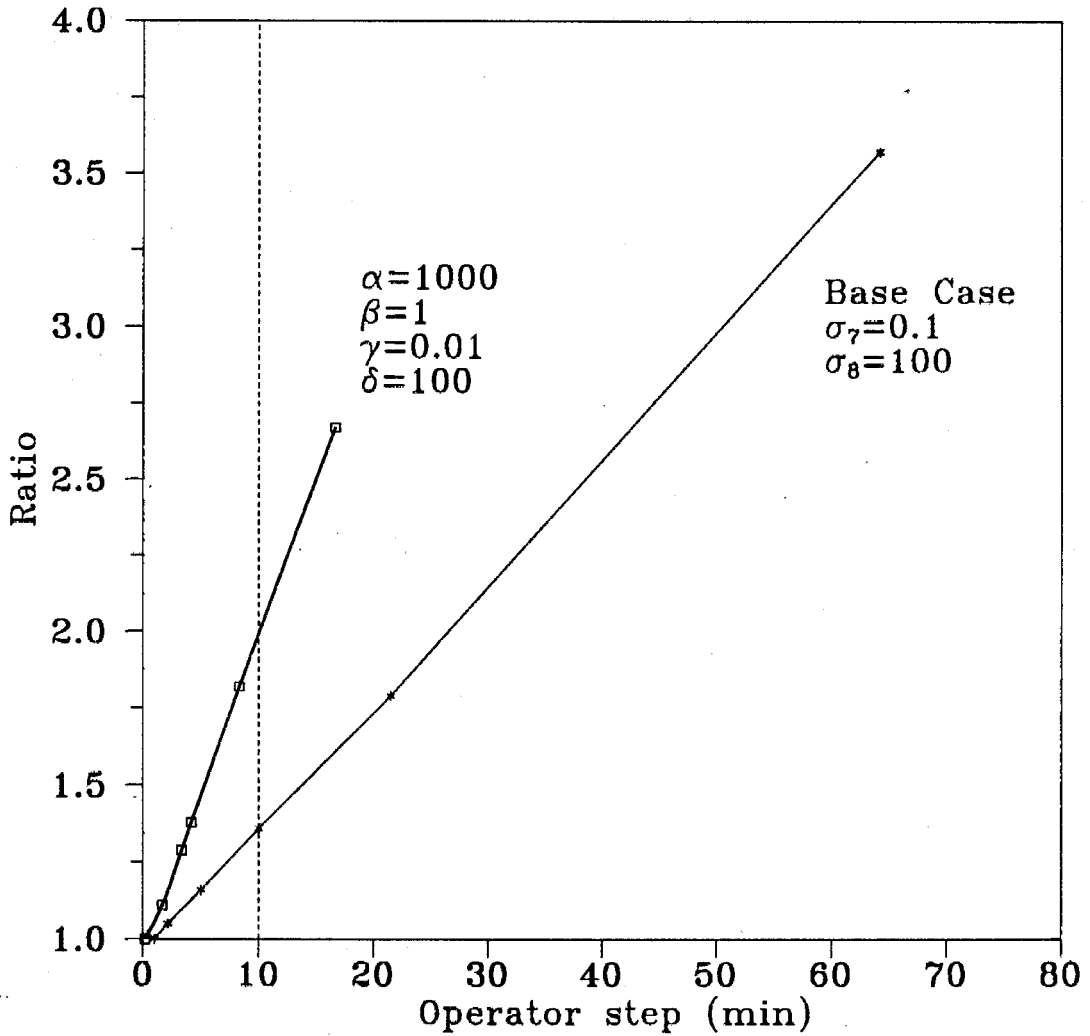


Figure 9 Ratio of the total deposited mass as calculated by the operator splitting scheme over the full solution as a function of the operator time step.

Conclusions

The study of three idealized problems has demonstrated that equilibration processes between two atmospheric phases that are removed with different rates can significantly influence the amount of material deposited on the ground and the residence times of material in the atmosphere. The larger the difference of deposition velocities between the two phases the more the equilibration processes affect the removal processes. If the two phases have the same deposition velocities, the equilibration processes just alter the material distribution between the two phases without affecting the total deposition.

The role of the equilibration processes is enhanced under conditions that cause large deviations from the system equilibrium state resulting in transfer of material between the two phases. The emission or gas-phase production of a vapor is the factor examined in this study. High emission or production rates cause supersaturations in the gas phase and material transfer to the aerosol phase. On the contrary, the absence of gas-phase sources causes subsaturation and evaporation of material from the aerosol or aqueous-phase.

The initial conditions of the system determine the relative magnitude of the material transferred between the two phases compared to the total system mass determining thus indirectly the importance of the equilibration processes.

In all cases examined the equilibration processes were able to enhance or suppress significantly the removal processes and therefore should not be neglected in deposition calculations. Furthermore, our analysis demonstrates that if an operator splitting scheme is used in a mathematical model, both equilibration and removal processes should be included in the same operator or very small operator steps (typically less than one minute) will be necessary.

Acknowledgement

This work was supported by State of California Air Resources Board Agreement A932-054.

References

- Bidleman T. F. (1988) Wet and dry deposition of organic compounds are controlled by their vapor-particle partitioning *Environ. Sci. Technol.* **22**, 361-367.
- Brost R. A., Delany A. C. and Heubert B. J. (1988) Numerical modeling of concentrations and fluxes of HNO₃, NH₃ and NH₄NO₃ near the surface *J. Geophys. Res.*, **93**, 7137-7152.
- Dollard G. J. and Unsworth M. H. (1983) Field measurements of turbulent fluxes of wind-driven fog drops to a grass surface **17**, 775-780.
- Jacob D. J (1985) The origins of inorganic acidity in fogs *Ph.D. thesis*, California Institute of Technology, Pasadena, CA.
- McMahon T. A. and Denison P. J. (1979) Empirical atmospheric deposition parameters-a survey *Atmos. Environ.* **13**, 571-585.
- McRae G. J. and A. G. Russel (1984) Dry deposition of nitrogen-containing species, in *Deposition Both Wet and Dry*, Ed. B. B. Hicks, 153-193, Acid Precipitation Series, Butterworth, Boston.
- National Center for Atmospheric Research (1982) *Regional Acid Deposition: Models and Physical Processes* Boulder, CO.
- Pandis S. N. and Seinfeld J. H. (1989a) Sensitivity analysis of a chemical mechanism for aqueous-phase atmospheric chemistry *J. Geophys. Res.*, **94**, 1105-1126.
- Pandis S. N. and Seinfeld J. H. (1989b) Mathematical modeling of acid deposition due to radiation fog *J. Geophys. Res.*, **94**, 12911-12923.
- Pandis S. N., Seinfeld J. H., and C. Pilinis (1990) The smog-fog-smog cycle and

acid deposition *Atmos. Environ.* (in press).

Pilinis C. and Seinfeld J. H. (1988) Development and evaluation of an eulerian photochemical gas-aerosol model *Atmos. Environ.* **22**, 9, 1985-2001.

Russel A. G. and Cass G. R. (1984) Acquisition of regional air quality model validation data for nitrate, sulfate, ammonium ion and their precursors *Atmos. Environ.* **18**, 9, 1815-1827.

Russel A. G. and Cass G. R. (1986) Verification of a mathematical model for aerosol nitrate and nitric acid formation and its use for control measure evaluation *Atmos. Environ.* **20**, 10, 2011-2025.

Schwartz, S. E. and W. H. White (1981) Solubility equilibrium of the nitrogen oxides and oxyacids in dilute aqueous solution, *Adv. Environ. Sci. Eng.*, **4**, 1-45.

Seinfeld J. H. (1986) *Atmospheric Chemistry and Physics of Air Pollution*. John Wiley, New York.

Stern J. E., Flagan R. C., Grosjean D., and Seinfeld J. H. (1987) Aerosol formation and growth in atmospheric aromatic hydrocarbon photooxidation, *Environ. Sci. Technol.*, **21**, 1224-1231.

Stafford M. A. (1988) The effects of partitioning between gas and aerosol phases on the dry deposition of acidity. Paper presented at American Chemical Society Meeting, Toronto, June 5-11, 1988.

Stelson A. W. and Seinfeld J. H. (1982) Relative humidity and temperature dependence of the ammonium nitrate dissociation constant, *Atmos. Environ.*, **16**, 983-993.

Tao Y. and McMurry P. H. (1989) Vapor pressures and surface free-energies of C14-C18 monocarboxylic acids and C5-dicarboxylic and C6-dicarboxylic acids, *Environ. Sci. Technol.*, **23**, 1519-1523.

Wesely M. L. and Shannon J. D. (1984) Improved estimates of sulfate dry deposition

in Eastern North America, *Environ. Progress* 3, 78-81.

CHAPTER 6

THE SMOG-FOG-SMOG CYCLE AND ACID DEPOSITION

(Accepted for publication in *Journal of Geophysical Research*, April 1990)

The Smog-Fog-Smog Cycle and Acid Deposition

Spyros N. Pandis, John H. Seinfeld

Department of Chemical Engineering and Environmental Quality Laboratory,

California Institute of Technology, Pasadena, CA 91125, USA

and

Christodoulos Pilinis

AeroVironment Inc., 825 Myrtle Ave., Monrovia, CA 91016, USA

Abstract

A model including descriptions of aerosol and droplet microphysics, gas and aqueous-phase chemistry and deposition is used to study the transformation of aerosol to fog droplets and back to aerosol in an urban environment. Fogs in polluted environments have the potential to increase aerosol sulfate concentrations but at the same time to cause reductions in the aerosol concentration of nitrate, chloride, ammonium and sodium as well as in the total aerosol mass concentration. The sulfate produced during fog episodes favors the aerosol particles that have access to most of the fog liquid water which are usually the large particles. Aerosol scavenging efficiencies of around 80% are calculated for urban fogs. Sampling and subsequent mixing of fog droplets of different sizes may result in measured concentrations that are not fully representative of the fogwater chemical composition and can introduce errors in the reported values of the ionic species deposition velocities. Differences in the major ionic species deposition velocities can be explained by their distribution over the aerosol size spectrum and can be correlated with the species average diameter. Two different expressions are derived for use in fog models for the calculation of the liquid water deposition velocity during fog growth and dissipation stages.

Introduction

Historically, urban fogs have frequently been interconnected with severe pollution episodes (Wilkins, 1954). A cyclical relationship between the occurrence of smog and fog in the Los Angeles basin has been proposed by Munger et al. (1983) and was termed the smog-fog-smog cycle. A polluted atmosphere with high aerosol concentration assists the formation of late night and early morning fogs which appear to enhance smog production, visibility reduction, and aerosol sulfate levels during the following day.

Fogs can be viewed as a physicochemical processor of the ambient aerosol and of various gaseous pollutants. As the relative humidity of an air parcel, in contact with the ground, increases, water condenses on the aerosol particles in accordance with water vapor equilibrium. If the relative humidity of the parcel reaches a critical supersaturation, the value of which depends on the size and chemical composition of the aerosol present, the particles become activated, grow freely by vapor diffusion, and a fog forms. The growth of the aerosol particles to liquid droplets leads to the acceleration of particle removal from the atmosphere decreasing in this way the aerosol concentration. Soluble gaseous species such as nitric acid, sulfur dioxide, and ammonia are transferred to the aqueous phase and their deposition is also enhanced. At the same time the fog formation provides the reacting medium, the liquid water, for aqueous-phase reactions. Several species dissolve in fogwater and react giving products that remain in the aerosol phase after the fog dissipates, for example the dissolution of SO_2 , its ionization and its subsequent oxidation to sulfate. These species can attract additional gaseous species, for example ammonia and water, into the aerosol phase and therefore a fog may also increase the aerosol mass.

Cass and Shair (1984) reported a correlation between high aerosol sulfate concentrations in the Los Angeles basin and the occurrence of fog episodes, but the

quantitative effects of the fogs on the concentration of the major aerosol species are not yet fully understood. Pandis et al. (1990) and Hegg and Larson (1990) suggested that sulfate produced is not uniformly distributed over the droplet spectrum. Therefore it is necessary to investigate not only the effects of fogs on bulk aerosol concentration, but also the possible effects on the aerosol size/composition distribution.

A rigorous theoretical investigation of the smog-fog-smog cycle requires a mathematical model able to describe in detail the thermodynamics and dynamics of multicomponent aerosols, the microphysics of the condensational growth of a droplet distribution, the droplet removal processes, and the gas and aqueous-phase chemical processes occurring in a fog.

Such a model enables us to provide answers to several additional questions associated with the urban fog life cycle. These problems include the aerosol scavenging efficiencies of urban fogs, the uncertainties introduced by measuring in bulk a polydisperse fog droplet distribution, the difference in deposition velocities of different ionic species during fog episodes, and expression of the liquid water flux as a function of the liquid water content for fog models that do not include explicit treatment of droplet microphysics.

We begin with a short discussion of the distinction between aerosol and droplets. A brief description of the mathematical model employed in this study follows together with a presentation of the representative fog episode that will be simulated. Next, the effects of fogs on aerosol concentration and aerosol size/composition distribution are investigated. Predictions for the aerosol scavenging efficiency of urban fogs are then compared with field measurements. The possible problems posed by the differences in chemical composition of fog droplets of different sizes on fog sampling and on calculations of deposition velocities are presented next. Suggestions

for a more accurate calculation of liquid water deposition flux in fog models follow. Finally, a possible explanation is presented for the reported differences among the deposition velocities of different ionic species.

Aerosol or droplet?

There have been different approaches in the literature concerning the distinction between aqueous droplets and interstitial aerosol. In principle this distinction appears unnecessary because the same physicochemical processes, mass transfer, chemical reactions, etc., take place in both aerosol and droplets. However, the difference in size between aerosol and droplets and the subsequent difference in the characteristic times of the respective processes has led previous investigators to separate these particles into aerosol and droplets, using different definitions and creating some confusion.

In several studies a size cut is selected more or less arbitrarily and all the particles larger than this size are named droplets while all particles smaller than that are considered aerosol. A second definition, used in cloud physics, is based on the fundamental droplet microphysics. For every particle there is a corresponding critical diameter d_c and a critical supersaturation s_c corresponding to the maximum of the Köhler equations (Pruppacher and Klett, 1980). If the environment reaches a supersaturation equal to or larger than s_c , that particle is said to be activated. In the usual description of the activation process, the larger particles are activated first, and, as the supersaturation increases, smaller and smaller particles are successively activated. In cloud physics a particle is not considered to be a droplet unless its diameter exceeds its critical diameter. In this case, however, because of mass transfer limitations the larger particles may not be able to follow the changes of relative humidity (Hänel, 1987) and they may not be able to reach their critical

radius. Nevertheless, these large particles carry a significant part of the liquid water of the cloud or fog and should be included in the droplet population.

To overcome the arbitrary nature of the first definition (everything larger than a certain size is a droplet) and the omission of the larger particles from the droplet population in the second definition because of mass transfer limitations (their diameter often never exceeds their critical diameter during a fog episode), we propose a third definition. A particle is described as a droplet when either the supersaturation of the environment exceeds its critical supersaturation or its diameter exceeds its critical diameter. When both of these criteria are not met the particle will be referred to as interstitial aerosol.

In our model the same differential equations will be applied to all particles independently of their size and chemical composition. Later on, the definition suggested above will be used to distinguish between droplets and aerosol, so that a direct comparison between our work and previous studies will be possible.

Model Description

The mathematical model employed in this study describes gas-phase chemistry, aerosol dynamics and thermodynamics, aqueous-phase chemistry, droplet microphysics, and wet deposition in a closed homogeneous volume of air in which a fog is formed and dissipated. The primary input to the model is the temperature of the system. This model is an extended version of that developed by Pandis et al. (1990). The main addition is the inclusion of the wet removal processes to those described in the original work.

The fog physics suggests that the fog life cycle should be divided into three simulation periods, namely the conditioning period (relative humidity, RH, rises from the initial value to a threshold value RH_c close to saturation, chosen as 99%),

the rapid growth period ($RH > RH_c$), and the dissipation period (RH drops under RH_c).

During the fog conditioning stage the model simulates the gas-phase chemistry and the aerosol size/composition distribution evolution. Both aerosol dynamics and thermodynamics are considered (Pilinis and Seinfeld, 1988) and for computational purposes the continuous aerosol size distribution is discretized into n uniform sections (Warren and Seinfeld, 1985). The detailed SAPRC/ERT gas-phase chemical reaction mechanism (Carter et al., 1986) with the modifications and extensions of Carter and Atkinson (1988) is used for the calculation of the gas-phase reaction rates. This mechanism describes the complex chemical reactions of hydrocarbon/ NO_x / SO_2 mixtures in a polluted atmosphere, using 154 reactions and 62 species.

When the relative humidity of the system exceeds the threshold value RH_c , processes described by the model include gas-phase chemistry, aqueous-phase chemistry, microphysics of aerosol and droplets, and deposition. The droplet size distribution is discretized as before into n individual size sections but because of the magnitude of the size changes occurring each droplet size section is now allowed to move in the time-diameter space increasing its diameter when water condensation is taking place and decreasing its size in case of evaporation.

The change of the mass concentration of species i in droplet size section l , q_{il} , is calculated by:

$$\frac{dq_{il}}{dt} = \left[\frac{\partial q_{il}}{\partial t} \right]_{cond./evap.} + R_{il}^a(q_{1l}, q_{2l}, \dots, q_{nl}) - \frac{v_l}{H} q_{il} \quad (1)$$

where $\left[\frac{\partial q_{il}}{\partial t} \right]_{cond./evap.}$ is the mass transfer rate of species i from the gas phase to the aqueous droplets in moving section l , R_{il}^a is the rate of change of species i in section

l due to aqueous-phase reactions, v_l is the deposition velocity of droplets in section l and H is the fog height. For the water mass transfer rate, the detailed growth equation derived by Pruppacher and Klett (1980) is used and for the remainder of the volatile species, the expression used by Pandis and Seinfeld (1989a) is applied. The use of the detailed growth equation for the multicomponent, aqueous solution droplets enables us to describe the activation process exactly without the use of any further assumptions (Pruppacher and Klett, 1980). The reaction rates R_{il}^a are derived from the aqueous-phase chemical mechanism presented by Pandis and Seinfeld (1989a) which includes 49 individual aqueous-phase species, 17 aqueous-phase ionic equilibria and 109 aqueous-phase reactions. Field studies in fogs (Dollard and Unsworth, 1983) have indicated that for wind speeds less than 2 m s^{-1} , that are typical of radiation fogs, droplet sedimentation accounts for most of the droplet flux to the ground. Therefore, the deposition velocity of fog droplets is approximated by Stokes law as long as the diameter of the droplets remains less than $50 \mu\text{m}$.

Droplet coagulation is neglected and the number concentration of droplets in each section l , N_l , changes only due to droplet deposition and is described by

$$\frac{dN_l}{dt} = -\frac{v_l}{H} N_l. \quad (2)$$

The change in section diameter, D_l , is calculated by

$$\frac{dD_l}{dt} = \frac{2}{N_l \rho_l \pi D_l^2} \sum_{i=1}^{N_v} \left[\frac{\partial q_{il}}{\partial t} \right]_{\text{cond./evap.}} \quad (3)$$

where ρ_l is the density of droplets in section l , and N_v is the number of volatile species.

The turbulence induced by the radiative cooling of the fog top and the entrainment of air in the fog layer have been neglected in this study.

Representative Fog Episode for Evaluation

Unfortunately, no complete data set exists, to the best of our knowledge, for a full evaluation of the present model. Such a data set should include aerosol size/composition distributions before and after the fog episode and droplet size/composition distributions during the episode. Direct comparison of the model predictions with observations is problematic not only because of the difficulty of the required experimental measurements but also because in fog field studies samples are acquired in the same location and no attempt is made to follow the air parcel in which fog was created. Because of the above limitations, the current work should be viewed primarily as a sensitivity study investigating phenomena that have not yet been elucidated by field studies.

The case that will be considered is a typical urban radiation fog episode in the Los Angeles basin roughly corresponding to the fog episode of November 23, 1981, in Pasadena, California (Munger et al., 1983). The first stage of the simulation starts in the late afternoon with relative humidity 50% and dry aerosol particles. The temperature drops to 14°C and the relative humidity increases reaching 95% one hour before midnight. The main simulation begins with both gas and aqueous phase chemical processes being taken into account at this time. The initial conditions used are shown in Table I. The fog lasted roughly three hours with the temperature dropping to a minimum of 12.8°C at midnight ($t = 60$ min), increasing slowly to 13°C at $t = 130$ min, and to 14 °C at $t = 170$ min. A constant fog height of 200 m is assumed, typical of radiation fog episodes (Pandis and Seinfeld, 1989b). During the fog dissipation stage, the chemistry is followed until the relative humidity again reaches 95% and then the aerosol is allowed to dry until the relative humidity reaches the 50% point. Gas-phase chemical processes are neglected in the first and last stages.

Table I. Base case parameters and initial conditions.

<i>Model Parameter</i>	<i>Value</i>
Latitude	34.5
Time at start (full simulation)	23 : 00 PST
Relative humidity at start	95%
Fog Height	200 m

<i>Gas – phase species</i>	<i>Initial concentration (ppb)</i>
SO ₂	10.0
NH ₃	8.03
HNO ₃	5.17
HCl	3.90
O ₃	10.0
NO	50.0
NO ₂	50.0
H ₂ O ₂	1.0
HCHO	7.0
PAN	1.0
ETHE	85.0
Parafins	700.0
Olefins	45.0
Aromatics	150.0

<i>Aerosol species</i>	<i>Initial concentration (μg/m³)</i>
Sulfate	3.93
Sodium	3.38
Fe ³⁺	0.2
Mn ²⁺	0.01

The model has been applied with 7 logarithmically spaced sections covering initially the diameter range from 0.2 to 8 μm . This choice of section number represents a reasonable compromise between computational accuracy and keeping the required computing time at a reasonable level. Increasing the current number of sections causes an exponential increase in computing time without changing the conclusions reached in the present work. The initial sulfate and sodium have been distributed over these sections according to the measurements of Wall et al. (1988). The initial aerosol mass concentration distribution is calculated assuming thermodynamic equilibrium between the gas and aerosol phases for the sulfate, nitrate, chloride, sodium, ammonium, water system (Pilinis and Seinfeld, 1987).

Effects of fogs on aerosol concentration

At the beginning of the simulation the air parcel contains 26.4 $\mu\text{g m}^{-3}$ dry aerosol particles consisting mainly of NH_4NO_3 (12.1 $\mu\text{g m}^{-3}$), Na_2SO_4 (5.9 $\mu\text{g m}^{-3}$) NaNO_3 (4.7 $\mu\text{g m}^{-3}$) and smaller quantities of NH_4Cl , NaCl and $(\text{NH}_4)_2\text{SO}_4$. As the relative humidity increases, the salts deliquesce, and as the liquid water increases, more and more material is transferred to the aerosol phase. When the relative humidity reaches 95%, the aerosol nitrate has increased from 12.8 to 13.5 $\mu\text{g m}^{-3}$, the aerosol ammonium from 3.6 to 5.5 $\mu\text{g m}^{-3}$ and the chloride from 2.3 to 5.8 $\mu\text{g m}^{-3}$. At this moment the aerosol phase contains around 450 $\mu\text{g m}^{-3}$ water. Twenty minutes later the humidity exceeds 100% and the fog episode begins. At $t = 23$ min the system supersaturation reaches its maximum value of 0.06% and starts decreasing slowly following the familiar pattern (Pandis et al., 1990).

Deposition and aqueous-phase chemistry have opposite effects on the aerosol mass, with the net effect of fogs on the total and individual species aerosol concentrations depending on several factors that will be discussed next. For the case

discussed here, the total concentrations of the major ionic species in the aerosol and aqueous-phase are presented in Figure 1, for the period for which the relative humidity exceeds 95%. The reader is reminded that in Figure 1 a particle is described as a droplet at a certain moment, when either the supersaturation of the environment exceeds its critical supersaturation or its diameter exceeds its critical diameter. Because of the finite number of size sections used in the simulation, a discontinuity is created in the calculation of the aerosol mass every time the particles in a section are activated or deactivated and are transformed from aerosol particles to liquid particles or vice versa. These discontinuities appear as jumps in Figure 1 and in several of the following figures. The fog episode causes an increase of the sulfate aerosol concentration from $4.1 \mu\text{g m}^{-3}$ to $8.4 \mu\text{g m}^{-3}$, but causes a decrease in the concentration of aerosol nitrate from $13.5 \mu\text{g m}^{-3}$ to $8.5 \mu\text{g m}^{-3}$, of aerosol ammonium from 5.5 to $3.9 \mu\text{g m}^{-3}$, and of aerosol chloride from 5.8 to $3.8 \mu\text{g m}^{-3}$.

The increase in the sulfate concentration is mainly a result of the aqueous-phase production of S(VI) through oxidation of S(IV) by H_2O_2 . During this fog episode $6.8 \mu\text{g m}^{-3}$ of sulfate are produced while $2.5 \mu\text{g m}^{-3}$ are deposited to the ground. This increase in sulfate is in qualitative agreement with observations of high aerosol sulfate concentrations in the Los Angeles basin after fog episodes by Cass and Shair (1984). The above conclusion should not necessarily be generalized, because fogs can easily lead to reduction of the aerosol sulfate. Even in the specific fog episode considered here if the fog duration is prolonged from 2 h to 10 h, one observes that as the available H_2O_2 is depleted and the fog pH becomes lower than 5, the sulfate production rate decreases significantly while the deposition rate continues at the same level for the full 10 h. Therefore after the fog dissipates, one actually finds a reduction of the sulfate levels below those present in the pre-fog aerosol. Such a scenario has been considered by Pandis and Seinfeld (1989b) who predicted

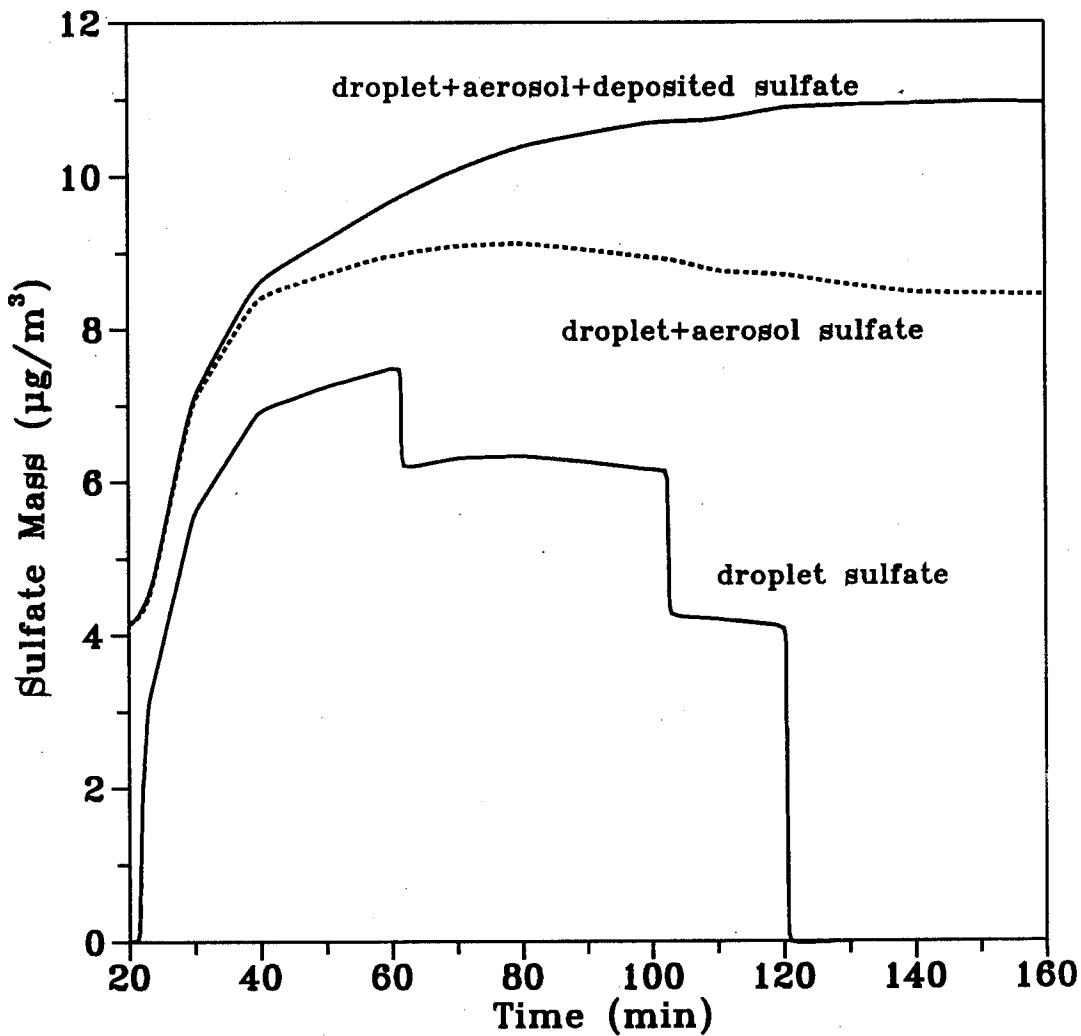


Figure 1a. Mass balances for the main ionic species for a simulated radiation fog episode.

(a) Sulfate

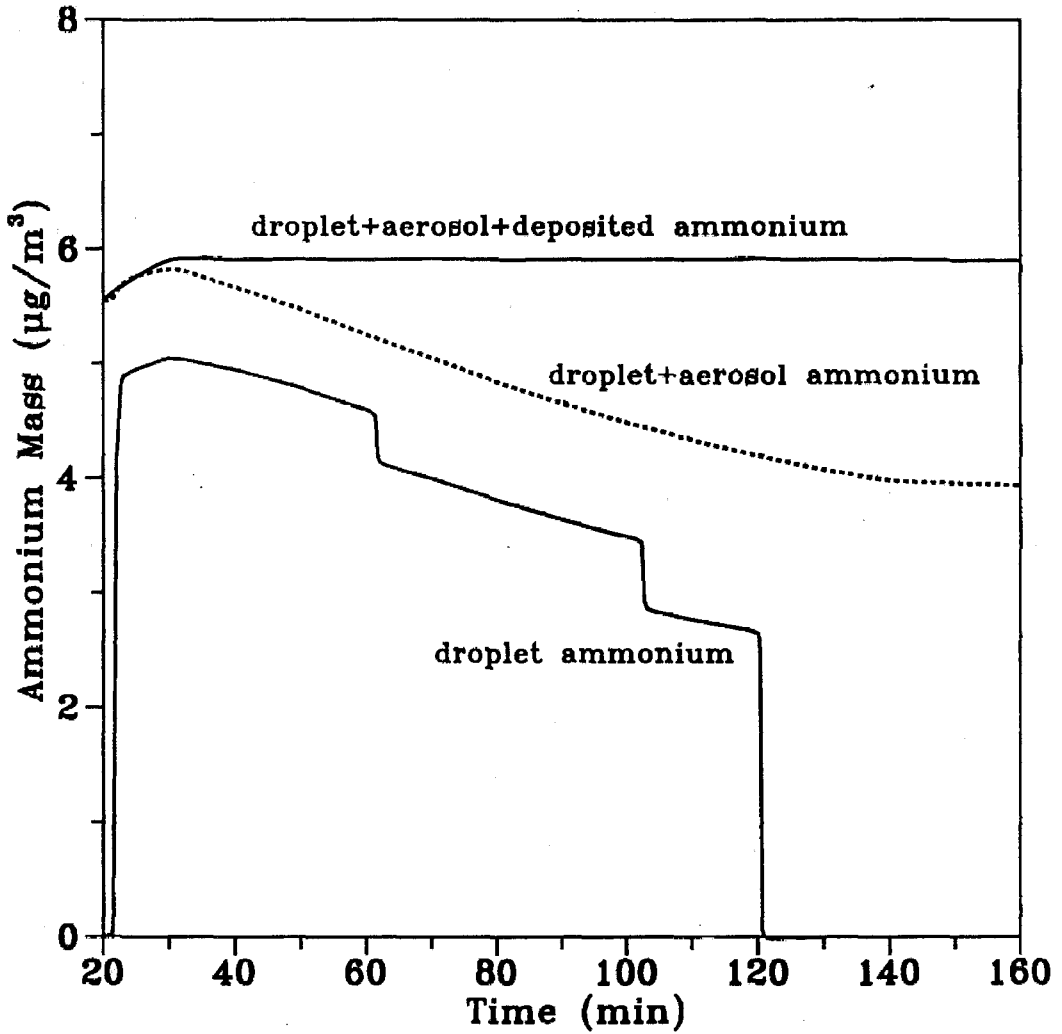


Figure 1b Mass balances for the main ionic species for a simulated radiation fog episode.

(b) Ammonium (the gaseous NH_3 is not included)

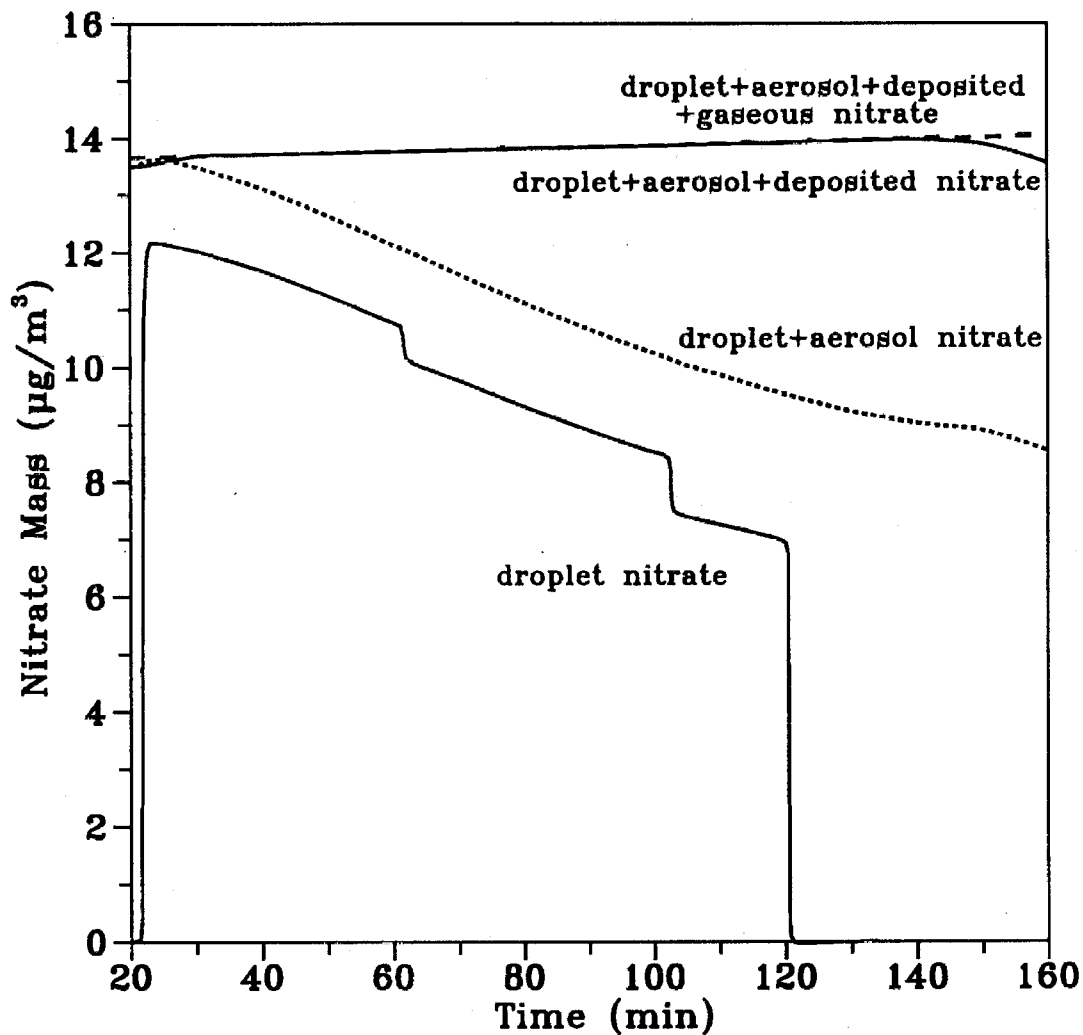


Figure 1c Mass balances for the main ionic species for a simulated radiation fog episode.
(c) Nitrate

reduction of the aerosol sulfate concentration for the radiation fog episode that they studied.

Previous sensitivity studies have showed that there are no major pathways for the aqueous-phase production of nitrate, and no chemical pathways for the production of chloride or ammonium (Pandis and Seinfeld, 1989a). Therefore the primary effect of fog is the reduction of the total concentrations of these species, gas plus aerosol, as a result of their removal to the ground. Existence of ammonia sources or gas-phase production of nitric acid can reverse these effects, but this is independent of the fog occurrence.

After the fog has dissipated and the relative humidity has decreased back to 50%, the total aerosol mass has decreased from the initial $26.4 \mu\text{g m}^{-3}$ to $19.7 \mu\text{g m}^{-3}$. It consists of $7.8 \mu\text{g m}^{-3}$ NH_4NO_3 , $7.8 \mu\text{g m}^{-3}$ Na_2SO_4 and $4.1 \mu\text{g m}^{-3}$ $(\text{NH}_4)_2\text{SO}_4$. The mass of sulfate has increased by 95%, but the masses of aerosol ammonium, nitrate, sodium, and chloride have been reduced by 24%, 53%, 30%, and 100%, respectively.

The decrease of the total aerosol mass can be explained by the fact that deposition dominates the chemical production of the main ionic species. On the other hand the decrease in the concentrations of all the aerosol species except sulfate is also due to the increase of the sulfate in the aerosol phase, sulfate that replaces volatile nitrate and chloride (Pilinis, 1989).

Effects of fogs on aerosol size/composition distribution

Fogs cause changes in the aerosol concentration levels and these changes are not uniform over the aerosol size distribution. During the smog-fog-smog cycle the large aerosol particles are transformed to large fog droplets and then back to aerosol particles. Because of the greater deposition of larger fog droplets, the depositional

losses of aerosol particles are mainly concentrated in the large size section of the aerosol distribution. On the other hand, most of the material that is produced by aqueous-phase reactions favors the droplet size that has access to most of the liquid water (Pandis and Seinfeld, 1990). The aerosol particles on which most of the liquid water condenses are determined by the aerosol distribution and by the cooling rate of the air parcel. Rapid cooling favors the small particles while slow cooling favors the larger, transport limited particles (Pandis and Seinfeld, 1990).

In the case examined here most of the fog liquid water content is predicted to have condensed on the larger particles (Figure 2); therefore, both the positive and negative effects of the fog are concentrated in this size range. The bimodal distribution of the droplets at $t = 40$ min and $t = 120$ min is due to the fact that the initial aerosol size spectrum is also bimodal. The dry aerosol distributions before and after the fog are presented in Figure 3. Most of the losses in mass are concentrated in the larger particle range where the losses in mass of the $>0.9 \mu\text{m}$ particles in diameter are around 50%. At the same time most of the sulfate that is produced during the fog is also found in the larger particles. The sulfate content of the particles larger than $0.5 \mu\text{m}$ increases by 130%, while for the particles smaller than $0.5 \mu\text{m}$ it increases only by 45%.

Aerosol Scavenging Efficiency

The aerosol scavenging efficiency of the fog determines the extent to which the fog droplet concentrations are influenced by the preexisting aerosol. This scavenging efficiency depends on the maximum supersaturation reached in the fog and on the preexisting aerosol size composition distribution.

Ten Brink et al. (1987) observed nearly complete scavenging of aerosol sulfate in clouds. Munger et al. (1990) reported aerosol scavenging ratios always lower

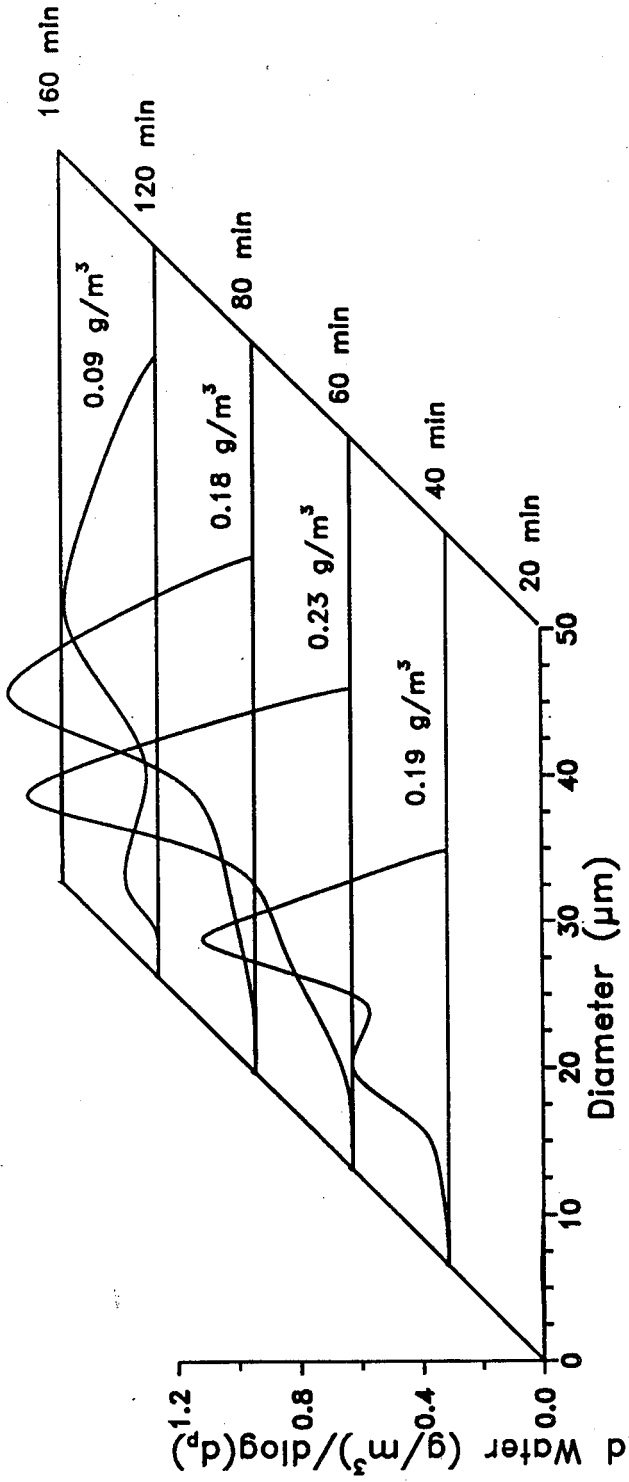


Figure 2 Evolution of the smoothed aqueous droplet mass distribution during the fog episode.

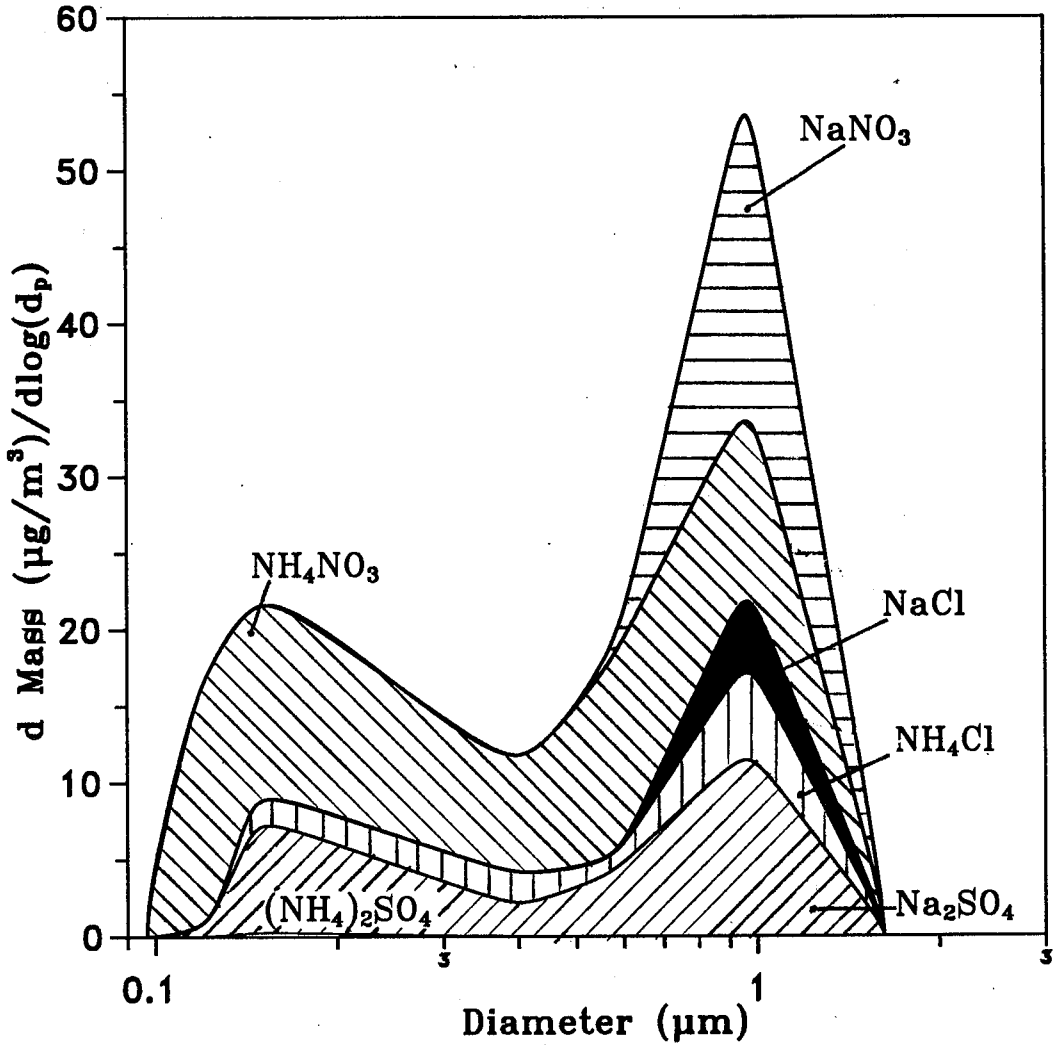


Figure 3a Comparison of the smoothed aerosol size/composition distributions before and after the fog episode.

(a) At 50% relative humidity before the fog episode.

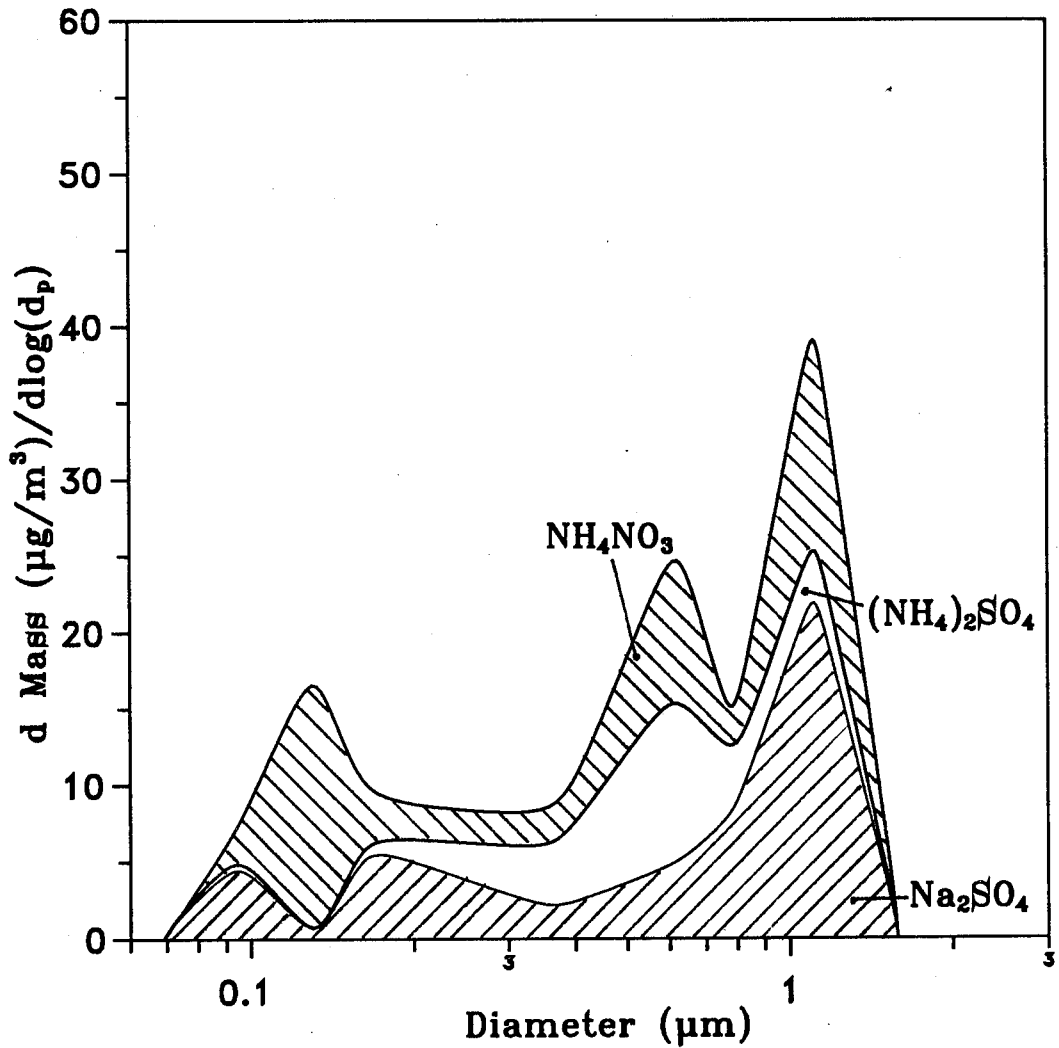


Figure 3b Comparison of the smoothed aerosol size/composition distributions before and after the fog episode.

(b) At 50% relative humidity after the fog episode.

than 100% and depending on the method used ranging from 10% to 90%. In a theoretical study of wet removal of atmospheric pollutants Jensen and Charlson (1984) calculated that for an average urban aerosol population nucleation scavenging efficiency is close to unity for convective clouds, but for stratiform clouds it decreases rapidly as the updraft velocity is lowered. Flossmann et al. (1985, 1987) reported calculated aerosol scavenging efficiencies equal to or larger than 90% in typical cloud environments.

The scavenging efficiencies for the fog episode under consideration are depicted in Figure 1. At $t = 20$ min the relative humidity reaches 100%, and at $t = 23$ min a maximum supersaturation of 0.06% is reached. Even at this relatively low supersaturation, most of the aerosol mass gets activated and is dissolved in the fog droplets, namely 70% of the sulfate, 80% of the nitrate and 85% of the ammonium. At the moment of maximum liquid water content ($t = 60$ min), the interstitial aerosol represents 16% of the sulfate, 11% of the nitrate and 12% of the ammonium. These interstitial aerosol concentrations will be even lower if one considers the coagulation of the aerosol particles with the fog droplets, a process that has been neglected in this study.

During the fog dissipation stage, the small droplets evaporate first with the larger droplets following, and the concentration of interstitial aerosol increases significantly. For example, at $t = 120$ min the interstitial aerosol represents 53% of the total sulfate concentration, 27% of the total nitrate concentration and 37% of the total ammonium, with these percentages reaching 100% five minutes later.

The above results can be used to improve the assumptions used in fog models like the one developed by Pandis and Seinfeld (1989b). In that model, explicit droplet microphysics is not considered and the initial fogwater concentrations are calculated by assuming that all the preexisting aerosol is scavenged by the fog

droplets. The evaluation of that model showed overprediction of the sulfate and ammonium concentrations for the first few hours of the fog episode. When no additional information is available it seems preferable to assume in such models an 80% scavenging efficiency for the main ionic species instead of 100%, at least for polluted urban conditions.

Sampling a Polydisperse Fog Droplet Population

Pandis et al. (1990) suggested that significant solute concentration differences can occur in aqueous droplets inside a cloud or a fog. The same qualitative behavior is observed (Figure 4) in this study even if a different initial aerosol size distribution has been used compared to that used by Pandis et al. (1990). At the moment of maximum liquid water content ($t = 60$ min), the total solute concentration in the 25 μm diameter droplets is 2.5 times larger than that in the 15 μm droplets.

If one samples this fog droplet population with one of the routinely used fog samplers (Jacob et al., 1984, 1985; Waldman, 1986), one collects most particles larger than the instrument cutoff size, mixes them and then reports an average concentration. If the droplet concentrations differ considerably, then the measured concentration may not be completely representative of the actual fogwater concentration. To investigate this we assume that three fog samplers were used to sample the fog episode studied here. Each sampler was able to sample all the droplets larger than its nominal cutoff size, 15 μm diameter for the first, 5 μm for the second, and the third sampler had zero cutoff and therefore was able to sample every particle. The concentrations measured by these three idealized samplers were divided by the concentration of the larger droplet section to give the concentration ratio.

We have chosen the concentration of the larger droplet section as the fogwater reference composition because most of the fog liquid water content has condensed on

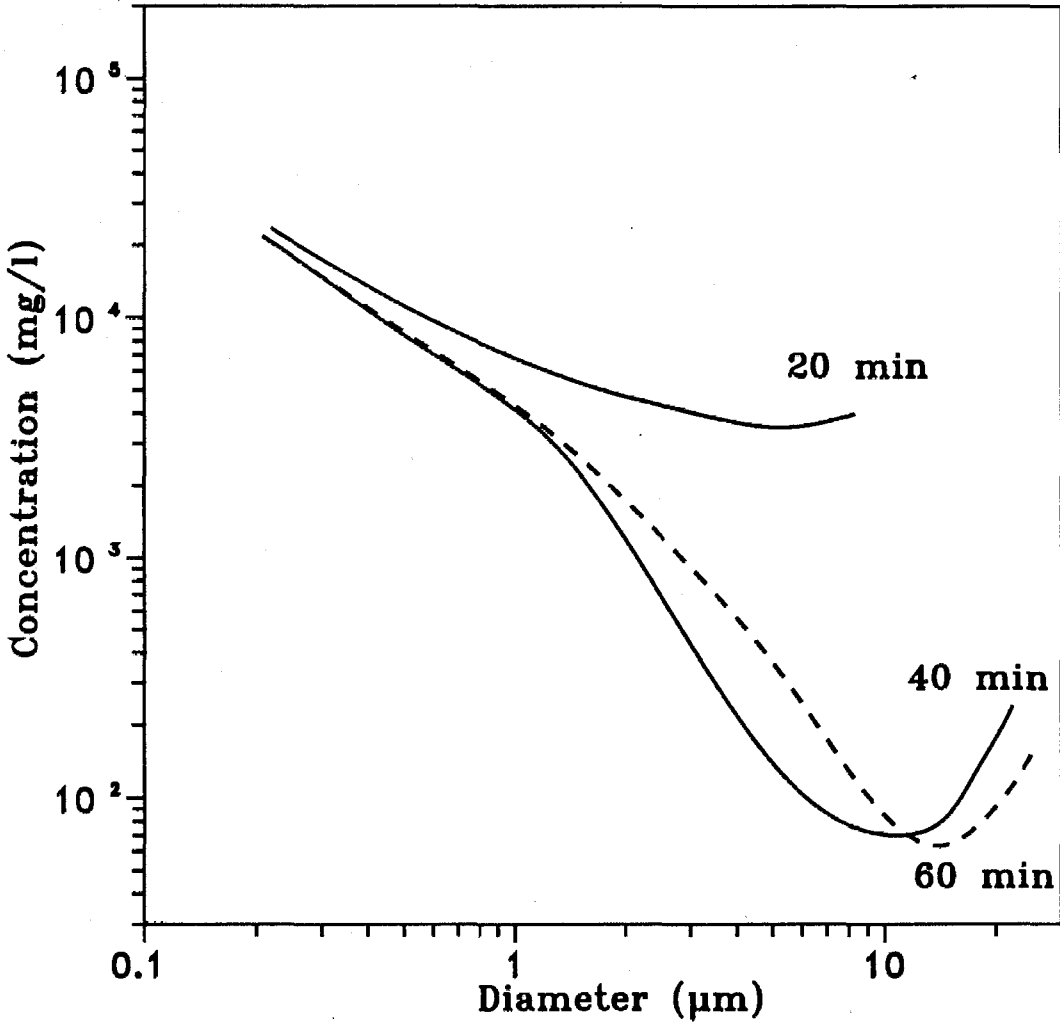


Figure 4a. Total solute concentration for particles (aerosol and droplets) of different sizes .

(a) During the fog growth period.

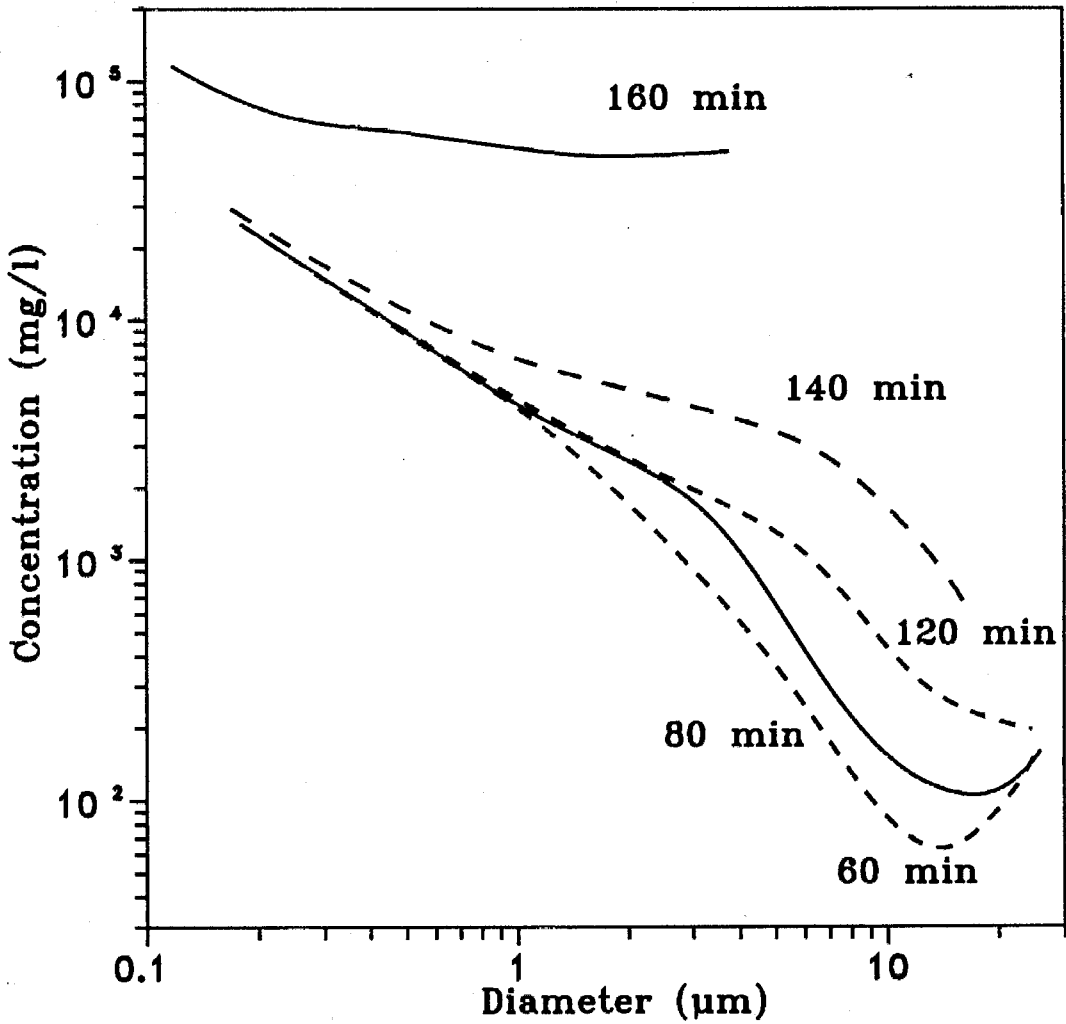


Figure 4b. Total solute concentration for particles (aerosol and droplets) of different sizes
(b) During the fog dissipation period

these droplets (55% at the fog peak) and because these droplets are responsible for most of the wet deposition. This choice is not unique, but for any choice of the most representative concentration, the concentration ratio calculations are indicative of the possible complications in fog sampling. The concentration ratios for sulfate and ammonium are shown in Figure 5. The discontinuities in the curves for the 5 and 15 μm samplers are also due to the finite number of sections used in this model application.

For this specific fog episode the 15 μm cutoff sampler collects droplets from the sixth and seventh sections and the sulfate concentration measured is always close to the concentration of the largest droplets. This sampler collects droplets only between $t = 25$ and $t = 142$ min and the concentration ratios cannot be defined outside this period. The largest deviation appears when the droplets of the sixth section start evaporating and then the measured concentration is 20% higher than the representative sulfate concentration. Use of a finer resolution drop size spectrum would make this difference more pronounced. The sampler with the 5 μm cutoff in the growth period of the fog collects droplets from the 4th, 5th, 6th and 7th droplet sections and the measured average concentration is lower than the representative concentration as the smaller droplets are less concentrated than the larger ones (Figure 4a). During the dissipation stage the smaller droplets evaporate first and their concentration becomes higher than that of the larger droplets. The sampler measures concentrations that are as much as 80% higher than the representative sulfate concentration. The total sampler collects all droplets and particles measuring average sulfate concentrations as much as a factor of 2.8 higher than the representative concentration.

The concentration ratio for ammonium (Figure 5b) and the other major ionic species exhibits the same qualitative behavior as that for sulfate but with signifi-

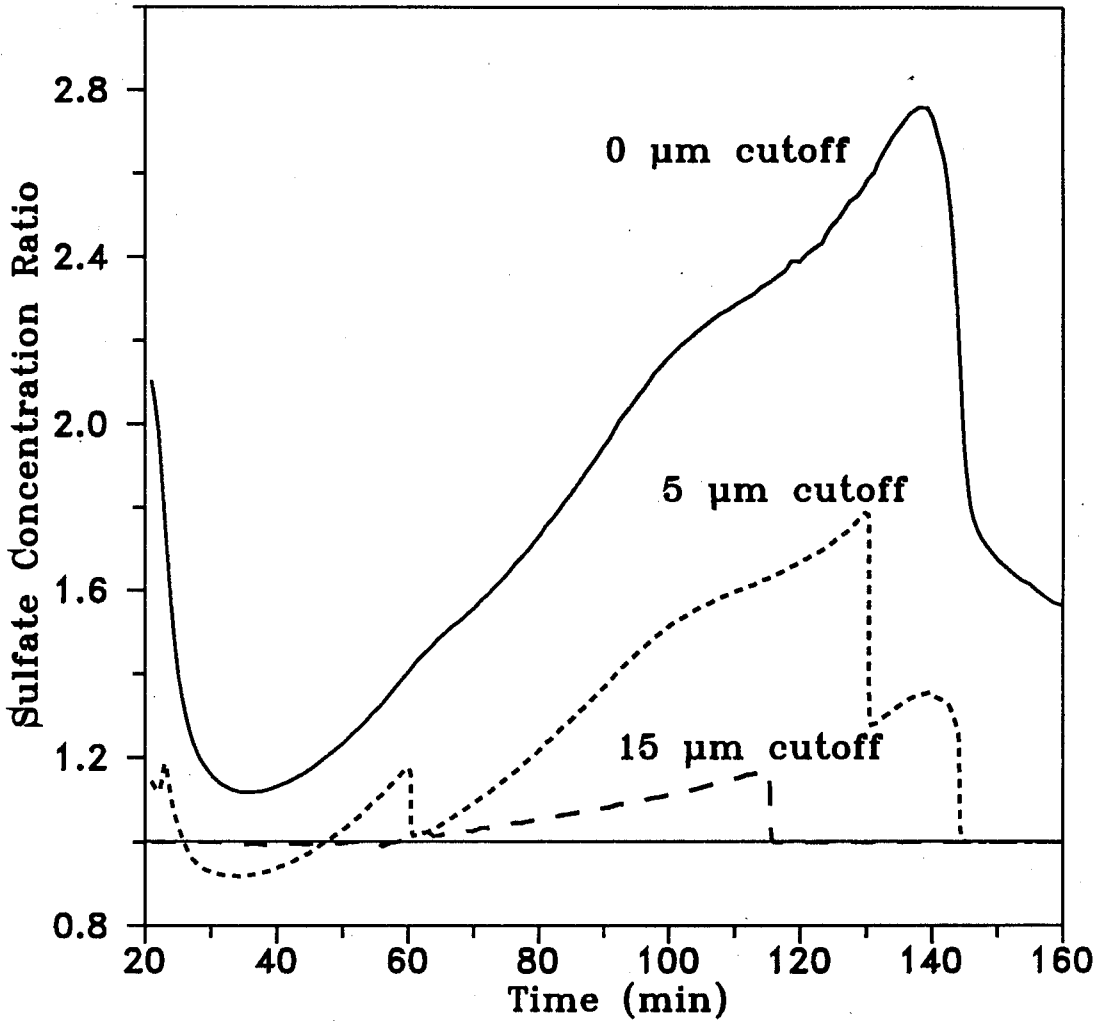


Figure 5a Concentration ratios (concentration measured by the sampler over the concentration of the larger droplet section) for three idealized fog samplers for (a) Sulfate.

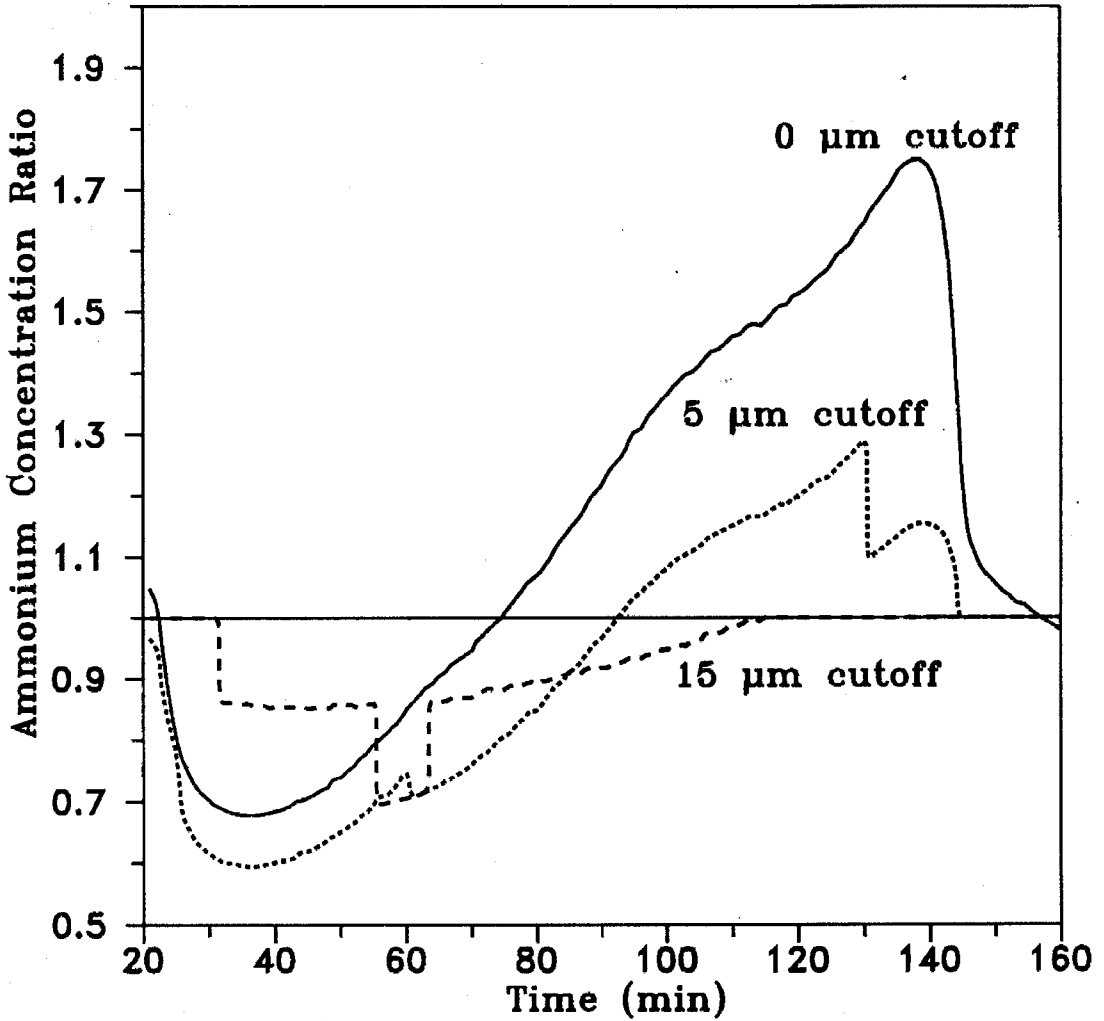


Figure 5b Concentration ratios (concentration measured by the sampler over the concentration of the larger droplet section) for three idealized fog samplers for
(b) Ammonium.

cantly lower values. The measured concentrations during the growth period can be as much as 40% lower than the representative ammonium concentration, and during the dissipation period as much as 80% higher. The lower values for the ammonium deposition ratio compared to the sulfate one are mainly due to the distribution of these species in the aerosol phase just before the onset of the fog. There is relatively more sulfate in the smaller droplets than ammonium, resulting in relatively low concentrations of sulfate in the larger droplets. For example at $t = 30$ min the sulfate concentration is $560 \mu\text{M}$ for the $18.5 \mu\text{m}$ droplets and $450 \mu\text{M}$ for the $7.3 \mu\text{m}$ droplets (a ratio of 1.2). At the same time the corresponding ammonium concentrations are $4060 \mu\text{M}$ and $890 \mu\text{M}$ (a ratio of 4.6). Therefore in the growth period the representative ammonium concentration is much higher than the concentration of the other droplets, resulting in concentration ratio values much lower than unity.

Generalization of the above results depends on the aerosol size/composition distribution before the fog episode as well as on the rates of temperature change in the fog. One conclusion is that sampling and mixing of fog droplets with different sizes can result in measured concentrations that are not completely representative of the actual fog composition. Furthermore, the measured concentrations can be very sensitive to the collection characteristics of the fog sampler. The choice at each time of a representative aqueous-phase concentration is a very difficult problem and should depend on the goals of the study. If one is concerned about fogwater composition, probably one should choose as the most representative the concentration of the droplets that carry most of the liquid water. If one is concerned about acid deposition, one should concentrate on the droplets that are responsible for most of the deposited material, and these are usually the larger droplets. If the representative concentration is that in the small droplets, the measurement will usually be higher than the actual value during the fog growth and lower during the fog

dissipation. The opposite is true if the representative concentration is that of the larger droplets.

Fogs and Deposition

The depositional flux of species i , F_d^i (g m^{-2}) is usually expressed as

$$F_d^i = v_d^i c^i \quad (4)$$

where v_d^i (m s^{-1}) is the deposition velocity of species i and c^i (g m^{-3}) its ambient concentration. If the species i exists in all three phases (gas, aerosol and aqueous), then one can define three deposition velocities and get

$$F_d^i = v_{d,gas}^i c_g^i + v_{d,aer}^i c_{aer}^i + v_{d,aq}^i c_{aq}^i \quad (5)$$

or define one deposition velocity for the condensed phases, $v_{d,cond}^i$, and express the depositional flux as

$$F_d^i = v_{d,gas}^i c_g^i + v_{d,cond}^i (c_{aer}^i + c_{aq}^i). \quad (6)$$

The size of the interstitial aerosol particles in a typical radiation fog is usually in the 0.1 to 1 μm diameter size range. For these particles neither Brownian diffusion, nor gravitational settling, nor inertial impaction are efficient removal mechanisms (Seinfeld, 1986) and as the mass carried by these particles is small, one can to a first order approximation neglect the aerosol deposition flux inside a fog.

After this approximation the expression (5) becomes quite simple but has the major disadvantage that the value of the deposition velocity depends on what one considers as aqueous phase. The application of the expression (6) requires measurement of the total concentration of species i in the condensed phases, but fortunately

is independent of what one defines as aerosol or droplet phase. The effect of the definition of deposition velocity for sulfate is presented in Figure 6. Depending on the droplet size fraction sampled, quite a range of deposition velocities is calculated. The higher the cutoff size, the higher the calculated deposition velocity. These differences increase during the early and late stages of fog life. For example at $t = 25$, $t = 65$, and $t = 145$ min the deposition velocity calculated with a cutoff size of $15 \mu\text{m}$ is, respectively, 170%, 30%, and 140% larger than the velocity calculated using a cutoff size of $5 \mu\text{m}$. These results suggest that the best way of calculating deposition velocities is by using the sum of the species concentrations in the aerosol and droplet phases. If one uses the concentration in droplets larger than a certain size, then the deposition velocities can be very sensitive to the choice of this cutoff size.

Calculation of Liquid Water Deposition in Fog Models

In fog models where there is no explicit treatment of the microphysics, the gravitational flux of liquid water G ($\text{g m}^{-2} \text{s}^{-1}$) is expressed as a function of the liquid water content, w (g m^{-3}). Brown and Roach (1976) used for a 10°C temperature

$$G = 0.078w^2 \quad (7)$$

while Forkel et al. (1984) proposed the expression

$$G = 0.032w^{1.6} \quad (8)$$

Pandis and Seinfeld (1989b) used

$$G = 0.120w^2 \quad (9)$$

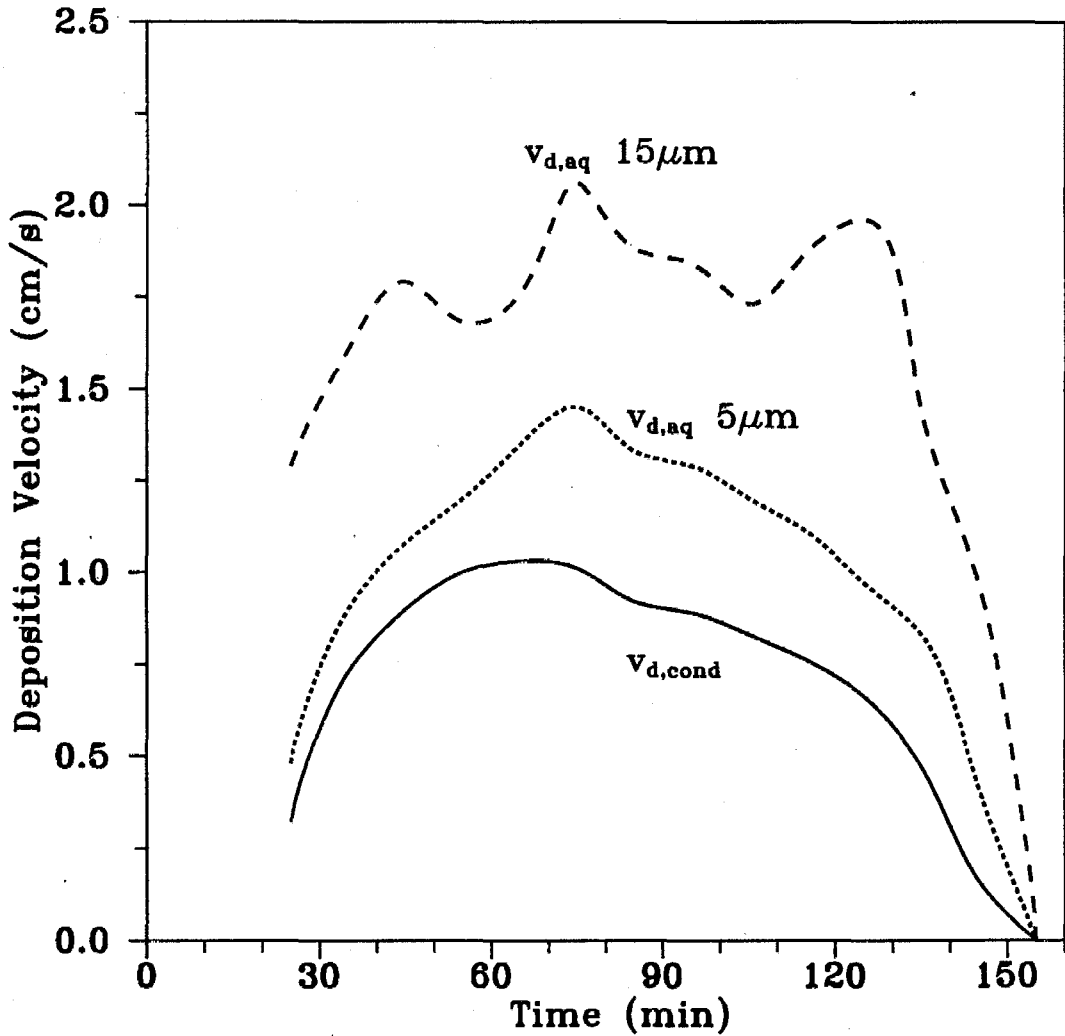


Figure 6 Calculated values of the sulfate deposition velocity for alternative definitions

Deposition velocity of the condensed phase $v_{d,cond}$

Deposition velocity of the aqueous-phase v_{aq} . Sampling cutoff $5\mu m$.

Deposition velocity of the aqueous-phase v_{aq} . Sampling cutoff $15\mu m$.

and found that their model overpredicted the depositional fluxes of the major ionic species for the high liquid water values and underpredicted these fluxes during the fog dissipation stage.

The water deposition rates predicted by the model here have been plotted versus the fog liquid water content in Figure 7. These data suggest something that has not been considered in the previous studies. Different deposition rates correspond to the same liquid water content value depending on whether the fog is in a growth or dissipation period. This behavior is due to the fact that the smaller droplets can easily follow the changes of the relative humidity, so that during the fog growth period small droplets have access to considerable amounts of the liquid water, resulting in relatively slower deposition rates. On the contrary during fog evaporation, the small droplets are the first to evaporate and most of the liquid water is left on the larger droplets resulting in faster deposition.

Figure 7 suggests that two different expressions should be used for the growth and the dissipation period. The modeling results for this specific episode suggest for the growth period

$$G = 0.027w^{1.67} \tag{10}$$

and for the dissipation period

$$G = 0.018w^{1.08} \tag{11}$$

For the period of almost constant liquid water content, the deposition rate appears to increase from the value suggested by equation 10 to the value corresponding to equation 11. Comparison of the expressions used in previous studies with the present results suggests that, at least for this fog episode, expressions 7

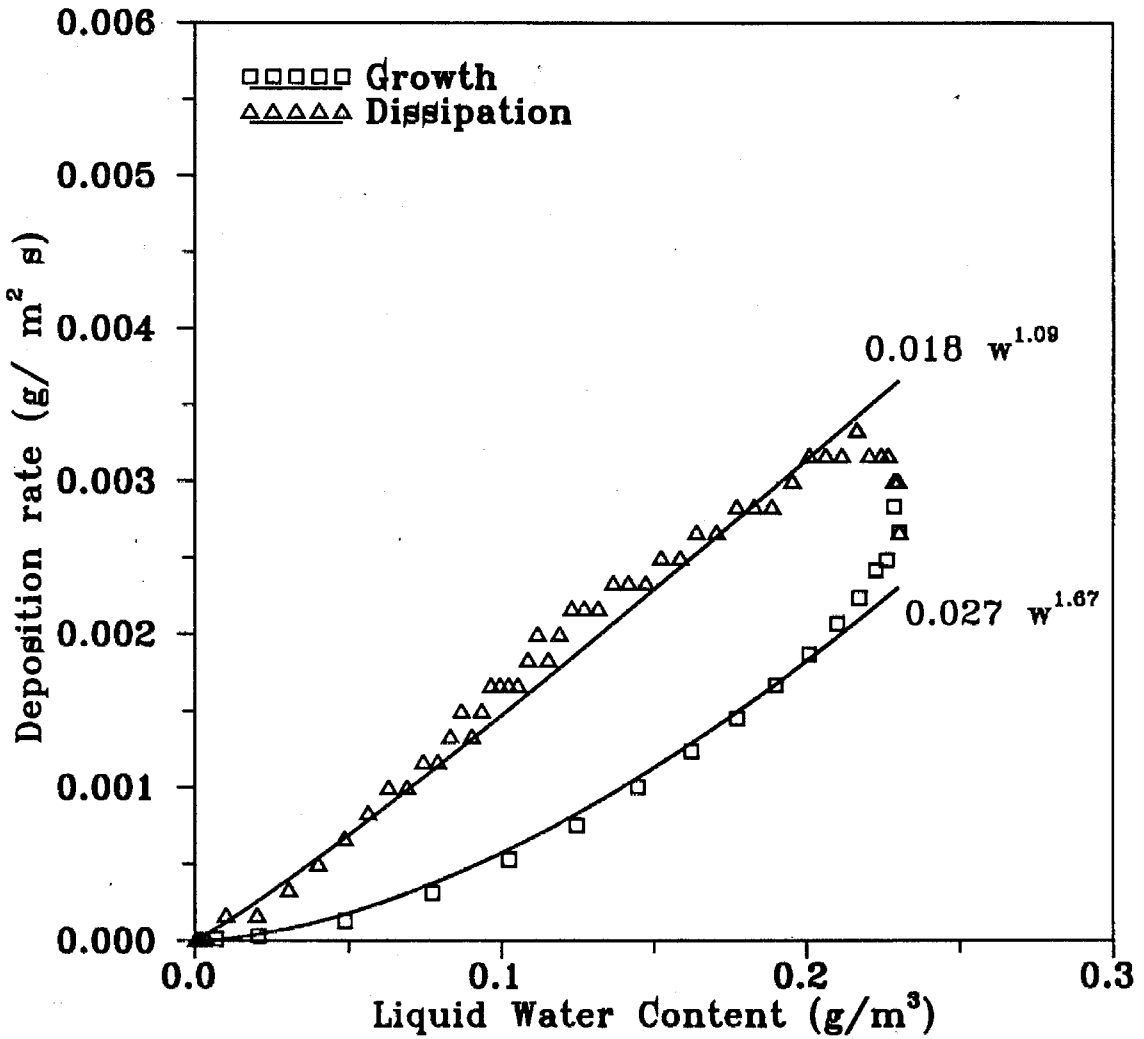


Figure 7 Water deposition rates versus fog liquid water content.

to 9 overpredict deposition for the growth and the constant liquid water period and underpredict deposition for the dissipation period. Equations 10 and 11 were derived using an urban radiation fog episode using a relatively crude resolution of the particle size distribution; therefore, their application, as well as the application of equations 7 to 9, to other fog episodes should be done with caution.

Deposition Velocity of Major Ionic Species

Field measurements have indicated that fog deposition velocities of different ionic species can be quite different (Waldman, 1986). One of the possible explanations for this phenomenon is the manner in which solute mass is distributed within the fog droplet spectrum. To investigate this, we have calculated the condensed phase deposition velocities for the major ionic species and water (Figure 8). The deposition velocities of all species exhibit the same qualitative behavior, but have in certain periods significantly different absolute values.

To explain these differences one can define the species average diameter \bar{D}_i for a sectional particle distribution as

$$\bar{D}_i = \left(\frac{\sum_j m_{ij} d_j^2}{\sum_j m_{ij}} \right)^{\frac{1}{2}} \quad (12)$$

where m_{ij} is the mass concentration per volume of air of species i in the j particle size section and d_j is the diameter of this section. If in a homogeneous fog the only deposition mechanism is fog droplet gravitational settling, and all particles have the same density, one can show that the depositional velocity of species i is given by

$$v_i = C \bar{D}_i^2 \quad (13)$$

where C is a constant depending on the particle density and temperature. Because all these variables are practically constant during the fog episode, C remains con-

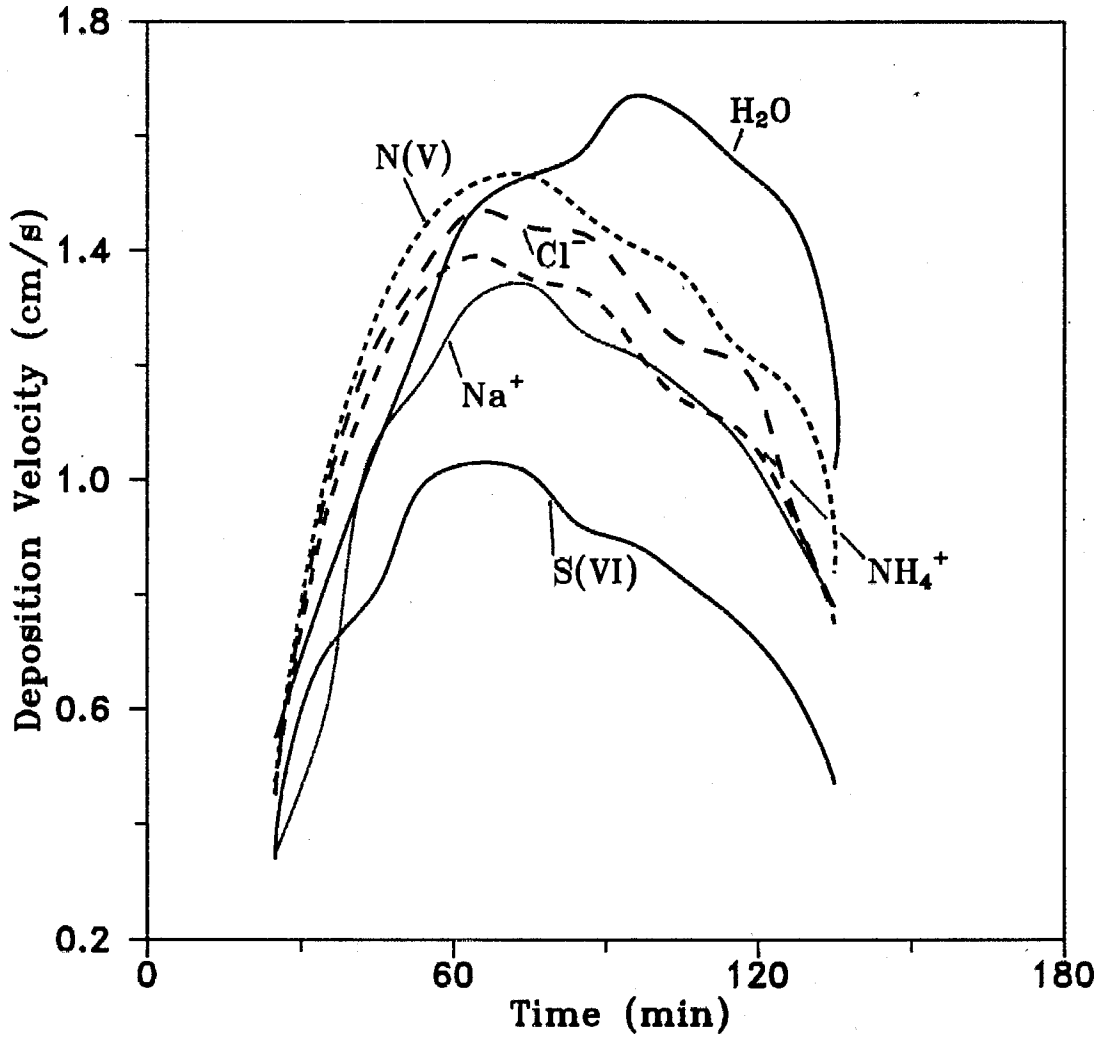


Figure 8 Condensed phase deposition velocities for the major species in fogwater.

$$(\text{Deposition Velocity}) = (\text{Deposition Flux}) / [(\text{aerosol concentration}) + (\text{droplet concentration})]$$

stant throughout the simulation and the deposition velocities of all species can be represented by the same curve (Figure 9). Therefore, the difference of the species deposition velocities (Figure 8) can be quantitatively explained by calculating the average diameter of each species as a function of time.

At the beginning of the fog episode a considerable fraction of the aerosol sulfate exists on the small particles resulting in a small initial sulfate average diameter and in a relatively small deposition velocity. Even if most of the sulfate production takes place in the large droplets, sulfate has the smallest average diameter among the major ionic species and therefore the smallest deposition velocity. On the contrary, in this fog episode, most of the nitrate is found in the large particles and the maximum deposition velocity of nitrate is almost 50% larger than the corresponding sulfate deposition velocity. The water deposition velocity reaches its maximum thirty minutes later than the major ionic species, during the fog dissipation stage. Even if the total fog liquid water decreases, the losses are located in the small droplet size range and the average water diameter increases for the first thirty minutes of the fog dissipation stage.

Conclusions

A model describing gas-phase chemistry, aerosol dynamics and thermodynamics, aqueous-phase chemistry, droplet microphysics, and wet removal processes has been used to study the smog-fog-smog cycle. Both aerosol and droplet size/composition distributions are discretized in size sections and their changes are followed during the simulation.

The fog episode under consideration increases considerably the sulfate content of the aerosol particles due to the aqueous-phase oxidation of sulfur dioxide. This increase should be expected in most urban fog episodes where a high potential for

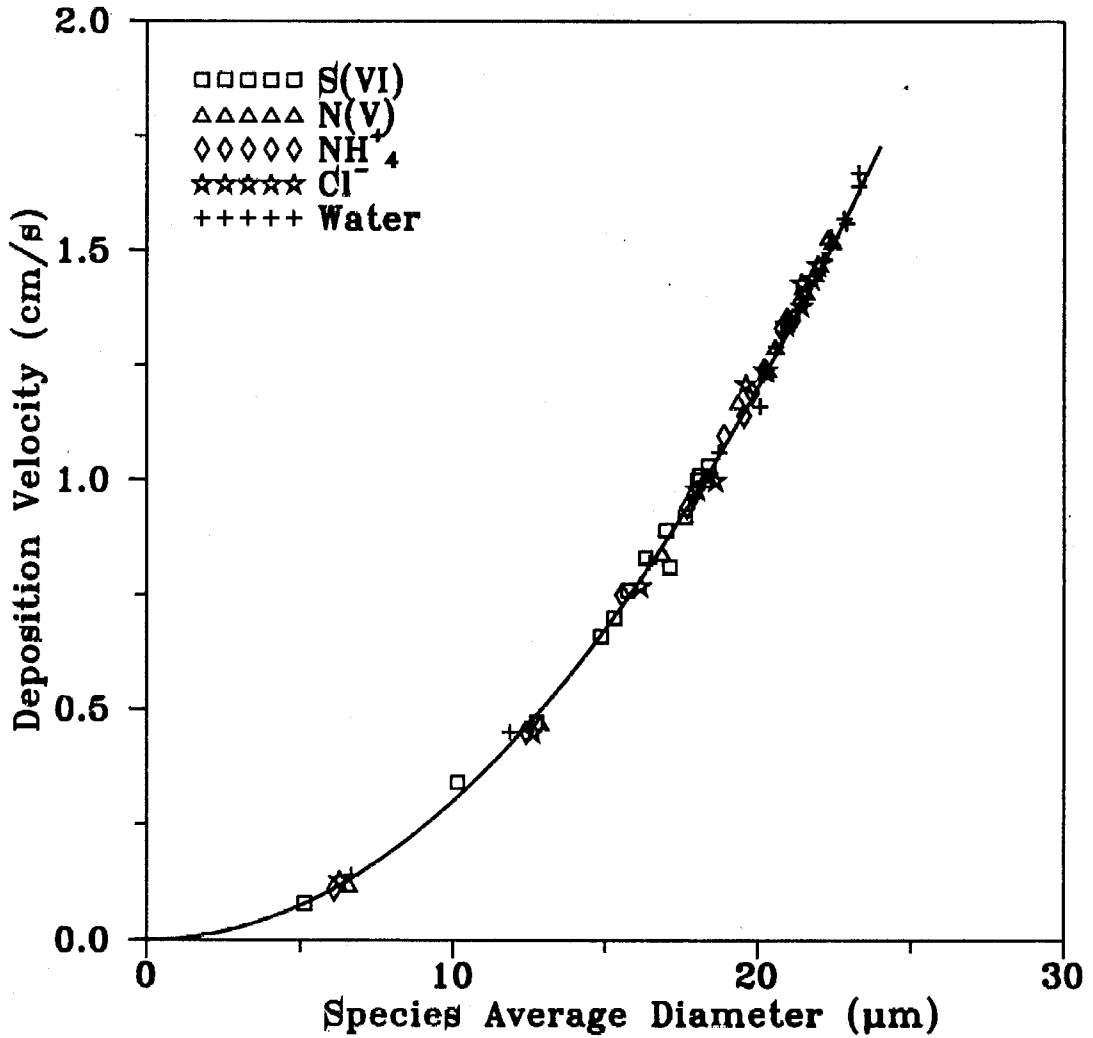


Figure 9 Calculated deposition velocity of selected species in fog as a function of their average diameter.

S(IV) exists. For urban fog episodes of long duration or fogs in rural environments where the sulfate production slows down after the first few hours due either to H_2O_2 depletion or pH decrease, deposition can dominate the chemical processes and sulfate may even decrease. The primary effect of fog is the reduction of the total concentrations, aerosol and gas phase, of ammonia, nitric, and hydrochloric acid due to their transfer to the aqueous phase and subsequent enhanced deposition. Even if aerosol sulfate increases, the enhancement in deposition of the inorganic aerosol species causes a 25% decrease in the total post-fog dry aerosol mass.

The fog effects on the aerosol are not uniform over the size spectrum. The sulfate produced during the fog episodes favors the aerosol particles that have access to most of the liquid water, and these are usually the large particles. In the case considered in this study, the sulfate content of the dry particles larger than $0.5 \mu m$ in diameter increases by 130% while for the particles smaller than $0.5 \mu m$ it increases only by 45%. Most of the losses in mass for the other major inorganic aerosol species are concentrated in the larger particle range with losses around 50% for the $> 0.9 \mu m$ dry particles.

The simulation indicates that aerosol scavenging ratios of around 80% should be representative for urban radiation fogs. The aerosol scavenging ratio for sulfate should be less than this average value, 70% under the conditions considered in this study, due to the preference of sulfate for the smaller particles. On the contrary, the ratio for nitrate should be higher than the average value.

Sampling and subsequent mixing of fog droplets and aerosol particles with different sizes may result in measured concentrations that are not fully representative of the fogwater chemical composition and can introduce errors in the reported values of the ionic species deposition velocities. The sampling bias will depend on the initial aerosol size/composition distribution, on the rate of temperature change

and on the cutoff size of the sampling device. The use of a sampling device with a smaller cutoff size does not guarantee a better measurement in all cases.

In fog models where the liquid water depositional flux is expressed as a function of the fog liquid water content because of the difference in liquid water distributions during the growth and dissipation stages, different expressions should be used for these two stages.

The difference in deposition velocities of the major ionic species during fog episodes can be explained by their different distributions over the droplet spectrum. The existence of a significant amount of sulfate in small particles before the fog starts results in a relatively small sulfate deposition velocity during the fog episode.

Acknowledgements

This work was supported by State of California Air Resources Board Agreement A932-079.

References

- Brown, R., and W. T. Roach, The physics of radiation fog, II, A numerical study, *Q. J. R. Meteorol. Soc.*, 102, 335-354, 1976.
- Carter, W. P. L., F. W. Lurmann, R. Atkinson, and A. C. Lloyd, Development and testing of a surrogate species chemical reaction mechanism. EPA-600/3-86-031, 1986.
- Carter, W. P. L., and R. Atkinson, Development and implementation of an up-to-date photochemical mechanism for use in airshed modeling, Summary final report to California Air Resources Board, 1988.
- Cass, G. R., and F. H. Shair, Sulfate accumulation in a sea breeze/land breeze circulation system, *J. Geophys. Res.*, 89, 1429-1438, 1974.

- Dollard, G. J., and M. H. Unsworth, Field measurements of turbulent fluxes of wind-driven fog drops to a grass surface, *Atmos. Environ.*, 17, 775-780, 1983.
- Flossmann, A. I., W. D. Hall, and H. R. Pruppacher, A theoretical study of the wet removal of atmospheric pollutants. Part I: The redistribution of aerosol particles captured through nucleation and impaction scavenging by growing cloud drops, *J. Atmos. Sci.*, 42, 583-606, 1985.
- Flossmann, A. I., H. R. Pruppacher, and J. H. Topalian, A theoretical study of the wet removal of atmospheric pollutants. Part II: The uptake and redistribution of $(\text{NH}_4)_2\text{SO}_4$ particles and SO_2 gas simultaneously scavenged by growing cloud drops, *J. Atmos. Sci.*, 44, 2912-2923, 1987.
- Forkel, R., W.-G. Panhans, R. Welch, and W. Zdunkowski, A one-dimensional numerical study to simulate the influence of soil moisture, pollution and vertical exchange on the evolution of radiation fog, *Beitr. Phys. Atmos.*, 60, 340-360, 1984.
- Hänel, G., The role of aerosol properties during the condensational stage of cloud: A reinvestigation of numerics and microphysics, *Beitr. Phys. Atmosph.*, 60, 321-339, 1987.
- Hegg, D. A., and T. V. Larson, The effects of microphysical parametrization on model predictions of sulfate production in clouds, *Tellus*, in press, 1990.
- Jacob, D. J., R.-F. T. Wang, and R. C. Flagan, Fogwater collector design and characterization, *Environ. Sci. Technol.*, 18, 827-833, 1984.
- Jacob, D. J., J. M. Waldman, M. Haghi, M. R. Hoffmann, and R. C. Flagan, Instrument to collect fogwater for chemical analysis, *Rev. Sci. Inst.*, 56, 1291-1293, 1985.
- Jensen, J. B., and R. J. Charlson, On the efficiency of nucleation scavenging, *Tellus*, 36B, 367-375, 1984.

- Munger, J. W., D. J. Jacob, J. M. Waldman, and M. R. Hoffmann, Fogwater chemistry in an urban atmosphere, *J. Geophys. Res.*, 88, 5109-5121, 1983.
- Munger, J. W., J. Collett, B. Daube, and M. R. Hoffmann, Fogwater chemistry at Riverside, California, *Atmos. Environ.*, in press, 1990.
- Pandis, S. N., and J. H. Seinfeld, Sensitivity analysis of a chemical mechanism for aqueous-phase atmospheric chemistry, *J. Geophys. Res.*, 94, 1105-1126, 1989a.
- Pandis, S. N., and J. H. Seinfeld, Mathematical modeling of acid deposition due to radiation fog, *J. Geophys. Res.*, 94, 12911-12923, 1989b.
- Pandis, S. N., J. H. Seinfeld, and C. Pilinis, Chemical composition differences in fog and cloud droplets of different sizes, *Atmos. Environ.*, in press, 1990.
- Pilinis, C., and J. H. Seinfeld, Continued development of a general equilibrium model for inorganic multicomponent atmospheric aerosols, *Atmos. Environ.*, 21, 2453-2466, 1987.
- Pilinis, C., and J. H. Seinfeld, Development and evaluation of an Eulerian photochemical gas-aerosol model, *Atmos. Environ.*, 22, 1985-2001, 1988.
- Pilinis, C., Numerical simulation of visibility degradation due to particulate matter: Model development and evaluation, *J. Geophys. Res.*, 9937-9946, 1989.
- Pruppacher, H. R., and J. D. Klett, *Microphysics of clouds and precipitation*, Reidel Pub. Co., The Netherlands, 1980.
- Seinfeld, J. H., *Atmospheric Chemistry and Physics of Air Pollution*, John Wiley, New York, 1986.
- Ten Brink, H. M., S. E. Schwartz and Daum, P. H., Efficient scavenging of aerosol sulfate by liquid water clouds, *Atmos. Environ.*, 21, 9, 2035-2052, 1987.
- Waldman, J. M., Depositional aspects of pollutant behavior in fog, *Ph.D. thesis*, California Institute of Technology, Pasadena, CA, 1986.
- Wall S. M., W. John, and J. L. Ondo, Measurement of aerosol size distributions for

nitrate and major ionic species, *Atmos. Environ.*, 22, 1649-1656, 1988.

Warren, D. R., and J. H. Seinfeld, Simulation of aerosol size-distribution evolution in systems with simultaneous nucleation, condensation and coagulation, *Aerosol Sci. Technol.*, 4, 31-43, 1985.

Wilkins, E. T., Air pollution aspects of the London fog of December 1952, *J. R. Meteorol. Soc.*, 80, 267-278, 1954.

CHAPTER 7

**AEROSOL FORMATION IN THE PHOTOOXIDATION OF
ISOPRENE AND β -PINENE**

(Accepted for publication in *Atmospheric Environment*, July 1990)

**Aerosol Formation in the Photooxidation of
Isoprene and β -pinene.**

Spyros N. Pandis, Suzanne E. Paulson, John H. Seinfeld and Richard C. Flagan

Department of Chemical Engineering

California Institute of Technology, Pasadena, CA 91125

Abstract

Isoprene and β -pinene, at concentration levels ranging from a few ppb to a few ppm were reacted photochemically with NO_x in the Caltech outdoor smog chamber facility. Aerosol formation from the isoprene photooxidation is found to be negligible even under extreme ambient conditions due to the relatively high vapor pressure of its condensable products. Aerosol carbon yield from the β -pinene photooxidation is as high as 8% and depends strongly on the initial HC/ NO_x ratio. The average vapor pressure of the β -pinene aerosol is estimated to be 37 ± 24 ppt at 31°C . Monoterpene photooxidation can be a significant source of secondary aerosol in rural environments and in urban areas with extended natural vegetation.

Key word index: Biogenic hydrocarbons, aerosol precursors, smog chamber, aerosol yield.

Introduction

Natural hydrocarbons like the monoterpenes $C_{10}H_{16}$ and isoprene C_5H_8 are emitted by various types of trees and plants. In the United States the biogenic hydrocarbon sources are estimated to produce 30 to 60 Mt of carbon per year (isoprene and monoterpenes) whereas anthropogenic hydrocarbon sources have been estimated to account for 27 Mt of carbon per year (Lamb et al., 1987; Zimmerman, 1979; Altshuller, 1983). Parameters used as a measure of the hydrocarbon reactivity include the rate of hydrocarbon disappearance, the rate of hydroxyl attack on the hydrocarbon, or the rate at which NO is oxidized to NO_2 . Laboratory investigations have indicated, using the above criteria, that biogenic hydrocarbons are moderately to extremely reactive when irradiated in the presence of oxides of nitrogen (Arnts and Gay, 1979). Despite the magnitude of the estimated amounts of biogenic hydrocarbons emitted and their considerable reactivity, our understanding of their role in atmospheric chemistry remains incomplete. The formation of aerosol from the oxidation of the biogenic hydrocarbons is one of the poorer understood phenomena.

Although the aerosol forming potential of the monoterpenes has been recognized since at least 1960 (Went, 1960), the aerosol formation processes have been neglected in most experimental and theoretical studies. The studies of Kamens et al. (1981,1982) indicated that the reaction of α -pinene with O_3 generates substantial aerosol even at concentrations of α -pinene as low as 20 ppb. In the same studies the isoprene-ozone system produced homogeneously nucleated aerosol at 4 ppm isoprene with a yield of around 1% but rapid nucleation did not occur during the reaction of low concentrations of isoprene. Hatakeyama et al. (1989) reported aerosol yields of 18.3 and 13.8% for the ozone reactions of α - and β -pinene, respectively. Recent aerosol measurements in Southern California showed that a substantial frac-

tion of fine aerosol carbon is modern and suggested that isoprene and terpenes may be important aerosol precursors (Global Geochemistry Corporation, 1989).

The lack of understanding of aerosol generation from biogenic hydrocarbons has caused problems in the extrapolation of previous gas-phase smog chamber data to ambient conditions. For example, Arnts and Gay (1979) expressed their concern about the high conversion of the reacting mixture to aerosol during their experiments, and suggested that if at atmospheric concentrations terpenes are not converted to aerosols with such high yields then the partially oxidized terpenes will remain in the gas phase, continue to participate in photochemical processes and probably produce more O_3 . The same investigators also postulated that the unaccounted carbon in their experiments (56% for the isoprene irradiation, 94% for the β -pinene) was due to a large extent to the condensation of these products to the aerosol phase.

This study was undertaken to investigate the significance of biogenic hydrocarbons as aerosol precursors in both rural and urban environments. The present study is focused on two representative natural hydrocarbons, namely isoprene and β -pinene. Isoprene is one of the major non-terpenoid compounds emitted by vegetation (Lamb et al., 1987) and is very efficient at forming O_3 when photooxidized in the presence of NO_x (Arnts and Gay, 1979). β -pinene is a representative monoterpene accounting for a major portion of the total terpene emissions (Zimmerman, 1979), and, together with α -pinene, is the most abundant monoterpene (Altshuller, 1983; Roberts et al., 1983, 1985).

In the next section we present a description of our experimental facility. Next we present our results concerning the aerosol yields during the isoprene and β -pinene photooxidation together with our measurements of the average vapor pressures of the corresponding condensable products. Finally, the implications of

our findings for the aerosol production from biogenic hydrocarbons in urban and rural areas is discussed.

Experimental Description

The experiments were performed during the summer and fall of 1989 in a flexible outdoor smog chamber on the roof of the Keck Laboratory on the Caltech campus (Leone et al., 1985; Stern et al., 1987). The smog chamber was constructed by heat-sealing 10 1.2×10 m panels of 2-mil thick Teflon to form a pillow shaped reactor with a volume of approximately 60 m³. Two Teflon ports were installed in the reactor and used for the injection of the reactants and for the sampling of the gas and aerosol products. The gas-phase sampling employed Teflon tubing and the aerosol sampling used copper tubing extending about 20 cm into the chamber. The bottom of the chamber was approximately 65 cm above the ground to allow for the circulation of air. A black tarpaulin was placed under the chamber to minimize reflective heating of the chamber. A full schematic of the experimental configuration is presented in Figure 1.

For each experiment the chamber, covered with a dark tarpaulin to shield solar radiation, was filled with purified air beginning the evening before the experiment. Laboratory compressed air was purified by passing through three consecutive packed beds containing in order, Purafil for the removal of NO_x (Purafil Inc.), drierite with 13X molecular sieves (Union Carbide), and activated charcoal for the removal of hydrocarbons. The purified air was then passed through a total particle filter to remove any aerosol particles and the purified particle free air was then injected to the chamber. Approximately 8-10 hours were required for the filling of the chamber. The gas-phase reactants were injected around 2 hours before the beginning of the experiment. The biogenic hydrocarbon was injected by syringe to a glass bulb,

CALTECH OUTDOOR SMOG CHAMBER FACILITY

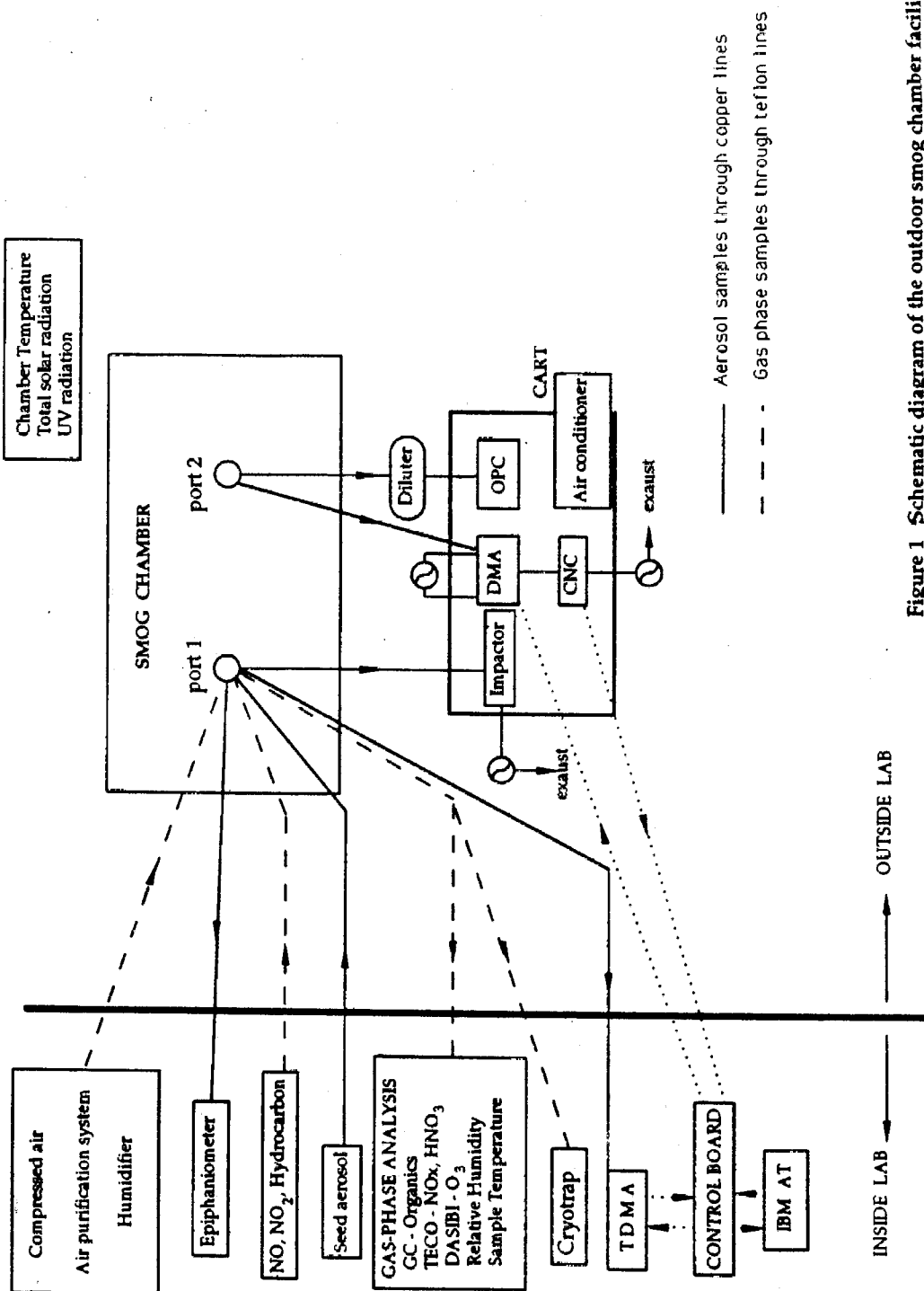


Figure 1 Schematic diagram of the outdoor smog chamber facility

the bulb was heated with a heat gun and the hydrocarbon was evaporated into the chamber. NO and NO₂ were then injected using certified cylinders containing about 600 ppm of the gas in ultrapure nitrogen (Scott-Marrin Inc.). For some experiments initial aerosol particles were injected into the chamber. The seed particles were ammonium sulfate aerosol generated using a stainless steel collision atomizer from a solution of 1 g l⁻¹ ammonium sulfate in water. The aerosol passed through a ⁸⁵Kr decharger and an evaporator before injection into the chamber. To minimize depositional losses before the experiment, the aerosol particles were added last. The reactants were allowed sufficient time to mix and when a constant concentration was reached the chamber was uncovered and exposed to sunlight. The moment of uncovering is considered as the inception of the experiment ($t = 0$).

The gas-phase parameters measured included concentrations of O₃ (Dasibi Model 1008-PC), NO and NO_x (Thermo Electron Model 14D/E), smog chamber and sample temperature, chamber relative humidity (Hygrometrix Model 8501), and total and UV solar radiation (Eppley laboratory pyranometer, Model 8-48). The gas-phase concentrations of isoprene, β -pinene, and of known major products of the photooxidation of the former, methylvinylketone and methacrolein were measured using a Hewlett-Packard Gas Chromatograph (Model 5890) equipped with a flame ionization detector. A sample trapping system (cryotrap) employing Tenax-TA (Alltech), with thermal desorption and cryo focussing, allowed gas sample analysis on a GC-mass spectrometer. The current work is focused on the aerosol processes; the gas phase measurements and their analysis will be the subject of a subsequent paper.

Several aerosol instruments were used to obtain comprehensive data concerning aerosol formation. The aerosol size distribution was measured using the newly developed Scanning Electrical Mobility Spectrometer (SEMS) (Wang and Flagan,

1990) for the 0.01 to 0.2 μm diameter range and an Optical Particle Counter (Royco Model 226) for the 0.12 to 5 μm size range. The SEMS consists of a Differential Mobility Analyzer (TSI Model 3071) and a Condensation Nucleus Counter (TSI Model 3760) as a particle detector and is able to generate a complete size distribution with 100 points in only 30 s. Since the OPC operates properly with number concentrations below 1500 cm^{-3} , a dilution system was used to dilute the aerosol sample by approximately a factor of 100. The OPC and the SEMS were housed inside a mobile temperature controlled cart placed next to the smog chamber to minimize sampling line length.

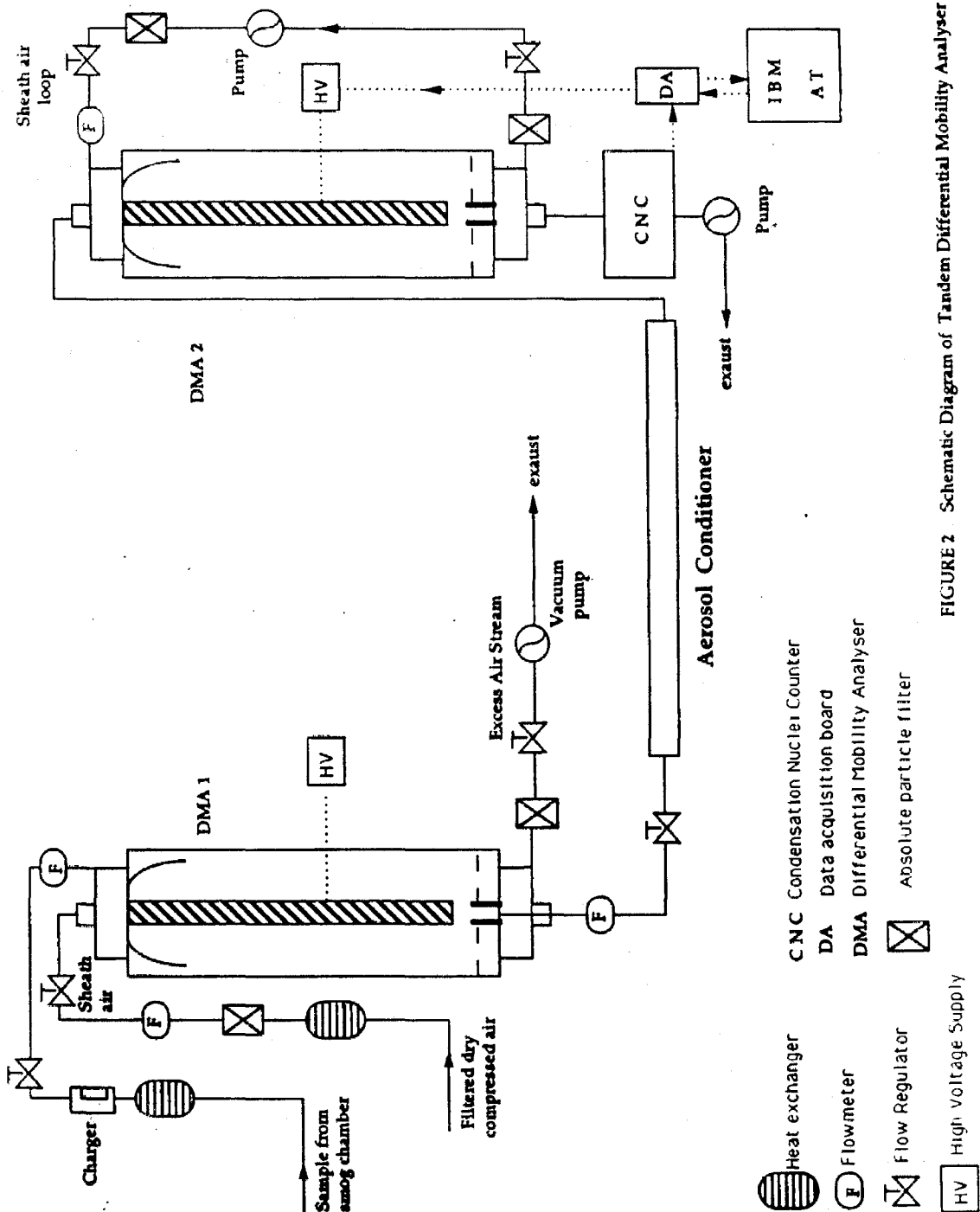
Losses in the sampling lines were estimated by sampling the chamber contents during one of the experiments with two SEMS. One was connected to the standard sampling line of length L and the other to a sampling line of length approximately $2L$. Comparison of the two results of showed agreement within 2%.

An eight stage Hering low pressure impactor (Hering et al. 1978; 1979) was also placed inside the cart and aerosol samples were collected once or twice during each experiment. The aerosol deposits on each stage were characterized using infrared spectroscopy (Palen and Allen, 1989). Also, bulk aerosol samples were obtained in selected experiments on quartz filters and analyzed using Mass Spectrometry. The results of these chemical composition characterizations will also be presented in a subsequent paper.

The Fuchs surface of the aerosol particles was measured using the epiphaniometer (Gäggeler et al., 1989). The Fuchs surface for a particle of diameter d is defined as πd^x where x a number between 1 and 2.

An average saturation vapor pressure of the condensing species was measured using a method based on the Tandem Differential Mobility Analyzer (TDMA) technique developed by Rader and McMurry (1986). A schematic diagram of the ex-

perimental set-up used for the TDMA is presented in Figure 2. The TDMA consists of a monodisperse aerosol generator (DMA 1), an aerosol conditioner (laminar flow evaporator), and a mobility detector (DMA2-CNC). The polydisperse aerosol sample is directly drawn from the smog chamber, equilibrates thermally with the laboratory atmosphere passing through a coil and enters DMA 1. Filtered, particle free compressed air that is also in thermal equilibrium with the laboratory air is also introduced in DMA 1. Under these conditions a narrow mobility slice is selected from the polydisperse input aerosol. Then these particles are diluted and separated from the surrounding organic vapors. Because the electric mobility of a spherical aerosol particle depends both on its particle diameter and on its charge, particles with a given mobility may consist of several discrete sizes corresponding to singly charged, doubly charged, etc., particles. Restricting the experiments to particles smaller than $0.2 \mu\text{m}$, one can minimize the effects of multiple charging and obtain a monodisperse aerosol flow leaving DMA 1 and entering the aerosol conditioner. The aerosol conditioner is a laminar flow evaporator consisting of a 3.66 m length of 2.292 cm i.d stainless steel tubing and associated connectors. Due to the existence of a parabolic velocity profile in the evaporator tube, the residence time of a given particle in the evaporator depends on its radial location. The size distribution of the aerosol exiting the evaporator is then measured with DMA 2 and a CNC. The control of DMA 2 and the data acquisition from the CNC are automated using an IBM AT and a Data Translation control system. The process occurring in the TDMA can be considered to be isothermal evaporation of organic aerosol particles with zero outside vapor concentration. Based on the measured diameter change of the aerosol particles and their residence time distribution in the evaporator, one calculates the corresponding evaporation rates and determines the average saturation vapor pressure (Rader and McMurry, 1986).





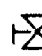
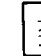
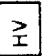




-  Heat exchanger
-  Flowmeter
-  Flow Regulator
-  Absolute particle filter
-  High Voltage Supply
-  CNC Condensation Nuclei Counter
-  DA Data acquisition board
-  DMA Differential Mobility Analyser
-  Absolute particle filter

FIGURE 2 Schematic Diagram of Tandem Differential Mobility Analyser

After each experiment the smog chamber was filled with purified air and "baked out" in the sunlight for one to two days to remove any residual products or reactants from the walls of the chamber. A continuous flow of clean air through the chamber was maintained during this period. Previous investigators (Stern et al., 1987) confirmed the reproducibility of experimental results using this cleaning process.

A total of 22 experiments, 11 for isoprene and 11 for β -pinene, were performed during the period between August 23, 1989, and November 30, 1989. A summary of these experiments is presented in Table I.

Aerosol Yields

The raw aerosol data from the SEMS and the OPC were inverted using the inversion code MICRON (Wolfenbarger and Seinfeld, 1990) to give the aerosol size distributions $dN/d\ln(D_p)$ as a function of time for each experiment. These aerosol distributions were then integrated to give the number (N), Fuchs surface (S_F), surface (S), and volume (V) concentration of the aerosol particles. A typical evolution of the number and volume aerosol concentrations is depicted in Figure 3. The aerosol carbon concentration (ACC) was then obtained from the aerosol volume concentration (V) using the expression proposed by Izumi et al. (1988),

$$ACC = 0.49V \quad (1)$$

where the constant 0.49 gC cm^{-3} represents the aerosol carbon density. Two aerosol yields were then calculated. First the aerosol volume yield per unit concentration of primary hydrocarbon (Y) expressed in $\mu\text{m}^3 \text{ cm}^{-3} \text{ ppm}^{-1}$ was determined as a function of time by dividing the aerosol volume concentration by the concentration of the hydrocarbon that had reacted up to that point

Table I
Initial Conditions and Results of the Smog Chamber Experiments

Expt	HC	HC (ppb)	Initial Concentrations			Time (min)	N_{max} Conc. (10^3 cm^{-3})	$(\text{O}_3)_{max}$	
			NO (ppb)	NO ₂ (ppb)	Seed cm ⁻³			Time (min)	Conc. (ppb)
1	ISO	730	47	23	—	40	205	50	395
2	ISO	1040	208	37	—	50	86	65	420
3	ISO	120	192	31	—	—	0.00	180 ^a	170 ^a
4	ISO	70	85	37	500	0	0.5	220	320
5	BPI	164	155	62	—	190	10	260	210
6	BPI	67	134	71	—	200	0.17	240	230
7	BPI	63	135	37	—	220	1	380	190
8	BPI	129	44	22	—	150	5.3	240	185
9	BPI	36	33	16	—	—	0.0	220	190
10	BPI	28	80	54	400	0	0.4	300	35
11	BPI	92	200	1600	—	15	8	10	300
12	ISO	1950	175	59	—	65	33	55	355
13	ISO	2200	202	43	—	60	47	65 ^b	369 ^b
14	ISO	1350	260	60	—	65	50	60	520
15	BPI	340	40	26	—	90	15	180	100
16	BPI	2000	770	212	—	65 ^c	4.5 ^c	260	350
17	ISO	4350	483	87	—	25	30	45	491
18	ISO	10000	862	280	—	35	38	32	570
19	BPI	10800	820	210	—	20 ^c	130 ^c	80	150
20	ISO	8300	1200	400	—	30	452	25	650
21	ISO	17000	0	0	—	N/A	N/A	0	20000
22	BPI	14500	0	0	—	N/A	N/A	0	25000

^a The experiment was interrupted before O₃ reached a maximum

^b Second O₃ maximum of 232 ppb at t=340 min

^c Double nucleation

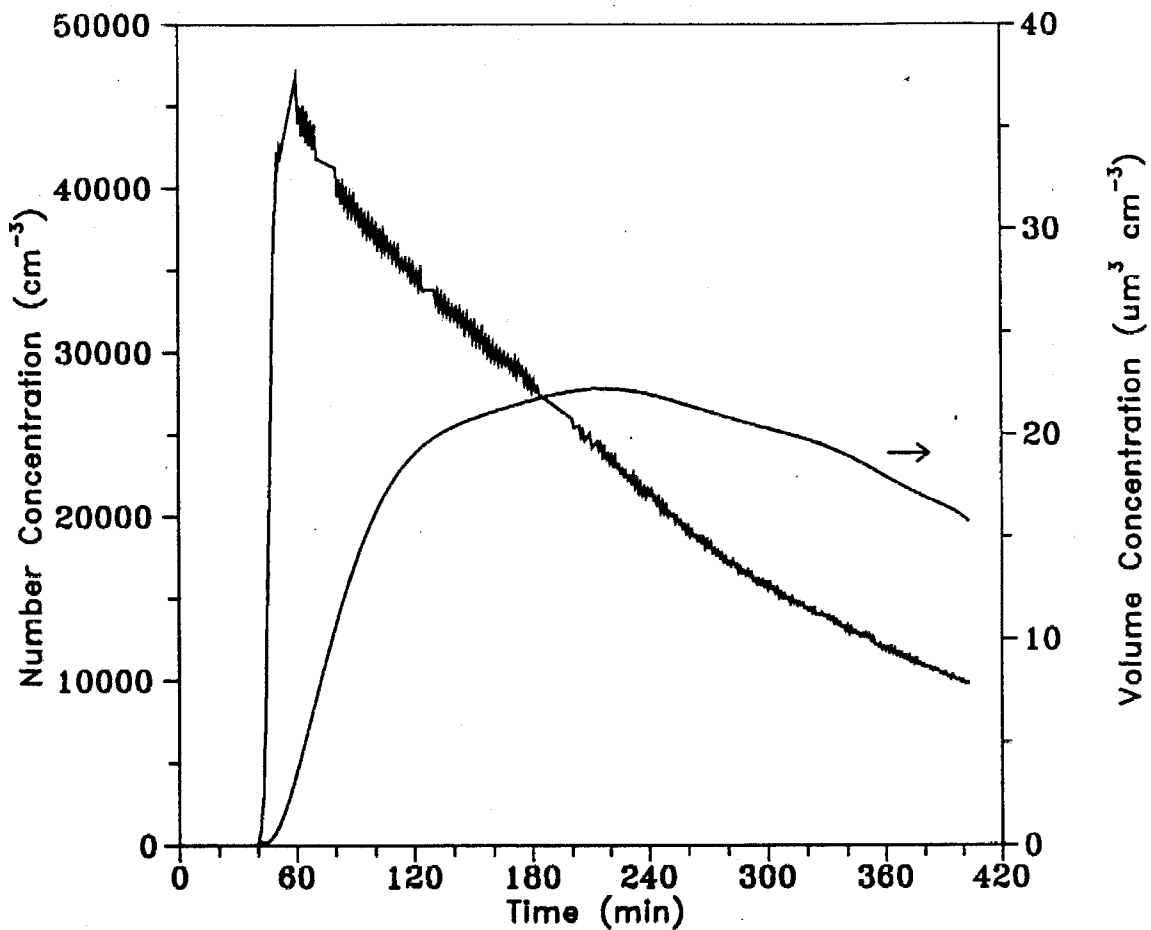


Figure 3. Number and volume concentrations of aerosol during experiment

$$Y(t) = \frac{V(t)}{[HC(0)] - [HC(t)]} \quad (2)$$

The aerosol carbon yield (Y_C) expressed as a carbon fraction was also determined by dividing the aerosol carbon content by the carbon content of the hydrocarbon that has reacted up to that point

$$Y_C(t) = \frac{ACC(t)}{f_c[HC(0)] - [HC(t)]} \quad (3)$$

where f_c is the carbon fraction of the hydrocarbon.

The aerosol volume yield for a typical experiment is presented in Figure 4. The yield is initially zero as condensable material is produced and accumulates in the gas phase. After 30 minutes of reaction and the consumption of almost 0.5 ppm of isoprene, the concentration of the condensable material has reached a critical supersaturation and nucleation begins. The yield reaches a maximum value and starts declining after 4 hours due to wall losses. The volume yield for that experiment is $18 \mu\text{m}^3 \text{ cm}^{-3} \text{ ppm}^{-1}$ and is reached after 1.5 ppm of isoprene has reacted.

Isoprene

The isoprene aerosol yield was investigated for isoprene concentrations ranging from 0.07 to 6 ppm (Figure 5). The aerosol carbon yield Y_C remained under 0.8% for the entire concentration range. In experiment 4, 0.12 ppm of isoprene was photooxidized, but no nucleation was observed. During experiment 5, 0.07 ppm of isoprene reacted in the presence of 0.23 ppm of NO_x and 500 cm^{-3} seed ammonium sulfate particles, without any condensation of material on the seed aerosol.

The experimental data points in Fig. 5 suggest a rather steep increase of the aerosol yield from a near zero value to around $25 \mu\text{m}^3 \text{ cm}^{-3} \text{ ppm}^{-1}$ for isoprene

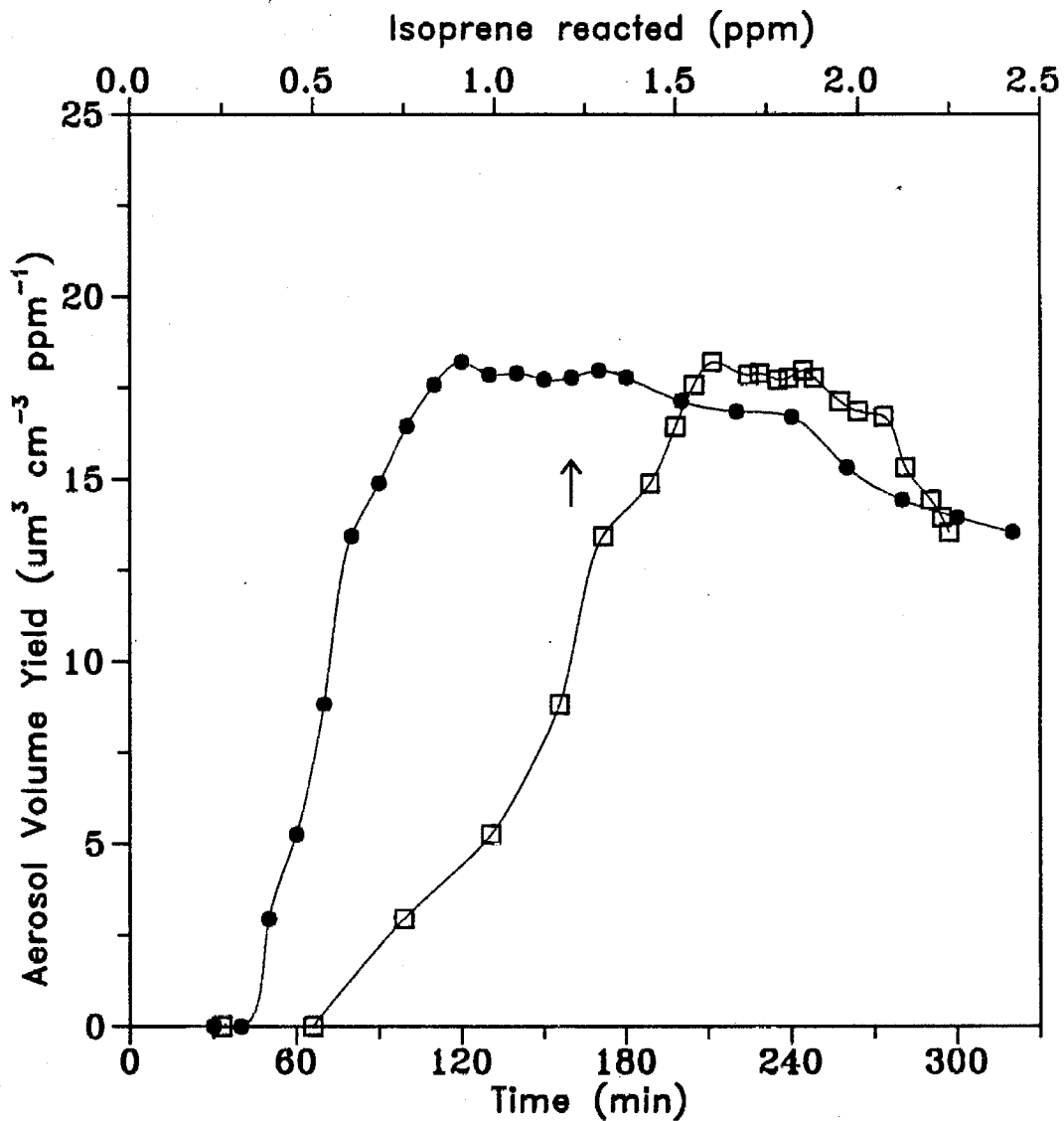


Figure 4 Aerosol volume yield as a function of time and isoprene reacted for experiment 13.

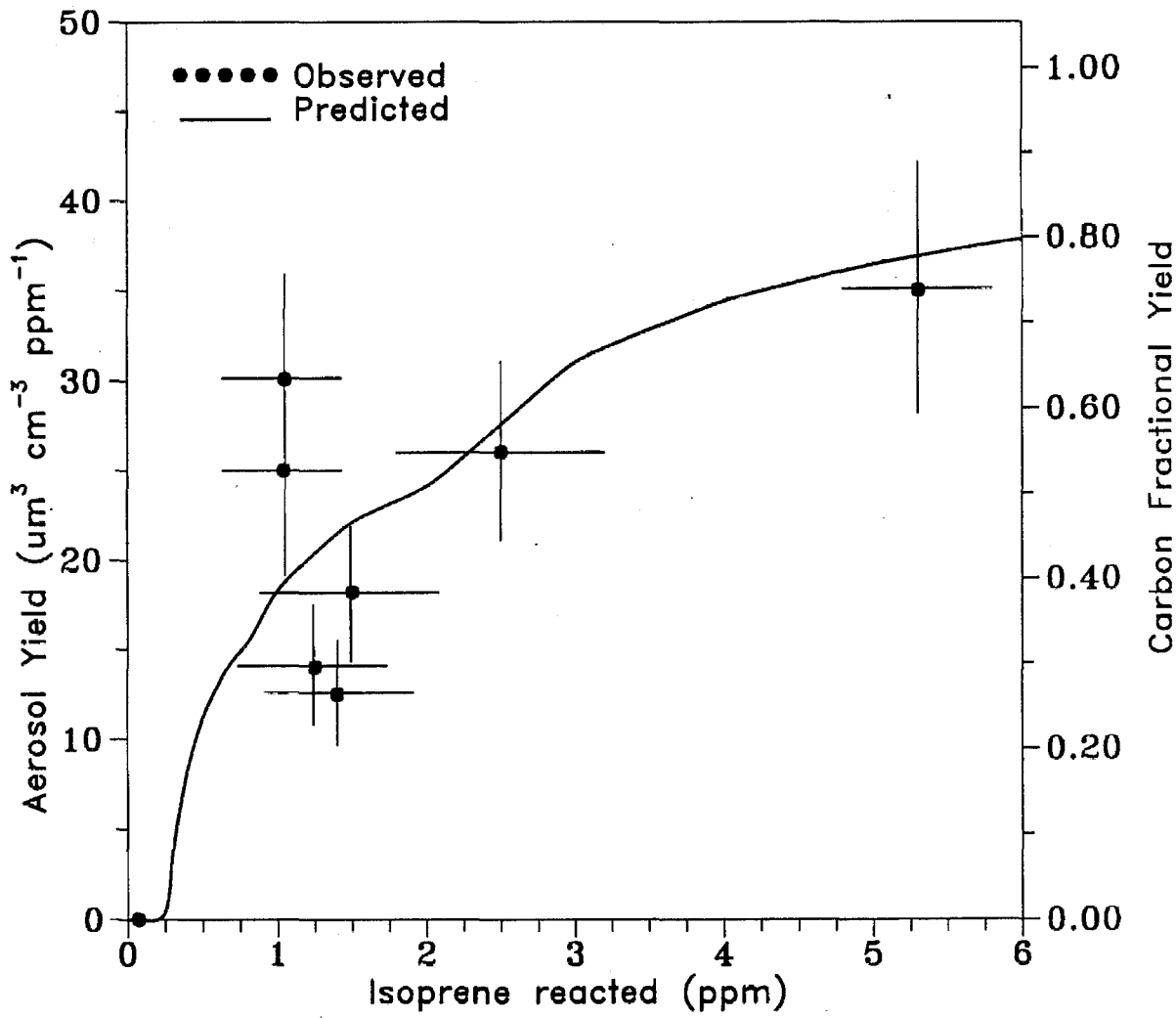
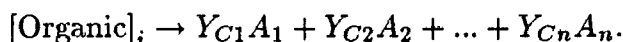


Figure 5 Measured maximum aerosol yields for the isoprene photooxidation versus the isoprene reacted. Also shown the predicted yields from the proposed model.

concentrations around 1.2 ppm. The yield then increases slowly up to its maximum value. This behavior can be explained by the formation of condensable species with relatively high vapor pressure. For example, formation of a species A with a 0.5% yield having a saturation vapor concentration of 1 ppb would require reaction of 0.2 ppm of isoprene to saturate the gas phase in A with an apparent aerosol yield of zero. If 0.4 ppm of isoprene reacted, then 2 ppb of A would be formed, only half of which would condense as aerosol, resulting in an apparent aerosol yield of 0.25% for reaction of 0.4 ppm of isoprene.

Generalizing the above, assume that organic species i reacts to produce n condensable species A_1, A_2, \dots, A_n . Also let these species be produced with fractional yields $Y_{C1}, Y_{C2}, \dots, Y_{Cn}$ and have saturation vapor concentrations, P_1, P_2, \dots, P_n ,



Without any loss of generality, one can assume that

$$\frac{P_1}{Y_{C1}} \leq \frac{P_2}{Y_{C2}} \leq \dots \leq \frac{P_n}{Y_{Cn}}. \quad (4)$$

If c is the concentration of the organic that reacts and Y_C is the aerosol yield, then

$$Y_C(c) = 0 \quad \text{for} \quad c \leq \frac{P_1}{Y_{C1}} \quad (5)$$

and no aerosol is formed for the reaction of organic concentrations less than P_1/Y_{C1} , or in other words P_1/Y_{C1} is the condensation threshold. For higher values of c ,

$$Y_C(c) = Y_{C1} - \frac{P_1}{c} \quad \text{for} \quad \frac{P_1}{Y_{C1}} \leq c \leq \frac{P_2}{Y_{C2}} \quad (6)$$

and more generally

$$Y_C(c) = \sum_{i=1}^{n-1} Y_{Ci} - \frac{\sum_{i=1}^{n-1} P_i}{c} \quad \text{for} \quad \frac{P_{n-1}}{Y_{C\ n-1}} \leq c \leq \frac{P_n}{Y_{Cn}}. \quad (7)$$

The best fit of our isoprene experimental data with the above model was obtained by assuming formation of three condensable products with carbon yields of 0.47%, 0.16%, and 0.31% and saturation vapor concentrations at 31°C of 1.2, 1.3 and 6.2 ppb. An implicit assumption in the application of the above model is that the yields $Y_{C1}, Y_{C2}, \dots, Y_{Cn}$ are constants not influenced by gas-phase conditions, such as the concentration of NO_x . This simplified model predicts that the reaction of around 250 ppb of isoprene is necessary for saturation of the gas phase with isoprene condensable products and the onset of condensation.

β -pinene

The aerosol carbon yields for the β -pinene photooxidations vary from 0.1% to around 8% (Figure 6) for β -pinene concentrations between 20 and 250 ppb. The aerosol carbon yield for experiment 16 that is not shown in Figure 6 was 5.8% for the reaction of 1.5 ppm of β -pinene. Formation of aerosol products was observed for β -pinene concentrations as low as 20 ppb, and nucleation of new particles for concentrations as low as 60 ppb.

There appears to be a small tendency of increase of the yield with increasing concentration of β -pinene. Application of equations (4) to (7) fails to explain the behavior of the yield, especially the 2% yield for 250 ppb of β -pinene and secondarily the 5.8% yield for 1500 ppb of β -pinene. Even if one neglects these data points, saturation of the gas phase with a condensable product, produced with 8% yield at 20 ppb of β -pinene, would require formation of a species with saturation concentration less than 1.6 ppb. But then the observed carbon yield for concentrations of β -pinene higher than 50 ppb should be more than 5%. Therefore,

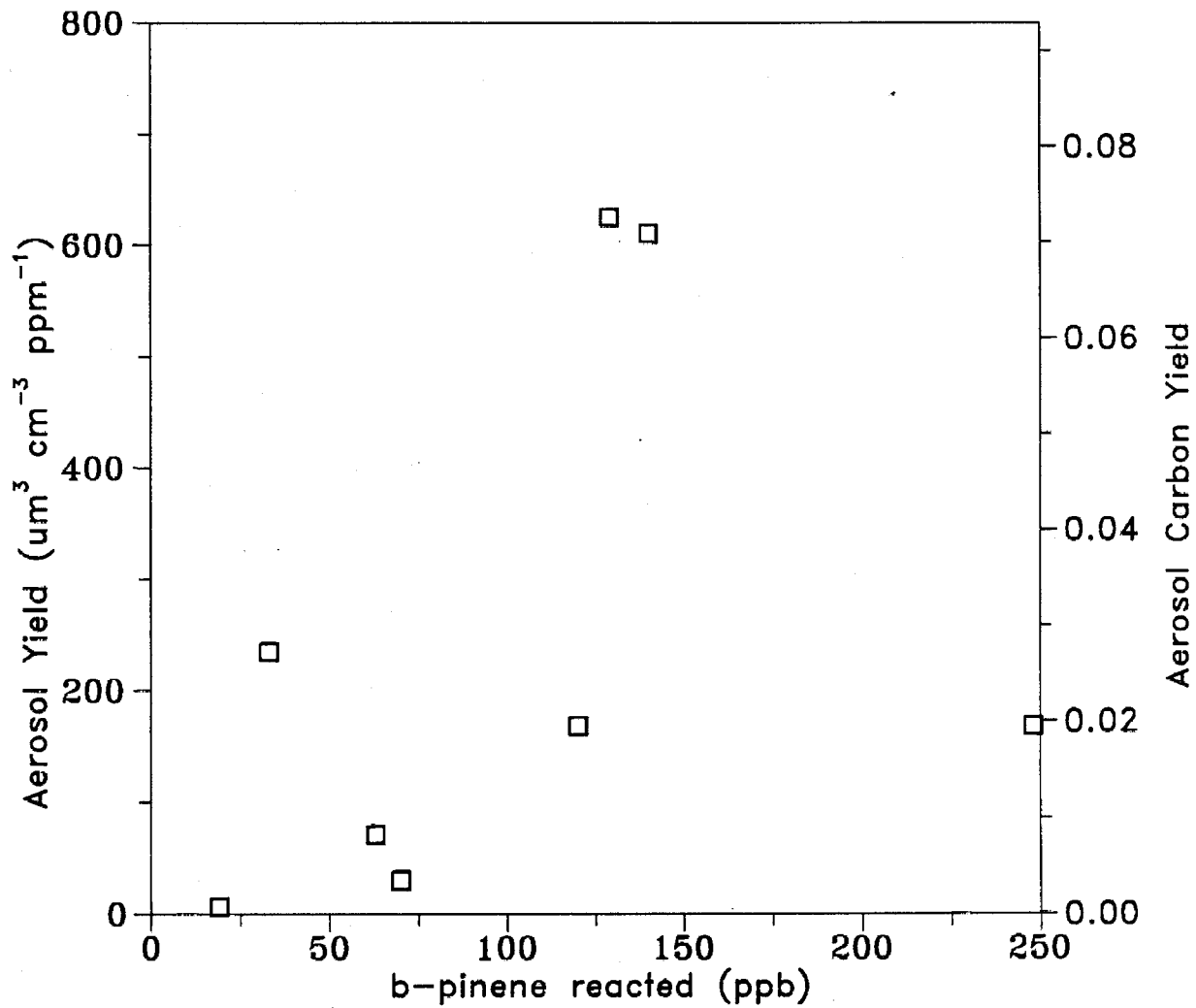
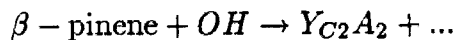
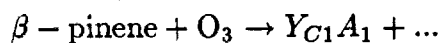


Figure 6 Measured maximum aerosol yields for the β -pinene photooxidation versus the β -pinene reacted.

it is evident that the assumption of the simplest reaction scheme β -pinene $\rightarrow Y_1 A_1$ with a constant yield Y_1 cannot explain the observed behavior for any choice of Y_1 and P_1 . It is also evident that the assumption of more than one condensable product formed does not improve the model's success.

Plotting the same aerosol yields as a function of the ratio r of the initial β -pinene concentration to the initial NO_x concentration reveals a strong dependence of the former on the latter (Figure 7). The aerosol yield is small for values of r smaller than 5, increases dramatically reaching a maximum for the range 10-15 and starts decreasing slowly as the ratio increases. The above results indicate that NO_x plays a major role in the production of aerosol during the β -pinene photooxidation. The appearance of this maximum suggests that there are two ways by which NO_x influences the aerosol production. In the first process NO_x enhances aerosol production causing the steep yield increase while during the second NO_x drives the reaction processes away from the formation of the condensable products reducing the aerosol production.

One possible mechanism involves the production of condensable products by two different pathways, attack of β -pinene by O_3 and OH with the ratio r determining the relative importance of these pathways:



with A_1, A_2 the only condensing species. Then with p_1 the fraction of β -pinene that reacted with O_3 during the photooxidation, and p_2 the fraction that reacted with OH , the total aerosol produced during the reaction of c β -pinene would be $(p_1 Y_{C1} + p_2 Y_{C2})c$ and the corresponding carbon aerosol yield is $Y_C = p_1 Y_{C1} + p_2 Y_{C2}$.

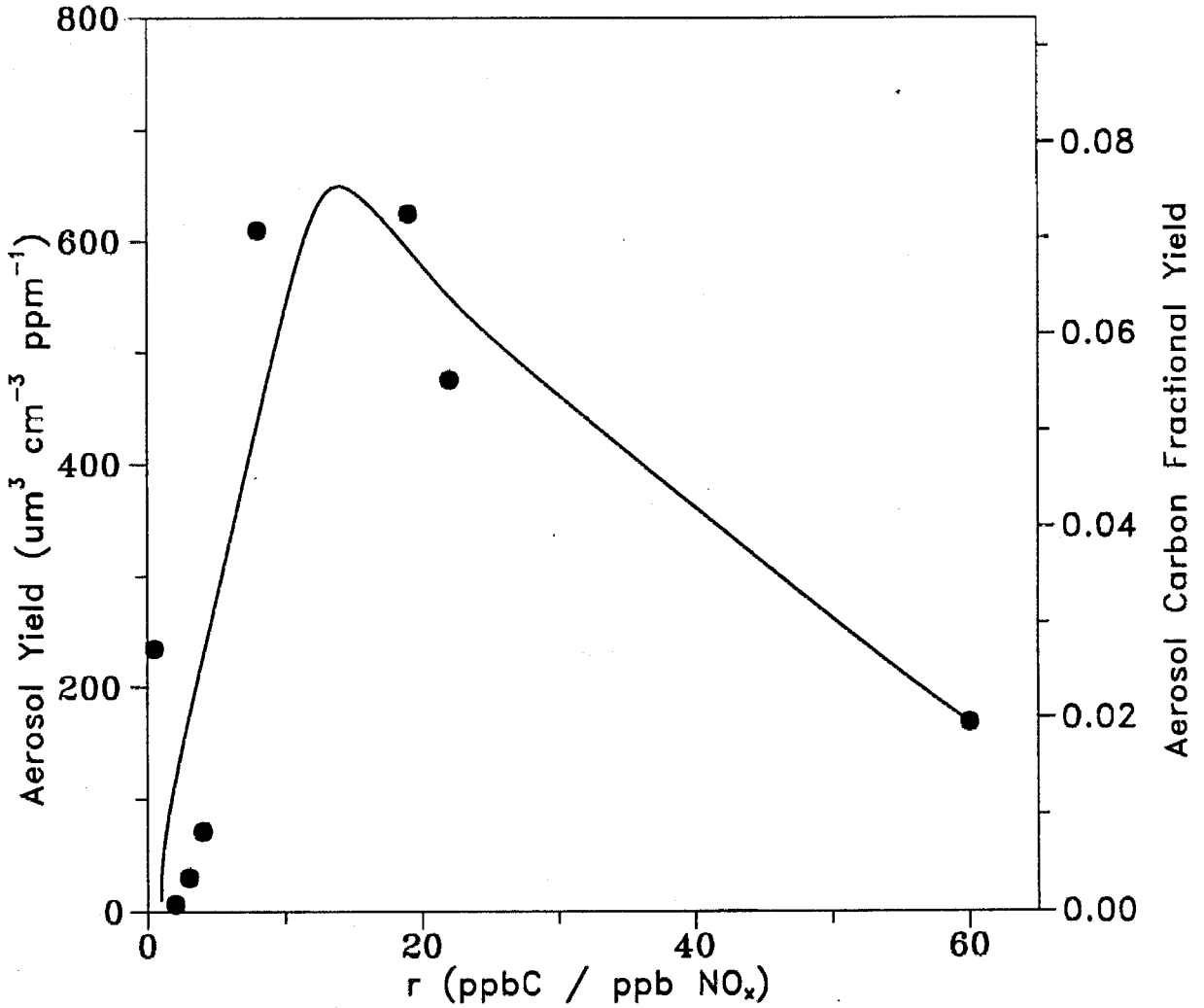


Figure 7 Measured maximum aerosol yields for the β -pinene photooxidation versus r , the ratio of the initial hydrocarbon to the initial NO_x concentration.

Assuming that the reactions with O_3 and OH are the only significant reaction pathways for β -pinene during the daytime then $p_2 = 1 - p_1$ and therefore

$$Y_C(p_1) = Y_{C2} + p_1(Y_{C1} - Y_{C2}). \quad (8)$$

If Y_{C1}, Y_{C2} are constants, then the aerosol yield would be a linear function of the fraction of the β -pinene that reacted with O_3 , p_1 . This fraction p_1 has been calculated for each experiment by integrating the product of the measured β -pinene and ozone concentrations and the corresponding reaction constant and has been plotted against the corresponding aerosol yield in Figure 8. The best linear fit suggests $Y_{C1} = 8.3\%$ and $Y_{C2} = 1.4$, but the correlation is very poor and evidently this second model does not explain the observed data satisfactorily.

Our understanding of the aerosol formation requires information on the nature of the condensable products and the gas-phase reaction pathways responsible for their production. At this time we will use the maximum observed yields in an attempt to obtain an upper limit of the aerosol forming potential of the β -pinene specifically and the monoterpenes more generally under ambient conditions.

Saturation Vapor Pressure Estimation

The saturation vapor concentration of the β -pinene condensable products was measured during experiment 11, at 31°C using the TDMA described above. Aerosol particles of diameters 103, 124 and 156 nm were evaporated during the experiment.

Assuming n aerosol species and monodisperse aerosol particles of diameter d_p , then the rate of change of mass M of these particles can be described by the Fuchs-Sutugin formula (Fuchs and Sutugin, 1971),

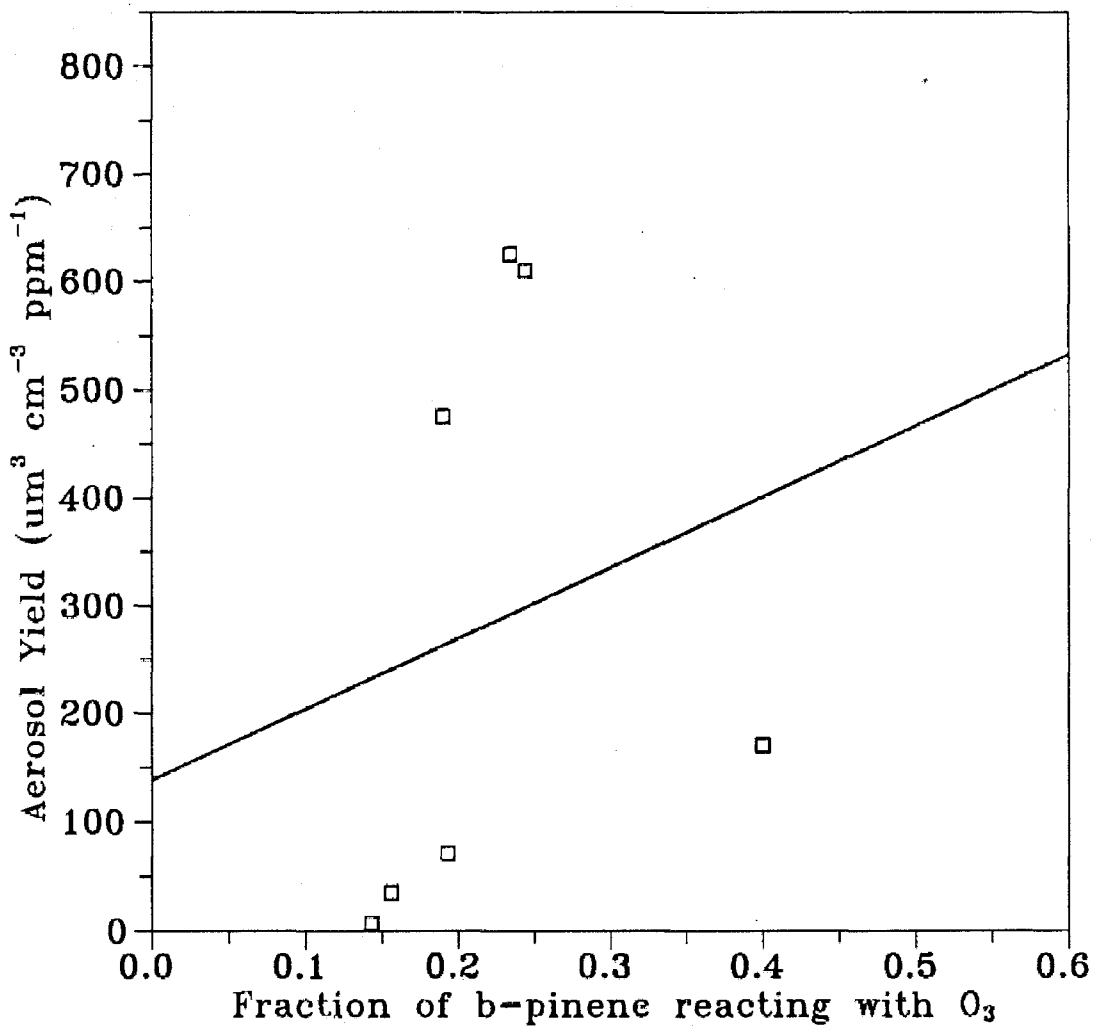


Figure 8 Measured maximum aerosol yields for the β -pinene photooxidation as a function of p_1 , the fraction of β -pinene that reacted with O_3 . The solid line is the best linear fit.

$$\frac{dM}{dt} = M \sum_{i=1}^n \frac{12D_i(p_i - p_{si})f_o(Kn)M_{wi}}{\rho d_p^2 RT} \quad (9)$$

where D_i is the molecular diffusion coefficient of species i in the gas phase, $(p_i - p_{si})$ is the difference between the partial pressure of species i in the bulk gas phase and that at the particle surface, $f_o(Kn) = (1 + kn)/(1 + 1.71Kn + 1.33Kn^2)$ with Kn the Knudsen number that is the ration of the mean free path of air to the particle radius, M_{wi} is the molecular mass of species i , ρ is the particle density, R the ideal gas constant and T the temperature (Pilinis et al., 1987). Assuming zero concentration of the organic vapor in the bulk gas phase, $p_i = 0$, $f_o(Kn) = 1$ for the droplets that will be evaporated, and that $D_i M_{wi} = DM_w$ for all the species then

$$\frac{dM}{dt} = -\frac{12MDM_w}{\rho d_p^2 kT} \sum_{i=1}^n p_{si} \quad (10)$$

This equation can be integrated from $t = 0$ to $t = t_r$ where t_r the residence time of the droplet in the evaporator assuming that the temperature and the sum of the vapor pressures does not change during this period resulting in

$$\sum_{i=1}^n p_{si} = \frac{(d_1^2 - d_2^2)\rho RT}{8DM_w t_r} \quad (11)$$

By measuring the initial and final diameters of the droplets and estimating the gas-phase diffusion coefficient D , the molecular weight M_w and the density ρ , the sum of the vapor pressures can be estimated. If one lumps all the condensable aerosol species into one, then the measured vapor pressure is the corresponding vapor pressure for that species. On the other hand if one treats the aerosol particles as a multicomponent mixture, then the measured vapor pressure is the sum of the vapor pressures of all these species and is an upper limit for the vapor pressures of the condensable species.

The average change of the squares of the diameters was $496 \pm 322 \text{ nm}^2$ for the β -pinene generated aerosol that was evaporated. The large uncertainty in this value is due to the small diameter changes for the particles used, at the most 3 nm, that are very close to the precision limit of the DMA and the SEMS. A molecular mass of 260 g mole^{-1} (suggested by preliminary GC-MS analysis of the aerosol products), a density 1.4 g cm^{-3} and a diffusion coefficient of $0.06 \text{ cm}^2 \text{ s}^{-1}$ were assumed and a saturation vapor concentration of $0.037 \pm 0.024 \text{ ppb}$ at 31°C was calculated from equation 11. Assuming that these condensable species behave similarly to the monocarboxylic and dicarboxylic acids studied by Tao and McMurry (1989), their vapor saturation concentration at 25°C should be around 0.009 ppb .

Isoprene as an Aerosol Precursor

Due to the relatively high vapor pressure of its reaction products, reaction of at least 250 ppb of isoprene is required for the saturation of the gas phase with any of the condensable products. The maximum isoprene concentration that has been measured under ambient conditions is 30 ppb, obtained by Ferman (1981) outside a forest canopy in south central Virginia. The ambient concentration of isoprene, interpreted as a steady state concentration, is a result of the balancing of the isoprene sources (emissions from trees) and the isoprene sinks (mainly reaction with OH, O_3 and NO_3). On the other hand, the ambient concentration of its condensable species can be also viewed as resulting from a balancing of their production rate (isoprene oxidation) and their loss due to deposition or possible reactions. If there are no significant chemical pathways for the transformation of these condensable species to species with much higher vapor pressure, the condensable species can accumulate under stagnant conditions reaching relatively high concentrations. To investigate this accumulation of the isoprene condensable products, we have used a simple box

model for isoprene and its condensable products

$$\frac{d[ISO]}{dt} = \frac{E(t)}{H(t)} - (k_{OH}OH + k_{O_3}O_3 + k_{NO_3}NO_3)[ISO] - \frac{v}{H(t)}[ISO] \quad (12)$$

$$\frac{d[COND_i]}{dt} = y_i(k_{OH}OH + k_{O_3}O_3 + k_{NO_3}NO_3)[ISO] - K_i[COND_i] - \frac{v_i}{H(t)}[COND_i] \quad (13)$$

where $[ISO]$ and $[COND_i]$ the gas-phase concentrations of isoprene and its i_{th} condensable product, $E(t)$ the isoprene emission rate, $H(t)$ the mixing height, k_{OH} , k_{O_3} , k_{NO_3} the reaction constants for the reactions of isoprene with OH, O_3 and NO_3 , correspondingly, v and v_i the deposition velocities of isoprene and the condensable product, y_i the yield for the production of the product and K_i the first order loss reaction rate for the condensable.

A stagnation episode has been investigated similar to the one studied by Peterson and Tingey (1980). Isoprene emissions are assumed to be close to zero during the nighttime and rise to $10,000 \mu\text{g m}^{-2} \text{hr}^{-1}$ during the daytime. The mixing height varied between 100 m at night and 1200 m at the early afternoon. The reaction loss rate constant of isoprene is assumed to remain constant during day and night and equal to 0.2 hr^{-1} and 0.55 hr^{-1} respectively. Deposition velocities of 0.1 cm s^{-1} were assumed and the reactions of the condensable product were neglected so that an upper limit of their concentration could be obtained.

The steady state diurnal profiles for isoprene and the first condensable product are presented in Figure 9. The isoprene reaches its steady state profile quickly due to the zero isoprene initial condition. The condensable species concentration increases from zero gradually reaching a maximum of 0.14 ppb the first day, 0.23 the second, 0.29 the third, 0.33 the fourth, etc. The steady state diurnal profile shown in Figure

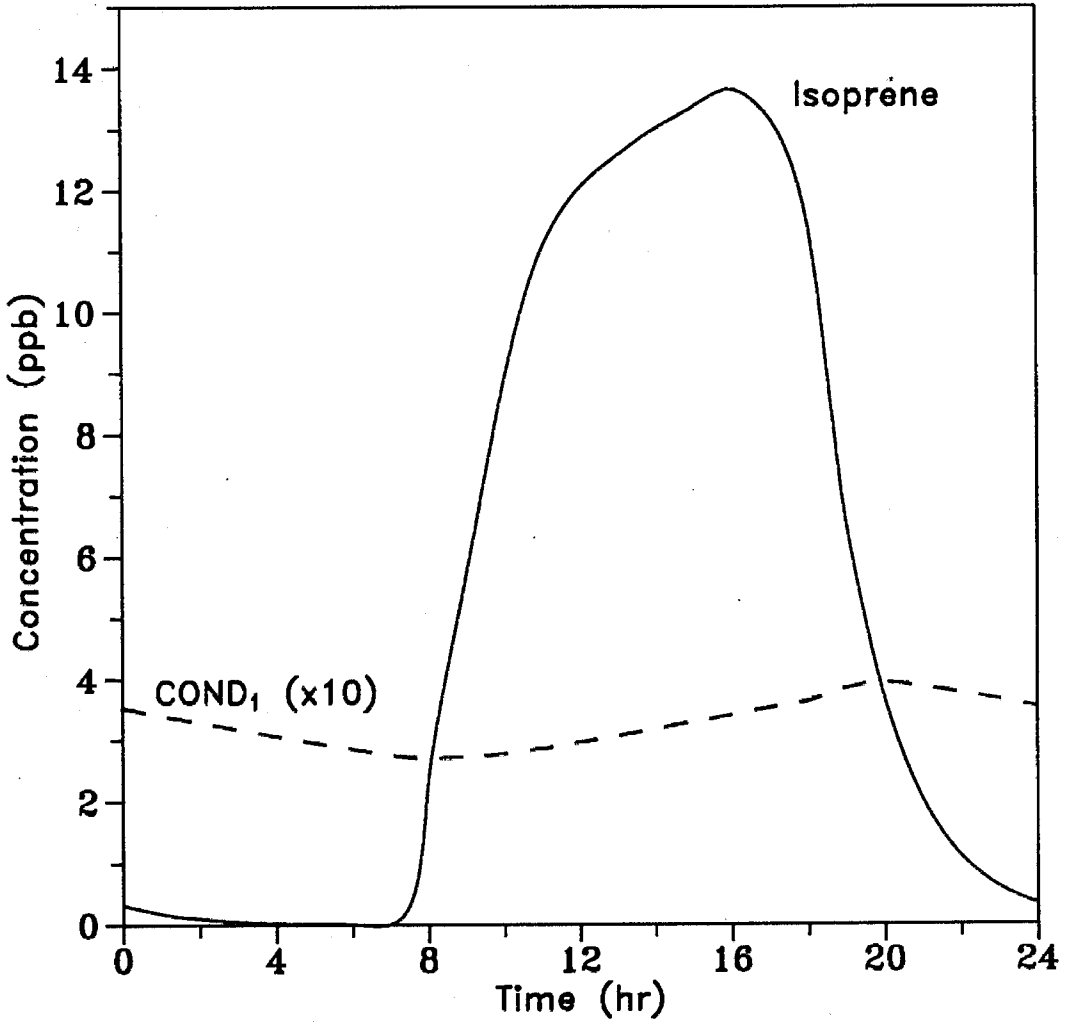


Figure 9 Steady state predicted diurnal variation of the concentrations of isoprene and one of its condensable products (COND₁) in a rural environment with atmospheric stagnation.

9 is attained after 6 days. The maximum concentration of isoprene is 13.6 ppb, higher than any reported ambient concentration of isoprene (Altshuller, 1983) with the exception of the 30 ppb reported by Ferman (1983), and our scenario is indeed an upper limit of the actual conditions. The maximum concentration of condensable species one is 0.39 ppb, a factor of 3 lower than its vapor concentration of 1.2 ppb at 31°C. Therefore, even under extreme conditions studied above, isoprene is not expected to contribute at all to the ambient aerosol loading.

β -pinene as an Aerosol Precursor

Pathways for production of condensable species

Hatakeyama et al. (1989) showed that the reaction of β -pinene with O_3 results in the production of aerosol. Preliminary results of Izumi et al. (1989) indicated that the reaction of β -pinene with OH also leads to aerosol formation. The present results provide indirect evidence that indeed both pathways contribute to the formation of condensable products that undergo gas-to-particle conversion.

In most β -pinene/ NO_x photooxidations, the nucleation of new particles proceeded in two stages. First relatively slow formation of new particles occurred for around 10 min and then an order of magnitude faster nucleation took place for another 10 min. This phenomenon (experiment 5) is illustrated in Figure 10, with 55 particles $cm^{-3} min^{-1}$ produced during the first stage (145-155 min) and 485 particles $cm^{-3} min^{-1}$ produced subsequently. At the beginning ($t = 145$ min) of the nucleation event, 73.4 ppb of β -pinene had already reacted with OH and 4.8 ppb had reacted with O_3 (assuming that these are the only reaction pathways for β -pinene). When the nucleation rate increased the β -pinene reacted with OH increased by 18% and the reacted with O_3 by 40%. The observed particle formation can be tentatively explained by the initial nucleation of a product of the

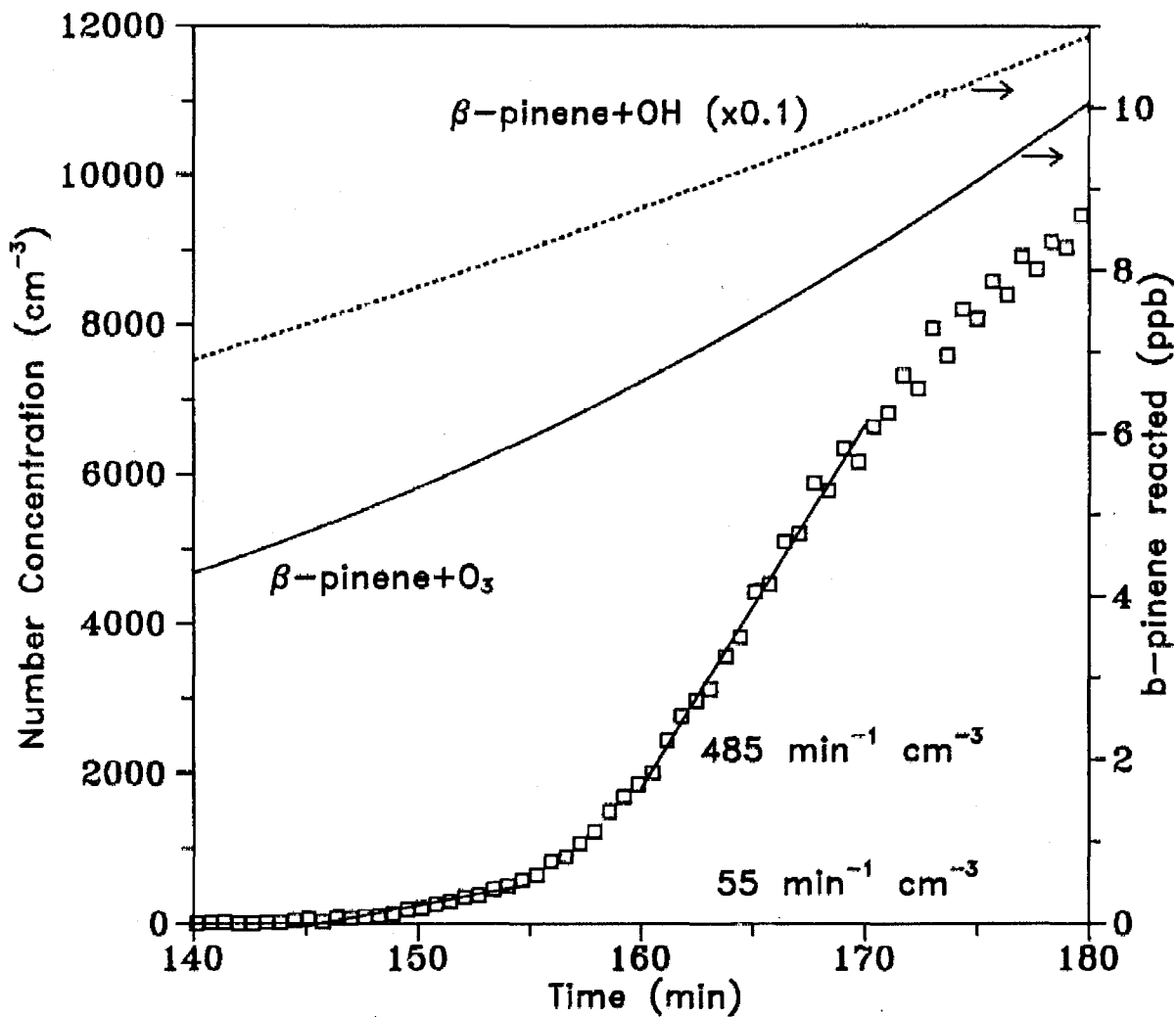


Figure 10 Nucleation of particles during experiment 5. Also shown the amounts of β -pinene that have reacted with O₃ and OH.

OH + β -pinene reaction followed by nucleation of a product of the $O_3 + \beta$ -pinene reaction at a 10 times higher rate. The same two different stages appeared in experiment 16 (Figure 11). The first nucleation event took place 40 min after the beginning of the experiment with 150 ppb of β -pinene having reacted all with OH because ozone remained zero up to that point. Two hours later O_3 started forming and at $t = 200$ min a second nucleation event occurred adding 1800 new particles cm^{-3} , in spite of the fact that 4,000 particles cm^{-3} existed in the system. The second nucleation events coincided with the rapid increase of O_3 and the rapid consumption of β -pinene by the $O_3 - \beta$ -pinene reaction. Both Figures 10 and 11 illustrate indirectly the two pathways forming aerosol during the β -pinene photooxidations. Detailed chemical information on the aerosol products is needed for the better understanding of these pathways.

Contribution of β -pinene and other monoterpenes to atmospheric aerosol levels

Because of incomplete understanding of the chemical pathways that lead to the formation of condensable species during the oxidation of β -pinene and the other monoterpenes only an approximate assessment of their contribution to ambient aerosol concentrations is possible at this point. Using the information provided by the current experiments, one can estimate an upper limit of this contribution by either performing emission calculations or using a simple box model like the one described by equations (12) and (13).

We shall illustrate these calculations for three different environments: Los Angeles, an urban area with 33% natural vegetation (Winer et al., 1983), Atlanta, an urban area with 57% wood coverage (Chameides et al., 1988) and a rural area represented by a coniferous forest in Norway (Hov et al., 1983). Most of the existing inventories lump all the monoterpenes into one category. The available data suggest

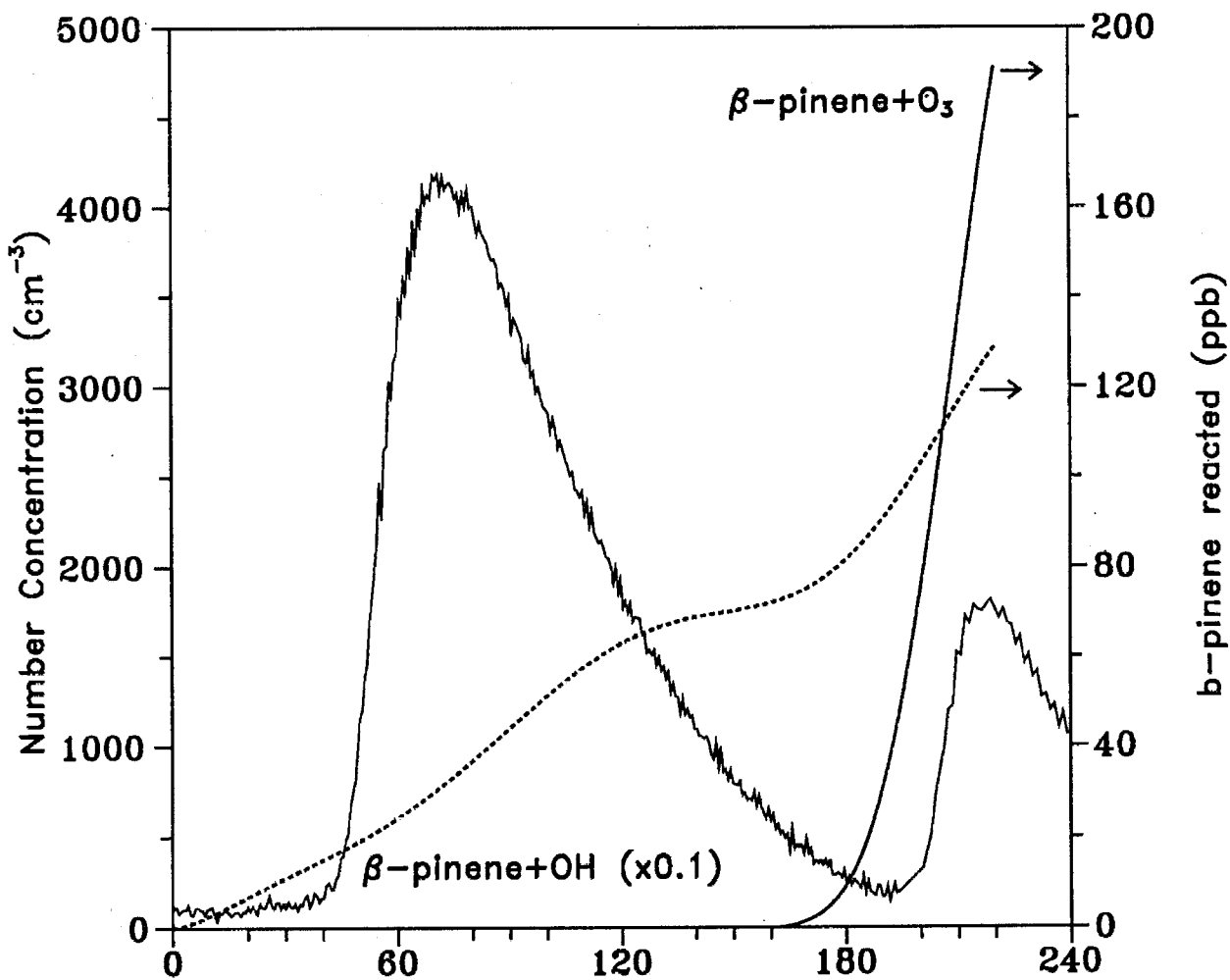


Figure 1*. Number concentration of particles smaller than 0.21 μm (DMA range) during experiment 16. Also shown are the amounts of β -pinene that have reacted with O₃ and OH.

that α -pinene represents around 25% of the monoterpene emissions in the United States (Lamb et al., 1987) with the β -pinene emissions accounting for roughly another 25%. Because of the unavailability of aerosol yield information for the other monoterpenes and the fact that the α -pinene yields exceed or are equal to the corresponding β -pinene yields (Hatakeyama et al., 1989; Izumi et al., 1989) a carbon aerosol yield of 10% will be assumed as an upper limit for all the monoterpenes. Twenty-five percent of the monoterpene emissions will be assumed to be β -pinene.

For the California South Coast Air Basin, monoterpene emissions of 10-40 tons day⁻¹ as estimated by Winer et al. (1983) lead to 1-4 tons day⁻¹ of organic aerosol. For the same area 1200 tons day⁻¹ of reactive organic gases (ROG) are emitted from anthropogenic sources which have been estimated to yield around 7.5 tons of organic aerosol (Grosjean and Seinfeld, 1989). Therefore even for an area like Los Angeles, with 58% urban vegetation and 33% natural vegetation, natural hydrocarbons could be responsible for up to 50% of the secondary organic aerosol. Analysis of the contemporary carbon (carbon of non-fossil origin) in the fine aerosol particles in Los Angeles showed that an average of 45% of the aerosol carbon in the summer and 38% in the fall is modern (Global Geochemistry Corporation, 1989). The above percentages are also an upper limit of the monoterpene contribution because other possible sources like volatilized food constituents, which contain only modern carbon, are also included in the above estimates.

For a case like Atlanta with 57% wood coverage, 300 tons day⁻¹ of monoterpenes have been estimated to be emitted (Chameides et al., 1988) which would correspond to approximately 30 tons day⁻¹ of aerosol. Over the same area anthropogenic ROG emissions are estimated to be 270 tons day⁻¹, and assuming the same average yield as in Los Angeles, these emissions correspond to only 2 tons day⁻¹ of secondary organic aerosol. Therefore, the aerosol produced by the monoterpenes

probably dominates the secondary ambient organic aerosol for highly vegetated urban areas.

Monoterpene emissions of $2000 \mu\text{g m}^{-2} \text{hr}^{-1}$ have been estimated for a coniferous forest (Hov et al., 1983) throughout the day. Using a box model, similar to the one used for isoprene, one can calculate an upper limit to the secondary organic aerosol concentration due to the monoterpenes' photooxidation. The mixing height varied again between 100 m at night and 1200 m at the early afternoon. The reaction loss rate constant is assumed to remain constant during day and night at 0.35 and 0.25hr^{-1} correspondingly. Deposition velocities of 0.1cm s^{-1} were assumed for the β -pinene and its condensable products and the possible reactions of the condensable species have been neglected. Our simulation indicated that under these stagnant conditions the monoterpenes reach a maximum concentration of around 12 ppb during the nighttime, and this concentration decreases to 1.1 ppb during the early afternoon due to the dilution of the mixed layer. The condensable species reach concentrations of $15 \mu\text{gC m}^{-3}$ the night of the first simulation day. Almost all of this amount will be transferred to the aerosol phase. If the stagnant conditions persist, the amount of condensable species will continue increasing reaching $30 \mu\text{gC m}^{-3}$ the second night, $39 \mu\text{gC m}^{-3}$ the third, etc. Although this is an extreme case, it is evident that the monoterpenes have the potential to contribute significantly to aerosol loadings in rural environments.

Conclusions

Aerosol formation and growth have been studied in the systems of isoprene/ NO_x and β -pinene/ NO_x in an outdoor smog chamber over hydrocarbon concentration levels of a few ppb to a few ppm.

The aerosol carbon yield remained under 0.8% for initial isoprene concentra-

tions as high as 6 ppm. The nucleation threshold was determined to exceed 0.12 ppm isoprene while the condensation threshold was more than 0.07 ppm of isoprene. The measured isoprene aerosol yields can be explained by the formation of condensable species with relatively high saturation vapor concentrations (> 1 ppb). The best fit of the observed aerosol levels was obtained by assuming formation of three condensable products with carbon yields of 0.47%, 0.16%, and 0.31% and saturation vapor concentrations at 31°C 1.2, 1.3 and 6.2 ppb, correspondingly. This simplified picture predicts that the reaction of about 250 ppb of isoprene is necessary for saturation of the gas phase with the first of the isoprene condensable products. Simulation of a stagnation episode in a rural environment indicates a maximum concentration of the first condensable product of 0.4 ppb, a factor of three lower than its saturation vapor concentration at the same temperature. Therefore, isoprene photooxidation should not contribute to the production of secondary aerosol under ambient conditions.

The carbon aerosol yields for the β -pinene photooxidations varied from 0.1% to around 8% for β -pinene concentrations between 20 and 250 ppb. The nucleation threshold was between 30 and 50 ppb of β -pinene and the condensation threshold below 20 ppb. The measured carbon aerosol yield depends nonlinearly on the initial HC/NO_x concentration ratio r , with a maximum occurring for values of r between 10 and 20. Reactions of β -pinene with O₃ and OH both appear to produce condensable species, but a simplified two pathway model failed to explain the observed nonlinearity. By using the tandem differential mobility analyzer method a single saturation vapor concentration of β -pinene produced aerosol of 0.037 ± 0.024 ppb was measured. Based on the data obtained, β -pinene specifically and the monoterpenes more generally appear to have the potential to contribute significantly to secondary aerosol, especially in areas with high vegetation coverage. A more complete assess-

ment of the monoterpene contribution to aerosol formation requires elucidation of the gas-phase mechanisms that lead to the formation of condensable species.

Acknowledgement

This work was supported by the Ford Motor Company.

References

- Altshuller A. P. (1983) Review: Natural volatile organic substances and their effect on air quality in the United States. *Atmospheric Environment*, **17**, 2131-2165.
- Arnts R. R. and Gay B. G. (1979) Photochemistry of some naturally emitted hydrocarbons. Rep. EPA-600/3-79-081.
- Chameides W. L., Lindsay R. W., Richardson J. and Kiang C. S. (1988) The role of biogenic hydrocarbons in urban photochemical smog: Atlanta as a case study, *Science*, **241**, 1473-1475.
- Ferman M. A., Rural nonmethane hydrocarbon concentration and composition (1981) In *Atmospheric Biogenic Hydrocarbons, Vol. 2, Ambient Concentrations and Atmospheric Science*, Ann Arbor, MI, 333-367.
- Fuchs N. A. and Sutugin A. G. (1971) In *Topics in Current Aerosol Research*, G. M. Hidy and J. R. Brock, eds. Pergamon Press, Oxford, Vol. II, pp. 1-60.
- Gäggeler H. W., Baltensperger U., Emmenegger M., Jost D. T., Schmidt-Ott A., Haller P. and Hofmann M. (1989) The epiphaniometer, a new device for continuous aerosol monitoring. *J. Aeros. Sci.*, **20**, 557-564.
- Global Geochemistry Corporation (1989) Estimation of contemporary carbon in fine particle aerosols, Final Report to the Coordinating Research Council, Atlanta, GA.

- Grosjean D. and Seinfeld J. H. (1989) Parameterization of the formation potential of secondary organic aerosols. *Atmospheric Environment*, **23**, 1733-1747.
- Hatakeyama S., Izumi K., Fukuyama T. and Akimoto H. (1989) Reactions of ozone with α -pinene and β -pinene in air: yields of gaseous and particulate products. *J. geophys. Res.*, **86**, 7210-7254.
- Hering S. V., Flagan R. C. and Friedlander S. K. (1978) Design and evaluation of a new low-pressure impactor: 1. *Environ. Sci. Tech.*, **12**, 667-673.
- Hering S. V., Friedlander S. K., Collins J. J. and Richards L. W. (1979) Design and evaluation of a new low-pressure impactor: 2. *Environ. Sci. Tech.*, **13**, 184-188.
- Hov O., Schjoldager J. and Wathne B. M. (1983) Measurement and modeling of the concentrations of terpenes in coniferous forest air. *J. geophys. Res.*, **88**, 10,679-10,688.
- Izumi K., Murano K., Mizuochi M. and Fukuyama T. (1988) Aerosol formation by the photooxidation of cyclohexene in the presence of nitrogen oxides. *Environ. Sci. Technol.*, **22**, 1207-1214.
- Izumi K., Hatakeyama S., Fukuyama T. and Washida N. (1989) Aerosol formation by the reaction of α - or β -pinene with OH radicals. Presented in PACIFICHEM, December.
- Kamens R. M., Jeffries H. E., Gery M. W., Wiener R. W., Sexton K. G. and Howe G. B. (1981) The impact of α -pinene on urban smog formation: an outdoor smog chamber study. *Atmospheric Environment*, **15**, 969-981.
- Kamens R. M., Gery M. W., Jeffries H. E., Jackson M., and Cole E. I. (1982) Ozone-isoprene reactions: product formation and aerosol potential. *Int. J. Chemical Kinetics*, **14**, 955-975.
- Lamb B., Guenther A., Gay D. and Westberg H. (1987) A national inventory of

- biogenic hydrocarbon emissions. *Atmospheric Environment*, **21**, 1695-1705.
- Leone J. A., Flagan R. C., Grosjean D. and Seinfeld J. H. (1985) An outdoor smog chamber and modeling study of toluene-NO_x photooxidation. *Int. J. Chem. Kinet.*, **17**, 177-216.
- Palen E. J. and Allen D. T. (1989) Size distributions of organic and inorganic functional groups in ambient Los Angeles aerosol. *Abstracts of the 1989 Annual Meeting of the American Association for Aerosol Research*, **245**, Reno, NV.
- Peterson E. W. and Tingey D. T. (1980) An estimate of the possible contribution of biogenic sources to airborne hydrocarbon concentration. *Atmospheric Environment*, **14**, 79-81.
- Pilinis C., Seinfeld J. H. and Seigneur C. (1987) Mathematical modeling of the dynamics of multicomponent atmospheric aerosols. *Atmospheric Environment*, **21**, 943-955.
- Rader D. J. and McMurry P. H. (1986) Application of the TANDEM differential mobility analyzer to studies of droplet growth or evaporation. *J. Aeros. Sci.*, **17**, 771-787.
- Roberts J. M., Fehsenfeld F. C., Albritton D. L., and Sievers R. E. (1983) Measurement of monoterpene hydrocarbons at Niwot Ridge, CO. *J. geophys. Res.*, **88**, 10,667-10,678.
- Roberts J. M., Hahn C. J., Fehsenfeld F. C., Warnock J. M., Albritton D. L. and Sievers R. E. (1985) Monoterpene hydrocarbons in the nighttime troposphere. *Environ. Sci. Technol.*, **19**, 364-369.
- Stern J. E., Flagan R. C., Grosjean D. and Seinfeld J. H. (1987) Aerosol formation and growth in atmospheric aromatic hydrocarbon photooxidation. *Environ. Sci. Technol.*, **21**, 1224-1231.
- Tao Y. and McMurry P. H. (1989) Vapor pressures and surface free energies of

C14-C18 monocarboxylic acids and C5-dicarboxylic and C6-dicarboxylic acids.

Environ. Sci. Technol., **23**, 1519-1523.

Wang S. C. and Flagan R. C. (1990) Scanning Electrical Mobility Spectrometer.

Aerosol Sci. Technol., in press.

Went F. W. (1960) Blue hazes in the atmosphere, *Nature*, **187**, 641-643.

Winer A. M., Fitz D. R., Miller P. R., Atkinson R., Brown D. E., Carter W. P.

L., Dodd M. C., Johnson C. W., Myers M. A., Neisess K. P., Poe M. P. and

Stephens E. R. (1983) Investigation of the role of natural hydrocarbons in photochemical smog formation in California. Final report A0-056-32, California

Air Resources Board, Sacramento, CA.

Wolfenbarger J. K. and Seinfeld J. H. (1990) Inversion of aerosol size distribution

data. *J. Aeros. Sci.*, in press.

Zimmerman P. R. (1979) Testing for hydrocarbon emissions from vegetation leaf

litter and aquatic surfaces, and development of a methodology for compiling

biogenic emission inventories. EPA Report 450/4-4-79-004.

CHAPTER 8

CONCLUSIONS

Conclusions

The major contributions of this work have been the formulation and computational implementation of mathematical descriptions of the physicochemical processes associated with acid deposition and the improvement of our understanding of secondary organic aerosol formation in the atmosphere.

The modeling systems developed incorporate detailed descriptions of gas and aqueous-phase chemistry, mass transfer between the two phases, aerosol dynamics and thermodynamics, aqueous droplet microphysics, turbulent diffusion, source emissions, surface removal processes and development and dissipation of radiation fogs. Descriptions of the above processes have been included in three modules of varying complexity, starting from a highly parametrized to a model based entirely on first principles. Each of the three models developed in this work can constitute the core of an urban-scale acid deposition model. The choice of the desired level of modeling treatment of acid deposition will depend on the available computing resources, on the desired level of basic prediction and on the available input information from field measurements.

The performance of the radiation fog model (second level of treatment) has been evaluated by comparing predicted and observed values of atmospheric variables, gas and aqueous-phase concentrations, and acid deposition rates for a well documented radiation fog episode. The agreement was found satisfactory, but of course there is always space for improvement. Some of this improvement can be accomplished by the use of the most detailed model (third level of treatment). The evaluation of this model requires an enormous amount of information that has not been available up to this point. Nevertheless, this detailed model can assist in improving the assumptions and parametrizations used in the less detailed models.

At the same time, the use of all the above models has helped improve our under-

standing of the fundamental processes contributing to acid deposition. Examples of this improved understanding include the relative importance of the various gas- and aqueous-phase chemical pathways contributing to the formation of acidic species, the mass transfer between gas and aqueous phases, the importance of parameters like the liquid water content, the increase of deposition rates during fog episodes, the differences between fog and cloud environments, the influence of the cloud or fog life cycle on the aerosol concentration and size-composition distribution, the differences in composition between cloud or fog droplets of different sizes, the interaction between equilibration processes and wet or dry deposition, the nucleation scavenging of aerosol particles by a fog or cloud, and some of the difficulties associated with sampling fog or cloud water.

An extensive set of experiments on the formation and growth of secondary aerosol in biogenic hydrocarbon/ NO_x systems was carried out. Outdoor smog chamber experiments were performed in order to study the gas phase kinetics, aerosol forming potential and aerosol physics for isoprene and β -pinene. Simple box models were used for the investigation of the aerosol forming potential of the biogenic hydrocarbons under ambient conditions. Aerosol formation from the isoprene photooxidation was found to be negligible even under extreme ambient conditions due to the relatively high vapor pressure of its condensible products. Aerosol carbon yield from the β -pinene photooxidation was as high as 8% and depended strongly on the initial HC/ NO_x ratio. These results indicate that monoterpene photooxidation could be a significant source of secondary aerosol in rural environments and in urban areas with extended natural vegetation.

APPENDIX A

BRIEF DOCUMENTATION OF ACID DEPOSITION MODULES 1-3

Appendix A

Brief Documentation for Acid Deposition Modules 1-3

The three acid deposition modules have been developed to answer some specific fundamental questions concerning acid deposition. A user-friendly interface will be added later together with the full three-dimensional model. At this stage we would recommend that anyone intending to use the codes contact the authors.

The computational requirements of the three modules developed are compared against the CIT gas and aerosol trajectory models in Table I. It has been found that the CPU time required for any simulation is strongly dependent on the initial and boundary conditions and can be in extreme cases even an order of magnitude different from the CPU times indicated in Table I. All the three modules (AQDRIVER, FOGMOD, DROPCHEM) have not yet been optimized for minimum computing time requirements and there is undoubtedly room for improvement.

A short description of the computer programs necessary for the three modules, as well as of the input and output files is given below.

Module 1

Purpose

Simulation of aqueous-phase chemistry in a homogeneous parcel of air containing water droplets (fog or cloud).

Reference

S. N. Pandis and J. H. Seinfeld, Sensitivity analysis of a chemical mechanism for aqueous-phase atmospheric chemistry, *J. Geophys. Res.*, **94** 1105-1126, 1989.

Main Input Variables

- Liquid Water Content.
- Droplet Radius.
- Temperature.
- Initial gas and aqueous-phase concentrations.

Main Output Variables

- Gas-phase species concentrations.
- Aqueous-phase species concentrations.

List of Programs

1. AQDRIVER.COM

Command File used for the test problem.

2. AQDRIVER.FOR

The driver used for the test program. It contains all the necessary input data.

3. AQCHEM.FOR

The main code for Module 1. It simulates the aqueous-phase chemistry for any number of computational cells for a prescribed period of time. Therefore it can be

used as a box model (1 computational cell), included in an n level trajectory model (n computational cells), or in a three-dimensional eulerian model.

4. VARIABL.FOR

Fortran code that is 'INCLUDE'd in several subroutines. It contains the number of computational cells for which the simulation will be performed.

5. AQSUB.FOR

Collection of subroutines called by the main code.

6. INTEGRB.FOR

The hybrid integrator used for the integration of the stiff ODEs of the model.

This module requires the use of subroutines from the IMSL library.

Input Files

All the input variables are included in the driving program AQDRIVER.FOR.

Output Files

AQRES.DAT

Contains all the gas-phase concentrations, aqueous-phase concentrations of main species (e.g., S(IV), S(VI), N(V), N(III), etc.) and the concentrations of ionic species (e.g., H^+ , HSO_3^- , SO_3^{2-} , NO_2^- , etc.).

Module 2

Purpose

Simulation of acid deposition due to radiation fog using parametrized droplet microphysics.

Reference

S. N. Pandis and J. H. Seinfeld, Mathematical modeling of acid deposition due to radiation fog, *J. Geophys. Res.*, **94**, 12,911-12,923, 1989.

Main Input Variables

- Initial temperature vertical profile.
- Initial relative humidity vertical profile.
- Initial gas concentrations vertical profile.
- Initial aerosol concentration profile.
- Average droplet diameter.
- Emission Inventory for NO_x , HC, SO_2 , NH_3 , etc.
- Wind speed.

Main Output Variables

- Liquid water content vertical profile for radiation fog.
- Relative humidity vertical profile.
- Temperature vertical profile.
- Fog height.
- Gas-phase concentrations vertical profiles.
- Aqueous-phase concentrations vertical profiles.
- Deposition rates of all ionic species.

List of Programs

1. FOGMOD.COM

Command File used for the test problem.

2. FOGMOD.FOR

Main program.

3. GASOPER.FOR

The operator for gas-phase chemistry (see reference for description).

4. AQOPER.FOR

The operator for aqueous-phase chemistry (see reference for description).

5. FOGOPER.FOR

The operator for the fog development and dissipation (see reference for description).

6. VARIABL.FOR

Fortran code that is 'INCLUDE'd in several subroutines.

7. MODLSPC.FOR

Fortran code that is 'INCLUDE'd in several subroutines.

8. RADCOM.FOR

Fortran code that is 'INCLUDE'd in the radiation subroutines.

9. FOGSUB1.FOR

Collection of subroutines called by the gas-phase operator.

10. FOGSUB2.FOR

Collection of subroutines called by the aqueous-phase operator.

11. FOGSUB3.FOR

Collection of subroutines called by the fog operator.

12. INTEGRB.FOR

Subroutine for the integration of stiff ODEs.

This module requires the use of subroutines from the IMSL library.

Input Files

1. ACIDE221.MOD

Standard file with the parameters of the gas-phase mechanism.

2. ACIDE221.RXP

Standard file with the parameters for the lumped species of the gas-phase mechanism.

3. INCON.DAT

Initial aqueous-phase concentration profiles.

4. INDAT.DAT

Initial conditions for the radiation fog.

5. INGAS.DAT

Initial values for gas species that are not treated by the gas-phase operator.

6. INMET.DAT

Concentrations of Fe^{3+} , Mn^{2+} , Na^+ .

7. INSPEC.DAT

Initial gas-phase concentrations, emission inventory and wind speed.

8. OPTIN.DAT

Standard data file for atmospheric radiation calculations (it should never be changed).

Output Files

SJV.DAT

Contains all the output information.

Module 3

Purpose

Simulation of the changes in the size-composition distribution of aqueous droplets as a result of water condensation on the aerosol particles and of chemical changes in the gas and aqueous-phases inside a spatially homogeneous air parcel (fog or cloud).

References

1. S. N. Pandis, J. H. Seinfeld and C. Pilinis, On the relation between the size and composition of fog and cloud droplets and the size and composition of atmospheric aerosol (presented at the *82nd APCA Annual Meeting*, Anaheim, California, June 1989).

2. S. N. Pandis, J. H. Seinfeld and C. Pilinis, Chemical composition differences in fog and cloud droplets of different sizes (accepted for publication in *Atmospheric Environment* June 1989).

Main Input Variables

- Temperature as a function of time.
- Initial relative humidity.
- Initial gas concentrations.
- Initial size distribution of the aerosol sulfate and sodium.

Main Output Variables

- Liquid water content of fog or cloud.
- Relative humidity.
- Water droplet and aerosol size-composition distributions.
- Gas phase concentrations.

List of Programs

1. DROPCHEM.COM

Command File used for the test problem.

2. DROPLET.FOR

Main program.

3. DGASOPER.FOR

The operator for gas-phase chemistry.

4. CLOUD2.FOR

Part of the aerosol dynamics and thermodynamics operators (see references for description).

5. CLOUD3.FOR

Part of the aerosol dynamics and thermodynamics operators (see references for description).

6. CLOUD4.FOR

Part of the aerosol dynamics and thermodynamics operators (see references for description).

7. CLOUD5.FOR

Part of the aerosol dynamics and thermodynamics operators (see references for description).

8. VARIABL.FOR

Fortran code that is 'INCLUDE'd in several subroutines.

9. DROPVAR.FOR

Fortran code that is 'INCLUDE'd in several subroutines.

10. DROPVAR1.FOR

Fortran code that is 'INCLUDE'd in several subroutines.

11. DROPVAR2.FOR

Fortran code that is 'INCLUDE'd in several subroutines.

12. MODLSPC.FOR

Fortran code that is 'INCLUDE'd in several subroutines.

13. DROPSUB1.FOR

Collection of subroutines called by the gas-phase operator (see references for description).

14. DROPSUB2.FOR

Collection of subroutines used for the aqueous phase chemistry calculations

15. RATES.FOR

Subroutine for the calculation of rates of change of droplet diameters and aqueous-phase concentrations.

16. TRANS.FOR

Subroutine that performs the necessary changes for the activation of the aqueous-phase operator.

17. SPRINT.FOR

Subroutines for the output of information.

This module requires the use of subroutines from the IMSL library.

Input Files

1. DINSPEC.DAT

Contains the initial gas phase concentrations.

2. ACIDE221.MOD

Standard file with the parameters of the gas-phase mechanism.

3. ACIDE221.RXP

Standard file with the parameters for the lumped species of the gas-phase mecha-

nism.

4. The rest of the necessary input (temperature variation, initial relative humidity and initial aerosol sulfate and sodium distributions) are included in DROPLET.FOR and RATES.FOR.

Output Files

1. DATGAS.DAT

Contains all the gas phase concentrations. Used for Plotting.

2. H2O2.DAT

Contains the aqueous-phase concentration of H_2O_2 . Used for Plotting.

3. HCHO.DAT

Contains the aqueous-phase concentration of HCHO. Used for Plotting.

4. HCl.DAT

Contains the aqueous-phase concentration of HCl. Used for Plotting.

5. HCOOH.DAT

Contains the aqueous-phase concentration of HCOOH. Used for Plotting.

6. HSO5.DAT

Contains the aqueous-phase concentration of HSO_5^- . Used for Plotting.

7. MASSEC.DAT

Contains the total solute mass in every size section. Used for Plotting.

8. MGAS.DAT

Contains the main gas phase concentrations. Used for Plotting.

9. NH3.DAT

Contains the aqueous-phase concentration of NH_3 . Used for Plotting.

10. NIIL.DAT

Contains the aqueous-phase concentration of HNO_2 . Used for Plotting.

11. NV.DAT

Contains the aqueous-phase concentration of HNO_3 . Used for Plotting.

12. RATSEC.DAT

Contains the total solute concentration in every size section. Used for Plotting.

13. SEC7-60.DAT

Contains the mass of every species in every section. Used for debugging purposes.

14. SEC7-70.DAT

Contains the aqueous-phase concentrations of every species in every section. Used for debugging purposes.

15. SIV.DAT

Contains the aqueous-phase concentration of S(IV). Used for Plotting.

16. SVI.DAT

Contains the aqueous-phase concentration of S(VI). Used for Plotting.

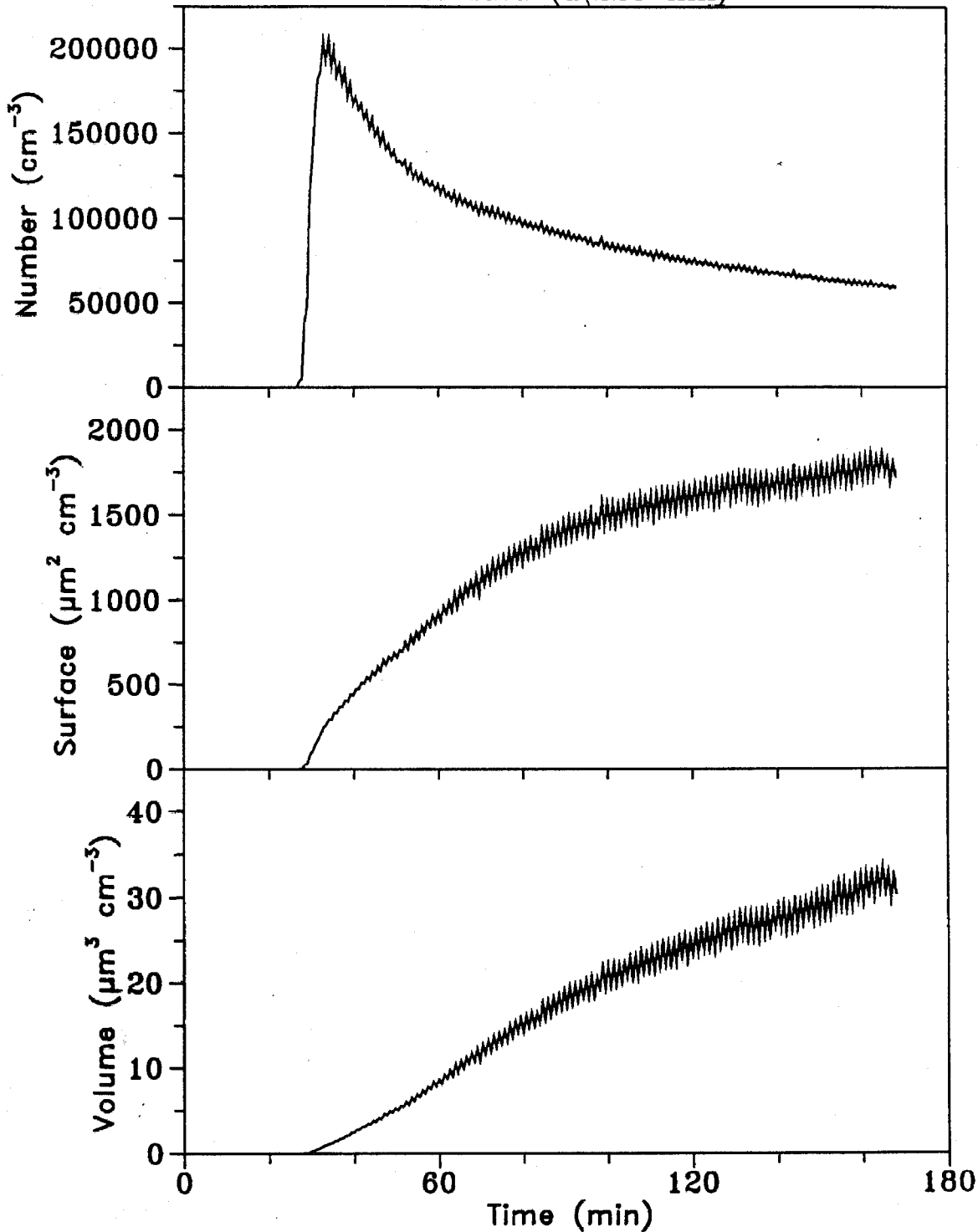
17. ACIDE221.DOC

Optional documentation of the gas-phase mechanism used in the module.

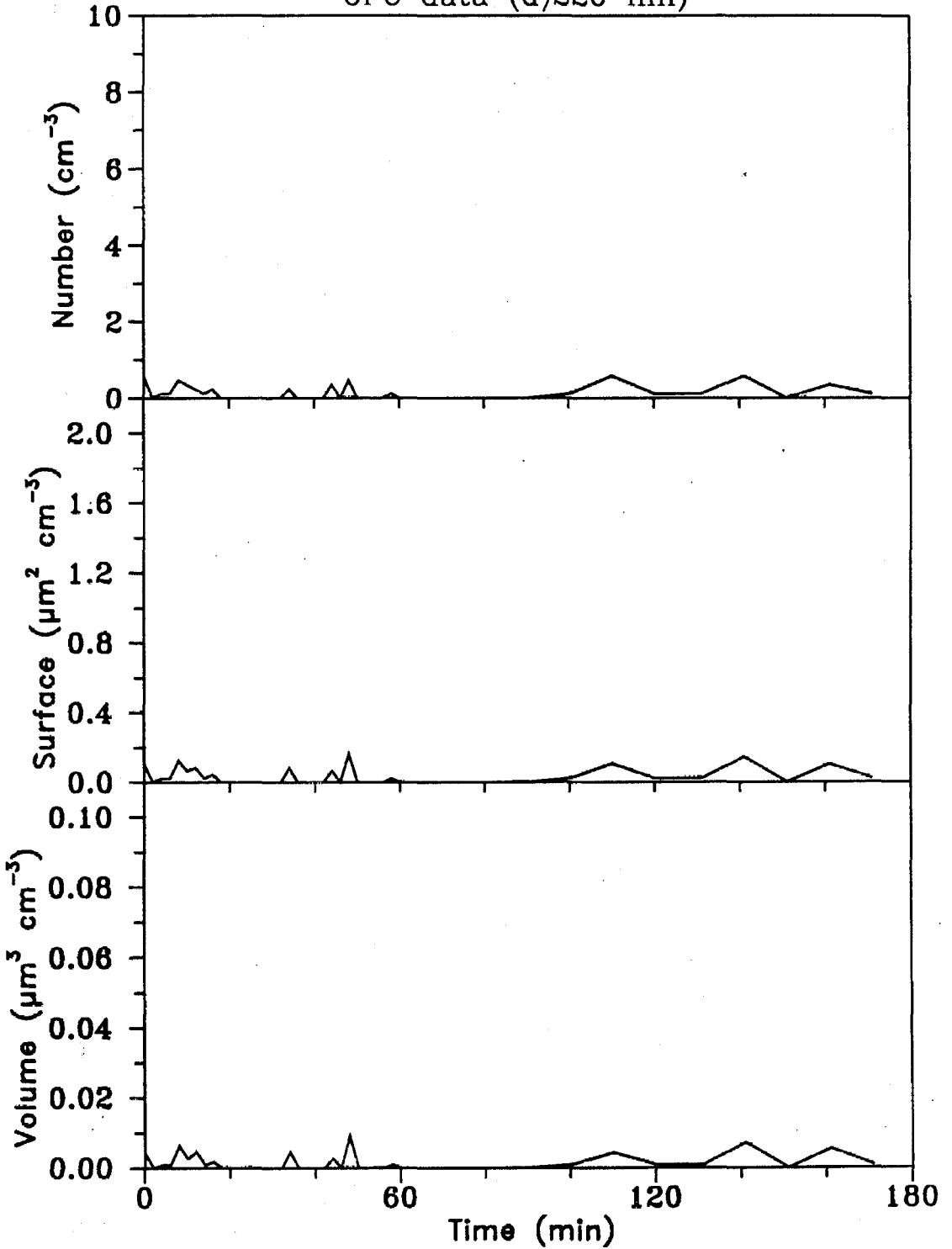
APPENDIX B

PLOTS OF SMOG CHAMBER AEROSOL DATA

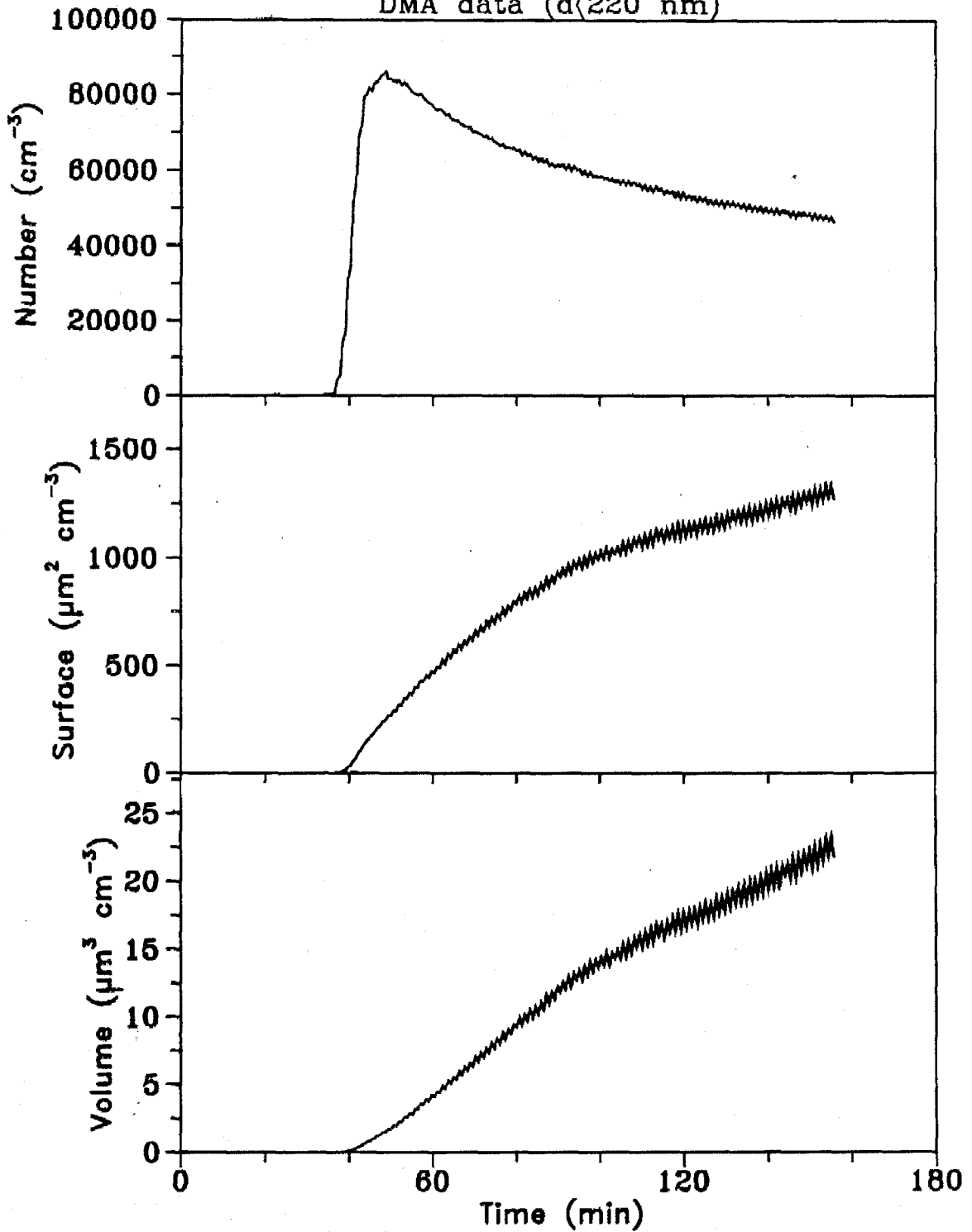
Experiment ISOA23
0.73 ppm isoprene, 0.07 ppm NO_x
DMA data (d < 220 nm)



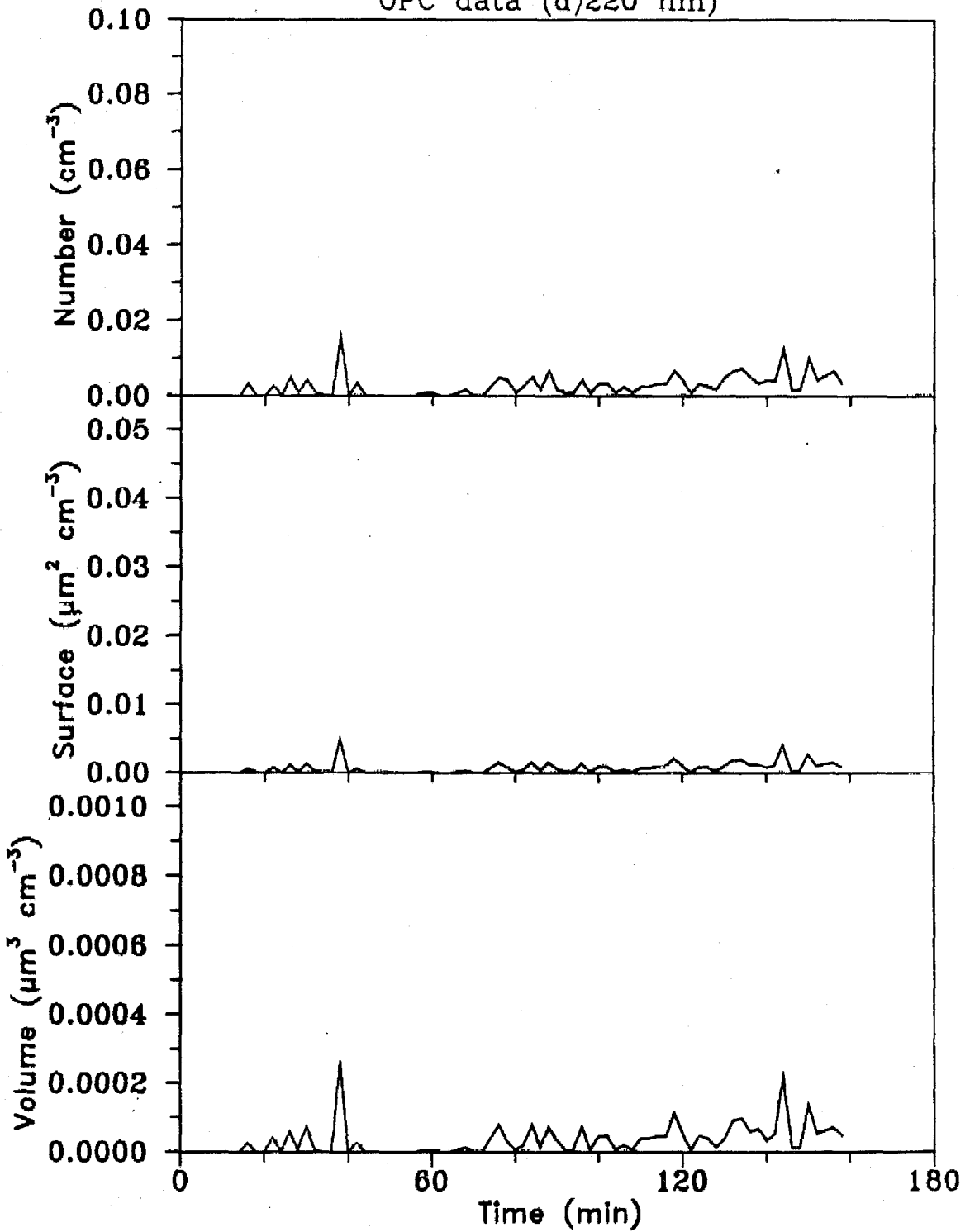
Experiment ISOA23
0.73 ppm isoprene, 0.070 ppm NO_x
OPC data (d)220 nm



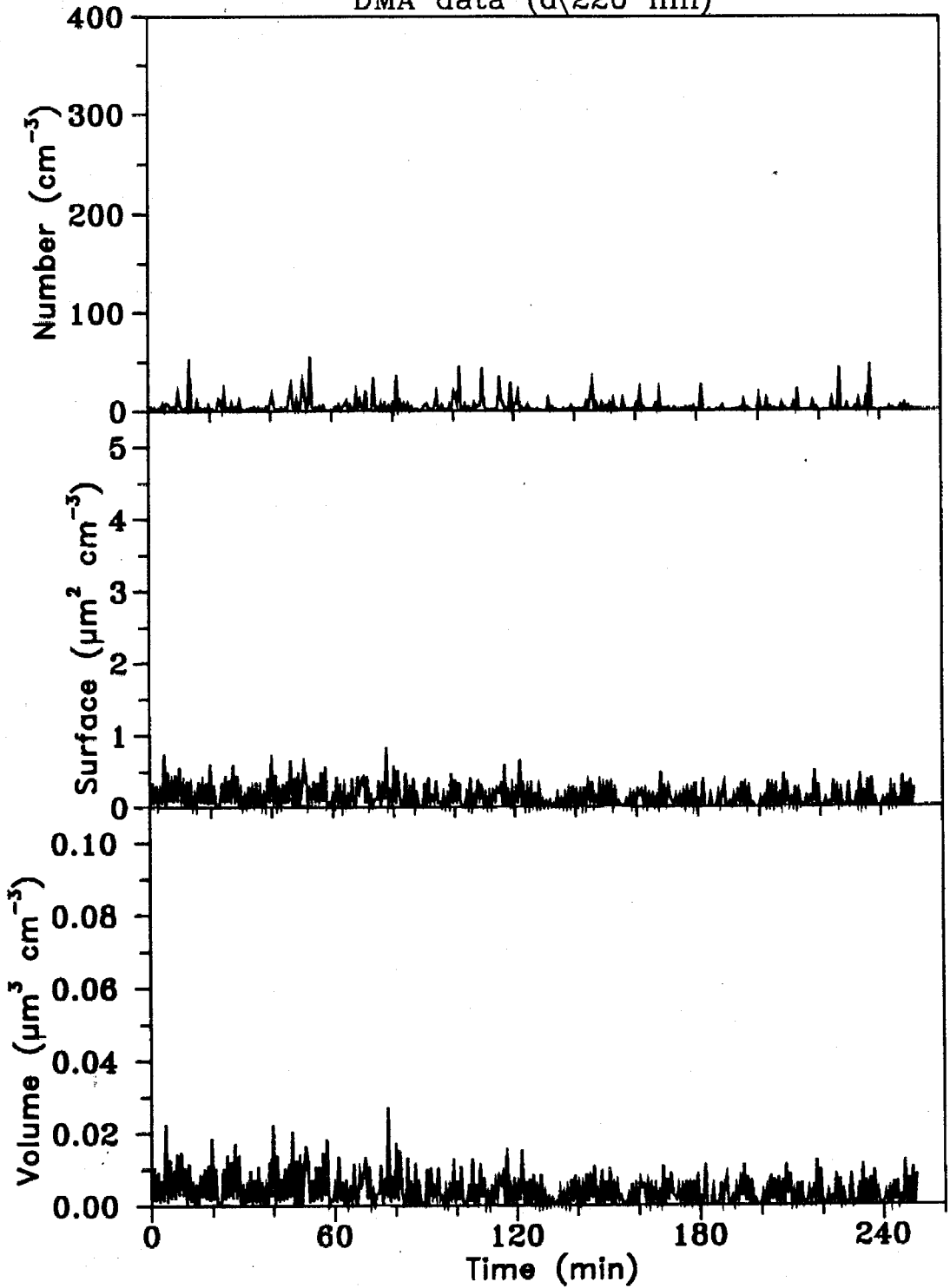
Experiment ISOA25
1.04 ppm isoprene, 0.245 ppm NO_x
DMA data (d < 220 nm)



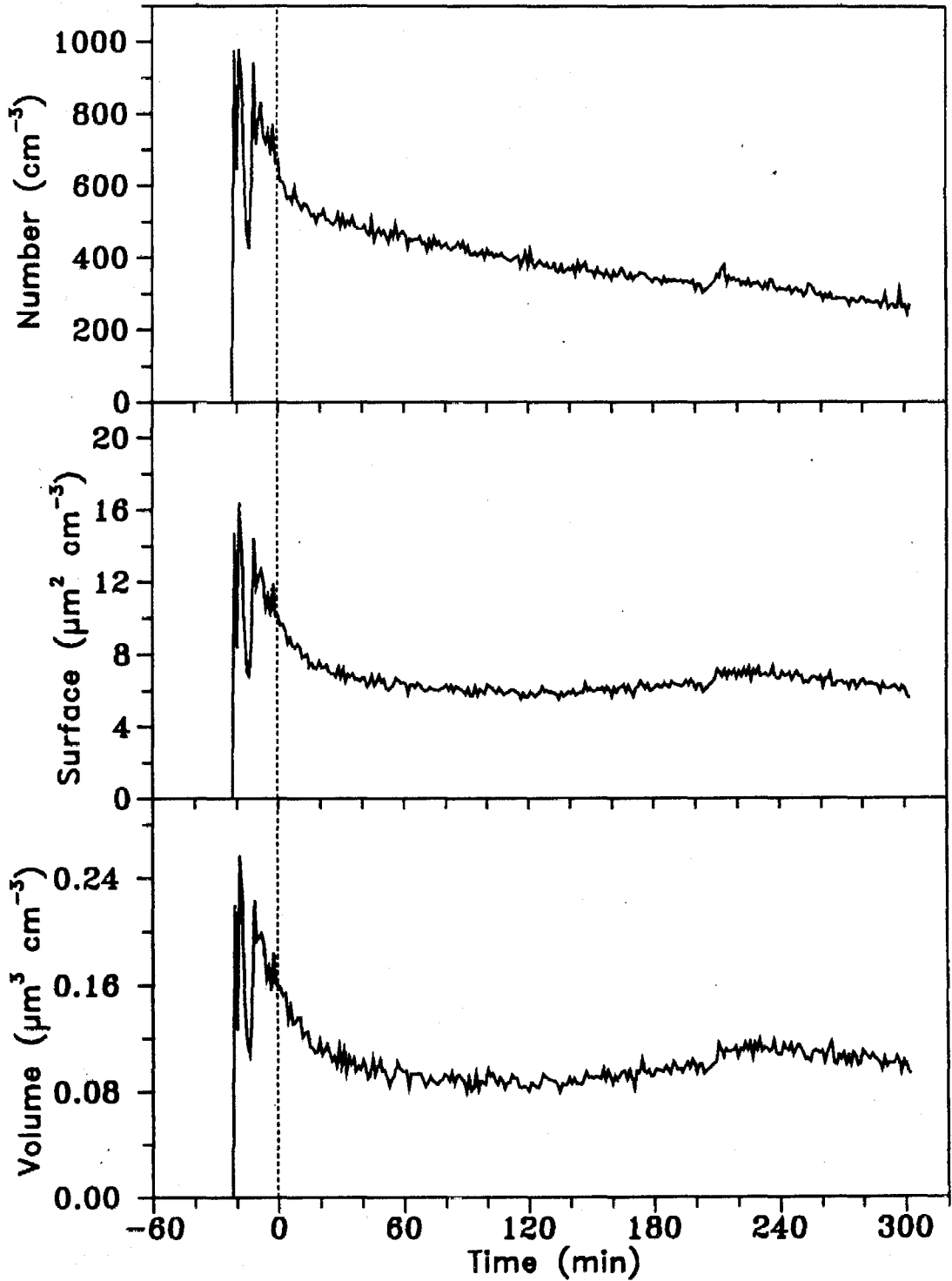
Experiment ISOA25
1.04 ppm isoprene, 0.245 ppm NO_x
OPC data (d)220 nm)



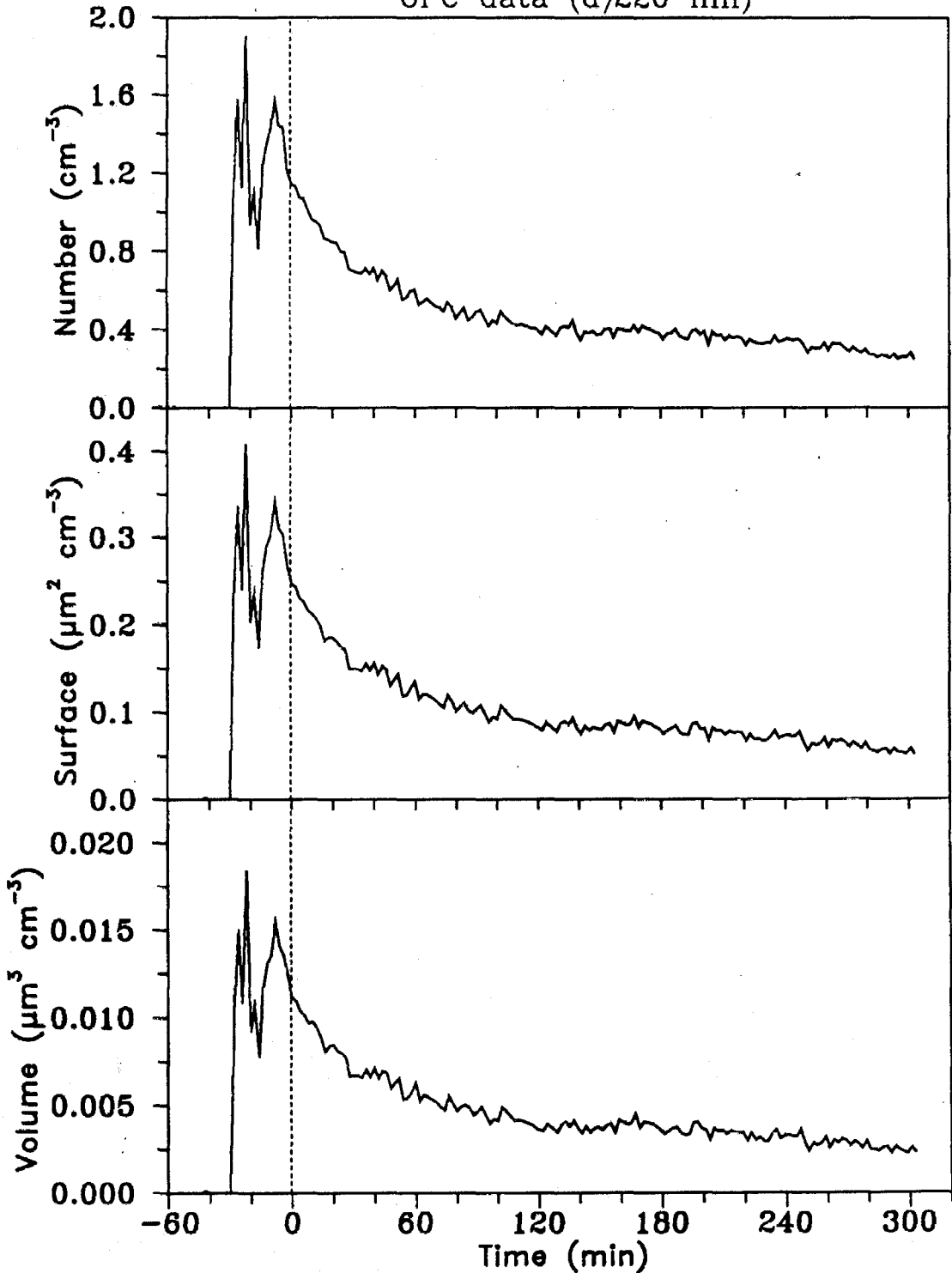
Experiment ISOA27
0.12 ppm isoprene, 0.223 ppm NO_x
DMA data (d(220 nm))



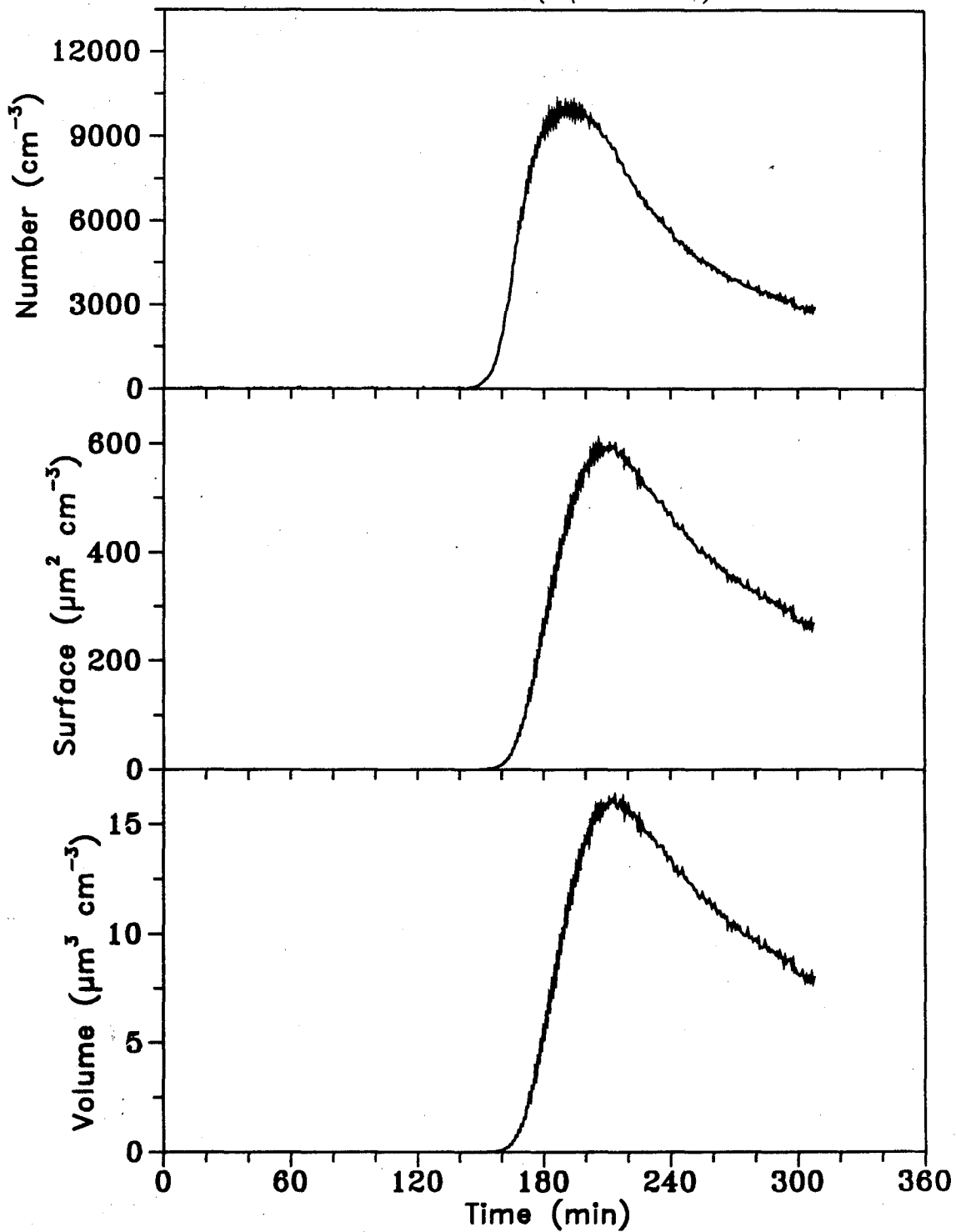
Experiment ISOA29
0.07 ppm isoprene, 0.122 ppm NO_x, seed particles
DMA data (d(220 nm))



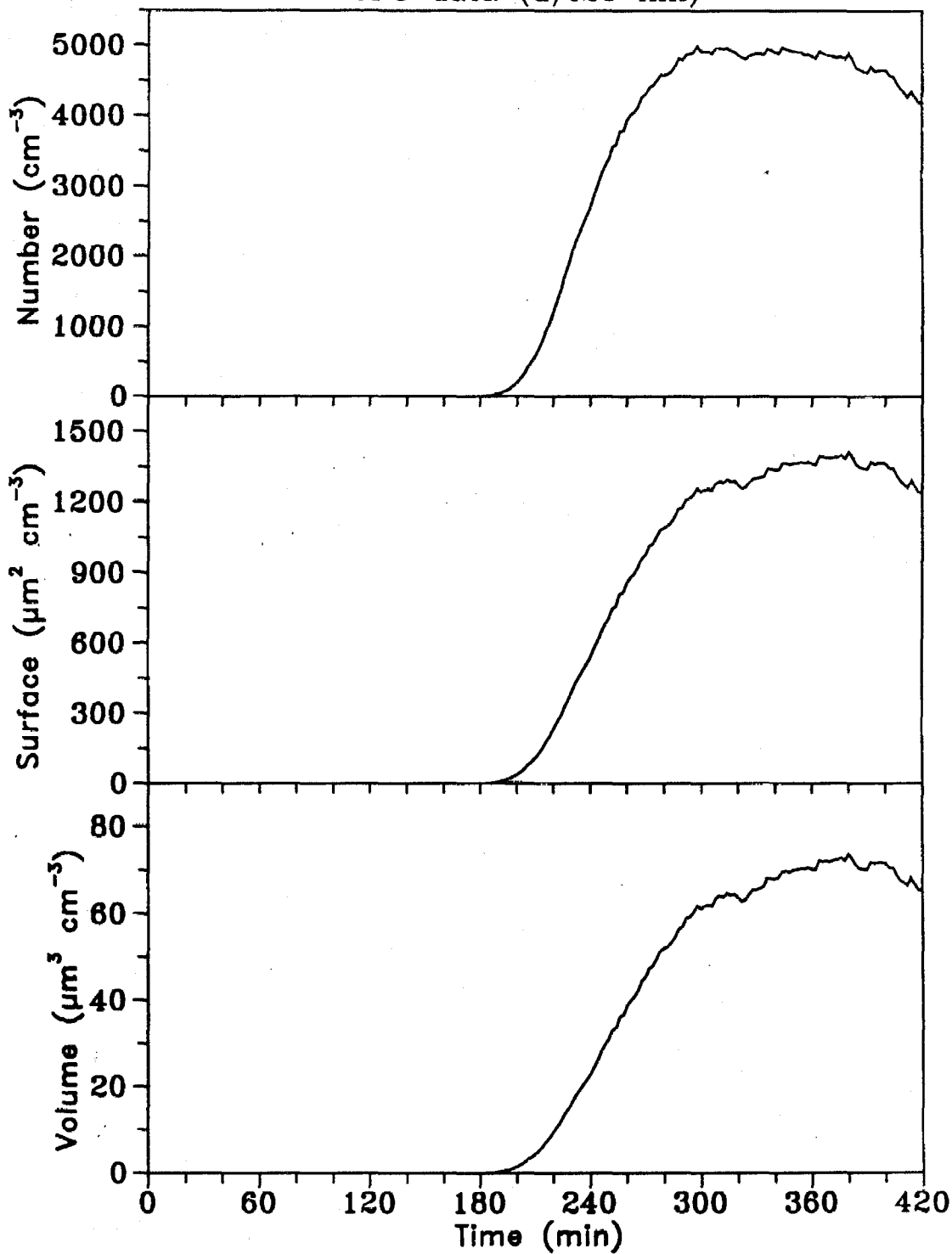
Experiment ISOA29
0.07 ppm isoprene, 0.122 ppm NO_x, seed particles
OPC data (d > 220 nm)



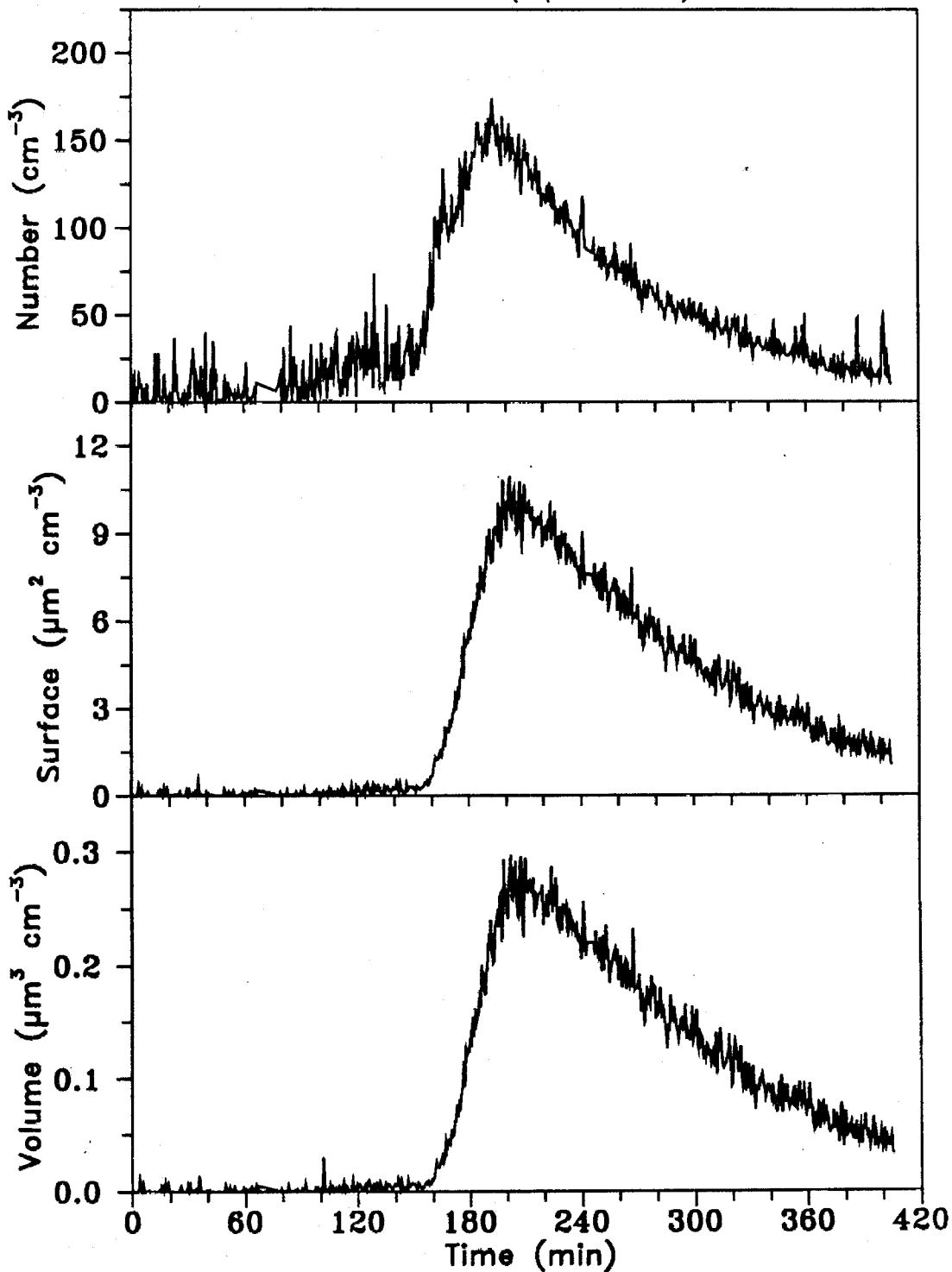
Experiment BPIA31
0.164 ppm β -pinene, 0.217 ppm NO_x
DMA data ($d \approx 220 \text{ nm}$)



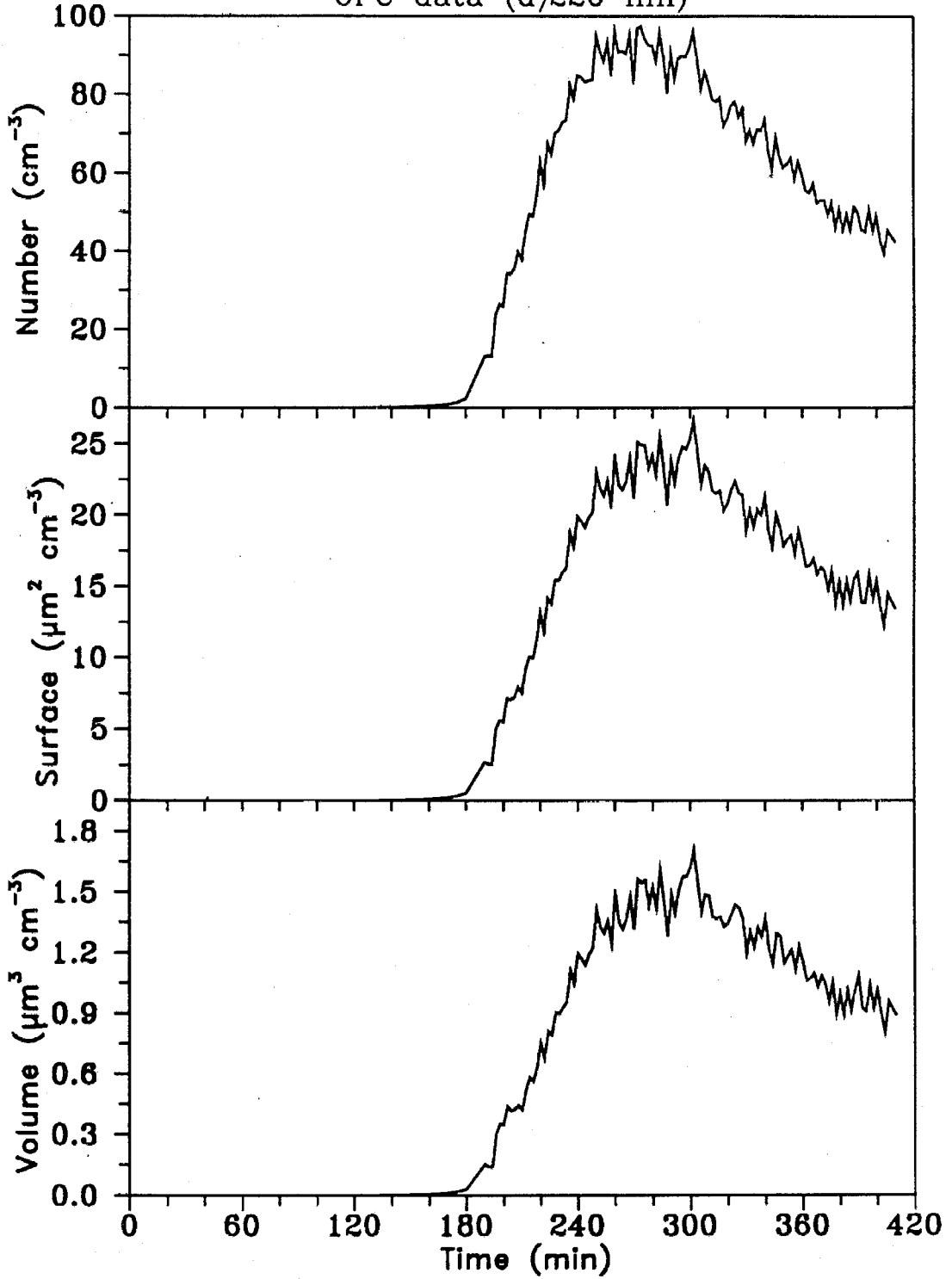
Experiment BPIA31
0.164 ppm β -pinene, 0.217 ppm NO_x
OPC data ($d \geq 220$ nm)



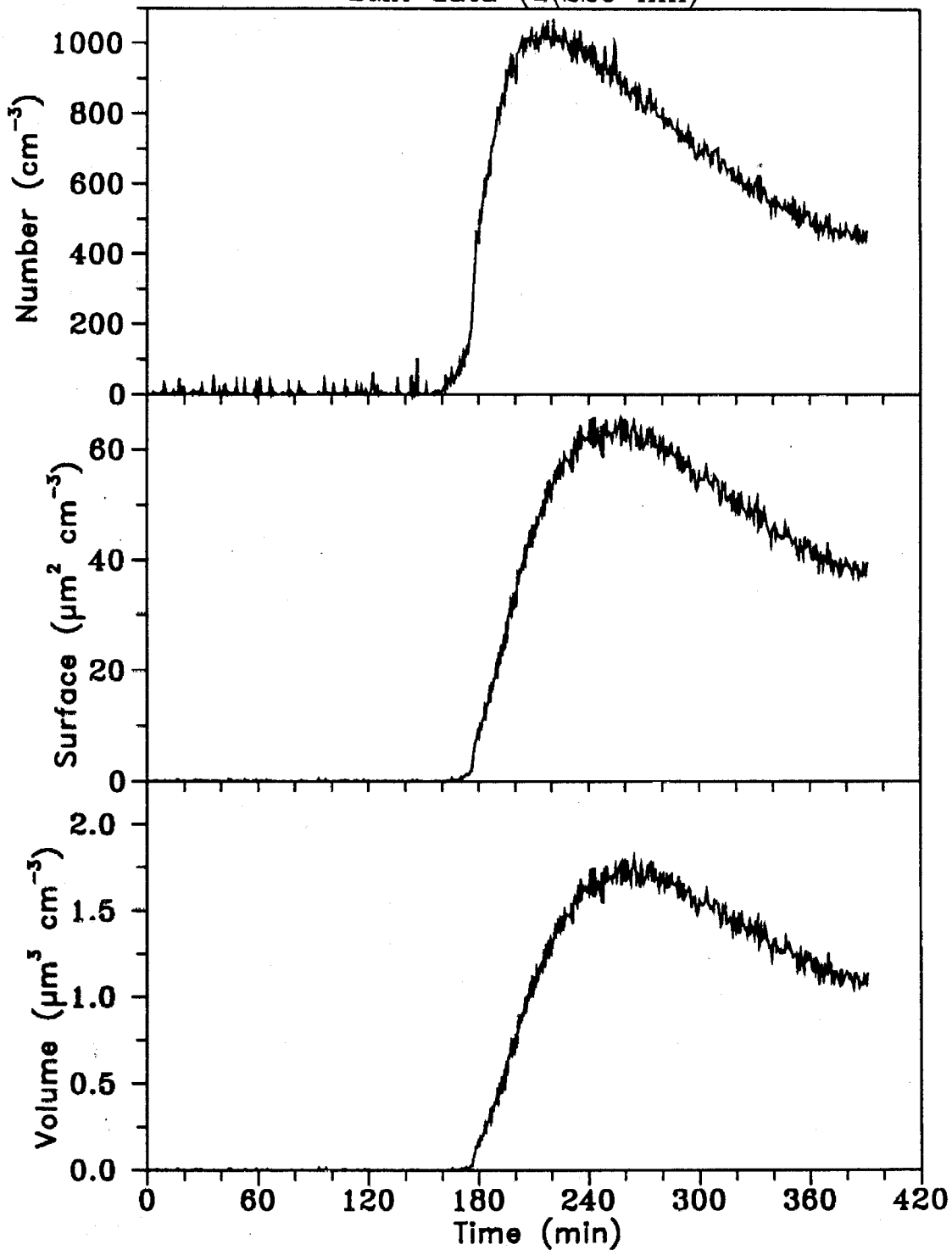
Experiment BPIS4
0.067 ppm b-pinene, 0.204 ppm NO_x
DMA data (d < 220 nm)



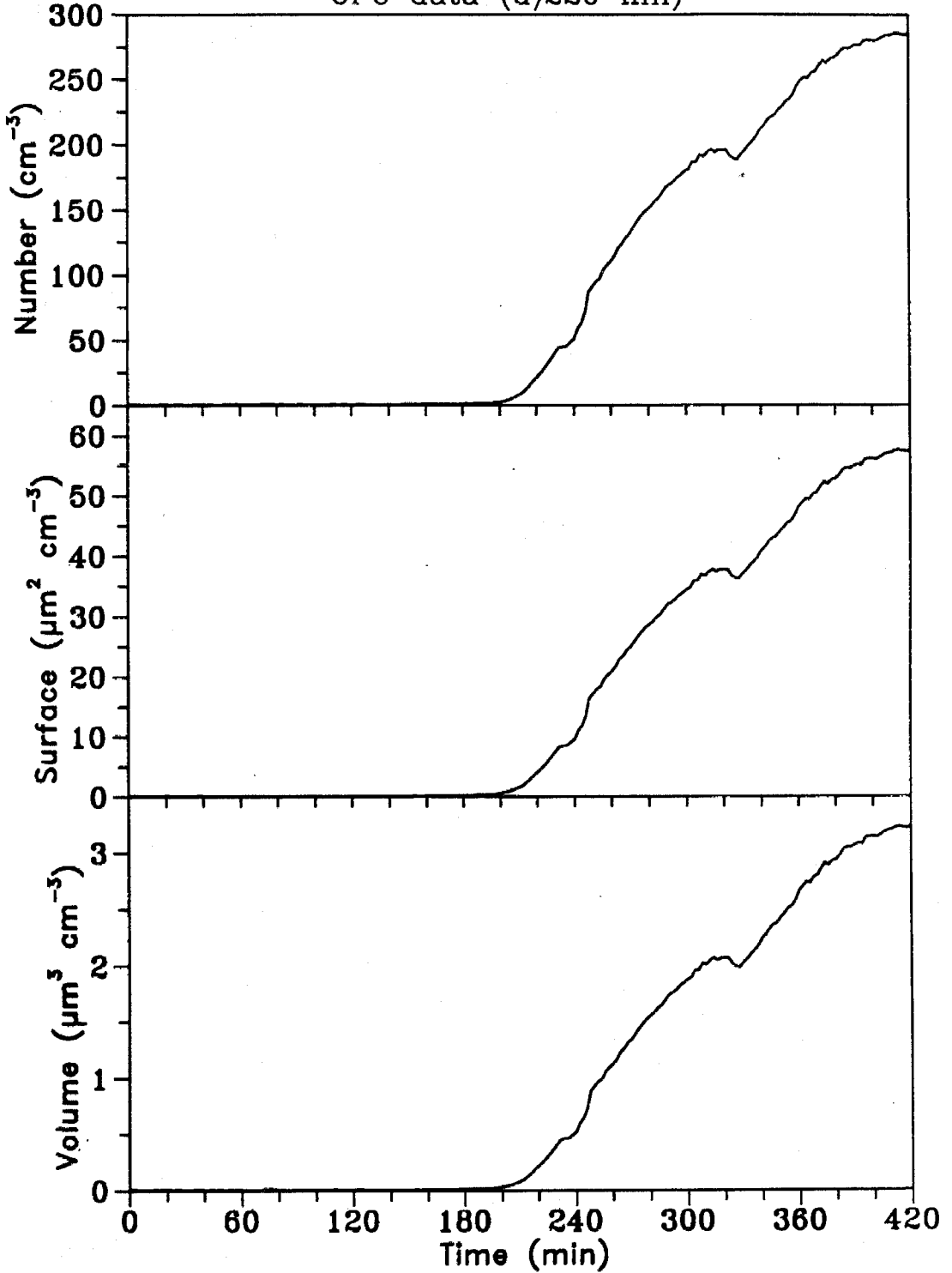
Experiment BPIS4
0.067 ppm β -pinene, 0.204 ppm NO_x
OPC data (d)220 nm



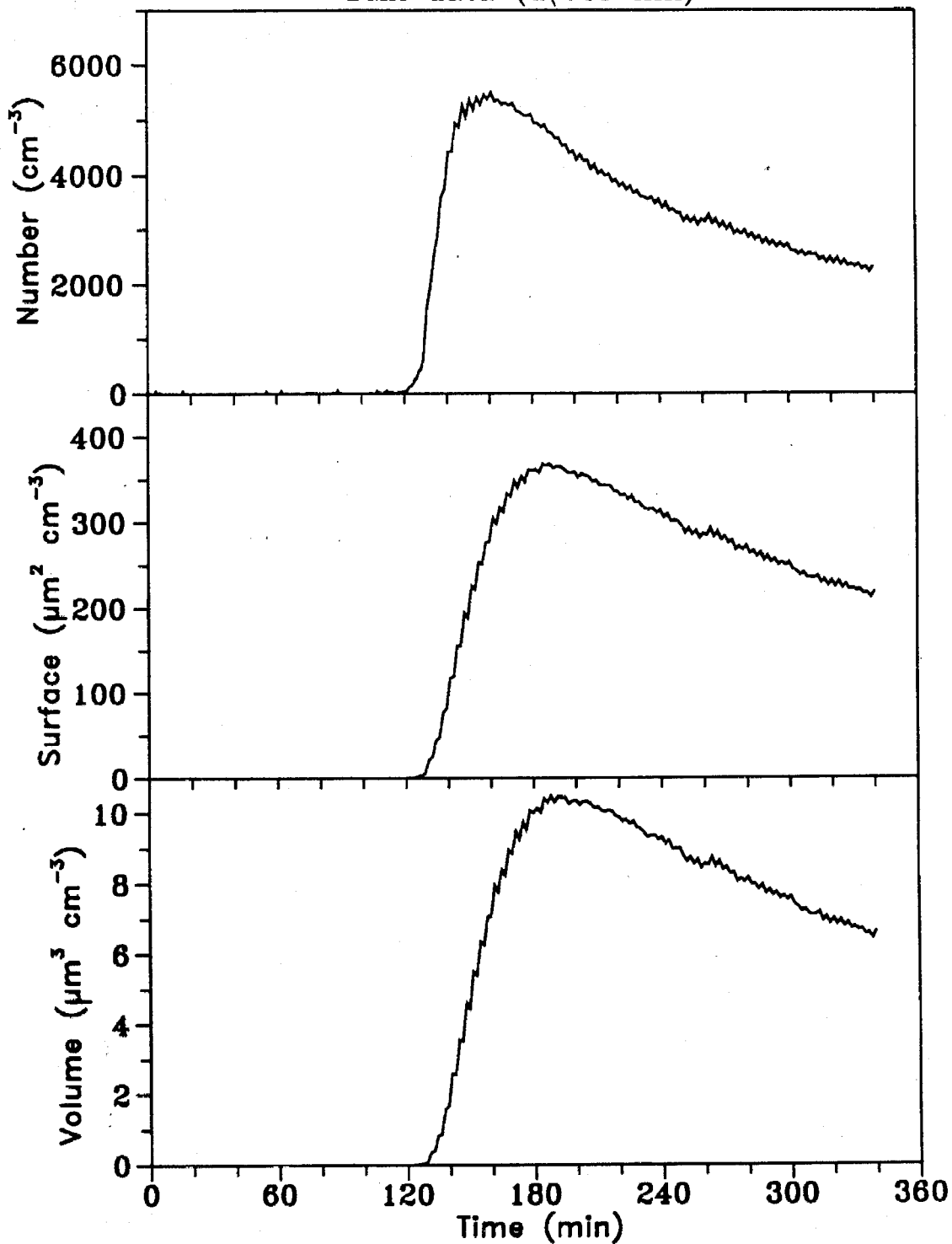
Experiment BPIS7
0.063 ppm β -pinene, 0.172 ppm NO_x
DMA data ($d \approx 220$ nm)



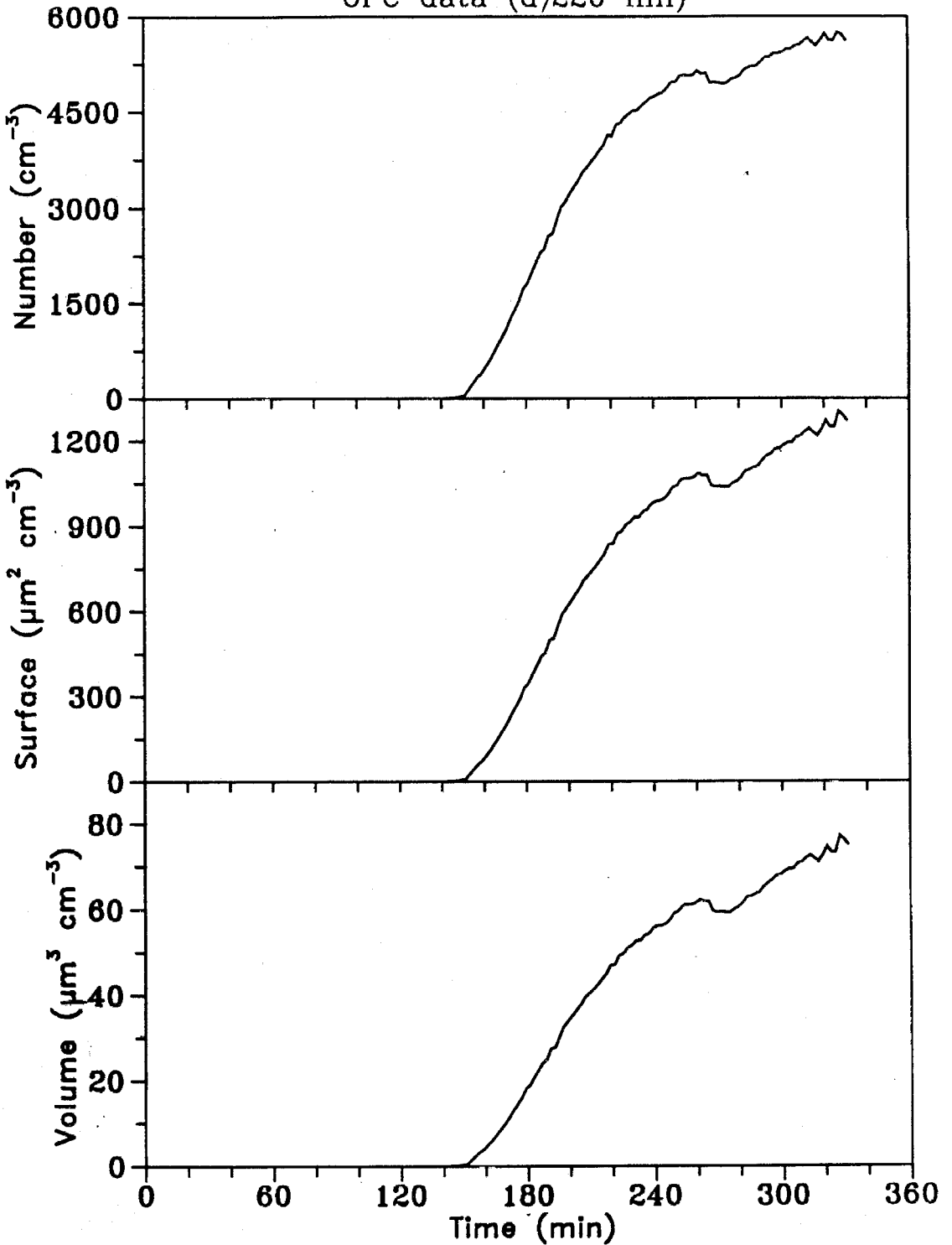
Experiment BPIS7
0.063 ppm β -pinene, 0.172 ppm NO_x
OPC data (d)220 nm



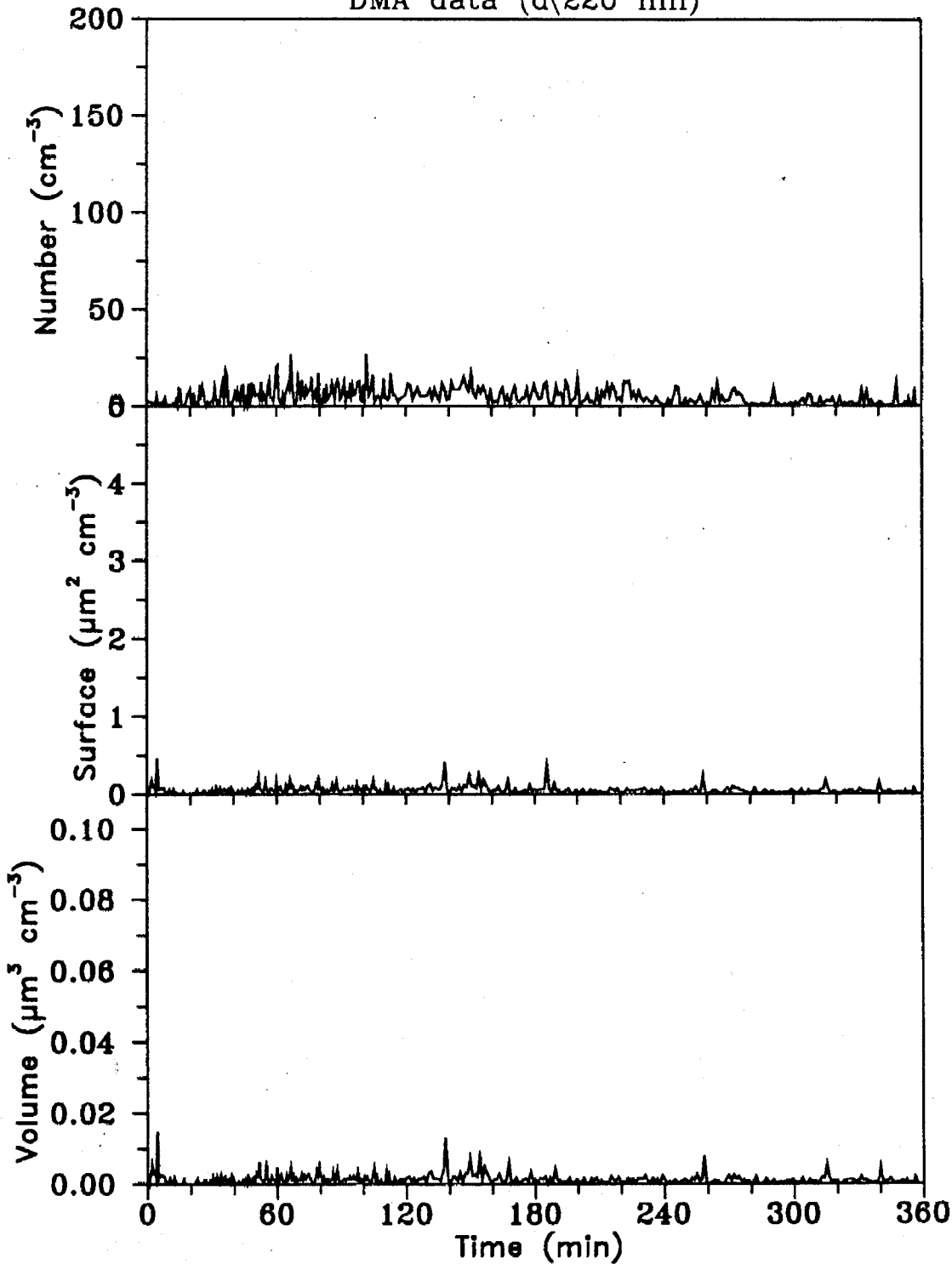
Experiment BPIS10
0.129 ppm β -pinene, 0.066 ppm NO_x
DMA data ($d(220 \text{ nm})$)



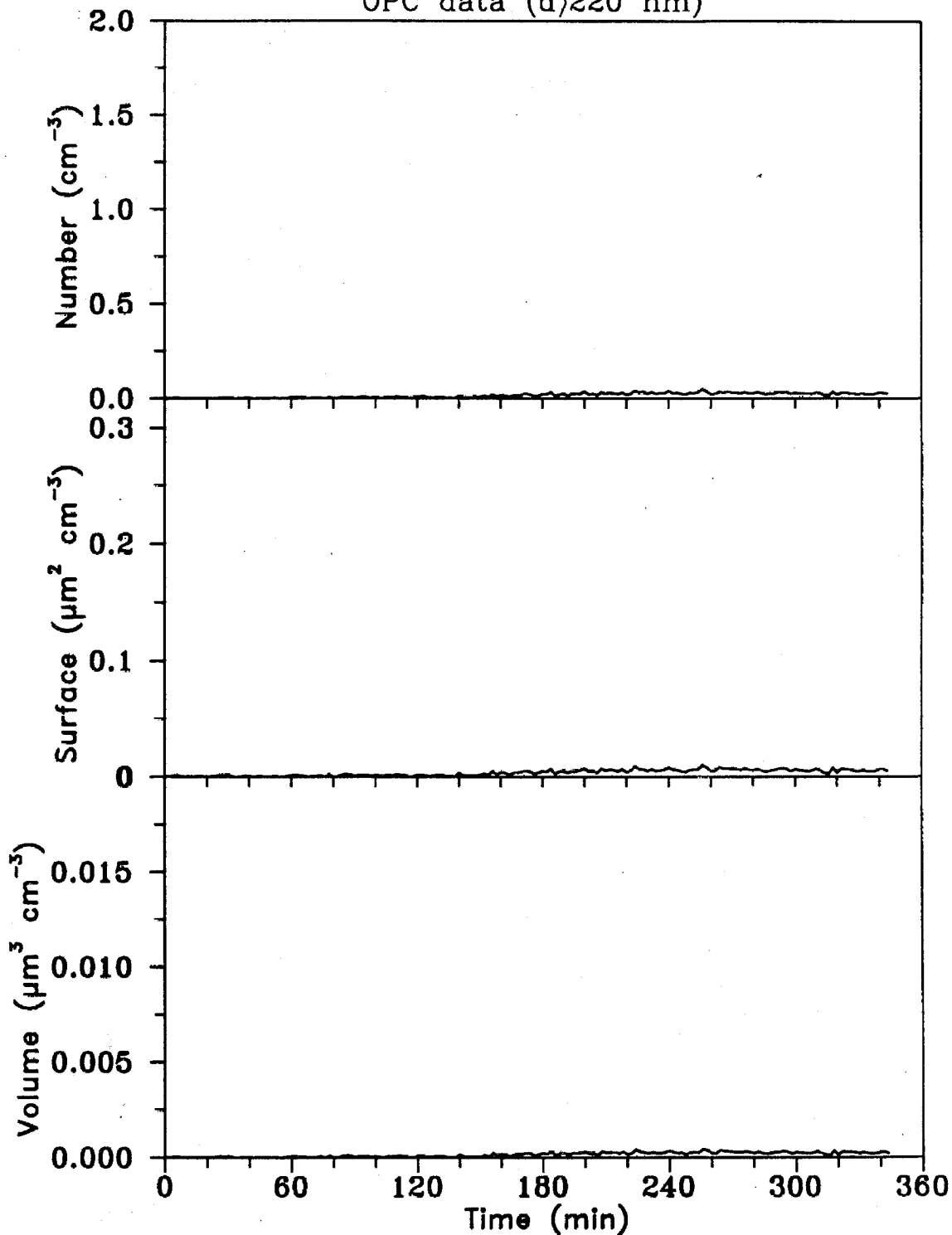
Experiment BPIS10
0.129 ppm b-pinene, 0.066 ppm NO_x
OPC data (d)220 nm



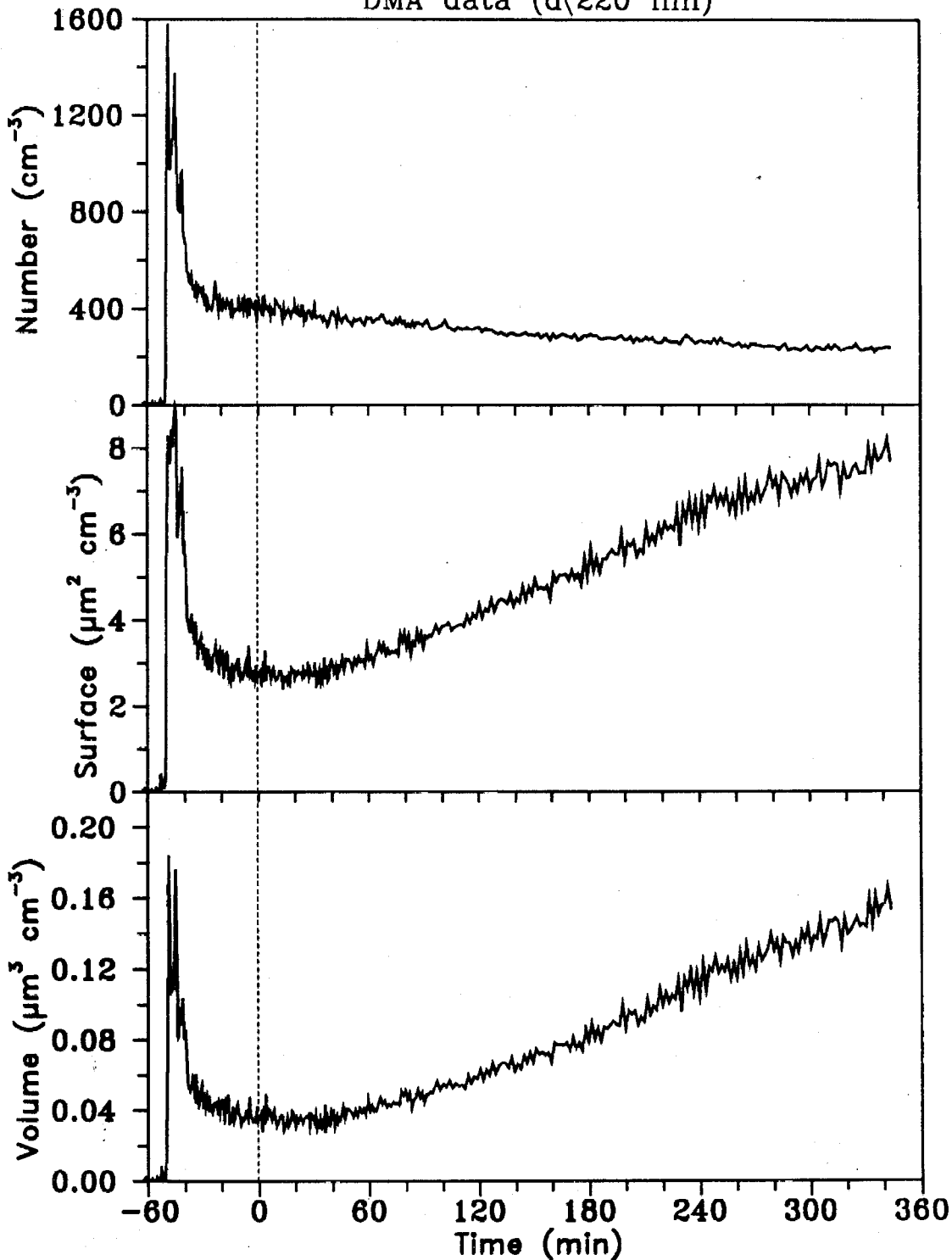
Experiment BPIS13
0.036 ppm b-pinene, 0.055 ppm NO_x
DMA data (d < 220 nm)



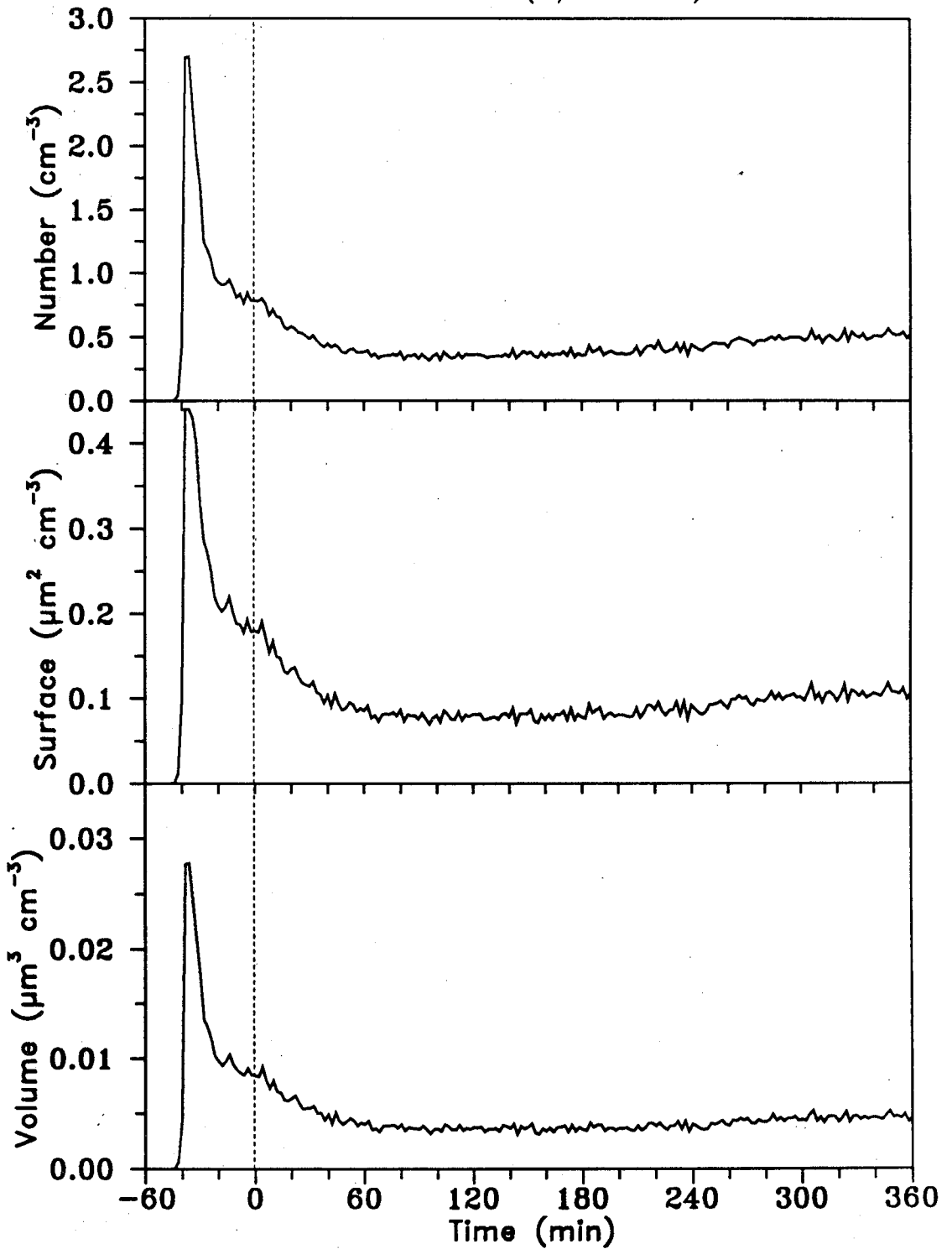
Experiment BPIS13
0.036 ppm β -pinene, 0.055 ppm NO_x
OPC data (d)220 nm



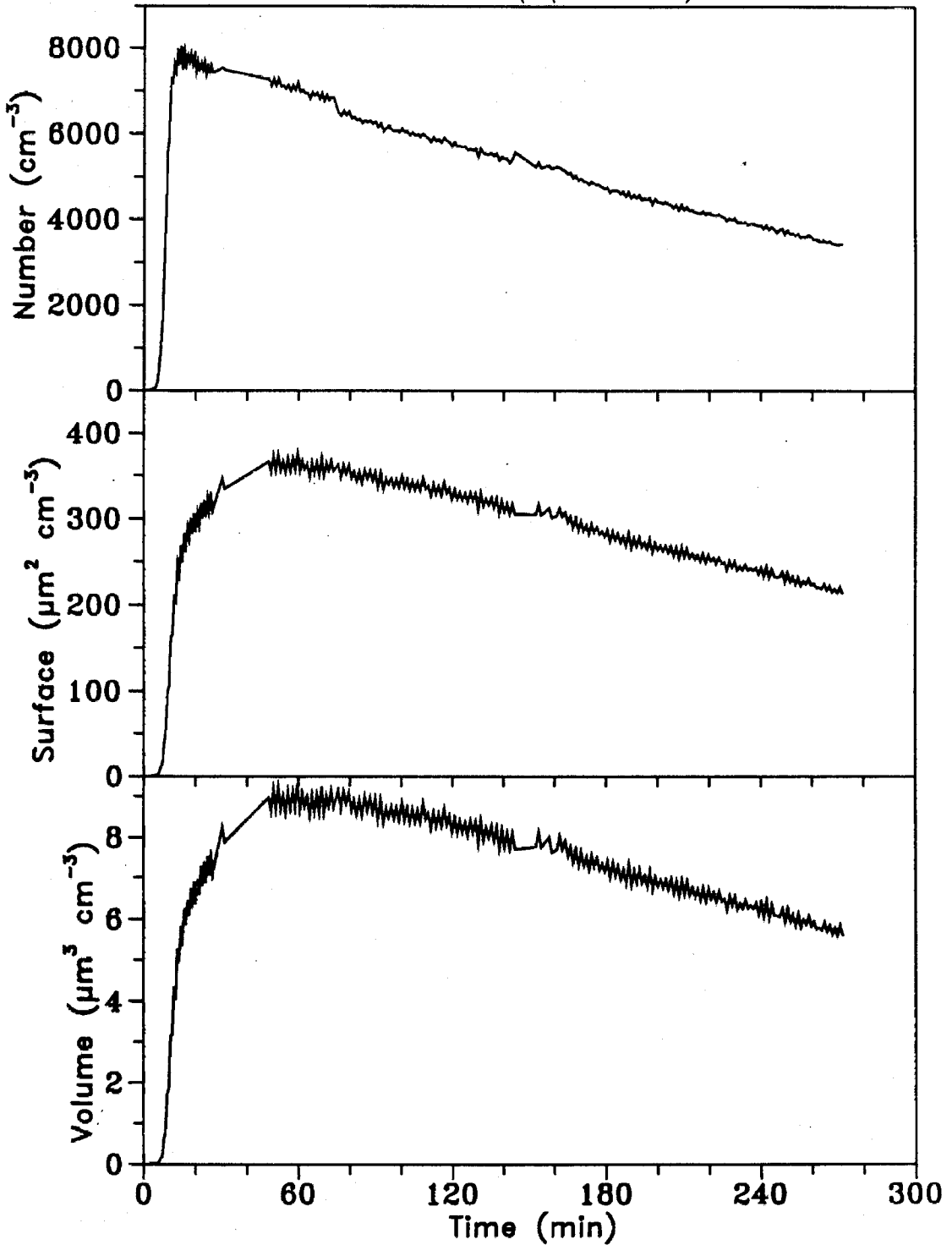
Experiment BPIS 20
0.028 ppm b-pinene, 0.130 ppm NO_x, seed particles
DMA data (d < 220 nm)



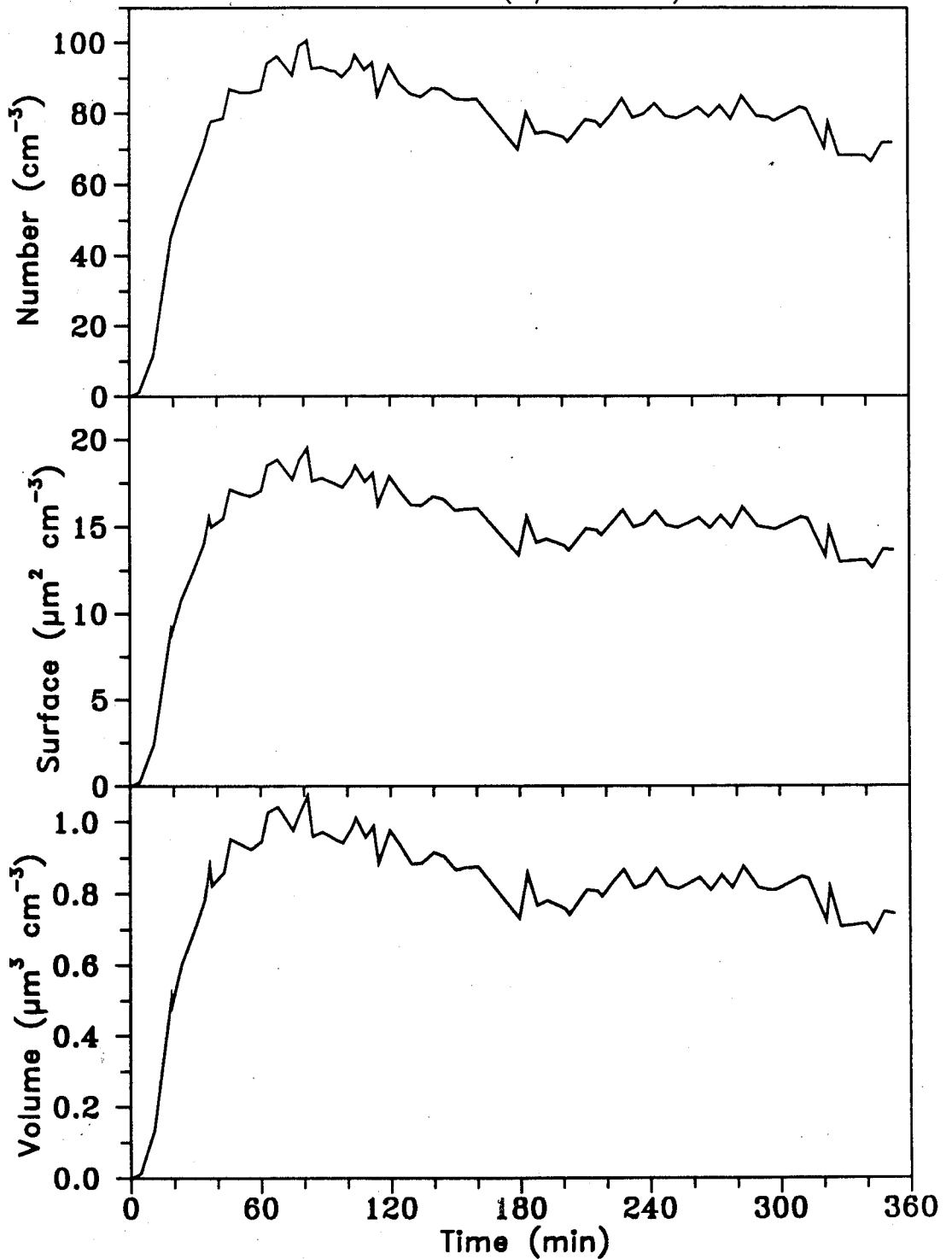
Experiment BPIS20
0.028 ppm b-pinene, 0.130 ppm NO_x, seed particles
OPC data (d)220 nm)



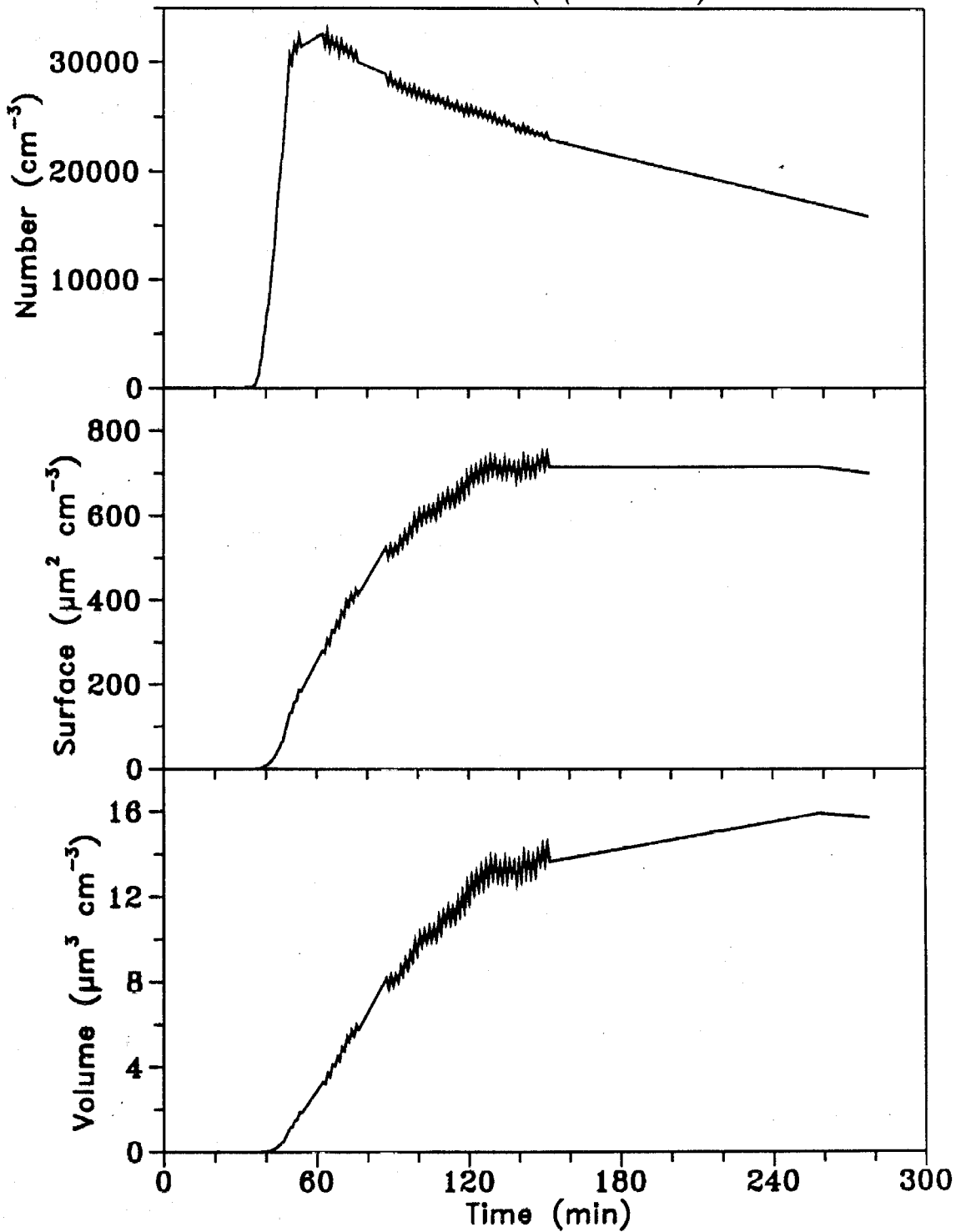
Experiment BPIS23
0.092 ppm β -pinene, 1.800 ppm NO_x
DMA data ($d < 220 \text{ nm}$)



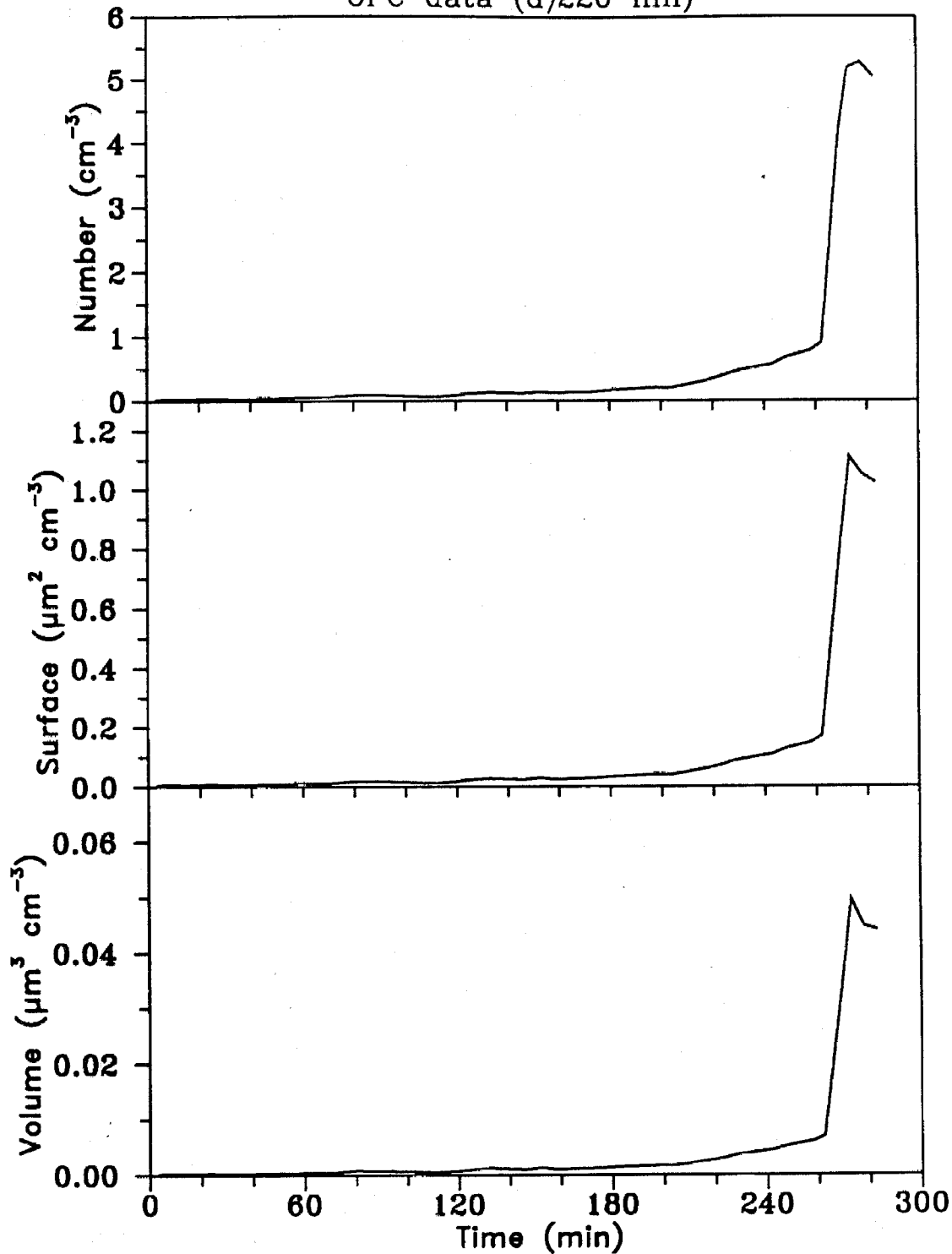
Experiment BPIS23
0.082 ppm b-pinene, 1.800 ppm NO_x
OPC data (d)220 nm



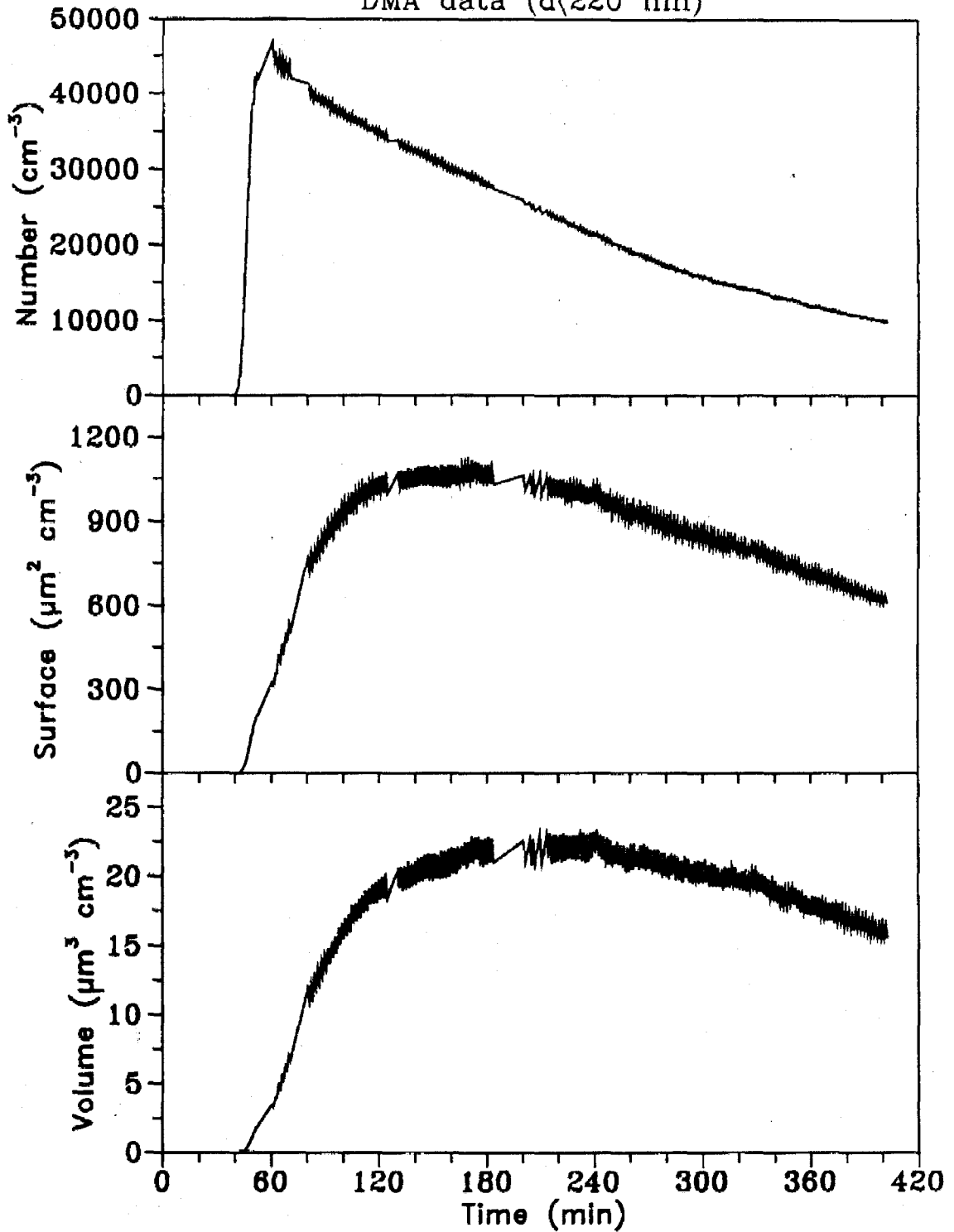
Experiment ISOS27
1.950 ppm isoprene, 0.238 ppm NO_x
DMA data (d < 220 nm)



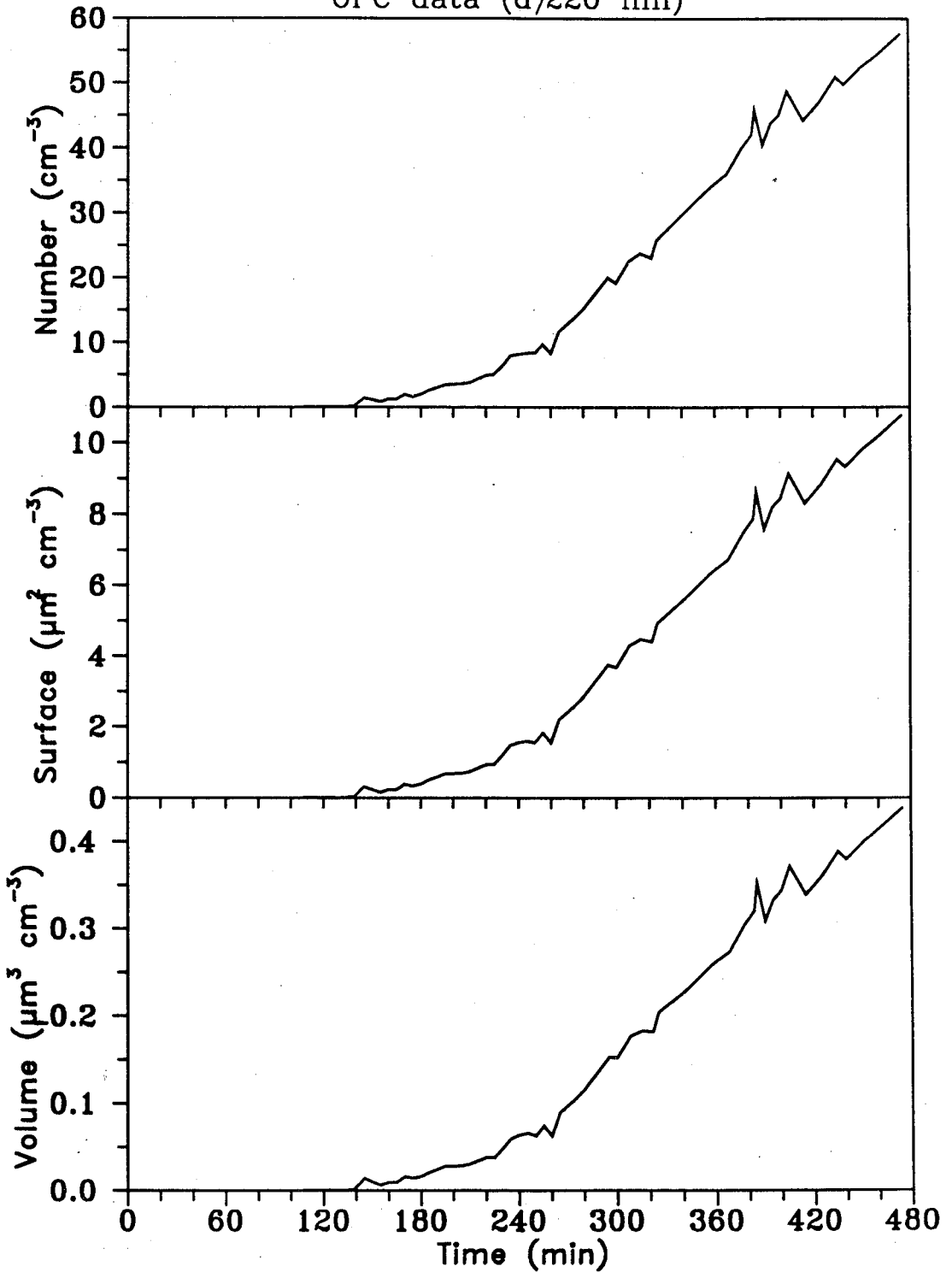
Experiment ISOS27
1.950 ppm isoprene, 0.238 ppm NO_x
OPC data (d)220 nm



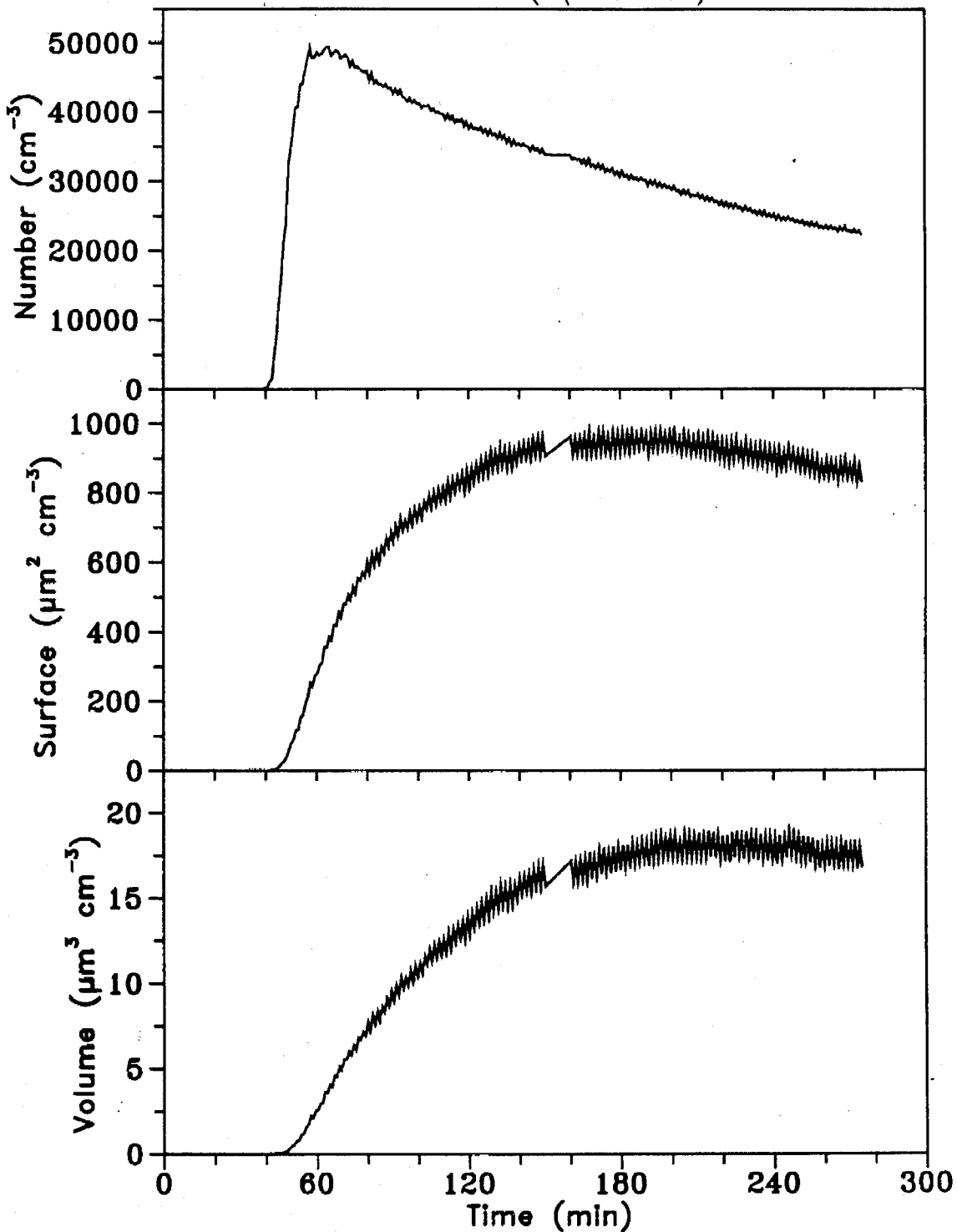
Experiment ISOS30
2.200 ppm b-pinene, 0.240 ppm NO_x
DMA data (d(220 nm))



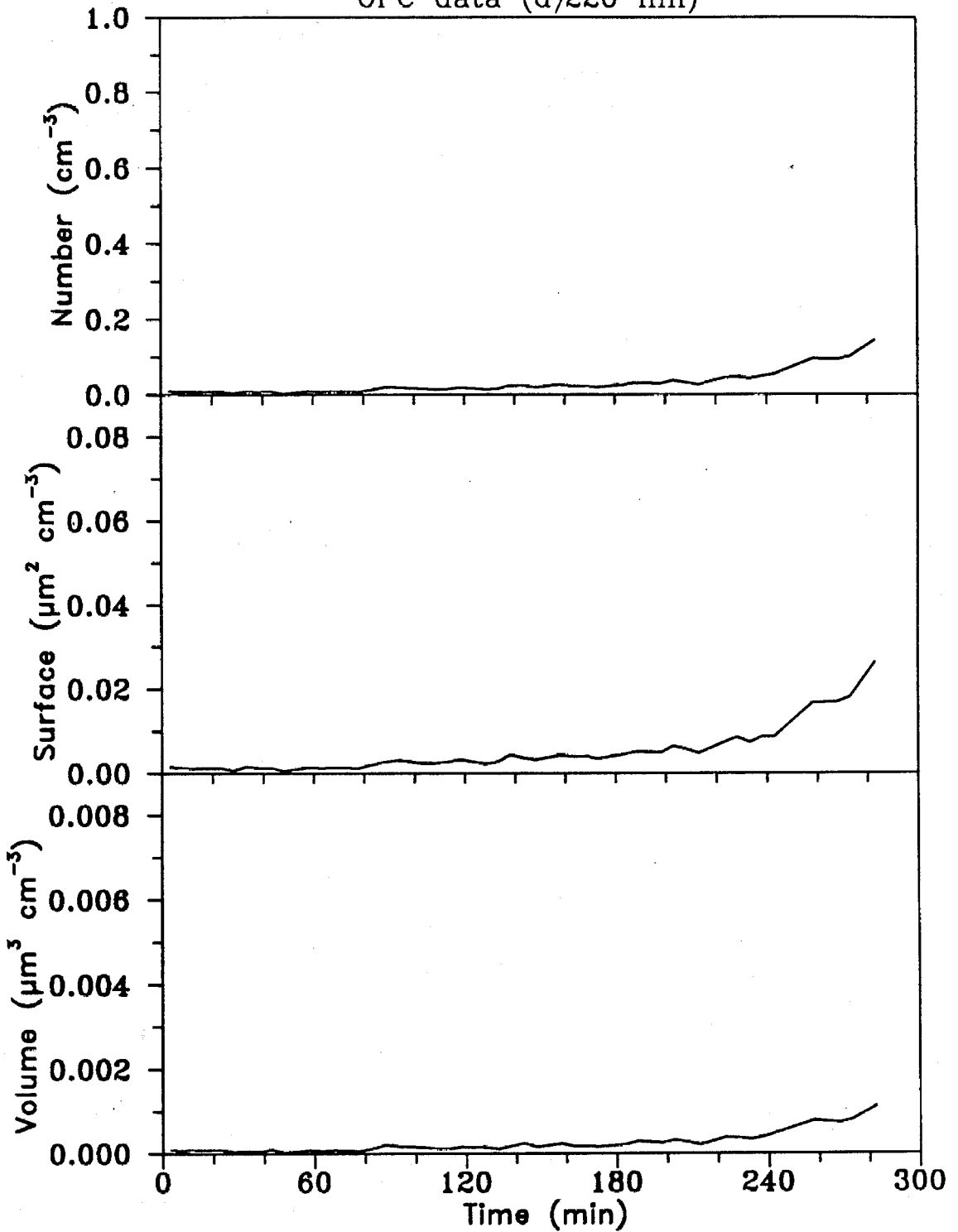
Experiment ISOS30
2.200 ppm isoprene, 0.240 ppm NO_x
OPC data (d)220 nm)



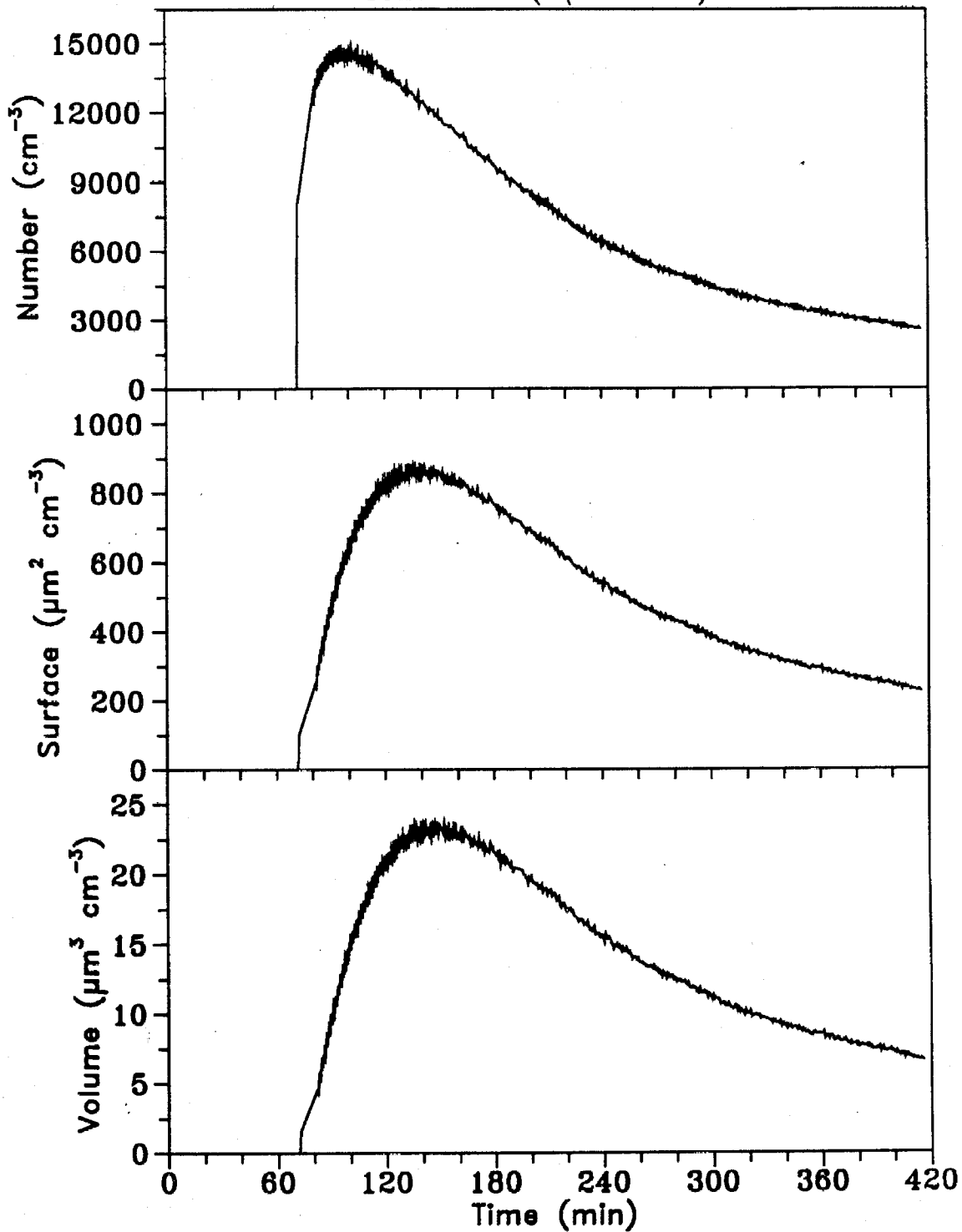
Experiment IS004
1.350 ppm isoprene, 0.320 ppm NO_x
DMA data (d<220 nm)



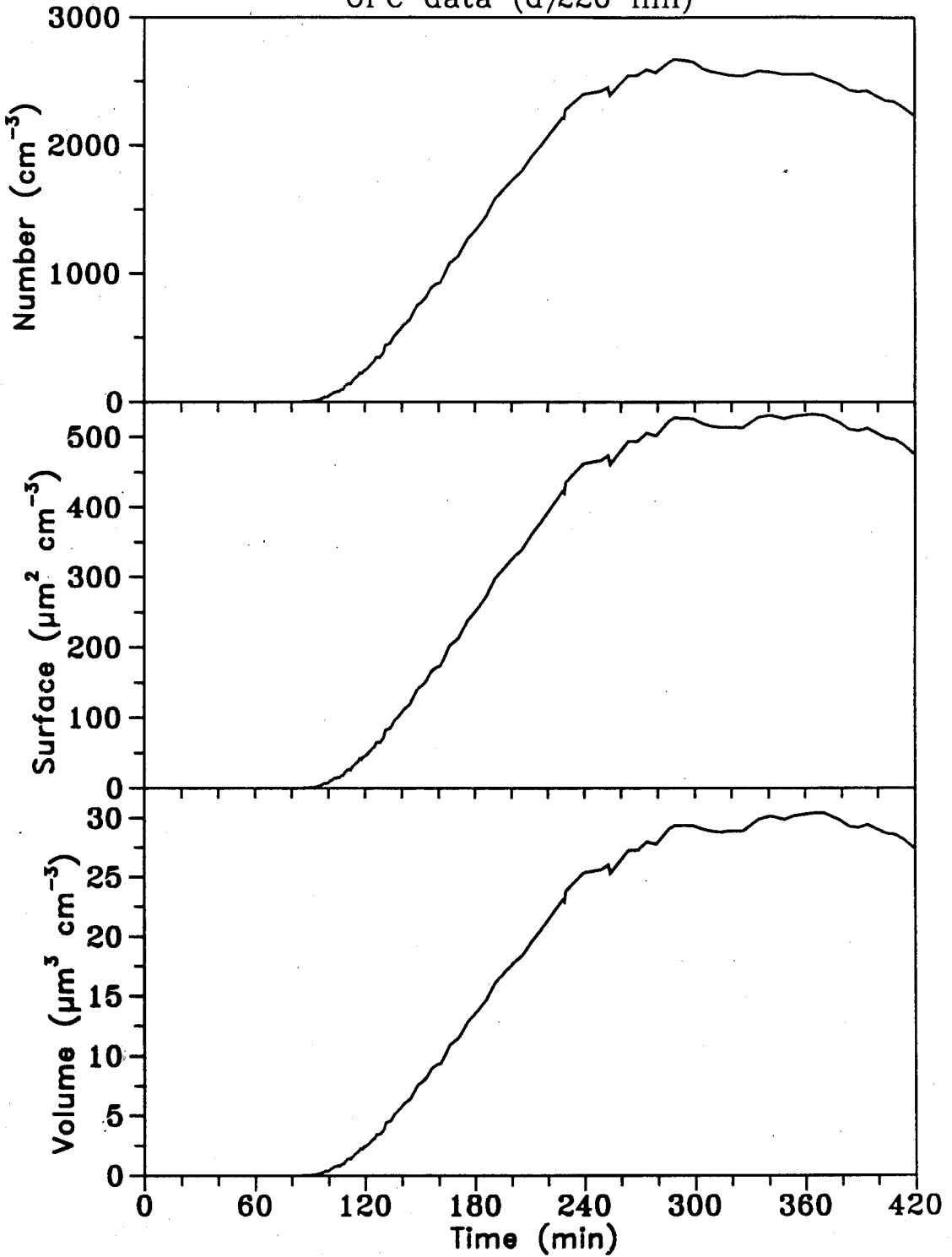
Experiment IS004
1.350 ppm isoprene, 0.320 ppm NO_x
OPC data (d)220 nm)



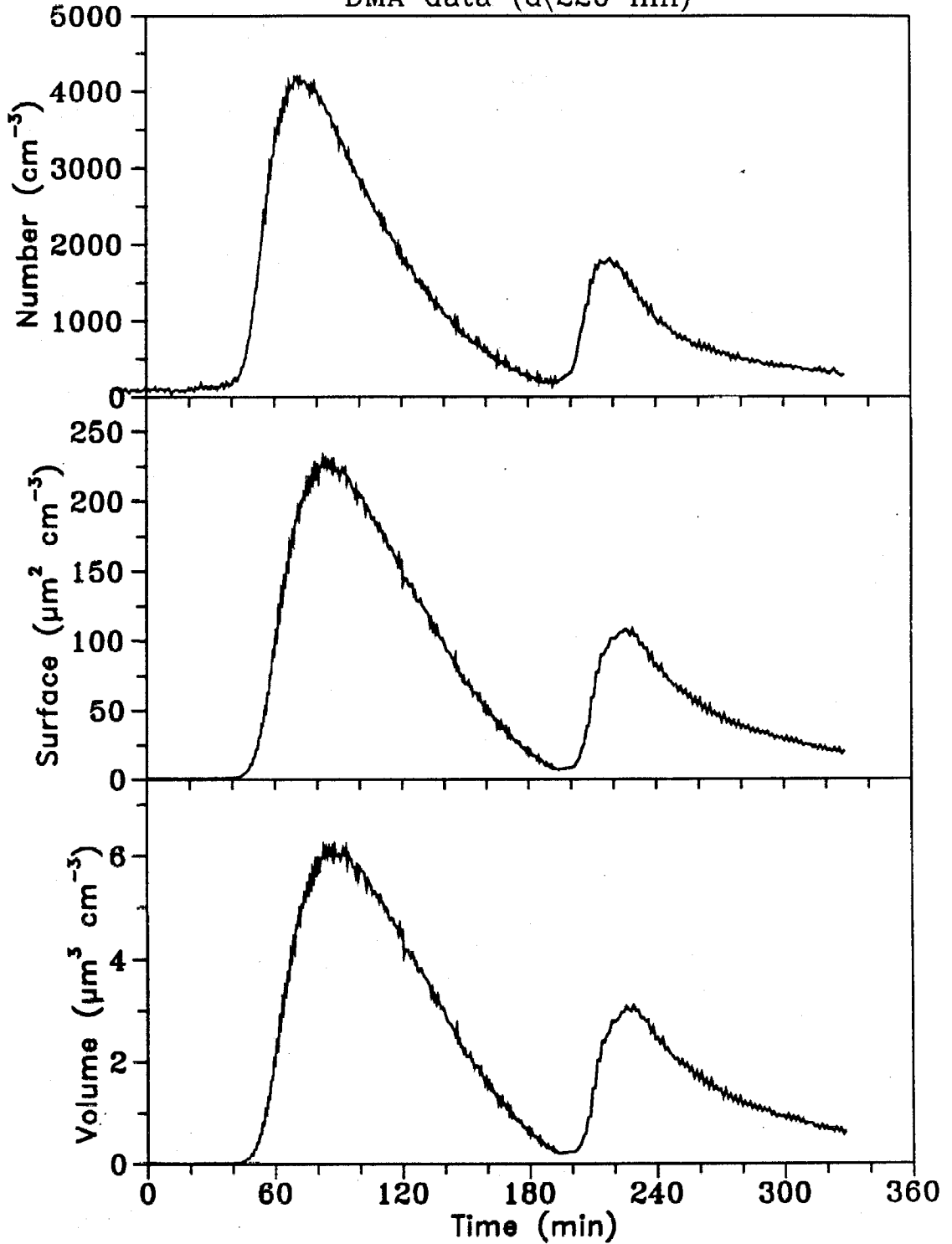
Experiment BPI07
0.340 ppm b-pinene, 0.066 ppm NO_x
DMA data (d < 220 nm)



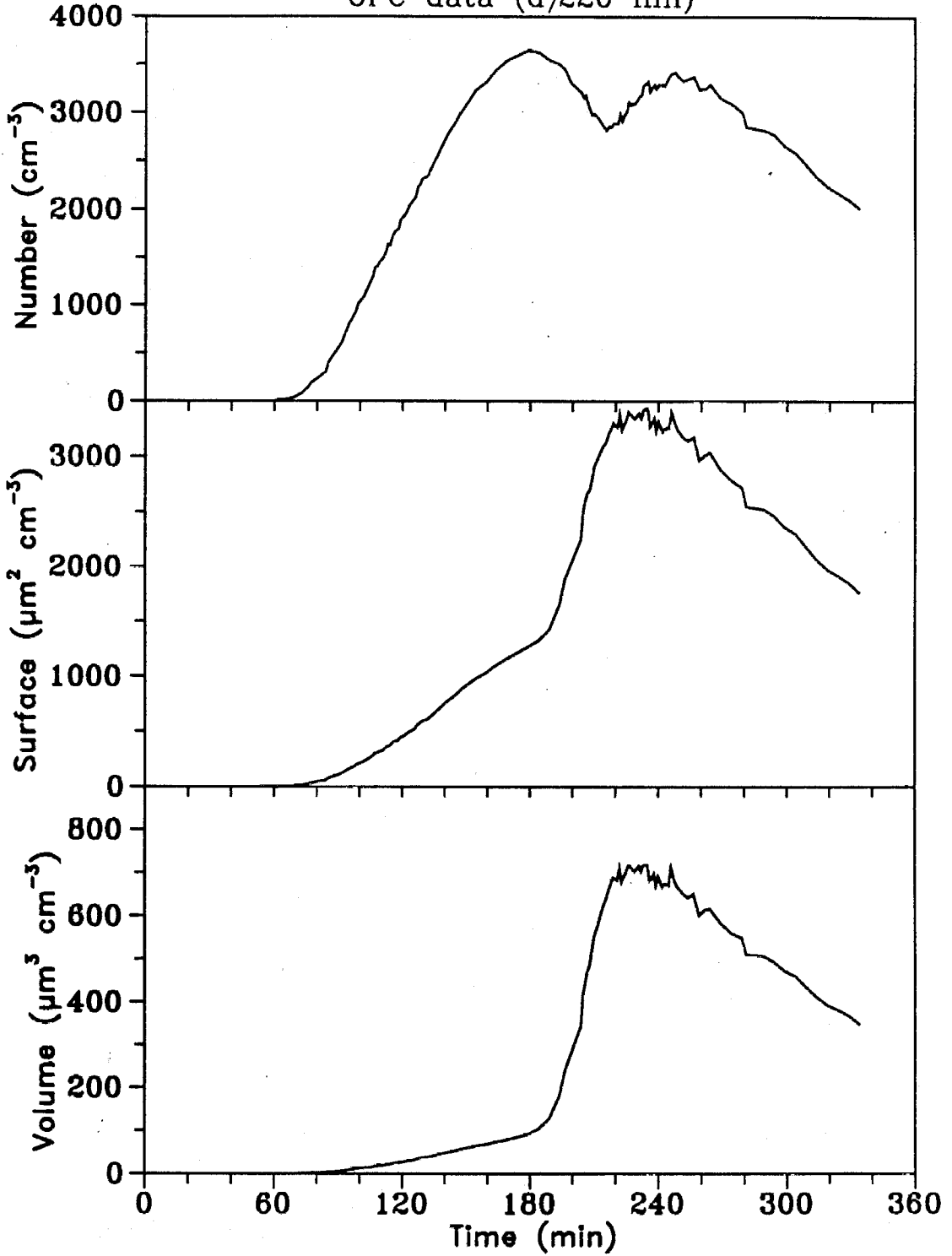
Experiment BPI07
0.340 ppm β -pinene, 0.068 ppm NO_x
OPC data (d)220 nm)



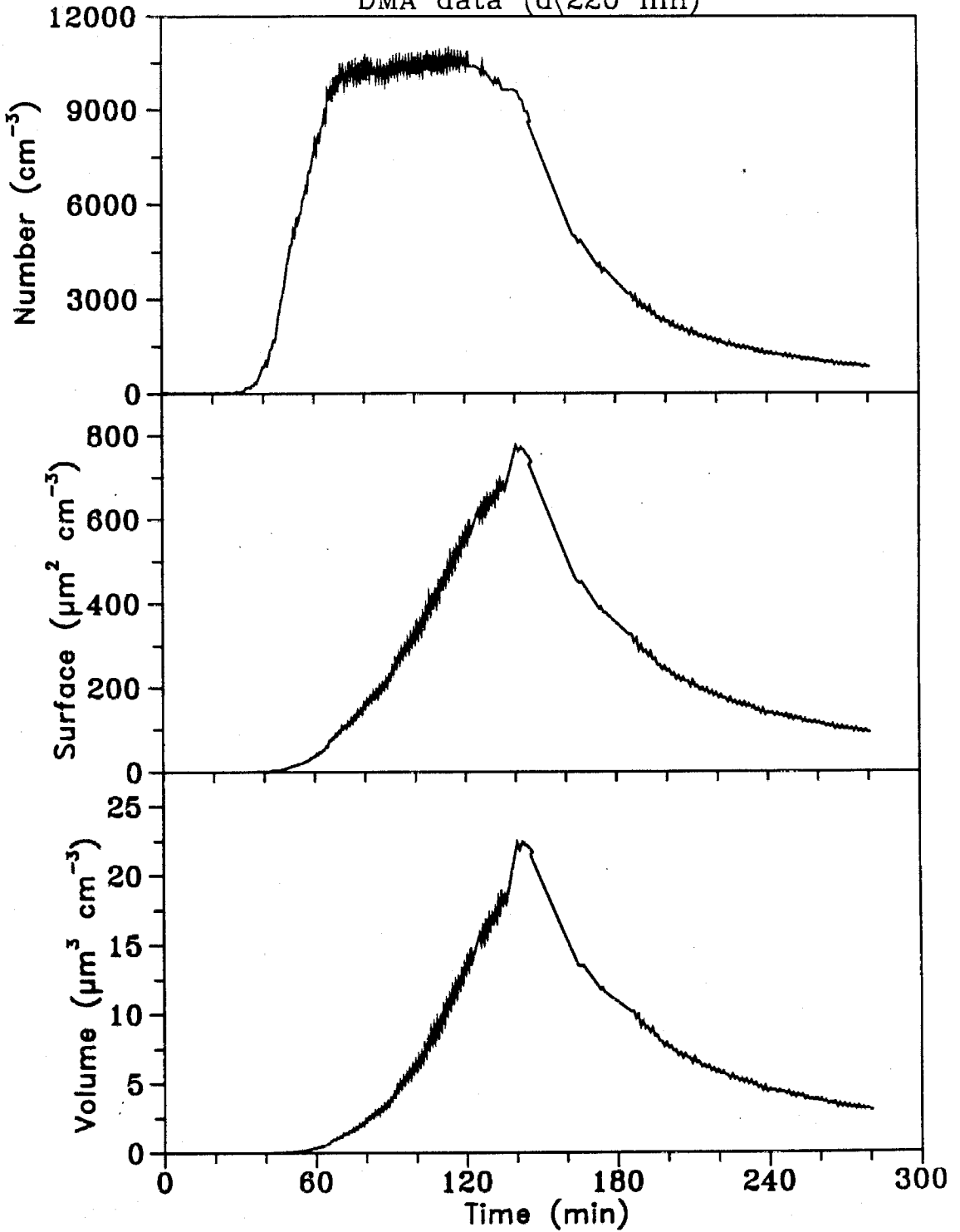
Experiment BPI016
1.990 ppm β -pinene, 0.982 ppm NO_x
DMA data ($d < 220 \text{ nm}$)



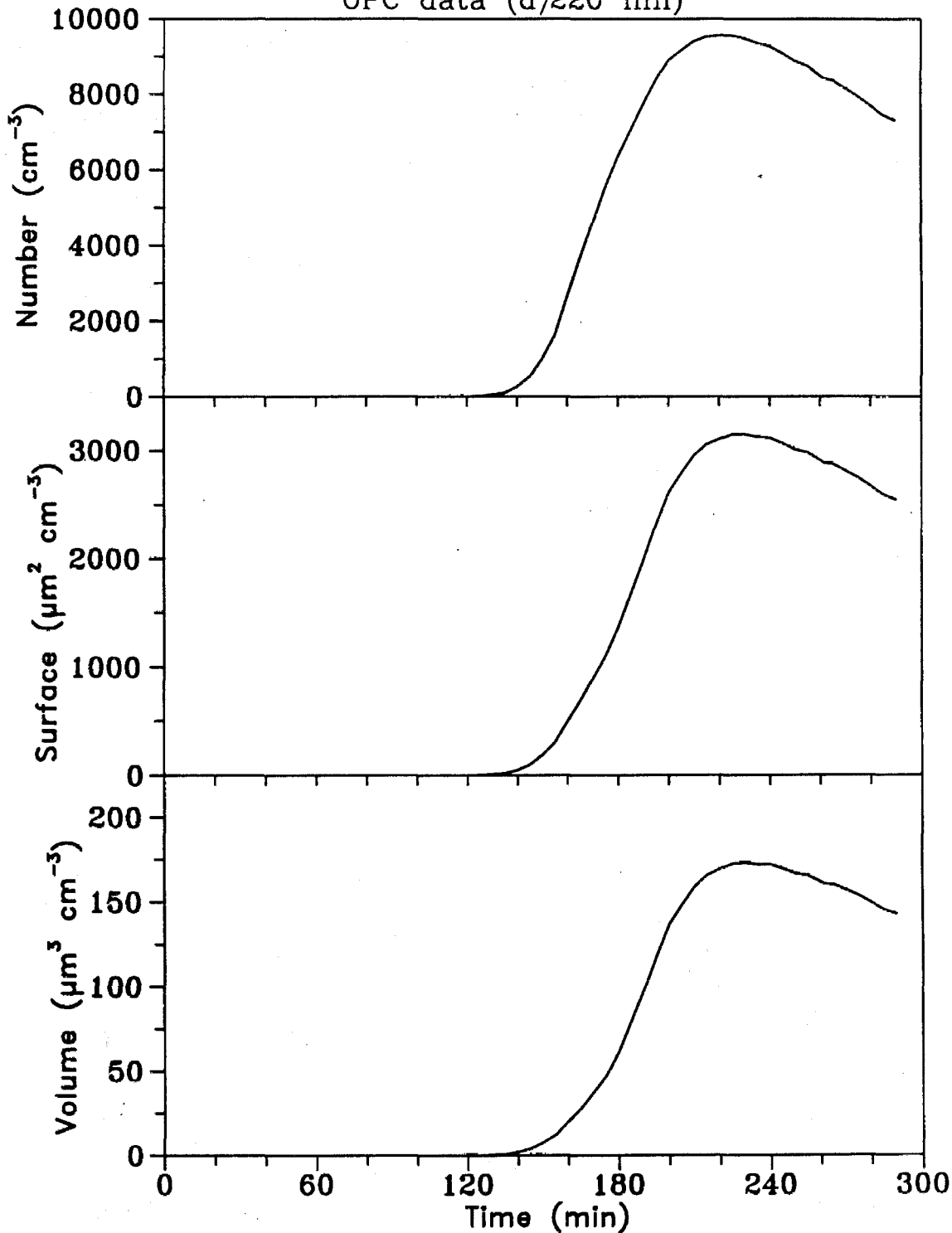
Experiment BPI016
1.990 ppm b-pinene, 0.982 ppm NO_x
OPC data (d)220 nm)



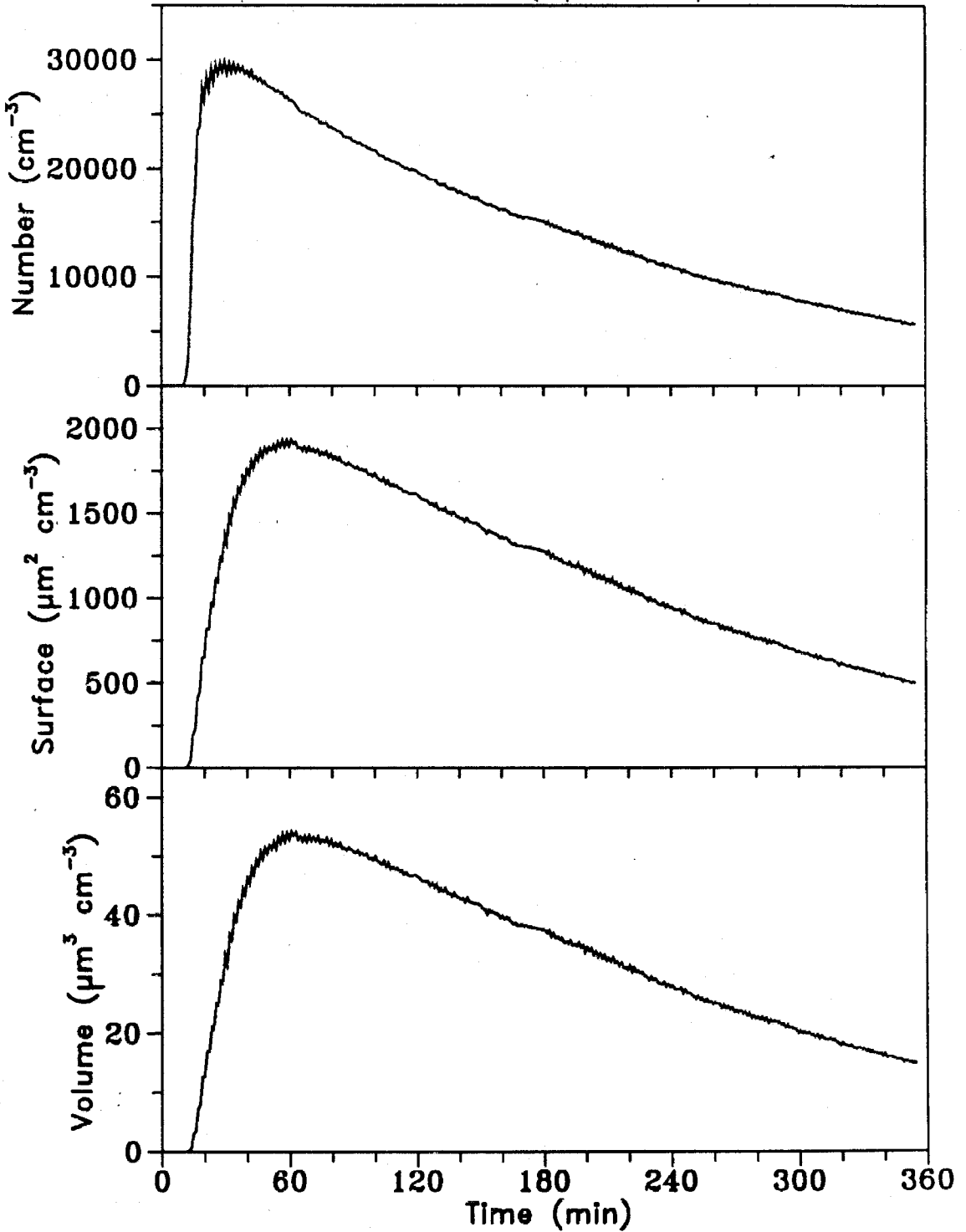
Experiment OCT026
4.60 ppm 1-octene, 0.70 ppm NO_x
DMA data (d(220 nm))



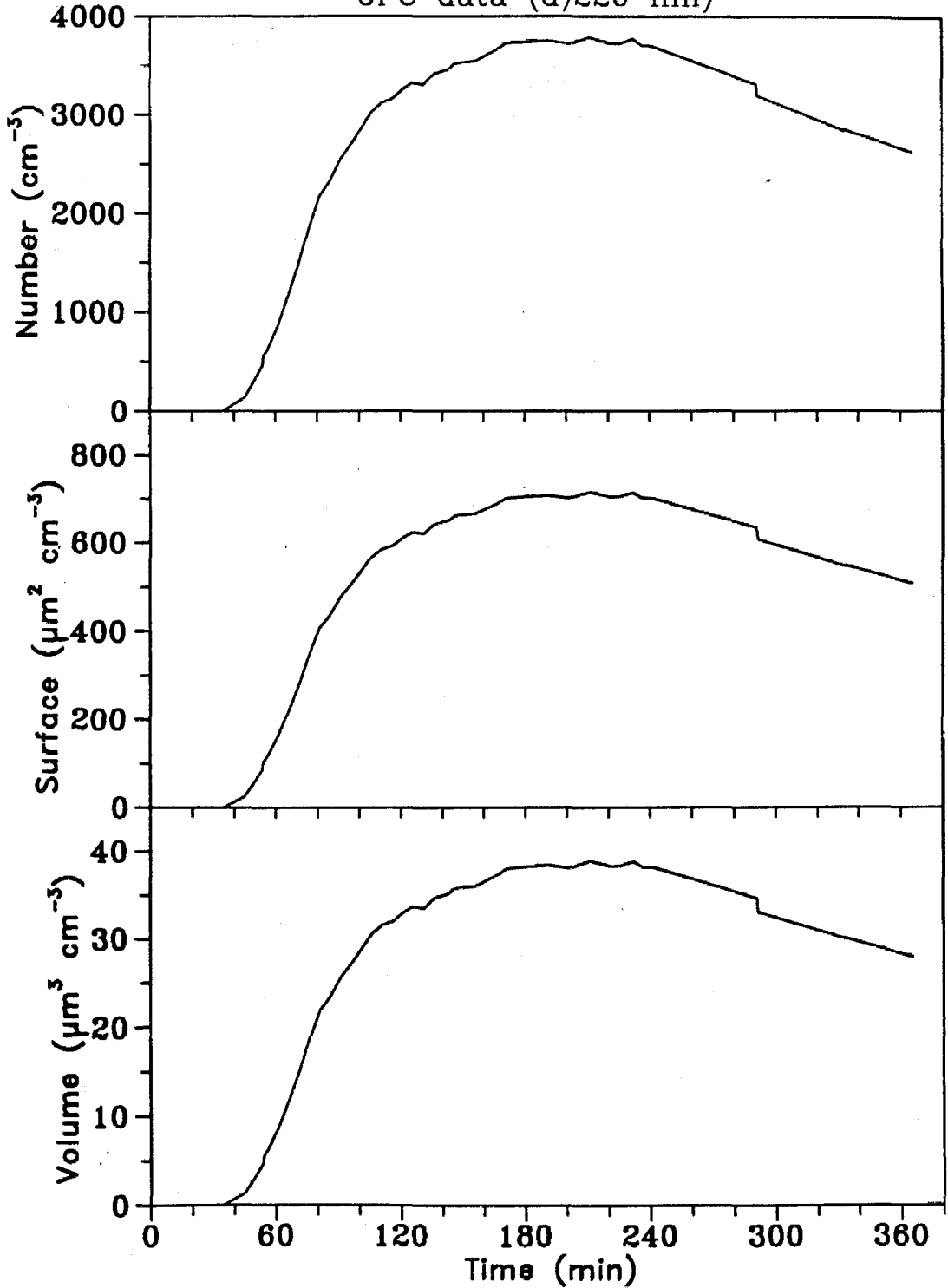
Experiment OCT026
4.60 ppm 1-octene, 0.70 ppm NO_x
OPC data (d)220 nm)



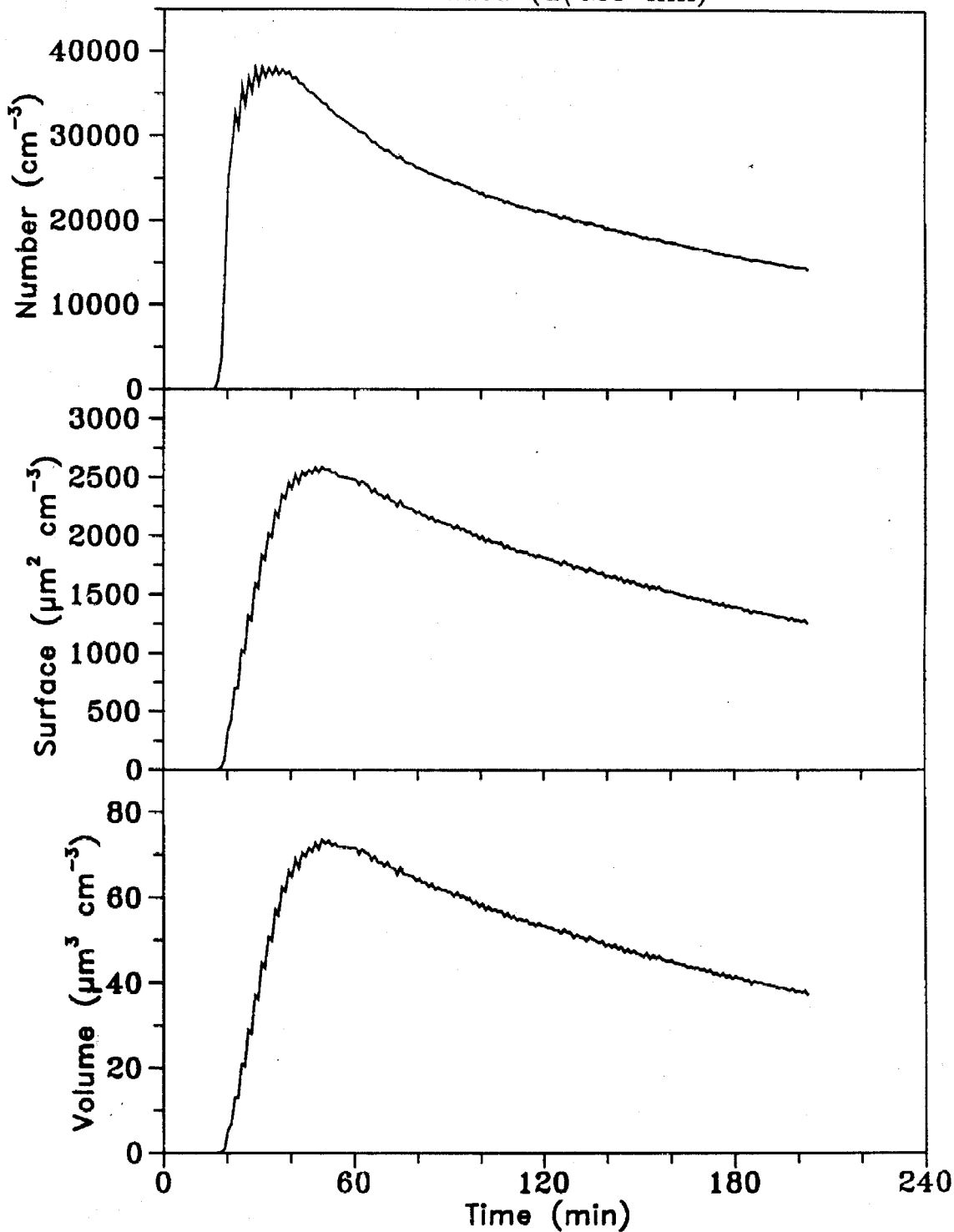
Experiment IS0029
4.450 ppm isoprene, 0.590 ppm NO_x
DMA data (d(220 nm))



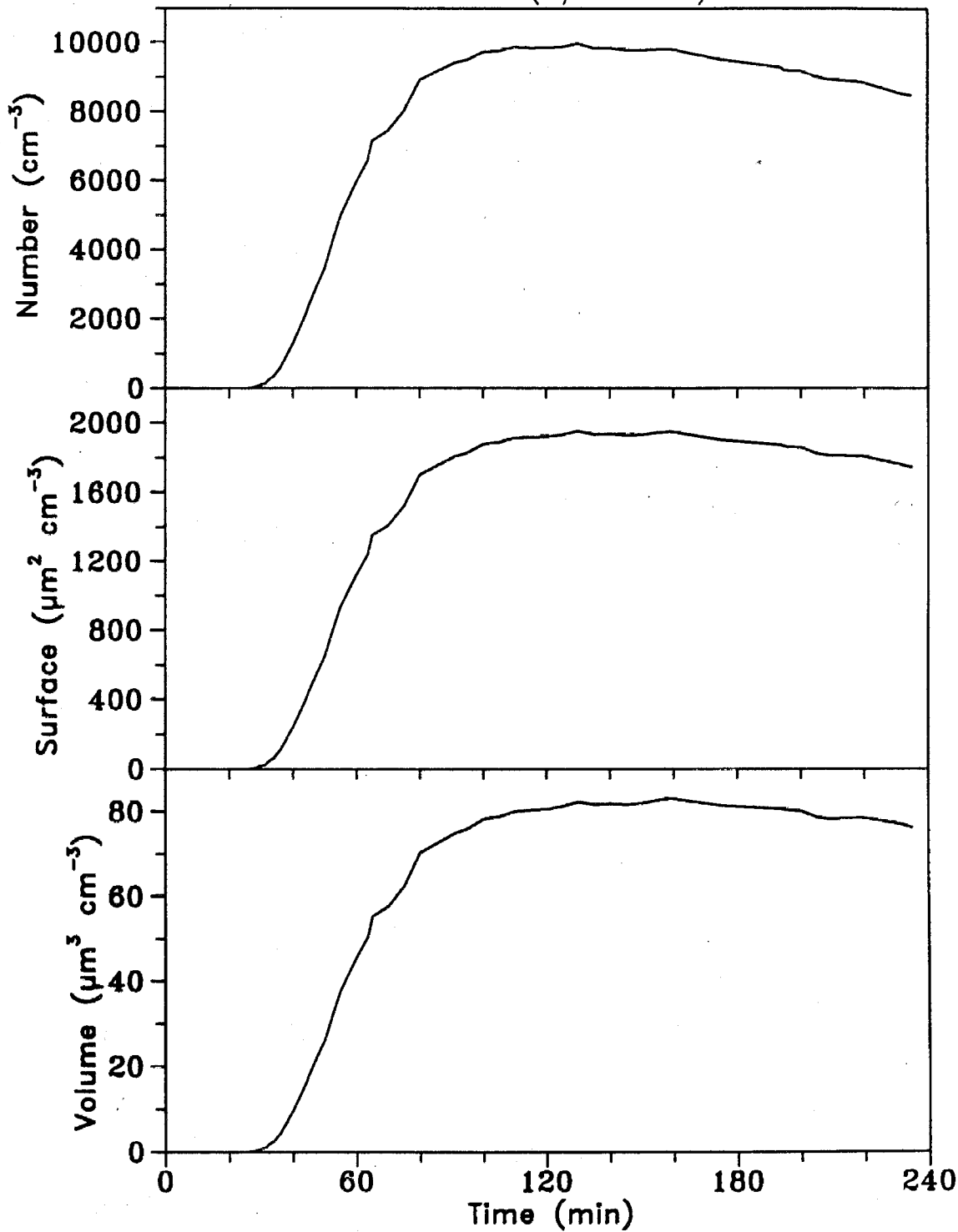
Experiment IS0029
4.450 ppm isoprene, 0.590 ppm NO_x
OPC data (d)220 nm)



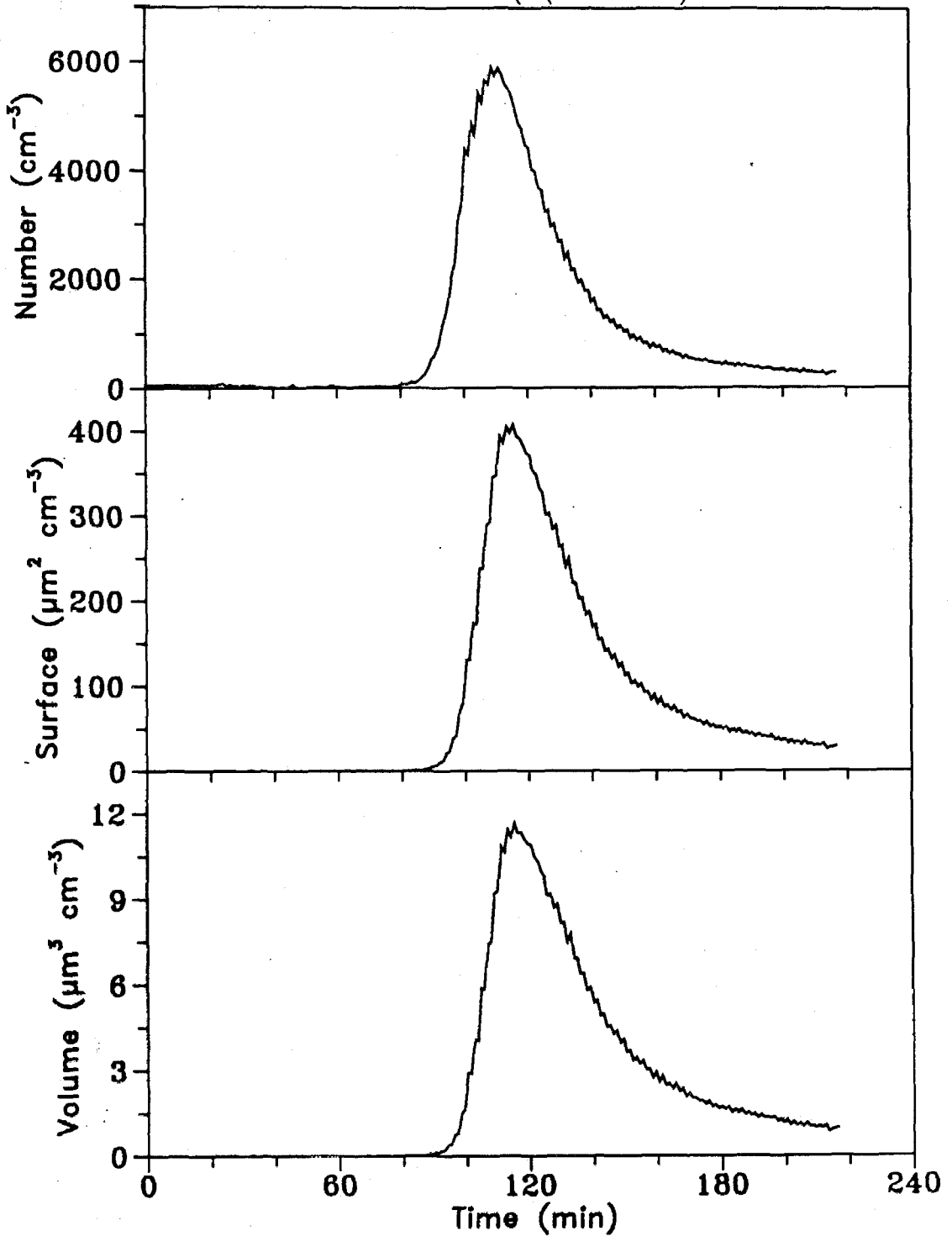
Experiment IS0031
10.00 ppm isoprene, 1.130 ppm NO_x
DMA data (d<220 nm)



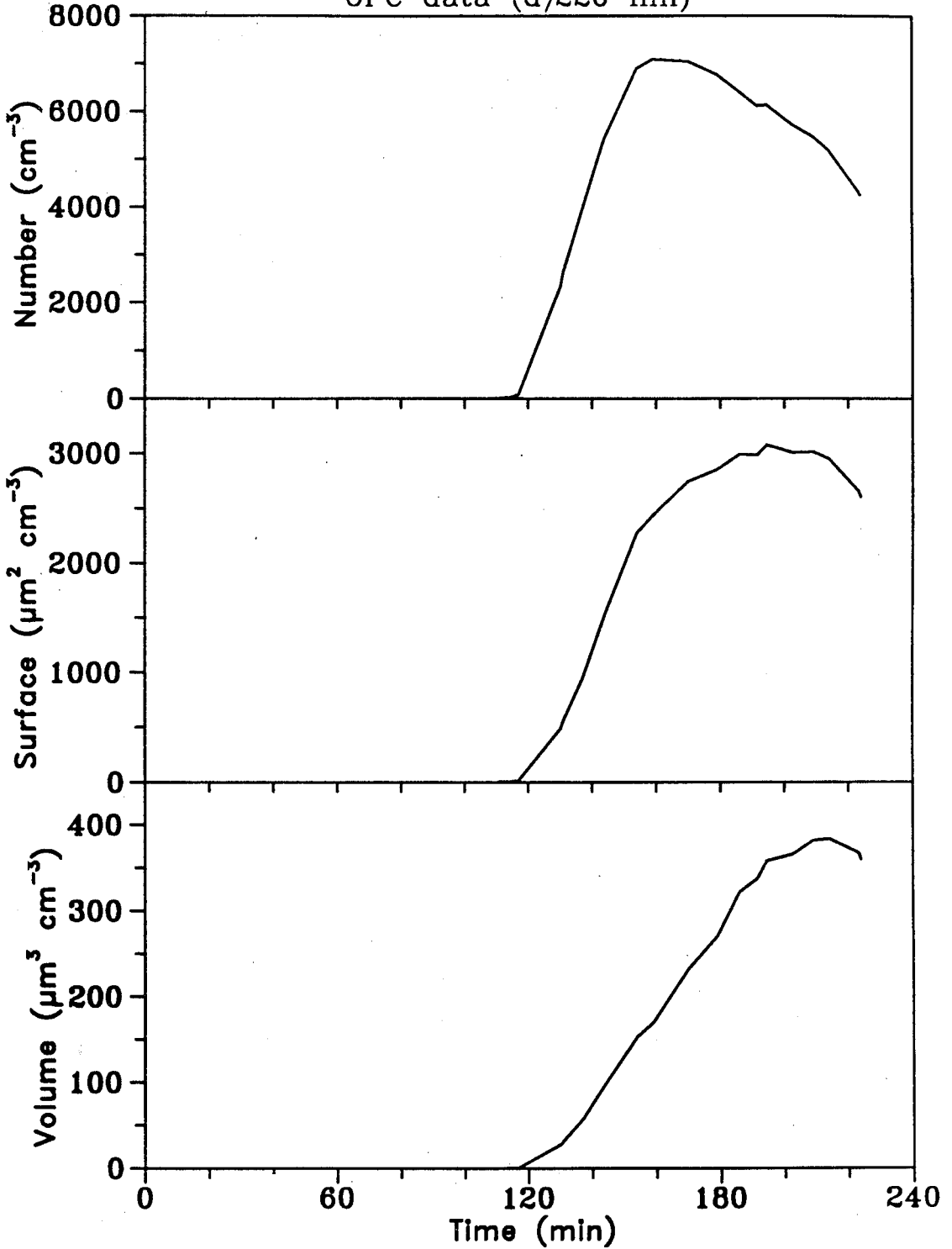
Experiment IS0031
10.00 ppm isoprene, 1.130 ppm NO_x
OPC data (d)220 nm)



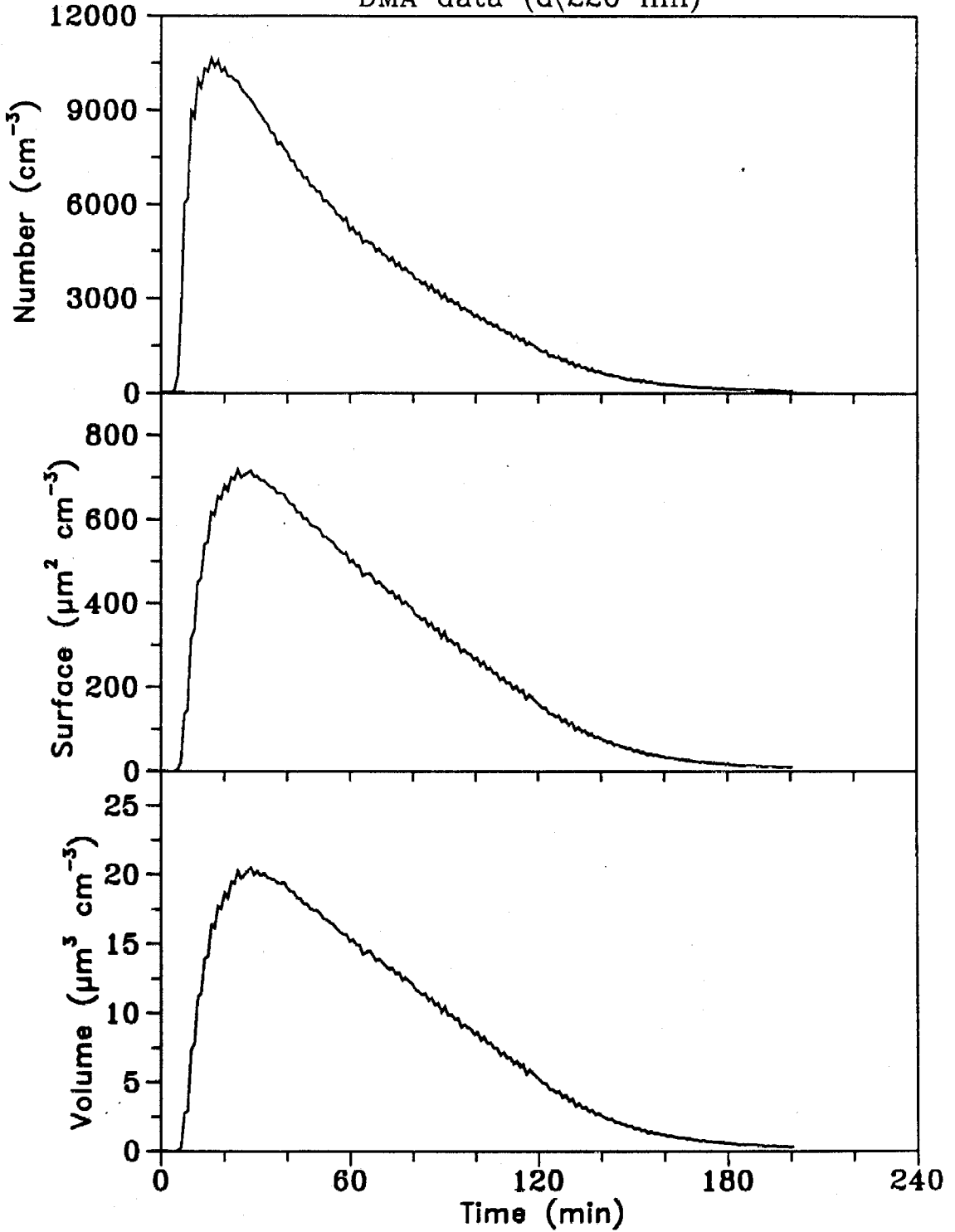
Experiment OCTN2
4.50 ppm 1-octene, 0.900 ppm NO_x
DMA data (d < 220 nm)



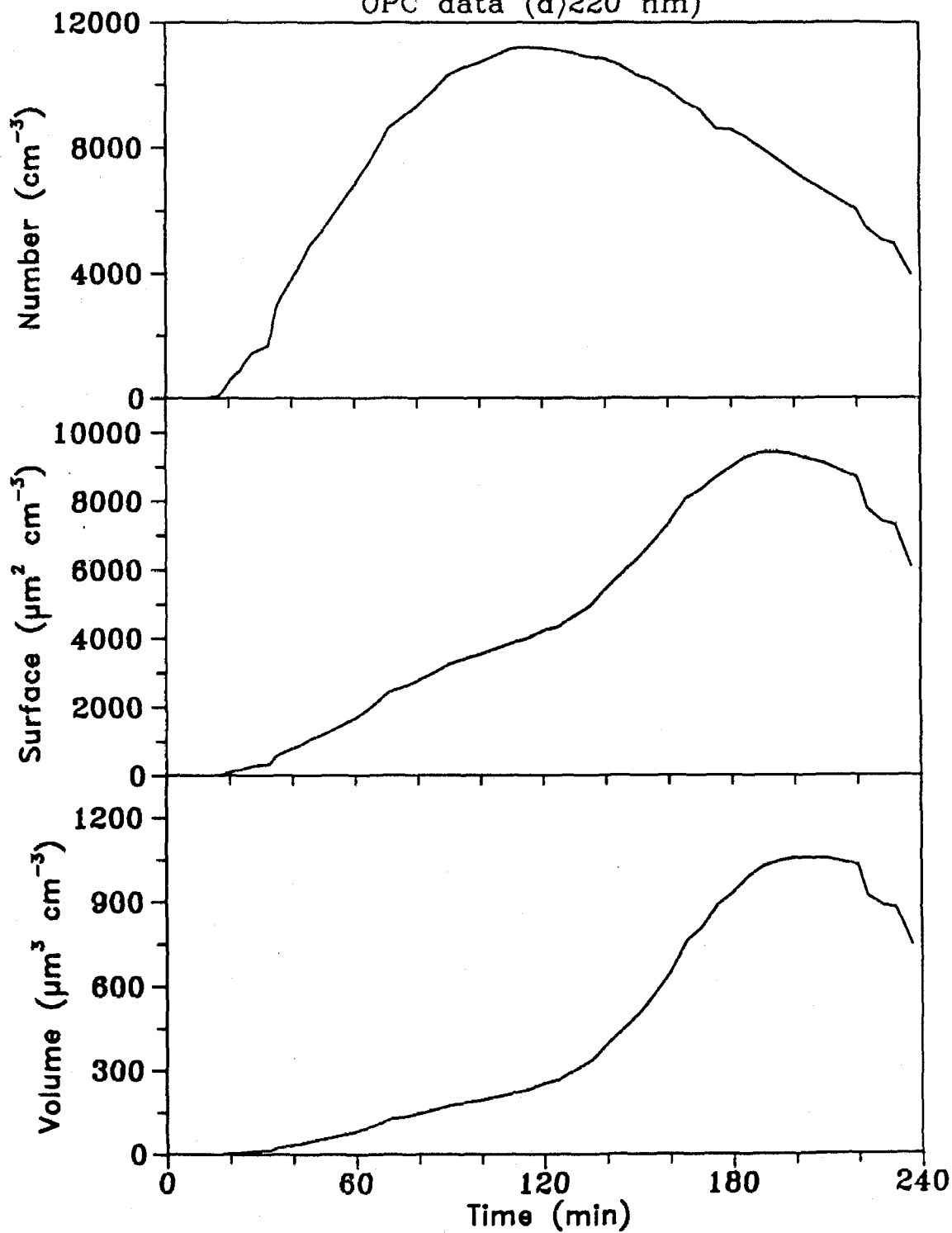
Experiment OCTN2
4.500 ppm 1-octene, 0.900 ppm NO_x
OPC data (d)220 nm



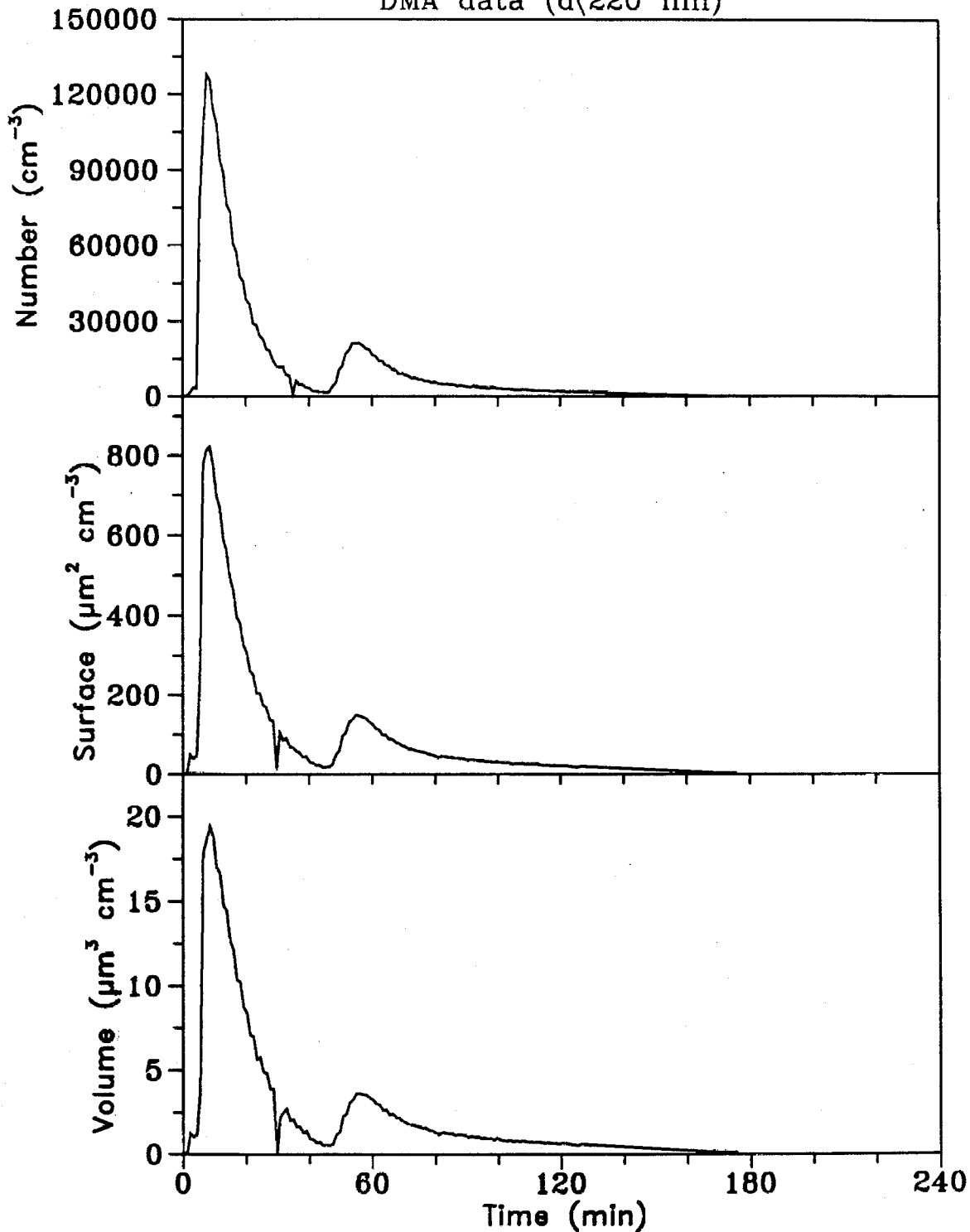
Experiment OCTN4
20.00 ppm 1-octene, 3.00 ppm NO_x
DMA data (d(220 nm))



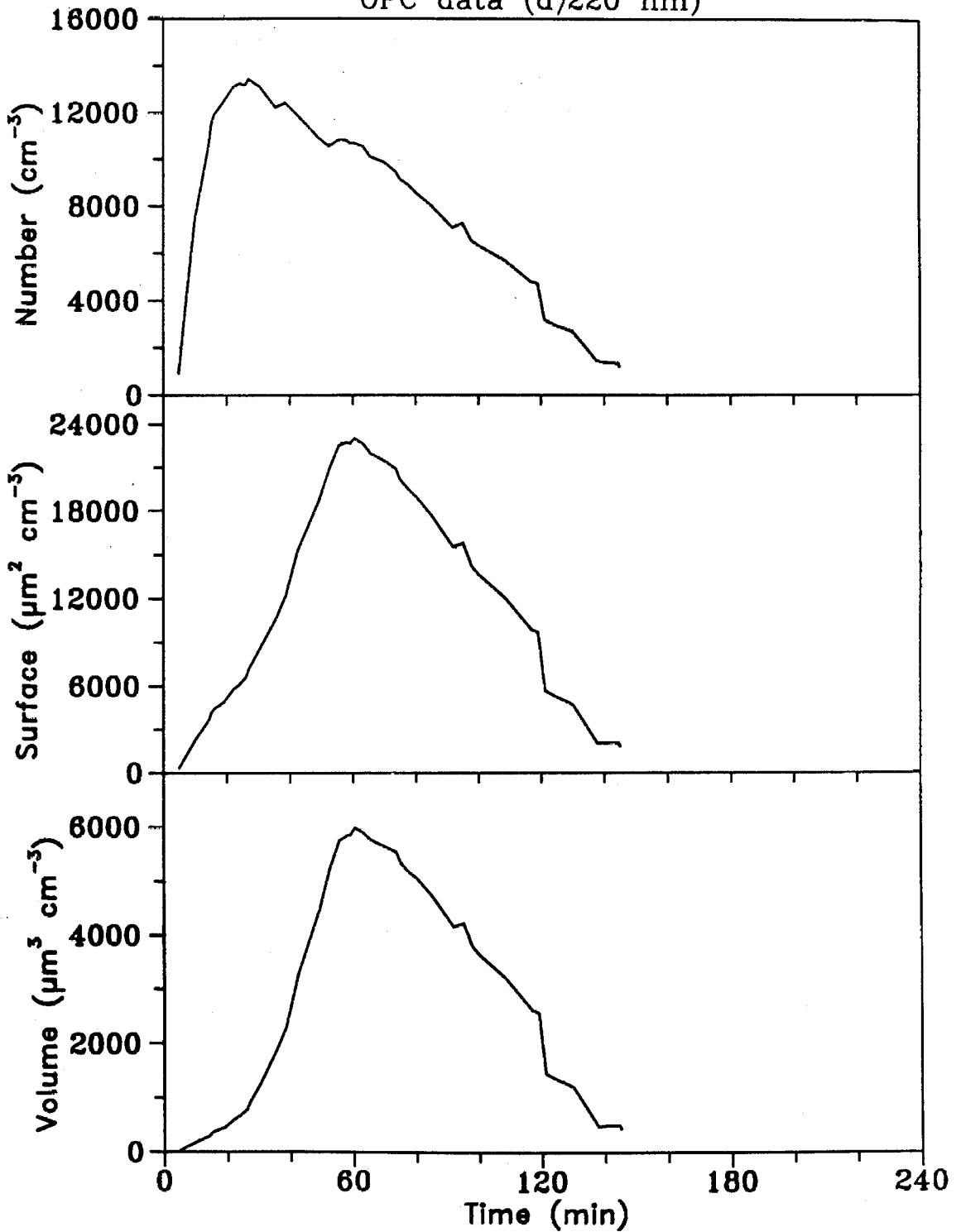
Experiment OCTN4
20.00 ppm 1-octene, 3.00 ppm NO_x
OPC data (d)220 nm)



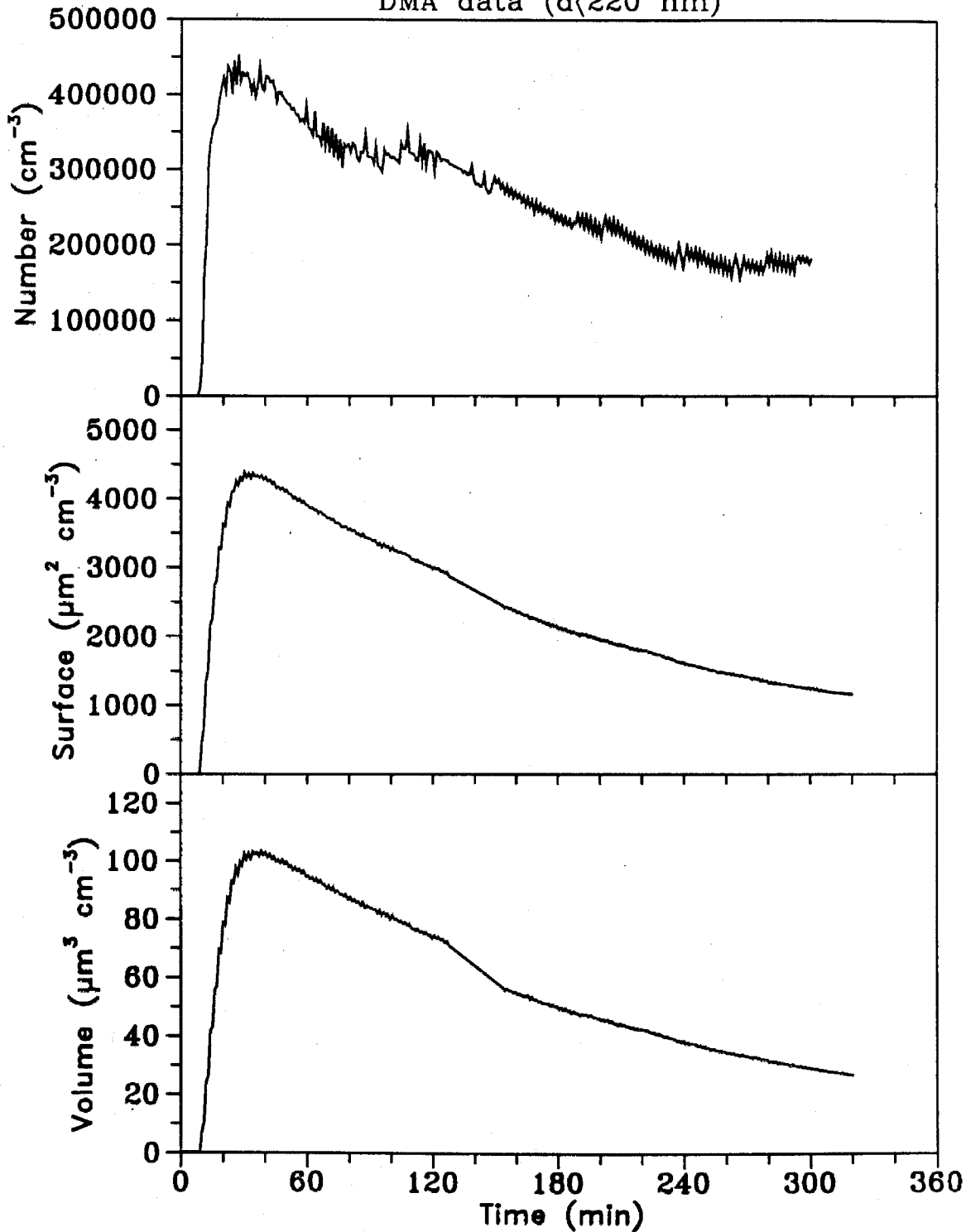
Experiment BPIN10
10.50 ppm β -pinene, 1.306 ppm NO_x
DMA data ($d < 220 \text{ nm}$)



Experiment BPIN10
10.50 ppm b-pinene, 1.308 ppm NO_x
OPC data (d)220 nm



Experiment ISON16
8.350 ppm β -pinene, 1.600 ppm NO_x
DMA data ($d < 220 \text{ nm}$)



Experiment ISON16
8.350 ppm β -pinene, 1.600 ppm NO_x
OPC data ($d > 220 \text{ nm}$)

